esa

→ THE EUROPEAN SPACE AGENCY

PROCEEDINGS OF SEASAR 2023

2-6 May 2023
Longyearbyen; Norway

NERSC
NANSEN ENVIRONMENTAL AND REMOTE SENSING CENTER

UNIS
The University Centre in Svalbard

SIOS
SVALBARD INTEGRATED ARCTIC EARTH OBSERVING SYSTEM

Organizing Committee

Yves-Louis Desnos, ESA, Italy
Catherine Downy, NERSC, Norway
Marcus Engdahl, ESA, Italy
Shridhar Jawak, SIOS, Norway
Johnny A. Johannessen, NERSC, Norway
Sabrina Lodadio, Serco c/o ESA, Italy
Nicolas Longepe, ESA, Italy
Jøran Idar Moen, UNIS, Norway
Fabrizio Pera, Serco c/o ESA, Italy
Lasse H. Pettersson, NERSC, Norway
Diego Fernandez Prieto, ESA, Italy
Eero Rinne, UNIS, Norway
Ulla Vayrynen, Serco c/o ESA, Italy

Scientific Committee

Bertrand Chapron, Ifremer, France
Fabrice Collard, OceanDataLab, France
Maria Michela Corvino, ESA, Italy
Yves-Louis Desnos, ESA, Italy
Wolfgang Dierking, The Arctic University of Norway/Alfred Wegner Institute, Germany
Craig Donlon, ESA, NL
Alejandro Egido, ESA, NL
Ralph Foster, University of Washington, Seattle, USA
Lucile Gaultier, OceanDataLab, France
Christine Gommenginger, NOC, UK
Benjamin Holt, NASA JPL, USA
Romain Husson, CLS, France
Johnny A. Johannessen, NERSC, Norway
Malin Johansson, The Arctic University of Norway, Norway
Harald Johnsen, NORCE, Norway
Cathleen Jones, NASA JPL, USA
Marcel Kleinherenbrink, DELFT, NL
Anton Korosov, NERSC, Norway
Ronald Kwok, University of Washington Seattle, USA
Paco Lopez-Dekker, Delft University of Technology, NL
Artem Moiseev, NERSC, Norway
Alexis Mouche, Ifremer, France
Francisco Ocampo-Torres, CEMIE-Océano, Mexico
William Perrie, Bedford Institute of Oceanography, CA
Marcos Portabella, CSIC/ICM, Spain
Diego Fernandez Prieto, ESA, Italy
Roland Romeiser, RSMAS, University of Miami, USA
Robert Shuchman, Michigan Technological Univ., USA
Ad Stoffelen, KNMI, NL
Justin Stopa, SOEST, USA
Douglas Vandemark, Univ. of New Hampshire, USA

Sponsored by: *European Space Agency*

Publication: *Proceedings of the SeaSAR 2023 Workshop, 2-6 May 2023, Svalbard, Norway*

Editors: *Johnny A. Johannessen, Lasse Pettersson, Catherine Downy.*
Nansen Environmental Remote Sensing Center, Bergen, Norway

DOI: *10.5281/zenodo.20391075*

Contents

Foreword

Twenty years after the workshop on Coastal and Marine applications of SAR the SeaSAR2023 workshop returned to Svalbard from 2-6 May 2023 (https://seasar2023.esa.int). The workshop was sponsored by ESA and organized jointly with the Nansen Environmental and Remote Sensing Center (NERSC), the University Centre of Svalbard and Svalbard Integrated Arctic Earth Observing System (SIOS).

SeaSAR2023 was arranged around keynote presentations and thematic discussions in plenary followed by thematic panel working group discussion and reporting. The themes included:

- Wave Retrievals
- Near Surface Wind Retrievals and Detection of Extremes
- Doppler Shift Retrievals
- Sea Ice Retrievals
- Sensor Synergy
- Methodology and Techniques
- Applications (Oil Spill, Ship Detection, etc)
- Future Missions

Covering these 8 themes the main workshop objectives included:

- Review state-of-the-art in SAR-based geophysical parameter retrievals.
- Identification of knowledge gaps and deficiencies.
- Novel approaches for advancing scientific research and applications.
- Importance and needs for validation.

The workshop brought together around 80 experts and researchers (see list of participants) from around the world to share the latest advancements and challenges in coastal and marine applications of satellite-based Synthetic Aperture Radar (SAR) technology. In addition, 76 individuals attended the on-line WebEx transmissions of the plenary and the eight breakout sessions throughout the week. The YouTube broadcasting of the first day plenary session was viewed 148 times, mostly in real-time.

Thanks to more than 3 decades of continuity of SAR missions the coastal and marine SAR scientific research and applications community have significantly advanced the quantitative understanding of SAR imaging capabilities. This is highlighted in these Proceedings of the SeaSAR 2023 regarding upper ocean currents and mesoscale structures, wave spectra, internal waves, sea ice field, surface slicks, near surface wind fields, marine atmosphere boundary layer processes and extremes as well as advances in methodologies and techniques and applications for oil spills and ship detection. Moreover, the outlook beyond 2030 and towards 2040 clearly evidences the continuity and sustainable access to data from future approved satellite SAR missions. However, as pointed out during the workshop there are deficiencies and challenges regarding design and implementation of a more comprehensive satellite SAR-based calibration-validation approach, jointly with systematic use of sensor synergy across the broad range of complementary satellite radar altimeters, scatterometry, interferometry, and high-resolution optical radiometer and spectrometer. This will require dedicated international collaboration with involvement of the space agencies, in particular to enable multi-frequency and multi-look direction SAR-based observations with shorter imaging interval. Combined with continuous free and open available SAR data this will strengthen the generation of training datasets for machine learning development.

List of Extended Abstracts

Wave Retrievals

Pleskachevsky, Andrey; Tings, Björn; Jacobsen, Sven
Multiparametric Sea State Fields from Synthetic Aperture Radar using Method combining CWAVE Approach and Machine Learning

Kleinherenbrink, Marcel; Ehlers, Frithjof; Gibert, Ferran; Hernandez, Sergi; Nouguier, Frederic; Chapron, Bertrand; Lopez-Dekker, Paco
SAR altimetry cross-spectra

Rikka, Sander; Nõmm, Sven; Alari, Victor; Björkqvist, Jan-Victor; Simon, Martin
Wave Spectra, Spread, and Direction in the Baltic Sea from Sentinel-1 SAR Imagery Using the LSTM Model

Khan, Salman Saeed
Temporal Consistency of Sentinel-1 SAR Wave Mode Level-2 Ocean Swell Spectra

Ocampo-Torres, Francisco J; Osuna, Pedro; Rascle, Nicolas G.; García-Nava, Héctor; Díaz Méndez, Guillermo M.; Esquivel-Trava, Bernardo; Villarreal-Olavarrieta, Carlos E.; Mora-Escalante, Rodney; Hasimoto-Beltrán, Rogelio
Assessment Of A Quasi-linear Inversion Scheme To Retrieve Ocean Surface Wave Spectrum from Synthetic Aperture Radar Image Spectrum: Results from Measurements in the Gulf of Mexico.

Benchaabane, Amine; Husson, Romain; Mouche, Alexis; Frederic, Nouguier; Johnsen, Harald
Wind-sea significant wave heights retrieval from Sentinel-1 with Deep Learning

Nouguier, Frederic; Mouche, Alexis; Chapron, Bertrand; Kleinherenbrink, Marcel
Ocean Wave Mapping By SAR: Numerical And Theoretical Perspectives

Aouf, Lotfi; Hauser, Danièle; Collard, Fabrice; Chapron, Bertrand
On The Complementary Assimilation Of SAR And SWIM Wave Spectra In The CMEMS Global Wave System

Amir, Malik Muhammad Haris; Bogoni, Antonella; Dekker, Paco Lopez
Unlocking the Potential of Distributed SwarmSAR for High-resolution Imaging of Ocean Waves

Pouplin, Clément; Mouche, Alexis; Chapron, Bertrand; Yurovskaya, Maria; Filipot, Jean-François
Tropical Cyclones Generated Waves: Processes And Contribution Of A Multi-Platform Approach

Collard, Fabrice; Guitton, Gilles; López Radcenco, Manuel; Nouguier, Frederic; Chapron, Bertrand
Swell Propagation and Forecast Across the North Atlantic Using Combined Sentinel1 Wave Mode, IW Mode and CFOSAT SWIM Observations.

Near Surface Ocean Wind Retrievals & Detection of Extremes

Stoffelen, Ad; Ni, Weicheng; Xu, Xingou; Portabella, Marcos; Makarova, Evgeniia; Cossu, Federico; Sánchez Rabaneda, Alberto
Extreme Winds From SAR And Their Use For Ku- And C-Band Wind Scatterometer Resolution Enhancement

Zecchetto, Stefano; Zanchetta, Andrea; Sclavo, Mauro; Shamsaddini, Parsa; Keshavarz, Ahmad
High-Resolution SAR Winds from Deep Learning in Coastal Areas

Khan, Salman; Young, Ian; Ribal, Agustinus; Canto, Marites; Davy, Robert; Hemer, Mark
Australian Coastal SAR Ocean Winds: Data, Portal, and Next products

Dimitriadou, Krystallia; Badger, Merete; Hasager, Charlotte Bay; Olsen, Bjarke Tobias
SAR for Offshore Wind Fields in the Mediterranean Sea

Hindberg, Heidi; Espeseth, Martine; Johnsen, Harald; Tollinger, Mathias
Operational Wind Retrieval Using Cross-Polarization And Doppler Data

Marquart, Robin; Mouche, Alexis; Chapron, Bertrand
Analysis Of SAR Ocean Scenes Texture For Wind Direction Retrieval And Generation Of Synthetic Images

Doppler Shift Retrievals

Kleinherenbrink, Marcel; Yuan, Yan; Theodosiou, Andreas; Gaultier, Lucile; Collard, Fabrice; Chapron, Bertrand; Lopez-Dekker, Paco
Multiscale Effects on Harmony's High-resolution Ocean Observations

Elyouncha, Anis; Eriksson, Leif; Gommenginger, Christine
Observations of the Agulhas Current by Along-track Interferometric Synthetic Aperture Radar

Romeiser, Roland
Review of TerraSAR-X Based Current Retrieval Activities at the University of Miami

Martin, Adrien; Macedo, Karlus; McCann, David; Portabella, Marcos; Marié, Louis; Marquez, José; Carrasco, Ruben; Duarte, Rui; Meta, Adriano; Gommenginger, Christine; Martin-Iglesias, Petronilo; Casal, Tania
OSCAR: A New Airborne Instrument To Image Ocean-Atmosphere Dynamics At The Sub-Mesoscale

Moiseev, Artem; Collard, Fabrice; Johannessen, Johnny A
Ocean Surface Currents from Sentinel-1 Doppler observations
Guitton, Gilles; Collard, Fabrice; Johnsen, Harald; Engen, Geir; Recchia, Andrea; Cotrufo, Alessandro; Bras, Sergio; Miranda, Nuno; Pinheiro, Muriel
Towards Calibrated Sentinel-1 OCN RVL Products

Domps, Baptiste; Guérin, Charles-Antoine
Evaluation of Surface Currents Derived from Sentinel-1 SAR Doppler Shift in the Northwestern Mediterranean Sea Using Coastal HF Radars

Sea Ice Retrievals

Wiehle, Stefan; Murashkin, Dmitrii; Frost, Anja; König, Christine; König, Thomas
Preliminary results of Sea Ice Classification using combined Sentinel-1 and Sentinel-3 data

Karvonen, Juha
Copernicus Marine Service SITAC SAR-Based Baltic Sea Ice Products

Lohse, Johannes; Dierking, Wolfgang
Combining C- And L-band SAR Data For Automated Sea Ice Classification & Segmentation

Frost, Anja; Imber, James; Murashkin, Dmitrii; Kortum, Karl; Gregorek, Daniel
Towards Multitemporal Sea Ice Classification By Means Of Spaceborne SAR Image Time Series

Wang, Qiang; Johansson, Malin; Lohse, Johannes; Doulgeris, Anthony P.; Eltoft, Torbjørn
The Impact of Input Features in Deep Learning Based Sea Ice Mapping

Eltoft, Torbjørn; Taelman, Catherine; Johansson, Malin; Lohse, Johannes; Gerland, Sebasitan; Dierking, Wolfgang
The CIRFA-2022 Cruise to the Western Fram-Strait: Objectives, Ground Measurements, and Preliminary Results

Li, Haiyan; Yang, Kun; Perrie, William
Fine Sea Ice Classification with Gaofen-3 Quad- Polarization SAR Observation

Demchev, Denis; Eriksson, Leif E.B.; Hildeman, Anders; Dierking, Wolfgang
Investigation of Multifrequency SAR Image Alignment by Ice Drift Compensation In The Marginal Ice Zone

Johansson, Malin; Singha, Suman; Spreen, Gunnar; Howell, Stephen
High resolution L- and C-band polarimetric variability during MOSAiC

Taelman, Catherine; Lohse, Johannes; Doulgeris, Anthony P.
Tracking Backscatter Signatures Of Individual Sea Ice Floes Using In-Situ Ice Drift Observations

Wulf, Tore; Buus-Hinkler, Jørgen; Singha, Suman; Kreiner, Matilde Brandt
Operational SAR-based Sea Ice Concentration Retrieval Using Convolutional Neural Networks
Korosov, Anton; Kleinherenbrink, Marcel
Potential Application of the Earth Explorer 10 candidate Harmony for Sea Ice Model Validation

Aparício, Sara

A Multisensory SAR-Based Approach For Melt Ponds Retrievals

Kim, Ekaterina; Skjetne, Roger; Høyland, Knut Vilhelm
Quadruple Helix Framework for Sea Ice Monitoring: Next Steps

Sensor Synergy

Taillade, Thibault; Engdahl, Marcus; Fernandez, Diego
Can We Retrieve Sea Surface Salinity with SAR Measurements?

Zhang, Biao; Perrie, William; Zhang, Mingyu
Polar Low Recognition and Tracking from Multi-Temporal Synthetic Aperture Radar and Radiometer Observations

Rascle, Nicolas Gilles; Grouazel, Antoine; Mouche, Alexis; Nouguier, Frederic; Villarreal Olavarrieta, Carlos Eduardo; Mora Escalante, Rodney Eduardo; Diaz Mendez, Guillermo; Chapron, Bertrand; Ocampo-Torres, Francisco J.
Satellite Measurement Of Waves And Currents: SAR Vs Optical Sensors

Holt, Benjamin; Lockhart, Brittany; Porter, Mitchell; Comer, Douglas
Fronts, Eddies, and Other Features in the Western Pacific and Micronesia from SAR and Other Multi-Sensor Data

Husson, Romain; Ollivier, Annabelle; Chehade, Bassam; Peureux, Charles; Quet, Victor; Goimard, Gaël; Soulat, François; Tourain, Cédric; Lachiver, Jean-Michel
Comparing and Combining S1 and SWIM Spectral Wave Measurements

Methodology and Techniques

Tings, Björn; Pleskachevsky, Andrey; Wiehle, Stefan; Jacobsen, Sven
Ship Wake Detectability in TerraSAR X, CosmoSkymed, Sentinel 1 and RADARSAT 2 Imagery – Summary and Applications for Wake Detection

Arthurs, David
Open and Reproducible Science: The Role of Computing Platforms for Research and Applications that use SAR

Gade, Martin; Peters, Sebastian; Schäfers, Simon
On the Use of SAR Data to Monitor Coastal Erosion and Morphodynamics in Intertidal Areas

Hajduch, Guillaume; Pinheiro, Muriel; Valentino, Antonio; Vincent, Pauline; Recchia, Andrea; Cotrufo, Alessandro; Franceschi, Niccolo; Piantanida, Ricardo; Benchaabane, Amine; Peureux, Charles; Husson, Romain; Schmidt, Kersten; Mouche, Alexis; Grouazel, Antoine; Nouguier, Frédéric; Johnsen, Harald; Hindberg, Heidi; Guiton, Gilles; Collard, Fabrice
Sentinel-1 product performance

Shamshiri, Roghayeh; Eide, Egil; Rangriz Rostami, Fazel; Vilhelm Høyland, Knut

Sentinel-1 Extra Wide Thermal Noise Removal Using a Deep Learning Model

Yitayew, Temesgen Gebrie; Grydeland, Tom; Larsen, Yngvar; Engen, Geir
Processing of High Squint Bistatic SAR Data: The Case of Harmony

Hoffman, Lauren Alexandra; Mazloff, Matt R; Gille, Sarah T; Giglio, Donata; Bitz, Cecilia M; Heimbach, Patrick
Machine Learning for Evaluating the Drivers of Variability in Arctic Sea-ice Motion.

Grydeland, Tom; Yitayew, Temesgen Gabrie; Larsen, Yngvar;DuBois, Pierre; Armstrong, Thomas; Gombert, Baptiste; Soulat, Francois; Monnier, Goulven; Hellouvry, Yann-Herve; Camus, Benjamin; Lopez-Dekker, Paco; Lajas, Dulce; Rommen, Bjorn; deWitte, Erik
Signal Processing for Harmony: Illustrations with Simulated Data over Ocean

Colin, Aurélien; Tandeo, Pierre; Husson, Romain; Fablet, Ronan; Peureux, Charles
MediSAR: An Exhaustive Augmented Dataset Of Segmented Sentinel-1 SAR Ocean Observations Of The Mediterranean Sea and the Black Sea regions

Stopa, Justin E.; Foster, Ralph; Vandemark, Doug; Wang, Chen; Chapman, Jonathan; Glaser, Yannik; Sadowski, Peter; Mouche, Alexis; Chapron, Bertrand
Using Ocean Surface Imagery to Estimate Atmospheric Boundary Layer Stratification

Foster, Ralph; Mouche, Alexis; Chapron, Betrand
Using SAR Imagery to Diagnose Tropical Cyclone Boundary Layer Mean State

Larsen, Yngvar; Engen, Geir; Grydeland, Tom; Yitayew, Temesgen G.
An Alternative Approach for Estimation of Doppler Centroid Anomaly Based on Level-0 SAR Data

Alpers, Werner R.; Bignami, Franceco
Sar Observation Of Internal Waves Generated By Sub-mesoscale Features In The Strait of Sicily

Applications: Maritime Security

Frost, Anja; Kortum, Karl; Wiehle, Stefan; Tings, Björn**.**
Ship Navigation Assistance For Polar Waters By Providing Information On Sea Ice Drift And Deformation Zones Using TerraSAR-X Data

Yang, Yi-Jie; Singha, Suman); Goldman, Ron
Integration of a Deep Learning Based Oil Spill Detection System into an Early Warning System for the Southeastern Mediterranean Sea

Blondeau-Patissier, David; Schroeder, Thomas; Suresh, Gopika; Li, Zhibin; Diakogiannis, Foivos; Steven, Andrew
Detection Of Marine Oil-like Features In Sentinel-1 SAR Images By Supplementary Use of Deep Learning and Empirical Methods

McGourty, Sara; Kaczor, Scott; Capsey, Austin

A Feasibility Study Into The Use of High-resolution Synthetic Aperture Radar (SAR) As A Novel Way Of Identifying Aids To Navigation

Gade, Martin; King, Dana
On the SAR Image Visibility of Heavy Fuel Leaking From the Wreck of a Sunken Vessel

Jones, Cathleen E, Johansson, Malin, Holt, Benjamin
Automation of Slick Detection and Classification for Improved Monitoring with SAR

Del Prete, Roberto; Graziano, Maria Daniela; Renga, Alfredo
AI-based Route Reconstruction on Multifrequency Multitemporal SAR Images

Ali, Muhammad; Schirinzi, Gilda; Afzal, Zeeshan; Hussain, Sajid
Impact of Sea Water Intrusion on Surface Deformation along the coastal areas of Pakistan using SAR Interferometry

Holt, Benjamin; Jones, Cathleen; Monaldo, Frank; Garcia, Oscar
Try, Try Again: Recent Steps Toward An Operational SAR-based Algorithm for Oil Spill Thickness Measurements

Bou-laouz, Moujahid; Vadaine, Rodolphe; Hajduch, Guillaume; Fablet, Ronan
Deep Learning For Ship Classification On Medium Resolution SAR Imagery

Zavagli, Massimo; Pastina, Debora; Santi, Fabrizio; Testa, Alejandro; Corvino, Michela; Morando, Elena; Pratola, Chiara; Costantini, Mario
Inverse SAR Processing for Maritime Situational Awareness

Lanz, Peter; Marino, Armando; Simpson, Morgan; Brinkhoff, Thomas; Köster, Frank; Möller, Matthias
Developing Refugee Vessel Detection Capabilities with Polarimetric SAR

Future Missions

Garcia-Mondéjar, Albert; Freer, Bryony; López-Zaragoza, Juan Pedro; McKeown, Charlie; Gibert, Ferran; Mank, Enrico; Recchia, Lisa; Hendricks, Stefan; Scagliola, Michele; Fornari, Marco; Di Bella, Alessandro; Bouffard, Jerome; Cipollini, Paolo; Borde, Franck.
Enhanced Sea Ice Performances from CRISTAL Mission

Jawak, Shridhar; Lauknes, Tom Rune; Rouyet, Line; Sivertsen, Agnar
Airborne SAR Sensor in Svalbard; User Perspective on Mission Requirements and Observational Needs

Fu, Jiayu; Li, Yuanhao; Chen, Zhiyang; Hu, Cheng
A New Distributed ATI SAR System: GEO-LEO SAR ATI Concept

Suess, Martin; de Witte, Erik; Rommen, Björn
The Harmony SAR Instrument

Lauknes, Tom Rune; Sivertsen, Agnar; Gebrie Yitayew, Temesgen; Rouyet, Line; Werner, Charles; Jenning, Michael; Plettemeier, Dirk; D. Jawak, Shridhar
Development of a Dual-Frequency Airborne SAR Sensor in Svalbard

Donlon, Craig
Future Missions at the European Space Agency

Gommenginger, Christine; Martin, Adrien; Nagamine, Katia; Gracheva, Valeria; Egido, Alejandro; Hall, Kevin; Casal, Tania; Martin-Iglesias, Petronilo
SEASTAR - Earth Explorer 11 Mission Candidate: Imaging Small-Scale Ocean Dynamics

Lopez Dekker, Paco; Chapron, Bertrand; Pasquero, Claudia; Stoffelen, Ad; Buongiorno Nardelli, Bruno; Masina, Simona; Kleinherenbrink, Marcel; Theodosiou, Andreas; Rommen, Björn; Desbiolles, Fabien
Multistatic High-Resolution Observations of the Ocean with the Harmony Mission: Science, Products, and Expected Performances

Dubois, P.; Monnier, G.; Lopez-Dekker, P.; Yitayew, T. G.; Armstrong, T.; Gombert, B.; Soulat, F.; Hellouvry, Y.-H.; Camus, B.; Grydeland, T.; Lajas, D.; Rommen, B.; De Witte, E.
Harmony End-o-End Performance Simulator: Evaluating The Performance Of A Bi-static ATI SAR Mission For Ocean Observations

Lopez Dekker, Paco; Kleinherenbrink, Marcel; Theodosiou, Andreas; Eleveld, Marieke; Zijl, Firmijn; Macedo, Karlus; Luiz, Thiago; Kubanek, Julia
WaddenSAR campaign: first results

List of Proceedings Papers

Korosov, Anton, Malin Johansson, Anja Frost, Juha Karvonen, Ekaterina Kim, Ron Kwok, Nicolas Longépé, Johannes Lohse, Robert Shuchman, Catherine Taelman, and Stefan Wiehle, *Recent advances in SAR remote sensing of sea ice and recommendations for the future: Summary from SEASAR 2023.*

Johannessen, Johnny A., Bertrand Chapron, Fabrice Collard, Ben Holt, Jose da Silva, Artem Moiseev, Werner Alpers, Thibault Taillade, Lucile Gaultier, Biao Zhang, William Perrie, Antonio Bonaduce, Nicolas Rascle, Lasse Pettersson, and Craig Donlon, *Satellite Sensor Synergy to strengthen spatial and temporal coverage and shortcut interpretation challenges*

Stopa, Justin, Ralph Foster, Aurélien Colin, Martin Gade, Lauren Alexandra Hoffman, Roghayeh Shamshir, and Björn Tings, *Advancements in methodologies using machine learning – SEASAR2023.*

Jones, Cathleen E., Maria Michela Corvino, Benjamin Holt, Elena Morando, Roberto Del Prete, Martin Gade, Scott Kaczor, Peter Lanz, Bou-Laouz Moujahid, and Yi-Jie Yang. *SEASAR Applications: Status and Outlook.*

Wave Retrievals

Wave Retrievals

Pleskachevsky, Andrey; Tings, Björn; Jacobsen, Sven
Multiparametric Sea State Fields from Synthetic Aperture Radar using Method combining CWAVE Approach and Machine Learning

Kleinherenbrink, Marcel; Ehlers, Frithjof; Gibert, Ferran; Hernandez, Sergi; Nouguier, Frederic; Chapron, Bertrand; Lopez-Dekker, Paco
SAR altimetry cross-spectra

Rikka, Sander; Nõmm, Sven; Alari, Victor; Björkqvist, Jan-Victor; Simon, Martin
Wave Spectra, Spread, and Direction in the Baltic Sea from Sentinel-1 SAR Imagery Using the LSTM Model

Khan, Salman Saeed
Temporal Consistency of Sentinel-1 SAR Wave Mode Level-2 Ocean Swell Spectra

Ocampo-Torres, Francisco J; Osuna, Pedro; Rascle, Nicolas G.; García-Nava, Héctor; Díaz Méndez, Guillermo M.; Esquivel-Trava, Bernardo; Villarreal-Olavarrieta, Carlos E.; Mora-Escalante, Rodney; Hasimoto-Beltrán, Rogelio
Assessment Of A Quasi-linear Inversion Scheme To Retrieve Ocean Surface Wave Spectrum from Synthetic Aperture Radar Image Spectrum: Results from Measurements in the Gulf of Mexico.

Benchaabane, Amine; Husson, Romain; Mouche, Alexis; Frederic, Nouguier; Johnsen, Harald
Wind-sea significant wave heights retrieval from Sentinel-1 with Deep Learning

Nouguier, Frederic; Mouche, Alexis; Chapron, Bertrand; Kleinherenbrink, Marcel
Ocean Wave Mapping By SAR: Numerical And Theoretical Perspectives

Aouf, Lotfi; Hauser, Danièle; Collard, Fabrice; Chapron, Bertrand
On The Complementary Assimilation Of SAR And SWIM Wave Spectra In The CMEMS Global Wave System

Amir, Malik Muhammad Haris; Bogoni, Antonella; Dekker, Paco Lopez
Unlocking the Potential of Distributed SwarmSAR for High-resolution Imaging of Ocean Waves

Pouplin, Clément; Mouche, Alexis; Chapron, Bertrand; Yurovskaya, Maria; Filipot, Jean-François
Tropical Cyclones Generated Waves: Processes And Contribution Of A Multi-Platform Approach

Collard, Fabrice; Guitton, Gilles; López Radcenco, Manuel; Nouguier, Frederic; Chapron, Bertrand
Swell Propagation and Forecast Across the North Atlantic Using Combined Sentinel1 Wave Mode, IW Mode and CFOSAT SWIM Observations.

Multiparametric Sea State Fields from Synthetic Aperture Radar using Method combining CWAVE Approach and Machine Learning

Andrey Pleskachevsky[a], Björn Tings[a], Sven Jacobsen[a]

[a] DLR, Maritime Safety and Security Lab Bremen, Am Fallturm 9, 28359 Bremen, Germany
Andrey.Pleskachevsky@dlr.de

Abstract

This study presents the algorithm SAR-SeaStaR (SAR Sea State Retrieval) for estimating series of integrated sea state parameters from satellite-borne synthetic aperture radar (SAR): total significant wave height H_s, dominant and secondary swell and windsea wave heights, first and second moment wave periods, mean wave period and period of wind sea. SAR-SeaStaR applies a combination of classical approach using linear regression with machine learning. It comprises the complete processing chain with a series of steps each needed to reach high accuracy: denoising, filtering image artefacts, SAR features estimation and control, model functions (linear regression and machine learning models) for estimation of sea state parameters and control of results using filtering procedures. SAR-SeaStaR is applied to C-band Sentinel-1 (S1) Interferometric Wide Swath Mode (IW), Extra Wide (EW) and Wave Mode (WM) Level-1 (L1) and to X-band TerraSAR-X (TS-X) StripMap (SM) products. The wide scenes are processed in raster format, resulting in continuous sea state fields. For each S1 WV 20 km × 20 km imagette, averaged values of each sea state parameter are derived. Validated with worldwide data the reached RMSE for H_s is 0.25 m for S1 WV, ~0.35 m for TS-X SM, ~0,50 m for the coarser S1 IW and ~0.60 m for S1 EW. The method was realized in Sea State Processor (SSP) software using modular architecture and allowing processing SAR-data from different satellites and modes in near real time (NRT).
In scope of ESA's SARWave study **[1]** the S1 IW archive was processed for 2020 with a raster of 5 km (ca. 1,600 subscenes/image). The validation with MFWAM (CMEMS, **[2]**) model results in an RMSE=0.51 m for significant wave height (H_s) and 0.78 s for crossing zero wave period (T_{m2}).

1. Methodology

The ongoing development of space-borne SAR sensors together with corresponding data transfer and data processing infrastructures has made a series of oceanographic applications possible in near real time (NRT), e.g. **[3,4,5]**. Also, in the past few years, machine learning techniques have taken a leading position in science, as their results are superior to those of analytical and simple empirical solutions when sufficiently large databases are available. Even though a few years ago, these applications did not noticeably provide more accurate solutions than the classical approaches, today they already exceed them. For example, in 2017, the accuracy of H_s obtained by applying neural networks (NN) in comparison to a traditional CWAVE **[6]** method had not improved significantly (RMSE of ca. 0.50 m for H_s) **[7]**, whereas by using a deep learning technique in 2020 the accuracy had significantly been improved to an RMSE of around 0.30 m **[8]**. In last year, the accuracy of ca. 0.25 m was reached **[9]**.

When comparing the application of the empirical approaches based on linear regression (LR) models and machine learning (ML) models, the following can be noted: the advantage of the LR is that an analytical solution exists. The coefficients can be obtained comparatively quickly, extensive machine learning training is not necessary. Although the linear solution is inferior in accuracy to that obtained by adding ML, this solution is already stable with around 1/10 samples needed for ML by a normal distribution of data used for tuning. In addition, as practice shows,

LR extrapolates much more successfully, if the modelled conditions are outside the training data conditions while the ML models can give an error with outliers significantly exceeding three times the RMSE.

Further, in addition to ML training (can take months), the developed ML model is many orders of magnitude larger (takes Gigabytes) than the list of coefficients for the LR model (takes Kilobytes). LR outperforms ML in terms of parsing speed of the model, which is important for NRT services. This point is important, as a migration of the sea state processing for direct installation on a satellite for on-board-processing has been developed **[10]**. In this case, no huge amount of SAR raw data will be transferred from satellite to earth, before the processing can be done, but only already derived sea state parameters. This technology will significantly simplify the data transfer and reduce the delay.

Based on all these reasons, the proposed SAR-SeaStaR algorithm combines both: LR (based on CWAVE approach **[6]** extended by series of additional features **[9]**) and ML model (using support vector machine (SVM) technique) for sea state processing. The solution of LR model (H_s) is used as first guess value for ML (additional feature) and also is applied for control of results.

2. Algorithm basic parameters

In a classic way, the estimation of sea state parameters is based on a normalized radar cross-section (NRCS) analysis of subscenes. One of the basic variables represents the SAR image spectrum obtained using fast Fourier transformation FFT applied to the ground range detected, radiometrically calibrated, filtered, denoised land-masked and normalised subscenes with a size of 1,024×1,024 pixels in wave number domain as introduced in **[5]**. SAR features estimated from a subscene are of five different types:

- NRCS and NRCS statistics (variance, skewness, kurtosis, etc.).
- Geophysical parameters (wind speed using CMOD-5 algorithms for C-band **[11]** and XMOD-2 for X-Band **[11]**).
- Grey Level Cooccurrence Matrix (GLCM) parameters (entropy, correlation, homogeneity, contrast, dissimilarity, energy, etc.).
- Spectral parameters, based on image spectrum integration of different wavelength domains (0-30 m, 30-100 m, 100-400 m, etc.) and spectral width parameters (Longuet-Higgins, Goda).
- Spectral parameters using products of normalized image spectrum with orthonormal functions (CWAVE approach) and cutoff wavelength estimated using autocorrelation function (ACF).

3. Sea state processor (SSP)

SSP was designed in a modular architecture for S1 IW, EW, WV and TS-X SM/SL modes. The DLR Ground Station "Neustrelitz" applies the SSP as part of a near real-time demonstrator service that involves a fully automated daily provision of surface wind and sea state parameters estimated from S1 IW images of the North and Baltic Sea. Due to implemented parallelization, a fine raster can be processed. For example, S1 IW image with coverage of 200 km × 250 km can be processed using a raster with 1 km sized grid cells (~50,000 subscenes) during minutes. Each of maritime information products, i.e. sea state retrieval, wind speed retrieval, ship detection and AIS defines each one independent data layer. The data layers are combined for processor-internal information exchange and presentation to the operator **[9]**.

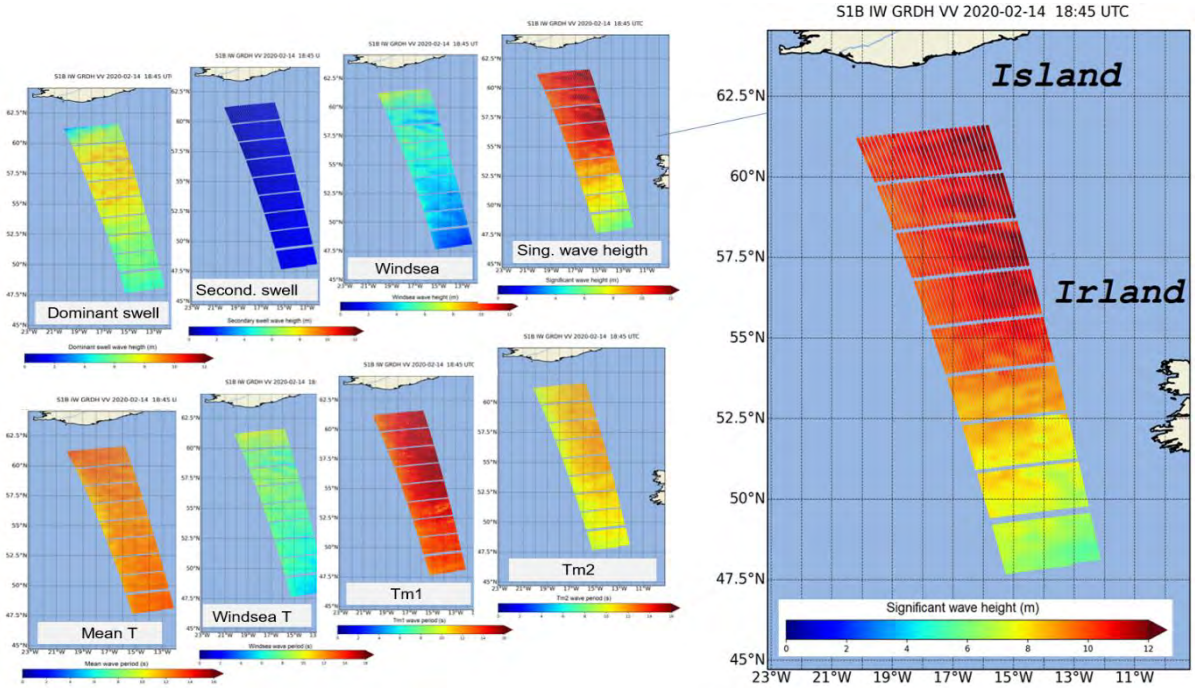

Figure 1: *Example of eight sea state fields processed from S-1 IW scene with ~1600 km by ~200 km coverage acquired during a storm in North Atlantic with H_s reaching ~14 m*

Using the SSP, the complete archive of S1 WV data from December 2014 until February 2021 with around 60 overflights/day, each including around 120 imagettes, was processed. The validation using the WFWAM/CMEMS **[2]** model resulted in an RMSE of 0.245/0.273 m for wv1/wv2 imagettes, respectively. Comparisons to 61 NDBC buoys **[13]**, collocated at distances shorter than 50 km to worldwide S1 WV imagettes, result into an RMSE of 0.41 m. The data is available to the public within the scope of ESA's climate change initiative CCI **[14]**.

References

[1] SARWAVE. www.sarwave.org
[2] CMEMS. Copernicus Marine Environment Monitoring Service. https://marine.copernicus.eu/
[3] Schwarz, E., Krause, D., Berg, M., Daedelow, and H. Maas, 2015. Near Real Time Applications for Maritime Situational Awareness. Proc. 36th Int. Symp. On Remote Sensing of Environment, Berlin, Germany, Remote Sensing and Spatial Information Sciences, vol. XL-7/W3, 6p.
[4] Pleskachevsky, A., W. Rosenthal, and S. Lehner, 2016: Meteo-Marine Parameters for Highly Variable Environment in Coastal Regions from Satellite Radar Images." JPRS, Vol. 119, pp. 464-484., 2016.
[5] Pleskachevsky, A., Jacobsen, S., Tings, B., and E. Schwarz, 2019. Estimation of sea state from Sentinel-1 Synthetic aperture radar imagery for maritime situation awareness. IJRS, Vol. 40-11, pp. 4104-4142.
[6] Schulz-Stellenfleth, J., König, Th., and S. Lehner, 2007. An empirical approach for the retrieval of integral ocean wave parameters from SAR data. JRL, Vol. 112, pp. 1-14.
[7] Stopa, J., and A. Mouche, 2017. Significant wave heights from Sentinel-1 SAR: Validation and Applications. JGR, Vol., 122, pp. 1827-1848..
[8] Quach, B., Glaser, Y., Stopa, J., Mouche, A., Sadowski, P., 2020. Deep Learning for Predicting Significant Wave Height From Synthetic Aperture Radar, IEEE TRANSACTIONS ON GEOSCIENCE AND REMOTE SENSING, 10.1109/TGRS.2020.3003839
[9] Pleskachevsky, A., Tings, B., and J, Jacobsen, 2022: Multiparametric Sea State Fields from Synthetic Aperture Radar for Maritime Situational Awareness, RSE, vol. 280, 22 pp.
[10] Wiehle, S., Breit, H., Günzel., D., Mandapati, S., and U. Balss, 2022. Synthetic Aperture Radar Image Formation and Processing on an MPSoC, IEEE Transactions on Geoscience and Remote Sensing, DOI: 10.1109/TGRS.2022.3167724
[11] Hersbach, H., 2008. CMOD5.N: A C-band geophysical model function for equivalent neutral wind.
[12] Li, X. -M. and S. Lehner, 2014. Algorithm for Sea Surface Wind Retrieval From TerraSAR-X and TanDEM-X Data, IEEE Transactions on Geoscience and Remote Sensing, vol. 52, no. 5, pp. 2928-2939.
[13] https://www.ndbc.noaa.gov/
[14] ESA, CCI, Sea State Project. http://cci.esa.int/seastate

SAR-altimetry cross-spectra

M. Kleinherenbrink, F. Ehlers, F. Gibert, S. Hernandez,
F. Nouguier, B. Chapron, P. Lopez-Dekker

January 31, 2023

1 Introduction

The normalized radar cross section (NRCS) from Synthetic Aperture Radar (SAR) depends on the short-scale roughness of the ocean surface[10]. Modulations of the NRCS result from the presence of long gravity waves, such as swell. Since the 1970s these intensity modulations have been studied to infer wave parameters. The mapping of wave spectra into SAR intensity spectra[5, 8] led to the first retrieval algorithms[2], which are now operational for SAR satellite missions such as Sentinel-1.

Distortions of intensity by long waves have also been observed in high-resolution delay/Doppler altimetry, which affects the accuracy to which geophysical parameters can be retrieved[9]. The limited along-track resolution prevents the interpretation of swell-related waveform distortions. With Focused SAR-altimetry processing, which is applicable to delay/Doppler altimeters, it is possible to compute SAR spectra from distortions in the waveform tails in a comparable way as the side-looking SAR systems. Instead of two ambiguities in side-looking SAR[4], the SAR-altimetry spectra contain four ambiguities because both sides of the ground track are illuminated[1]. Under moderate sea states it should be possible to retrieve swell-wave parameters from nadir altimeters. However, an inversion or retrieval of swell-wave parameters has not been performed yet as the SAR-altimetry spectra are still poorly understood.

This paper will describe SAR-altimetry spectra in more detail using a closed-form solution and simple model simulations, which are compared to Sentinel-6 data. It extends the description of Altiparmaki et al.[1] and introduces the concept of the cross-spectral stack, a set of cross-spectra using multiple sublooks from the overpass. We will show that the cross-spectra vary during the overpass, which can help to constrain the estimation of swell-wave parameters.

2 Closed-form model

The closed-form model [5, 8], suffers from limitations and is not accurate for the steep incident angles of nadir altimetry (more details in Kleinherenbrink et al. (2023), in preparation). However, the closed-form model can provide a local approximation for the observed spectrum and helps to understand the SAR-altimetry spectral properties. We define the two-dimensional SAR spectrum for the right side of the ground-track as [4]

$$P(k_x,k_y) = \frac{1}{(2\pi)^2} e^{-k_x^2\rho_{xx}(0,0)-k_y^2\rho_{yy}(0,0)-k_xk_y(\rho_{xy}(0,0)+\rho_{yx}(0,0))} \int\int e^{k_x^2\rho_{xx}+k_y^2\rho_{yy}+k_xk_y(\rho_{xy}+\rho_{yx})} L e^{-i(k_xx+k_yy)} dxdy, \tag{1}$$

with $L = 1 + \rho_{II} + ... \ \rho_{ab}$ cross-correlation functions computed from ocean-wave spectrum $S(k_x, k_y)$ and transfer functions for ground-range shifts, Doppler shifts and tilt modulation as [6, 4]

$$\begin{aligned} T_x &= -\frac{1}{\tan(\theta)} \\ T_y &= -i\frac{R}{V}\omega_k \\ T_I &= -ik_x\frac{1}{\sigma_0}\frac{\delta\sigma_0}{\delta\theta}, \end{aligned} \tag{2}$$

where θ is the local incident angle, R/V the reciprocal of the angular satellite velocity, ω_k the angular velocity of the ocean waves and σ_0 the NRCS. This formulation explicitly takes into account the non-linear range shifts (range bunching). The exponential terms outside of the integral provide us a clue on the resolution in the along- and cross-track directions, approximated as

$$\begin{aligned} \lambda_{al} &\propto \pi\sqrt{\rho_{yy}(0,0)} = \pi\frac{H}{V}\sqrt{\sigma_v^2} \\ \lambda_{ct} &\propto \pi\sqrt{\rho_{xx}(0,0)} = \pi\sqrt{\frac{\sigma_e^2}{\tan^2(\theta)}} = \pi\frac{\mathrm{SWH}}{4\tan(\theta)}, \end{aligned} \tag{3}$$

with σ_v^2 the velocity variance [7], and the Significant Wave Height (SWH) as a function of the elevation variance σ_e^2. This yields an ellipsoidal roll-off in the spectral domain. In case the range direction and the azimuth direction are not perpendicular, the orientation and size of the ellipse changes.

3 Numerical model

A surface is modelled on a regular grid using as input an Elfouhaily wind-wave spectrum[3] and a Gaussian swell-wave spectrum. Using Discrete Fourier Transforms we compute the elevation h, upward velocity v_r and two-dimensional slope. The local in-plane and out-of-plane incident angles are used to compute the tilt modulation using the well-known equation for specular reflections[10]. For the zero-Doppler case, the surface velocity is used to reproject scatterers in the Doppler along-track direction

$$\Delta y = \frac{R}{V}v_r \tag{4}$$

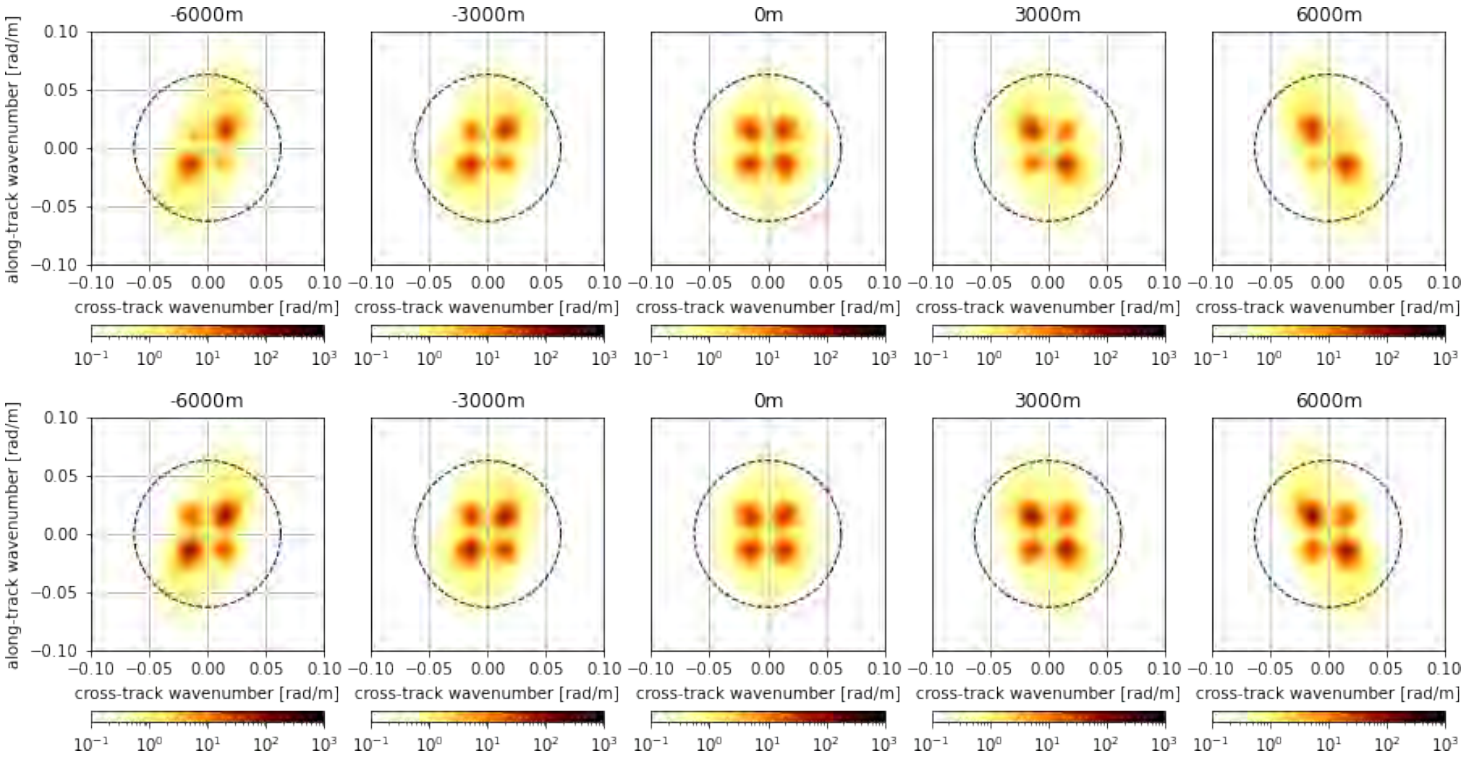

Figure 1: Absolute values of numerically modeled satellite nadir altimetry cross-spectra based on ten realizations at five along-track distances. The inputs consist of swell systems with a peak wavelength of 277 m propagating at 45 (top) and 135 (bottom) degrees from cross track (right), and a wind-sea system based on a wind speed of 10 m/s, a fetch of 200 km at a mean direction of 45 degrees from cross track.

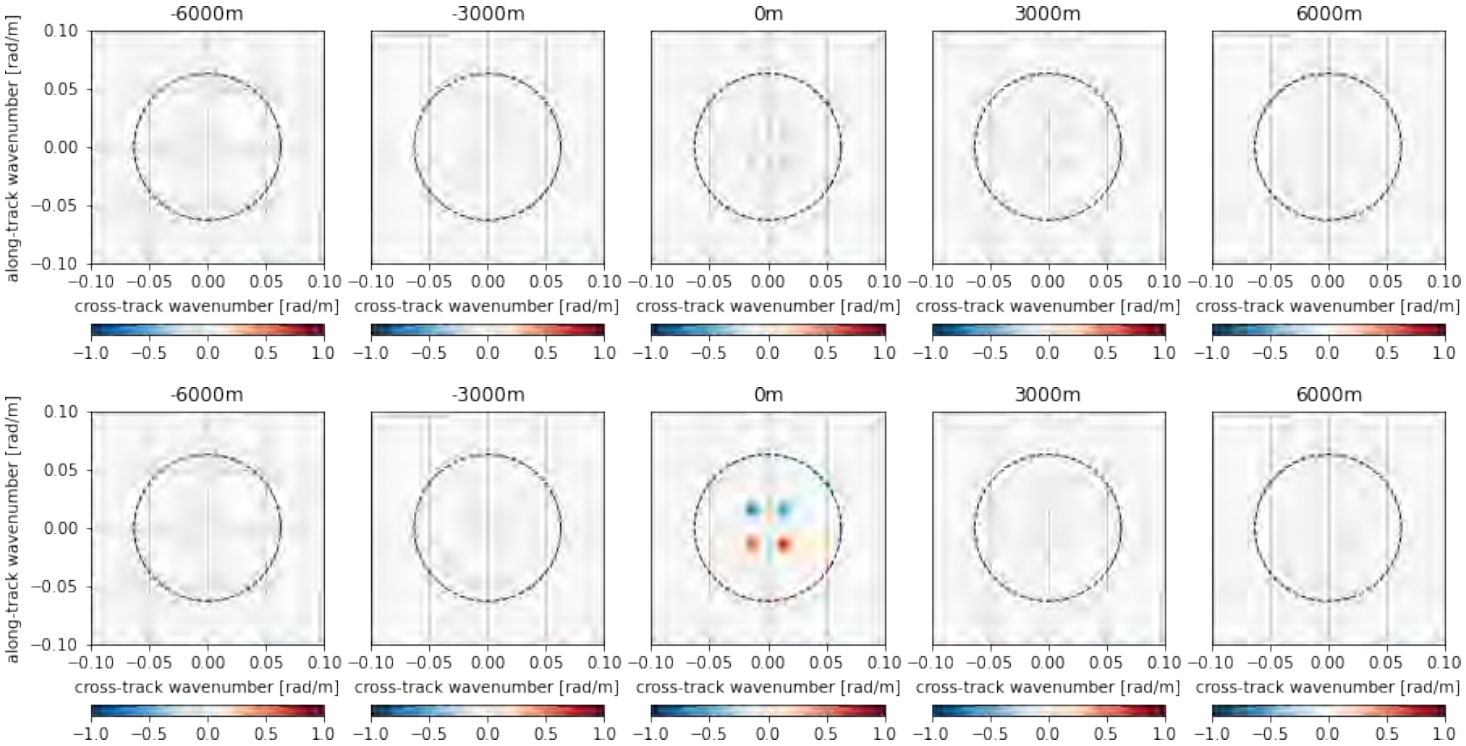

Figure 2: Imaginary values of numerically modeled satellite nadir altimetry cross-spectra based on ten realizations at five along-track distances. The input consists of a swell system with a peak wavelength of 277 m propagating at 45 (top) and 225 (bottom) degrees from cross track (right), and a wind-sea system based on a wind speed of 10 m/s, a fetch of 200 km at a mean direction of 45 degrees from cross track.

and the elevation to move scatterers is the ground-range (cross-track) direction by

$$\Delta x = -\frac{1}{\tan(\theta)}. \quad (5)$$

The latter two effects are responsible for the resolution losses in the along-track and the cross-track direction, respectively, and also for the accompanied velocity and range bunching.

4 Cross-spectral stack

The 3dB-beamwidth of radar altimeters is typically in the order of 1.3 degrees. At a platform velocity of approximately 7 km s^{-1} scatterers are a few seconds in view. Only using part of the overpass for SAR processing is sufficient to get the necessary along-track resolution for spectral analysis. By dividing the overpass in multiple sublooks, we get observations and spectra of the surface from various view angles leading to varying spectral densities. Cross-spectra are computed from two consecutive sublooks [4], which provides additional information on the phase change of the intensity modulations.

Without considering the phase, the history of the spectral density emerging from a swell signal varies by four effects. First, the tilt modulation varies as the relative satellite position with respect to the slopes changes. Second, the ground-range direction is at non-zero Doppler not aligned anymore with the cross-track direction. Surface elevations still cause reprojections of scatterers in the cross-track direction, but their effects are 'filtered' and depend on the width of the Doppler strip, which leads to an adjustment of Eqs. 2 and 5. Third, vertical velocity causes Doppler shifts that move scatterers in the along-track direction. However, as they are constrained by their range, reprojection occurs effectively over the range isoline. This introduces a cross-track shift and adds a term to the ground-range transfer function T_x (Eq. 2) and to the shift in Eq. 5. Fourth, the range and Doppler shifts are not perpendicular anymore, which causes the cross-term outside of the integral (Eq. 1) to becomes non-zero. This will rotate the cut-off and lowers the power spectral density in two quadrants.

The combined effect results in different power spectral density variations in the spectral quadrants (Fig. 1). It appears that the power spectral density in a non-zero Doppler cross-spectrum depends on the wind-wave and swell directions. The imaginary terms of the cross-spectra also vary during the overpass (Fig. 2). The phases or imaginary parts of the cross-spectra cannot directly be coupled to the wave direction, as the location of maximum intensity also varies due to the changing phases of the three imaging mechanisms by the geometrical variations induced by the satellite velocity. The relative phase change of the 'static' intensity modulation (comparable to SAR, see Nouguier et al. (2023), in preparation) interferes with the phase change caused by wave motion. The cross-spectral stack might therefore be used to remove ambiguities, but it is non-trivial and the precise mechanism is not fully understood yet.

5 Conclusions

This study provides the most extensive description of the SAR-altimetry spectra up to date. It also introduces the cross-spectral analysis for SAR altimeters. The long overpass time of the altimeters allows to estimate a cross-spectral stack. The cross-spectral stack adds information for retrieval algorithms, but is not yet fully understood. It also shows potential to remove swell-direction ambiguities.

The next step is the inversion of swell-wave parameters from the SAR-altimetry cross-spectra. If swell-wave parameters are retrieved from altimeters this will greatly increase the number of ocean-wave observations. In combination with the backscatter (roughness), the SWH and the velocity variance, the SAR altimeter will have a more synoptic view of the ocean surface. Finally, the additional information resulting from such an inversion would help to constrain the sea-state bias.

References

[1] O. Altiparmaki, M. Kleinherenbrink, M. Naeije, C. Slobbe, and P. Visser. SAR Altimetry Data as a New Source for Swell Monitoring. *Geophysical Research Letters*, 49(7), Apr. 2022.

[2] B. Chapron, H. Johnsen, and R. Garello. Wave and wind retrieval from sar images of the ocean. *Annales Des Télécommunications*, 56(11-12):682–699, Nov. 2001.

[3] T. Elfouhaily, B. Chapron, K. Katsaros, and D. Vandemark. A unified directional spectrum for long and short wind-driven waves. *Journal of Geophysical Research: Oceans*, 102(C7):15781–15796, July 1997.

[4] G. Engen and H. Johnsen. SAR-ocean wave inversion using image cross spectra. *IEEE Transactions on Geoscience and Remote Sensing*, 33(4):1047–1056, July 1995.

[5] K. Hasselmann and S. Hasselmann. On the nonlinear mapping of an ocean wave spectrum into a synthetic aperture radar image spectrum and its inversion. *Journal of Geophysical Research*, 96(C6):10713, 1991.

[6] F. C. Jackson. THE physical basis for estimating wave-energy spectra with the radar ocean-wave spectrometer. *Johns Hopkins APL Technical Digest*, 8(1), 1987.

[7] V. Kerbaol, B. Chapron, and P. W. Vachon. Analysis of ERS-1/2 synthetic aperture radar wave mode imagettes. *Journal of Geophysical Research: Oceans*, 103(C4):7833–7846, Apr. 1998.

[8] H. E. Krogstad. A simple derivation of Hasselmann's nonlinear ocean-synthetic aperture radar transform. *Journal of Geophysical Research*, 97(C2):2421, 1992.

[9] T. Moreau, E. Cadier, F. Boy, J. Aublanc, P. Rieu, M. Raynal, S. Labroue, P. Thibaut, G. Dibarboure, N. Picot, L. Phalippou, F. Demeestere, F. Borde, and C. Mavrocordatos. High-performance altimeter Doppler processing for measuring sea level height under varying sea state conditions. *Advances in Space Research*, 67(6):1870–1886, Mar. 2021.

[10] R. Valenzuela. Theories for the Interaction of Electromagnetic and Oceanic Waves - A Review. *Boundary-Layer Meteorology*, 13:61–85, 1978.

Wave Density Spectra in the Baltic Sea from Sentinel-1 SAR Imagery Using the LSTM Model

Sander Rikka [1], Sven Nõmm[2], Victor Alari[1], Jan-Victor Björkqvist[3,4], Martin Simon[2]

[1]Department of Marine Systems, School of Science, Tallinn University of Technology TalTech, Akadeemia tee 15a, 12618, Tallinn, Estonia,
sander.rikka@taltech.ee
[2]Department of Software Science, School of Information Technology, Tallinn University of Technology, Akadeemia tee 15 a, 12618, Tallinn, Estonia, [3]Norwegian Meteorological Institute, 5007, Bergen, Norway. [4]Finnish Meteorological Institute, 00560, Helsinki, Finland,

Abstract

This paper presents preliminary results on the use of a long-short-term memory (LSTM) deep recurrent neural network to estimate 1D wave density spectra from Sentinel-1 (S1) Interferometric Wide (IW) swath images. In total, 165 locations in the Baltic Sea are used to extract image spectra from custom ground-range detected data. The training data set consists of approximately 80000 individual data points divided into training, validation, and testing data sets by 70-15-15, respectively. WAM wave model spectra from the MET Norway repository are used as ground truth. The LSTM model shows correlations greater than 0.80 between wave periods of 2 and 9 seconds for the wave density spectra.

1. Introduction

Estimation of various surface wave parameters (e.g. significant wave height H_S) from SAR imagery has been the focus of many studies [1], [2] and [3]. However, the accurate retrieval of 2D wave density spectra has been the ultimate goal of the SAR data. Various inverse methods have been developed to extract 2D wave information for the open ocean [4], [5] where high resolution wave mode data are acquired and swell waves dominate the sea state. The lack of long-swell waves in closed wind-wave dominant regional seas, e.g. the Baltic Sea [6], [7], and lower-resolution ScanSAR (TOPS mode for S1) acquisitions have been the limiting factor for using the inverse methods for such environments.

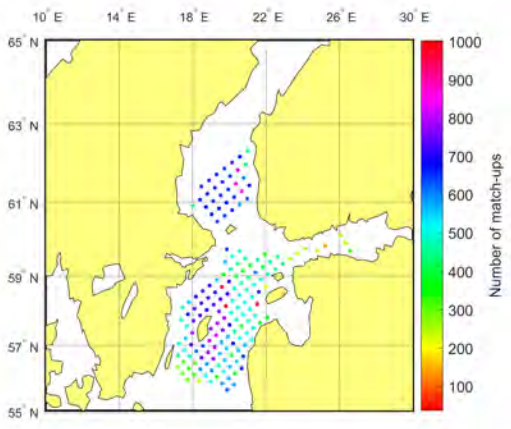

Figure 1: Map of the Baltic Sea with locations of SAR data collection. Colors represent the amounts of SAR match-ups with model spectra.

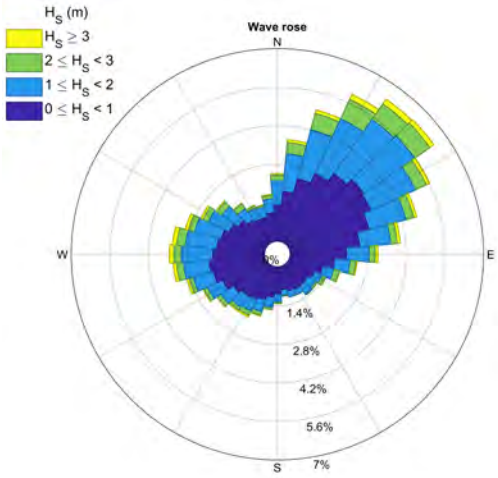

Figure 2: NORA3 significant wave height distribution over mean propagation directions (going to) for the matching dataset.

Recently, recurrent deep learning neural network methods (e.g., long-short-term memory - LSTM [8]) have been used to estimate 1D wave density spectra from S1 IW data in the Baltic Sea [9]. The aim of this study is to extend

the data set by using NORA3 wave model spectra and train LSTM networks to estimate wave density spectra between 2 and 10 s with a much larger and more variable data set compared to the previous study.

2. Data and Methods

2.1 NORA3 data

We used the NORA3 wave hindcast, which is based on the WAM wave model [10], [11]. The hindcast covers the pan-Arctic domain, including also the Baltic Sea with a 3 km resolution. However, the spectra were only outputted with a 30 km resolution. The model spectra are discretized using 30 frequencies logarithmically spaced in the range of 0.0345-0.5476 Hz and 24 equally spaced directions covering a full circle.

2.2 SAR processing

S1 IW Single Look Complex (SLC) sub-images were calibrated and speckle filtered with a Frost (5x5) filter. During the multi-look operator, pixels were not averaged to represent squares, and the images were left in radar projection. The image spectra (ISP) are calculated from both polarisations (VV and VH) with the fast Fourier transform (FFT). Subsequently, the values of the ISP components ISP_x and ISP_y were interpolated to fixed wavelength values between 215 and 30 m (39 values with variable intervals). Image spectra and other metadata (e.g. satellite heading ($PASS$), incidence angle (IA), image texture, etc.) were saved for later processing. SAR data was collected around the location of the model spectra (Figure 1) from the beginning of 2015 until the end of 2021. On average, around 550 independent sub-images were processed at each location. The resulting distribution of H_S in the mean propagation direction is shown in Figure 2. In total, around 80000 collocation pairs were formed for the study.

2.3 LSTM configuration and experiments

Spectra estimation was performed by a deep LSTM type neural network. The network architecture is shown in Figure 3. The best configuration was found when the input data for the LSTM model had a shape of $(40, 4)$, where the four variables are IA and ISP_{VV_x}, $PASS$ and ISP_{VV_y}, IA and ISP_{VH_x}, $PASS$ and ISP_{VH_y}. Before training, the values IA and $PASS$ are normalized between 0 and 1; the logarithm base e is applied to ISP and wave energy.

3. Results and discussion

Bin-by-bin comparison in Figure 4 between test data and LSTM model predictions show correlations greater than 0.80 for all predicted spectra between 2 and 9 s, which corresponds to most of the sea states dominated by wind waves. Although the correlation coefficient for the energy density around 10 s in [9] is greater, the prediction accuracies for higher frequencies are similar or even better for the current study. Moreover, the custom SAR processing (without squaring pixels during multi-look) allows for avoiding complex image upsampling which was required previously to estimate energies in higher frequencies.

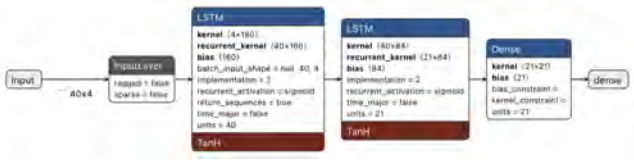

Figure 3: LSTM model structure.

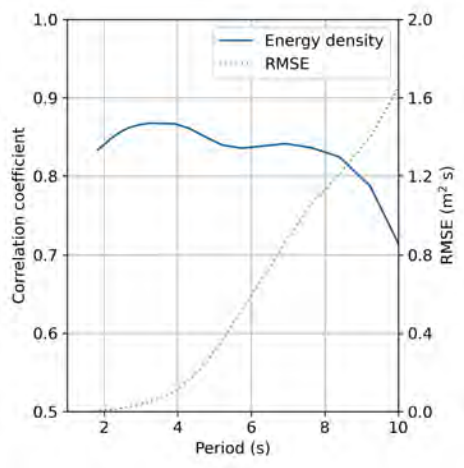

Figure 4: LSTM model prediction average correlation coefficients on test data for wave energy per frequency/period band and standard deviation of errors.

Acknowledgements

We thank MET Norway for its open data policy and data availability. The corresponding author expresses sincere gratitude to the co-authors. The work of S. Nõmm and M. Simon is in the project "ICT programme" which was partially supported by the European Union through the European Social Fund.

References

[1] S. Lehner, A. Pleskachevsky, D. Velotto, and S. Jacobsen, "Meteo-marine parameters and their variability: Observed by high-resolution satellite radar images," *Oceanography*, vol. 26, no. 2, pp. 80–91, 2013.

[2] F. Ardhuin, J. E. Stopa, B. Chapron, F. Collard, R. Husson, R. E. Jensen, J. Johannessen, A. Mouche, M. Passaro, G. D. Quartly *et al.*, "Observing sea states," *Frontiers in Marine Science*, p. 124, 2019.

[3] A. Pleskachevsky, B. Tings, S. Wiehle, J. Imber, and S. Jacobsen, "Multiparametric sea state fields from synthetic aperture radar for maritime situational awareness," *Remote Sensing of Environment*, vol. 280, p. 113200, 2022. [Online]. Available: https://www.sciencedirect.com/science/article/pii/S0034425722003108

[4] K. Hasselmann and S. Hasselmann, "On the nonlinear mapping of an ocean wave spectrum into a synthetic aperture radar image spectrum and its inversion," *Journal of Geophysical Research: Oceans*, vol. 96, no. C6, pp. 10 713–10 729, 1991.

[5] J. Schulz-Stellenfleth, S. Lehner, and D. Hoja, "A parametric scheme for the retrieval of two-dimensional ocean wave spectra from synthetic aperture radar look cross spectra," *Journal of Geophysical Research: Oceans*, vol. 110, no. C5, 2005.

[6] J.-V. Björkqvist, S. Pärt, V. Alari, S. Rikka, E. Lindgren, and L. Tuomi, "Swell hindcast statistics for the baltic sea," *Ocean Science*, vol. 17, no. 6, pp. 1815–1829, 2021. [Online]. Available: https://os.copernicus.org/articles/17/1815/2021/

[7] L. Tuomi, K. K. Kahma, and H. Pettersson, "Wave hindcast statistics in the seasonally ice-covered Baltic Sea," *Boreal Environ. Res.*, vol. 16, no. 6, pp. 451–472, 2011.

[8] S. Hochreiter and J. Schmidhuber, "Long Short-Term Memory," *Neural Computation*, vol. 9, no. 8, pp. 1735–1780, 11 1997. [Online]. Available: https://doi.org/10.1162/neco.1997.9.8.1735

[9] M. Simon, S. Rikka, S. Nõmm, and V. Alari, "Application of the lstm models for baltic sea wave spectra estimation," *IEEE Journal of Selected Topics in Applied Earth Observations and Remote Sensing*, vol. 16, pp. 83–88, 2023.

[10] Ø. Breivik, A. Carrasco, H. Haakenstad, O. J. Aarnes, A. Behrens, J.-R. Bidlot, J.-V. Björkqvist, P. Bohlinger, B. R. Furevik, J. Staneva, and M. Reistad, "The impact of a reduced high-wind charnock parameter on wave growth with application to the north sea, the norwegian sea, and the arctic ocean," *Journal of Geophysical Research: Oceans*, vol. 127, no. 3, mar 2022. [Online]. Available: https://doi.org/10.1029\%2F2021jc018196

[11] "Norwegian meteorological institute, spectra database," https://thredds.met.no/thredds/catalog/windsurfer/mywavewam3km_spectra/catalog.html, accessed: 2022.

Temporal Consistency of Sentinel-1 SAR Wave Mode Level-2 Ocean Swell Spectra

Salman Khan

Commonwealth Scientific and Industrial Research Organisation, Environment, Aspendale, Victoria, Australia.

Sentinel-1 C-SAR platforms (A/B) acquire small wave mode images covering most of the global ocean up to ~100 km close to the coast [1]. Ocean surface wave information is routinely extracted from these images such as in the ESA Sentinel-1 level-2 ocean swell (OSW) spectra product [2]. The swell spectra derived from SAR (including Sentinel-1) are limited by the azimuth cut off wavelength and generally cannot capture high frequency ocean waves. Despite this limitation, they are useful in monitoring and analysing longer scale swell systems, and prior to CFOSat's (China France Oceanography satellite) launch, they were the only satellite-derived ocean swell spectra measurements that were routinely produced.

The algorithm that sits behind the production of the OSW product has matured over time through several updates [3,4]. It would be ideal to reprocess the whole Sentinel-1 wave mode archive at each OSW processor update to have a product that is the most accurate and consistent in time, but that is not currently the case and may be too costly a prospect. Nevertheless, it is important to examine the temporal consistency of the OSW product before potentially using these data for various applications.

In this brief work, a temporal consistency analysis of the OSW product has been carried out in the Australian region. In this region, there are not many wave buoy measurements as one moves further away from the coast. Therefore, one viable option for a mission duration temporal consistency analysis is through comparisons with regional wave model runs. We have taken this approach and have carried out the comparison of the OSW product against an Australian-produced global wave model (WaveWatch III) hindcast [5]. The matching criteria between OSW observations and the wave hindcast are within 100 km and +/- 30 mins. The wave spectra from the hindcast are also truncated using the ellipsoidal azimuth cut off from the matching OSW spectra as done in [6].

The comparison is performed using bulk statistics of significant wave height, zero-crossing period, and mean direction (Hs, tm02, and dm) to assess the consistency of wave parameters over time. In each comparison, the time series of the mean monthly bias and standard deviation (Sentinel-1 - WW3) are analysed after grouping the data by platform, polarisation, incidence angle, and Sentinel-1 IPF (Instrument Processing Facility) versions [4]. This approach gives clues into the dependency of the wave parameters/swell spectra on the above characteristics and the processor version. The results for the three cases are shown in figs. 1-3.

The results clearly show that the biases and standard deviations are reduced with improvement to the Sentinel-1 IPFs generally for all combinations of satellite characteristics with only some exceptions. Especially, the results since IPF 3.30+ are quite encouraging. Resources permitting, there is value in reprocessing historical Sentinel-1 wave mode data with the latest IPF version. Until that is possible, the users of this dataset need to consider its limitations due to evolving IPF versions before their use.

A subsequent analysis on potential calibration consistency of the Sentinel-1 affecting wave mode data was also carried out. The calibration consistency was analysed on the normalised radar cross section (NRCS) time series. The NRCS is a function of incidence angle, operating frequency, and transmit-receive polarisation. Daily NRCS mean and standard deviation on Sentinel-1 wave mode time series were computed to check for inconsistencies after grouping the data by platform, incidence angle, polarisation and IPF version (fig. 4). The NRCS stats of Sentinel-1 A and B wave mode level-2 data for overlapping periods, matching polarisation and incidence angles closely follow each other and no alarming inconsistency is observed. Slightly higher fluctuation of mean NRCS value is possibly observed in the beginning of the time series (IPF 2.50, fig. 4).

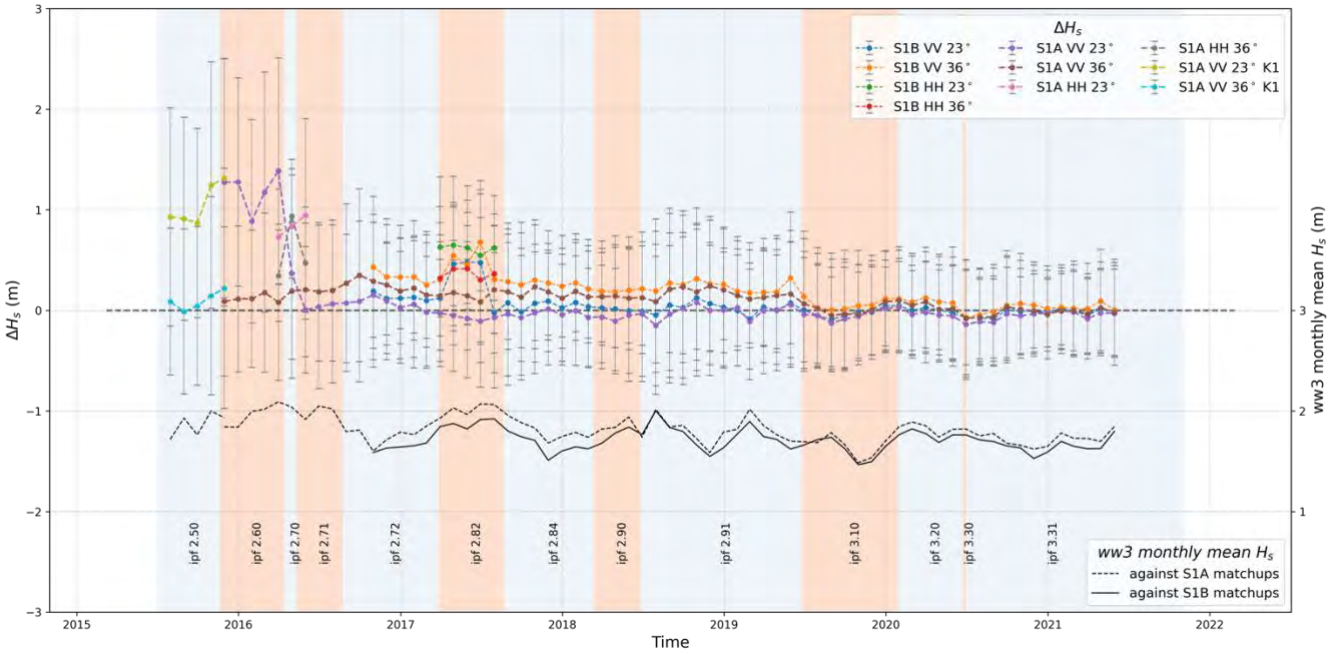

Figure 1: (left y-axis) ΔHs (Sentinel-1 – WW3) monthly mean and standard deviation time series of Sentinel-1A/B wave mode data as a function of platform, polarisation, and incidence angle, and (right y-axis) WW3 monthly mean Hs computed against Sentinel-1 A A and B matchups. Sentinel-1 IPF version evolution through time is highlighted.

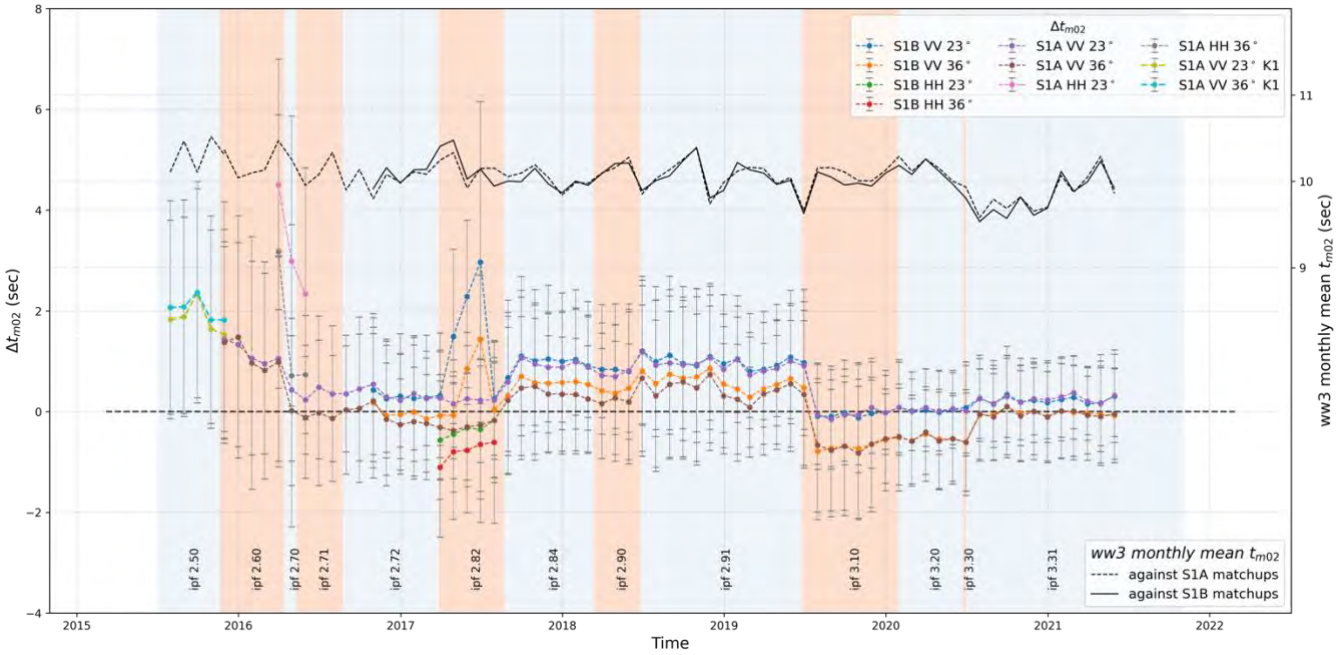

Figure 2: Figure 7: (left axis) $\Delta tm02$ (Sentinel-1 – WW3) monthly mean and standard deviation time series of Sentinel-1A/B wave mode data as a function of platform, polarisation, and incidence angle, and (right axis) WW3 monthly mean $tm02$ computed against Sentinel-1 A and B matchups. Sentinel-1 IPF version evolution through time is highlighted.

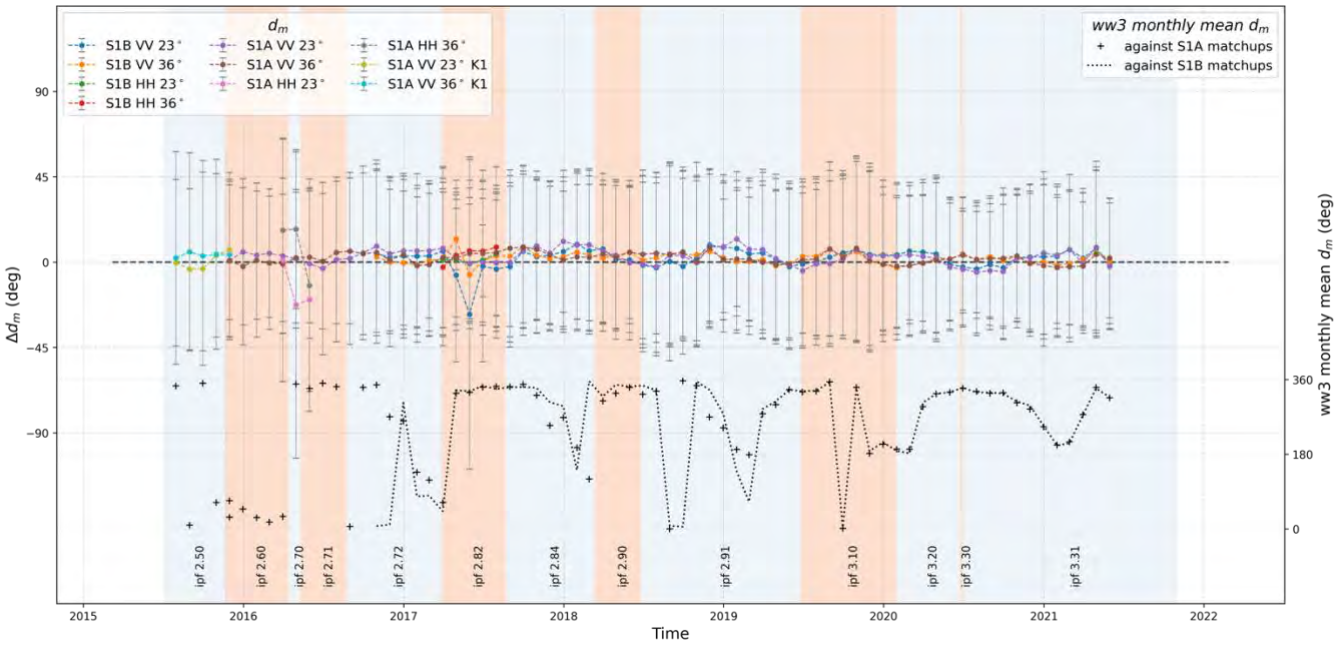

Figure 3: Figure 8: (left axis) Δdm (Sentinel-1 – WW3) monthly mean and standard deviation time series of Sentinel-1A/B wave mode data as a function of platform, polarisation, and incidence angle, and (right axis) WW3 monthly mean dm computed against Sentinel-1 A and B matchups. Sentinel-1 IPF version evolution through time is highlighted.

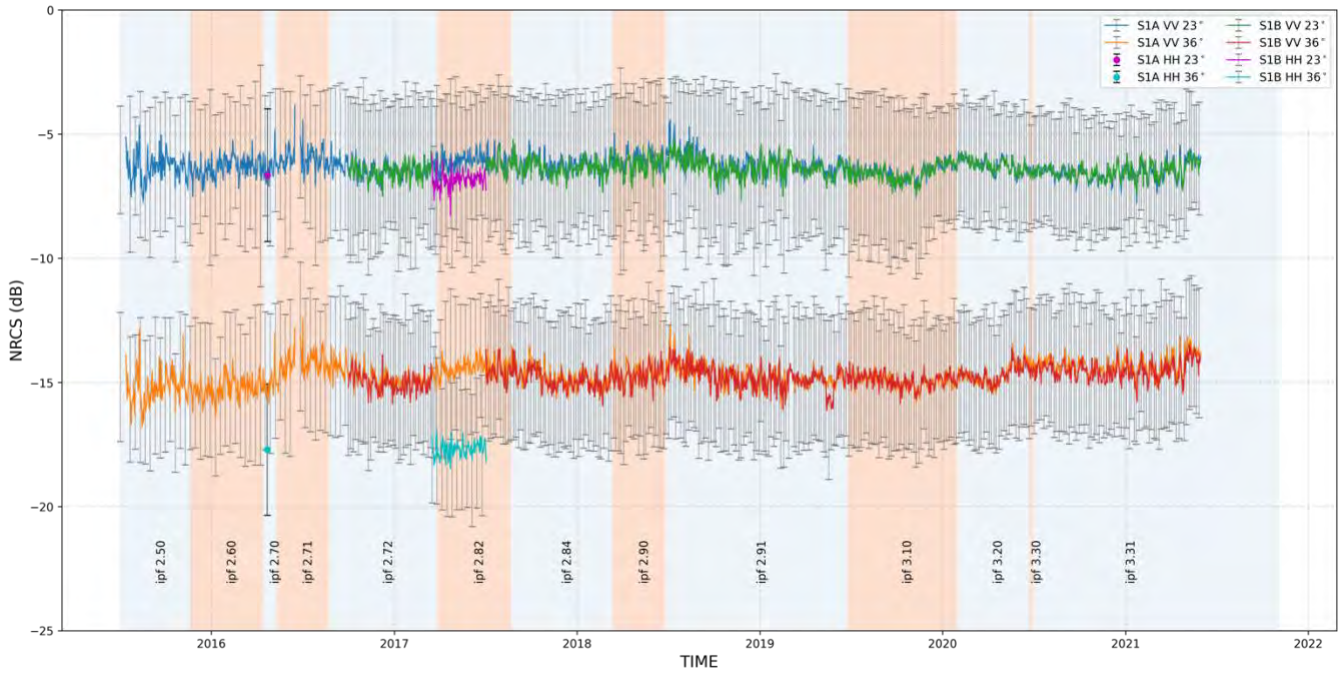

Figure 4: Figure 5: NRCS daily mean and standard deviation time series of Sentinel-1A/B wave mode data as a function of platform, polarisation, and incidence angle. Sentinel-1 IPF version evolution through time is highlighted.

REFERENCES

[1] Torres, R., Snoeij, P., Geudtner, D., Bibby, D., Davidson, M., Attema, E., et al. GMES Sentinel-1 mission. Remote Sensing of Environment, 120, 9–24 (2012).
[2] Sentinel-1 Product Definition. Collecte Localisation Satellites (CLS). Ref: S1-RS-MDA-52-7440. Issue 2.7. 25th Mar. 2016.
[3] Sentinel-1 Ocean Swell Spectra (OSW) Algorithm Theoretical Basis Document (2020a). Northern Research Institute (Norut). Ref: S1-TN-NRT-52-7450. Issue 1.3. 11th Feb 2020.
[4] Sentinel-1 Mission Performance Centre. https://sar-mpc.eu/.
[5] Smith, GA, Hemer, M, Greenslade, D, Trenham, C, Zieger, S, Durrant, T. Global wave hindcast with Australian and Pacific Island Focus: From past to present. *Geosci. Data J.*. 2021; 8: 24– 33. https://doi.org/10.1002/gdj3.104
[6] Khan, S. S., Echevarria, E. R., & Hemer, M. A. (2021). Ocean swell comparisons between Sentinel-1 and WAVEWATCH III around Australia. Journal of Geophysical Research: Oceans, 126, e2020JC016265. https://doi.org/10.1029/2020JC016265

Assessment of a quasi-linear inversion scheme to retrieve ocean surface wave spectrum from synthetic aperture radar image spectrum: results from measurements in the Gulf of Mexico.

F. J. Ocampo-Torres(1), P. Osuna(2), N. G. Rascle(3), H. García-Nava(4), G. Díaz Méndez(2), B. Esquivel-Trava(2), Carlos E. Villarreal-Olavarrieta(2), Rodney E. Mora-Escalante(2), R. Hasimoto-Beltrán(5).

1.CEMIE-Océano, Inst. Ingeniería UNAM, México, pocampotorres@gmail.com
2.Physical Oceanography Department, CICESE, Ensenada, México
3.IFREMER, LOPS, Brest, France, nicolas.rascle@ifremer.fr
4.Institute of Oceanology Research, UABC, Ensenada, México, hector.garcia.nava@uabc.edu.mx
5. CIMAT, Guanajuato, México, hasimoto@cimat.mx

Abstract.
Ocean surface wave full directional spectrum as estimated directly from measurements obtained with a spar buoy is used in order to assess the wave spectrum retrieval procedure from synthetic aperture radar images of the sea surface. Our ultimate goal is to obtain a rather comprehensive view of the dynamical behaviour of surface waves, while we focus our study in sea state conditions under varying winds, when frequently mixed sea and swell systems are present. Encountered field conditions are characterized by non-equilibrium wind-wave systems and uppermost ocean dynamics under rapidly varying wind field. Atmospheric cold front passage through the measuring site imposed a unique wind-wave system information, especially under the occurrence of cases when swell propagation opposes locally generated wind-waves. Of particular importance is the variety of environmental conditions and the analysis of the wave field making use of synthetic aperture radar images of the sea surface. Making use of quasi-linear inversion scheme (Krogstad et al, 1994) the wave field at both sides of the atmospheric fronts are analyzed. Limitations of the quasi-linear scheme being used in association with the full non-linear behavior of the SAR imaging process are recognized, nevertheless results are promising and an extensive assessment of the method is carried out with the use of several SAR images acquired during the various months sea trials in the Gulf of Mexico. Furthermore, the inversion to retrieve ocean wave spectra is assessed taking into account some spectral features such as directional spread and the presence of more than one wave systems.

Introduction.
Air-sea interaction studies represent a key component of CIGoM, the National Consortium for scientific research, technology integration and consulting services, specialized in multidisciplinary projects to assess and manage environmental impacts caused by the oil and gas industry, in the marine ecosystems of the Gulf of Mexico. As part of CIGoM buoy network, Oceanography and Marine Meteorology Buoys (BOMM for Spanish acronyme) were developed, built, integrated and deployed in the Gulf of Mexico, between 2016 and 2019. This type of buoys is similar to Air-Sea Interaction Spar (ASIS) buoys already deployed for previous studies (Graber, et al., 2000; Ocampo-Torres et al., 2011).
Direct measurements at sea are essential to improve our knowledge of air-sea interaction processes, which play a key role in determining the sea state and weather and influencing our planet climate and its changes. The description of waves through directional wave spectrum is essential and we aim to establish the best relation with momentum and energy fluxes between ocean and atmosphere. Furthermore, our research is focused in non-equilibrium cases, when wind is varying, for instance, instead of dealing only with analysis of stationary and homogeneous forcing wind fields. Ultimately, improvements in our knowledge of upper ocean and lower atmosphere processes will lead us to implement better models with more precise parameterizations to be used to forecast weather and climate.

Direct measurements of relevant environmental and dynamical variables are required to be complemented with observations from a different points of view that can be achieved through remote sensing techniques. Synthetic aperture radar images of the sea surface are a proper example of information that can be used to retrieve ocean surface wave parameters and directional spectrum, as well as other wind field characteristics. Even more, SAR images would provide us with a synoptic view of the ocean surface in the area where field campaign measurements were acquired.
It is the purpose of this work to estimate directional wave spectra under non-stationary conditions in order to determine the waves effect on air-sea momentum transfer and the influence of Stokes drift in the upper ocean currents velocity. Spatial variability of the wave field is to be determined through SAR images in order to relate it to momentum fluxes behaviour, specially when non-homogeneous wind field is present. Furthermore, the inversion to retrieve ocean wave spectra is assessed taking into account some spectral features such as directional spread and the presence of more than one wave systems. The quasi-linear inversion scheme proposed originally by Krogstad et al. (1994) and used by Vachon et al (1994), is being considered in this work.

Field campaign.
As part of CIGoM oceanographic buoys network, BOMM1 (an oceanography and marine meteorology spar buoy) was deployed at 24o 36.20' N (see Fig. 1) and 96o 37.50' W (see Fig. 1), approximately 98 km offshore Tamaulipas coastline at an 840-m depth location. BOMM1 was operational recording gathered data onboard in solid state disks and transmitting real time hourly data from 18 July 2018 until 19 April 2019, when service vessel Bourbon Fulmar reported BOMM1 adrift and towed it to Tampico Port waterway entrance.

Figure 1. BOMM1 and tether buoy at Perdido region in the Gulf of Mexico.

During the BOMM1 operations period several SAR images were acquired in the area of interest as can be seen in Fig. 2, where time series of wind speed significant wave height are also shown. Atmospheric fronts were encountered when some of those images were acquired.

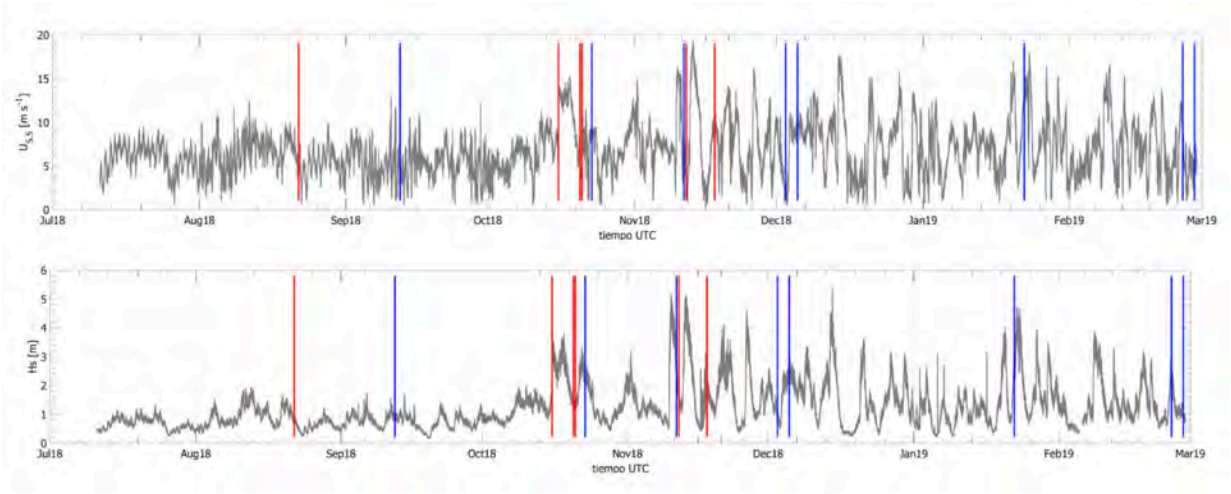

Figure 2. Wind speed and significant wave height from BOMM1 at Perdido region (Gulf of Mexico). Vertical lines indicate acquired SAR image (TerraSAR-X or TanDEM-X; Sentinel-1A or -1B).

Perspectives.
Detailed analysis of directional wave spectra are carried out and the advantages as well as the limitations in the cuasi-linear scheme to retrieve wave spectrum from SAR images are determined. Special cases are being considered such as this depicted in Fig 3.

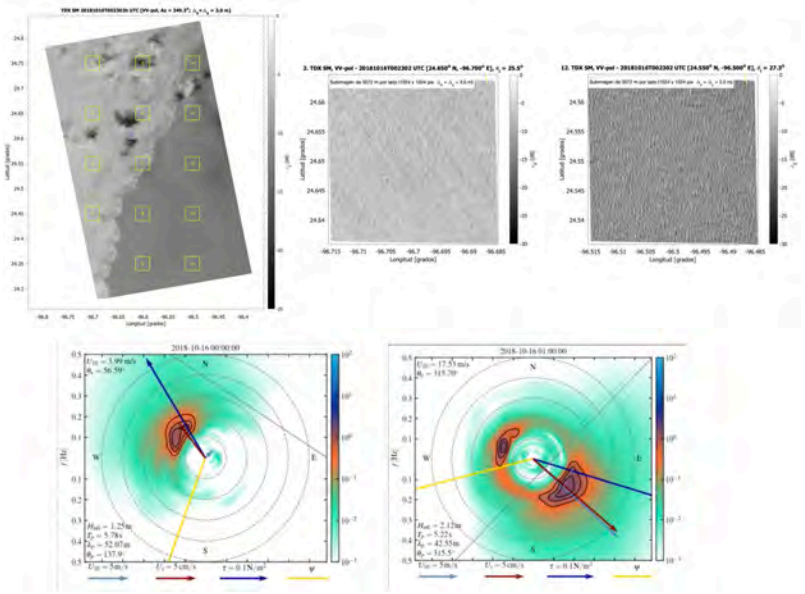

Figure 3. SAR image from Tandem-X SM 20181016T002302h UTC, and sub-images 2 and 12. Bottom plots are directional spectra from BOMM1 at 00h and 01h same day.

References.
-Graber, H. C., E. A. Terray, M. A. Donelan, W. M. Drennan, J. C. V. Leer, D. B. Peters (2000). ASIS-a new Air-Sea Interaction Spar buoy: design and performance at sea. J. Atmos. Ocean. Technol. 17:708-720.
-Krogstad, H. E., O. Samset, P. W. Vachon (1994). Generalizations of the non-linear ocean-SAR transform and a simplified SAR inversion algorithm, Atmosphere-Ocean, 32(1):61-82.
-Ocampo-Torres, F. J., H. García-Nava, R. Durazo, P. Osuna, G. M. Díaz Méndez, and H. C. Graber (2011). The INTOA Experiment: A study of ocean-atmosphere interactions under moderated to strong offshore winds and opposing swell conditions in the Gulf of Tehuantepec, Mexico. Bound.-Layer Meteorol., 138, 433-451.
-Vachon, P. W., H. E. Krogstad, J. S. Paterson, 1994. Airborne and spaceborne synthetic aperture radar observations of ocean waves, Atmosphere-Ocean, 32(1):83-112.

Wind-sea significant wave heights retrieval from Sentinel-1 with Deep Learning

Benchaabane Amine[1], Husson Romain[1], Mouche Alexis[2], Frederic Nouguier [2], Johnsen Harald[3]

1- Collecte Localisation Satellites (CLS), Brest, France
2- Institut français de recherche pour l'exploitation de la mer (IFREMER), Brest, France
3- NORCE, Bergen, Norway

Abstract

Wind blowing over the sea surface generates wind waves that grow in time and space by absorbing wind energy. Wind waves cover a wide range of wavelengths from a few centimeters to several hundred meters. The shortest centimetric waves are used as a proxy to measure the sea surface wind speed and the longest waves, often referred to as swell, can be estimated through a quasi-linear inversion to provide directional swell spectra [1]. As for the locally generated wind waves, a.k.a. wind-sea, the azimuthal cut-off limitation prevents from imaging this component of the wave spectrum. Yet, the azimuth cut-off is itself a signature of the wind sea component and similarly, other wind-sea related variables can be derived from the SAR measurements.

This paper focuses on a new method to estimate the wind-sea significant wave height (Hs) based on Sentinel-1 Synthetic Aperture Radar (SAR) Level-2 products using a deep-learning (DL) approach. The method was tested on data from Sentinel-1A and -1B Wave Mode (WV) acquisition for both incidences angle 23.8° (WV1) and 36.8° (WV2) collocated with global numerical wave spectra given by WAVEWATCH III (WW3) over the period from July 2021 to August 2022. We use a Deep Neural Networks (DNN) Regressor to relate the input geophysical waves parameters derived from SAR and the output WW3 wind waves Hs. As a first experimentation, the DNN performs well on the tested SAR dataset with R2 score more than 0.82 for WV1 data and more than 0.86 for WV2. The newly developed method extends the capability of SAR to estimate extreme Hs wind-sea (above 5 m) which are almost difficult to estimate otherwise due to the azimuth cut-off limitation. For this work, we also address the problem that machine learning models suffer from, namely class imbalance, i.e., when the distribution of wind-sea Hs is skewed, resulting in a disproportionate number of observations over the different Hs ranges. Synthetic data are generated and used in such situations to balance the under-representation of extreme wind-sea Hs and to train models able to better generalize real wave observations.

Keywords: SAR wave spectrum, wind waves, Deep Learning, SAR wind speed, wave age, azimuth cut off.

1. State of the art

Wind waves are surface waves that derive their energy and their geophysical properties from wind blowing over the sea surface. However, the local wind forcing itself is not sufficient to define the local wave properties. While the swell component can be rather well imaged and then estimated by SAR instrument thanks to its quasi-linear properties, the wind-sea part presents more complex non-linearities and are only partially or totally removed from the SAR spectral signature. SAR-derived measurements are therefore difficult to use given the partial and complex spectral coverage of the wind waves. Nevertheless, some initiatives have shown the possibility to derive more exhaustive description of the ocean state, estimating the significant wave height, comparable to altimeters [2], [3], [4]. Similarly in this study, we attempt to estimate the wind-sea component from the SAR measurements even if it is not well imaged by the instrument. Yet, wind-sea component impacts the SAR spectral measurements and some SAR-derived parameters such as the sea surface wind, the azimuth cut-off, the wave age and the IMACS are closely related to it and can be used as proxies to estimate its contribution [5], [6]. The developed methodology is compared to the one currently used to produce the L2 OCN products [7], based on ENVISAT-inherited empirical relationship between SAR-derived wind speed and azimuth cut-off and WW3 wind sea Hs.

2. Data and Methods

a. Data description

The dataset consists in collocations between S1 wave spectra measurements and geophysical parameters derived from the SAR and WW3 numerical wave model outputs over the period from July 2021 to August 2022. On the SAR side, we only consider data acquired from Sentinel-1A with the wave mode acquisition (WV1 and WV2) in VV polarization.

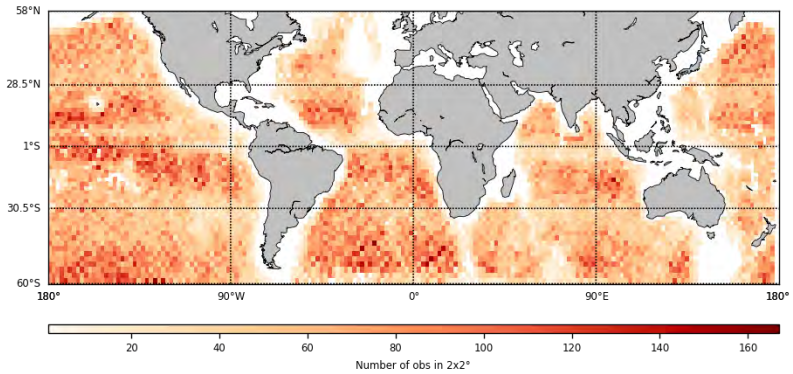

Figure 1: Density map for co-located data between the WV1 SAR acquisitions and WW3 over the period from July 2021 to August 2022.

Figure 1 illustrates the density maps of collocated data for WV1 (similar for WV2). The full dataset includes more than 348 000 pairs.

For this study, several variables were extracted from ESA-Copernicus WV level 2 (L2 OCN) products identified as potential features that are expected to explain the wind-sea significant wave height variability. These variables include both geophysical information such as wind speed and direction and other acquisition information like incidence angle and azimuth cut-off. The list of these variables is shown in Table 1. A whole feature engineering pipeline has been put in place to prepare data for learning.

SAR Features
Signal to Noise Ratio (SNR)
Normalized Radar Cross Section (NRCS)
Azimuth Cut-off
SAR wind speed
SAR wind direction in sensor convention
SAR wave spectrum Kurtosis
SAR wave spectrum Skewness
SAR wave normalized variance
Incidence angle of acquisition

Table 1: SAR features used as inputs of the DNN-Regressor.

As for the target, it is defined as the wind-sea Hs estimated from the WW3 spectra. To get such variables, the first step is to extract the wind sea spectra from the WW3 spectra collocated with the SAR, then we estimate the associated Hs. The distribution of this computed variable, presented by a range of Hs for both collocated WV1 and WV2 dataset, is shown in Figure 2.

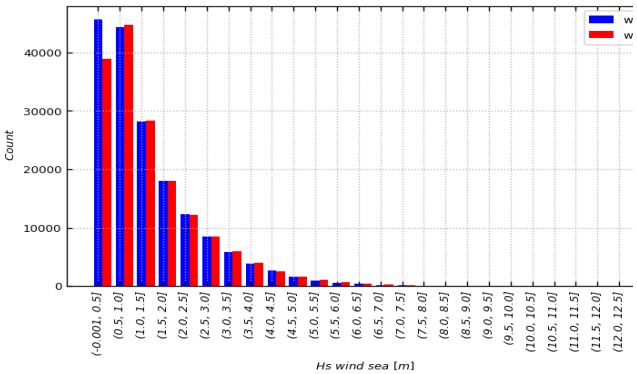

Figure 2 : Wind-sea Hs count by 0.5m bins for WV1 and WV2.

The obtained distribution of wind-sea Hs is not uniform and contains extreme values that are poorly represented. Initially, this database is used to define a baseline of learning performances. Then, it is than submitted to a specific balancing task to obtain a more homogeneous distribution of wind-sea Hs and to perform model accuracy. As for each machine learning model, the database was divided into three parts: a training data set (~122200 pairs), a validation data set (~26000 pairs) and a test data set (~26000 pairs).

b. Method

The first tests are performed using a simple deep learning architecture defined by a Deep Networks Regressor (DNN-Regressor). The SAR features are fed into 5 dense layers of 128,64,32,16,8 units respectively with Rectified Linear Unit (ReLU) as an activation function. Between each two hidden layers a Batch Normalization was applied to perform training. Finally, the wind-sea Hs prediction is performed by an output layer with linear activation function. This model is trained to minimize the mean squared error (MSE) using Adam optimizer with a batch size of 150 samples. A specific learning rate decay was applied to improve the optimization. Training was stopped when the validation loss did not improve after 10 epochs to avoid overfitting. The architecture, learning rate, early stopping and batch size was optimized by tuning and only for WV1. The same hyperparameters were used to train WV2 model to investigate the incidence angle sensitivity.

Metric	WV1	WV2
Bias	-0.02 m	-0.04 m
Standard deviation	0.49 m	0.45 m
Correlation	0.92	0.93
R2 score	0.83	0.86
RMSE	0.49 m	0.45 m

Table 2: Statistics of model's performances for WV1 and WV2.

3. Results and perspectives

a. Results

The first results obtained are very promising and the two models obtained for WV1 and WV2 generalize well on the test data (Figure 3). The performances indicators are displayed in Table 2. First, we notice that the models suffer a little from high wind-sea Hs values by underestimated them. This is starting to appear from Hs > 4m for WV1 and Hs > 2m for WV2. This finding is expected because this model has not been tuned as the case of WV1. Therefore, this confirms implicitly that there is a sensitivity to incidence and that the two modes should be treated separately since the acquisition noise differs according to incidence.

The extreme wind-sea Hs under-estimation is also explainable since they are poorly represented in the training distribution as introduced earlier. Work is in progress to balance the training data set for all ranges of wind-sea Hs.

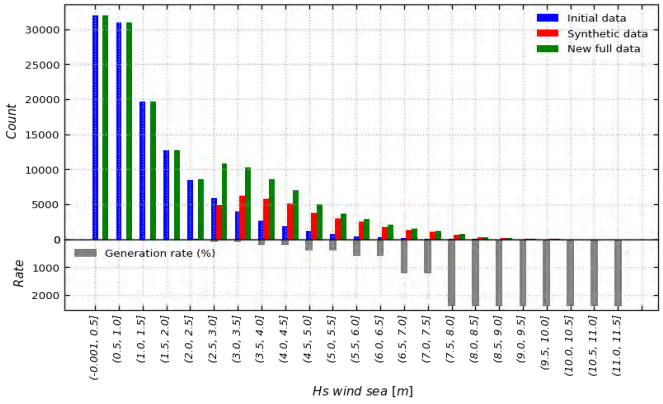

Figure 4: Histogram of wind-sea Hs for initial and synthetic datasets.

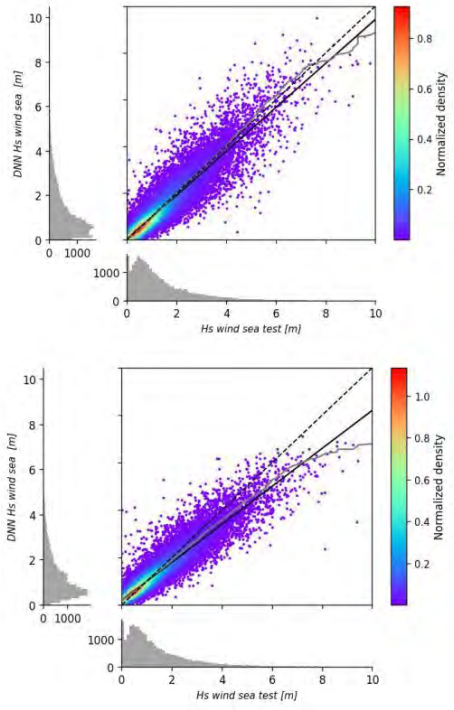

Figure 3: Scatterplot of wind-sea Hs estimated by the DNN-Regressor model against the WW3 target.

b. Perspectives

We have created a dataset of over 348000 collocations between SAR features, derived wind-sea Hs from WW3 and used it to train a DNN-Regressor model that predicts wind-sea Hs from SAR features. The obtained models underestimate extreme Hs which is tackled by a synthetic data generation to balance the training dataset. Figure 4 illustrates the generative potential of extreme Hs for the case of WV1 under validation: red bars indicate synthetic data; blue bars indicate initial data; green bars indicate assembled data and gray bars for rate of generation. To improve the performance of the two models, new variables will be introduced such as IMACS [5]. Then, with this new enriched and balanced database, the architectures will be redesigned to consider the sparse and dense nature of each learning SAR feature. The relative contribution of these chosen input features will be investigated to quantify their relative importance. The estimation of a SAR-derived wind-sea component, together with the already existing swell and "total significant wave height" paves the way for complete SAR-derived directional wave spectra.

4. References

[1] Engen, G., and H. Johnsen. "SAR-Ocean Wave Inversion Using Image Cross Spectra." IEEE Transactions on Geoscience and Remote Sensing 33, no. 4 (1995): 1047–56.

[2] Li, X. M., S. Lehner, and M. X. He. "Ocean Wave Measurements Based on Satellite Synthetic Aperture Radar (SAR) and Numerical Wave Model (WAM) Data – Extreme Sea State and Cross Sea Analysis." International Journal of Remote Sensing 29, no. 21 (2008): 6403–16. .

[3] Pleskachevsky, Andrey, Sven Jacobsen, Björn Tings, and Egbert Schwarz. "Estimation of Sea State from Sentinel-1 Synthetic Aperture Radar Imagery for Maritime Situation Awareness." International Journal of Remote Sensing 40, no. 11 (June 3, 2019): 4104–42. https://doi.org/10.1080/01431161.2018.1558377.

[4] Quach, Brandon, Yannik Glaser, Justin Edward Stopa, Alexis Aurélien Mouche, and Peter Sadowski. "Deep Learning for Predicting Significant Wave Height From Synthetic Aperture Radar." IEEE Transactions on Geoscience and Remote Sensing, 2020.

[5] Nilsen, Vegard, Geir Engen, and Harald Johnsen. "A Novel Approach to SAR Ocean Wind Retrieval." IEEE Transactions on Geoscience and Remote Sensing PP (May 6, 2019): 1–10. https://doi.org/10.1109/TGRS.2019.2909838.

[6] Li, H., Chapron, B., Mouche, A. A., & Stopa, J. E. (2019). A new ocean SAR cross-spectral parameter: Definition and directional property using the global Sentinel-1 measurements. Journal of Geophysical Research: Oceans, 124, 1566–1577. https://doi.org/10.1029/2018JC014638.

[7] Johnsen, Harald, Romain Husson, Benchaabane Amine, Pauline Vincent, and Guillaume Hajduch. "Sentinel-1 Ocean Swell Wave Spectra (OSW) ATBD - Sentinel Online.", S1-TN-NRT-52-7450, v1.5, 10 October 2022. shorturl.at/pqxX6

Ocean wave mapping by SAR: Numerical and theoretical perspectives

Frédéric Nouguier[1*], Alexis Mouche[1], Bertrand Chapron[1], Marcel Kleinherenbrink[3]

1 Introduction

Hasselmann and Hasselmann [2] and Krogstadt [3] paved the way of understanding the SAR imaging process of ocean waves by deriving the basic theoretical equations. Later on, Engen [1] reformulated them using characteristic functions and provided a stand alone methodology to remove wave propagation ambiguity using the evaluation of cross-spectra analysis between sublooks in azimuth. This technique elaborated during ESA ERS time was then applied on ENVISAT - ASAR acquisitions and is still currently applied for wave retrieval on Sentinel-1 acquisition over ocean without major evolution since the first derivation of the algorithm. Ocean wave spectrum retrieval from SAR observation remains a challenge due to its complex imaging mechanism and existing operational algorithms mainly rely on the exploitation of the so-called theoretical close-form. This close-form equation is a theoretical equation mapping the ocean wave spectrum into the back-scattered intensity SAR spectrum. Even if this equation exhibits most of the SAR imaging non-linear aspects (velocity bunching, azimuthal cut-off, ...), it still misses some key features that have not been correctly understood up to now. One striking example is that cross-spectra phase predicted by theoretical approach should be close to the waves dispersion relationship which is the dominant apparent displacement on the surface. Data analysis reveals that this wave dispersion relationship is strongly altered by non-linear imaging process of the SAR and can not be correctly predicted with the currently used close-form.

Since the first attempts to derive wave spectrum from SAR observations, new techniques have been developed to model and understand the complex imaging process of waves by SAR. Computational capabilities have strongly evolved and opened new perspectives in simulating the complete chain of a SAR acquisitions on realistic synthetic ocean scene. Coupled with a revisit of the assumptions of the close-form derivations and foreseen neural-network methodologies, the authors developed a coherent framework to better understand and model ocean wave spectrum mapping by existing Synthetic Aperture Radar systems and support the development of new concept missions.

To exemplify new perspectives offered by the aforementioned techniques, the authors selected some examples and the corresponding illustrations where they reveal themselves to provide interesting insights on the imaging process. In the coming years, it is planned to revisit the existing Sentinel-1 wave inversion algorithms and take benefit of these new techniques to better understand wave mapping by new coming SAR missions such as Harmony constellation based on innovative bistatic SAR configuration or Rose-L SAR operating at L band frequency.

2 The case of reversed swell propagation direction on Sentinel-1

Since the pioneer work of Engen et al. [1], it is commonly accepted that the sign of the imaginary part of the cross-spectrum computed between two looks extracted from Single Look Complex SAR data is directly linked to the ocean wave direction propagation. The wave displacement between the two looks (different acquisition time) is indeed assumed to be responsible for the non-vanishing phase of cross-spectrum between looks extracted from the azimuth Doppler Bandwidth. The resulting sign of the complex cross-spectrum is thus usually used to remove the ambiguity of the wave direction propagation in wave retrieval algorithms.

Figure 1 shows a succession of six Sentinel-1 vignettes (WM1) acquisitions on July 6th 2020 between 15h08m14s and 15h10m40s in the Indian ocean where a long swell is captured by the sensor. In this specific case, the swell propagates towards the East direction. In this low latitudes part of Sentinel-1 orbit, the SAR range direction is rapidly changing relatively to the swell direction of propagation. While the swell direction is located slightly below the range direction on the first vignette (horizontal axis), it is located above the range axis on the last acquired vignette with a continuous variation during the intermediate acquisitions.

Figures 2 show the imaginary part of the cross-spectrum for each acquisition. As observed, the sign of the swell peak energy is changing along the orbit (brown and purple colors are of opposite signs) while a constant positive sign is expected due to the established easterly swell system. At the middle acquisition (vignette #4 - 15h09m42s), the energy of the cross-spectrum is even split by the range axis in two parts with opposite signs. The theoretical close-form equation is unable to reproduce the change of sign in the cross-spectrum revealing some unexpected limitation of the theoretical approach. Several legitimate assumptions could be raised to explain the observed discrepancies such as the inaccuracy of the wave model compared to the true ground truth or the limiting assumption of the analytical approach such as the non-Gaussian nature of the ocean waves or a different look energy weighting leading to an inaccurate estimation of the separation time between looks. However, for the presented case, none of these assumptions explain the discrepancies and will be illustrated hereafter.

In real data analysis, it is usually very hard to distinguish the reasons of this apparent discrepancies between the SAR measurements and the sea-state conditions. On the contrary, numerical simulations can be of great help in doing such parameters analysis thanks to the ability of disabling other possible effects. In this case, we relied on the "Remote Sensing Simulation from Space" (R3S) numerical model to explore the possible parameters that could enter into the aforementioned problematic case. This numerical model is a brute force simulation

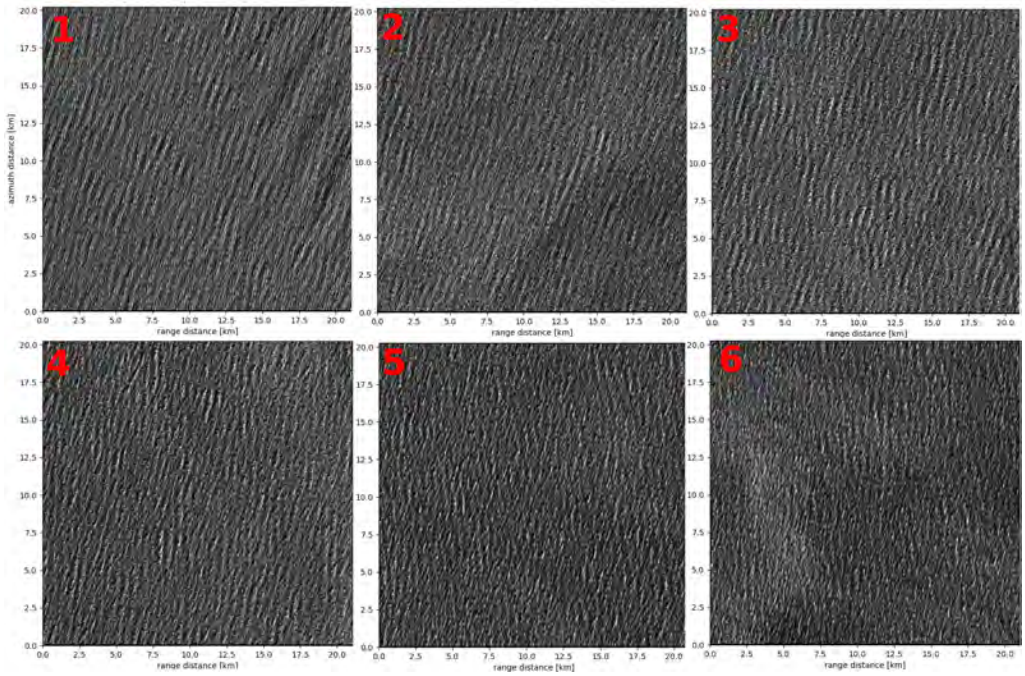

Figure 1: Succession of six Sentinel-1A vignettes (WM1) acquired in indian ocean. Vignette #1 was acquired at latitude -56.54 degree and vignette #6 at -48.4 deg. The same long swell (≈500m) is observed on all vignettes and its direction is slowing crossing the SAR range direction (horizontal axis).

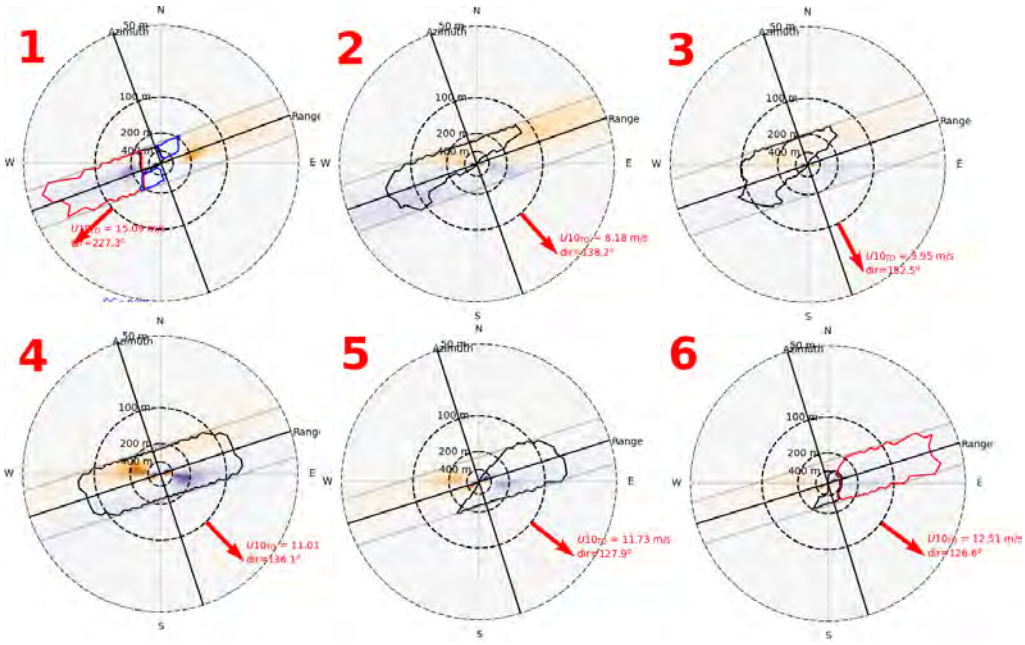

Figure 2: Imaginary part of the cross-spectra (between looks). Brown and purple colors are of opposite sign.. The sign of the energy corresponding to the observed swell around 500 m wavelength is changing from vignette #1 to vignette #6. Cross-spectrum #4 exhibits an energy blob splitted around the range axis with parts of opposite signs.

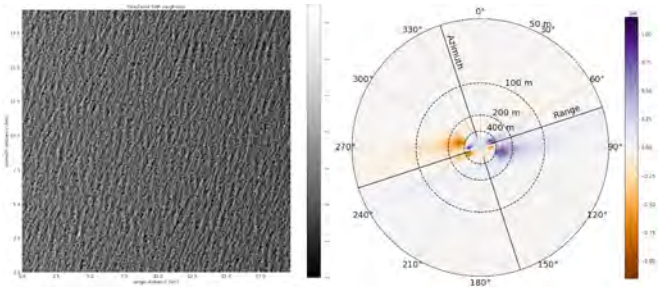

Figure 3: R3S numerical simulation. Left panel is synthetic Sentinel-1 vignette corresponding to vignette #4 of figure 1 and rigth panel is the corresponding imaginary part of cross-spectrum. On both real and simulated cross-spectrum, we can observe the energy slpitting over the range axis with opposite signs on each side of it.

intending to model as much physically as possible all the elements of the SAR observation chain of an ocean scene (ocean wave properties, scattering mechanisms of rough surface, satellite platform dynamics, antenna, SAR processing, ...).

Figure 3, left panel, shows the simulated imagette which was generated using the co-localized Wave Watch III wave model and Sentinel-1 configuration corresponding to the acquisition date of July 6th 2020 15h0942 (vignette #4). The resulting imaginary cross-spectrum (right panel) exhibits the same sign inversion and splitting around the range axis on the simulated data supporting the fact that non-simulated effects (such as nonlinear wave statistics, ...) are not responsible of it. To push further the analysis, another simulation (not shown here) was processed but with a "frozen swell" meaning that the swell propagation was disabled during the SAR acquisition simulation. While it was expected to have no imaginary part in the cross-spectrum (because of the absence of ocean movement), a significant signal in the imaginary part was found suggesting that other phenomenon was responsible for some phase in the cross-spectrum.

A joint theoretical and data analysis on both real and simulated data revealed that the small variation of the SAR observing geometry during the acquisition time has a significant contribution on the sub-look cross-spectra phase. This have an impact of the swell system signature and shall not be neglected when interpreting the cross-spectra for swell propagation ambiguity removal or, more generally, on phase exploitation strategies. A simple theoretical model has been developed to demonstrate the strong impact of this phenomenon on the cross-spectrum derivation and more specifically on its phase. We will show that this effect is linked to an important geophysical term that has been omitted in the classical literature leading to an incomplete SAR closed-form equation and, in turn to possible caveats in the operational wave inversion algorithm applied to Sentinel-1 products. In fact, considering this term is also critical to anticipate accurately future SAR missions performances

3 ESA Earth Explorer 10 - Harmony, understanding bistatic SAR

The European Space Agency has selected Harmony as tenth Earth Explorer Mission. Harmony is a constellation of two companion satellites around Sentinel-1 platform. Among other capabilities, the two Harmony satellites will provide interferometric measurements and bi-static SAR acquisitions. This is a unique opportunity to better map ocean surface dynamics thanks to its enhanced azimuthal diversity. Based on the existing mono-static theoretical close-form, efforts have already been done by the Harmony scientific team to extend it to the bi-static case. However, the basic assumptions are still questionable and their validation with respect to numerical simulations highly desirable. The authors developed joint theoretical and numerical approaches to better understand the ocean wave mapping with bi-static SAR and started to explore the benefits of this configuration comparatively to the mono-static case. Preliminary studies show very encouraging results an reveal new possible strategies for mitigating SAR undesired effects such as azimuthal cut-off.

4 ESA SARWAVE project - sea state retrieval from Sentinel-1 large swath acquisitions

The scientific teams involved in SARWAVE project (Ifremer-LOPS, Isardsat, TU Delft, ODL, DLR, CEOS-UP) proposed to develop and validate novel methods for sea state retrieval from Sentinel-1 Interferometric Wide Swath (IWS) products. This project, recently selected by ESA, started some month ago and recent results will be presented during a dedicated session of the Seasar 2023 workshop in Svalbard. Some of the methodologies presented in this abstract will be used in the algorithms development workpackage of the SARWAVE project. The latter is indeed an excellent opportunity to take benefit from the past and new research outputs dedicated to sea state retrieval from remote sensors (SAR, optical, altimeter, ...) and to exemplify the newly developed algorithm and produced sea-state L2 products over a one-year duration data-set of Sentinel-1 IWS acquisitions over European seas.

References

[1] G. Engen and H. Johnsen. Sar-ocean wave inversion using image cross spectra. *IEEE transactions on geoscience and remote sensing*, 33(4):1047–1056, 1995.

[2] K. Hasselmann and S. Hasselmann. On the nonlinear mapping of an ocean wave spectrum into a synthetic aperture radar image spectrum and its inversion. *Journal of Geophysical Research: Oceans*, 96(C6):10713–10729, 1991.

[3] H. E. Krogstad. A simple derivation of hasselmann's nonlinear ocean-synthetic aperture radar transform. *Journal of Geophysical Research: Oceans*, 97(C2):2421–2425, 1992.

On The Complementary Assimilation Of SAR And SWIM Wave Spectra In The CMEMS Global Wave System

Lotfi Aouf[1], Danièle Hauser[2], Fabrice Collard[3], Bertrand Chapron[4]

[1]Meteo France, France; [2]LATMOS/CNRS; [3]Ocean Data Lab; [4]IFREMER

corresponding author : lotfi.aouf@meteo.fr

Directional wave observations from satellite missions play a crucial role to improve integrated sea state parameters, particularly swell dominant ones. The global CMEMS wave system is using in operations (Near Real Time) both SAR wave spectra from Sentinel-1 and SWIM wave spectra from CFOSAT. SAR instrument covers ranges of waves from roughly 200 m to 800 m of wavelength, while SWIM detects shorter scale of waves starting from 60 m to 500 m of wavelength. The objective of this work is to examine the combined assimilation of wave data from CFOSAT and Sentinel-1 missions. We investigated particularly the impact of assimilating directional wave spectra in unlimited fetch conditions such as in the Southern Ocean. Two years of operational wave products from MFWAM model will be used in the analysis and a control model run without assimilation will be performed. Particular attention will be considered to examine the underestimation of spectral wave energy from SAR for high wave height generated in severe storms in austral winter. Figure 1 shows the mean difference of Significant Wave Height (SWH) from model runs with assimilation of wave spectra from SAR of Sentinel-1 and SWIM of CFOSAT. This clearly indicates the underestimation of SWH from the assimilation of SAR wave spectra in Southern Ocean dominated by shorter long waves still wind dependent because of unlimited fetch conditions. In these conditions SWIM can capture correctly such wind-wave of wavelengths ranging between 50 to 150 m of wavelength. The overestimation of SWH from the assimilation of SAR spectra as illustrated by in reddish color in figure 1, reveals the limitation of SWIM to capture very long waves exceeding 500 m of wavelength, typically in west coast of central America and tropical ocean regions.

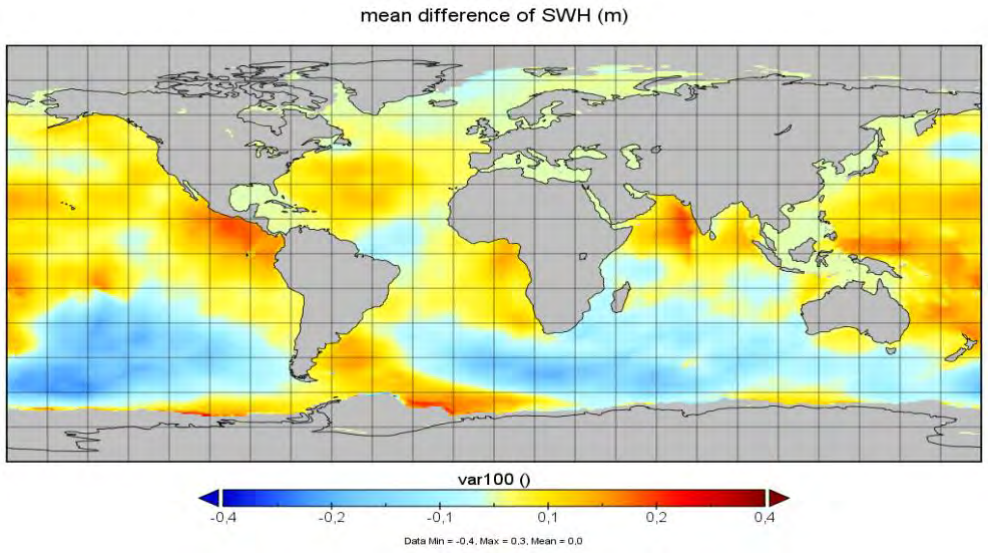

Figure 1 : Mean difference of SWH from MFWAM model runs A and B for the period of May 2020. Run A is with the assimilation of SAR wave spectra, while run B is with the assimilation of SWIM wave spectra.

The validation of model outputs has been performed with independent wave data from altimetry and also integrated sea state parameters provided by available drifting buoys. Figure 2 shows here the SWH bias maps in comparison with altimeters focused on Southern Ocean. We can easily see that the assimilation of SWIM wave spectra better reduces the bias in comparison with the assimilation of SAR wave spectra.

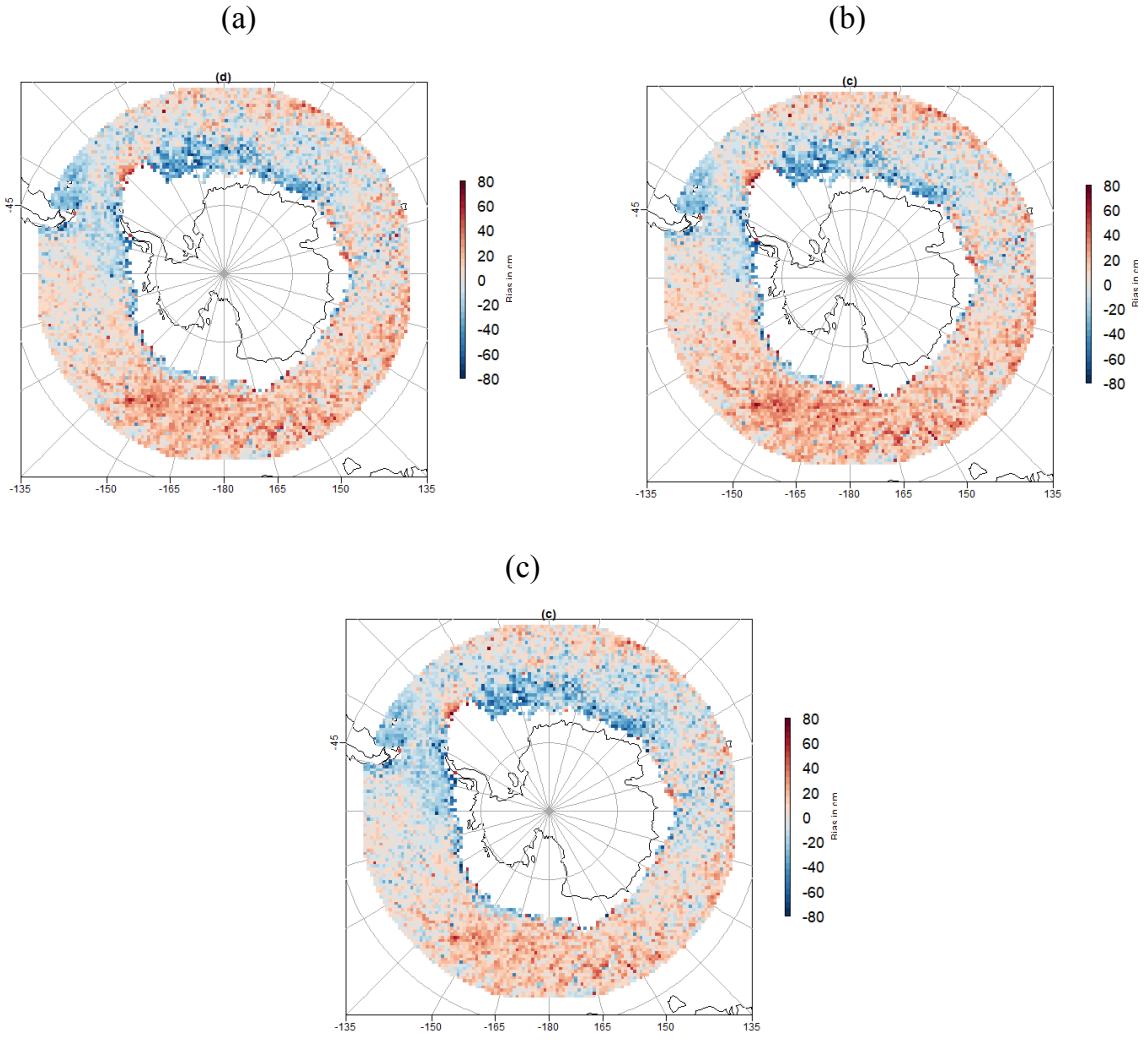

Figure 2 : bias maps of SWH from MFWAM model runs in comparison with altimeters (Jason-3, Saral and S3) for the period from May-August 2020. (a), (b) and (c) stand for runs without assimilation, with assimilation of SAR spectra only, and with assimilation of SWIM spectra only, respectively.

The results show the relevance of using jointly SAR and SWIM wave spectra to take benefits from the best capturing of different scales of waves. The SWIM wave spectra can also be used to improve or calibrate SAR wave spectra in storm conditions of Southern ocean. We also examined the impact of using upgraded level 2 retrieval algorithms for CFOSAT on the wave forecast. In

other respects we investigated the impact of using multi-mission directional wave observations on coupling parameters with ocean circulation model.

Further results will be presented in the final paper.

Unlocking the Potential of Distributed SwarmSAR for High-resolution Imaging of Ocean Waves

M. M. M. Amir[1], A. Bogoni[1], P. L. Dekker[2]

[1]TeCIP Institute, Scuola Superiore Sant'Anna, Pisa, Italy
email: {malikmuhammadharis.amir, antonella.bogoni}@santannapisa.it

[2]Delft University of Technology, Delft, The Netherlands
email: f.lopezdekker@tudelft.nl

Abstract: *The paper presents a novel concept of swarmSAR for improving azimuth resolution of decorrelating targets i.e., ocean surface in SAR imaging. SwarmSAR uses a swarm of small satellites to form a larger synthetic aperture, enabling higher resolution compared to traditional SAR. Results of the study show that swarmSAR offers a significant improvement in azimuth resolution compared to traditional SAR and provide insight into the limitations and future potentials. The paper suggests that this new technique has the potential to advance a range of applications, including environmental modelling, remote sensing, and oceanography. The study sheds light on the possibilities of using swarmSAR to tackle long-standing challenge in SAR imaging and promises to open up new avenues for research in this field.*

Introduction:

Synthetic Aperture Radar (SAR) is a highly sophisticated remote sensing technology that plays a vital role in mapping the earth's surface and obtaining detailed images. Its application spans across the fields, including geology, hydrology, meteorology, oceanography, and others [1]. SARs exploit the satellite movement to synthesize a long aperture antenna, observing the area of interest, and collecting radar echoes of the area while moving over it, to attain high azimuth resolution, which would otherwise need an antenna with an aperture of several kilometre.

The ability of SAR to provide high-resolution images is a result of coherent integration of radar returns during the time of flight of a radar pulse along its path. However, the quality of these images can be impacted by various factors, including the aperture length. The amount of information collected by the radar is directly proportional to the aperture length, and hence, the aperture length is a critical factor affecting the resolution and accuracy of SAR images. The decorrelating nature of the target, because of the changes in ground scene during the flight duration can limit the aperture length. On land, the decorrelation is frequently not an issue because the ground is not changing during the period when SAR data is being gathered. Oceans, on the other hand, vary quickly over the duration of flight time, causing severe decorrelations, and limiting the permitted synthetic aperture length, and as a result affecting the azimuth resolution and SAR image quality [2].

To address these limitations, swarmSAR concept has emerged as a promising solution. The approach involves using multiple antennas in a close formation cooperating in a multiple-input multiple-output (MIMO) fashion. The idea behind SwarmSAR is to install several nodes, each of which has a basic imaging capacity that can be used independently. However, when they work together, they increase azimuth resolution and imaging capabilities [3].

In this paper, we address the swarmSAR concept for decorrelating target, to enhance the azimuth resolution. First, we will present the signal model, which will be followed by the discussion of preliminary results, and finally conclusion. The detailed results will be presented in the final version of the paper.

Signal Model:

Let us consider a decorrelating point target, with point target amplitude A and a variable decorrelation amplitude A_d, having a correlation time $\tau_c \approx 3.29\,{}^{\lambda}/_{U}$, where U is the windspeed in this case we considered $U = 10\,{}^{m}/_{S}$ [4]. The total amplitude of decorrelating point target A_t, which is product of A and A_d. The decorrelating point target is illuminated by N phase centres. Let $\Phi_i(t, R)$ represent the phase history of i^{th} satellite, where $i = \{1, \dots, N\}$, t is the time and R is the range.

$$\Phi_i(t, R) = e^{-2k_0 R_i} \tag{1}$$

Where, $k_0 = {}^{2\pi}/_{\lambda}$, and R_i is the range history of i^{th} phase centre. The integration length is set according to the correlation time, i.e., $l_i \approx \tau_c . v_{sc}$, where v_{sc} is satellite velocity. The monostatic received signal based on the phase history of the i^{th} phase centre can be written as:

$$s_{r,i}(\Phi) = A_t . e^{j\Phi_i} \tag{2}$$

Once the azimuth direction of the target is estimated, the signal from each satellite can be compressed in azimuth direction, this can be performed by using Fourier Transform (FT).

$$S_{r,i}(\Phi) = \mathcal{F}\{ s_{r,i}(\Phi)\} \tag{3}$$

The compressed signals from different phase centres can then be combined and passed through the matched filter to generate azimuth compressed SAR image.

$$S = \sum_{i=1}^{N} S_{r,i}(\Phi) \tag{4}$$

Final SAR image can be expressed as;

$$I = \mathcal{F}^{-1}(S * M) \tag{5}$$

Here, M is the matched filter and $\mathcal{F}^{-1}$ represent inverse FT.

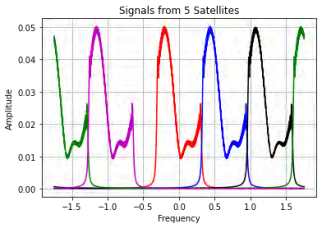

Figure 1 – Frequency Response for five satellites with the separation of 4 km between them

Table 1 – Simulation Parameters

Parameter	Value
Satellites Height	693 km
Satellites Speed	7000 m/s
Operating Frequency	2.9 GHz (S-Band)
PRF	4000
Number of Satellites	5

Results:

Before discussing the azimuth resolved images using monostatic and swarmSAR concept, let us discuss frequency response of signal from five satellites and simulation parameters, which are shown in figure 1 and table 1 respectively. Note that, since aperture length is same as the satellite separation, the frequency responses for different satellites is perfectly aligned together causing no overlapping or gaps between different apertures, and hence by combining all the apertures together, we are able to create a full long aperture, and hence increasing azimuth resolution. However, in a close to reality scenario, when the apertures are not perfectly aligned with each other, this will cause the frequency response to overlap which due to insufficient cut-off can lead to azimuth ambiguities.

In figure 2a, the azimuth resolved image using a monostatic satellite is plotted for non-decorrelating (red curve) and decorrelating target (dashed blue curve). It is evident that azimuth resolution is downgraded when resolving decorrelating target using a standalone satellite. Figure 2(b-d) shows the comparison of azimuth resolved image for monostatic case (dashed red curve) and swarmSAR case (solid blue curve) for perfectly aligned apertures, overlapping apertures and, gapped apertures respectively. It is evident that perfectly aligned apertures enhance the azimuth resolution without adding signficant sidelobes, however, overlapping, and gapped apertures add significant sidelobes along with the enhance resolution, that is because of the frequency jumps which are caused when frequencies from two different apertures are mixed with each other. Note, the results presented in figure 2 are preliminary, which shows the potential of using this technique to enhance image quality of ocean surface using swarmSAR concept. The detailed results will be presented in the final version of paper, where we will present the method for mitigating the sidelobes and maintaining high resolution for generation high resolution images of ocean surfaces.

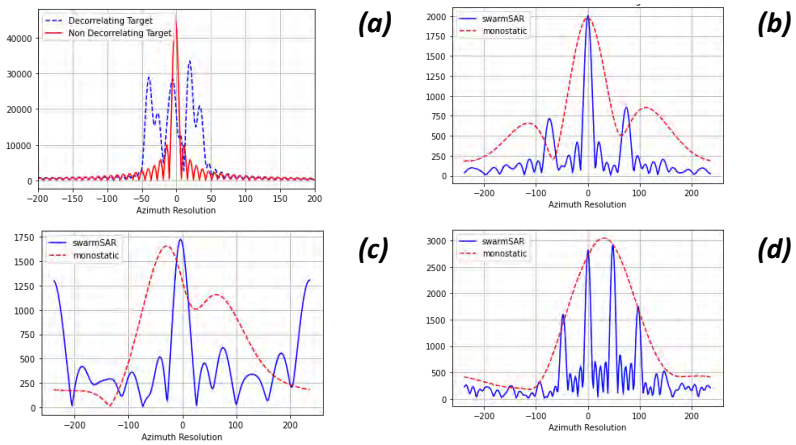

Figure 2* – Azimuth Resolved Image for decorrelating target *(a) Single Satellite, ***(b)*** Perfectly aligned swarmSAR configuration, ***(c)*** Overlapping swarmSAR configuration, ***(d)*** gapped aperture swarmSAR configuration

Conclusion:

In conclusion, the proposed concept of swarmSAR shows a great potential for improving azimuth resolution of decorrelating targets in SAR imaging, with results demonstrating its superiority over traditional SAR methods. The limitations and potentials of swarmSAR were analysed, providing a valuable information for further research. This study highlighted the significance of swarmSAR in advancing the capabilities of SAR systems.

Acknowledgement:

This paper has been partially funded under the COSMOS project (FISR2019_03476).

References:

[1] D. Amitrano *et al.*, 'Earth Environmental Monitoring Using Multi-Temporal Synthetic Aperture Radar: A Critical Review of Selected Applications', *Remote Sens.*, vol. 13, no. 4, Art. no. 4, Jan. 2021, doi: 10.3390/rs13040604.

[2] A. Leanza, A. Monti Guarnieri, A. Recchia, A. Broquetas Ibars, and J. Ruiz Rodon, 'Decorrelating Clutter Statistics for Long Integration Time SAR Imaging', vol. 731, p. 31, May 2015.

[3] L. Iannini, P. Lopez-Dekker, and P. Hoogeboom, 'A Highly Flexible and Scalable S-band SwarmSAR from Very Simple Nodes', in *2020 IEEE Radar Conference (RadarConf20)*, Sep. 2020, pp. 1–6. doi: 10.1109/RadarConf2043947.2020.9266527.

[4] S. Wollstadt, P. López-Dekker, F. De Zan, and M. Younis, 'Design Principles and Considerations for Spaceborne ATI SAR-Based Observations of Ocean Surface Velocity Vectors', *IEEE Trans. Geosci. Remote Sens.*, vol. 55, no. 8, pp. 4500–4519, Aug. 2017, doi: 10.1109/TGRS.2017.2692880.

Tropical cyclones generated waves: processes and contribution of a multi-platform approach

Clément Pouplin, Alexis Mouche, Bertrand Chapron, Maria Yurovskaya, Jean-François Filipot

January 2023

Abstract

This study assesses the potential of using jointly several wave observations sources in order to describe the properties of the wave field induced by a tropical cyclone. To this aim, wave measurements inside and outside the TC vortex are considered. A particular attention is paid on both the synergy and the consistency between the different data sources. A specific filtering is proposed for each of them to deal with their limitations and to finally gather only valid data into a single multi-mission product. This product is then used to discuss the performances of tropical cyclone dedicated parametric wave models. In this cocktail of data, it is shown that both Sentinel-1 SAR acquisitions in Wave and Wide Swath modes can play a complementary role.

1 Introduction

Tropical cyclones (TC) can generate long and energetic waves whose growth processes are complex. In the last decades, sensors dedicated to waves measurements, embedded on aircrafts, satellites and buoys allowed to acquire wind and waves data in such extreme meteorological events.

Airborne sensors sample the waves inside the TC vortex from the center up to the outer core with a high resolution (kilometer) (1). However most of the flights are limited to USA waters and only the Wide Swath Radar Altimeter provides directional wave spectra.

Several studies have used data from wave dedicated sensors embedded onboard satellites in the case of TCs. Altimeter is certainly the most used but it only provides significant wave height and wind speed (8). SAR is also promising to characterize the 2D wave spectrum but its limitations when observing severe sea state still hampers for a seamless and routine usage of this sensor (3). However, Sentinel-1 wide swath mode and the 5 rotating beams of SWIM onboard CFOSAT should help monitoring the wave field variability in the TC vortex.

Wave buoys, such as SOFAR ocean drifters and NDBC network, could allow to revisit the pioneer experiment conducted in 1962, when wave-buoy measurements had been used to track storm (including TC) induced swell systems across the pacific ocean (9).

This study proposes to apply this technique in the particular case of TC, combining several sources of data. The method is explained in section 2 while the results are presented in section 3, before a discussion in section 4.

2 Method

In this study, we rely on wave measurements from Sentinel-1 SAR, CFOSAT SWIM, SOFAR Spotter and NDBC wave-buoys to characterize TC induced wave fields. As wave measurements inside TCs are not numerous and of poor quality, measurements outside TCs are considered to extend the so-called back propagation technique to the case of TC waves - the measurements inside are left for another study. After a quality-filtering step depending on the measurement source, the past trajectory of wave groups is computed assuming those propagate along great circles without any impact of current and bathymetry on their wavelength and direction. Wave measurements whose back propagation trajectory do not cross the TC, or crossed the TC but were generated by another meteorological event are eliminated. Wave measurements are associated to their date and location of generation by the TC, and gathered into a multi-mission product. For more details on the method and other applications, the reader can refer to (9), (2) and (4).

3 Results

In this section, information included in the multi-sensor TC waves product in the case of TC Larry, North Atlantic, on 2021-09-09 at midnight, is analysed. On the map on figure 1 (right), all wave measurements generated by Larry at the selected date are scattered at their location, and their propagation trajectories from the cyclone to acquisition are plotted in color (color code represents days from 2021-09-09). In addition, the TC track is drawn in black. Each measurement is also scattered on one of 4 wave roses depending on the sensor (left). On these polar plots, the peak wavelength of measurements (distance to center of the rose) can be analysed as function of the direction of propagation with respect to TC direction (given by the polar angle). The multi-sensor wave rose (middle) is a superposition of the 4 individual wave roses on the top.

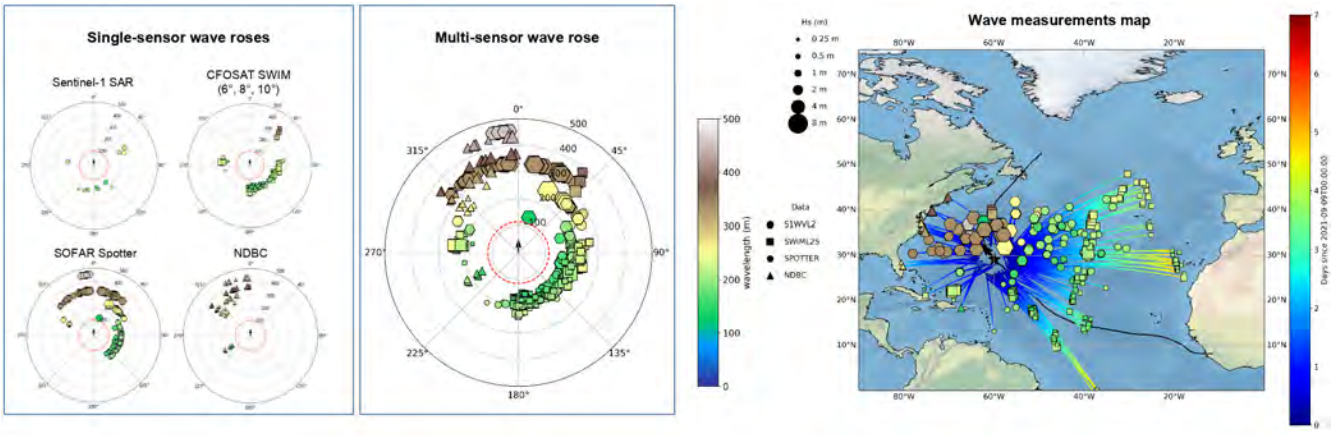

Figure 1: (Left) Wave roses for Tropical cyclone Larry on 2021-09-09 00:00:00, for each of the 4 different sensors. (Middle) multi-sensor wave rose. (Right) Measurements map.

The 4 different sensors are in agreement as markers corresponding to different sensors overlap. Synergy between sensors allows to get wave information in every direction of propagation. Moreover, this multi-sensor wave rose provides observational evidence of the extended fetch effect that leads to longer waves propagating towards the front of the TC than towards the rear, because of TC translation speed.

4 Discussion

Several parametric approaches to characterize the TC induced wave field have been proposed, and can be compared to the multi-sensor product presented in section 3. In particular, (10) estimates the extended fetch encountered by translating TC waves through a second order polynomial function of the wind velocity and TC translation speed. The maximum significant wave height inside a tropical cyclone is estimated from this model and the designed parametric function is corrected to match significant wave height altimeter measurements. In (6), a Lagrangian parametric wave model is developed to provide fast estimates of the 2D sea state in the TC, at low computational cost compared to spectral wave models, as an extention of the 1D formulation presented in (5). In (7) this ray tracing model is run for a large amount of TC conditions to quantify the effect of TC translation on the energy and wavelength enhancement or reduction, at any location in a TC.

Both models presented in (10) (based on an experimental fit) and (5) (based on wave growth theory) provide an estimate of the spectral peak wavelength and significant wave height for the most energetic waves generated by a TC (those that propagate in the TC direction to encounter an extended fetch). Unlike significant wave height, wavelength is assumed to be conserved through propagation in deep water conditions. Then, peak wavelength observations from the multi-sensor product performed outside the TC vortex, and peak wavelength estimations from the 2 models should be equivalent. We compare model maximum peak wavelength estimation to the 90^{th} percentile of longest peak wavelengths coming from the TC front at each 3 hours step of Larry track. The results are provided on figure 2.

During Larry's maturity phases (between 2021-09-03 and 2021-09-09), Kudryavtsev's maximum peak wavelength estimations better matches observations than Young, which sligthly overstimates it. Interestingly, both models match the trends of the observed wavelength. However, outside the mature phase of the TC, models can be

significantly different from observations. Several hypotheses may explain these differences.

Regarding the multi-sensor product, it can be due to a too small amount of observations or wave observations wrongly associated to a TC while they were generated by another meteorological event. Regarding models, they assume TC first order parameters (maximum wind speed, maximum wind radius and translation speed) to be constant in time. A rapid evolution of these TC vitals may provide inaccurate estimates of peak wavelength. The fetch laws considered may also not be appropriate because they do not take into account drag coefficient variations as function of the wind speed, in wind-wave growth processes. Our next objectives are to assess the validity of the classic fetch laws inside tropical cyclones and to extend such model / observations comparisons in 2 dimensions, taking into account the peak wavelength distribution as function of the direction of propagation and time.

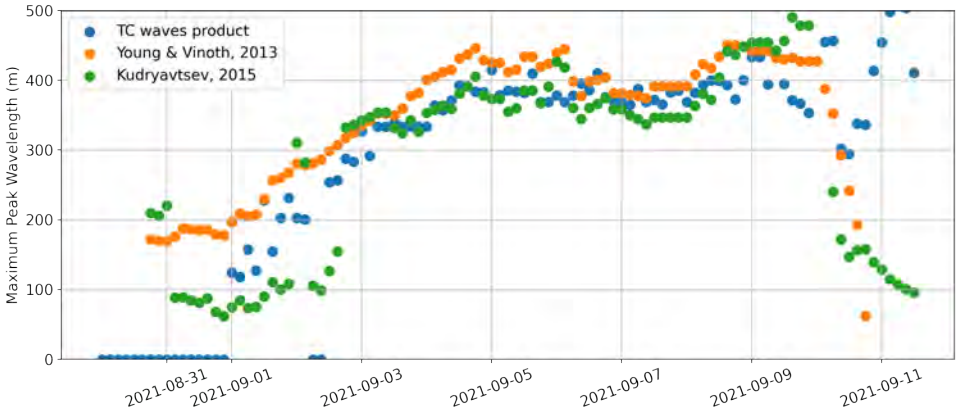

Figure 2: Estimation of maximum peak wavelength from observations (blue), Young 2013 model (orange) and Kudryavtsev 2015 model (green) as function of time in the case of TC Larry, 2021

References

[1] *Validation of Significant Wave Height Retrievals by the KaIA Airborne Radar (AMS 35th conference on Hurricanes and Tropical Meteorology)*, 2022.

[2] Fabrice Collard, Fabrice Ardhuin, and Bertrand Chapron. Monitoring and analysis of ocean swell fields from space: New methods for routine observations. *Journal of Geophysical Research: Oceans*, 114(C7), 2009.

[3] Klaus Hasselmann and Susanne Hasselmann. On the nonlinear mapping of an ocean wave spectrum into a synthetic aperture radar image spectrum and its inversion. *Journal of Geophysical Research*, 96:10713, 1991.

[4] Momme C Hell, Alex Ayet, and Bertrand Chapron. Swell generation under extra-tropical storms. *Journal of Geophysical Research: Oceans*, 126(9):e2021JC017637, 2021.

[5] Vladimir Kudryavtsev, Pavel Golubkin, and Bertrand Chapron. A simplified wave enhancement criterion for moving extreme events. *Journal of Geophysical Research: Oceans*, 120(11):7538–7558, 2015. _eprint: https://onlinelibrary.wiley.com/doi/pdf/10.1002/2015JC011284.

[6] Vladimir Kudryavtsev, Maria Yurovskaya, and Bertrand Chapron. 2D Parametric Model for Surface Wave Development Under Varying Wind Field in Space and Time. *Journal of Geophysical Research: Oceans*, 126, April 2021.

[7] Vladimir Kudryavtsev, Maria Yurovskaya, and Bertrand Chapron. Self-similarity of surface wave developments under tropical cyclones. *Journal of Geophysical Research: Oceans*, 126(4), 2021.

[8] Yves Quilfen, Jean Tournadre, and Bertrand Chapron. Altimeter dual-frequency observations of surface winds, waves, and rain rate in tropical cyclone isabel. *Journal of Geophysical Research: Oceans*, 111(C1), 2006.

[9] F E Snodgrass. Propagation of ocean swell across the pacific.

[10] Ian Young. A review of parametric descriptions of tropical cyclone wind-wave generation. *Atmosphere*, 8(12):194, 2017.

Swell Propagation and short term forecast across the North Atlantic using Combined Sentinel1 Wave Mode, IW Mode and CFOSAT SWIM Observations.

fabrice Collard[1], gilles Guitton[1], manuel López Radcenco[1], frederic Nouguier[2], bertrand chapron[2]
Organisation(s): 1: Oceandatalab, France; 2: Ifremer

Swell propagation over the global ocean (so called firework) using Sentinel-1 wave mode is now an operational CMEMS product and can be used to plan the arrival of swell events on world shorelines. However, since Sentinel-1 is mostly operated in IW mode over the north Atlantic, very limited monitoring of swells on North European Shorelines is possible, especially since the loss of Sentinel1-B unit. Processing of IW mode into cross spectra allows to circumvent and even surpass this lack of wave mode coverage in the North Atlantic. Resulting potential for swell monitoring over the North Atlantic will be demonstrated. Complementarity and comparison with CFOSAT SWIM wave spectra potential for swell monitoring in the North Atlantic will also be demonstrated and discussed. Comparison of this new capability for swell monitoring with the one offered by wave buoys network along the European Atlantic coastline will be shown, highlighting the pro and cons of the two complementary observing systems.

Near Surface Ocean Wind Retrievals & Detection of Extremes

Near Surface Ocean Wind Retrievals & Detection of Extremes

Stoffelen, Ad; Ni, Weicheng; Xu, Xingou; Portabella, Marcos; Makarova, Evgeniia; Cossu, Federico; Sánchez Rabaneda, Alberto
Extreme Winds From SAR And Their Use For Ku- And C-Band Wind Scatterometer Resolution Enhancement

Zecchetto, Stefano; Zanchetta, Andrea; Sclavo, Mauro; Shamsaddini, Parsa; Keshavarz, Ahmad
High-Resolution SAR Winds from Deep Learning in Coastal Areas

Khan, Salman; Young, Ian; Ribal, Agustinus; Canto, Marites; Davy, Robert; Hemer, Mark
Australian Coastal SAR Ocean Winds: Data, Portal, and Next products

Dimitriadou, Krystallia; Badger, Merete; Hasager, Charlotte Bay; Olsen, Bjarke Tobias
SAR for Offshore Wind Fields in the Mediterranean Sea

Hindberg, Heidi; Espeseth, Martine; Johnsen, Harald; Tollinger, Mathias
Operational Wind Retrieval Using Cross-Polarization And Doppler Data

Marquart, Robin; Mouche, Alexis; Chapron, Bertrand
Analysis Of SAR Ocean Scenes Texture For Wind Direction Retrieval And Generation Of Synthetic Images

EXTREME WINDS FROM SAR AND THEIR USE FOR KU-BAND AND C-BAND WIND SCATTEROMETER RESOLUTION ENHANCEMENT

Ad Stoffelen[1], Weicheng Ni[2], Xingou Xu[3], Marcos Portabella[4], Evgeniia Makarova[4], Federico Cossu[4] and Alberto Rabaneda[5]*

1. Royal Netherlands Meteorological Institute KNMI, 3730 AE,De Bilt, Utrecht, The Netherlands
2. National University of Defense Technology,Changsha 410073, China
3. Key Laboratory of Microwave Remote Sensing, National Space Science Center, CAS, Beijing, 100190, China
4. Barcelona Expert Centre (BEC), Institut de Ciències del Mar (ICM-CSIC) Barcelona, Spain
5. Norwegian Meteorological Institute, Oslo, Norway

* ad.stoffelen@knmi.nl

Introduction

Tropical cyclones (TC), or hurricanes cause severe damage during their land-falls, in China alone, the average 9.3 land-fall TCs cause more than $1 billion property loss while they take thousands of human lives each year. At the same time, remotely sensed data have the potential of providing vital information for improved forecasts. Among them, Synthetic Aperture Radar (SAR) images capture the most dynamic detail. European, Canadian and Chinese efforts to capture TCs have resulted in a considerable data base of a few hundred TC SAR acquisitions. Exploiting these data, we report on SAR image classification of TC features [1], TC wind direction retrieval using features in all polarizations [2,3], intercalibration of ECMWF, SAR and ASCAT scatterometer winds in a triple collocation [4].

While SARs provide detail, wind scatterometers provide the capability to track TCs when exploiting the extending scatterometer virtual constellation. Scatterometers have been providing high-quality ocean surface wind products for more than 40 years [11], while they provide good extreme-wind retrieval on their native resolution of about 25 km [5]. Ku-band scatterometers have in principle similar capability, but suffer from heavy rain contamination and where quality control and rain correction are in progress [6,7]. Recently, with reference to the Step-Frequency-Multichannel-Radiometer (SFMR) products [8], the quality of the C-band extreme wind speeds have been well proven and extension to Ku-band scatterometers is ongoing, tackling the problem of contamination by precipitation, as further illustrated below. Furthermore, improved extreme wind vector retrieval is being explored for C-band and later Ku-band scatterometers by resolution enhancement with reference to the extended SAR data base mentioned above using parametric high-resolution TC models [9]. Since sufficient SAR and scatterometer collocations for statistical enhancement techniques for varying hurricane categories are now available, the standard 2DVAR processing for scatterometer ambiguity removal [10] is employed for resolution enhancement of scatterometer winds in TCs, as illustrated in next secction.

Work in Progress

In-situ wind speeds are inconsistent for winds higher than 15 m/s, which poses a problem for wind speed calibration in TCs. The highest quality regular winds are from moored buoys and these are available up to about 25 m/s in sufficient statistical quantity for analysis [12]. Dropsondes from airplane campaigns by the NOAA hurricane hunters [13], which generally available above 20 m/s and are used to calibrate the Step-Frequency Microwave Radiometer (SFMR) winds. SFMR winds may subsequently be used for satellite wind calibration, due to their abundance. At 25 m/s there is an approximate 40% difference in wind strength between wind calibrations based on SFMR/dropsondes and moored buoys, affecting all satellite wind retrievals and physical modelling attempts of exchange processes at extreme winds. A more detailed assessment of dropsonde characteristics is needed [12], hence probably also affecting all SAR wind products [4].

For reconciliated speeds between satellite instruments [4], we attempt spatial resolution enhancement and tracking of TCs or polar lows using the virtual constellation of microwave sensors, both active and passive. The ASCAT C-band scatterometer TC acquisitions are now being tested as depicted in Figure 1.

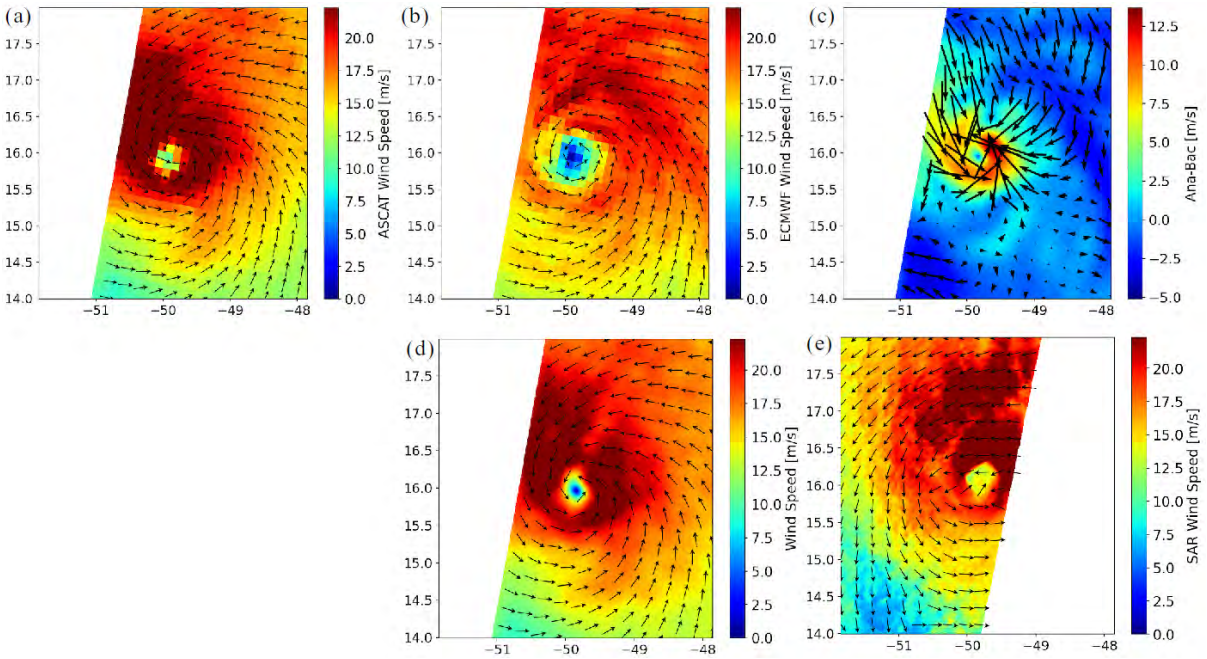

Figure 1. Illustration of ASCAT resolution enhancement: (a) TC TEDDY (acquired on September 16, 2020) imaged by ASCAT VV winds; (b) ECMWF forecast TC TEDDY winds resampled onto ASCAT; (c) 2DVAR wind analysis increments corresponding to (a) and (b). An apparent TC eyewall is generated around the TC center; (d) Super resolution ASCAT result; (e) TC TEDDY imaged by collocated SAR winds.

In the 2DVAR analysis the typical spatial errors in the ECMWF forecasts need to be characterized in terms of longitudinal and transverse wind components. These spatial errors are particular to the hurricane under analysis and depend on the hurricane intensity and Radius of Maximum Wind (RMW), which can be estimated from the ASCAT inputs. The next step is to extend the resolution enhancement work to Ku-band scatterometers, thereby profiting from ongoing advancements in wind calibration, quality control and in particular rain screening and possibly rain correction for Ku-band scatterometers [6,7].

Conclusions

The extensive SAR campaigns on acquisitions of tropical cyclones have resulted in a data base that allows the innovation of SAR wind products for TCs, providing unprecedented detail on the surface winds, supplementing detailed wind information, otherwise only available from hurricane campaigns.

The many SAR TC acquisitions provide a good statistical basis for enhancing TC winds from the extending virtual wind scatterometer constellation, allowing improved tracking of TCs over their lifetime. Some of these enhancement techniques for surface winds may also be employed for microwave radiometers winds in future work.

References

[1] Weicheng Ni, Ad Stoffelen & Kaijun Ren (2022), Hurricane eye morphology extraction from SAR images by texture analysis. Front. Earth Sci. 16, 190–205. https://doi.org/10.1007/s11707-021-0886-9.

[2] Weicheng Ni, Ad Stoffelen & Kaijun Ren (2023),Tropical Cyclone Wind Direction Retrieval From Dual-Polarized SAR Imagery Using Histogram of Oriented Gradients and Hann Window Function", IEEE Journal of Selected Topics in Applied Earth Observations and Remote Sensing, vol. 16, pp. 878-888, https://doi.org/10.1109/JSTARS.2022.3230441.

[3] Weicheng Ni, Ad Stoffelen & Kaijun Ren (2022),"Tropical Cyclone Wind Direction Retrieval Using Histogram of Oriented Gradients on Dual-Polarized Synthetic Aperture Radar Images", IGARSS 2022 - 2022 IEEE International Geoscience and Remote Sensing Symposium, Kuala Lumpur, Malaysia, pp. 6967-6970, https://doi.org/10.1109/IGARSS46834.2022.9884396.

[4] Weicheng Ni, Ad Stoffelen, Kaijun Ren, Xiaofeng Yang, and Jur Vogelzang (2022), "SAR and ASCAT Tropical Cyclone Wind Speed Reconciliation" Remote Sensing 14, no. 21: 5535. https://doi.org/10.3390/rs14215535.

[5] Federica Polverari et al. (2022), "On High and Extreme Wind Calibration Using ASCAT", IEEE Transactions on Geoscience and Remote Sensing **60**, 1-10, Art no. 4202210, https://doi.org/10.1109/TGRS.2021.3079898.

[6] Xingou Xu, Ad Stoffelen, Marcos Portabella, Wenmig Lin and Xiaolong Dong (2021), "A Comparison of Quality Indicators for Ku-Band Wind Scatterometry & for Typhoons Lekima and Krosa", 2021 IEEE International Geoscience and Remote Sensing Symposium IGARSS, Brussels, Belgium, 7584-7587, https://doi.org/10.1109/IGARSS47720.2021.9553678.

[7] Ke Zhao, Ad Stoffelen, Jeroen Verspeek, Anton Verhoef and Chaofang Zhao (2023), Bayesian algorithm for rain detection in Ku-band scatterometer data, IEEE Transactions on Geoscience and Remote Sensing, in revision.

[8] F. Polverari, J. W. Sapp, M. Portabella, A. Stoffelen, Z. Jelenak and P. S. Chang (2022), "On Dropsonde Surface-Adjusted Winds and Their Use for the Stepped Frequency Microwave Radiometer Wind Speed Calibration", IEEE Transactions on Geoscience and Remote Sensing, vol. 60, pp. 1-8, Art no. 4208308, https://doi.org/10.1109/TGRS.2022.3189310.

[9] W. Ni, A. Stoffelen, K. Ren and X. Yang, "Tropical Cyclone Intensity Estimation From Spaceborne Microwave Scatterometry and Parametric Wind Models", IEEE Journal of Selected Topics in Applied Earth Observations and Remote Sensing, vol. 15, pp. 4719-4729, 2022, https://doi.org/10.1109/JSTARS.2022.3180281.

[10] Jur Vogelzang, Ad Stoffelen (2018), Improvements in Ku-band scatterometer wind ambiguity removal using ASCAT-based empirical background error correlations. Q J R Meteorol Soc. 144: 2245– 2259. https://doi.org/10.1002/qj.3349.

[11] Jur Vogelzang & Ad Stoffelen (2021). Quadruple collocation analysis of in-situ, scatterometer, and NWP winds. Journal of Geophysical Research: Oceans, 126, e2021JC017189. https://doi.org/10.1029/2021JC017189.

[12] Ad Stoffelen et al., "Hurricane Ocean Wind Speeds", 2021 IEEE International Geoscience and Remote Sensing Symposium IGARSS, Brussels, Belgium, 2021, pp. 1182-1185, https://doi.org/10.1109/IGARSS47720.2021.9554667.

[13] https://www.aoml.noaa.gov/hurricane-research-division/.

Analysis of SAR ocean scenes texture for wind direction retrieval and generation of synthetic images

Robin Marquart, Alexis Mouche, Bertrand Chapron

January 2023

Abstract

This paper provides an extensive analysis of high resolution C-band ocean SAR scenes. Now routinely provided by Sentinel-1 acquisitions at global scale in wide swath and wave modes, C-band detected ocean surface roughness changes generally trace local air-sea marine-atmosphere layer conditions. Building on these large data sets, a brute force approach is first applied to establish a robust relationship between the local radar texture and the wind direction. Training a convolutional neural network model, performances can be assessed against co-located WindSat radiometer estimates, with respect to the radar configuration (polarization, incidence angle, antenna-to-wind direction), the wind speed and the nature of the air-sea interactions. In presence of atmospheric rolls, the key textural information lies between 800 and 1600 m. Moreover, to interpret and then synthesize a realistic scene, the texture spectral information is solely necessary. This does not apply for scenes where convective cells dominate the texture. For such cases, the detected scale organisation matters. To interpret and synthesize a realistic scene, both spectral and phase distributions must be considered. The present analysis thus provides new means to derive improved estimates of very local air-sea marine-atmosphere layer conditions.

1 Introduction

It has long been recognized that high-resolution SAR ocean scenes quite systematically exhibit atmosphere signatures. For scales larger than 300m, filtering out ocean swell contributions and slick impacts, most radar detected roughness changes characterize the nature of the stability above the sea surface. Several studies thus already largely investigated the relationship between these amplitude modulations with stability to possibly retrieve the Monin-Obhukov length from SAR large scenes [4] or to characterize the surface layer stratification regime associated to particular patterns [1]. Based on Sentinel-1 global Wave Mode data, these authors evidenced that signatures of atmospheric rolls were prevalent for near-neutral conditions while signatures of convective cells were appearing for unstable conditions.

Recently, methodologies based on convolutional neural networks (CNN) has been used to provide efficient multi-scale decomposition of instantaneous SAR ocean image textures. In particular, [3] applied such an approach to classify wave mode images into 10 different geophysical classes. An other study [5] also relies on such a decomposition to evidence links with the local wind direction estimates. In that context, CNN methods largely extend Fourier-based methodology, mostly useful to estimate the local direction of atmospheric rolls.

In the present study, the objective is to primarily follow and extend the approach presented in [5] to a broader frame, including all sea conditions and Sentinel-1 modes. From the extended analysis, a more precise investigation of the small-scale organisation, spectral and phase distributions, are then performed. The proposed methodology is especially useful to better understand the links between SAR texture statistical properties, the surface wind direction and local air-sea marine-atmosphere layer conditions.

2 Methodology

2.1 Dataset and neural network

A dataset was built for each of the following Sentinel-1 exclusive acquisition modes: Extra-Wide swath (EW), Interferometric swath (IW), Wave (WV). These are three collections of collocated patches extracted from SAR acquisitions and a reference wind direction. Each patch is defined by a size and a resolution. As a first choice, we set the size to be around 18 km, corresponding to the size of an image acquired in WV. A pixel resolution of 400 m is then considered to filter most of the swell signature in the signal. The reference wind direction is given by

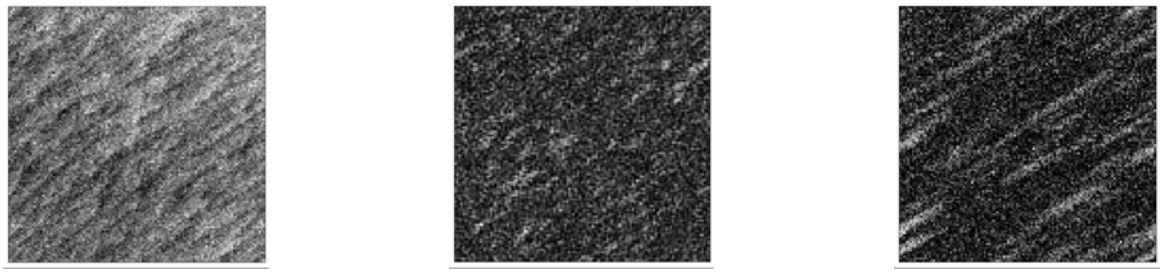

Figure 1: (a) A streaks scene as fed to the CNNs. (b) Previous streaks scene with randomized phase. (c) Artificially generated streaks.

satellite passive microwave WindSat estimates. A pair is considered to be robust when the WindSat wind direction estimates is consistent ($\pm 10°$) to the one given by the ERA-5. WindSat observations may greatly deteriorate in presence of heavy precipitations [2]. Only cases with a zero rain rate are kept. Note, heavy rain signatures on SAR images can hide features related to the wind direction to possibly prevent any learning from the neural network.
For each of these datasets, several deep residual networks (ResNet) are trained. As each model is initialized randomly and trained independently, this allows to predict an ensemble of different wind direction values and then determine which direction is the most probable for a given patch as well as the associated uncertainty. The patches resolution has been degraded to the same 400 m resolution for the three acquisition modes, the size chosen to fit in the wavemode swath, to take benefit of the transfer learning method. The models are first trained on patches extracted from WV acquisitions for which we have a much larger dataset. The WV model coefficients are then transferred on IW and finally on EW for which less data is available.

2.2 Synthetic images

In this study we also attempt to create synthetic SAR scenes. Two methods have been tested : the modification of an existing image and the creation from scratch. This is done in order to help discussing the results given by the neural networks, further analyze the signature of phenomena of interest and to allow for data augmentation or multi-resolution analysis. Here is presented how those artificial scenes are synthesized.
To begin with, starting from patches used in the validation datasets, we removed the part of the signal related to the organization of the phases in the Fourier domain : we only kept the modulus of the spectrum and randomized the phase component. This is done by replacing the phase component of the considered patch by the one of a Gaussian white noise.
We also directly synthesized streaks scenes by modulating white noise with a correlation function defined such as the noise level, width, length, regularity and orientation of the streaks. These parameters can then be can be tweaked to test different configurations. An example is given on figure 1.
Finally, to examine the importance of the scales studied, we also applied low pass and high pass filters to the patches of interest at different lengths.

3 Results & Discussion

The neural networks trained on each acquisition mode provide reliable estimations of the wind direction. In average, the Mean Absolute Error (MAE) between the prediction and the reference value is inferior to 12° with a standard deviation (STD) below 19° for IW and WV. For EW the MAE is lower than 15° with a STD below 24°. The bias is lower than 2° across all acquisition modes. The best wind estimations are obtained for wind speeds between 10 and 20 m/s. In this specific range, the MAE drops below 7° for IW, 9° for WV and 11° for EW. Moreover, the predictions do not seem to be dependent of the incidence angle in the case of WV or IW where plenty of data is available across the whole incidence range. In EW, the lower amount of data available in the training dataset at incidence inferior to 27° does seem to have an impact on the performances. The error linearly decreases from 20° to 15° between incidence angles of 20° and 27°.
In the contrary, the quality of inference is significantly impacted by the nature of the atmospheric phenomena visible in a given patch. The performances of the model with respect to 10 different geophysical classes as defined in [3] for WV has been assessed. The best results were obtained on streaks events where the mean difference between predictions and reference is lower to 9° for both WV1 and WV2. On micro convective cells or rain cells situations, this difference increases by more than 4°. An illustration of those results is given on figure 2.
Even tough the model was trained only on the VV polarization channel, it is still possible to infer on the VH polarization channel. In fact, in the case of extreme waves events, the swell signature can hinder the wind direction

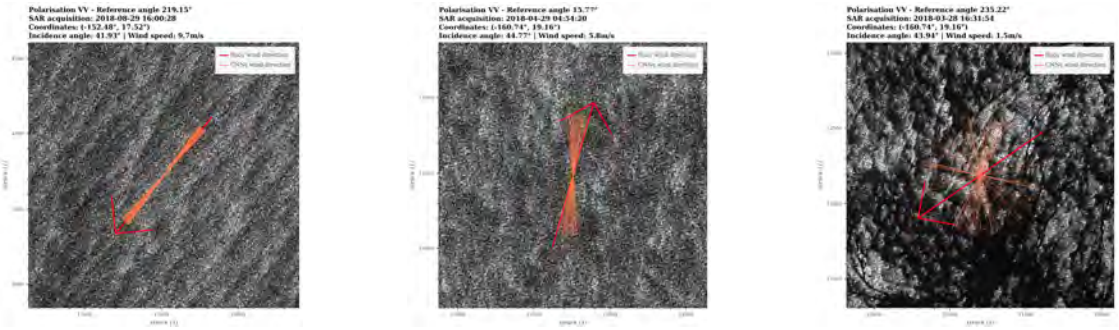

Figure 2: Example of the results obtained on different type of scenes.

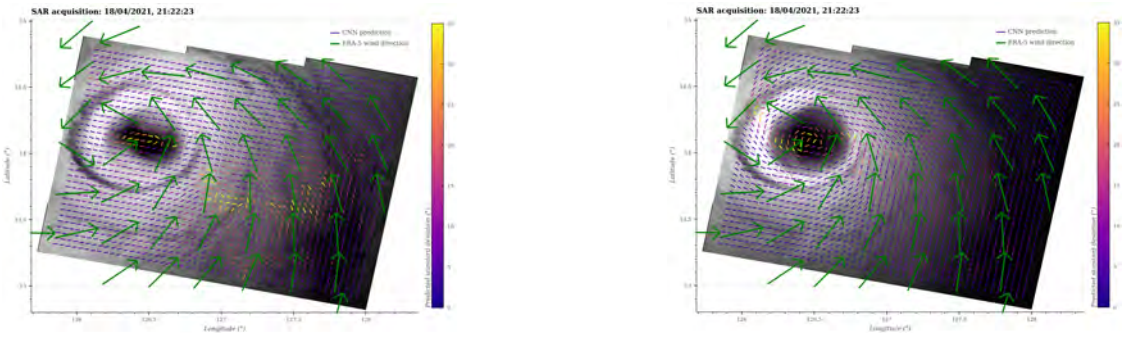

(a) (b)

Figure 3: Sentinel-1 acquisitions of the tropical cyclone Surigae with windfield estimation from the neural networks. (a) Polarization VV. (b) Polarization VH

retrieval because its unusually large wavelength can be mixed up with rolls by the neural models. This is expected to impact more importantly the VV than the VH polarization channel as the wave modulation is higher in VV than in VH due to the tilting effect. Considering the VH channel is thus interesting in these cases. The figure 3 illustrates this aspect on a Sentinel-1 acquisition over the Surigae cyclone where the inference made on the VH channel seems more realistic (wind swirling around the eye on the right hand side of TC tracks where swell are expected to be the longest) than the one from the VV channel.

The models were also used to predict the wind direction on synthetic patches. In the case of wind streaks, when the phases of a given patch are randomized in the Fourier domain, the models are still able to perform a reliable estimation. However, this does not apply in the case of micro convective cells. This means that the organisation of the cells-induced structure is essential to retrieve the wind direction.

Progressively filtering different levels of scales using low pass and high pass filters allowed to estimate what are the most important ones for the wind direction retrieval. It appears that it is between 800 m and 1600 m that lies the majority of features directly related to wind direction estimation.

References

[1] Justin E. Stopa, Chen Wang, Doug Vandemark, Ralph Foster, Alexis Mouche, and Bertrand Chapron. Automated global classification of surface layer stratification using high-resolution sea surface roughness measurements by satellite synthetic aperture radar. *Geophysical Research Letters*, 49(12).

[2] Meissner Thomas and Frank Wentz. Wind-vector retrievals under rain with passive satellite microwave radiometers. *Geoscience and Remote Sensing, IEEE Transactions on*, 47:3065 – 3083, 10 2009.

[3] Chen Wang, A. Mouche, P. Tandeo, J. Stopa, B. Chapron, R. Foster, and D. Vandemark. Automated geophysical classification of sentinel-l wave mode sar images through deep-learning. *IGARSS 2018 - 2018 IEEE International Geoscience and Remote Sensing Symposium*, pages 1776–1779, 2018.

[4] George S Young, Todd D Sikora, and Nathaniel S Winstead. Inferring marine atmospheric boundary layer properties from spectral characteristics of satellite-borne sar imagery. *Monthly weather review*, 128(5):1506–1520, 2000.

[5] Andrea Zanchetta and Stefano Zecchetto. Wind direction retrieval from sentinel-1 sar images using resnet. *Remote Sensing of Environment*, 253:112178, 2021.

HIGH-RESOLUTION SAR WINDS FROM DEEP LEARNING IN ARCTIC FJORDS

Stefano Zecchetto[1,2], Andrea Zanchetta[3], Mauro Sclavo[1], Ahmad Keshavarz[2], and Parsa Shamsaddini[2]

[1]*Istituto di Scienze Polari, National Research Council of Italy, Padova, Italy*
[2]*Faculty of Intelligent Systems Engineering and Data Science, Persian Gulf University, Bushehr, Iran*
[3]*Department of Music, Hong Kong Baptist University, Hong Kong SAR, China*

Abstract

A deep learning methodology based on a residual neural network (ResNet), developed to retrieve wind directions from SAR at 500 m grid without external information, opens the possibility to investigate the spatial characteristics at mesoscale γ in small semi-enclosed areas, like lagoons and Arctic fjords. Avoiding to illustrate technical details concerning the ResNet methodology, this contribution is focused on showing a ResNet wind field over Svalbard fjords. The richness of details provided makes the comparison with other data sets (models/in-situ) somehow insufficient, simply because they do not have a resolution similar to that of SAR wind. We tackle this issue by adding other approaches to the standard co-located comparisons, like the analysis of the spatial gradient of wind. In the example reported in this work and in literature it turns out that the structure of the ResNet wind fields is compatible with some of the meso-scale γ features of the wind.

Key words: Deep residual network, Arctic Fjords, Synthetic Aperture Radar (SAR), Wind field.

1. INTRODUCTION

Retrieval of wind field from SAR needs, among others, the knowledge of the wind direction. The main techniques at present available are reviewed in Zecchetto and Zanchetta (2022), to which the interested reader is addressed. Summarizing by considering only the methods evaluating wind direction directly from the SAR images, we pointed out that the intrinsic limitations of the existing methodologies (requiring the presence of wind-induced streaks or weakly divergent fields or working only in deep water open sea) claim for a robust methodology able to derive high resolution (below 1 km) wind fields both in open sea and coastal areas. Thus, a deep learning methodology based on the residual convolutional neural network, hereafter referred as ResNet, has been developed using Sentinel-1 SAR images (Zanchetta and Zecchetto, 2021) and tested over different meteorological situations and areas (Zecchetto and Zanchetta, 2022). From a statistical point of view, the ResNet wind directions agree very well with those from ECMWF and *in-situ* data; from the applicative point of view, the 500 m spatial grid of ResNet SAR winds attains an exhaustive coverage of small enclosed sea areas, like the Venice Lagoon, allowing the investigation of the inner structure of the wind fields up to the meso-scale γ (Orlanski, 1975), i.e. below 10 km. In our knowledge, there is not any other methodology to derive the wind from SAR with such richness of detail and without any external information.

2. THE DATA

The C-band Sentinel-1 images IW GRDH L1 at VV polarization and pixel size of 10 meters (European Space Agency, 2013), downloaded from the ESA Sentinels Scientific Data Hub[1], have been used in this work. In-situ and model data have been used here as reference: they are the *in-situ* data in the western coast of Svalbard, downloaded from the Norwegian Meteorological Institute[2], and the AROME Arctic 2.5 km model wind data are the forecasts at 1 hour sampling by the Norwegian Meteorological Institute.

[1]https://scihub.copernicus.eu/
[2]frost.met.no/api.html

3. IMAGE PRE-PROCESSING AND WIND DIRECTION COMPUTATION BY RESNET

The original SAR images underwent to a pre-processing, carried out using SNAP[3] free software, i.e. precise orbit determination, thermal noise reduction, calibration, de-speckle filtering, terrain correction, land-sea mask and down-sampling to 50 m. ResNet works from these pre-processed images on partitioned, partly overlapping, sub-images of 64 × 64 pixels (3.2 km × 3.2 km), centered on a regular grid of 500 m, previously filtered with a Gauss filter to remove the ocean wave signatures. Therefore, the vectors closest to the land are at least 1.5 km offshore. ResNet has been trained with 806139 samples derived from 25 Sentinel-1 images, in a similar way as in Zanchetta and Zecchetto (2021).

4. RESULTS

Figure 1 reports a Sentinel-1 image of the southwestern part of Svalbard (left panel), along with the ResNet wind field (right panel). The image was taken in wintertime, and sea-ice is present both as pancake and first year ice. As the wind cannot be derived over ice, we developed a methodology (Shamsaddini et al., 2023), based on the Gray Level Co-occurrence Matrix, to obtain sea-ice masks, contoured by white lines in the left panel. The image shows a tongue of high backscatter in the Isfjorden area, (between 9.5° and 17.5° E and 77.8° and 78.4° N), well visible in the ResNet wind (left panel), showing an impressive number of details: the down-fjord wind in Isfjorden, the katabatic flows west of Prins Karls long island (≈ 10° E, 78° N). The bias between AROME model and SAR winds shows a good agreement (0.4 m/s and 3°), but cannot show whether the several short scale variations provided by SAR are artifact of the method used or indeed represent meso-scale γ characteristics of the wind. For this reason, we investigate the wind speed and direction variability of the down-fjord wind in the Isfjorden shown in the right panel of Figure 1. Figure 2 reports the wind speed

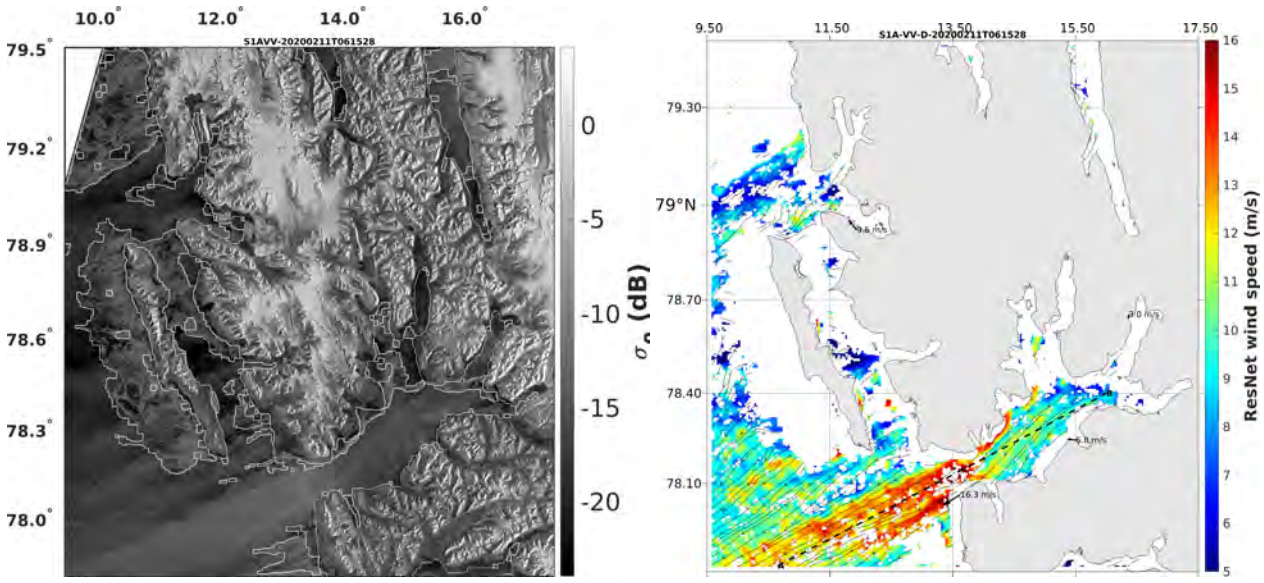

Figure 1. Example of SAR wind field over the Svalbard. Left panel: Sentinel-1A of 2 February 2020, 06:15 UTC. The white contours identify the presence of ice. Right panel: ResNet wind field in the sea areas (sea-ice areas in white). Black arrows are in-situ winds (not in scale). The black dashed line is the transect along which the wind variability is studied.

and direction variability along the transect from ResNet, AROME and ECMWF model data. Apart from the obvious difference in details between ResNet and model winds because of the different grid size, the models variations differ in both wind speed and direction, with some space lag with variations of the SAR winds. This shows the issues arising when comparing SAR winds with models in small areas. The spatial variability of the wind speed and direction are of 0.8 $(m/s)/km$ and $8°/km$, with a dominant wavelength of 7.1 km, numbers close to those obtained from the analysis of high frequency in-situ and SAR winds in the northern Adriatic sea (Zecchetto and Zanchetta, 2022) (not possible with the 1 h in-situ data available here). This indirectly confirms the reliability of the estimates provided by ResNet.

[3]https://step.esa.int/main/toolboxes/snap/

5. FINAL CONSIDERATIONS

The ResNet SAR wind fields describe, in unprecedented detail, the spatial characteristics of the wind even in very demanding areas as the Arctic fjords. The richness of details provided makes somehow insufficient the comparison with other data set, simply because the present available data set (models/in-situ) do not have resolutions comparable to that provided by ResNet. Thus, we have to envisage other approaches, different from the standard co-located data comparison, approaches testing the compatibility rather than bias of RMS difference. One of these is the analysis of the wind spatial gradient that has shown, in the example reported here as well as in Zecchetto and Zanchetta (2022), that the spatial structure of the ResNet wind fields is compatible with some features of the wind in the meso-scale γ range. An other approach could be the comparison with other methods deriving the wind from SAR without external information, such as the 2D Continuous Wavelet Transform (Zecchetto, 2018).

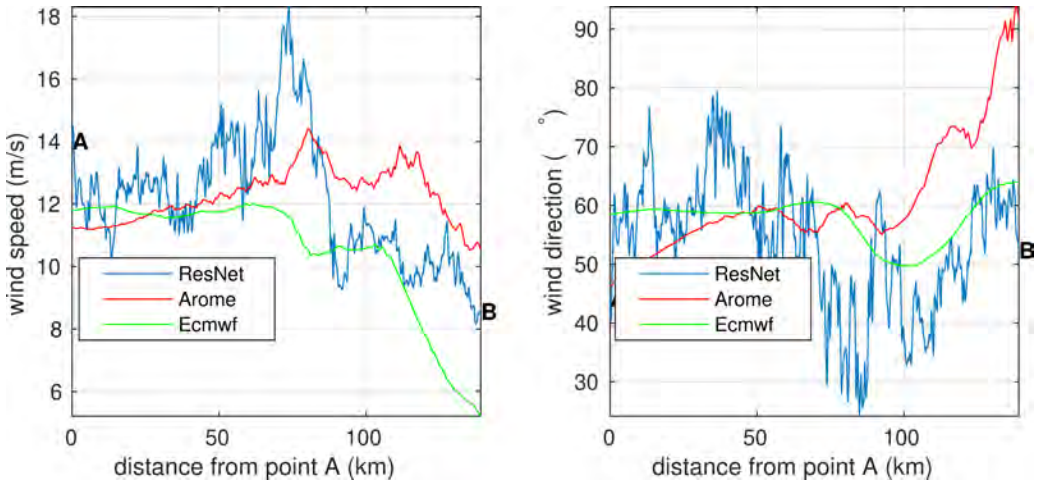

Figure 2. Variability of wind speed (left panel) and direction (right panel) along the transect depicted in the right panel of Fig. 1.

ACKNOWLEDGMENTS

The Sentinel-1 images have been downloaded from the ESA Sentinels Scientific Data Hub. The in-situ data have been obtained from the Norwegian Meteorological Institute web site www.met.no. The work has been partially funded by the Italian Space Agency (ASI), Contract Call ASI DC-UOT-2019-017, Project APPLICAVEMARS n. 2021-4-U.0 (CUP F65F21000070005).

REFERENCES

European Space Agency (2013). *Sentinel-1 User Handbook*. ESA Standard Document. Available online at https://sentinel.esa.int/.

Orlanski, I. (1975). A rational subdivision of scales for atmospheric processes. *Bull. Amer. Meteor. Soc.*, 56:527–530.

Shamsaddini, P., Keshavaz, A., and Zecchetto, S. (2023). Wind-robust sea-ice discrimination from sentinel-1 texture features. In *ICEE 2023*, volume submitted.

Zanchetta, A. and Zecchetto, S. (2021). Wind direction retrieval from Sentinel-1 SAR images using ResNet. *Remote Sensing of Environment*, 253.

Zecchetto, S. (2018). Wind Direction Extraction from SAR in Coastal Areas. *Remote Sensing*, 10(2):261.

Zecchetto, S. and Zanchetta, A. (2022). Structure of high resolution SAR winds over the Venice lagoon area. *IEEE Trans. Geos. and Remote Sensing*.

Australian coastal SAR ocean winds: data, portal, and next products

Salman Khan[1], Ian Young[2], Agustinus Ribal[2,3], Marites Canto[4], Robert Davy[5], Mark Hemer[6]

[1]Commonwealth Scientific and Industrial Research Organisation, Environment, Aspendale, Victoria, Australia. [2]Department of Infrastructure Engineering, University of Melbourne, Parkville, Victoria, Australia. [3]Department of Mathematics, Faculty of Mathematics and Natural Sciences, Hasanuddin University, Makassar, Indonesia. [4]Commonwealth Scientific and Industrial Research Organisation, Environment, James Cook Dr, Townsville, Australia. [5]Commonwealth Scientific and Industrial Research Organisation, IM&T, Black Mountain, Canberra, Australia. [6]Commonwealth Scientific and Industrial Research Organisation, Environment, Castray Esplanade, Hobart, Tasmania, Australia.

Despite Australia having an abundance of offshore industries (e.g., oil and gas, fisheries), and an emerging offshore wind energy industry, there are few sustained in-situ nearshore ocean surface wind measurements around Australia. The collected data are commercial-in-confidence or confounded by land effects on reefs, jetties, and coastal infrastructure. To fill this measurement gap, Sentinel-1 A/B Synthetic Aperture Radar (SAR) acquisitions over Australian nearshore areas have been exploited to build a regional, high resolution (1km) SAR ocean surface winds database [1; under review at the time of writing]. Such a high-resolution coastal winds database also compliments global Scatterometer wind measurements which contain limited data closer to the shore. Two similar SAR nearshore winds databases that exist in other geographical regions, include NOAA's operational SAR derived wind products [2] primarily focused on North America and DTU (Technical University of Denmark) Wind Energy's SAR winds database [3] with a European focus.

SAR winds are derived using input data from Sentinel-1 level-2 ocean winds (OWI) product [4] sourced from the Copernicus Australasia regional data hub (https://www.copernicus.gov.au/). For consistency, the whole Sentinel-1 archive is processed using the same wind inversion scheme and geophysical model function (GMF). The OWI product contains all the input variables necessary to derive SAR winds at 1 km resolution including normalised radar cross section (NRCS), local incidence angle, satellite heading, and collocated model wind speed and direction from ECMWF. The algorithm applied for wind inversion is based on the variational Bayesian inversion approach as proposed in [5], and the Sentinel-1 Ocean wind algorithm definition document [6] with CMOD5.N as the underlying GMF [7]. The winds are also quality flagged in a systematic manner. Calibration of SAR wind speed is performed opportunistically against calibrated Metop-A and B Scatterometer winds database [8] with a relatively relaxed matchup criteria (within 50km and 3 hours) to increase the number of data points. Calibrated SAR wind speeds are then validated against an independent Altimeter wind speed database [9].

The database has been recently made available through the Australian Ocean Data Network (AODN) portal (https://portal.aodn.org.au), which provides access through a graphical user interface that facilitates search and filtering by date, spatial extent, percentage of map containing wind data, satellite platform, and swath as well as quick display of wind maps of interest. At the time of writing, the portal hosts historical SAR winds data with approx. 6 monthly updates, but the intention is to also include a near real time feed.

The online database at this stage comprises wind maps arranged in satellite swath-style grids i.e., aligned along SAR azimuth and range directions (commonly referred to as a curvilinear grid). But regularly gridded and interpolated (rectilinear grid) experimental data products have also been developed with the advantage of easier use with regularly gridded numerical model or other satellite data, easier stitching/scaling of data in space and time for regular monitoring and/or visualisation. A challenge here is to find the grid resolution that retains small scale variability captured in SAR wind maps without being prohibitively large. One potential approach is to have separate datasets with different levels of detail and spatial extents.

Such a coastal winds archive has numerous uses for various applications. It is envisaged that the data will be of use to Australian marine science and industry sectors, such as for offshore industry needs, better understanding of coastal wind climatology alongside other regional/global model hindcast and reanalyses products, and verification of model wind fields.

REFERENCES

[1] Khan, S., Young, I., Ribal, A., and Hemer, M. (under review). High-resolution, calibrated and validated Synthetic Aperture Radar Ocean surface wind data around Australia. *Sci Data* (under review)

[2] Monaldo, F. M., Jackson, C. R., Li, X.; Pichel, W. G. Sapper, J., Hatteberg, R. (2016). NOAA high resolution sea surface winds data from Synthetic Aperture Radar (SAR) on the Sentinel-1 satellites. *NOAA National Centers for Environmental Information*. Dataset. https://doi.org/10.7289/v54q7s2n

[3] Hasager, C.B., Barthelmie, R.J., Christiansen, M.B., Nielsen, M. and Pryor, S.C. (2006), Quantifying offshore wind resources from satellite wind maps: study area the North Sea. *Wind Energ.*, 9: 63-74. https://doi.org/10.1002/we.190

[4] Sentinel-1 Product Specification. (2020). Collecte Localisation Satellites (CLS). Ref: S1-RS-MDA-52-7441. Issue 3.7. Feb 2020.

[5] Portabella, M., Stoffelen, A., and Johannessen, J. A., (2002). Toward an optimal inversion method for synthetic aperture radar wind retrieval, *J. Geophys. Res.,* 107(C8), doi:10.1029/2001JC000925.

[6] Sentinel-1 Ocean Wind Fields (OWI) Algorithm Theoretical Basis Document (ATBD). (2019). Collecte Localisation Satellites (CLS). Ref: S1-TN-CLS-52-9049 Issue 2.0. Jun 2009.

[7] Hersbach, H. (2010). Comparison of C-Band Scatterometer CMOD5.N Equivalent Neutral Winds with ECMWF, *Journal of Atmospheric and Oceanic Technology*, *27*(4), 721-736.

[8] Ribal, A., & Young, I. R. (2020). Calibration and Cross Validation of Global Ocean Wind Speed Based on Scatterometer Observations, *Journal of Atmospheric and Oceanic Technology*, 37(2), 279-297. https://doi.org/10.1175/JTECH-D-19-0119.1

[9] Ribal, A., Young, I.R. (2019). 33 years of globally calibrated wave height and wind speed data based on altimeter observations. *Sci Data* 6, 77. https://doi.org/10.1038/s41597-019-0083-9

SAR for offshore wind fields in the Mediterranean Sea

Krystallia Dimitriadou[1], Merete Badger[1], Charlotte Bay Hasager[1], Bjarke Tobias Olsen[1]

1. Technical University of Denmark, Department of Wind and Energy Systems, Frederiksborgvej 399, 4000 Roskilde, Denmark

The current energy supply in the Mediterranean Sea is highly linked with fossil fuels. Offshore wind farm development is the next step towards the green energy transition. Robust planning and deployment of wind farms though, require the quantification of wind potential in the offshore areas with high quality wind measurements.

Precise wind speed evaluations are notably important in the Mediterranean basin, which is mostly surrounded by mountain ranges which strongly affect the wind circulation and create a local wind climate. Under specific weather conditions, orography may funnel wind flows that can reach gale strengths. Therefore, modelling of offshore wind conditions in such areas is challenging. On the other hand, in-situ measurements are sparse and their quality in terms of continuity and accuracy is highly variable. Another caveat with the above-mentioned model datasets, is that model outputs are constrained in finite grid boxes and in-situ data refer only to point locations. Wind fields from Sentinel-1 satellite Synthetic Aperture Radar (SAR) can resolve wind variability in detail since they have an adequate spatial coverage of 500 m. SAR may be a useful alternative for capturing the local wind effects and variations in complex terrain as well as the calculation of the wind resource potential in the near shore and offshore areas of the Mediterranean Sea.

This study focuses on the North-Western Mediterranean, in the Gulf of Lion, which currently is the most progressed spot for the placement of floating wind turbines in the Mediterranean. This region is frequently affected by two strong local winds, the Mistral and Tramontane. The Mistral is a North wind that develops between the Alps and the Massif Central along the Rhône valley, and the Tramontane is a North-Western wind that flows through the Aude valley between the Massif Central and the Pyrénées (Fig. 1).

SAR wind speed retrievals using CMOD5.N are driven with three different numerical model wind directions: GFS and ERA-5 with a 27 km spatial resolution and the WRF model used for the production of the New European Wind Atlas (NEWA) with a 3 km spatial resolution for the year of 2018. Their respective temporal resolutions are 3, 1 and ½ hour.

A SAR scene from 21st of January 2018 is presented on Fig. 2., for the three datasets (SAR-GFS, SAR-ERA5 and SAR-NEWA). Fig. 2 indicates the wind speed at 10 m and the areas of the potential wind farms (black circles). In this figure, the SAR scene clearly displays the presence of the Tramontane wind, which is channeled through the two mountain ranges. Apparent lee waves come as a result of the Tramontane passing through Massif Central Mountain range.

The scatter plots of wind speed and direction between the three datasets for the potential wind farm site 1 are displayed on Fig. 3 and Fig. 4, respectively. SAR fields indicate that SAR data driven with NEWA wind directions indicate higher wind speeds of 1-2 m/s than the data driven with GFS and ERA5 wind directions. The respective wind directions on Fig. 4 display 2 to 4 degrees difference from the other two datasets.

This objective of this study is twofold. First, to highlight that the SAR satellite winds can yield detailed spatial information about the wind potential at future wind farm sites, especially in coastal places near complex topography. Second, to reveal the importance of a correct coupling between SAR and numerical inputs to CMOD5.N in order to demonstrate the true wind conditions in the area of interest.

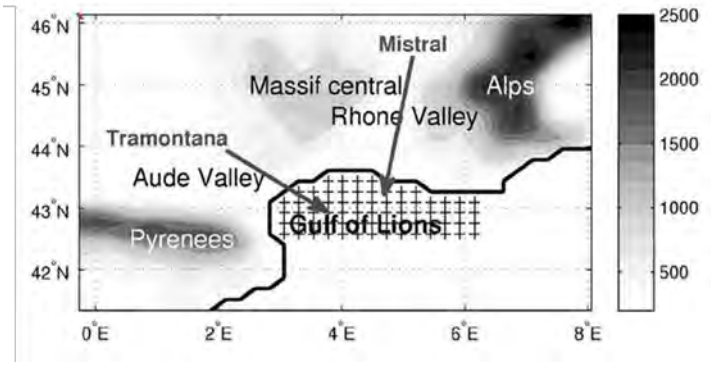

Fig. 1. Topography of the Gulf of Lion (adapted from (Omrani et al., 2017))

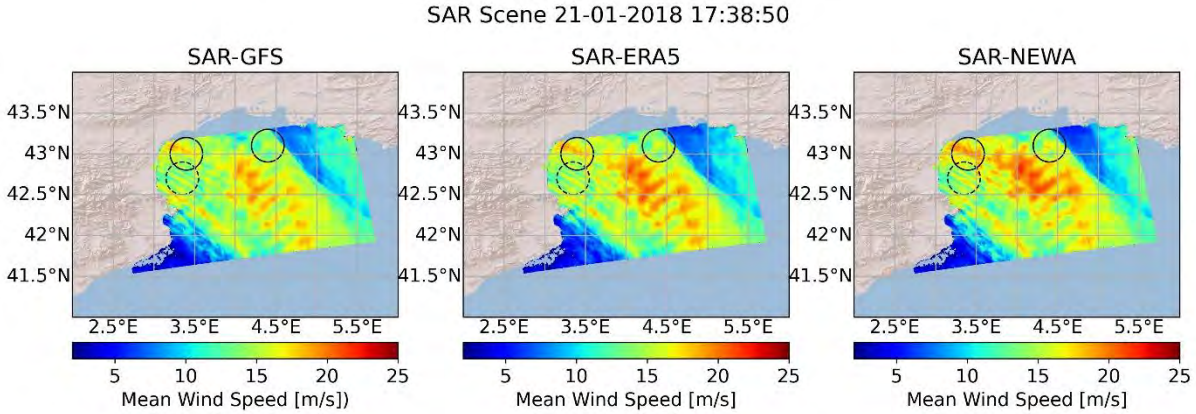

Fig. 2. Sentinel-1 SAR wind fields from CMOD5.N processed with GFS (left), ERA5 (middle) and NEWA (right) wind directions. The black circles indicate the potential areas for wind farm placement.

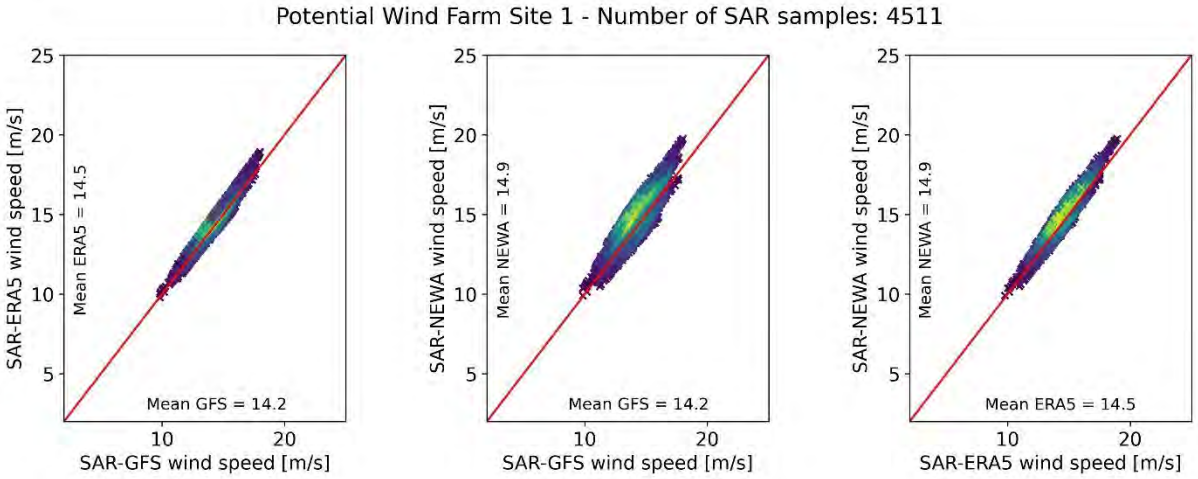

Fig. 3. Wind speed scatter plots between the three SAR datasets with input of wind directions from GFS (left), ERA5 (middle) and NEWA (right) for the potential wind farm site 1 (dotted circle on Fig.2). The mean value of each dataset is displayed along the respective axis.

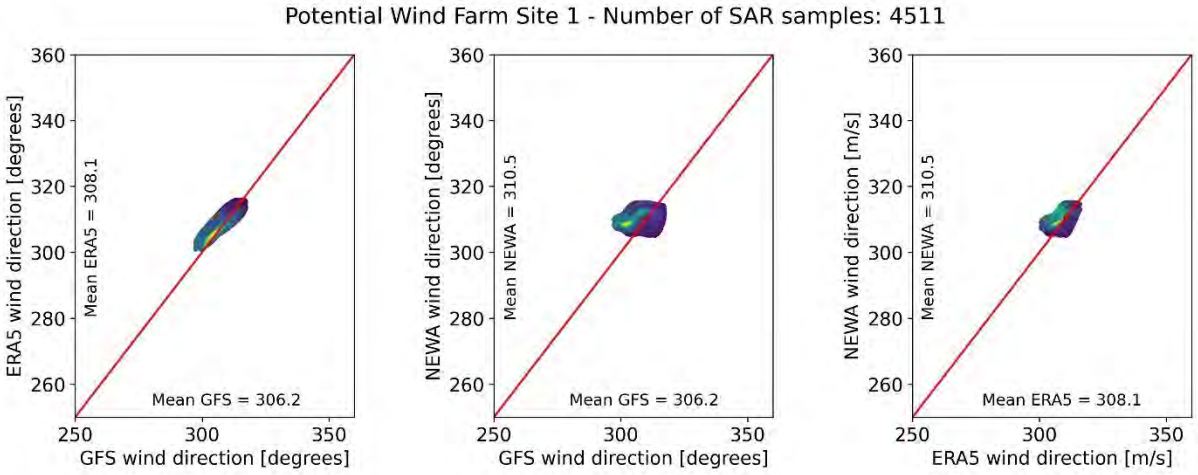

Fig. 4. Wind direction scatter plots between the three datasets: GFS (left), ERA5 (middle) and NEWA (right) for the potential wind farm site 1 (dotted circle on Fig.2). The mean value of each dataset is displayed along the respective axis.

Operational Wind Retrieval Using Cross-Polarization And Doppler Data

H. Hindberg[1], M. Espeseth[2], H. Johnsen[1], M. Tollinger[3]

[1]NORCE, Norway.

[2]Kongsbert Satellite Services (KSAT), Norway

[3]UiT The Arctic University of Norway

***Abstract*— The usage of synthetic aperture radar (SAR) co-polarized data to retrieve information about the wind speed over the ocean surface is an established operational service. We investigate how to include the cross-polarized and the Doppler Centroid Anomaly (DCA) data in an operational setting. Including more data sources can alleviate the dependency on weather model data, but also requires rules for how to balance the influence of the different data sources.**

Keywords— SAR wind, dual-polarization, operational service

I. INTRODUCTION

SAR data can be used to measure the wind over the ocean surface for most sea states, since the backscatter is dominated by wind-induced ripples. The measured co-polarized backscatter is compared to semi-empirical forward models describing the relation between the wind speed vector and the SAR signal. Compared to most numerical weather models the resolution achieved from SAR data (1-by-1 km) is quite good. However, the problem is underdetermined, both the speed and direction of the wind will affect the co-polarized backscatter signal, and we only have one measurement. Traditionally this has been solved by combining numerical weather model data to the inverse problem. We typically use the weather model wind direction and determine the corresponding wind speed from the backscatter signal. Ideally, we would also like to update the wind direction based on the measured signal. In addition, in an operational context we have now introduced a dependency on weather model data meaning that if the model data provider is down the wind production will also stop.

With the launch of Sentinel-1 the availability of dual-polarization data has increased, resulting in a lot of interest in the use of cross-polarization data in wind retrieval. Especially over hurricanes and other high-wind events, since cross-polarized data does not saturate at high winds like co-polarized data (e.g. [1], [2]). Cross-polarized data taken over the ocean is not sensitive to the wind direction, only to the wind speed [3]. Using the cross-polarized data in the wind retrieval can decrease the dependency on weather model data and allow us to infer about the direction as well as the speed. For Sentinel-1 data, we can also utilize the doppler centroid anomaly (DCA) data which is also dominated by ocean wind and current effects [4]. In theory this should allow us to discard the dependency on model wind data, but the DCA product from Sentinel-1 is still in a prototype stage.

Standard wind retrieval from SAR has been in operational use for years at KSAT, especially within the oil detection service to obtain the detection capability map. In this work we investigate how to include cross-polarization backscatter and DCA in an operational setting, meaning that all SAR scenes are processed by the same system regardless of if it is a low or high wind situation. This is done in the framework of the CryoniteOcean software, developed by NORCE and running operationally at KSAT. We analyse all the Sentinel-1A data for 2022 over a point of the coast of Norway, as well as 34 Radarsat-2 scenes taken in 2010 and 2016. Wind retrieval based on four different combinations of data sources is performed and compared to measurement station Norne.

II. DATASETS

A. SAR datasets

The Sentinel-1 data set comprises 151 Sentinel-1A IW DV scenes of the coast of Norway from all of 2022. Of these, 80 contain land which is currently a requirement for using the DCA data. Both the level 1 GRD and level 2 OCN data were used. The Radarsat-2 dataset is 34 SCNA DV scenes covering the same area, 8 from 2010 and 26 from 2016.

Areas of low backscatter in SAR scenes can be severely affected by additive noise. For most ocean surfaces the cross-pol backscatter signal will be low, and the additive noise quite visible. Also, the multi-swath acquisition mode of S1 and RS2 SCN will cause an intensity difference in each swath and the swath seams will be visible in the detected image. We apply the standard thermal denoising procedure [5], which has well-known weaknesses. This will be visible in the end wind speed and direction results, as we can see the sub-swaths in the results. Radarsat-2 data is similarly corrected using the reference noise levels annotated in the products.

The S1 level 2 OCN contains denoised backscatter so no further denoising is needed. However, the DCA is not calibrated in the standard product. We adjust the DCA at ocean pixels by subtracting the mean DCA over all land pixels.

B. In situ dataset

The in-situ wind speed and direction measurements are taken from https://seklima.met.no/, from the Norne platform located at 66.0256º N, 8.085º E. The wind is typically measured ~100moh but is adjusted to 10m height, and the time

resolution is 10 min. The median wind speed for every 10 minutes is used, indicating that wind gusts are ignored. Figure 1 below shows the wind direction and speed from the platform, where the majority of the wind comes from south-west, west, and north-west. The average wind is 7.6 m/s, the middle wind is 7.2, and the maximum wind is 27 m/s throughout the year 2022.

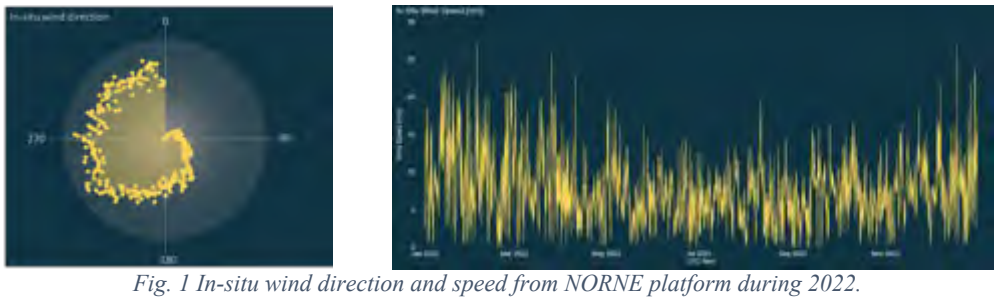

Fig. 1 In-situ wind direction and speed from NORNE platform during 2022.

III. INVERSION METHOD

SAR wind retrieval is typically done by defining a cost function which is a function of the true wind vector (speed and direction) and depends on the measured SAR backscatter and a prior wind vector as an input. The measured SAR backscatter is related to the wind vector using a forward model. Working from [6], the full cost function is defined as

$$J(w,\phi) = (1 - W(\sigma_{obs}^{VH}))\left(\frac{\sigma_{mod}^{VV}(w,\phi) - \sigma_{obs}^{VV}}{s_{VV}}\right)^2 + \left(\frac{\phi_{prior} - \phi}{s_\phi}\right)^2 + W(\sigma_{obs}^{VH})\left(\frac{\sigma_{mod}^{VH}(w,\phi) - \sigma_{obs}^{VH}}{s_{VH}}\right)^2 + \left(\frac{dca_{mod}(w,\phi) - dca_{obs}}{s_{dca}}\right)^2 \quad (1)$$

Here, we use the CMOD5.n [7] model for co-polarization backscatter σ_{mod}^{VV}, the MS1A [8] model for cross-polarization backscatter σ_{mod}^{VH}, and the CDOP [4] model for the DCA dca_{mod}^{V}. The true wind vector is described by its speed w and its direction ϕ, and the prior wind direction ϕ_{prior} is the ERA5 ECMWF [9] model wind direction. The model wind speed is not used directly in the cost function; however, the model wind speed and direction are both used as starting points in the inversion procedure. The selection of the weights in the denominators will assign the relative importance of matching this particular term in the cost function. For instance, with a high s_ϕ it will be less important in the inversion procedure to match ϕ with ϕ_{prior}. In this case we select $s_{VV} = s_{VH} = 0.1$, $s_{dca} = 0.4$ and $s_\phi = 5$.

Over ocean the cross-polarization backscatter will hit the noise floor for low wind cases, and the co-polarization backscatter will saturate for high wind cases. Ideally, we should use the cross-pol signal for high wind and the co-pol signal for low wind. This is regulated through the $W(\sigma_{obs}^{VH})$ term in (1). We select a wind speed interval $[w_l, w_h]$, where for all wind speeds below the interval we only use co-pol and for wind speed above the interval we only use cross-pol. We use an interval of [8,30] m/s and define the weight function as

$$W(\sigma_{obs}^{VH}) = \begin{cases} 0 & \text{for } \sigma_{obs}^{VH} < \sigma_{mod}^{VH}(\omega_l) \\ 1 & \text{for } \sigma_{obs}^{VH} > \sigma_{mod}^{VH}(\omega_h) \\ 3x_s(\sigma_{obs}^{VH})^2 - 2x_s(\sigma_{obs}^{VH})^3 & \text{elsewhere} \end{cases} \quad (2)$$

$$x_s(\sigma_{obs}^{VH}) = \frac{\sigma_{obs}^{VH} - \sigma_{mod}^{VH}(\omega_l)}{\sigma_{mod}^{VH}(\omega_h) - \sigma_{mod}^{VH}(\omega_l)}$$

Wind inversion is performed with four combinations of input data and thus four different cost functions:

- based on co-polarization data alone (copol), using terms 1 and 2 in (1).
- based on a combination of co-polarization and cross-polarization (dual), using terms 1, 2, and 3 in (1).
- based on the DCA and co- and cross-polarization data (full), using all terms in (1).
- based on co-polarization data and the DCA (codop), using terms 1, 2 and 4 in (1).

The copol and dual scheme is applied to both S1 and RS2 datasets, and the results are processed from the standard GRD products using the CryoniteOcean software running at KSAT. The full and codop is limited to the S1 dataset as the DCA is not available for the Radarsat-2 dataset, and we perform the inversion starting from the S1 level 2 OCN products.

IV. PRELIMINARY RESULTS

Figure 2 shows the results for the four different inversion methods for a S1 scene on 20220508. Here we see that the copol, dual and full results for wind speed are quite similar, while the codop has some higher winds at near range. Either way the SAR wind speed is much more detailed than the model wind speed. The DCA is estimated at a resolution of 3x3 km, while the SAR wind has a resolution of 1x1 km, we can see this difference in resolution in the level of details comparing

codop/full with copol/dual. For the direction, as expected the copol direction is very close to the model direction. The dual direction has more variations. We can also see the 3 swath seams in the dual direction, this is due to the inferior noise correction applied on the cross-pol backscatter.

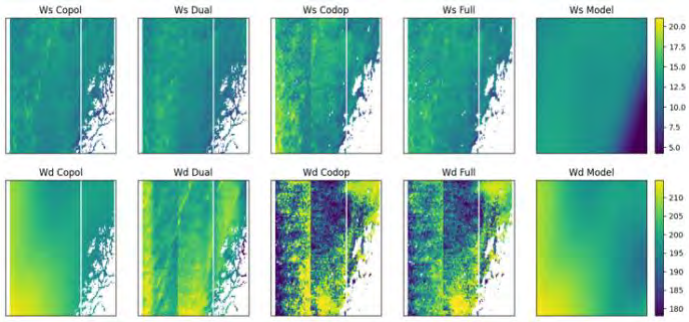

Fig. 2 Results for S1A IW GRDH 1SDV 20220528T055454. Upper row is wind speed and lower is wind direction, using the four different inversions and the ECMWF model data.

Figure 3 shows screenshots from an interactive dashboard with statistics of the in-situ wind speed and direction from NORNE versus the four methods (copol, dual, codop, and full). The boxes below the scatter plots show the standard deviations of SAR wind and SAR wind directions versus in-situ. Codop and full-pol deviates the most from the in-situ wind data compared to the other methods, while the copol and dual-pol show similar performance. Preliminary results indicate that the use of cross-pol is useful for increasing the information about the wind direction. Visually the retrieved wind speed seems deteriorated because of the swath seams, showing the need for more robust noise corrections. The use of DCA deteriorates the results, the weighting needs to be investigated further.

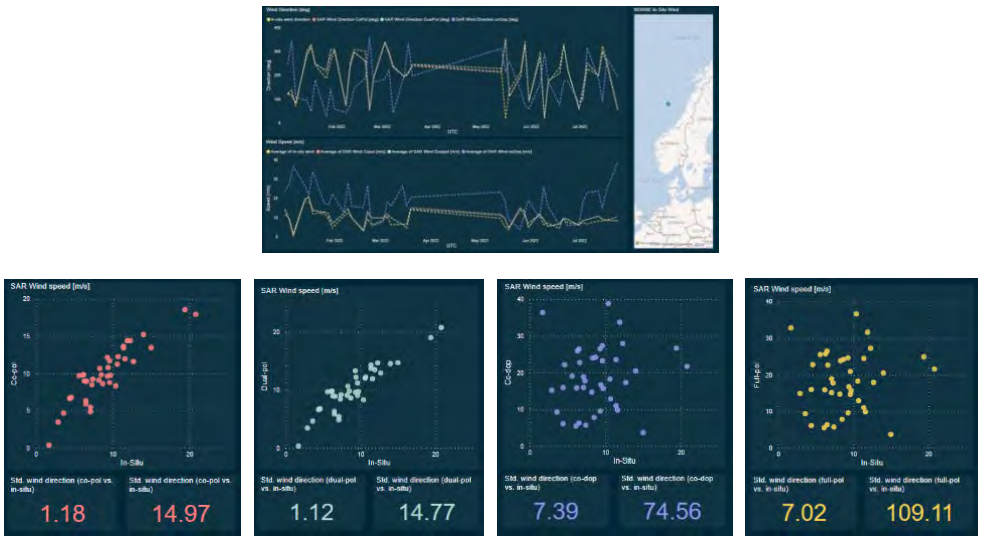

Fig. 3 Upper: Time series of SAR wind and direction from in-situ, copol, codop, and dual-pol. Lower: Scatterplots of SAR winds versus in-situ wind from copol, dual, co-dop, and full, respectively.

REFERENCES

[1] Horstmann, J.; Schiller, H.; Schulz-Stellenfleth, J.; Lehner, S. "Global wind speed retrieval from SAR". IEEE Trans. Geosci. Remote. Sens. **2003**, 41, 2277–2286.

[2] Vachon, P.W.; Wolfe, J. "C-band cross-polarization wind speed retrieval". IEEE Geosci. Remote. Sens. Lett. **2010**, 8, 456–459.

[3] Zhang, B.; Perrie, W. "Cross-polarized synthetic aperture radar: A new potential measurement technique for hurricanes". Bull. Am.Meteorol. Soc. **2012**, 93, 531–541.

[4] Mouche, A.A.; Collard, F.; Chapron, B.; Dagestad, K.F.; Guitton, G.; Johannessen, J.A.; Kerbaol, V.; Hansen, M.W. "On the use of Doppler shift for sea surface wind retrieval from SAR". IEEE Trans. Geosci. Remote Sens. **2012**, 50, 2901–2909.

[5] S-1 Mission Performance Centre, "Thermal Denoising of Products Generated by the S-1 IPF", https://sentinel.esa.int/documents/247904/2142675/Thermal-Denoising-of-Products-Generated-by-Sentinel-1-IPF

[6] Tollinger M.; Graversen R.; Johnsen H. "High-Resolution Polar Low Winds Obtained from Unsupervised SAR Wind Retrieval", Remote Sens. **2021**, 13(22), 4655; https://doi.org/10.3390/rs13224655

[7] Hersbach H., "CMOD5.N: A C-band geophysical model function for equivalent neutral wind," ECMWF, Reading, U.K., **2008**. Tech. Memo. 554.

[8] Mouche, A.A.; Chapron, B.; Zhang, B.; Husson, R. "Combined co-and cross-polarized SAR measurements under extreme wind conditions". IEEE Trans. Geosci. Remote Sens. **2017**, 55, 6746–6755.

[9] Hersbach, H. et al., "The ERA5 Global Reanalysis" May 2020

Doppler Shift Retrievals

Doppler Shift Retrievals

Kleinherenbrink, Marcel; Yuan, Yan; Theodosiou, Andreas; Gaultier, Lucile; Collard, Fabrice; Chapron, Bertrand; Lopez-Dekker, Paco
Multiscale Effects on Harmony's High-resolution Ocean Observations

Elyouncha, Anis; Eriksson, Leif; Gommenginger, Christine
Observations of the Agulhas Current by Along-track Interferometric Synthetic Aperture Radar

Romeiser, Roland
Review of TerraSAR-X Based Current Retrieval Activities at the University of Miami

Martin, Adrien; Macedo, Karlus; McCann, David; Portabella, Marcos; Marié, Louis; Marquez, José; Carrasco, Ruben; Duarte, Rui; Meta, Adriano; Gommenginger, Christine; Martin-Iglesias, Petronilo; Casal, Tania
OSCAR: A New Airborne Instrument To Image Ocean-Atmosphere Dynamics At The Sub-Mesoscale

Moiseev, Artem; Collard, Fabrice; Johannessen, Johnny A
Ocean Surface Currents from Sentinel-1 Doppler observations

Guitton, Gilles; Collard, Fabrice; Johnsen, Harald; Engen, Geir; Recchia, Andrea; Cotrufo, Alessandro; Bras, Sergio; Miranda, Nuno; Pinheiro, Muriel
Towards Calibrated Sentinel-1 OCN RVL Products

Domps, Baptiste; Guérin, Charles-Antoine
Evaluation of Surface Currents Derived from Sentinel-1 SAR Doppler Shift in the Northwestern Mediterranean Sea Using Coastal HF Radars

Multiscale effects on Harmony's High-resolution Ocean Observations

M. Kleinherenbrink, Y. Yuan, A. Theodosiou, L. Gaultier,
F. Collard, B. Chapron, P. Lopez-Dekker

January 31, 2023

1 Introduction

The two satellites of the Harmony mission will fly in constellation with a Sentinel-1 Synthetic Aperture Radar (SAR) satellite. Harmony's passive radar instruments will receive signals transmitted by Sentinel-1 after reflection from the surface. The multistatic system uses three lines-of-sight to observe high-resolution normalized radar cross section (NRCS) and Doppler. With Harmony's high-resolution observations we aim to observed high-resolution O(1 km^2) wind-stress anomalies and ocean-surface currents.

The interpretation of high-resolution signals is not trivial as they are affected by non-locally generated waves. Long waves O(>5 m) have relaxation scales much larger than the intended resolution of the Harmony level-2 products. The long waves affect the NRCS and the Doppler in different ways [6, 7, 5, 3]. Estimation of wind stress and ocean-surface current should therefore not be done on a pixel basis, but it requires multi-scale dynamical approaches.

In this paper, we show the result of forward modelled polarimetric NRCS and Doppler for Harmony and Sentinel-1. Input for our models are wind (stress) and ocean current grids from models. We use an equilibrium short-wave spectrum with a parametric long-wave spectrum to estimate the NRCS and Doppler. Alternatively, we use the Simulating WAves Nearshore (SWAN) model[1] for the long waves to capture non-local effects of wind and currents. By comparing both, we demonstrate why a pixel-based inversion is not suitable for high-resolution products.

2 Methodology

The modelling of NRCS and Doppler is based on a bistatic implementation of the Radar Imaging Model (RIM)[6, 7] and the Doppler RIM (DopRIM)[5]. The forward models require as input a wave spectrum at each grid cell that is computed from the wind and ocean currents in the scene.

2.1 Wave spectra

The wave spectrum is split at ten times the peak wavenumber, $k_l = 10k_p$, into a short- and a long-wave spectrum. The two-dimensional curvature spectrum depends on the wavenumber vector $\vec{k}$ and is described by

$$B(\vec{k}) = \phi(k, k_l)B_{lw}(\vec{k}) + (1 - \phi(k, k_l))B_{sw}(\vec{k}), \qquad (1)$$

where $\phi(\vec{k}, k_l)$ is a roll-off function. The parametric long-wave spectrum used in this study is from Elfouhaily et al.[2], while the short-wave spectrum is based on an equilibrium approach described by Kudryavtsev et al.[6] with the implementation as in Kudryavtsev et al. (2014)[8].

To take the relaxation and direction changes of long waves into account, we replace in a second run the Elfouhaily long-wave spectra by those from a SWAN model run. We additionally apply a linear model to account for the effects of currents on the short-wave spectrum[9]. From here on we refer to both models simply as Elfouhaily and SWAN.

2.2 NRCS and Doppler

The implementation of the RIM and DopRIM models from the monostatic case follow Kudryavtsev et al.[6] and Hansen et al.[3] The RIM accounts for three scattering mechanisms: specular scattering, Bragg scattering and scattering from wave breaking. This results in a monostatic NRCS as given by

$$\sigma_0^m = \sigma_{sp}(1 - q) + \sigma_{Br}(1 - q) + \sigma_{wb}q, \qquad (2)$$

where q the fraction of the surface covered by breakers. The derivation of the bistatic NRCS is rather elaborate and is discussed in an upcoming publication (Kleinherenbrink et al. 2023, in preparation). A principal polarization basis as defined in [4] is used, which results in different weighting of the scattering mechanisms, which is summarized as

$$\sigma_0^b = w_{sp}^b\sigma_{sp}(1 - q) + w_{Br}^b\sigma_{Br}(1 - q) + w_{wb}\sigma_{wb}^b q, \qquad (3)$$

where the weights depend on the bistatic geometry. We establish one description for the monostatic and bistatic Doppler

$$f_D^{m,b} = \sigma'_{sp}f_{sp} + \sigma_{Br}^{HH'}f_{Br}^{HH} + \sigma_{Br}^{VV'}f_{Br}^{VV} + \sigma'_{wb}f_{wb}, \qquad (4)$$

which depends on the scattering ratios σ'_{xx} where the superscript (b, m) is omitted for clarity. Due to the geometry, the bistatic Doppler can be described as a function of both HH and VV components (see Kleinherenbrink et al. (2023), in preparation) even though Sentinel-1's transmission is in VV. For the monostatic case $\sigma_{Br}^{HH'}$ becomes zero.

3 Results

Fig. 1 shows the NRCS, in the major polarizations, computed from a run of a coupled ocean-atmosphere model near the coast of Calfornia. The top panels (based on the Elfouhaily long-wave spectrum) clearly show the directional dependence of backscatter. The line-of-sight or Harmony-A is more aligned with the wind than the line-of-sight of Harmony-B, resulting in a higher NRCS. Several linear and meandering features are visible that closely coincide with wind-speed anomalies and currents.

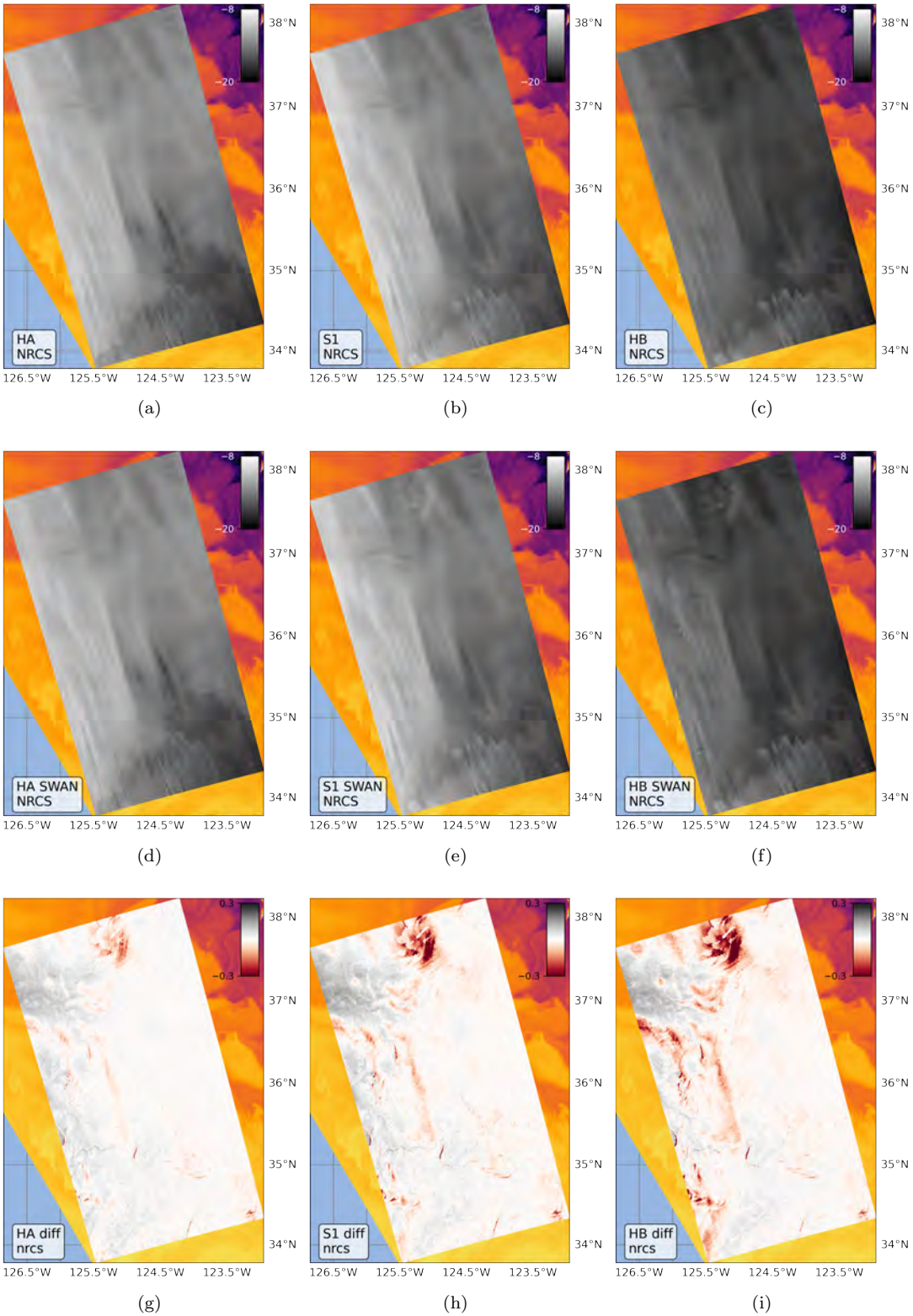

Figure 1: Modelled observed NRCS (dB) in the major polarization near California using the output of a scientific workbench run. The top panels (a-c) are computed using an equilibrium approach with a Elfouhaily long-wave spectrum. The middle panels (d-f) are generated with SWAN as the long-wave spectrum. The bottom panels (g-i) show the normalized linear differences between (a-c) and (d-f) with in the background the sea surface temperature.

The second row of panels shows the results of the SWAN model. The differences with the Elfouhaily model are shown in the bottom panels. The effects of currents on the wave spectrum are not explicitly modelled in the Elfouhaily model, which results in the largest discrepancies between the two models. The enhanced short-scale roughness near currents primarily result from enhanced wave breaking [8], which is primarily a local effect. Wind anomalies and currents can also introduce directional changes to the long-wave spectra, resulting in changes in the energy exchanges between long waves and short waves. Large-scale differences between the Elfouhaily and the SWAN model also arise from differences in wave age and (asymmetric) spreading leading to changes in short-wave energy balances. As differences in NRCS are typically in the order of 10-20% and vary with direction, there are consequence for the inversion of high-resolution stress-equivalent wind products.

Fig. 2 shows the observed geophysical Doppler from the Elfouhaily and SWAN models. Whereas the NRCS is primarily regulated by short waves in the form of Bragg and wave breaking, the wave-Doppler results from line-of-sight-projected surface velocities of longer waves, O(10 m), and their tilt and hydrodynamic modulations of shorter waves [3]. The interpretation of the wave-Doppler is due to its dependence on both short and long waves even less trivial than the NRCS. A change in observed Doppler direction and magnitude might therefore arise from either a current, a change in the short-wave spectrum or a change in the long-wave spectrum. Longer waves are refracted by currents and slowly react to wind variations, as their relaxation scales are large O(10 km)[7]. Shorter waves react more rapidly to changing conditions and therefore change the tilt and hydrodynamic modulations. To help with the interpretation, or inversion, of Harmony's observations at high-resolution, a classification based on the scene's features might therefore be required.

4 Conclusions

At small scales, the observed NRCS and Doppler deviate substantially from stead-state conditions. Both multistatic radar observations are affected by currents, winds and depend on the inverse wave age. The retrieval of high-resolution stress-equivalent wind and ocean-surface currents is therefore non-trivial and we cannot rely on traditional GMFs designed for low resolutions. Removal of the wave-Doppler based on solely stress-equivalent wind and inverse-wave age is not suitable for high resolutions, as other relaxation scales are involved. The inversion of both parameters requires an integrated approach involving multiple scales, SAR-spectral parameters and might even profit from an adjoint approach.

References

[1] N. Booij, R. C. Ris, and L. H. Holthuijsen. A third-generation wave model for coastal regions: 1. Model description and validation. *Journal of Geophysical Research: Oceans*, 104(C4):7649–7666, Apr. 1999.

[2] T. Elfouhaily, B. Chapron, K. Katsaros, and D. Vandemark. A unified directional spectrum for long and short wind-driven waves. *Journal of Geophysical Research: Oceans*, 102(C7):15781–15796, July 1997.

[3] M. Hansen, V. Kudryavtsev, B. Chapron, J. Johannessen, F. Collard, K.-F. Dagestad, and A. Mouche. Simulation of radar backscatter and Doppler shifts of wave–current interaction in the presence of strong tidal current. *Remote Sensing of Environment*, 120:113–122, May 2012.

[4] L. Iannini, D. Comite, N. Pierdicca, and P. Lopez-Dekker. Rough-Surface Polarimetry in Companion SAR Missions. *IEEE Transactions on Geoscience and Remote Sensing*, 60:1–15, 2022.

[5] J. A. Johannessen, B. Chapron, F. Collard, V. Kudryavtsev, A. Mouche, D. Akimov, and K.-F. Dagestad. Direct ocean surface velocity measurements from space: Improved quantitative interpretation of Envisat ASAR observations. *Geophysical Research Letters*, 35(22):L22608, Nov. 2008.

[6] V. Kudryavtsev. A semiempirical model of the normalized radar cross section of the sea surface, 2. Radar modulation transfer function. *Journal of Geophysical Research*, 108(C3):8055, 2003.

[7] V. Kudryavtsev. On radar imaging of current features: 1. Model and comparison with observations. *Journal of Geophysical Research*, 110(C7):C07016, 2005.

[8] V. Kudryavtsev, B. Chapron, and V. Makin. Impact of wind waves on the air-sea fluxes: A coupled model. *Journal of Geophysical Research: Oceans*, 119(2):1217–1236, Feb. 2014.

[9] N. Rascle, J. Molemaker, L. Marié, F. Nouguier, B. Chapron, B. Lund, and A. Mouche. Intense deformation field at oceanic front inferred from directional sea surface roughness observations: DIRECTIONAL ROUGHNESS AT OCEANIC FRONT. *Geophysical Research Letters*, 44(11):5599–5608, June 2017.

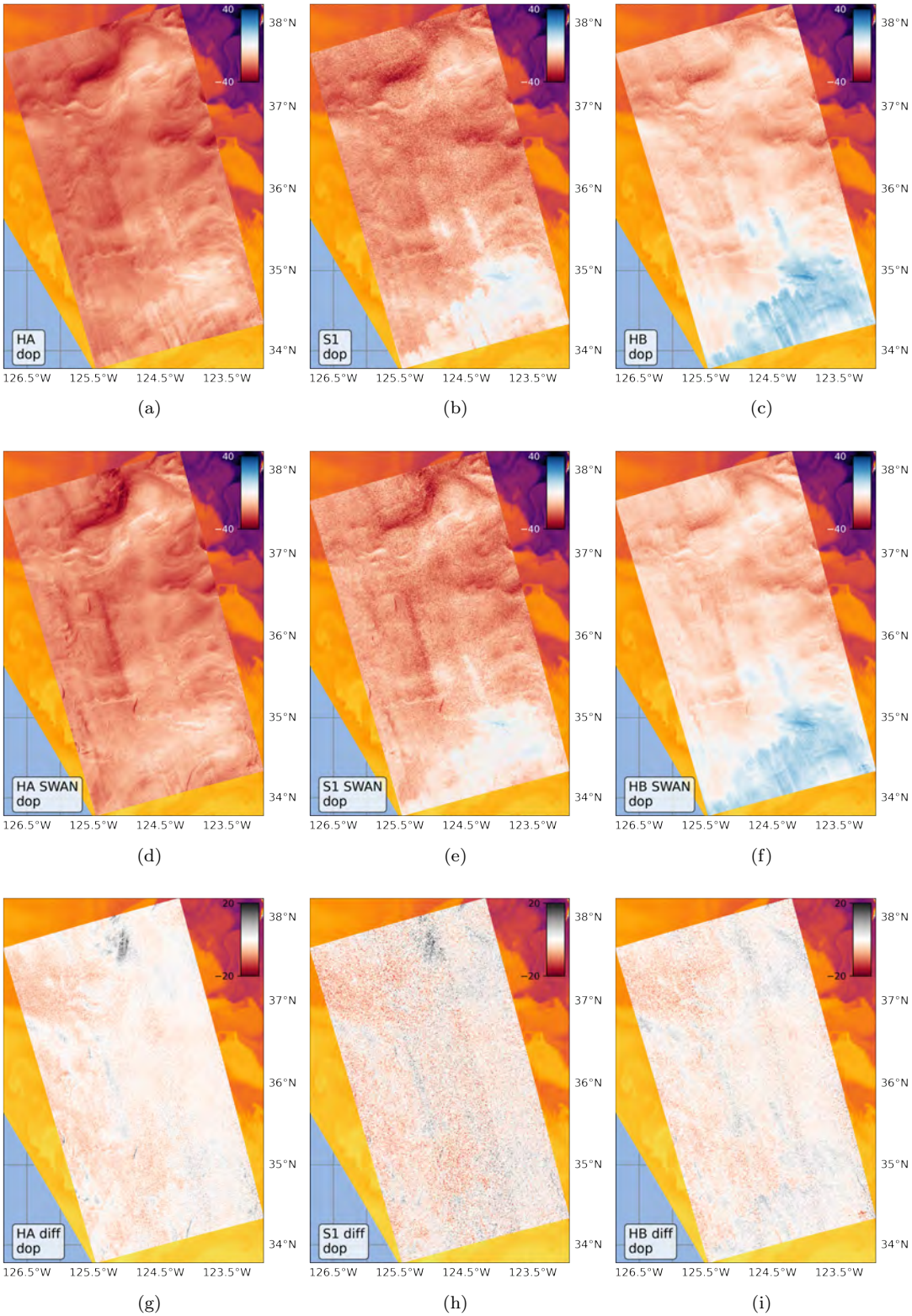

Figure 2: Modelled observed Doppler (Hz) in the major polarization near California using the output of a scientific workbench run. The top panels (a-c) are computed using an equilibrium approach with a Elfouhaily long-wave spectrum. The middle panels (d-f) are generated with SWAN as the long-wave spectrum. The bottom panels (g-i) show the linear difference between (a-c) and (d-f) with in the background sea surface temperature.

OBSERVATIONS OF THE AGULHAS CURRENT BY ALONG-TRACK INTERFEROMETRIC SYNTHETIC APERTURE RADAR

Anis Elyouncha[1], *Leif E. B. Eriksson*[1], *Christine Gommenginger*[2]

[1]Chalmers University of Technology, Gothenburg, Sweden
[2]National Oceanography Center, Southampton, UK

Synthetic aperture radar (SAR) offers the possibility to observe the sea surface circulation with very high spatial resolution. These observations are particularly relevant in coastal areas and shelf seas, where the ocean circulation is complex and highly variable. SAR has been routinely providing valuable information on sea surface winds and waves for many decades. During the last decade, a new application of SAR measurements based on the analysis of the Doppler shift has emerged [1, 2], opening the possibility to measure directly the surface currents. There are still however many unresolved questions and challenges. One of the challenging questions is the wind-wave-current interaction and its effect on the wind and wave retrieval. There are two major techniques for extracting ocean surface currents from SAR data: Along-track interferometry (ATI) and the Doppler centroid anomaly (DCA) analysis. The retrieval of surface velocity using these two techniques has been demonstrated in several papers, e.g. [3, 4, 1, 5].

A known effect that makes the retrieval of the ocean currents from SAR data challenging is the so-called wave-induced Doppler shift or velocity bias. This effect is due to the correlation between the normalized radar cross section (NRCS) and Doppler shift modulations, which are generated by the long modulating waves. Thomson [6] was probably the first to show that the Doppler spectrum was considerably shifted from the frequency of the Bragg waves. He attributed this to the fact that both the radar cross section and the radial surface velocity are functions of the position of the radar footprint along the wave.

The Agulhas Current is the strongest western boundary currents in the southern hemisphere. The region of the Agulhas Current is characterized by a complex upper ocean dynamics involving a wide range of mesoscale and submesoscale processes. It thus provides an ideal natural laboratory for oceanographers and for testing remote sensing sensors and techniques. It is known that oceanic currents modify the wave filed properties, e.g. [7]. The Agulhas region has attracted the attention due to the rich interaction of the Agulhas Current system with wave field, e.g. [8]. This interaction is manifested in the SAR and optical images [8]. The manifestation of this interaction has has been reported by previous authors using the C-band SAR on-board Envisat [9] and Sentinel-1 [10] and also using Sentinel-2 imagery, e.g. [11].

In this paper the manifestation of the interaction of the Agulhas Current with the wind and the wave fields is presented and discussed based on the acquisitions provided by the X-band ATI-SAR TanDEM-X. To our knowledge this is the first time the Agulhas Current is mapped with an X-band spaceborne ATI-SAR. The backscatter and the Doppler shift derived from these unique acquisitions of the interferometric SAR over the Agulhas Current with very high spatial resolution (few hundreds of meters) are analyzed. Collocated existing products of ocean surface wind, ocean surface current, sea surface temperature and significant wave height are also analyzed to help the interpretation of these SAR observations.

1. PRELIMINARY RESULTS

Figure 1 shows an example of the preliminary results from a TanDEM-X acquisition on 2015-11-05, together with model data for sea surface current and sea surface temperature (SST). Panels (a) and (b) depict the observed NRCS and Doppler centroid (DC), respectively. These observations contain complex signatures of the varying wind and current fields in addition to surface and internal waves. The DC image captures accurately the boundary and the intensity of the Agulhas Current. Moreover, these maps show unprecedented fine structure of the Agulhas Current and its interaction with the wave field. The core of the Agulhas Current is clearly detected by a increase in the DC image around -35 degrees latitude. The pattern depicted by the backscatter images is on the other hand much more dependent on the wind and sea state than on the current velocity. This is manifested by a sharp enhancement of the NRCS at the northern edge of the current. The structure of the current core can also be discerned by increase in the NRCS image around the same latitude as of the DC maximum.

Panel (c) depicts the model current speed. It can be observed that the northern boundary around -34.5 degrees latitude depicted by the NRCS and DC images is unresolved by the model. This is probably an indication that it is due to a wind front

rather than an oceanic front. The wind field will be analyzed later to investigate this. Panel (d) depicts the azimuth profile of the model current speed, SAR-derived radial velocity and the sea surface temperature. The model current and SST are provided by the Copernicus product GLOBAL_MULTIYEAR_PHY_001_030. It can be observed that the SAR-derived velocity locates correctly the current core which reaches 1.5 m/s. The model current and SST both peak roughly at the same location but the variation is much more smoother than SAR observation.

The influence of the Agulhas Current on the wind and wave field retrieval will be investigated. The inversion of the backscatter to wind speed, without taking the current into account, would lead artificially high estimates of SAR-derived wind speeds in the regions of enhanced backscatter. Note that the effect of the current on the wind and wave field retrieval will also impact the current retrieval via the wave-induced Doppler shift.

To summarize, this paper analyses collocated NRCS and DC images acquired by the along-track interferometric SAR TanDEM-X over the Agulhas Current. These observation present rich manifestations of the wave-current and wind-current interaction at very high resolutions not observed before from satellites. The roughness and velocity signatures depend on the wind, wave and the current fields. A case of particularly enhanced roughness, which is probably due to a convergent wind front is reported. More detailed investigation of the cause of this sharp enhancement of the NRCS in regions of strong current shear will be carried out. Finally, more cases from other TanDEM-X acquisitions will be shown at the conference.

2. REFERENCES

[1] B. Chapron, F. Collard, and F. Ardhuin, "Direct measurements of ocean surface velocity from space: Interpretation and validation," *Journal of Geophysical Research*, vol. 110, Mar 2005.

[2] R. Romeiser and D. R. Thompson, "Numerical study on the along-track interferometric radar imaging mechanism of oceanic surface currents," *IEEE Transactions on Geoscience and Remote Sensing. Vol. 38-II, 446-458, 2000.*, vol. 38, no. 2, pp. 446–458, Jan 2000.

[3] R. Romeiser, H. Runge, S. Suchandt, R. Kahle, C. Rossi, and P. S. Bell, "Quality assessment of surface current fields from TerraSAR-X and TanDEM-X along-track interferometry and doppler centroid analysis," *IEEE Transactions on Geoscience and Remote Sensing*, vol. 52, no. 5, pp. 2759–2772, 2014.

[4] A. Elyouncha, L. E. B. Eriksson, R. Romeiser, and L. M. H. Ulander, "Measurements of sea surface currents in the Baltic Sea region using spaceborne along-track InSAR," *IEEE Transactions on Geoscience and Remote Sensing*, vol. 57, no. 11, pp. 8584–8599, Nov 2019.

[5] J. A. Johannessen, B. Chapron, F. Collard, V. Kudryavtsev, A. Mouche, D. Akimov, and K.F. Dagestad, "Direct ocean surface velocity measurements from space: Improved quantitative interpretation of Envisat ASAR observations," *Geophysical Research Letters*, vol. 35, no. 22, 2008.

[6] D. R. Thompson and J. R. Jensen, "Synthetic aperture radar interferometry applied to ship generated internal waves in the 1989 Loch Linnhe experiment," *Journal of Geophysical Research: Oceans*, vol. 98, no. C6, pp. 10259–10269, 1993.

[7] Fabrice Ardhuin, Sarah T. Gille, Dimitris Menemenlis, Cesar B. Rocha, Nicolas Rascle, Bertrand Chapron, Jonathan Gula, and Jeroen Molemaker, "Small-scale open ocean currents have large effects on wind wave heights," *Journal of Geophysical Research: Oceans*, vol. 122, no. 6, pp. 4500–4517, 2017.

[8] Vladimir Kudryavtsev, Alexander Myasoedov, Bertrand Chapron, Johnny A. Johannessen, and Fabrice Collard, "Imaging mesoscale upper ocean dynamics using synthetic aperture radar and optical data," *Journal of Geophysical Research: Oceans*, vol. 117, no. C4, 2012.

[9] M. Krug, A. Mouche, F. Collard, J. A. Johannessen, and B. Chapron, "Mapping the agulhas current from space: An assessment of asar surface current velocities," *Journal of Geophysical Research: Oceans*, vol. 115, no. C10, 2010.

[10] Y. Quilfen, M. Yurovskaya, B. Chapron, and F. Ardhuin, "Storm waves focusing and steepening in the agulhas current: Satellite observations and modeling," *Remote Sensing of Environment*, vol. 216, pp. 561–571, 2018.

[11] Vladimir Kudryavtsev, Maria Yurovskaya, Bertrand Chapron, Fabrice Collard, and Craig Donlon, "Sun glitter imagery of surface waves. part 2: Waves transformation on ocean currents," *Journal of Geophysical Research: Oceans*, vol. 122, no. 2, pp. 1384–1399, 2017.

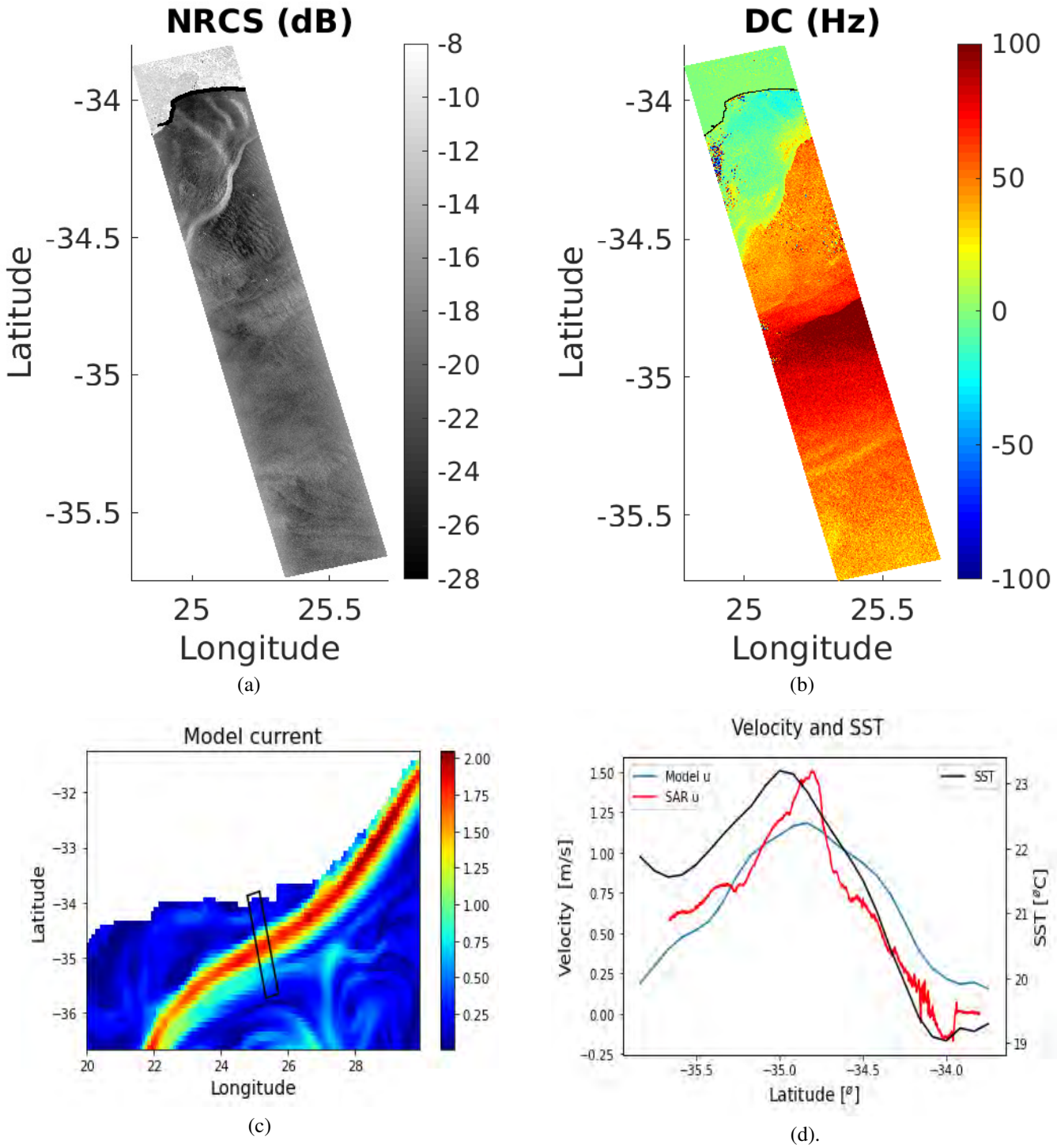

Fig. 1. Example of ATI-SAR observations and model data illustrating part of the Agulhas Current system. (a) NRCS, (b) DC estimated from the ATI phase, (c): Model current speed (the black rectangle depicts the satellite scene), (d): Azimuth profile of SAR radial velocity (red), model current speed (blue) and SST (black).

Review of TerraSAR-X Based Current Retrieval Activities at the University of Miami

Roland Romeiser

Rosenstiel School of Marine, Atmospheric, and Earth Science
University of Miami, Florida, USA
rromeiser@miami.edu

20 years ago, at the 2003 Second Workshop on Coastal and Marine Applications of SAR in Svalbard, the author of this abstract presented a first surface current field from a spaceborne interferometric SAR, based on a Shuttle Radar Topography Mission (SRTM) data set acquired over the Dutch Wadden Sea in February 2000 and provided to him by H. Runge of the German Aerospace Center (DLR) [1]. Subsequently, a "white paper" on findings from the workshop regarding the state of the art in current measurements by spaceborne SAR was published [2]. At SeaSAR 2012 in Tromsø, Norway, we discussed early along-track InSAR results from TerraSAR-X and made contributions to another conference paper [3]. SeaSAR 2023 in Svalbard is a good opportunity to review our TerraSAR-X / TanDEM-X results obtained since the launch of these satellites and offer them as input to the next "white paper" on the state of the art. In this abstract we will discuss a few examples that can be shown.

TerraSAR-X, launched in 2007 and still in good condition at the time of writing this abstract in early 2023, can be operated in an experimental divided-antenna mode that permits along-track interferometry with an effective baseline on the order of 1 m as well as polarimetry [4]. Numerical simulations before the launch predicted a performance for surface current measurements comparable to, or a little better than, the one of SRTM, with a residual uncertainty better than 0.1 m/s at a spatial resolution better than 1000 m [5]. First results based on actual TerraSAR-X data, acquired in 2008 and processed by S. Suchandt of DLR, confirmed that the data quality was at the expected level [6],[3]. In another paper from 2015, we demonstrated on the basis of divided-antenna mode data how the quantitative interpretation of SAR signatures of oceanic internal waves could be improved when Doppler velocity signatures were available in addition to the usual intensity signatures [7].

Significantly improved current measuring capabilities became available with the launch of a second TerraSAR-X type satellite in 2010, built specifically to fly in close formation with the first one for the TanDEM-X mission, with the main objective to obtain a global high-resolution map of the Earth's land topography [8]. As discussed in [5], the optimal effective along-track baseline for current measurements by X-band along track InSAR is on the order of 30 m, a factor of 20-30 longer than what is possible with the divided-antenna mode of a single TerraSAR-X satellite. To enable useful cross-track baselines for topographic measurements without colliding or drifting apart from each other, the two TanDEM-X satellites were on orbits that made them revolve around each other in such a way that the effective along-track baseline varied between 0 near the north and south pole and 700-900 m near the equator during every orbit, such that the best along-track baselines were achieved still near the poles and the baselines at more interesting latitudes were too long. However, there were a few opportunities for current measurements with good baselines at lower latitudes, as shown in a paper by R. Kahle of DLR [9].

Again with help from our colleagues at DLR, we were able to obtain two TanDEM-X images of a region with strong tidal currents between the Orkney Islands (Scotland) in early 2012. The effective along-track baselines in the two cases were about 25 m and 40 m, respectively. An analysis of these data was presented in [10], together with a comparison with a divided-antenna mode data set and reference currents from a numerical model. In addition, C. Rossi of DLR performed Doppler centroid anomaly analysis (DCA) with single images from the interferometric data sets to evaluate the capabilities of that technique, which can be applied to raw data from any conventional SAR, as well. It was shown that the quality of the DCA results was close to that of the divided-antenna interferometry results, which is not surprising in view of the fact that the effective baseline of the divided-antenna setup is just a small fraction of the optimal baseline, causing a low sensitivity to scatterer velocities and a lot of noise that needs to be reduced by averaging over many pixels. In contrast, the TanDEM-X results with near-optimal baselines exhibited a much better data quality, with a residual uncertainty of 0.1 m/s at an effective resolution on the order of 30 m instead of the ~1000 m of the DCA, divided-antenna mode, and SRTM results. This was consistent with our predictions and shown to be sufficient to resolve orbital motions of swell waves. An example figure from [10], showing wave signatures in the intensity Doppler velocity images, is reproduced in Fig. 1 below.

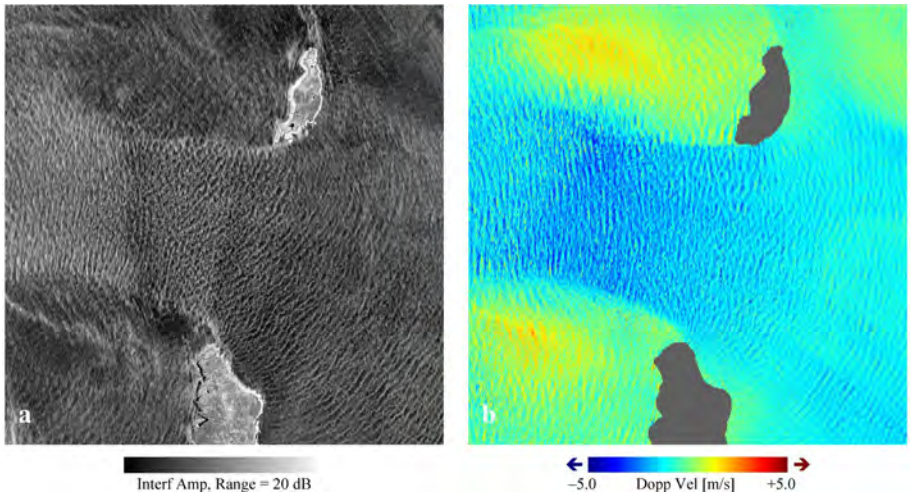

Fig. 1: Subsection of a TanDEM-X interferogram amplitude (left) and Doppler velocity (right) image with clear wave signatures, acquired at Orkney, 26 Feb 2012, from [10]. Area size ≈ 10 km × 10 km, multilooked pixel size = 8.40 m × 8.46 m.

Other activities with TanDEM-X data include the acquisition of two series of image pairs over the open ocean with slowly changing along-track baselines, initiated by H. Runge with the idea to measure the temporal decay of the signal autocorrelation function (equivalent to a decrease in coherence) directly instead of deriving it from Doppler bandwidths or estimating it based on numerical simulations. Preliminary results, which once again indicated good agreement with numerical model predictions, were presented at EUSAR 2014 [11]. S. Suchandt published a paper based on similar TanDEM-X data in 2017 [12]. Other TanDEM-X studies that should be mentioned here are the ones by Dammann, Elyouncha, Eriksson, and coworkers in Sweden on various aspects on current and sea ice motion retrievals, to which the author of this abstract made small contributions [13][14].

A totally different approach to current measurements with TerraSAR-X was demonstrated in [16]. It makes use of spotlight-mode images acquired with dwell times of up to several seconds. While the long dwell time can make images of the moving ocean surface look blurry initially, it is possible to reprocess the data into short time series of images with shorter dwell times, in which wave motions become visible like in a video. This permits the computation of wavenumber-frequency spectra and the use of analysis methods similar to the ones developed for marine radar data [17]: The theoretical dispersion relation of ocean waves can be used to separate actual ocean wave patterns from other contributions, such as the ones of higher harmonics of the waves and nonlinearities of the SAR imaging mechanism, as well as noise. As a result, a clean spectrum of the linear signatures of ocean waves is obtained, which is easier to invert into an ocean wave spectrum than the full image spectrum of a single SAR image. In addition, water depths and surface current vectors can be obtained as byproducts of the process of fitting the theoretical dispersion relation to the observed spectral energy distribution. An example of extracted wave signatures and the corresponding depths is shown in Fig. 2. Unfortunately, we do not have a good example of an extracted current field so far.

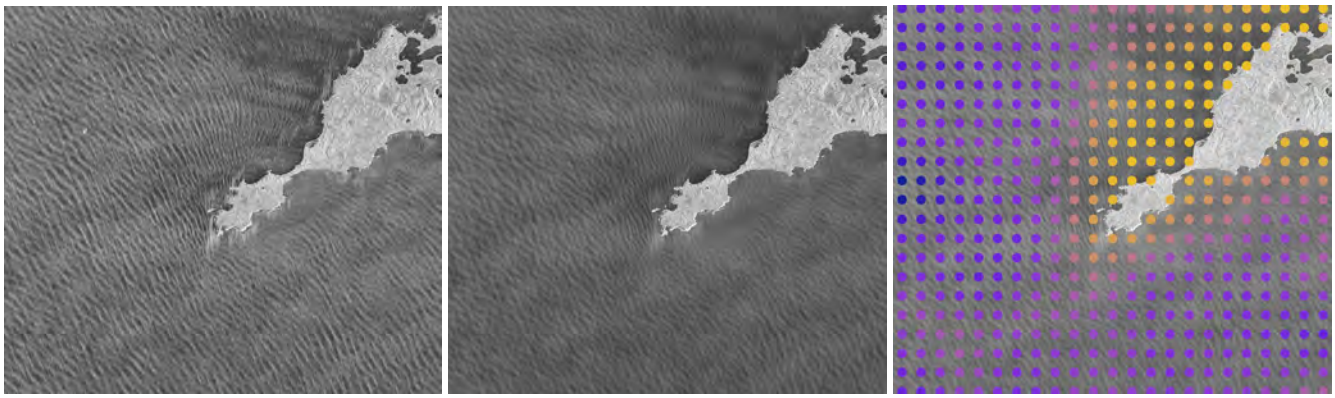

Fig. 2: Example of a wave pattern and water depth extraction result for an area at Rottnest Island (Australia), after [16]. Left: TerraSAR-X Sliding Spotlight Mode image from 20 Oct 2009, 11.7 km × 10.4 km, integration time = 1.22 s; center: extracted wave signatures; right: extracted depths between 60 m (blue) and 0 (yellow), grid spacing = 512 m × 512 m.

References

[1] Werner, M., Shuttle Radar Topography Mission (SRTM): Mission overview, *J. Telecommun. (Frequenz)*, *55*, 75-79, 2001.

[2] Romeiser, R., S. Ufermann, and S. Kern, Status report on the remote sensing of current features by spaceborne synthetic aperture radar, *Pro. Second Workshop on Coastal and Marine Applications of SAR*, 111-129, ESA Special Publication SP-565, 2004.

[3] Johannessen, J.A, B. Holt, B. Chapron, F. Collard, V. Kudryavtsev, R. Romeiser, and A. Mouche, Ocean current retrievals and applications, *Proc. SeaSAR 2012*, 7 pp., ESA Special Publication SP-709, 2013.

[4] Mittermayer, J., and H. Runge, Conceptual studies for exploiting the TerraSAR-X dual receive antenna, in Proc. IGARSS 2003, 2140-2142, IEEE, 2003.

[5] Romeiser, R., and H. Runge, Theoretical evaluation of several possible along-track InSAR modes of TerraSAR-X for ocean current measurements, *IEEE Trans. Geosci. Remote Sens.*, *45*, 21-35, 2007.

[6] Romeiser, R., S. Suchandt, H. Runge, U. Steinbrecher, and S. Grünler, First analysis of TerraSAR-X along-track InSAR-derived current fields, *IEEE Trans. Geosci. Remote Sens.*, *48*, 820-829, 2010.

[7] Romeiser, R., and H.C. Graber, Advanced remote sensing of internal waves by spaceborne along-track InSAR – a demonstration with TerraSAR-X, *IEEE Trans. Geosci. Remote Sens.*, *53*, 6735-6751, 2015.

[8] Krieger, G., A. Moreira, H. Fiedler, I. Hajnsek, M. Werner, M. Younis, M. Zink, TanDEM-X: a satellite formation for high-resolution SAR interferometry, *IEEE Trans. Geosci. Remote Sens.*, *45*, 3317-3341, 2010.

[9] Kahle, R., H. Runge, J.S. Ardaens, S. Suchandt, and R. Romeiser, Formation flying for along-track interferometric oceanography – first in-flight demonstration with TanDEM-X, *Acta Astronautica*, *99*, 130-142, 2014.

[10] Romeiser, R., H. Runge, S. Suchandt, R. Kahle, C. Rossi, and P.S. Bell, Quality assessment of surface current fields from TerraSAR-X and TanDEM-X along-track interferometry and Doppler centroid analysis, *IEEE Trans. Geosci. Remote Sens.*, *52*, 2759-2772, 2014.

[11] Romeiser, R., and H. Runge, Measuring the temporal autocorrelation function of backscattered X-band signals from the ocean with TanDEM-X, *Proc. 10th European Conference on Synthetic Aperture Radar (EUSAR 2014)*, 1299-1301, VDE Verlag, Berlin / Offenbach, Germany, 2014.

[12] Suchandt, S., and R. Romeiser, X band sea surface coherence time inferred from bi-static SAR interferometry, *IEEE Trans. Geosci. Remote Sens.*, *55*, 3941-3948, 2017.

[13] Dammann, D.O., L.E.B. Eriksson, J. Jones, A.R. Mahoney, R. Romeiser, F.J. Meyer, and H. Eicken, Instantaneous sea ice drift from TanDEM-X interferometry, *The Cryosphere*, *13*, 1395-1408, 2019.

[14] Elyouncha, A., L.E.B. Eriksson, R. Romeiser, and L.M.H. Ulander, Measurements of sea surface currents in the Baltic Sea region using spaceborne along-track InSAR, *IEEE Trans. Geosci. Remote Sens.*, *57*, 8584-8599, 2019.

[15] Elyouncha, A., L.E.B. Eriksson, R. Romeiser, and L.M.H. Ulander, Empirical relationship between the Doppler centroid derived from X-band spaceborne InSAR data and wind vectors, *IEEE Trans. Geosci. Remote Sens.*, *60*, 20 pp., 2022.

[16] Romeiser, R., and H.C. Graber, Advanced coastal bathymetry retrieval from moving wave patterns in reprocessed spotlight SAR data, in *Proc. 13th European Conference on Synthetic Aperture Radar (EUSAR 2021)*, 185-187, VDE Verlag, Berlin / Offenbach, Germany, 2021.

[17] Senet, C.M., J. Seemann, and F. Ziemer, The near-surface current velocity determined from image sequences of the sea surface, *IEEE Trans. Geosci. Remote Sens.*, *39*, 492-505, 2001.

OSCAR: A NEW AIRBORNE INSTRUMENT TO IMAGE OCEAN-ATMOSPHERE DYNAMICS AT THE SUB-MESOSCALE

Adrien Martin[1], *Karlus Macedo*[2], *David McCann*[1], *Marcos Portabella*[3], *Louis Marié*[4], *José Marquez*[5], *,Ruben Carrasco*[6], *Rui Duarte*[7], *Adriano Meta*[2], *Christine Gommenginger*[1], *Petronilo Martin-Iglesias*[8], *and Tania Casal*[8]

[1]National Oceanography Centre, Southampton, United Kingdom of Great
[2]MetaSensing, Italy
[3]ICM-CSIC, Spain
[4]Ifremer, France
[5]Radarmetrics, Spain
[6]Hereon, Germany
[7]France Energies Marines, France
[8]ESTEC, ESA, Netherlands

Abstract – OSCAR (Ocean Surface Current Airborne Radar) is a new airborne instrument which provides unique 2D synoptic views of ocean and atmosphere dynamics (currents, waves, winds) below km-scale. OSCAR is the airborne demonstrator of SeaSTAR, an innovative satellite mission concept currently under study in Phase 0 of ESA Earth Explorer 11. SeaSTAR aims to observe ocean submesoscale dynamics and small-scale atmosphere-ocean processes in all coastal, shelf and polar seas by providing simultaneous measurements of current and wind vectors at 1 km resolution with accuracy better than 0.1 m/s and 2 m/s respectively. A key objective of SeaSTAR is to characterize, for the first time, the magnitude, spatial structure, regional distribution and temporal variability of upper ocean dynamics on daily, seasonal and multi-annual time scales, with particular focus on coastal seas, shelf seas and Marginal Ice Zone boundaries.

OSCAR was flown over the Iroise Sea (West of Brittany, France) in May 2022 during the SEASTARex campaign. The OSCAR operations and products are representative of the spaceborne concept, with geophysical parameters and accuracies that directly relate to those of the SeaSTAR satellite mission. In itself, OSCAR provides a new observing capability that will improve our understanding of microwave Doppler sensing of the ocean thanks to its unique Doppler and scatterometry capabilities in three azimuth directions. OSCAR's high-resolution images (8 metres pixels resolution) over a 5km swath provide 2D synoptic views of ocean and atmosphere dynamics below km-scales that are highly relevant to support and complement scientific investigations of fine-scale ocean-atmosphere processes based on in-situ, satellite and model data.

In this paper, we give an overview of the OSCAR system, of the SEASTARex campaign over the Iroise Sea in May 2022 and present the main preliminary results about the performance and imaging capability of the instrument.

OSCAR (Ocean Surface Current Airborne Radar) is a new airborne instrument which provides unique 2D synoptic views of ocean and atmosphere dynamics (currents, waves, winds) below km-scale.

OSCAR is a Ku-band (13.5 GHz) SAR system with Doppler and scatterometry capabilities in three azimuth look directions. It is an evolution of the Wavemill instrument where only squinted beams in two directions where only considered [1]. The OSCAR instrument features an along-track interferometric (ATI) baseline in two lines-of-sight squinted 45° fore and aft from the broadside direction. The fore and aft antenna pairs provide interferometric Doppler measurements in two views angularly separated by 90 degrees. This ensures two orthogonal measurements of the ocean surface motion velocity that enable the retrieval of the total ocean surface current vector. In addition, backscatter measurements from the broadside antenna in the zero-Doppler direction serve to retrieve wind direction and wind speed, which are critical to correctly measure total ocean surface currents.

In each line-of-sight, the ocean surface motion sensed by the microwave radar (after correcting for navigation and geometry) has two constituents: the total ocean surface current – consisting of all currents contributing to actual horizontal

transport of water – and a measurement bias associated with the Doppler signature of the surface scatterers responsible for the backscatter, a term known as Doppler wave bias or Wind-wave induced Artefact Surface Velocity — WASV [2]. The WASV is caused by the phase velocity of the surface scatterers responsible for the microwave backscatter (e.g. Bragg waves) and the effect of the orbital motion of longer ocean waves. The magnitude of the WASV can reach 0.5-1 m/s and is, at first order, a function of the wind direction. A number of geophysical model functions (GMFs) have been published in recent years to correct this effect

OSCAR is the airborne demonstrator of SeaSTAR, an innovative satellite mission concept currently under study in Phase 0 of ESA Earth Explorer 11 [3]. SeaSTAR aims to observe ocean submesoscale dynamics and small-scale atmosphere-ocean processes in all coastal, shelf and polar seas by providing simultaneous measurements of current and wind vectors at 1 km resolution with accuracy better than 0.1 m/s and 2 m/s respectively. A key objective of SeaSTAR is to characterize, for the first time, the magnitude, spatial structure, regional distribution and temporal variability of upper ocean dynamics on daily, seasonal and multi-annual time scales, with particular focus on coastal seas, shelf seas and Marginal Ice Zone boundaries.

OSCAR was flown over the Iroise Sea (West of Brittany, France) in May 2022 during the SEASTARex campaign. The OSCAR operations and products are representative of the spaceborne concept, with geophysical parameters and accuracies that directly relate to those of the SeaSTAR satellite mission. In itself, OSCAR provides a new observing capability that will improve our understanding of microwave Doppler sensing of the ocean thanks to its unique Doppler and scatterometry capabilities in three azimuth directions. OSCAR's high-resolution images (8 metres pixels resolution) over a 5km swath provide 2D synoptic views of ocean and atmosphere dynamics below km-scales that are highly relevant to support and complement scientific investigations of fine-scale ocean-atmosphere processes based on in-situ, satellite and model data.

Figure 3 presents first results from OSCAR. The aircraft is heading North with the antennas looking on the left side. The figure shows a general pattern of strong current flowing to the South-West. The position of the gradient agrees well with the satellite NovaSAR roughness image taken close to the OSCAR acquisition. On the southern part of the OSCAR acquisition we observe a secondary circulation which is in agreement with numerical model and X-band marine radar.

In the presentation, we will give an overview of the OSCAR system, of the SEASTARex campaign over the Iroise Sea in May 2022 and present the main results about the performance and imaging capability of the instrument.

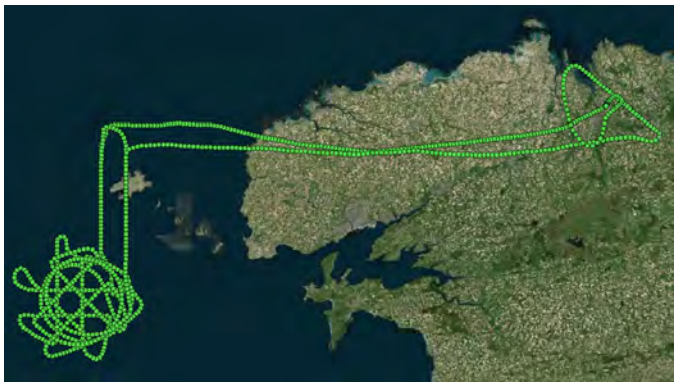

Figure 1 Flight path during the Brest campaign execution.

Figure 2 The aircraft and belly pod where the the OSCAR system and gimbal are installed.

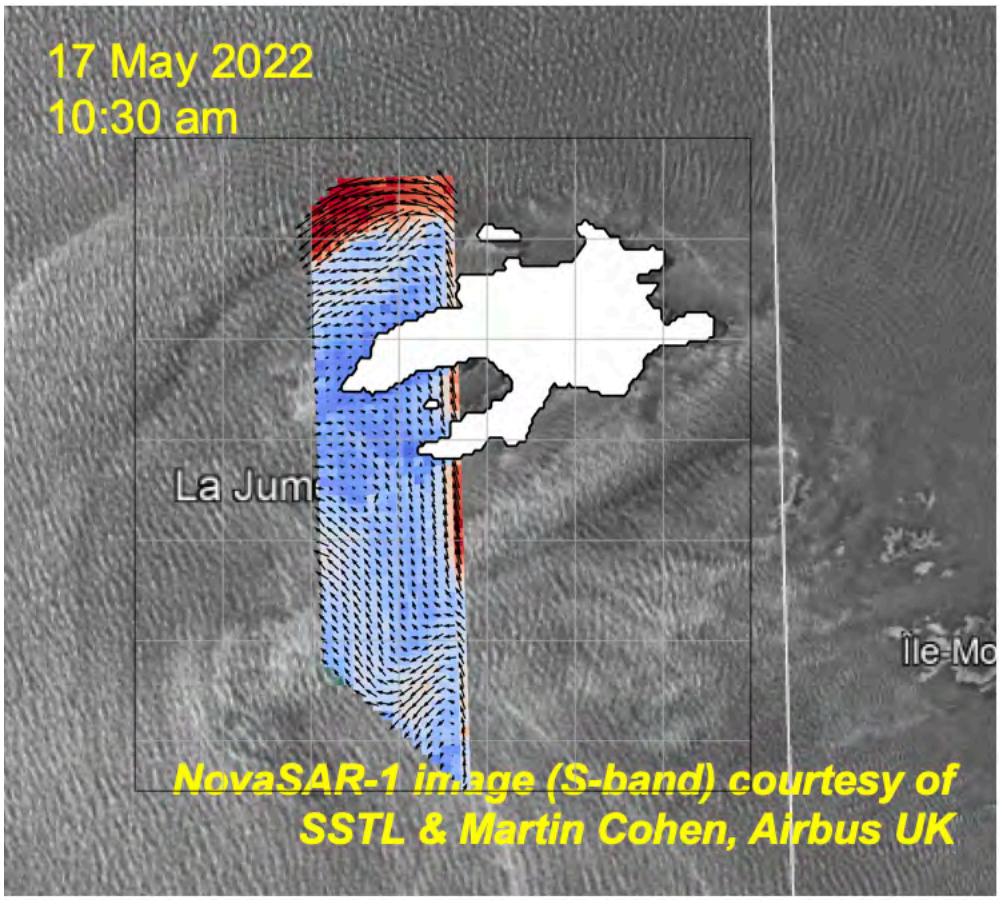

Figure 3: (background) NovaSAR roughness image in S-band at the time of OSCAR acquisition. (in color) OSCAR retrieved 2D current along the track. Near range is on the East part of the image.

ACKNOWLEDGEMENTS

This work was supported by ESA/ESTEC Contract Number 4000116410/16/NL/BJ for the OSCAR development and ESA/ESTEC contract number 400017623/22/NL/IA for the campaign over Iroise Sea.

REFERENCES

[1] Adrien C.H. Martin, Christine Gommenginger , "Towards wide-swath high-resolution mapping of total ocean surface current vectors from space: Airborne proof-of-concept and validation", *Remote Sensing of Environment*, Volume 197, 2017, Pages 58-71

[2] Adrien C.H. Martin, Christine Gommenginger, Jose Marquez, Sam Doody, Victor Navarro, Christopher Buck, "Wind-wave-induced velocity in ATI SAR ocean surface currents: First experimental evidence from an airborne campaign", *Journal of Geophysical Research: Oceans*, Volume121, Issue3, March 2016, Pages 1640-1653

[3] Gommenginger, Christine et al. , "SEASTAR: A Mission to Study Ocean Submesoscale Dynamics and Small-Scale Atmosphere-Ocean Processes in Coastal, Shelf and Polar Seas," *Frontiers in Marine Science*, Volume 6, p.457, 2019.

Ocean Surface Currents from Sentinel-1 Doppler observations

Artem Moiseev[1], Fabrice Collard[2], Johnny A. Johannessen[1,3]

[1]Nansen Environmental and Remote Sensing Center (NERSC), Bergen, Norway
[2]OceanDataLab (ODL), Locmaria-Plouzané, France
[3]Geophysical Institute, University of Bergen, Norway

Observations from satellite Synthetic Aperture Radars (SARs) can complement existing ocean observing systems with systematic kilometer-resolution observations of the total surface radial current velocity in the open ocean and coastal zones. Reliable and systematic observations of the total ocean surface currents are essential for monitoring, model validation, search and rescue operations, pollution applications, and climate research. However, such observations are challenging and expensive to acquire and, hence, rarely available on a systematic basis. In this study focusing on the greater Agulhas Current, the surface current retrieval algorithm for Sentinel-1 developed and validated in the ESA WOC project is presented.

We retrieved surface current radial velocities from the SAR Doppler Centroid Anomaly (DCA). This DCA is derived from the frequency difference between transmitted and backscattered signals after correcting for the satellite motion (geometric Doppler). Over the ocean, the DCA is a measure of the surface motion induced by the combination of the wind and waves (sea state) and ocean surface currents in the antenna line-of-sight direction. The sea-state-induced contribution to the DCA can be estimated from Empirical Geophysical Model Functions (GMFs), such as CDOP3SiX, for given radar incidence and polarization, based on wind and wave fields from collocated models. We evaluated the impact on the DCA of different global wind (ECMWF, NCEP GFS, ERA5) and wave (MFWAM, WAVERYS, WW3) model forecasts and reanalysis.

Although usage of the model fields is convenient due to their regular availability, it also yields limitations related to the accuracy and representativeness of the model product which will strongly impact the estimate of the sea state contribution to the DCA and, consequently, the SAR-derived radial surface current retrievals. As such we explore the potential of using SAR-derived wind and wave information to estimate the sea state DCA. We used wind fields routinely provided in Sentinel-1 L2 OWI product. For the wave field, we tested Sentinel-1 L2 OSW product as well as cross-spectra estimates provided for the Wave (WV) mode acquisitions. The new product was then compared with the previous product (see Figure 1b). Moreover, it was compared with the QG current product derived from altimetry (Figure 1c). Both SAR- and altimetry-derived surface current products agree on the location of the main ocean surface current features. We also demonstrated the potential of using the Sentinel-1-derived ocean surface current to validate model forecasts in the region. We collocated the SAR RVLs with ocean model fields from Mercator 1/12 deg. model (available from CMEMS) along the southern African coast. The model can reproduce the Agulhas Current features, however, disagreement with observations in terms of the location and velocity of meanders and eddies are evident.

In summary, we have demonstrated that the Sentinel-1 acquisition can provide valuable observations of the ocean surface current which are essential for systematic model validation, applications, and climate research. We also demonstrated the potential of using SAR-derived surface currents for model validation. The accuracy of the ocean surface current radial velocity retrieved from SAR, on the other hand, relies on the precise removal of the sea-state-induced signal. We developed and demonstrated a new approach for estimating this sea state contribution based on the wind and wave information which can be directly extracted from SAR observations. This approach provides a more reliable way to estimate sea state DCA compared to using auxiliary model fields. However, the algorithm requires more testing and systematic validation. The developed methodology is promising and ready to be applied to the operational Sentinel-1 mission (sustained operation until 2030) as well as for candidate future satellite missions designed for monitoring of the upper ocean circulation (e.g., SEASTAR and Harmony).

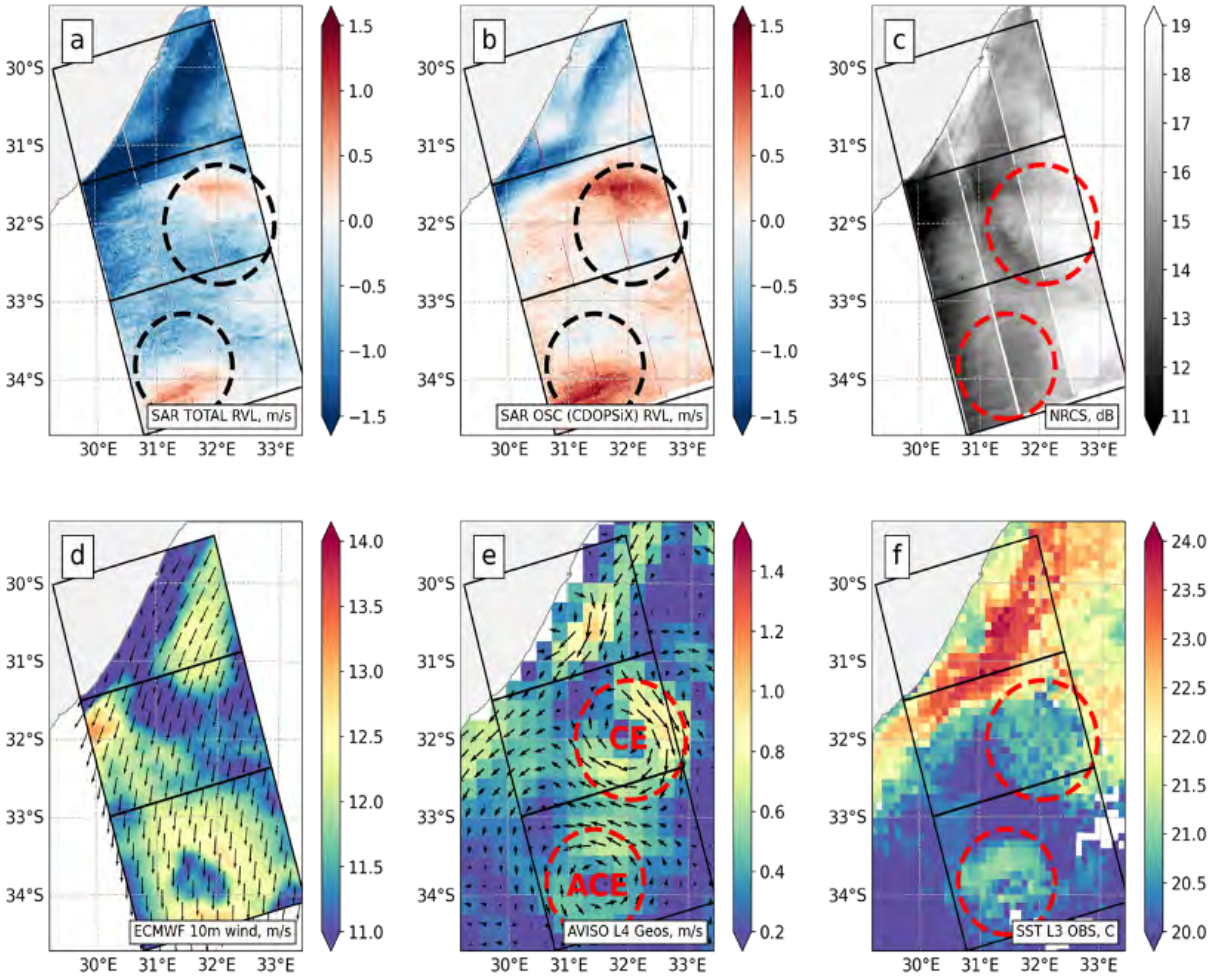

Figure 1. The Sentinel-1A SAR scene acquired in ascending pass on 7 July 2019 at 16:36:36: (a) Total surface radial velocity (i.e., wave- and surface-current-induced signal) from the Doppler shift; (b) Ocean surface current radial velocity (i.e., after removal of the sea-state-induced signal) from the Doppler shift;

(c) Normalized radar cross-section. The blue/red color in a, b indicates south-westward/north-eastward velocity. The SAR scene is collocated with: (d) Wind speed (color) and direction (arrows) at 10m height from the ECMFW; (e) Geostrophic velocity from altimetry observations; (f) Satellite-derived Sea Surface Temperature field. The black frames indicate the footprint of the SAR acquisition frames. The dashed contours in subplots b, c, e, f represent the position of the cyclonic (CE) and anticyclonic (ACE) eddies detected in the geostrophic velocity field

Towards Calibrated Sentinel-1 OCN RVL Products

G. Guitton[1], F. Collard[1], H. Johnsen[2], G. Engen[2], A. Recchia[3], A. Cotrufo[3], S. Brás[4], N. Miranda[5], M. Pinheiro[5]

[1]OceanDataLab, Locmaria, Plouzane, France.

[2]NORCE Norwegian Research Center AS, Tromsø, Norway.

[3]Aresys Ltd, Milano, Italy

[4]ESTEC/ESA, Noordwijk, The Netherlands

[5]ESRIN/ESA, Frascati, Italy

Corresponding author: G. Guitton (gilles.guitton@oceandatalab.com)

Co-author: F. Collard (dr.fab@oceandatalab.com), H. Johnsen (hjoh@norceresearch.no), G. Engen (geen@norceresearch.no), A. Recchia (andrea.recchia@aresys.it), A. Cotrufo (alessandro.cotrufo@aresys.it), M. Pinheiro (muriel.pinheiro@esa.int), N. Miranda (nuno.miranda@esa.int), S. Brás (sergio.bras@esa.int)

Abstract

The Doppler Centroid (DC) frequency shift recorded over ocean surfaces by Synthetic Aperture Radar (SAR) is a sum of contributions from satellite attitude/antenna and ocean surface motion induced by waves and underlying ocean currents. A precise calibration of the DC is needed in order to predict and subsequently remove contributions from attitude/antenna.

Recently, a novel data calibration technique based on combining gyroscope telemetry data and global Sentinel-1 WV OCN products has demonstrated promising capabilities to quantify the Sentinel-1 (S1) attitude and hence provide calibrated estimates of the corresponding DC frequency shift. For validation purpose, one year of S1 a and b WV OCN products, orbit data and gyroscope data are combined providing one year of restituted attitude data (AUX_ESTATT). For the same time period, mean DC bias versus elevation angle is computed on a daily basis from S1 IW land acquisitions (AUX_DCBIAS). The AUX_ESTATT and AUX_DCBIAS products are subsequently used to generate global data set of calibrated S1 WV OCN products as well as subsets of calibrated S1 IW OCN products from predefined super sites (Norwegian Coast, Agulhas, Mediterranean). In this paper we assess the accuracy and precision of the calibrated DC frequency of S1 WV and IW acquisitions acquired over both land and ocean areas. The DC standard deviation (STD) and bias show significant reduction for both satellites and for all swaths. Assessment of the performance of global WV data shows a STD around or less than 6Hz, while the BIAS is less than 2 Hz. The performance is very similar for both satellites and for both swaths. For IW the STD is similar, but small DC bias between sub-swaths is sometimes observed.

The remaining errors are mainly due to change in antenna characteristics on a timescale not captured with the procedure used to generate the mean DC bias stored in the AUX_DCBIAS file. Such changes may come from thermo-elastic effects and/or temperature compensations applied to the antenna. This directly affects the IW mode DC, where it is also clearly visible in some scenes. For WV mode it mainly impacts the statistics.

S1 WV mode has achieved a performance (i.e. accuracy and precision) within the requirement for climatology mapping of global ocean current features. It will be demonstrated on a longer time serie than the validation year.

For IW mode, we have achieved a precision within the requirement, but use of land areas within the scene is still required to achieve the required accuracy over all sub-swaths. Improved accuracy using DC over nearest land will be demonstrated and the limitations discussed. Remaining issues related to antenna temperature compensation and Level 0 Doppler estimates will also be discussed.

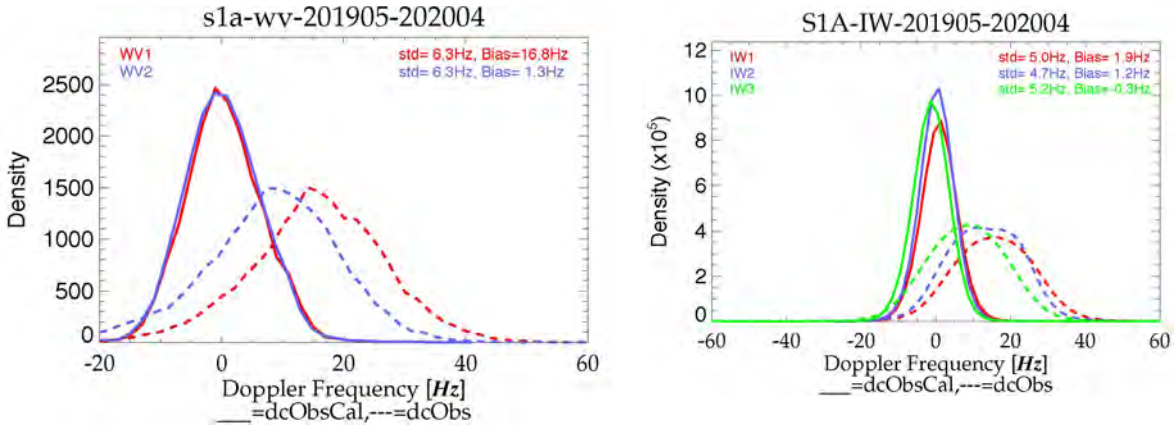

Figure: Histograms of observed (---) and calibrated (___) DC from S1a WV (left) and S1a IW (right) modes. Data acquired over land areas within the period 01 May 2019 to 30 April 2020.

EVALUATION OF SURFACE CURRENTS DERIVED FROM SENTINEL-1 SAR DOPPLER SHIFT IN THE NORTHWESTERN MEDITERRANEAN SEA USING COASTAL HF RADARS

Baptiste Domps

Degreane Horizon
Cuers, France
baptiste.domps@degreane-horizon.fr

Charles-Antoine Guérin

Univ. Toulon Aix-Marseille Univ.,
CNRS, IRD, MIO
Toulon, France
guerin@univ-tln.fr

ABSTRACT

We evaluate the estimations of oceanic surface currents retrieved from C-band synthetic aperture radar onboard Sentinel-1A/B. The assessment is carried out using reference measurements provided by a network of coastal high-frequency radars on the French Rivieira over 6 months.

1. INTRODUCTION

Real-time observations of coastal ocean surface currents have been routinely performed by high-frequency radars (HFR) for nearly half a century, starting with the pioneering works of Crombie [1] and Barrick [2]. Nowadays, the vast majority of HFR operate from shore in the HF and UHF frequency bands, typically from 5 to 50 MHz. Within this range, commercial HFR are proved to provide reliable estimates of surface currents at high spatial (typically 5 km) and temporal (typically 30 min) resolution, up to 100 km from coast [3]. The Mediterranean Institute of Oceanography (MIO) and the University of Toulon have been operating for more than one decade a network of such systems, manufactured by Helzel Messtechnik GmbH [4]. The network is located on the Western French Riviera, in the vicinity of Toulon, and consists in an original arrangement of spatially diverse systems with 2 distinct transmitters and receivers on 3 remote sites [5]. Such multistatic geometry allows to derive the total vector surface current on a $1\,\mathrm{km} \times 1\,\mathrm{km}$ Cartesian grid cell every 20 min whose quality have been assessed through two campaigns of *in situ* measurements [6]. Besides a wide range of oceanographic and operationnal applications, the Toulon HFR network is also an experimental ground for developing new signal processing techniques [7, 8].

Aside from ground-based systems, the measurement of the total suface current velocity from space at high resolution remains a challenge partially met by synthetic aperture radars (SAR) such as ASAR (formerly onboard ENVISAT) and C-SAR (currently onboard Sentinel-1). It is well known that SAR does not only measure the magnitude of the backscattered signal but also the Doppler frequency offset induced by the velocity of the scatterers. However, the Doppler shift is not simply proportionnal to the line-of-sight surface current. The surface current actually represents a minor contribution to the total frequency anomaly. The measurement is affected by a number of instrumental and environmental biases. While the former can be withdrawn by calibrating the frequency measurements (see, e.g., [9, 10]), doing so is less straightforward for the latter. The geophysical Doppler shift is yet dominated by wave-induced surface displacements whose contribution to the frequency anomaly can not be evaluated directly from the SAR measurements. One popular way to determine the wave-induced Doppler bias is to use a geophysical modeling function (GMF) such as CDOP [11]. This empirical GMF relates the wave bias to the surface wind speed and direction than can be routinely obtained from SAR measurements.

As of now the use of surface currents inferred from SAR measurements has not received a place within the oceanographic community. Such current estimations yet suffer from a lack of evaluation and uncertainty analysis. In the past few years, there have been isolated atempts to assess the validity of surface currents retrieved from Sentinel-1A/B using coastal HF radars [12, 13]. The results of these studies are promising and we contribute to this effort by using reference estimates provided by the HF radar network of Toulon.

2. EVALUATION OF SURFACE CURRENTS

Sentinel-1A/B measurements have been processed using the standard scheme (we refer to Fig. 1 of [9] for a description). The vector surface currents provided by the HFR network have been interpolated along the Sentinel-1 cartesian grid and projected along the SAR line-of-sight. An example of comparison between S1A/B and HFR currents is given on Figs. 1c and f. After visual inspection of the whole dataset, a total of 6 months of colocalized measurements have been compared from July 2020 to March 2021, accounting for about 150,000 individual comparisons.

Extended abstract submitted to SEASAR 2023

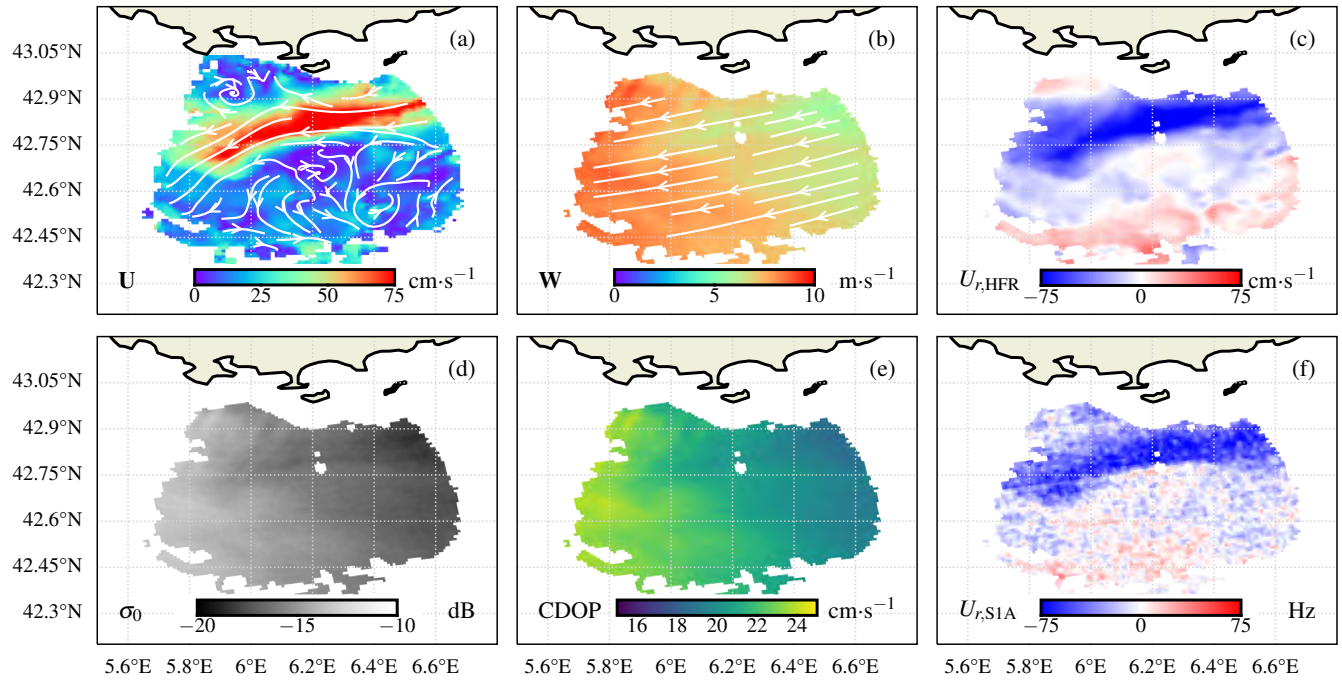

Fig. 1. Maps (colorscale) obtained off of Toulon on March 1st, 2021, at 17:30 UTC: (a) 2D surface current measured by the coastal HFR network of Toulon; (b) 2D 10-m wind obtained using CMOD7; (c) HFR surface current projected along S1A line-of-sight; (d) SAR NRCS; (e) wind-wave Doppler bias computed with CDOP; (f) radial surface current obtained from S1A measurements [14].

2.1. Overall Results

Fig. 2 shows the estimated surface velocity inferred from S1A/B SAR versus the projected surface velocity retrieved by the HFR network of Toulon. The root mean square error (RMSE) is of 21 cm s^{-1}. Thorough comparisons between ascending and descending orbits, Sentinel-1A and -1B or surface wind velocities will be presented during the conference.

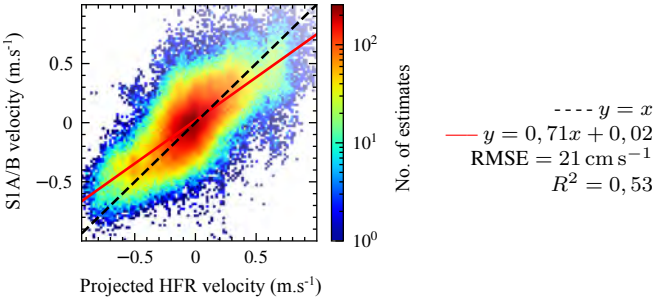

Fig. 2. Scatter plot (color scale, counts) of estimated surface velocities using the HFR network versus S1A/B.

2.2. Wave-induced bias

Within the classical processing scheme for inverting the radial surface current from the SAR Doppler shift, the wave-induced Doppler bias is given by a model (such as CDOP) as a function of the relative wind speed and direction

$$f_{ww} = \mathrm{CDOP}_{\mathrm{VV}}(u_{10}, \theta_{10}) \quad (1)$$

and is then substracted from the measured Doppler anomaly to give the current-induced Doppler shift

$$f_c = f_{dca} - f_{ww} \quad (2)$$

where $f_c = 2U_r/\lambda_0$. Here we use the surface current velocity provided by the HFR network as an a priori information for the frequency shift, plus the wind information retrieved from the SAR NRCS, to retrieve the wave-induced bias. This observed bias is then used to train a simple neural network, CDOP-TLN, as an alternative to CDOP suited for the observations in the vicinity of Toulon. This simple, empirical model yields to better estimates of the wave-induced bias than CDOP (Fig. 3), being however only valid in the coastal Mediterranean sea.

3. CONCLUSIONS AND FUTURE WORK

This study shows a remarkable agreement between the estimations of surface currents provided by Sentinel-1A/B and the HFR network of Toulon. Our ongoing research focuses on the thorough evaluation of these estimations. Furthermore,

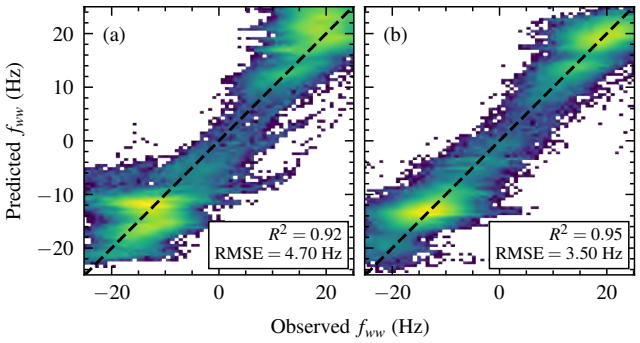

Fig. 3. Scatters plots (color scale, counts) of the wave induced bias observed versus predicted by: (a) CDOP; (b) CDOP-TLN.

we wish to refine our CDOP-TLN model by using the wave height information retrieved from the HFR.

4. REFERENCES

[1] D. D. Crombie, "Doppler Spectrum of Sea Echo at 13.56 Mc./s.," *Nature*, vol. 175, no. 4459, pp. 681–682, Apr. 1955.

[2] D. Barrick, "Remote Sensing of Sea State by Radar," in *IEEE Int. Conf. Eng. Ocean Env.*, 1972, pp. 186–192.

[3] H. Roarty et al., "The Global High Frequency Radar Network," *Front. Mari. Sci.*, vol. 6, 2019.

[4] K.-W. Gurgel, G. Antonischki, H.-H. Essen, and T. Schlick, "Wellen Radar (WERA): a New Ground-Wave HF Radar for Ocean Remote Sensing," *Coastal Engineering*, vol. 37, no. 3, pp. 219–234, 1999.

[5] C.-A. Guérin, D. Dumas, A. Gramoullé, C. Quentin, M. Saillard, and A. Molcard, "The Multistatic Oceanographic HF Radar Network in Toulon," in *IEEE Int. Radar Conf.*, Toulon, FR, 2020.

[6] D. Dumas, A. Gramoullé, C.-A. Guérin, A. Molcard, Y. Ourmières, and B. Zakardjian, "Multistatic Estimation of High-Frequency Radar Surface Currents in the Region of Toulon," *Ocean Dyn.*, vol. 70, pp. 1485–1503, 2020.

[7] B. Domps, D. Dumas, C.-A. Guérin, and J. Marmain, "High-Frequency Radar Ocean Current Mapping at Rapid Scale With Autoregressive Modeling," *IEEE J. Ocean. Eng.*, vol. 46, no. 3, pp. 891–899, 2021.

[8] D. Dumas and C.-A. Guérin, "New Signal Processing Techniques for Phased-Array Oceanographic Radars: Self-Calibration, Antenna Grouping and Denoising," *J. Atmos. Ocean. Technol.*, under revision.

[9] Morten Wergeland Hansen, Fabrice Collard, Knut-Frode Dagestad, Johnny A. Johannessen, Pierre Fabry, and Bertrand Chapron, "Retrieval of Sea Surface Range Velocities From Envisat ASAR Doppler Centroid Measurements," *IEEE Trans. Geosci. Remote Sens.*, vol. 49, no. 10, pp. 3582–3592, 2011.

[10] A. Moiseev, H. Johnsen, J. Johannessen, F. Collard, and G. Guitton, "On Removal of Sea State Contribution to Sentinel-1 Doppler Shift for Retrieving Reliable Ocean Surface Current," *J. Geophys. Res. Oceans*, vol. 125, Sept. 2020.

[11] Alexis A. Mouche, Fabrice Collard, Bertrand Chapron, Knut-Frode Dagestad, Gilles Guitton, Johnny A. Johannessen, Vincent Kerbaol, and Morten Wergeland Hansen, "On the Use of Doppler Shift for Sea Surface Wind Retrieval From SAR," *IEEE Trans. Geosci. Remote Sens.*, vol. 50, no. 7, pp. 2901–2909, 2012.

[12] A. Moiseev, H. Johnsen, M. Hansen, and J. Johannessen, "Evaluation of Radial Ocean Surface Currents Derived from Sentinel-1 IW Doppler Shift Using Coastal Radar and Lagrangian Surface Drifter Observations," *J. Geophys. Res. Oceans*, vol. 125, Mar. 2020.

[13] A. C. H. Martin, C. P. Gommenginger, B. Jacob, and J. Staneva, "First Multi-Year Assessment of Sentinel-1 Radial Velocity Products Using HF Radar Currents in a Coastal Environment," *Remote Sens. Environ.*, vol. 268, Jan. 2022.

[14] B. Domps and C.-A. Guérin, "Comparaison des courants de surface mesurés par radar côtier HF et par SAR spatial en Méditerranée," in *Journées d'études propagation radioélectrique*, Rennes, FR, 2021.

Sea Ice Retrievels

Sea Ice Retrievals

Wiehle, Stefan; Murashkin, Dmitrii; Frost, Anja; König, Christine; König, Thomas
Preliminary results of Sea Ice Classification using combined Sentinel-1 and Sentinel-3 data

Karvonen, Juha
Copernicus Marine Service SITAC SAR-Based Baltic Sea Ice Products

Lohse, Johannes; Dierking, Wolfgang
Combining C- And L-band SAR Data For Automated Sea Ice Classification & Segmentation

Frost, Anja; Imber, James; Murashkin, Dmitrii; Kortum, Karl; Gregorek, Daniel
Towards Multitemporal Sea Ice Classification By Means Of Spaceborne SAR Image Time Series

Wang, Qiang; Johansson, Malin; Lohse, Johannes; Doulgeris, Anthony P.; Eltoft, Torbjørn
The Impact of Input Features in Deep Learning Based Sea Ice Mapping

Eltoft, Torbjørn; Taelman, Catherine; Johansson, Malin; Lohse, Johannes; Gerland, Sebasitan; Dierking, Wolfgang
The CIRFA-2022 Cruise to the Western Fram-Strait: Objectives, Ground Measurements, and Preliminary Results

Li, Haiyan; Yang, Kun; Perrie, William
Fine Sea Ice Classification with Gaofen-3 Quad- Polarization SAR Observation

Demchev, Denis; Eriksson, Leif E.B.; Hildeman, Anders; Dierking, Wolfgang
Investigation of Multifrequency SAR Image Alignment by Ice Drift Compensation In The Marginal Ice Zone

Johansson, Malin; Singha, Suman; Spreen, Gunnar; Howell, Stephen
High resolution L- and C-band polarimetric variability during MOSAiC

Taelman, Catherine; Lohse, Johannes; Doulgeris, Anthony P.
Tracking Backscatter Signatures Of Individual Sea Ice Floes Using In-Situ Ice Drift Observations

Wulf, Tore; Buus-Hinkler, Jørgen; Singha, Suman; Kreiner, Matilde Brandt
Operational SAR-based Sea Ice Concentration Retrieval Using Convolutional Neural Networks

Korosov, Anton; Kleinherenbrink, Marcel
Potential Application of the Earth Explorer 10 candidate Harmony for Sea Ice Model Validation

Aparício, Sara
A Multisensory SAR-Based Approach For Melt Ponds Retrievals

Kim, Ekaterina; Skjetne, Roger; Høyland, Knut Vilhelm
Quadruple Helix Framework for Sea Ice Monitoring: Next Steps

Preliminary results of Sea Ice Classification using combined Sentinel-1 and Sentinel-3 data

Stefan Wiehle, Dmitrii Murashkin, Anja Frost, Christine König, Thomas König

***Abstract*—A sea ice classification is trained using a combination of Synthetic Aperture Radar (SAR) from Sentinel-1 and an existing sea ice classification using optical-thermal data from Sentinel-3. Compared to a SAR-only classification, preliminary results show improved classification reliability especially in open water areas.**

Sea ice is constantly changing: wind and ocean currents can push together large ice masses and close leads; the pack ice formed by these processes is often not navigable even by icebreakers. Combining radar measurements of Sentinel-1 and results of a sea ice classification using the optical/thermal measurements of the SLSTR instrument onboard Sentinel-3 offers the possibility to improve the sea ice situation awareness. In radar data, different ice classes can mostly be distinguished by different radar backscatter, but some ice classes exhibit a similar backscatter, limiting the applicability of radar-based classification. Sentinel-3 data contain optical/thermal information of water, ice, and snow, allowing a refined ice class separation after classification, but the observations are in lower resolution and clouds may obstruct the view. The fused classification is based on a Convolutional Neural Network (CNN) classifier and discriminates 6 surface types. Its input data are the HH and HV polarization channels of the Sentinel-1 image plus pre-classified Sentinel-3 images with continuous RGB labels. Improved sea ice classification allows planning of safer routes and better awareness for possible dangerous situations for polar ships.

***Index Terms*—Synthetic Aperture Radar, SLSTR, Sea Ice Classification, Sentinel-1, Sentinel-3, Sensor Fusion**

I. Introduction

Navigation through ice-infested waters is a challenge even for icebreakers. With the ongoing decline of polar sea ice cover, more shipping is expected in polar waters, especially commercial shipping along North-East- and North-West-Passage. Knowledge of the presence and type of sea ice is crucial for vessel safety. While sea ice charts are provided on a regular basis by several national sea ice services, their usabilty in changing sea-ice conditions is limited by their coarse resolution and low update frequency. An automated processing chain making high-resolution sea ice information generated from satellite data available directly to ship navigators will increase maritime safety in ice-infested waters. Such a processing chain is currently being developed using two sources of satellite data: Sentinel-1 (S-1) Synthetic Aperture Radar (SAR) data and Sentinel-3 (S-3) optical/thermal data from the Sea and Land Surface Temperature Radiometer (SLSTR).

S. Wiehle, D. Murashkin and A. Frost are with German Aerospace Center (DLR), Maritime Safety and Security Lab Bremen, Germany (email: {stefan.wiehle, dmitrii.murashkin, anja.frost}@dlr.de)

Ch. König and Th. König are with König und Partner Fernerkundung GbR, Dießen am Ammersee, Germany (email: rs.iceoffice@googlemail.com)

SAR detection is based on surface backscatter, in case of sea ice the SAR backscatter depends on the ice surface roughness and is used to discrimitate between different ice ages and types. The SLSTR data contains optical and thermal information, the sea ice classification is based on the surface (and sub-surface) reflectivity in different bands. Both sensors, hence, use different phenomena for sea ice observations and a fused classification is expected to have a higher quality than individual classifications using only one type of data. This submission covers the methods and workflow of the fused classification and preliminary results.

II. Method

This section covers the generation of the SLSTR classfication, data preparation for machine learning, and a description of the applied CNN classification.

A. SLSTR sea ice classification

The sea ice classfication from SLSTR data was presented in [1] and more details are provided therein. The classification uses the 9 bands of the SLSTR instrument for optical and thermal discrimination of ice classes and was extensively validated using official ice charts, comparisons to higher resolution satellite imagery, and webcam recordings. Its output is a continuous, three channel (RGB) sea ice classification with 19 surface types, of which 8 classes include open water and sea ice with up to approximately $50\,\mathrm{cm}$ thickness. Clouds are masked out using information from three of the SLSTR channels. The current processor was further improved compared to the version presented in [1], for example with refined cloud masking and better operational useability.

B. Data preparation

Two sources of satellite data are merged in this process: Sentinel-1 L1B scenes and the Sentinel-3 L2 classifed images. The S-1 data is acquired in Extended Wide Swath mode (EW) with a swath width of $410\,\mathrm{km}$ and consists of two channels, one for each polarizations (HH, HV). The data are delivered in GeoTiff format with a pixel spacing of $40\,\mathrm{m}$. The images are oriented in satellite flight direction and not projected in a Coordinate Reference System (CRS); georeferencing is supplied by Ground Control Points (GCPs). The S-3 data are ingested as pre-classified 3-channel RGB GeoTiffs, projected in a polar-stereographic CRS, with a swath width of $1420\,\mathrm{km}$ and a pixel spacing of $500\,\mathrm{m}$.

For further processing, both images have to be aligned, i.e. they need to have the same coverage, projection, and pixel

spacing. Therefore, first the S-1 data is warped to the CRS of the S-3 data. An intersection polygon of both scenes is then made and both scenes are cut to the extensions of this polygon. Since the S-1 image has lower coverage than the corresponding S-3 image, it is only cut in case of partial overlaps. The S-3 scene is then upsampled to the higher resolution of the S-1 scene, which finishes the alignment.

A binary validity mask in the same alignment is then created, marking areas where both scenes have valid data. Invalid data areas are clouds in the S-3 classification and black boundaries from reprojecting in both S-1 and S-3 data. Only pixels with valid data are later used in the training and classification.

The full stack of files for training consists of four files and seven channels:

- S-1 σ_0-calibrated image (HH, HV channels)
- S-3 classification (R, G, B channels)
- binary validity mask
- S-1 preview image of HH channel

The latter S-1 preview of the HH channel is saturation-adapted for better useability during the data labeling process, allowing the separation of ice classes by visual inspection. This channel is only used for training and not for inherence. One stack of files is generated for each S-1/S-3 scene pair.

C. CNN classification

The classification is conducted using a Convolutional Neural Network (CNN) using the previously described 6 channels (3 channels optical, 2 channels SAR, mask layer) as input data. A similar setup and method of classification was introduced before for SAR-only sea ice classification [2], more details on the classification algorithm are presented therein. The outcome is an image classified into six sea ice classes

- Open leads / water (smooth)
- Open leads / water (rough)
- New ice
- First Year ice
- Multi-Year ice
- Rough ice

plus an additional no-data entry used for areas with clouds (S-3 image) or geometrically not covered by both sensors.

III. Preliminary Results

The results presented in this section are derived from an early, limited training data sample of 12 data stacks as described in Section II-B. Figure 1 shows an exemplary set of input data (SAR, SLSTR) and a comparison of the classification results. The SAR scene in panel (a) is shown almost in full, only a small corner was removed during cutting. It is located at the boundary of the SLSTR scene and, hence, does not overlap fully. Panel (b) shows the SLSTR classification, here variations of red colors show sea ice with different ages of snow cover (darker: older, brighter: younger), while the green and green-brown tones show open water with different surface temperature (green: warmer, green-brown: colder, ready to freeze). Clouds are shown in different shades of grey, seen here at the right side of the panel. For a full description of the SLSTR classification and its colors, the reader is referred to [1]. Only a small part of the SLSTR scene is used since it was cut to the extends of the SAR scene. A SAR-only classification is shown in panel (c), using only the SAR data for training and inherence but otherwise identical to the fused classification. This does not correctly classify the bright open water sections in the lower right of the image. In comparison, the fused classification shown in panel (d) classifies most of these areas correctly as open water. Note that for this comparison, the validity mask derived from SAR and SLSTR (panels (a) and (b)) was applied to both classifications shown (panels (c) and (d)), visible by black borders and the cloud cutouts on the right side. In operational use, the SAR-only classification would not need to such a mask, it would only be applied to the fused classfication.

IV. Conclusions and Outlook

The presented preliminary results show that the fused sea ice classification from SAR and optical images can improve the results especially in the task of open water and lead detection. The inclusion of more training data samples and an extended comparison of results will allow more detailed findings in the future.

Automated satellite-based sea ice information services can benefit from using and combining both sources of data. It was demonstrated here already with the preliminary results that fused information can provide a better accuracy of sea ice class determination and thereby improve the safety of ships sailing through ice-infested waters.

The presented classification is to become part of a near-real time sea ice information generation and delivery chain. The high coverage and acquisition frequency of the SLSTR scenes results in regularly possible fused classifications, as long as there is no cloud cover blocking the acquisitions. Nevertheless, also the individual classifications from SAR and SLSTR are made available to the end users due to their much higher availability, as the fused classification is only available where both sensors have acquired spatially overlapping data within a time interval of several hours.

Acknowledgements

This work was prepared in the scope of the project EisKlass2, funded by the German Federal Ministry for Digital and Transport's mFUND programme under grant 19F2122.

References

[1] C. König, T. König, S. Singha, A. Frost, and S. Jacobsen, "Combined Use of Space Borne Optical and SAR Data to Improve Knowledge about Sea Ice for Shipping," *Remote Sensing*, vol. 13, no. 23, 2021.

[2] D. Murashkin and A. Frost, "Arctic Sea ICE Mapping Using Sentinel-1 SAR Scenes with a Convolutional Neural Network," in *2021 IEEE International Geoscience and Remote Sensing Symposium IGARSS*, 2021, pp. 5660–5663.

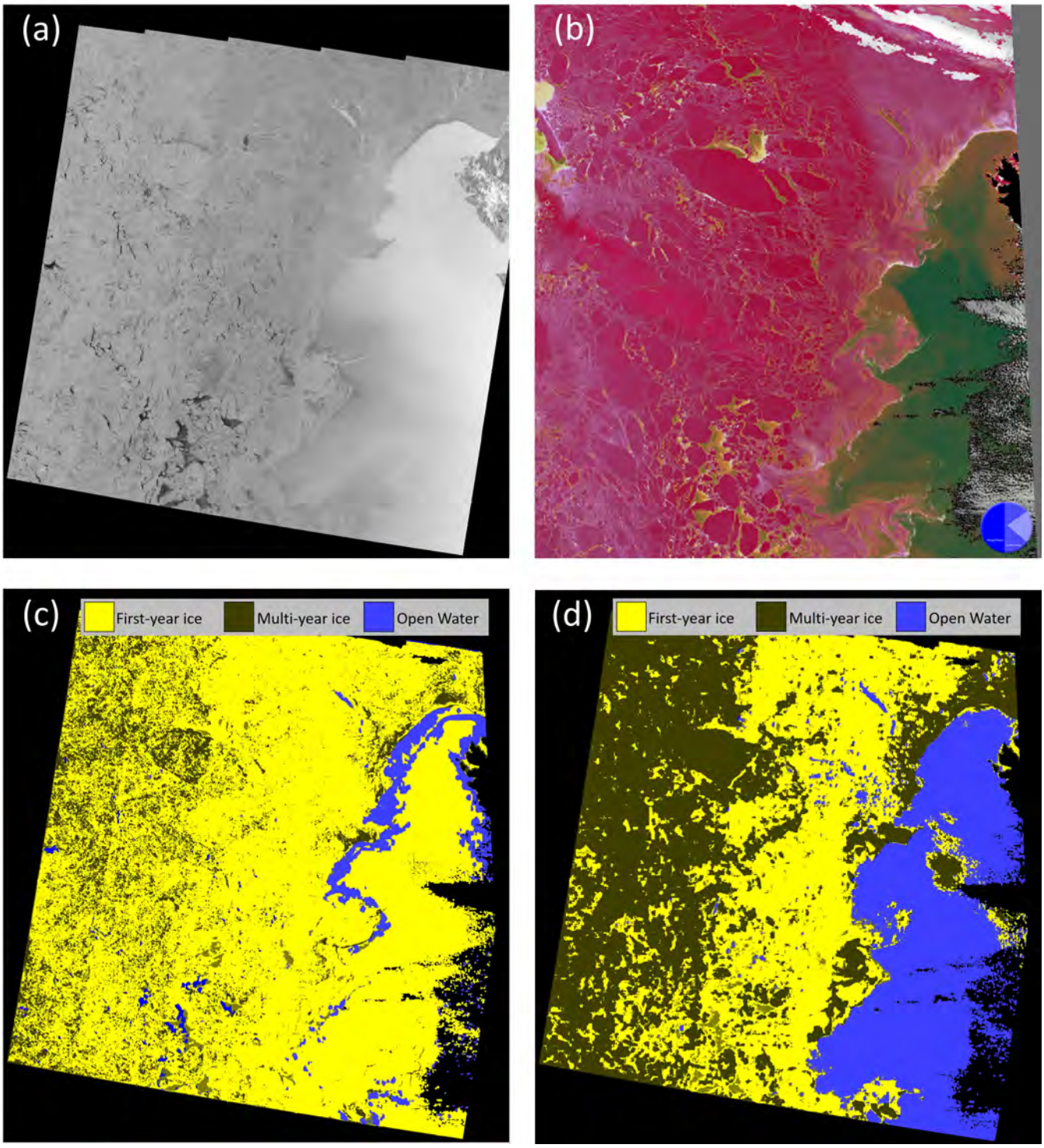

Fig. 1. Example data stack and classification results. (a) Sentinel-1 acquisition (HH, HV), (b) SLSTR classification (RGB); contains modified Copernicus Sentinel data (2020) (c) SAR classification using only Sentinel-1 data, (d) fused classification using SAR data and SLSTR classification. The open water areas in the lower right part of the figure are identified more correctly by the fused classification.

Copernicus Marine Service SITAC SAR-Based Baltic Sea Ice Products

Finnish Meteorological Institute (FMI) is providing automated sea ice products as part of the Copernicus Marine Service (CMS, part of the European Commission Copernicus Programme) sea ice thematic assembly center (SITAC) coordinated by MET Norway. The spatial cover of the products is the whole Baltic Sea and a typical temporal coverage is 1-3 days, depending on the availablility of SAR imagery. In the presentation an overview of the automated FMI SAR-based Baltic Sea ice products, their processing chain and their estimated quality will be presented, including examples of the products. Also plans for improvements and future new products will be discussed. The current products estimate three essential sea ice parameters: sea ice thickness (SIT), sea ice concentration (SIC) and sea ice drift (SID). During each Baltic Sea ice season, lasting approximately from the beginning of December until late May hundreds of SAR-based sea ice products are delivered to CMS by FMI. In Figure 1 the monthly amounts of delivered products grouped by product category for the season 2021-2023 are shown.

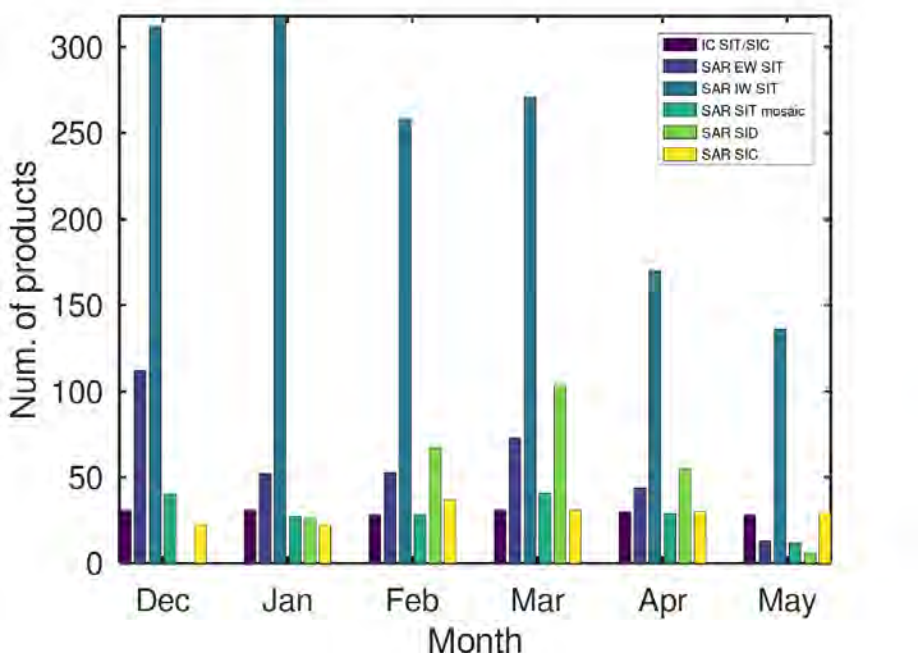

Figure 1. FMI CMS SITAC Baltic Sea ice products during the season 2021-2022 by category. The IC SIC and IC SIT are based on the daily ice charts made by the ice analysts at FMI/SMHI, the other products are automated and based mainly on SAR data.

The data quality is evaluated after each season and the bias, L1 difference (L1D) and root-mean-square difference (RMSD) for the estimates with respect to reference data sets are provided.

Sea ice Thickness (SIT)

SIT is currently based on SAR imagery supported by background information of the previous day ice chart. From SAR imagery only qualitative SIT information can be derived. For this reason quantitative background information of SIT is required. The current operational algorithm (Karvonen et al., 2003) uses ice chart ice thickness as its background information. It has also been shown that the background information can be produced by an ice model (Karvonen et al. 2008). The operational SIT algorithm was developed for C-band HH polarized data and it is applied to Sentinel-1 extra wide swath (EW) GRDM mode HH/HV-polarized data and to Radarsat-2 wide swath mode (WSM) HH/HV data. A slightly modified SIT algorithm is applied to Sentinel-1 IW mode VV/VH polarized data. The SIT products are given in 500m resolution and provided to the

CMS service in near-real-time (NRT), CMS time requirement being four hours from the SAR acquisition. In addition to the SIT grids, corresponding to each SAR image, a daily SIT mosaic is provided. In the daily SIT mosaic the most recent SIT information is overlaid over the older information and each grid point then contains the most recent SIT information available at the moment of the mosaic generation.

The reference data in evaluation of the SIT estimates are SIT measurements made by the Finnish and Swedish ice breakers. In the 2021-2022 evaluation the bias for the EW/WSM data was -0.7 cm (slight underestimation), L1D 8.5 cm and RMSD 10.2 cm. For the IW mode data the corresponding measures were 3.2 cm, 11.2 cm and 15.3 cm, indicating that SIT estimation using VV/VH data has slightly worse estimation accuracy than HH/HV data. The SIT estimation accuracy during 2021-2022 was similar as in the previous seasonal evaluations.

Sea Ice Concentration (SIC)

SIC is the fraction of sea ice within an area, which can be a grid point area or a segment defined by SAR segmentation or polygon drawn by hand. In the FMI SAR based products the reference areas are SAR segments produced by a segmentation algorithm. The algorithm provides SIC in percents, i.e. 0 % represents all open water and 100% all sea ice over the reference area. Baltic Sea SIC is provided daily in the morning after the Radarsat-2 and Sentinel-1 morning passes over the Baltic Sea. The product is a daily mosaic and generated from single image SIC grids in the same manner as the SIT mosaic. SIC is provided in 500m resolution. The SIC algorithm currently uses C-band HH(HV-polarized SAR data from Sentinel-1 and Radarsat-2 an additionally also microwave radiometer data from AMSR2. The algorithm is based on a multilayer perceptron (MLP) neural network combining texture measure inputs based on the SAR data and polarization and gradient ratios based on the AMSR2 brightness temperatures of different frequency channels. The algorithm is described in detail in (Karvonen, 2017).

In evaluation of the SIC data, the FMI ice chart SIC and 3.125 km resolution ASI algorithm (Spreen et al. 2008) SIC, also based on AMSR2 data, are used as reference SIT data sets. For the season 2021-2022 data the bias, L1D and RMSD were -3.7 (underestimation), 10.4 and 26.2 percentage points, respectively. The corresponding values when compared to ice chart SIC were -1.0, 7.0 and 22.3 percentage points. Also the 2021-2022 SIC estimation accuracy has remained similar as during the previous seasons.

Sea Ice Drift (SID)

SID is estimated based on matching two SAR images acquired at different time instants over the same area, i.e. based on multitemporal SAR analysis. Sentinel-1 EW mode and Radarsat-2 SCW data are currently used in the SID estimation. Because during longer time periods sea ice may deform too much for reliable matching of the multitemporal SAR data, we restrict the time difference between the SAR images to be less than three days. Baltic Sea SID was for a long time estimated using a two-resolution phase correlation approach (Karvonen 2012). However, since 2020 a new algorithm was established. The new algorithm also operates in two resolutions, first a coarse resolution pattern matching by the ORB algorithm (Rublee et al. 2011) is performed and the resulting coarse resolution SID is then refined in fine resolution by applying Lucas-Kanade optical flow (Lucas and Kanade 1981). Optical flow has the capability of estimating the movement from an image to another with a sub-pixel resolution. SID estimates are evaluated using ice drifter buoys deployed almost every winter. The evaluation is performed separately for short drift and larger drift. For larger drift both direction and magnitude are evaluated, for short drift only magnitude. In general, the estimated drift and buoy drift correspond to each other quite well. However, there exist

some outliers that typically give short SID estimates for some significantly longer buoy motions. It seems that these cases occur near the boundary of static and drift ice.

Product development

We are continually developing the products and try to involve new SAR data in the production chain. Currently the integration or Radarsat Constellation Mission (RCM) HH/HV C-band SAR data is under construction. The RCM rdata reireval and preprocessing have already been implemented but RCM data are not used for the products yet. Also X-band SIT algorithm utilizing X-band HH-polarized SAR data from TerraSAR-X, Cosmo-SkyMED and PAZ is currently in operational test phase. We are also studying good ways to estimate the degree of ice deformation and identifying single large pressure ridges based on SAR imagery. We expect that this work will later result into a SAR degree of deformation classification product to be included in the FMI CMS SITAC product portfolio. To improve estimation accuracy we have plans to utilize convolutional neural netrorks (CNN) in SIC estimation and possibly for other sea ice parameters as well. We have already successfully applied CNN to Sentinel-1 SAR data for SIC estimation (Karvonen 2022) and integrating AMSR2 microwave radiometer data in the CNN model is well under construction.

References

J. Karvonen, M. Simila, I. Heiler, Ice Thickness Estimation Using SAR Data and Ice Thickness History, Proceedings of the IEEE International Geoscience and Remote Sensing Symposium 2003 (IGARSS'03), 2003.

J. Karvonen B. Cheng, M. Simila, Ice Thickness Charts Produced by C-Band SAR Imagery and HIGHTSI Thermodynamic Ice Model, Proc. of the Sixth Workshop on Baltic Sea Ice Climate, pp. 71–81, Lammi, Finland , 2008.

J. Karvonen, Operational SAR-based sea ice drift monitoring over the Baltic Sea, Ocean Sci., 8, 473-483, doi:10.5194/os-8-473-2012, 2012. http://www.ocean-sci.net/8/473/2012/os-8-473-2012.html

J. Karvonen, Baltic Sea Ice Concentration Estimation Using SENTINEL-1 SAR and AMSR2 Microwave Radiometer Data, IEEE Transactions on Geoscience and Remote Sensing, v. 55, n. 5, pp. 2871 - 2883, 2017.

J. Karvonen, Baltic Sea Ice Concentration Estimation From C-Band Dual-Polarized SAR Imagery by Image Segmentation and Convolutional Neural Networks, in *IEEE Transactions on Geoscience and Remote Sensing*, vol. 60, pp. 1-11, 2022, Art no. 4301411, doi: 10.1109/TGRS.2021.3097885, 2022.

B. D. Lucas and T. Kanade, An iterative image registration technique with an application to stereo vision. Proceedings of Imaging Understanding Workshop, pages 121–130, 1981.

E. Rublee, V. Rabaud, K. Konolige and G. Bradski, ORB: An efficient alternative to SIFT or SURF, *2011 International Conference on Computer Vision*, Barcelona, Spain, pp. 2564-2571, doi: 10.1109/ICCV.2011.6126544, 2011.

Spreen, G., L. Kaleschke, and G.Heygster (2008), Sea ice remote sensing using AMSR-E 89 GHz channels J. Geophys. Res.,vol. 113, C02S03, doi:10.1029/2005JC003384.

Combining C- And L-band SAR Imagery For Automated Sea Ice Classification And Segmentation

Johannes Lohse[1] and Wolfgang Dierking[1,2]

1) UiT The Arctic University of Norway
2) Alfred Wegener Institute, Helmholtz Center for Polar and Marine Research

Abstract

Operational activities and environmental studies in the Arctic both require robust and reliable mapping of sea ice conditions. Because of its 24/7 imaging capability, synthetic aperture radar (SAR) is the main data source for operational ice charting in national ice services worldwide. At present, the daily distributed ice charts are largely produced manually by visual interpretation of the SAR imagery. The most commonly used frequency is C-band, and data is available for example through the Sentinel-1 or Radarsat-2 satellites. Future missions, such as for example ROSE-L or Sentinel-1 NG, are expected to further increase the total amount of available SAR images and will in addition provide data at different frequencies, in particular L-band, for operational monitoring. The huge amount of data will require (semi-)automated analysis, and studies are needed in order to determine the ideal configuration of future satellites missions. Here, we use a set of 161 aligned image pairs acquired at C- and L-band to investigate the benefits of combining both frequencies for multi-frequency classification and segmentation of sea ice types. The image pairs were acquired over three different test sites, located in Fram Strait, Lincoln Sea, and Belgica Bank. Sea ice drift between image acquisitions is compensated, using an algorithm developed at Chalmers University of Technology, such that we can stack the C- and L-band data pixel-by-pixel. We then perform supervised classification and unsupervised segmentation of the image pairs, using both single-frequency (C- and L-band as stand-alone) and dual-frequency approaches. We evaluate the classification results in terms of classification accuracy, and the segmentation results in terms of how many statistically separable clusters are found in each data set. Our results presented here clearly show the benefits of combining the complementary information from both frequencies, in particular for the classification of young ice, open water, and newly formed ice in lead areas.

I. Introduction

Monitoring and continuous mapping of the Arctic sea ice is essential to support marine traffic and navigation in the Arctic and to assess the state of the sea ice cover for environmental and climate studies. Hence, daily sea ice charts are provided by national ice services around the world. Because of its independence of sunlight and cloud conditions, synthetic aperture radar (SAR) is the main data source for operational ice charting. Production of the ice charts is at present done manually via visual interpretation of the imagery by expert ice analysts; a time-consuming process that depends on the training and experience of the individual analyst. Automation or semi-automation of the ice chart production ("computer-assisted ice charting") is thus a desirable goal. Furthermore, the operational workflow in many ice services is predominantly based on imagery acquired at C-band, even though it has been shown that other frequencies, such as for example L-band, can offer valuable complementary information [1]. This focus on C-band is mostly caused by the fact that L-band data is not yet routinely available for operational purposes. However, by the end of this decade, ESA's upcoming ROSE-L mission [2] will consistently provide L-band data which can be exploited for ice charting.

The work presented here is part of the ESA project *Synergistic Use of L- and C-Band SAR Satellites for Sea Ice Monitoring* (LC-ICE). In this study, we investigated the benefits of combining C- and L-band SAR imagery in a dual-frequency approach for automated mapping of sea ice types. This type of analysis requires perfectly aligned SAR data from both frequencies; the data set that we used is introduced in Section II. In Section III we briefly describe the algorithms and the layout of our experiment. We summarize and discuss the main results in Section IV.

II. Data Set

Multi-frequency classification and segmentation of sea ice imagery requires spatially overlapping image pairs at C- and L-band, acquired close in time. For the LC-ICE project, such image pairs were collected over different test sites in the Arctic. Here, we use data from the *Belgica Bank*, *Fram Strait*, and *Lincoln Sea*. The C-band images are acquired by Sentinel-1 (S1) and the L-band data by ALOS-2 PALSAR, respectively. All S1 data used in this study are in extra-wide swath (EW) mode. We use the ground range detected format at medium resolution (GRDM), which at present is the most commonly used S1 data format in operational sea ice charting. Our ALOS-2 data is available in both wide beam (WB) and fine beam (FB) mode. Specifications of the sensor acquisition modes used in this study are listed in Table 1.

TABLE I
SENSOR ACQUISITION MODES USED IN THIS STUDY

	S1 EW GRDM	**ALOS-2 WB**	**ALOS-2 FB**
swath width (km)	410	350	70
pixel spacing (m)	40x40	25x25	6.25x6.25
looks	ENL: 10.7	5(r)x3(a)	2
polarizations	HH, HV	HH, HV	HH, HV

For a joint, multi-frequency analysis, the individual images in each image pair must be perfectly aligned, so that they can be stacked to a multi-dimensional data cube. Here, we use a set of 161 aligned image pairs, for which the sea ice drift during the time interval between the C- and L-band acquisition was compensated using an algorithm developed at Chalmers University of Technology [3]. The aligned image pairs are calibrated, noise-corrected, and geocoded; the backscatter intensities are converted to decibel (dB).

III. METHOD

A. Selection of areas of interest within image pairs

We have visually inspected all image pairs to ensure correct alignment and to check for undesired alignment artifacts in the imagery. We have then selected an area of interest (AOI) within each pair that is suitable for the study of multi-frequency classification. The main goal of the AOI selection is to choose areas that are as large as possible, but small enough to:

- avoid too wide IA range
- avoid visible swath boundaries and influence of sensor noise
- exclude areas with mis-alignment or alignment artifacts

B. Classification and segmentation

We apply both supervised classification and unsupervised segmentation on the selected AOIs, using algorithms developed by Lohse et al. (2020) [4] and Doulgeris (2015) [5], respectively. Both algorithms are based on well-established statistical methods that use multi-variate probability density functions and Bayesian decision rules.

The classification algorithm assigns each image pixel to a set of class labels that are defined based on training data. We evaluate its performance in terms of classification accuracy (CA), which is estimated from a set of validation data. Regions of interest (ROIs) of different ice types for training and validation are selected manually based on visual interpretation of the combined C-/L-band image pairs.

The segmentation algorithm automatically determines the number of clusters based on the statistics of the input data. As we gradually increase the sensitivity of the algorithm, the number of resulting clusters increases. We then use the Jeffries-Matusita (JM) distance to asses the separability of the clusters. Finally thresholding the JM distance allows us to find the optimal number of clusters and thus quantify the statistically separable information in the imagery in an unsupervised approach.

We perform both classification and segmentation using single-frequency (C-band and L-band as stand-alone) and dual-frequency data as input, which allows us to assess the added value of combining both frequencies.

IV. RESULTS AND DISCUSSION

Our results clearly show the benefit of combining C- and L-band data for automated separation of sea ice types. With the segmentation approach, the combination of C- and L-band on average separates 2.4 more clusters than C-band alone, and 1.0 more clusters than L-band alone. For the classification, we find that the dual-frequency approach achieves the highest CA in 98.1 % of all cases. In some cases, in particular for regions of deformed ice, the L-band stand-alone classification performs almost or equally as well as the dual-frequency classification. However, especially in lead areas with open water, newly formed ice, and young ice, the combination of C- and L-band is usually superior to either of the single-frequency approaches.

An example AOI with selected ice type ROIs and a comparison of classification results is shown in Figure 1. It demonstrates the superiority of L-band for separating level and deformed ice compared to C-band; the good separation of these ice types at L-band is retained in the multi-frequency scenario. Furthermore, a lead stretching from east to west in the lower part of the image is generally identified in the stand-alone classification results at both C-band and L-band. However, at L-band, almost the entire lead is classified as *Young Ice*, while at C-band the lead is split up into *OW/New Ice*, *Young Ice*, and *Level Ice*. Only the combination of both frequencies manages to capture the lead as a mixture of *OW/New Ice* and *Young Ice*, with small parts in the northern area being open, and the majority of the lead being re-frozen. At the conference, we will present further examples with corresponding CAs and discuss differences between C- and L-band.

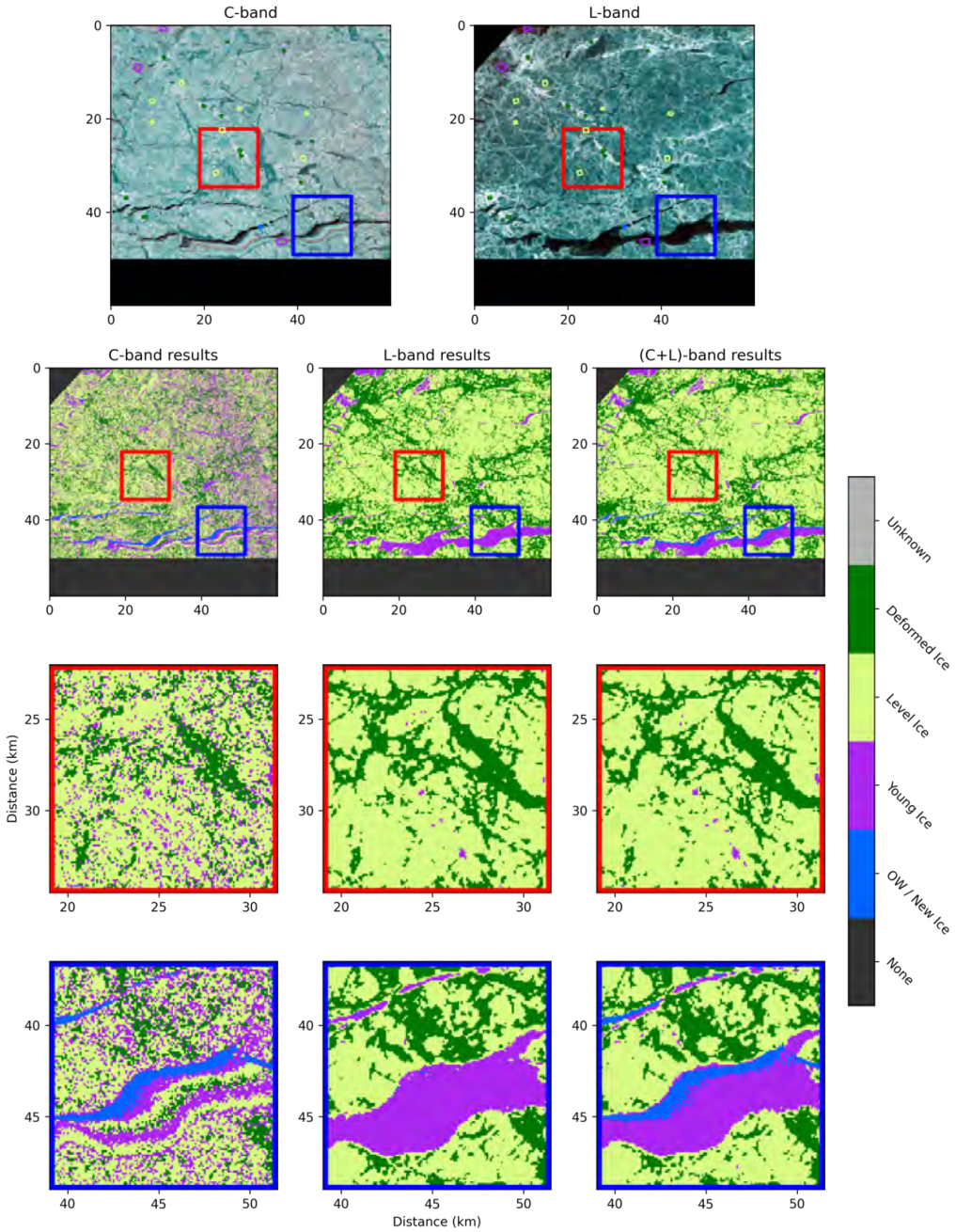

Fig. 1. Classification example from Fram Strait test site, 2019/12/10, acquisition time difference $\Delta t = 1.7$hours. C- and L-band false-color RGB images (R-HV, G-HH, B-HH) with training and validation ROIs for different ice types are shown at the top, single- and multi-frequency classification results below, including close-ups of the areas marked by red and blue squares.

References

[1] W. Dierking and H. Skriver, "What is Gained by Using an L-band SAR for Sea Ice Monitoring? (84)," in *Envisat & ERS Symposium*, vol. 572, 2005.

[2] W. Dierking, "Synergistic Use of L-and C-Band SAR Satellites for Sea Ice Monitoring," in *2021 IEEE International Geoscience and Remote Sensing Symposium IGARSS*. IEEE, 2021, pp. 877–880.

[3] L. Eriksson, D. Demchev, A. Hildeman, and W. Dierking, "Alignment of L-and C-Band SAR Images for Enhanced Observations of Sea Ice," in *IGARSS 2022-2022 IEEE International Geoscience and Remote Sensing Symposium*. IEEE, 2022, pp. 3798–3801.

[4] J. Lohse, A. P. Doulgeris, and W. Dierking, "Mapping sea-ice types from Sentinel-1 considering the surface-type dependent effect of incidence angle," *Annals of Glaciology*, vol. 61, no. 83, pp. 260–270, 2020.

[5] A. P. Doulgeris, "An Automatic $\mathcal{U}$-Distribution and Markov Random Field Segmentation Algorithm for PolSAR Images," *IEEE Transactions on Geoscience and Remote Sensing*, vol. 53, no. 4, pp. 1819–1827, 2015.

Towards Multitemporal Sea Ice Classification By Means Of Spaceborne SAR Image Time Series

Anja Frost[1], James Imber[1], Dmitrii Murashkin[1], Karl Kortum[1], Daniel Gregorek[2]

[1]DLR (German Aerospace Center), Remote Sensing Technology Institute, Maritime Safety and Security Lab Bremen, Germany

[2]MARUM, Center for Marine Environmental Sciences, Bremen, Germany

The greatest threat to the Arctic is climate change. Nowhere else is the earth warming up faster than here: Within the last 100 years, the average annual temperature here has risen by five degrees Celsius. Permafrost is thawing. Sea ice is disappearing, more precisely; Multiyear ice has been replaced by seasonal ice, and ice-covered areas have been partially replaced by open water [1]. Therefore, there is a high demand to monitor the Arctic and its sea ice, not only by extend but also by age.

Synthetic Aperture Radar (SAR) satellites are able to observe small- and large-scale structures in the sea ice in any weather, through clouds and darkness, due to their active Radar antenna. This makes them well suited to monitor changings in remote areas of the Arctic. However, to analyze large amounts of data sufficiently, automatic algorithms for classifying the sea ice in terms of their stages of development are requested. The development of these algorithms has long been a focus of research ever since the advent of satellite borne SAR [2].

Since then, an abundance of approaches for SAR based sea ice classification have been developed, summarized comprehensively in [3]. The most promising approaches have been transferred to operational services. Nevertheless, obtaining accurate classifications year-round is still a challenge. Different ice classes can show similar radar backscatter responses, which limits the performance of sea ice classification. Seasonally, the radar backscatter signal can be affected by precipitations e.g. wet snow obscures information about underlying ice types [4].

In order to stabilize automated classification, we show here the first tests on multitemporal sea ice classification. That is, we use collocated, sequential SAR acquisitions taken over a region of interest, and – as sea ice is driven by winds and ocean currents – run our sea ice drift retrieval algorithm, which we presented in [5, 6] and improvements of it, for capturing fine-scale sea ice motions especially at the borders of different ice sheets in [7]. Using the retrieved drift vector information, we are able to track drifting pieces of ice (such as an ice floe) from one SAR acquisition to the next, and collect more SAR measurements about the floe. The collected SAR measurements are then used jointly to classify the sea ice.

In the study presented here, we only use pairs of SAR images. Larger time series will be considered in future work. We present preliminary test results with Sentinel-1 (S1) data taken over the Arctic Ocean offshore close to Cape Morris Jesup between the Lincoln and Wandel Seas during December 2021, when the ocean showed a closed cover of drift ice (according to dmi ice charts), which most probably consisted of mainly multiyear ice [8-10] and some small leads of open water. East of Cape Morris Jesup, the concentration of multiyear ice may have decreased.

Sea ice classification

The core of the sea ice classification algorithm is an adjusted UNET++ convolutional neural network architecture described by [11]. In our specific implementation, the classification is done tile-wise, i.e. a S1 acquisition is divided into tiles, classified, and then the results are joined back to generate an ice map as shown in [12]. We differentiate six sea ice types: multiyear ice (MYI), first-year ice (FYI), young ice (YI), open leads (split in so-called dark leads (DL) and bright leads (BL)) and rough ice (RI). For each ice type (and each pixel) a discrete probability distribution over ice type is output. In general, the ice type with the highest probability is then selected for the final ice map.

As an example, Fig. 1 shows sea ice classifications (most likely ice type) of two S1 acquisitions taken on 6th Dec. 2021 11:25 UTC and 7th Dec. 2021 17:01 UTC over the study area. Although the sea ice has not changed significantly in the two days according to visual inspection of the radar backscatter signal, both classification results differ a lot. The sea ice classification for the 6th Dec. shows young ice in large areas. The result for the 7th Dec. appears to better reflect the real sea ice situation offshore.

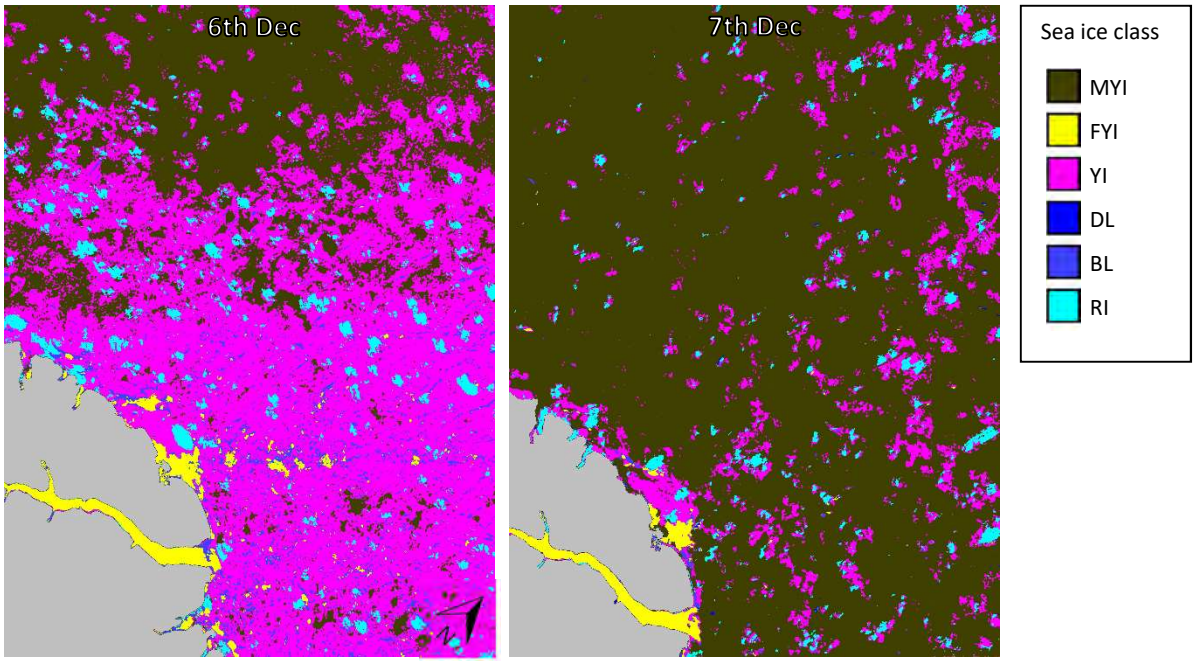

Fig. 1: Examples of sea ice classification individually performed on two subsequent Sentinel-1 (S1) acquisitions taken on 6th Dec. 2021 11:25 UTC (left) and 7th Dec. 2021 17:01 UTC (right) over the Arctic Ocean offshore close to Cape Morris Jesup, which is mainly covered with MYI. Even though sea ice has not changed significantly, the classifications differs a lot.

Fusion

We fuse the discrete probability distributions of the subsequent acquisitions considering the underlying drift. Fig. 2 shows the sea ice drift vector field used for the drift compensation. In the given case, the sea ice moved quite homogeneously eastwards with up to 500 m/h.

Fig. 3 is generated out of the two individual classifications, more precisely, the most likely class from both probability distributions is selected after drift compensation. The unlikely presence of “young ice” over Lincoln Sea on 6th Dec. gets automatically corrected in most parts as there is a higher probability of "multi-year ice" the following day. This example showcases the strength of multitemporal sea ice classification. It provides the basis to overcome misclassifications and overall to generate sea ice classifications with increased reliability.

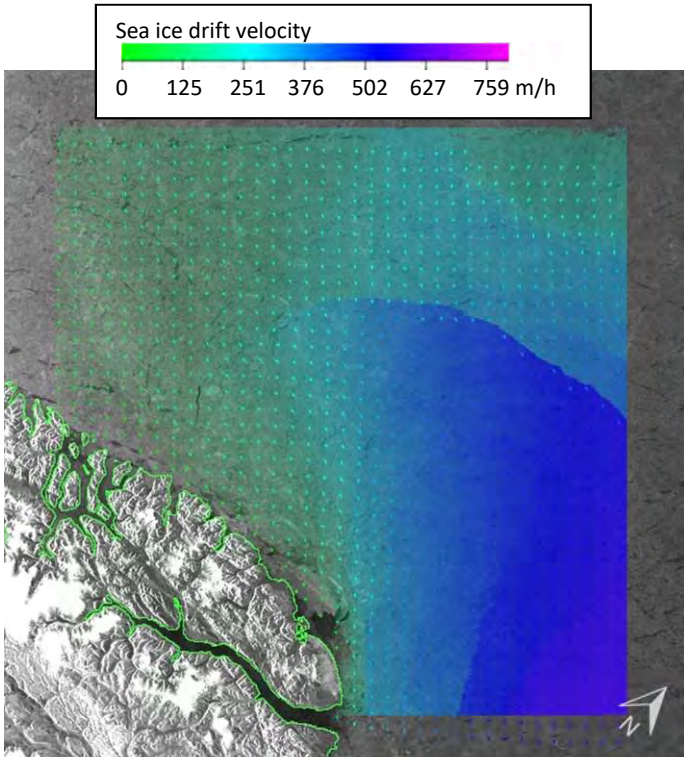

Fig. 2: Sea ice drift estimated from the two S1 acquisitions used for the sea ice classifications in Fig. 1. Grey scales show S1 HH data from 7th Dec. 2021. Overlaid colours represent retrieved sea ice drift velocity in 500 m resolution and arrows illustrate sea ice drift vectors (10 km spacing).

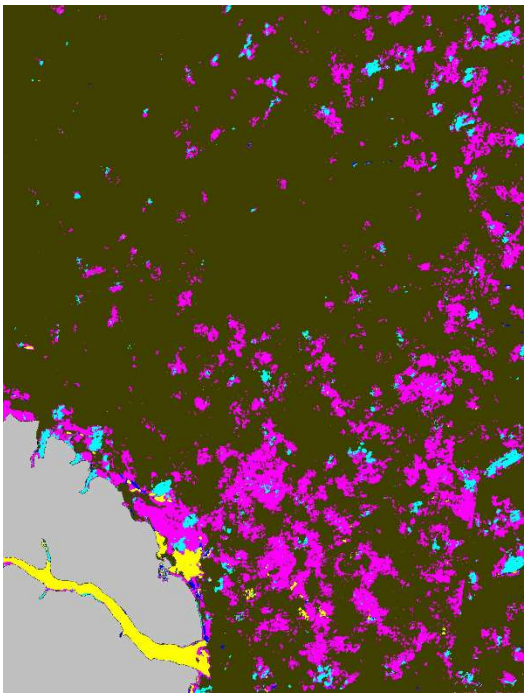

Fig. 3: Sea ice classification based on the two S1 acquisitions used for the sea ice classifications in Fig. 1. The unlikely presence of "young ice" over Lincoln Sea on 6th Dec. gets corrected in most parts. Colour legend see Fig. 1 top right.

Discussion

For fusing probabilities, various approaches can be applied, namely Kalman filter, Bayesian networks, and Dempster-Shafer. In ongoing work, we consider Kalman filtering and incorporate a priori knowledge to forbid impossible class changes e.g. from "young ice" to "multiyear ice" and vice versa.

References

[1] Planck, C., Perovich, D. K., & Light, B. (2017, December). Summertime heat and Arctic ice retreat: the role of solar heat on bottom melting of Arctic sea ice. In AGU Fall Meeting Abstracts.

[2] Ressel, R., Frost, A., & Lehner, S. (2015). Navigation assistance for ice-infested waters through automatic iceberg detection and ice classification based on TerraSAR-X imagery. The International Archives of Photogrammetry, Remote Sensing and Spatial Information Sciences, 40(7), 1049.

[3] Zakhvatkina, N., Smirnov, V., & Bychkova, I. (2019). Satellite SAR data-based sea ice classification: An overview. Geosciences, 9(4), 152.

[4] Kortum, K., Singha, S., & Spreen, G. (2022). Robust Multiseasonal Ice Classification From High-Resolution X-Band SAR. IEEE Transactions on Geoscience and Remote Sensing, 60, 1-12.

[5] Frost, A., Jacobsen, S., & Singha, S. (2017, July). High resolution sea ice drift estimation using combined TerraSAR-X and RADARSAT-2 data: First tests. In 2017 IEEE International Geoscience and Remote Sensing Symposium (IGARSS) (pp. 342-345).

[6] Frost, A., Wiehle, S., Singha, S., & Krause, D. (2018, July). Sea Ice Motion Tracking from Near Real Time Sar Data Acquired During Antarctic Circumnavigation Expedition. In IGARSS 2018-2018 IEEE International Geoscience and Remote Sensing Symposium (pp. 2338-2341). IEEE.

[7] Frost, A., Kortum, K. Wiehle, S., & Tings, B. Ship Navigation Assistance For Polar Waters By Providing Information On Sea Ice Drift And Deformation Zones Using TerraSAR-X Data. Submitted to SeaSAR 2023.

[8] Multiyear ice concentration data from 6th and 7th Dec. 2021 are from https://www.meereisportal.de (Förderung: REKLIM-2013-04)

[9] Ye, Y.; Shokr, M.; Heygster, G. and Spreen, G. (2016), Improving multiyear ice concentration estimates with ice drift, Remote Sensing, 8(5), 397, doi:10.3390/rs8050397.

[10] Ye, Y.; Heygster, G. and Shokr, M. (2016), Improving multiyear ice concentration estimates with air temperatures, IEEE Transactions on Geoscience and Remote Sensing, 54(5), 2602–2614, doi:10.1109/TGRS.2015.2503884.

[11] Z. Zhou, M. M. R. Siddiquee, N. Tajbakhsh, and J. Liang, "Unet++: Redesigning skip connections to exploit multiscale features in image segmentation," IEEE transactions on medical imaging, 39(6), 1856-1867. 2019.

[12] D. Murashkin, and A. Frost, "Arctic Sea Ice Mapping Using Sentinel-1 SAR Scenes with a Convolutional Neural Network," IEEE International Geoscience and Remote Sensing Symposium, pp. 5660-5663. 2021.

The impact of input features in deep learning based sea ice mapping

Qiang Wang, Malin Johansson, Johannes Lohse, Anthony P. Doulgeris and Torbjørn Eltoft

Abstract

Here we present a semantic based segmentation model for separating sea ice from open water in Sentinel-1 imagery. The study utilizes Sentinel-1 intensity imagery, together with sea surface temperature (SST) obtained from Sentinel-3 data, to train a UNET based semantic segmentation model for separating sea ice from open water. The imagery were all acquired over an area between Greenland and Svalbard, and contains images from all seasons. Two network configurations were studied: A "baseline model", which used the HH, HV intensities and the incident angle, and an "advanced model", which in addition included the SST as inputs. We compared the models' performances on independent Sentinel-1 scenes acquired over different seasons. The results indicate that both the baseline and the advanced models are able to separate the open water and sea ice classes well. Improvements were identified in the delineation of the sea ice edge for the advanced model.

I. Introduction

Monitoring sea ice and its changes in extent and concentration has drawn more attention with the ongoing global warming [1]. Wunderling et al [1] indicated that the Arctic Ocean might become ice-free during summer within the 21st century. Meanwhile, Post et al [2] reported that sea ice loss could influence terrestrial productivity and diversity, species interactions, etc. Hence, a better understanding of temporal and spatial changes in sea ice is important for improving climate modelling, understanding the Arctic ecology, as well as supporting safe marine navigation and offshore operations.

Ship-based expeditions are a good way to observe sea ice conditions with high accuracy, though are expensive and time consuming and hence not feasible to be carried out regularly over large spatial scales. Remote sensing can provide data for regular monitoring. For example, Spreen et al [3] developed a sea ice concentration algorithm called ARTIST (ASI) using data from Advanced Microwave Scanning Radiometer (AMSR-E) and Advanced Microwave Scanning Radiometer 2 (AMSR2). The maps are openly available, regularly updated and has a km resolution. However, such relatively coarse spatial resolution might not be sufficient for accurate marine navigation. Synthetic aperture radar (SAR) sensors, e.g. Sentinel-1, on the other hand, can provide measurements at much finer spatial resolution on the order of tens of meters resolution.

Park et al [4] developed a machine learning sea ice type classifier by using the texture features from Sentinel-1 and retrieved three generalized ice types (open water, mixed first-year ice, old ice) with an overall accuracy of 87% (winter)and 67% (summer). Wang and Li et al [5] developed an approach for deriving a high-resolution sea ice product for the Arctic Ocean by employing an integrated stacking model to combine multiple UNET [6] classifiers with diverse specializations with Sentinel-1 imagery. It obtained an overall accuracy of 96.10% by using the HV-polarization, polarization ratio and polarization difference as input features.

Here we propose in this paper two simplified UNET configurations for sea ice and open water separation. One model, denoted the "baseline model", uses the HH, HV intensities and the incident angle (IA) as input features, whereas the second model, denoted the "advanced model", also includes sea surface temperature (SST) as input. The networks were trained using Sentinel-1 (baseline), and SST from Sentinel-3 (advanced), and their performances were subsequently validated with regard to accuracy and robustness.

II. Data and methodology

A. Data

We utilized Sentinel-1 Ground Range Detected (GRD) in the Extra Wide (EW) swath mode over the area between Greenland and Svalbard. Sentinel-1A + 1B offers a 6 day exact repeat cycle. At medium resolution, the GRD product is provided at a spatial resolution of 40 × 40 m and each scene covers roughly 10,000 × 10,000 pixels. In total, 32 Sentinel-1 images acquired during all the months of 2021 were used to generate the training samples for our experiment. Scenes in both ascending and descending mode were used in order to prevent biased model fitting. Daily SST was obtained from the Copernicus climate change service with the spatial resolution of 0.05° × 0.05°, and were re-sampled to match the spatial resolution of the Sentinel-1 images.

B. Methodology

We trained two deep learning models for segmenting sea ice and water in the Arctic region. Back-scatter coefficients from the HH and HV polarization, IA, and SST are used as input features. A baseline model was trained using only the SAR features (HH, HV, IA), whereas the advanced model also included the SST.

The original 4-layer UNET was used as a baseline, and we thereafter re-designed the network architecture using a trade-off between computation cost and training accuracy. Finally, a three-layer down-sampling and up-sampling network was determined. The detailed architecture of the model is shown in Fig 1. For the configuration of the model (advanced UNET) training procedure a Stochastic gradient descent (SGD) optimization method was used. The learning rate was set as 0.001 with the moment of 0.9. Focal loss [7] is used to control the training process for compensating the class imbalance in the training data.

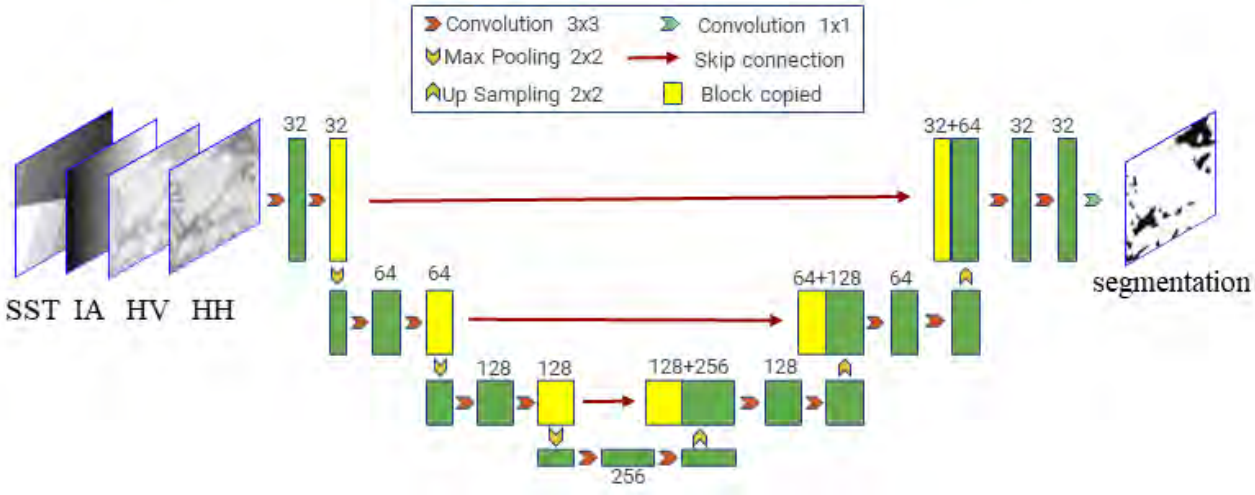

Fig. 1. Architecture of the simplified UNET

III. Results

We validated the model performance by computing the inference of the advanced model and the baseline model for four independent validation images covering different seasons, whose scene IDs are listed in Table I. The corresponding inference by baseline model and advanced model are shown in Fig 2.

TABLE I
Sentinel-1 scene IDs for the images used for validation

scene	scene ID
(a)	S1A_EW_GRDM_1SDH_20220308T075349_20220308T075453_042227_050850_B0B3
(b)	S1A_EW_GRDM_1SDH_20220502T074631_20220502T074731_043029_05233F_CC06
(c)	S1A_EW_GRDM_1SDH_20220706T075459_20220706T075559_043977_053FDB_3D18
(d)	S1A_EW_GRDM_1SDH_20221122T074535_20221122T074639_046004_05816B_9FC9

It can be seen from Fig. 2 that the water ice boundary is well delineated by both the baseline and the advanced model. However, the advanced model can identify the newly formed ice better than the baseline model (see areas marked by red rectangles). Meanwhile, both models may mis-classify the smooth ice as water, shown in the green rectangle in Fig. 2c. It should be denoted that this mis-classification occurred during the summer season, where wet snow or melt-ponds on the sea ice surface may render classification difficult.

IV. Conclusion

We have trained two simplified UNET models to segment ice and water, where the baseline model used the HH, HV and IA from Sentinel-1 imagery as input features and the advanced model used SST derived Sentinel-3 in addition to HH, HV and IA from Sentinel-1 observation as input features. Results indicate that by including the SST, the advanced model can delineate the water ice boundary well and newly formed ice inclusion in the sea ice class is improved. This can serve as a baseline model for segmenting water and ice over the Arctic Ocean. In the future, a better training

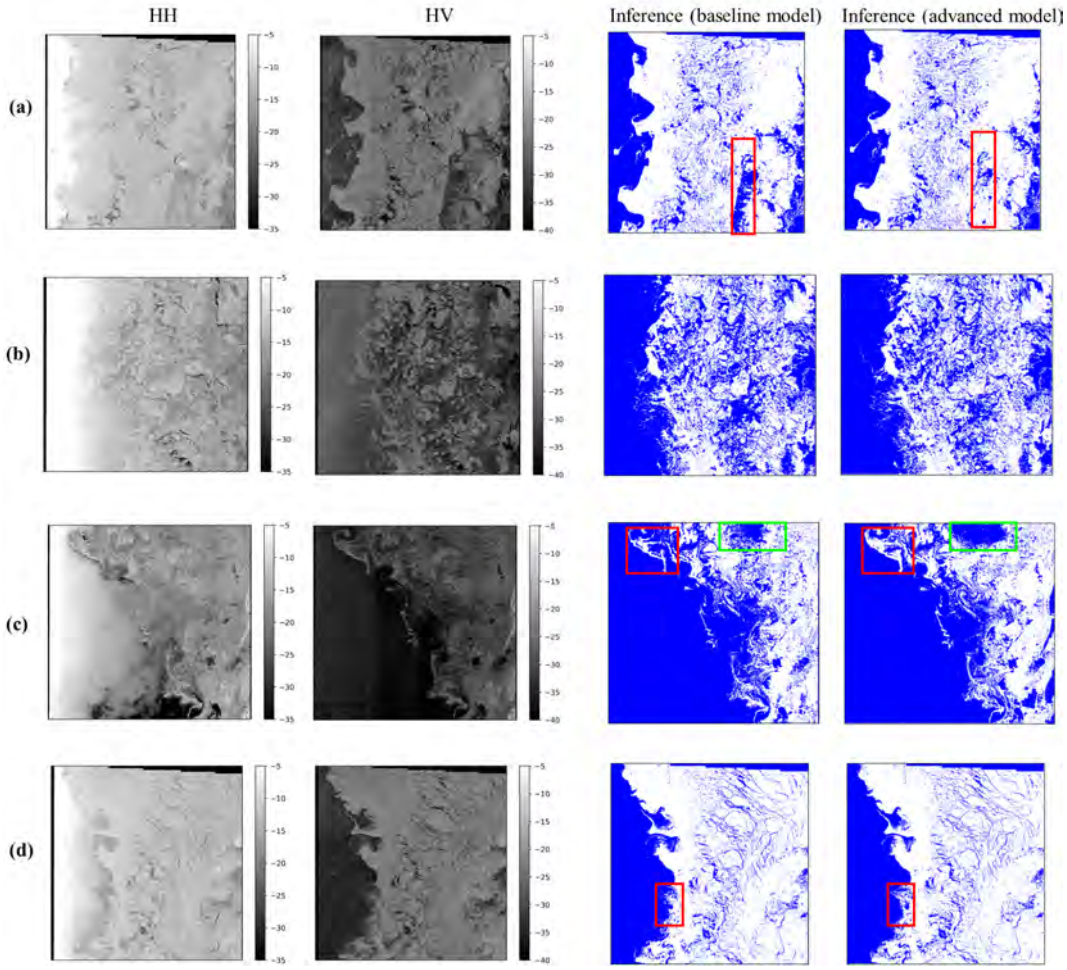

Fig. 2. From left to right: HH (in dB), HV (in dB), baseline model inference, and advanced model inference for the four S1 example images. The a-d letters corresponds to the Scene IDs in Tab. I. Water is blue and ice is white. Regions of particular interest are highlighted by colored rectangles.

data set should be further developed (wet ice in the summer, windy water, etc) to improve the model generalization. Moreover, high resolution SST data can be further explored to replace the existing SST for achieving a high accuracy sea ice vs. open water segmentation model.

References

[1] N. Wunderling, M. Willeit, J. F. Donges, and R. Winkelmann, "Global warming due to loss of large ice masses and Arctic summer sea ice," *Nature communications*, vol. 11, no. 1, pp. 1–8, 2020.

[2] E. Post, U. S. Bhatt, C. M. Bitz, J. F. Brodie, T. L. Fulton, M. Hebblewhite, J. Kerby, S. J. Kutz, I. Stirling, and D. A. Walker, "Ecological consequences of sea-ice decline," *Science*, vol. 341, no. 6145, pp. 519–524, 2013.

[3] G. Spreen, L. Kaleschke, and G. Heygster, "Sea ice remote sensing using AMSR-E 89-GHz channels," *Journal of Geophysical Research: Oceans*, vol. 113, no. C2, 2008.

[4] J.-W. Park, A. A. Korosov, M. Babiker, J.-S. Won, M. W. Hansen, and H.-C. Kim, "Classification of sea ice types in Sentinel-1 synthetic aperture radar images," *The Cryosphere*, vol. 14, no. 8, pp. 2629–2645, 2020.

[5] Y.-R. Wang and X.-M. Li, "Arctic sea ice cover data from spaceborne sar by deep learning," *Earth Syst. Sci. Data Discuss*, vol. 2020, pp. 1–30, 2020.

[6] O. Ronneberger, P. Fischer, and T. Brox, "U-net: Convolutional networks for biomedical image segmentation," in *Medical Image Computing and Computer-Assisted Intervention–MICCAI 2015: 18th International Conference, Munich, Germany, October 5-9, 2015, Proceedings, Part III 18*. Springer, 2015, pp. 234–241.

[7] T.-Y. Lin, P. Goyal, R. Girshick, K. He, and P. Dollár, "Focal loss for dense object detection," in *Proceedings of the IEEE international conference on computer vision*, 2017, pp. 2980–2988.

THE CIRFA-2022 CRUISE TO THE WESTERN FRAM STRAIT: OBJECTIVES, GROUND MEASUREMENTS, AND PRELIMINARY RESULTS

T. Eltoft[1], C. Taelman[1], M. Johansson[1], J. P. Lohse[1], S. Gerland[2], and W. Dierking[3,1]

[1] *UiT The Arctic University of Norway, Norway*
[2] *Norwegian Polar Institute, Norway*
[3] *Alfred Wegener Institute, Germany*

Abstract

In this paper, we give an overview of the CIRFA-2022 Cruise with *RV Kronprins Haakon* to the north-eastern coast of Greenland in the period April 22nd to May 9th, 2022. The cruise was motivated by a need to validate and assess remote sensing products resulting from the research in the "*Centre for Integrated Remote Sensing for Arctic Operations (CIRFA)*". CIRFA's research spans a wide spectrum of activities which together aim to develop new remote sensing (RS) algorithms, methods and technologies, that through integration of multi-sensor data with model predictions and surface observations enable improved detection, characterisation, and monitoring of the geophysical environment of the Arctic. In this regard, remote sensing of sea ice and icebergs is of particular interest, and a significant amount of resources has been devoted to analysis and interpretation of synthetic aperture radar (SAR) data for sea ice classification and iceberg detection. Additionally, CIRFA has contributed to advances in numerical modelling through the development of the Barents-2.5 ocean circulation and sea ice model for use in operational ocean forecasting. The CIRFA-2022 Cruise was carried out in collaboration between CIRFA and the European Space Agency (ESA), and was financially supported by The UiT the Arctic University of Norway, ESA, and CIRFA partners.

1. WHAT WAS DONE

The cruise track followed a profile at 78.5° N, moving westwards from Svalbard towards Belgica Bank which is located between 78 – 80°N and 12 – 16°W in the western Fram Strait and offshore North East Greenland Figure 1. A major focus of the CIRFA-2022 Cruise was on linking field observations of sea ice properties and icebergs with the analysis of satellite SAR images in a region of highly variable ice cover characteristics close to the Northeast coast of Greenland. Ground-based measurements of small-scale ice surface and volume

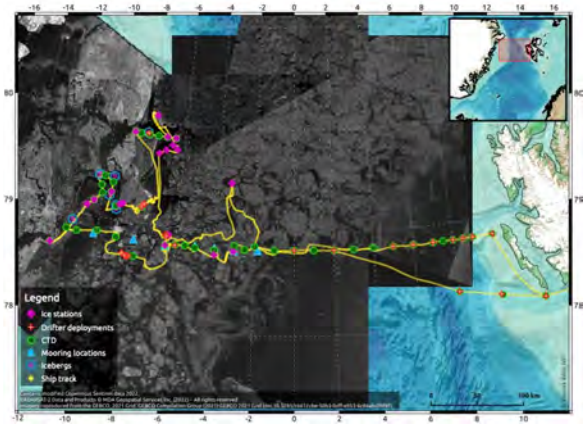

Figure 1. Map of Fram Strait showing the ship track along with markings of the various stations overlaid on a Sentinel-1 scene. (Made by Yannick Kern (Norwegian Polar Institute)).

parameters, as well as of snow properties, were carried out using a suite of different instruments. Large-scale ice cover characteristics and iceberg occurrences were monitored by means of drone and ship-based sensors. The ground truth measurements conducted included:

- *Physical properties of sea ice*, i.e. ice thickness, salinity, temperature, volume structure and inhomogeneities, surface roughness (mm-cm scale), frost flower properties
- *Physical properties of snow*. Layering, grain size, salinity, wetness, presence of snow ice or superimposed ice were measured in snow-pits. Snow thickness and snow layer profiles were also measured on transects by a snow micropenetrometer and by a snow radar mounted on a drone.
- *Layering in snow and ice* was also investigated by a ground-based tomographic radar.
- *Large scale sea ice characteristics* like ice type, floe size distribution, occurrence of open water leads and icebergs were imaged in optical and IR spectral bands by drones.
- *Sea ice and ocean drift patterns* were monitored by a network of GPS-trackers on ice floes and in the ocean.
- *Local hydrography properties* were recorded as CTD-profiles at predefined stations.
- *Local current conditions* were measurred by a network of Lagrangian current drifters.
- *Meteorological conditions* such as air temperature, wind data, humidity, precipitation, and visibility were recorded.

Coordinated with the on-ice measurements, radar images from a suite of satellites were collected. These included high-resolution, full-polarimetric scenes from RADARSAT-2 and ALOS-2, and ScanSAR scenes from RADARSAT-2, ALOS-2, TerraSAR-X, and COSMO-SkyMed, in addition to all available scenes from the Sentinel satellites.

2. PRELIMINARY RESULTS

2.1. Sea Ice Classification

CIRFA has investigated several approaches for sea ice classification from SAR data. During the CIRFA-2022 Cruise the performances of some of these were assessed against observations made in the field. Figure 2 shows the result of applying a supervised statistical classification algorithm on a Sentinel-1 scene. The algorithm is trained on a data set for multiple sea ice types, which is based on the visual analysis and interpretation of overlapping Sentinel-1 SAR and optical images from Sentinel-2 and Landsat-8. The colours in the right panel of Figure 2 represent different ice types and open water. Visual comparison against the drone image (left) indicates good agreement between the classified and observed sea ice classes.

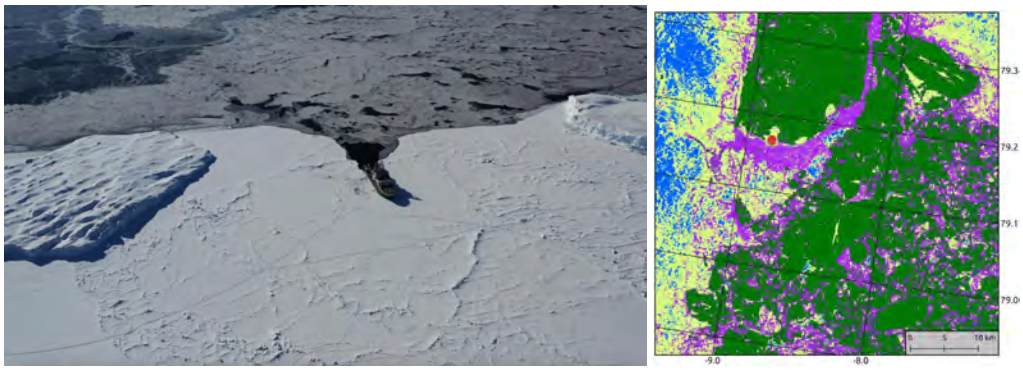

Figure 2. Example of sea ice classification. Left: Drone photo, with the ship in the image (Made by Maritime Robotics). Right: Classification result based on a section of a Sentinel-1 scene. Dark Green represents Deformed Ice. Light Green represents Level Ice. Purple represents Young Ice. Blue represents Open Water. The red dot indicates the ship position.

2.2. Polarimetric analysis

CIRFA has been able to acquire a time series of 11 RADARSAT-2 scenes over fast ice in the Belgica Bank in the period April 11th to June 18th. The scenes cover a site where the CIRFA team had a field work station on April 27th-29th. The SAR images were acquired at incidence angles ranging from 30 to 44 degrees, and

display several types of snow-covered sea ice areas, including levelled first-year ice, deformed multi-year ice, and thin young ice in refrozen leads. Figure 3 illustrates how the changes in the meteorological conditions are reflected in the Pauli signatures of the ice floes denoted A, B, and C in the scenes from April 11th (left) , May 4th (middle), and June 18th (right). Ice area C, which is thin lead ice, had broken off and disappeared on June 18th. The time series allows for a comprehensive study of the consistency and stability of the polarimetric properties of sea ice with varying temperatures and meteorological conditions.

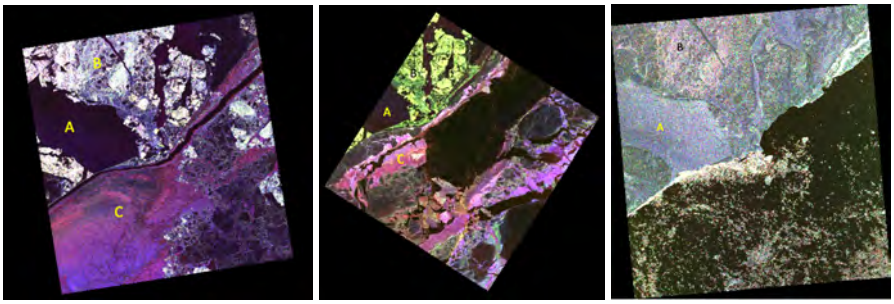

Figure 3. Pauli images of RS-2 images from April 11, May 4, and June 18.

2.3. Sea ice drift patterns from drifter network

As part of the CIRFA-2022 Cruise, a total of 20 drifters were manufactured in-house at UiT The Arctic University of Norway and consequently deployed in Fram Strait. Of the 20 drifters, 15 were deployed manually on sea ice, while the remaining 5 were deployed on sea ice and icebergs by drones. Deploying a drifter by a drone allows to set it out further away, at locations up to 3 km from the ship. The sea ice drifters sample GPS positions every 30 minutes and perform a wave motion measurement every 3 hours for a duration of 20 minutes. The iceberg drifters collect a GPS position every 12 hours and do not perform wave measurements. The wave motion measurements are collected in order to determine when a sea ice drifter transitions into an ocean drifter, which occurs when the sea ice melts or breaks up. This ice-to-water transition moment can be detected by analysing the wave spectra.

Drifter deployments were carried out at a range of different longitudes in Fram Strait, from 03° 4.532’ W to 09°15.630’ W, thus covering sea ice drift from the marginal ice zone towards the fast-ice. For the sea ice drifters that were deployed manually, auxiliary measurements of snow and ice properties were performed at the deployment sites: ice thickness, snow depth stake measurements, salinity of snow-ice interface samples, and snow-water equivalent. Figure 4 shows the trajectories of all drifters deployed during the CIRFA cruise. Note that for the sea ice drifters these trajectories are showing both the sea ice drift and the ocean drift part.

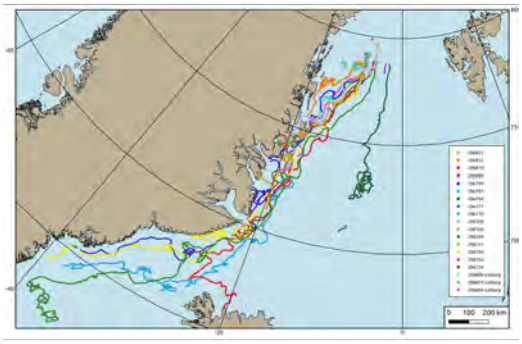

Figure 4. Trajectories of drift tracks from north to southwest along the east coast of Greenland.

3. CONCLUSION

The CIRFA-2022 Cruise succeeded in collecting a large amount of ground-based measurements coincident with satellite overflights. This data will be subject to thorough investigations in the months and years to come. The proposed presentation will summarise the objectives, give an overview on the data sets, and present more details on some results.

Fine Sea Ice Classification with Gaofen-3 Quad- Polarization SAR Observation

Haiyan Li[1,2*] *Kun Yang* [1] William Perrie[3]

1. Key Laboratory of Computational Geodynamics, Chinese Academy of Sciences/University of Chinese Academy of Sciences, Beijing, China. *lihaiyan@ucas.ac.cn,
2. Institute of Oceanology, Chinese Academy of Sciences, Qingdao, China.
3. Fisheries & Oceans Canada, Bedford Institute of Oceanography, Dartmouth, Nova Scotia, Canada

EXTENDED ABSTRACT

Sea ice in the Arctic, as an amplifier of global climate change, has undergone dramatic changes because of global warming. Arctic sea ice changes mainly include continuous decreases in sea ice, thinning of multi-year ice thickness, and the conversion of multi-year ice to first-year ice, which makes first-year sea ice ever more complex, especially in summer. During the growth and development processes, sea ice possesses different radar scattering characteristics, which vary according to the various sea ice types, and according to its stage of development. From the Canadian Ice Service (www.canada.ca/en/environment-climate-change/services/ice-forecasts-observations/latest-conditions/educational-resources /sea/types-forms.html), sea ice can be considered in different ice types: new ice (NI), young ice (YI), first-year ice (FYI) and multi-year ice (MYI). NI is a general term for newly formed ice, which is composed of ice crystals and has no definite fixed form. YI is ice in the transitional stage between new ice and first-year ice with thickness of about 10-30 cm. FYI is sea ice that grows for no more than one winter and develops from younger ice with 30 cm or more thickness. MYI is sea ice that has undergone at least one summer of melting.

Accurate sea ice information can significantly improve Arctic sea ice predictions and global atmospheric environment forecasts. Thus, it is important to have detailed information of first year sea ice. Synthetic aperture radar (SAR) is an important tool for sea ice monitoring because of its low sensitivity to clouds, rain and fog, and its ability to achieve all-day, almost all-weather, high-resolution earth observations. Quad-pol SAR with the amplitude and phase information of the backscattered signal can be recorded for four transmit/receive polarizations (HH, HV, VH and VV) which contains polarization characteristics of sea ice which are closely related to the physical scattering mechanisms of the sea ice. The differences in the scattering mechanisms can be described by polarimetric parameters. There are many parameters that have been proposed for sea ice classification (Espeseth et al., 2017; Li et al., 2021; Liu et al., 2015).

However, there are two facts that hinder fine-resolution sea ice classification. *Firstly*, sea ice is complex, unpredictable, highly connected with environmental factors, particularly FYI (Bi et al., 2020; Winski et al., 2021), and it is difficult to collect actual sea ice observations with large coverage and high resolution. *Secondly*, even though a large number of SAR characteristics have been used to classify sea ice, it remains unclear which parameters are the most effective. Determining the best SAR parameters for fine-resolution sea ice categorization is quite challenging.

In this study, our focus is to develop a methodology for fine-resolution sea ice classification and particularly to classify first-year ice. The types of sea ice in SAR images are calibrated using visible images as a significant source of actual sea ice data. The key point of this work is to determine optimal parameters, among the possible different parameters identified, using separability index (SI) methods. Based on the selected optimal parameters, we can distinguish among open water (OW), NI, YI and FYI types, using the support vector machine (SVM) machine learning method. The classification results are validated by manually interpreted ice maps derived from Landsat-8 data.

Funding: This work was supported by the National Key R&D Program of China (No. 2022YFC3104904), the Fundamental Research Funds for the Central Universities, the Canadian Space Agency SWOT (Surface Water Ocean Topography) program, and MAXSS – Marine Atmosphere eXtreme Satellite Synergy project by ESA, the European Space Agency.

Acknowledgements: We would like to thank the ECMWF for providing ERA5 reanalysis data, and the National Satellite Ocean Application Service for providing GF-3 data. the U.S. Geological Survey (USGS), NASA National Snow and Ice Data Center and Goddard Space Flight Center for providing Landsat-8 images.

INVESTIGATION OF MULTIFREQUENCY SAR IMAGE ALIGNMENT BY ICE DRIFT COMPENSATION IN THE MARGINAL ICE ZONE

Denis Demchev, Leif E. B. Eriksson,
Anders Hildeman*

Chalmers University of Technology
Gothenburg, Sweden
*A.H. is currently with the AstraZeneca AB

Wolfgang Dierking

The Arctic University of Norway
Tromso, Norway

Alfred Wegener Institute
Helmholtz Centre for Polar and Marine Research
Bremerhaven, Germany

ABSTRACT

A recently proposed SAR image alignment framework based on ice drift compensation is examined for applicability in the marginal ice zone where ice analysis is complicated by ice floe rotations, fast changing local ice concentration, local wind variations, and changing wetness of the ice surface. Here, we use L-band ALOS-2 and C-band Sentinel-1 images that were acquired over the Greenland Sea in the summer period of 2019. Preliminary results show that L-C SAR image alignment is possible in the marginal ice zone during melting conditions with a time span of a few hours and with ice speeds of $>$10 cm/s. The main challenges and directions of future work to improve the alignment performance in the transitional zone between open sea and dense drift ice are formulated.

Index Terms— Alignment, sea ice drift, marginal ice zone, SAR, Arctic

1. INTRODUCTION

The marginal ice zone (MIZ) denotes the transition between the open sea and dense drift ice or fast ice and is of large interest for research on sea dynamics as it is characterized by various features comprising ice edge dispersion/compacting, formation of ice bands, intense air-sea interaction which presence of oceanic eddies [1]. Satellite data from synthetic aperture radar (SAR) are extremely valuable for sea ice monitoring including the MIZ. However, the automated retrieval of ice movements in the MIZ from pairs of SAR images can be complicated because of ice floe rotations, wind-induced changes of the water surface roughness, and wetness of the ice surface. The usage of SAR images acquired at different frequencies is beneficial as it provides richer information for monitoring and retrieval of sea ice parameters. Most often the images at different frequencies are not acquired from the same satellite but rather from different satellites observing the same region at slightly different points in time. This poses a problem for their joint analysis as ice drifts due to wind and sea currents will transform the ice in-between the two paired acquisitions. To collocate the SAR sea ice images, a recently proposed SAR ice imagery alignment method based on ice drift compensation [2] is used to assess the feasibility of alignment in the marginal ice zone.

2. SAR IMAGES AND TEST SITE

We collected L-C image pairs from Level-1.5 Ground Range Detected (GRD) data from ALOS-2 (Advanced Land Observing Satellite-2) and Sentinel-1A/B GRD Extra Wide Swath Mode (EW) data taken over the ice edge area in the Greenland Sea. Two different ALOS-2 data modes are used, namely ScanSAR Nominal and Stripmap Fine. The backscattering coefficient σ^0 was computed and the data were projected onto a Polar Stereographic grid with a pixel size of 100 m.

3. SAR ALIGNMENT METHOD AND QUALITY ASSESSMENT

Alignment of SAR images acquired at L- and C-band was demonstrated in [2]. This study examines the performance of the alignment method in the marginal ice zone. An L-C pair has been selected in the Greenland Sea area (10.8191°W, 79.2014°N) in the summer period (2019/06/22) with a time gap between acquisitions of around 4 hours (Figure 1 A, B).

A SAR drift algorithm [3] is used to estimate the ice drift for the overlapping parts of the SAR images, which provides the ice displacement vectors on a regular grid with a step size of 50 pixels, corresponding to 5 km.

The alignment is carried out by local piece-wise affine image transforms on a triangular mesh obtained based on the ice displacements. The alignment framework was demonstrated with pairs of ALOS-2 and Sentinel-1 images, but can be used for data at other frequencies and from other sensors.

For the alignment quality evaluation, we use the Structural Similarity Index (SSIM) [4] which is a similarity measure comprising brightness, contrast, and structural components. Its values range from -1 to 1, with the latter indicating a perfect alignment. For consistency in the assessment of alignment quality, we apply SSIM for the original L-band image L, and image L^{FB} which is obtained after forward transform T_F followed by backward transform T_B: $L^{FB} = T_B(T_F(L))$. But it should be noted that we use the two-times transformation as some kind of proxy for assessing one-time transformation to exclude the influence of the signature difference.

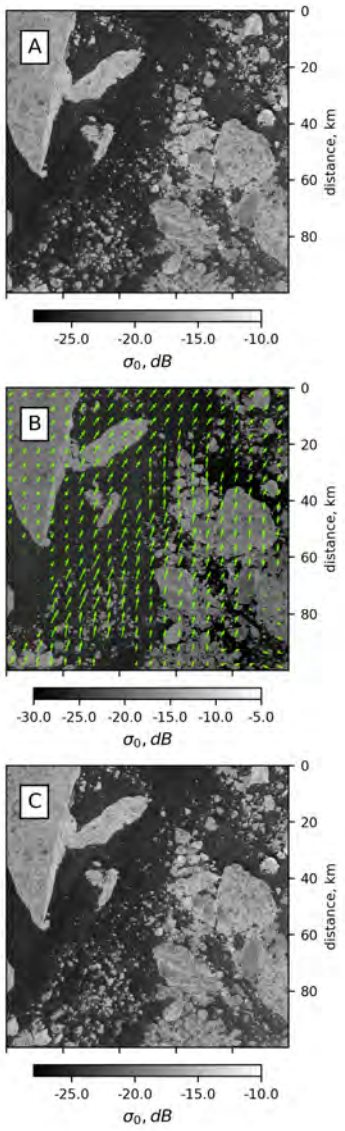

Fig. 1. A - L-band ALOS-2 HH image from 2019/06/22 13:45:11; B - C-band Sentinel-1 HH image from 2019/06/22 17:40:12; C - aligned ALOS-2 image by ice drift compensation. The derived ice displacement vectors are depicted in green on the Sentinel-1 image (B).

4. RESULTS AND DISCUSSION

Ice drift retrieval in the marginal ice zone becomes more complex compared to pack ice mainly due to two factors: (1) more intense dynamics of ice floes including their rotations and (2) the influence of open water patches that constrains the ice signature recognition. As the drift algorithm [3] handles the rotational movement of ice, we obtained displacement vectors for almost each grid point, which have been visually checked for correctness. According to the drift algorithm output, the mean ice speed in the period was 14.7 cm/s with a dominating drift towards NE and N. Individual ice floes with a horizontal size from a few hundred to tens of kilometers can be recognized in Figure 1. A result of the alignment of the ALOS-2 image to the Sentinel-1 image by ice drift compensation is shown in Figure 1 C. Visually, it is seen that the aligned ALOS-2 image has not been significantly distorted after alignment and compared to the original image (Figure 1 A). This indicates the correctness of the obtained drift vectors and successful transformation by the alignment method.

To assess the quality of the alignment quantitatively, we used the SSIM values. Here we assess the transformation quality but not the differences caused by sea ice signature changes at the different bands, therefore we applied the metric for the original ALOS-2 image and its forward-backward transformed version. Figure 2 shows that the SSIM values close to 1 are prevailing across much of the aligned image, while the lower values correspond to a relatively small fraction of pixels.

The mean air temperatures over the area between 13:00 and 18:00 on 2019/06/22 were derived from the ERA5 reanalysis dataset [5] and are depicted in Figure 2. According to the data, the prevailing air temperature at 2 m over the entire region was above 0°C in previous days, and in the period between image acquisitions, hence we can expect melting conditions.

5. CONCLUSIONS

In this case study, we assessed the applicability of the recently proposed alignment framework for SAR sea ice imagery in presence of granular ice covers consisting of relatively small, thin ice floes, which are common in the marginal ice zone. Such analysis is more challenging compared to pack ice due to the complex nature of the MIZ as described above. Successful alignment has been demonstrated for a pair of L-band ALOS-2 and C-band Sentinel-1 images from 2019/06/22 acquired over the Greenland Sea with a difference in acquisition time of 4 hours. The feasibility of alignment has been examined visually by the presence of distortion as well as quantitatively by the Structural Similarity Index. Both the .visual assessment and the SSIM confirm the applicability and efficiency of the alignment method based on the piecewise affine transform in summer conditions, rotational ice

movement, and locally varying ice concentrations. Despite promising results, it has to be proven that the alignment can be applied for time gaps longer than a few hours and under different weather conditions. The ice drift algorithm used in this study has demonstrated reliable performance for multi-frequency SAR images over the marginal ice zone, but the image alignment can also be assessed for other SAR drift algorithms.

6. ACKNOWLEDGEMENT

This work was done as part of the European Space Agency contract no. 4000130509/20/NL/FF/ab, "Synergistic Use of L- and C-band SAR Satellites for Sea Ice Monitoring". ALOS-2/PALSAR-2 data are provided by JAXA through the 2019 to 2022 mutual cooperation project between ESA and JAXA on Using Synthetic Aperture Radar Satellites in Earth Science and Applications. Sentinel-1 data (European Union Copernicus program) were downloaded from the NASA Alaska Satellite Facility (ASF) SAR Distributed Active Archive Center (DAAC).

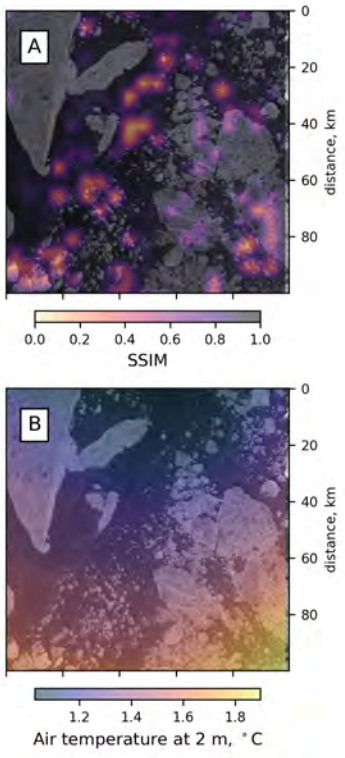

Fig. 2. A - Structural Similarity Index (SSIM) from the original L and forward-backward transformed image L^{FB}; B - the mean air temperature at 2m from ERA5 reanalysis between 13:00 and 18:00 on 2019/06/22.

7. REFERENCES

[1] Matti Leppäranta, *The drift of sea ice*, Springer Science & Business Media, 2011.

[2] Leif EB Eriksson, Denis Demchev, Anders Hildeman, and Wolfgang Dierking, "Alignment of l-and c-band sar images for enhanced observations of sea ice," in *IGARSS 2022-2022 IEEE International Geoscience and Remote Sensing Symposium*. IEEE, 2022, pp. 3798–3801.

[3] Anders Berg and Leif EB Eriksson, "Investigation of a hybrid algorithm for sea ice drift measurements using synthetic aperture radar images," *IEEE transactions on geoscience and remote sensing*, vol. 52, no. 8, pp. 5023–5033, 2013.

[4] Zhou Wang, Alan C Bovik, Hamid R Sheikh, and Eero P Simoncelli, "Image quality assessment: from error visibility to structural similarity," *IEEE transactions on image processing*, vol. 13, no. 4, pp. 600–612, 2004.

[5] Hans Hersbach, Bill Bell, Paul Berrisford, Shoji Hirahara, András Horányi, Joaquín Muñoz-Sabater, Julien Nicolas, Carole Peubey, Raluca Radu, Dinand Schepers, et al., "The era5 global reanalysis," *Quarterly Journal of the Royal Meteorological Society*, vol. 146, no. 730, pp. 1999–2049, 2020.

High resolution L- and C-band polarimetric variability during MOSAiC

A. Malin Johansson[1], S. Singha[2], G. Spreen [3], S. Howell [1]
[1]UiT The Arctic University of Norway
[2]National Center for Climate Research (NCKF), Danish Meteorological Institute (DMI)
[3] Institute of Environmental Physics, University of Bremen
[4] Climate Processes Section, Science and Technology Branch, Environment and Climate Change Canada / Government of Canada

Abstract

The polarization difference (VV-HH) for different sea ice types observed in L- and C-band SAR images during the MOSAiC drift study is investigated here. The drift lasted from the freeze-up to the early melt season, ensuring that the temperature dependency is also examined. PD has positive values for open water and new ice areas, i.e. HH > VV, whereas the values turn negative for the young ice stage and stabilise around 0 for the thicker sea ice types. L-band SAR PD values appeared to have a higher sensitivity to the melt onset compared to C-band SAR.

I. Introduction

In September 2019, the German research icebreaker R/V Polarstern started the drift across the Arctic Ocean as a part of the MOSAiC (Multidisciplinary drifting Observatory for the Study of Arctic Climate) drift experiment. During the course of MOSAiC thousands of SAR images were acquired in different imaging mode and frequency supported by various international space agencies and research organizations (e.g. CSA, JAXA, ESA, DLR, KARI, ASI, CONAE, INTA). In this study we focus on SAR images from the ALOS-2 and RADARSAT-2 satellites acquired through joint ESA-JAXA collaboration. Here we evaluate the effects of seasonal changes on C- and L-band backscatter in respect to four different sea ice types, i.e., newly formed sea ice (NI), Young Ice (YI), Smooth Ice (SI) and Deformed Ice (DI), as well as the stability of radar backscatter in different polarization, for polarimetric parameters acquired under different environmental conditions and at different incidence angles.

Previous studies e.g., [1–3] have shown that L-band SAR can provide improved separability between different sea ice types. The different wavelengths means e.g., different penetration depths and different sensitives to the onset of melting e.g. [4]. In [2] L-band data was shown to provide easier separation between first year ice (FYI) and second/multi-year ice (MYI) in the early and advanced melt season. Upcoming L-band missions such as NISAR, ALOS-4 and ROSE-L will offer the advantages of fully polarimetric acquisitions along with higher ground coverage to achieve a optimal scenario for L-band SAR based sea ice monitoring.

In this study we found that the polarization difference (PD) can be used to separate out younger sea ice types in both C- and L-band SAR images, provides a complement to the co-polarization ratio that can primarily separate the newer sea ice types, and PD provide good separability between high backscatter young ice and MYI. PD could also be used as an indicator of early melt stages, due to the shift from stronger VV to stronger HH channel data in L-band SAR images. The same trend could not be observed in the C-band images, and as such the two frequencies complemented one another.

II. Data set

SAR data overlapping the drift of R/V Polarstern during the MOSAiC expedition from 1 October 2019 until 31 July 2020. The sea ice observed in the larger area around R/V Polarstern for the first floe is the main focus of this study. R/V Polarstern drifted towards the polar hole (ca. above 86.6^{o}N) around the end of 2019 and the beginning of 2020. Some sensor specifics are listed in Table I.

TABLE I
Specifics of satellite data used in this study. The values presented are average values for the different missions.

Mission	Frequency	Range x Azimuth resolution*	Range x Azimuth spacing *	IA range	NESZ
RADARSAT-2	C (5.41 GHz)	5.2 m x 7.6 m	4.7 m x 5.1 m	18 ^{o}–49 ^{o}	-32.9db ±1.5dB
ALOS-2	L (1.2 GHz)	5.1 m x 4.3 m	2.9 m x 3.2 m	29 ^{o}–41 ^{o}	-36.0 dB(HH), -46.0 dB (HV)

III. Method

Here we analyse the polarimetric SAR information for four different sea ice types, NI, YI, SI and DI, and how they vary with incidence angles, SAR frequencies and temperature. The NI was predominantly observed within leads and the YI was predominantly the younger sea ice surrounding the MOSAiC floe at the start of the campaign. This YI had on 14th October an average thickness of 30 cm.

The SAR images were calibrated so that the pixel values could be directly related to the radar backscatter coefficient (σ^0) values. The backscatter coefficients are derived from the mean intensity of the complex scattering coefficient S, where $\langle\cdot\rangle$ is averaging over a neighbourhood of N pixels. Here N is equal to 7x7 pixels. The polarization difference (PD) was calculated as;

$$PD = \langle|S_{VV}|^2\rangle - \langle|S_{HH}|^2\rangle. \quad (1)$$

Note that PD is defined on a linear scale, and using PD the non-polarized component can be separated from the polarized one in the analysed data, and is less sensitive to the closeness to the NESZ than many other polarimetric features. A poor signal-to-noise ratio (SNR) was in, e.g., [5], shown to result in an over representation of perceived volume scattering when SNR is less than 10 dB. A low SNR primarily affects the NI areas as well as the refrozen melt pond parts of the MOSAiC floe and similar floes in the vicinity. The sea ice growth during the season means that poor SNR is a larger problem at the start of the campaign, with the overall thinner sea ice as well as a larger proportion of refrozen melt pond floes. Moreover, during the melt season stage when R/V Polarstern was located in the marginal ice zone poor SNR was more prominent.

Region of interests (ROIs) representing the four different ice types were manually identified. During the selection of these areas we mainly relied on ice charts, ice concentration map and expert visual judgment of the Pauli RGB compositions. The areas were selected in such a way that they adequately represent the incidence angle variation from near to far range. Not all ice types were available within all images, in particular were the NI and YI not always present. When possible was the MOSAiC floe included in the ROIs.

IV. Results and Discussion

During the The MOSAiC drift expedition the sea ice drift remained reasonably stable from the start until December, and during this time period we also observe stable backscatter values that primarily vary with incidence angle. Once R/V Polarstern drifted out of the polar hole increased overall sea ice deformation could be observed.

In all frequency bands the co-pol power ratio has been proven to be an excellent measure to distinguish open water and newly formed sea ice from the thicker sea ice types, SFYI and RFMYI ([1, 6]). In the case of younger ice types, the co-pol power ratio is not as powerful in discriminating thin ice from open water. PD shows some promise in the separability of the NI and YI areas as well as separation from thicker ice types. In this study we focus on changes in backscatter and PD within the SAR images from the freeze-up to the melt onset.

For background do open water and NI have high PD values, though once the transition to YI areas occur the PD values are reduced and for thicker sea ice the mean values stabilise around 0. This follows the trend seen at other sea ice campaigns such as N-ICE2015 and Beaufort 2015 during the freeze-up and winter months. In Figure 1 the PD evolutions for the L- and C-band images during MOSAiC is shown. For all ice types does L-band data have lower variability than overlapping C-band data.

The transition in PD values from the NI to YI is likely dependent on the penetration depth as the transition occurs later in time in the L-band data compared to the C-band data for the sea ice areas surrounding the MOSAiC floe co-inside with the thermodynamic sea ice growth. The L-band images had higher (and positive) PD values at the start of the freeze-up than the C-band images for the thin ice areas (30 cm thick) surrounding the ship and the MOSAiC floe, though these values stabilised once the sea ice had grown in thickness and transitioned to negative values by mid-November. The negative values for both C- and L-band lasted all the time until R/V Polarstern entered the polar hole. Analysis of the scattering mechanisms in the area indicate predominant surface scattering for the thinner sea ice area from the freeze-up to the end of December.

Starting with the freeze-up season we can observe that the SI largely have low PD values and a low variability whereas the DI have mean values close to 0 but with larger standard deviation (std). PD overall has a larger variability for deformed sea ice compared to the other ice types for both frequencies, and as such can the coefficient of variation (CV) or std over an area be used to separate the DI from the surrounding sea ice types. This was also confirmed by investigating MYI areas in Canada. For the MOSAiC floe this meant that the refrozen melt pond areas had low PD values with low std, and the deformed part of the floe had high std values.

Once Polarstern drifted out of the polar hole the temperatures started to increase and by mid-April they were above -10^{o}C, with temperatures around 0^{o}C in mid-April. A PD temperature dependency was observed once the temperatures remained above 0^{o}C the mean value and the std increased significantly in the L-band data, meaning that this parameter may be possible to use to indicate melt onset. For the C-band data there was an increase in variability

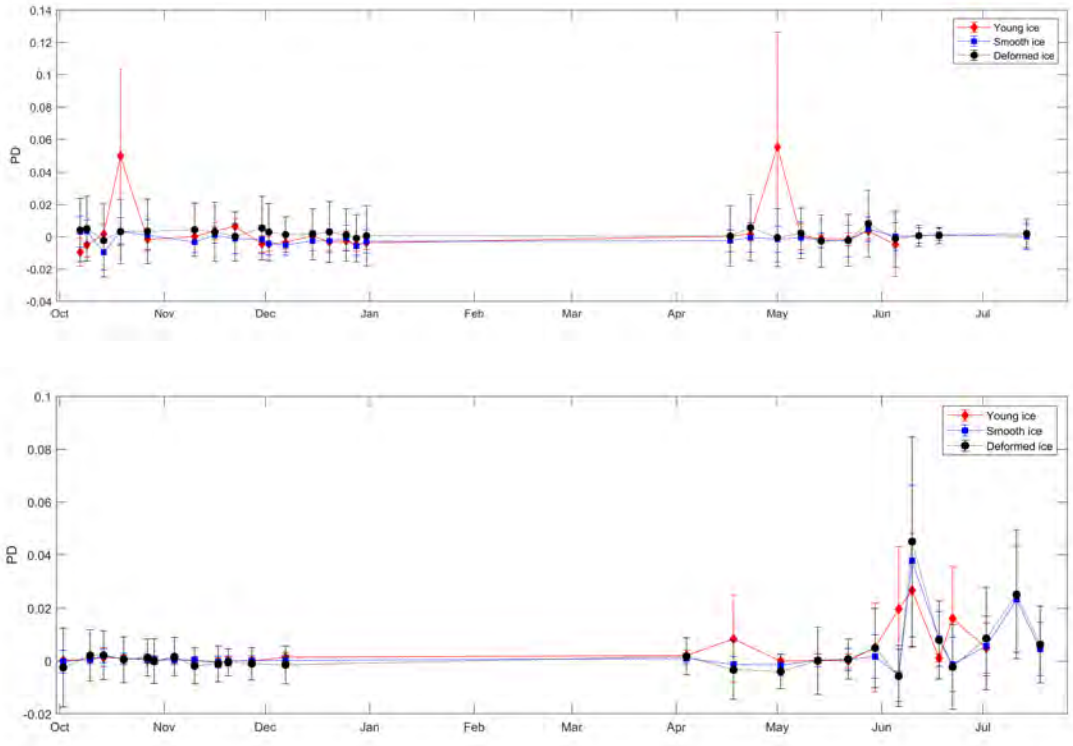

Fig. 1. The PD evolution for RADARSAT-2 (top) and ALOS-2 (bottom).

for the SI and a decrease for the DI. Combining the PD evolution for the different sea ice types and frequencies makes the two frequencies complementary for sea ice type separation and classification.

V. Conclusions

The polarization difference was found to provide separability between younger ice types and thicker sea ice and provide good separability between high backscatter young ice and MYI. The variability in PD was in L-band SAR was found to be a useful indicator of early melt stages, due to the shift from stronger VV to stronger HH data. SAR images from the CIRFA cruise in 2022 at the Belgica Bank fast ice was found to confirm this analysis and the usefulness of PD will be further investigated using both the MOSAiC, N-ICE2015 and the CIRFA cruise data, utilizing overlapping L- and C-band images that co-inside with in-situ measurements.

Acknowledgement

The work was funded through the Research Council of Norway Grant no. 237906. RADARSAT-2 Data and Products © MDA Geospatial Services Inc. 2019/2020. RADARSAT is an official mark of the Canadian Space Agency

References

[1] A. M. Johansson, C. Brekke, G. Spreen, and J. A. King, "X-, C-, and L-band SAR signatures of newly formed sea ice in Arctic leads during winter and spring," *Remote Sensing of Environment*, vol. 204, pp. 162 – 180, 2018.

[2] M. Mahmud, V. Nandan, S. Howell, T. Geldsetzer, and J. Yackel, "Seasonal evolution of l-band sar backscatter over landfast arctic sea ice," *Remote Sensing of Environment*, vol. 251, p. 112049, 2020.

[3] T. Toyota, J. Ishiyama, and N. Kimura, "Measuring deformed sea ice in seasonal ice zones using l-band sar images," *IEEE Trans. Geosci. Remote Sens.*, vol. 59, no. 11, pp. 9361–9381, 2020.

[4] J. A. Casey, S. E. Howell, A. Tivy, and C. Haas, "Separability of sea ice types from wide swath C- and L-band synthetic aperture radar imagery acquired during the melt season," *Remote Sensing of Environment*, vol. 174, pp. 314 – 328, 2016.

[5] M. Espeseth, C. Brekke, C. Jones, and A. Holt, B. abd Freeman, "The impact of system noise in polarimetric sar imagery on oil spill observations," *IEEE Trans. Geosci. Remote Sens.*, vol. 58, no. 6, pp. 4194–4214, 2020.

[6] T. Geldsetzer and J. J. Yackel, "Sea ice type and open water discrimination using dual co-polarized C-band SAR," *Canadian Journal of Remote Sensing*, vol. 35, no. 1, pp. 73–84, 2009.

Tracking Backscatter Signatures of Individual Sea Ice Floes Using In-Situ Ice Drift Observations

Catherine Taelman[1], Johannes Lohse[1], Anthony P. Doulgeris[1]

1) UiT The Arctic University of Norway

Abstract

Studies on seasonal variations in radar backscatter exist for landfast ice, but seem sparse for drifting sea ice. Here, we introduce a new in-situ sea ice drift data set collected by 17 drifters deployed during the CIRFA-22 cruise in Fram Strait in April-May 2022. The data set covers the transition from freezing conditions to melt onset in Fram Strait and the Greenland Sea. These drift trajectories provide the rare opportunity to track individual sea ice floes and study the temporal evolution and incident angle dependence of their radar backscatter signatures as they undergo physical changes during melt onset. We furthermore demonstrate how the amount of tracked floes can be increased by identifying distinct surface structures in the vicinity of the drifter location in consecutive radar images.

I. Introduction

Because of its fine spatial resolution and its independence of daylight and cloud conditions, synthetic aperture radar (SAR) is a primary tool for operational sea ice monitoring. The appearance of different sea ice types in SAR imagery is determined by radar parameters, such as polarization, frequency, and incident angle (IA), and surface parameters, such as small-scale roughness, large-scale deformation, and the dielectric properties of the ice and snow layers. At present, most of the SAR data that is routinely available for sea ice monitoring is acquired in wide-swath mode at C-band, for example by Sentinel-1 (S1) or Radarsat-2 (RS2). For these sensors, the backscatter signal from a given sea ice type varies with IA across the swath [1], and it is strongly affected by changes in temperature and snow properties [2]. Understanding these variations in backscatter is crucial for the interpretation and automated analysis of the imagery.

The effect of melt onset and the seasonal evolution of C-band radar backscatter over the yearly cycle has been extensively studied for landfast ice (for example [3, 4]). However, studies tracking the backscatter signature of individual drifting sea ice floes seem sparse. Here, we use a set of in-situ drift trajectories to track individual ice floes in the Greenland Sea over several months, covering the transition from freezing temperatures to warmer melting conditions. We automatically identify the individual drifter locations in overlapping S1 imagery and extract backscatter intensities from the pixels around the drifter. Furthermore, we visually identify and track the backscatter of distinct surface features in the vicinity of the drifters that can be followed over time. On short timescales (days), this allows us to investigate the IA dependence of the exact same sea ice, while on longer timescales (weeks), we can study the backscatter evolution of drifting ice floes with changes in temperature during melt onset.

The main focus of this work can be summarized in three points:

- We introduce a unique data set of in-situ drift observations in the Greenland Sea in the time period from April until December 2022.
- We demonstrate the use of the drifter trajectories to track individual sea ice floes and investigate the IA dependence and the temporal evolution of their backscatter signature.
- We conceptually show how to expand the tracked ice areas by identifying distinct surface structures that are clearly visible in the vicinity of the drifter locations.

II. Data Set

A. In-situ sea ice drift data

We use in-situ sea ice drift observations collected from drifters that were deployed during the CIRFA-22 cruise to Fram Strait and Belgica Bank in the time period from April 22nd to May 10th 2022. A total of 17 sea ice drifters were manufactured in-house at UiT after the design of Rabault et. al. [5]. They sample a GPS position at a 30 minutes interval and measure wave motion for a duration of 20 minutes every 3 hours. Of the 17 sea ice drifters, 15 were deployed manually on the sea ice, while 2 were set out by a drone. At the sites of manual deployment, additional in-situ measurements were acquired: ice thickness, snow depth, snow-water equivalent (SWE), and snow salinity at the snow-ice interface.

The floes tagged with drifters continuously move southwards into the Greenland Sea, where they eventually break up or melt. The sea ice drifters then end up in the open water and transition into ocean drifters. They float in the water and continue sampling location and wave motion. By analyzing the wave motion measurements, we can determine when this ice-to-water transition takes place (see Section III).

B. Sentinel-1 data

We use freely available Sentinel-1 (S1) imagery to study the temporal evolution of SAR backscatter from the sea ice at the drifter deployment sites. S1 operates at C-band and is at present one of the main data sources for operational sea ice monitoring. All S1 data used in this study was acquired in dual-polarimetric extra-wide swath (EW) mode and processed to ground range detected format at medium resolution (GRDM). The EW GRDM product is provided at 40x40 m pixel spacing at a swath width of 410 km.

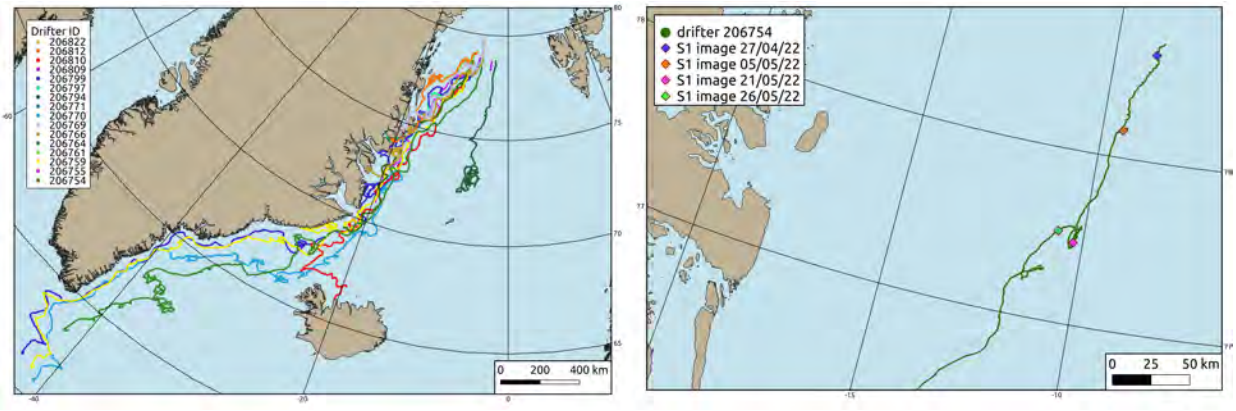

Fig. 1. Left: Full drift trajectories of all 17 drifters that were deployed during the CIRFA-22 cruise. Right: Partial trajectory of the example drifter (ID 206754) used in this abstract. The markers indicate the drifter location at the time of the overlapping S1 images shown in Figure 2.

III. Method

A. Drifter data processing

A full drifter trajectory consists of a sea ice part, followed by an ocean part. By careful analysis of the wave spectra time series, which are obtained from the wave motion measurements, we identify 3 stages in each trajectory: sea ice - transition - ocean. In the sea ice stage, there is little to no wave motion, and the drifter is clearly on sea ice. During the transition phase, the floe with the drifter starts breaking up or melting as it reaches the marginal ice zone, which is reflected by an increase in wave motion. Finally, the drifter ends up in the open water (ocean). This stage is characterized by a major rise in wave motion. We flag all drifter trajectories according to these three stages, and only use data from stage 1 (sea ice) for this study.

B. Identifying overlapping Sentinel-1 data

To find S1 scenes that overlap with the drifter positions, we loop through the time series of each individual drifter as long as it is on sea ice. For every data point, we use the *SentinelAPI* from the *sentinelsat* python package to search for overlapping S1 images. As the drifters sample a GPS location every 30 minutes, we search over a time interval from 15 minutes before until 15 minutes after the drifter location timestamp. This results in a maximum time difference of 15 minutes between the S1 image acquisition and the recorded drifter location. Note that the ice floe can drift a distance that corresponds to several image pixels during this time. Assuming a drift speed of 0.1 $\frac{m}{s}$, the covered distance will be 90 m (that is 2.25 pixels) in 15 minutes.

C. Extracting backscatter intensities

The drifters enable us to track backscatter intensities in two different ways.

1) The most straightforward approach is to extract a patch of pixels directly around the location of the drifter, and compare these patches throughout the time series. This more conventional way of tracking sea ice is, however, limited when the drifter is close to the edge of the floe, or when the sea ice deforms or breaks up in the direct vicinity of the drifter. Moreover, the drifter locations in the S1 imagery need to be drift-corrected if the time difference between image acquisition and GPS timestamp is large enough to result in a significant location offset in the SAR image.
2) We expand this conventional method by tracking distinct surface structures that are clearly recognizable in the SAR image in the area close to the drifter location. As a proof of concept, we identify these structures manually. At a later stage, this step can be automated using feature tracking and pattern matching algorithms.

We investigate the IA dependence by comparing backscatter values of one floe imaged in two consecutive S1 scenes, once in near-range and once in far-range. Using both proposed workflows to track sea ice, we study the temporal evolution of the backscatter signatures of distinct sea ice structures and floes.

IV. Preliminary Results

We collected a unique data set of in-situ sea ice drift observations in the Greenland Sea during the transition from freezing to melting conditions in 2022. The trajectories of the 17 drifters are shown in Figure 1. Note that these trajectories include the entire time series (sea ice - transition - ocean), ranging from April to December 2022. (see Section II-A). A small selection of the overlapping S1 image time series for one example drifter is shown in Figure 2 (top). The drifter location is marked with a red star. We identified two distinct sea ice structures throughout the time series and selected a region of interest (ROI) in each of them, visualized as purple (ROI 1) and blue (ROI 2) rectangles. Note that ROI 2 is not drawn in the S1 image of 26/05/22, as it is not clearly recognizable there. Scatterplots of the Sigma Nought backscatter values in HV versus HH polarization for a small area around the drifter location and for both ROI's at the timestamps of the S1 images is shown in Figure 2 (bottom).

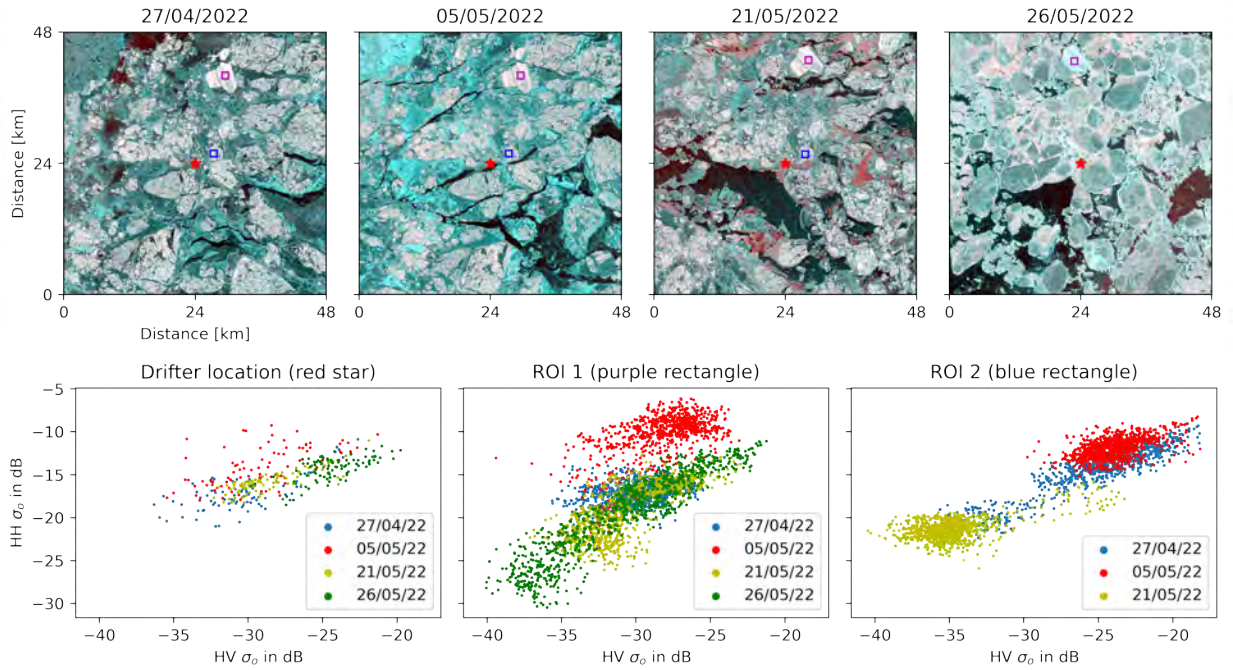

Fig. 2. Top: False-color RGB images (R-HV, G-HH, B-HH) of four S1 scenes that overlap with the drift trajectory of drifter 206754. The images are cropped to areas of 48x48 km around the drifter location at the time of image acquisition, as indicated in Figure 1 (right). The drifter location is indicated with a red star. Purple and blue rectangles indicate ROI's on distinct sea ice structures. Bottom: Scatterplots of HH versus HV backscatter values for a small area around the drifter location and for the two ROI's at the timestamps of the selected S1 images.

Future work includes tracking the backscatter signatures over the full temporal time series for this case study and for more floes and distinct surface structures, using the CIRFA-22 drift data set. The larger sample size will allow for a representative analysis of the temporal variations and incidence angle dependence of radar backscatter during melt onset.

References

[1] J. Lohse, A. P. Doulgeris, and W. Dierking, "Mapping sea-ice types from Sentinel-1 considering the surface-type dependent effect of incidence angle," *Annals of Glaciology*, vol. 61, no. 83, pp. 260–270, 2020.

[2] D. Barber, E. LeDrew, D. Flett, M. Shokr, and J. Falkingham, "Seasonal and diurnal variations in SAR signatures of landfast sea ice," *IEEE transactions on geoscience and remote sensing*, vol. 30, no. 3, pp. 638–642, 1992.

[3] J. Yackel and D. Barber, "Melt ponds on sea ice in the Canadian Archipelago: 2. On the use of RADARSAT-1 synthetic aperture radar for geophysical inversion," *Journal of Geophysical Research: Oceans*, vol. 105, no. C9, pp. 22 061–22 070, 2000.

[4] R. Scharien, J. Yackel, M. Granskog, and B. Else, "Coincident high resolution optical-SAR image analysis for surface albedo estimation of first-year sea ice during summer melt," *Remote sensing of environment*, vol. 111, no. 2-3, pp. 160–171, 2007.

[5] J. Rabault, T. Nose, G. Hope, M. Müller, Ø. Breivik, J. Voermans, L. R. Hole, P. Bohlinger, T. Waseda, T. Kodaira *et al.*, "Openmetbuoy-v2021: An easy-to-build, affordable, customizable, open-source instrument for oceanographic measurements of drift and waves in sea ice and the open ocean," *Geosciences*, vol. 12, no. 3, p. 110, 2022.

Sea ice cover and drift by Sentinel-1 SAR and the support for Arctic shipping

Xiao-Ming Li
Aerospace Information Research Institute, Chinese Academy of Sciences

Widely used sea ice cover and drift data in polar regions are derived mainly from spaceborne microwave radiometer and scatterometer data, and the typical spatial resolution of these products ranges from several to dozens of kilometers. Due to dramatic changes in polar sea ice, high-resolution sea ice data are drawing increasing attention for polar navigation, environmental research, and offshore operations. In this paper, we focused on developing methods for deriving a high-resolution sea ice volume and dynamics data, i.e. sea ice cover and drift using Sentinel-1 (S1) SAR dual-polarization data in extra wide swath (EW) mode.

The approach (Fig.1) for discriminating sea ice from open water by S1 HH and HV (denoised, as examples shown in Fig.2) data is based on a modified U-Net architecture (Fig.3), a deep learning network. By employing an integrated stacking model to combine multiple U-Net classifiers with diverse specializations, sea ice segmentation is achieved with superior accuracy over any individual classifier (example shown in Fig.4). We applied the proposed approach to over 28,000 S1 EW 15 images acquired in 2019 to obtain sea ice cover products in a high spatial resolution of 400 m. By converting the S1-derived sea ice cover to concentration and then compared with Advanced Microwave Scanning Radiometer 2 (AMSR2) sea ice concentration data, showing an average absolute difference of 5.55 % with seasonal fluctuations (Fig.5). A direct comparison with Interactive Multisensor Snow and Ice Mapping System (IMS) daily sea ice cover data achieves an average accuracy of 93.98 %. These results show that the developed S1-derived sea ice cover results are comparable to the AMSR and IMS data in terms of overall accuracy but superior to these data in presenting detailed sea ice cover information, particularly in the marginal ice zone. So far we have generated the S1-derived sea ice cover dataset from 2019-2022.

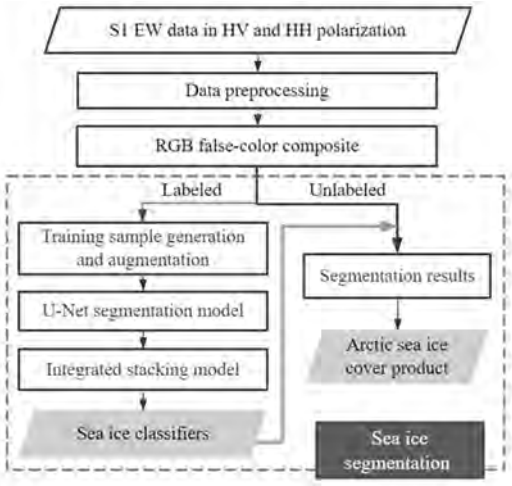

Fig.2 Flowchart of the proposed method for deriving sea ice cover information from S1 EW images in HV and HH polarization.

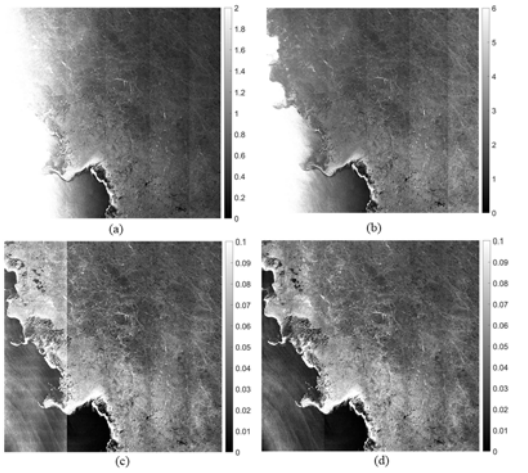

Fig.1 Example of the process of S1 data: (a) original HH-polarized data (b) incidence angle-corrected HH-polarized data (c)original HV-polarized data and (d)denoised HV-polarized data using the method proposed by Sun and Li (2020).

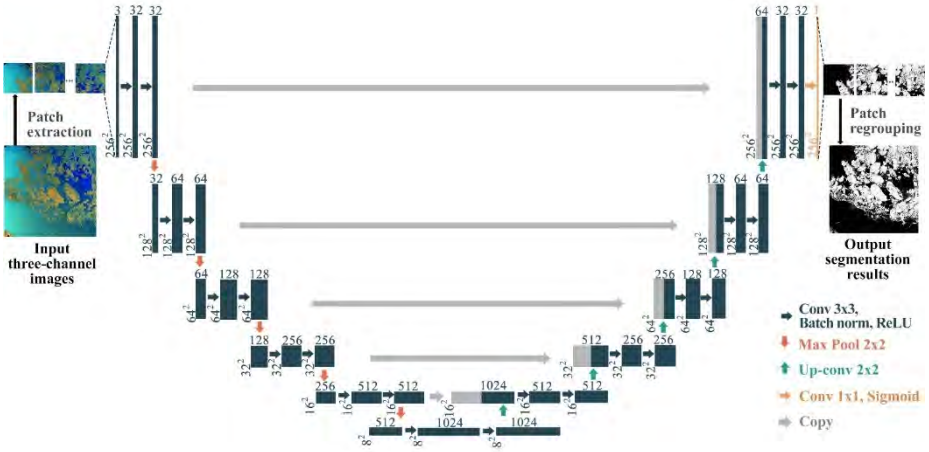

Fig.3 The overall architecture of the proposed sea ice segmentation model for the S1 EW data based on the U-Net deep learning algorithm.

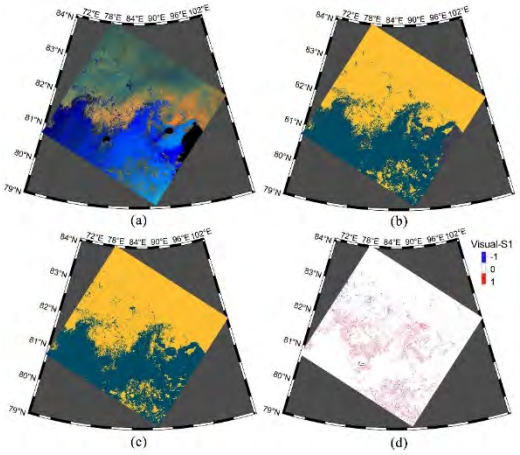

Fig.4 An example of S1-derived sea ice cover and its comparison with the visual interpretation result. (a) RGB false-color composite image. (b) and (c) S1-derived and visual interpretation of sea ice cover, with yellow indicating sea ice and cyan indicating open water. (d) Differences in sea ice cover between (b) and (c) (visual interpretation - S1 derive).

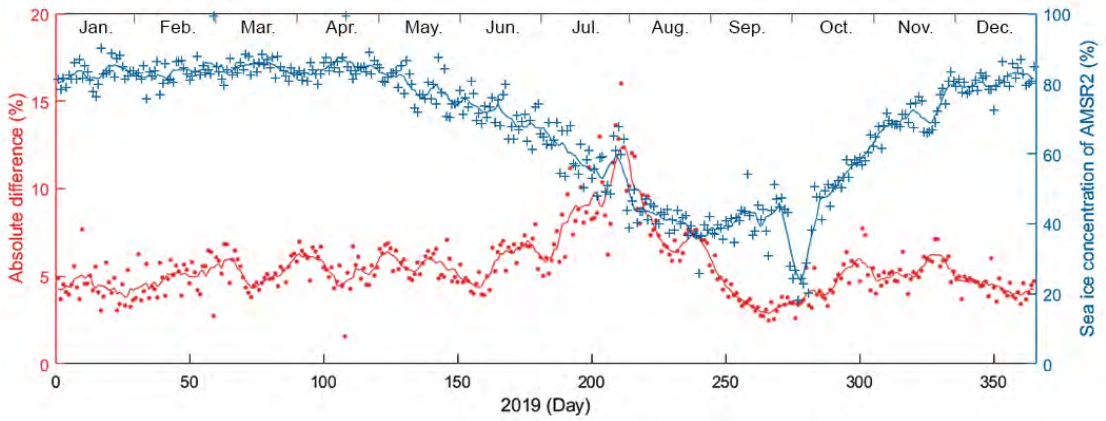

Fig.5 Comparison between the S1-derived Arctic sea ice concentration data and AMSR2 data for the whole year of 2019. The red dots reflect the absolute daily difference, and the red line is the 7-day average absolute difference. The blue crosses are the daily sea ice concentrations in the S1-covered area calculated based on the AMSR2 data, and the blue line is the 7-day average sea ice concentration.

A state of-the-art method (Fig.6) combining feature tracking (FT) and pattern matching (PM) techniques was applied to sequential S1 SAR data in 2020 to derive sea ice drift from the central

Arctic to the Fram Strait. The SAR retrievals were validated with drifting buoys. For temporal intervals of S1 data of approximately 24 h, 15254 collocations (Fig.7) were collected from January to June and from October to December, yielding a 0.00 cm/s bias for the drift velocity magnitude and 0.27◦ for direction with corresponding root mean square error (RMSE) of 0.47 cm/s and 4.73◦ (Fig.8). Using temporal intervals of S1 data of less than 24 h, we retrieved SID from July to September. A total of 644 collocations yields a comparison with a bias of 0.52 cm/s and 4.62◦ for the drift magnitude and direction, respectively. The corresponding RMSE values are 1.85 cm/s and 20.73◦. The comparisons demonstrate better performance than the operational SAR-based sea ice drift product using the maximum cross correlation (MCC) method and are consistent with seasonal trends in drift velocity with the coarse resolution product. We also analyzed the variations in SAR retrievals and further estimated appropriate temporal intervals, making it feasible to conduct long-term SID retrievals based on spaceborne SAR data at high spatial resolution in the Arctic.

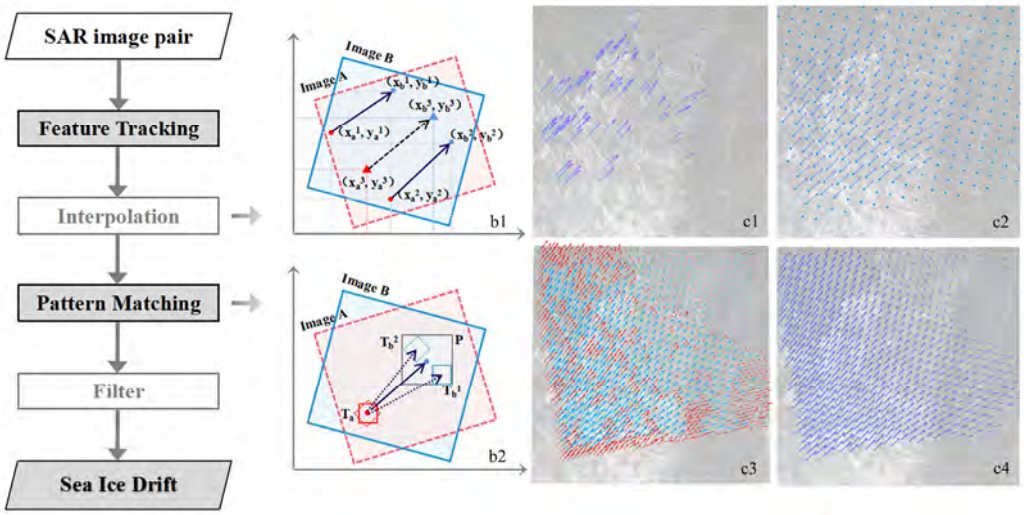

Fig.6 The combined method for retrieving SID from S1 image pairs. (a) The main flowchart of the combined method. (b) Illustrations of the interpolation (b1) and PM module (b2). (c) Vectors derived by the steps. (c1) The sparse vectors extracted by the FT module. (c2) The vectors full of the regular grid by the interpolation. (c3) The good vectors (blue) and the filtered vectors (red) derived by the PM module. (c4) The final output vectors.

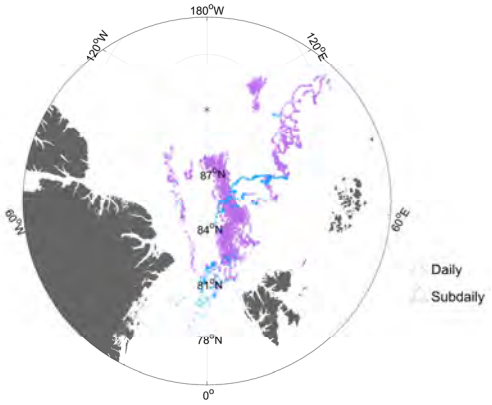

Fig.7 Distribution of 15,898 SAR-derived SID vectors compared with MOSAiC buoy data (Daily temporal (purple markers): 15254 collocations)

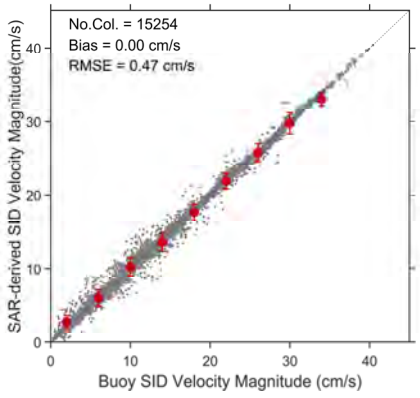

Fig. 8 Comparisons between SAR-derived SID based on daily-scale temporal intervals and MOSAiC buoys in the velocity magnitude

Operational SAR-based Sea Ice Concentration Retrieval Using Convolutional Neural Networks

The Arctic is undergoing unprecedented changes due to anthropogenic warming, and the thinning of the Arctic sea ice is leading to increased human activity in the region. The growing maritime user group accessing wider parts of the Arctic calls for detailed and timely information about the state of the Arctic sea ice for maritime safety and planning purposes. Synthetic Aperture Radar (SAR) imagery enables detailed year-round mapping of sea ice conditions due to the high spatial resolution (<100m), the independence of solar illumination and the fact that SAR is unimpeded by cloud cover. SAR imagery is therefore an important source of information for the National Ice Centres around the world, where ice analysts produce sea ice charts for maritime users by manual interpretation of primarily SAR imagery. With the ever-expanding archives of readily available satellite imagery, the task of manually interpreting these data becomes laborious and time-consuming. A partial automation of this process can assist the ice analysts in the delivery of high-resolution sea ice products in near-real time, and a fully automated sea ice mapping system can provide high-resolution sea ice products to be integrated into forecast models to potentially improve forecast quality.

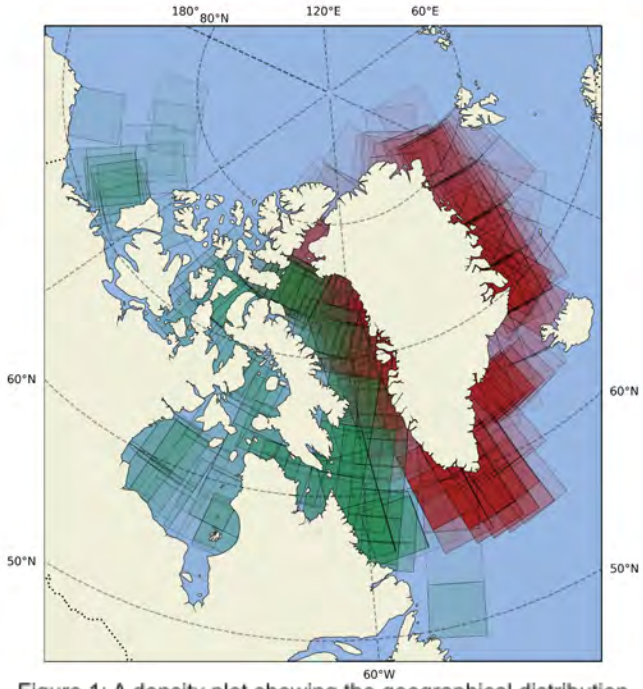

Figure 1: A density plot showing the geographical distribution of the dataset used to train our CNN. Each square corresponds to a single Sentinel-1 scene. Red squares are Sentinel-1 scenes that have been matched up with an ice chart from the Greenland Ice Service, while green squares are from the Canadian Ice Service.

For several decades the design of SAR-based sea ice classification schemes has been studied within the sea ice community. Traditional machine learning (ML) and computer vision techniques have been applied to the task of SAR-based sea ice mapping with limited success. SAR data is inherently ambiguous, and many ML methods therefore rely on manually engineered texture features, like GLCM-based features, that capture contextual information [Clausi, 2001]. Such approaches, however, have a common bottleneck in that they depend on the quality and usefulness of the engineered features, and humans are bound to miss important latent features.

Advances in deep learning (DL) and computing technology over the last decade have paved the way for the use of advanced computer vision techniques, such as Convolutional Neural Networks (CNNs), for the automatic analysis of high-resolution satellite imagery. CNNs automatically learn spatial representations relevant to the task at hand, and therefore bypasses the need for manually engineered image features. In recent years, Fully Convolutional Networks (FCNs) have been applied to the task of automatic sea ice concentration mapping using Sentinel-1 SAR dual-polarized imagery, generally with promising results [Malmgren-Hansen et al., 2020; Stokholm et al., 2022; Gélis et al., 2021].

The main challenge faced by all data-driven sea ice property retrieval algorithms is the shortage of in-situ information. The collection of comprehensive in-situ data over sea ice is a resource-intensive process and is often not feasible. Despite this, several National Ice Centers regularly produce manually drawn ice charts with a history spanning several decades. As of today, these ice charts provide the best alternative for generating large training datasets, which are necessary for the development of modern deep learning-based models. In our approach, we train a CNN in a supervised setting using manually produced ice charts as label data. Our CNN fuses high-resolution Sentinel-1 SAR imagery and Passive Microwave Radiometer (PMR) observations from AMSR-2 to generate high-resolution maps of sea ice. The CNN has been trained on a vast dataset containing ice charts from the Greenland and Canadian ice services co-located with Sentinel-1 EW imagery and AMSR-2 observations. A subset of this dataset as well as get-started tools has been made publicly available as part of ESA's AutoICE challenge (https://platform.ai4eo.eu/auto-ice). The geographical distribution of the dataset is shown in figure 1.

Classifying sea ice in SAR imagery is not a trivial task. While microwave signatures in SAR imagery show patterns related to ice formations, the differentiation between different sea ice conditions is challenged by ambiguities in backscatter intensities, noise phenomena and wind-induced surface roughness, etc., which is apparent in previous studies [Malmgren-Hansen et al., 2020; Stokholm et al., 2022; Gélis et al., 2021]. Our approach tackles this obstacle by increasing the receptive field of the CNN and by fusing the SAR imagery with PMR observations to exploit the advantages of both instrument types - that is, the high spatial resolution of the SAR imagery, and the more reliable discrimination of sea ice and open water in the PMR observations.

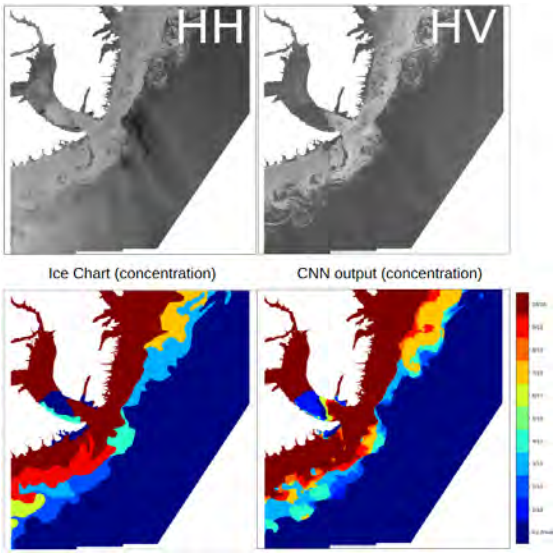

Figure 2: Example of a Sentinel-1 EW scene from the Scoresbysund Fjord in East Greenland. Upper left: Sentinel-1 HH polarisation. Upper right: Sentinel-1 HV polarisation. Bottom left: Manually drawn ice concentration chart (Greenland Ice Service). Bottom right: Ice concentration output from the CNN.

Our CNN processes Sentinel-1 EW and IW GRD products resampled to an 80 m grid, which is close to the native spatial resolution of Sentinel-1 EW products. Similarly, the output of the CNN is on an 80 m grid. The Sentinel-1 HH and HV bands have been noise-corrected using the accompanying metadata and the CNN is largely unencumbered by any remaining noise-related artifacts.

We set aside a test dataset that we use to evaluate the performance of the CNN. Figure 2 illustrates an example of a Sentinel-1 scene from the test dataset. The imagery was acquired in May 2018 and covers the Scoresbysund Fjord in East Greenland. The figure shows the HH and HV bands as well as a manually produced ice chart and the output sea ice concentration map from our CNN. Overall, the CNN achieves an R^2-score of 92% against the manually produced ice concentration charts in the test dataset, indicating a good level of agreement between the CNN and the ice analysts. Note, that while manually produced ice charts are relatively

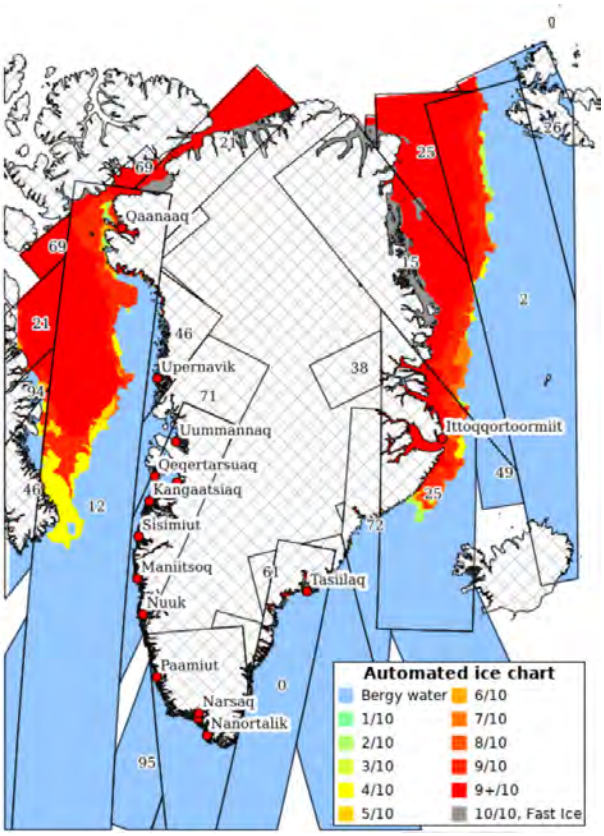

Figure 3: Example of a concentration mosaic of several days of Sentinel-1 imagery processed by the CNN. The mosaic was generated on November 7th 2022.

high-resolution and available at scale, and thus an obvious choice as label data, the charts have inherent uncertainties that are not well-documented - such as analyst subjectivity, inter- and intra-analyst variation and mislabeling errors. Any systematic biases introduced by the manual ice charting method (e.g. an overestimation of intermediate sea ice concentrations) might therefore be reproduced by the CNN. Given the size and diversity of the training dataset, we believe inter- and intra-analyst variability is not reproduced by the CNN.

The CNN is implemented in operations at DMI and provides high-resolution sea ice concentration in near-real-time for the benefit of the ice analysts in the DMI Greenland Ice Service that use the sea ice information from the CNN as input to the ice charting process.
Products based on the CNN are also distributed within the Copernicus Marine Service (since November 2022) as the “DMI-ASIP sea ice classification - Greenland” dataset [Dinessen et al. 2022]. From March 2023 similar products for the Antarctic will be distributed in Copernicus Marine Service. The Greenland and Antarctic products include sea ice concentration information and associated uncertainties.

The failure of Sentinel-1B in December 2021 has affected the coverage and update frequency of derived sea ice products. Robustness against such events calls for the development of ‘sensor-agnostic’ models that allows for the ingestion of additional SAR products in the processing chain, such as SAR imagery from the Radarsat Constellation Mission. A robust system with good coverage and update frequency delivering near real-time SAR-based sea ice products for both hemispheres is an attractive alternative to the manually produced ice charts or PMR-based sea ice products (which lack in temporal and/or spatial resolution) that is being used for data assimilation in sea ice forecasting systems. Manually produced ice charts are valuable for deep learning model training since they are available at scale and they can be accurately matched, spatially and temporally, with SAR images. However, due to the manner in which the ice charts are drawn (as homogeneous polygons consisting of partial concentrations), they are not a physically realistic representation of the state of the sea ice. In order to properly validate these deep learning models, we need a higher resolution dataset from which the state of the sea can be reliably extracted and that can be matched, spatially and temporally, with SAR images, e.g. optical imagery. While most research into the field of automatic sea ice mapping has been concerned with sea ice concentration mapping, the National Ice Centers also mention *Stage of Development* (ice type) and *Floe Size* as important sea ice properties for their users.

References

D. A. Clausi, “Comparison and fusion of co-occurrence, Gabor and MRF texture features for classification of SAR sea-ice imagery,” Atmos.-Ocean, vol. 39, no. 3, pp. 183–194, 2001.

Dinessen, F., Korosov, A., Wettre, C., Lavergne, T., and Kreiner, M. B. (2022). “Product user manual: Arctic sea ice concentration arctic sea ice type greenland sea ice concentration,” in Copernicus Marine service, product SEAICE ARC PHY AUTO L4 NRT. 011 015 1.1. doi: 10.48670/moi-00122

A. Stokholm, T. Wulf, A. Kucik, R. Saldo, J. Buus-Hinkler and S. M. Hvidegaard, "AI4SeaIce: Toward Solving Ambiguous SAR Textures in Convolutional Neural Networks for Automatic Sea Ice Concentration Charting," in *IEEE Transactions on Geoscience and Remote Sensing*, vol. 60, pp. 1-13, 2022, Art no. 4304013, doi: 10.1109/TGRS.2022.3149323.

I. de Gélis, A. Colin and N. Longépé, "Prediction of Categorized Sea Ice Concentration From Sentinel-1 SAR Images Based on a Fully Convolutional Network," in *IEEE Journal of Selected Topics in Applied Earth Observations and Remote Sensing*, vol. 14, pp. 5831-5841, 2021, doi: 10.1109/JSTARS.2021.3074068.

D. Malmgren-Hansen *et al*., "A Convolutional Neural Network Architecture for Sentinel-1 and AMSR2 Data Fusion," in *IEEE Transactions on Geoscience and Remote Sensing*, vol. 59, no. 3, pp. 1890-1902, March 2021, doi: 10.1109/TGRS.2020.3004539.

Potential Application of the Earth Explorer 10 candidate Harmony for Sea Ice Model Validation

Sea ice in the Arctic Ocean is in continuous motion under influence of wind, ocean, and internal stress. Sea ice deformation (computed as a spatial derivative of the drift field) is localized in space and time and forms elongated, narrow zones, also called Linear Kinematic Features (LKFs). The frequency distribution of deformation rates as well as the pattern, density, orientation, and intersection angle of LKFs are a characteristic feature of sea ice.

Sea ice drift and deformation can be observed by pattern matching techniques applied to passive microwave, or scatterometer, or synthetic aperture radar (SAR) satellite data. The disadvantage of the type of ice drift product is the large time delta required between the image acquisitions, and a relatively low spatial resolution.

Harmony is a candidate for the Earth Explore 10 mission. The two Harmony satellites will fly in a reconfigurable formation with Sentinel-1D. Both will be equipped with a multi-angle thermal infrared sensor and a passive radar receiver, which receives the reflected Sentinel-1D signals using two antennas. In the stereo formation, the Harmony satellites will fly approximately 300 km in front and behind Sentinel-1, which allows for the estimation of instantaneous sea-ice drift vectors. As it was shown by Kleinherenbrink et al., [2021] the sea ice drift and deformation can be derived from simulated Harmony data, but the signal-to-noise ratio is quite low.

The goal of this study is to evaluate the applicability of the Harmony data for statistical characterisation of sea ice deformation in the Arctic Ocean and feasibility in utilisation for tuning parameters of the next generation sea ice model (neXtSIM, [Olason et al., 2022]). NeXtSIM can realistically simulate the sea ice motion and deformation. Both the LKFs and the spatial scaling of the sea ice deformation rate simulated by neXtSIM compare quite well to PMW and SAR observations. Sensitivity of synthetic Harmony data to neXtSIM rheological parameters is studied. A scenario of model validation against instantaneous sea ice drift satellite estimates is suggested.

Denoising Doppler shift data

Computing the Doppler shift signal and adding thermal noise is performed with the same forward model (F_M) as in [Kleinherenbrink et al. 2021]:

$D, N_D = F_M (U)$

This yields 2D fields of Doppler shift from Concordia, Discordia, and Sentinel ($D_C(R,A)$, $D_D(R,A)$, $D_S(R,A)$) and the thermal noise equivalent sigma zero (NESZ) of the Doppler signal ($N_D(R,A)$). Each Doppler shift field is further treated separately and the subscripts and (R,A) dependence is omitted for clarity.

Thermal noise is added as a product of NESC profile and normally distributed noise (N):

$D^N = N_D * N$

Noise correction is further performed for each field of D individually.

Given that the profile of NESZ is known *a priori* we can perform “texture noise” correction suggested by Park et al. [2019] for reducing amplitude of signal variations near inter-swath boundaries where NESZ is the highest:

$D^1 = Gf(D^N)*N_N + D^N*(N_N – 1),$

Where Gf is a 2D Gaussian filter with size of 10 pixels (20 km) and N_N is N_D normalized into range 0 – N_{MAX}, with N_{MAX} = 0.7 being found empirically.

Next, the low-pass filter is applied to D^1 as suggested in [Kleinherenbrink et al. 2021, eqs. 19 – 22]:

$D^2 = Kf(D^1, D)$.

Note, that the original fields with Doppler shift (D, prior to adding noise) are required to compute the cut-off frequency.

Finally, the anisotropic diffusion filter [Perona and Malik, 1990] is applied is applied for smoothing homogeneous U/V fields and preserving high contrasts:

$D^3 = ADf(D^2, gamma=0.25, kappa=5)$.

Denoising instantaneous sea ice drift velocities

Velocity fields (U) are reconstructed from D, D^N and from D^3 using the same retrieval model (R_M) as in [Kleinherenbrink et al. 2021], and the low-pass filter (Kf) is applied for comparing results of the initial denoising approach (U^M) and the new one (U^3):

$U^N = R_M(D^N)$; $U^M = Kf(U^N, U)$; $U^3 = R_M(D^3)$

Figure 1 shows that velocities reconstructed from denoised Doppler shift (U^3) seem cleaner than the denoised velocities (U^M) and have a lesser effect of thermal noise range variations.

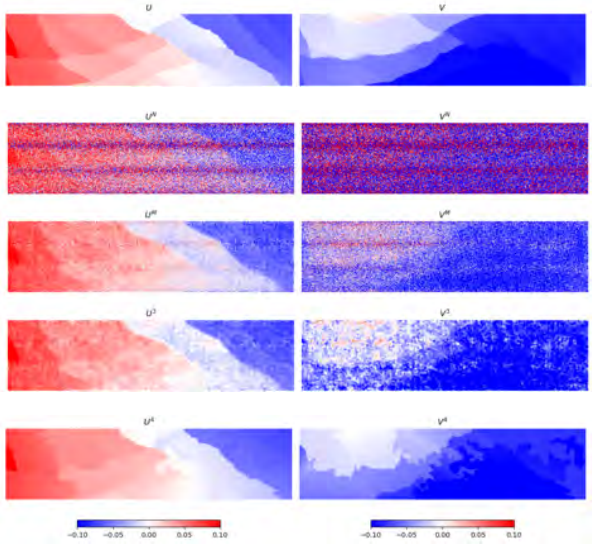

Figure 1. Velocity components after the steps of processing: U – initial range and azimuth components, U^N – from raw noisy Doppler shift, U^M – Kleinherenbrink method, U^3 – new smoothing, U^4 – smoothing and clustering.

The next step of denoising the velocity fields is clustering. The clustering can be described as grouping of objects (in our case pixels) with similar characteristics (in our case velocities and coordinates). The clustering is applied under assumption that sea ice deforms as a solid body with low elasticity and ability for brittle break-up. Therefore, the neighbour elements can have either the same velocity (when they belon to an unbroken ice, i.e., an ice floe) or differ substantially (when they belong to different ice floes). After the clustering is performed, the small-scale variability on the edges of clustering is reduced by applying a median filter to the image with labels (Figure 1).

Computing deformations

The discontinuities (dU^{M1}) in the field of U^M were identified the same way as suggested in [Kleinherenbrink et al. 2021]. This method was slightly optimized for computing discontinuities dU^{M2} by reducing resolution, smoothing U^M with a Gaussian filter and thresholding geometrically averaged X- and Y- gradients. Divergence (∇) and shear (τ) components of sea ice deformation of the velocity fields U, and U^A was computed by calculating the velocity gradients (Vg) in neighbour elements and then using equations 23 and 24 from [Kleinherenbrink et al. 2021].

A mosaic of sea ice deformations was created by generating 15 swaths of Harmony observations for the 1 January 2019 and interpolating the swath data onto a grid in Polar Stereographic projection. Daily mean deformation map was created by averaging the individual swaths. Two neXtSIM runs with distinctly different parameters of rheology were used to generate Harmony data, retrieve / denoise velocities and compute deformations.

Figure 2 shows that neXtSIM rheology parameters significantly affect the pattern of sea ice deformation. Methods M2 and A were tuned for denoising and computing deformations on the first run and obviously work better with the synthetic data generated from the first run: the major deformation features north of Greenland, Canadian Archipelago and Laptev Sea are well visible. Method A seems to be better capturing also small deformation features and producing a less noisy map. Both methods perform poorer on the data from the second neXtSIM run: large deformation zones north of Greenland, near Novaya Zemlya and in the Laptev Sea are not reconstructed, small features are almost not visible, the maps look quite noisy.

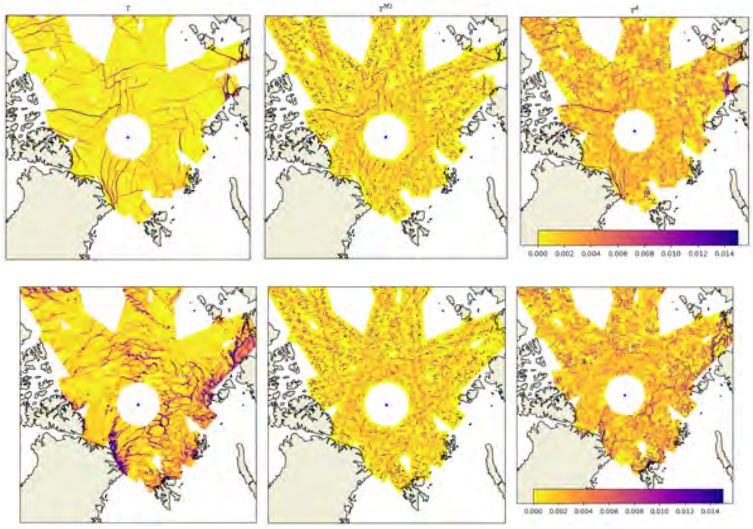

Figure 2. Maps of divergence (∇) and shear (τ) computed from the two neXtSIM runs (upper and lower rows) from original velocities (left) and from Harmony denoised velocities U^{M2} (middle) and U^A (right).

Analysis of PDFs of deformation (not shown here) indicates that not only the pattern, but also the PDF of the neXtSIM ice deformation is sensitive to neXtSIM rheology parameters: the second run generally produces lager deformation, and the skewness of PDFs is lower, indicating lesser localisation of deformation zones (wider LKFs).

Nevertheless, the PDFs of deformation from two runs (computed either by M2 or by A methods) seem almost equal. That indicates low sensitivity of the noisy ice drift velocity field and corresponding ice deformation to the actual rheology of sea ice and high sensitivity to the processing method.

SeaSAR 2023 Abstract

A Multisensory SAR-Based Approach For Melt Ponds Retrievals

Much of the current understanding of melt ponds (and corresponding sea ice albedo evolution) is based on in-situ studies (e.g. Eicken et al., 1994, Perovich et al., 2012, Tschudi et al., 2008), however, satellite-based observation are the way to map and monitor melt ponds and albedo changes on a pan-Arctic scale. In fact, given that melt ponds are generally small and change rapidly it is of great interest the use of remote sensing data with high spatial and temporal resolution to monitor melt ponds on different types of sea ice during the melting season.

The application of satellite data to understand spatial and temporal variations in melt pond coverage has been traditional though estimates using optical sensors (during cloud-free conditions) (e.g. Tschudi et al., 2008, Rösel et al. 2012, Istomina et al., 2020). However, the enhanced spatial resolution of synthetic aperture radar (SAR) compared to radiometers and scatterometers along with SAR's ability to image our Planet's surface irrespective of cloud cover, is gaining a lot of interest by researchers to bridge the gap between current knowledge of evolving ice-ocean-atmosphere between melt onset and freeze up (Scharien et al., 2010).

However, the availability of spatial resolution to perform large scale monitoring in the high regions is limited. Optical missions like Sentinel-2 provide a very interesting temporal resolution however the availability of cloud-free data is scarce at higher latitudes. Some works have been focusing on the derivation of melt pond fraction and proxy estimates of surface albedo in order to understand the evolution of summer ice albedo and to evaluate the potential of SAR for aiding the parameterization of sea ice and climate models (Scharien et al., 2014).

Furthermore, due to the difficulty in collecting data from polar regions, the relatively expensive costs, and logistics, it is important to maximize the potential benefits deriving from data. According to Rolnick et al. (2019), the number of applications of machine learning to study polar regions is not high although it has been increasing over the past decade. The combination of satellite imagery with machine learning holds the potential to address global challenges by remotely estimating environmental conditions in data-poor regions – such as the Arctic region.

The proposed approach focuses on using multi sensors to increase the temporal resolution and enhance spatial resolution and accuracy of previous melt ponds and melt pond fraction products or studies. A main focus will be given to synthetic aperture radar (SAR) data in different incidence angles for various ice types. The main reason for using SAR is due to its weather independence, meaning it is not constrained by cloud coverage as optical imagery - which has been the main source of information for melt ponds monitoring. In addition, the heterogeneity of other datasets will be merged with SAR data due to its potential to extent help bridging possible gaps of non-existence data to guarantee the continuous monitoring and understanding of melt ponds formation and dynamics during melting period. The multi source datasets will be used to train models to achieve the following key objectives:

1) Classification of melt ponds
2) Prediction of melt pond fraction

Three additional additional and major expected outcomes or by products are:

1) The capability of tracking evolution of melt ponds, as well as extracting the feature importance (i.e. for the case where random forests are applied) to understand the importance of each variable on the prediction results.

2) The creation of training datasets specifically focused on melt ponds, which to our knowledge are not currently available.

3) The retrieval of statistical information such as the relationship between the polarimetric signatures and microwave emissivity of melt ponds, and retrieve information on spectral and radiometric properties, along with other variables that impact melt pond formation.

References

Tschudi, M. A., Maslanik, J. A. and Perovich, D. K.: Derivation of melt pond coverage on Arctic sea ice using MODIS observations, Remote Sensing of Environment, 112 (5), 2605-2614, https://doi.org/10.1016/j.rse.2007.12.009, 2008.

Eicken, H., T. C. Grenfell, D. K., Perovich, J. A. Richter-Menge, and Frey, K.: Hydraulic controls of summer Arctic pack ice albedo, J. Geophys. Res., 109, C08007, https://doi.org/10.1029/2003JC001989, 2004.

Perovich, D. K., and Polashenski, C. (2012), Albedo evolution of seasonal Arctic sea ice, *Geophys. Res. Lett.*, 39, L08501, doi:10.1029/2012GL051432.

Rösel, A., Kaleschke, L. and Birnbaum, G.: Melt ponds on Arctic sea ice determined from MODIS satellite data using an artificial neural network, The Cryosphere, 6 , pp. 431-446 . doi: http://doi.org/10.5194/tc-6-431-2012, 2012.

Istomina, L., Marks, H., Huntemann, M., Heygster, G., and Spreen, G.: Improved cloud detection over sea ice and snow during Arctic summer using MERIS data, Atmos. Meas. Tech., 13, 6459–6472, https://doi.org/10.5194/amt-13-6459-2020 , 2020a.

Scharien, R. K., Hochheim, K., Landy, J., and Barber, D.G.: First-year sea ice melt pond fraction estimation from dual polarisation C-band SAR – Part 2: Scaling in situ to Radarsat-2, The Cryosphere, 8, 2163-2176, https://doi.org/10.5194/tc-8- 2163-2014, 2014.

Rolnick, D., et al.: Tackling Climate Change with Machine Learning, Association for Computing Machinery, 55, 0360-0300, https//doi.org/10.1145/3485128, 2019.

Quadruple Helix Framework for Sea Ice Monitoring: Next Steps

Ekaterina Kim, Roger Skjetne, Knut Høyland
Norwegian University of Science and Technology, Trondheim, Norway

The Arctic - one of the most desolate and sparsely populated areas on our planet - plays a crucial role in regulating the world's climate. Despite Arctic's importance for the Earth's climate, this area remains severely under-monitored and not well known to the broad public. Few humans are directly involved in monitoring (this is mostly done using remote sensing tools). As urbanization continues, there is limited human engagement, and participation in monitoring of nature and a further disassociation with it. In view of this challenges, we readopted a quadruplex helix framework for monitoring of sea ice. The framework relates sea ice knowledge at different spatial and temporal resolutions to each other (i.e., remote sensing, in-situ scientific measurements, citizen science, and indigenous knowledge)

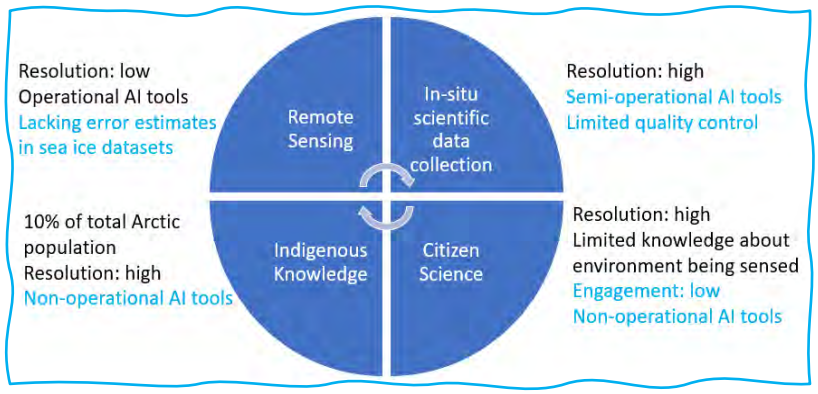

Fig. 1. Quadruplex helix framework for sea ice monitoring and its challenges.

In addition to the challenges with local data collection, access to (and processing) the Arctic data is a persistent and important multidimensional problem; not all Arctic countries are willing to share their knowledge, but for those who do share, the amount of shared data now outpaces experts' ability to check, interpret, and make complex decision based on these data. As a result, our ability to predict rapid changes of the environment and manage the effects of environmental change is severely limited. Traditional remote sensing techniques (using satellites) suffer from significant uncertainties near the coast, close to the sea ice edge, etc. Uncrewed aerial vehicles and sail drones have limited coverage and operability window (e.g., darkness, heavy snow, etc.). We are not always able to validate & trust the Arctic satellite products when looking at rapid & localized events or changes on the ground – a recognized shortcoming by the Arctic Council, Copernicus, and International Ice Chart Working group communities. Solving this shortcoming has been difficult in the past due to the lack of technology for automated collection, processing, and quality control of the ground-truth Arctic data. Empirical testing of the popular state-of-the-art machine learning algorithms applied to sea ice revealed a need for pre/post training and systematic evaluations. Fig. 2 is a typical example of false negative errors in some of the analysed algorithms.

In addition, sea ice data users (fisheries, forecasting agencies, etc.) increasingly require spatially explicit information on the uncertainty of sea ice parameters for evaluating the risk that a specific outcome of further analysis of the information will be incorrect. However, error estimates are lacking in practically all the sea ice datasets available today. It is, therefore, a priority to develop and standardize methods to compute consistent and comparable error estimates. This is

particularly important for in-situ observations since realistic uncertainty estimates are essential for meaningful integration of these data in remote sensing and other higher-level products and studies (automated sea ice charting, climate modelling, etc.).

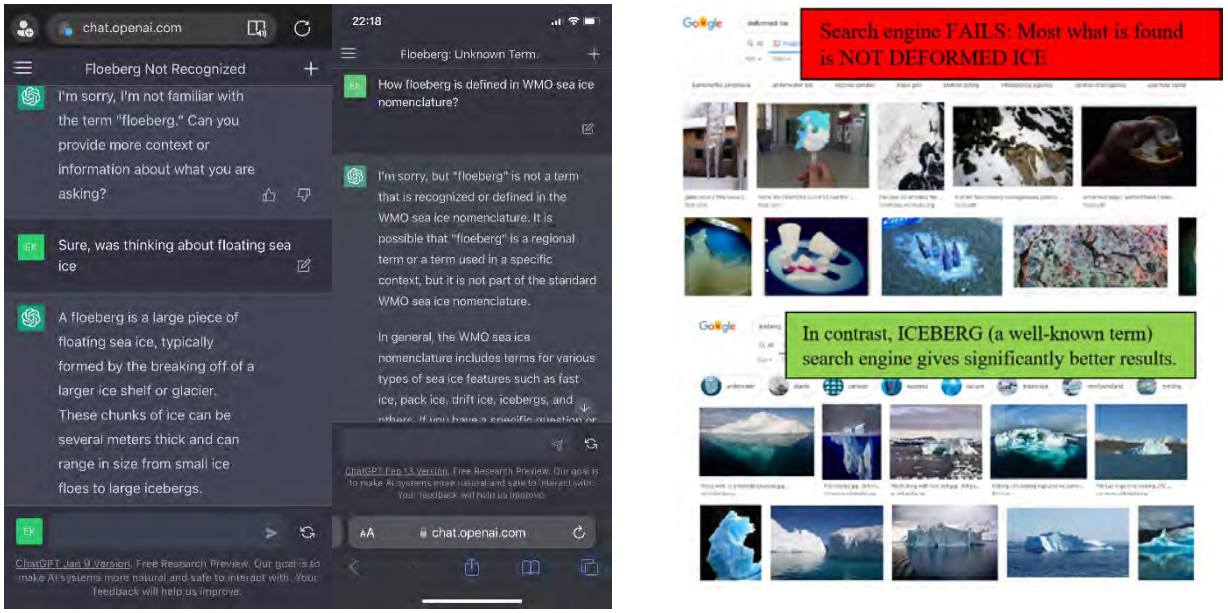

Fig. 2 False negative output errors (ChatGPT Jan 9 and Feb 13 versions; Google search engine)

During the workshop, the first significant results from two (or more) parallel projects will be presented with the focus on the blue colored elements in Fig. 1.

Digital Sea Ice

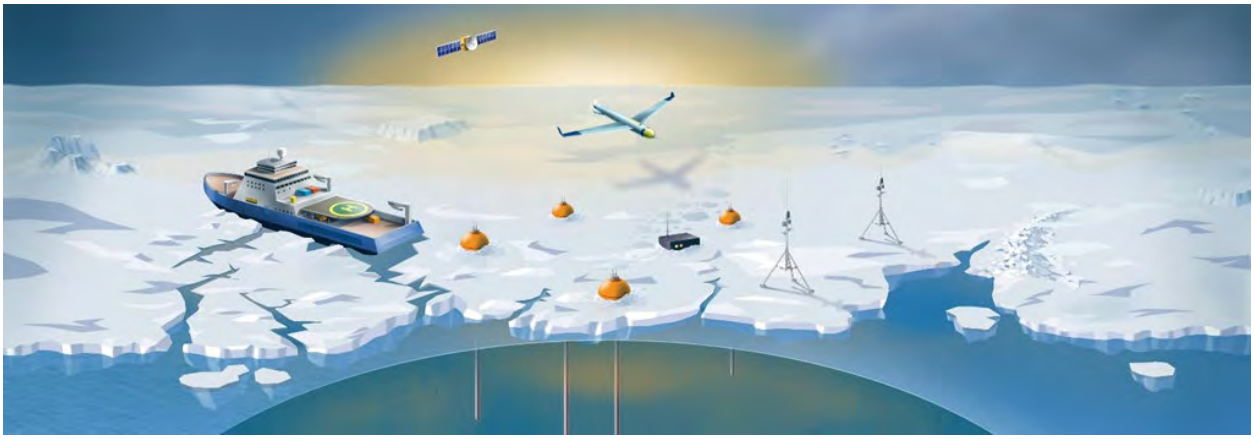

As a part of this project, a multiscale digital method and a system is being built by integrating regional sea ice forecasting models and local ice-ice/ice-structure numerical models with in-situ, shipboard, and space observations of the Arctic sea ice and of environmental conditions. This enables improved spatial and temporal resolution in the models, to achieve more precise forecasting of ice conditions in the Arctic – including better understanding of long-term variations in the polar ice cover. It involves development of novel methods for use of artificial intelligence (AI)-based analytics of synthetic aperture radar and optical imagery from satellites, marine radars

and lidars, visual and infrared cameras, and other enabling technologies. Further objectives are to accurately map the sea ice flow in high resolution and generate quality-controlled sea ice drift forecasting. Novel methods for monitoring and analysis of sea ice dynamics and fracturing processes based on data from heterogenous sources are being developed and will be used to update the multiscale model from the real observations.
The project aims at developing novel methods and a digital infrastructure for improved spatial and temporal forecasting and decision support in an increasingly dynamic Arctic environment due to climate changes. Such infrastructure will enable more accurate data and information to be produced, thus resulting in better insight on polar Earth systems, as well as improved safety for maritime voyages.

NTNU Oceans Pilot on Arctic marine environment

This project covers a university-wide aspects of topics from engineering, physics, biology to social anthropology. The Arctic marine environment (including Baltic and Europe's ice-covered inland waterways) with sea ice and icebergs distinguishes itself from open water environment further south in two vital ways: a) It is more complicated (e.g., more parameters are required to describe it) and b) the available data is scarce. We are working with models and methods to predict short - and long-term behavior of the environment and our human interaction with it, within the framework of risk, reliability, and data. One of the main outcomes is that there are important challenges (and possibilities) in combining measurements in different spatial and temporal scales. Data measured in-situ is usually very local (either in-situ field work with point measurements in space and time, or drifting buoys with continuous temporal records), whereas satellites based usually covers larger areas with a low frequency. In addition, the physics of how the diverse signals from satellites reflect from the ice cover is not completely understood. The uncertainties should be studied through collocated measurements with different sensors (from down on the ice to satellite sensors) and data analysis methods, but also through studying the physics of how signal reflect from different ice covers (wet/dry snow, melt ponds, etc.).

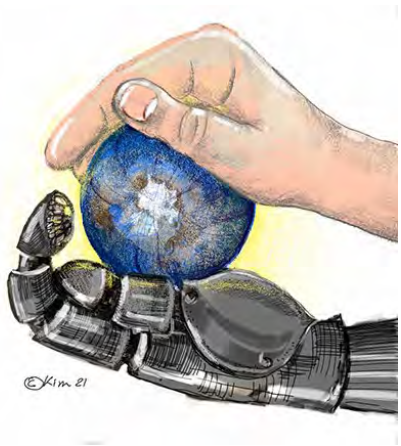

During the workshop, we want to engage in dialog with ESA and other members of the program committee and chairs on specific needs, priorities for in-situ observations of sea ice, functional requirements to the collected in-situ data (above, at, and below the sea ice surface) as well as for uncertainty representations, in view of the sensing technologies, data processing and quality control tools being developed at the Norwegian University Science and Technology (NTNU). This will help in achieving a broader impact from ongoing research projects, create the potential for researchers to collaborate across multiple dimensions of scale, and to build a more precise picture of harsh and unforgiving Arctic environment. This is urgently needed in a view of accelerating climate-change-driven events and impacts of human activities on our planet's ecosystems.

Sensor Synergy

Sensor Synergy

Taillade, Thibault; Engdahl, Marcus; Fernandez, Diego
Can We Retrieve Sea Surface Salinity with SAR Measurements?

Zhang, Biao; Perrie, William; Zhang, Mingyu
Polar Low Recognition and Tracking from Multi-Temporal Synthetic Aperture Radar and Radiometer Observations

Rascle, Nicolas Gilles; Grouazel, Antoine; Mouche, Alexis; Nouguier, Frederic; Villarreal Olavarrieta, Carlos Eduardo; Mora Escalante, Rodney Eduardo; Diaz Mendez, Guillermo; Chapron, Bertrand; Ocampo-Torres, Francisco J.
Satellite Measurement Of Waves And Currents: SAR Vs Optical Sensors

Holt, Benjamin; Lockhart, Brittany; Porter, Mitchell; Comer, Douglas
Fronts, Eddies, and Other Features in the Western Pacific and Micronesia from SAR and Other Multi-Sensor Data

Husson, Romain; Ollivier, Annabelle; Chehade, Bassam; Peureux, Charles; Quet, Victor; Goimard, Gaël; Soulat, François; Tourain, Cédric; Lachiver, Jean-Michel
Comparing and Combining S1 and SWIM Spectral Wave Measurements

Can We Retrieve Sea Surface Salinity with SAR Measurements?

Thibault Taillade, Marcus Engdahl, Diego Fernandez ESA/ESRIN, Frascati

Abstract

Sea Surface Salinity (SSS) is measured operationaly with Radiometers (e.g. SMOS) with a resolution from 25 to 40 km that is rather constraining for coastal areas and estuaries. In this contribution, we theoretically evaluate Synthetic Aperture Radar (SAR) sensitivity to SSS. This work focuses firstly on the variations of the dielectric properties of seawater with salinity at different SAR frequency bands (P-, L- and C-bands) and then evaluate the consequences on the Normalized Radar Cross Section (NRCS) simulated using Bragg models. The main challenge for SSS retrieval is to disentangle the sensitivity to dielectric properties from the surface roughness contribution in the SAR backscattered signals. The results show that the NRCS sensitivity with salinity increases with decreasing operating frequency, and NRCS sensitivity to roughness decreases with decreasing operating frequency providing potential retrieval strategies.

I. Introduction

Sea Surface Salinity is an important parameter driving ocean circulation and is currently measured at a 25 to 40km resolution with SMOS [1], [2]. Nevertheless, it might be interesting to derive SSS with higher resolution thanks to SAR sensors(sub-kilometric), especially in coastal areas. A classical observable used for geophysical parameter retrieval in oceanography is the NRCS (Normalized Radar Cross Section) in VV polarization at C-band because of its sensitivity to the sea surface roughness [3]. Indeed geophysical models have been developed in the past mainly at C-band for wind retrieval (CMOD5N, CMOD7N) [3].The purpose of this work is to investigate possible schemes for salinity retrieval using SAR imaging. A first experiment at P-band has been carried out in [4] with promising results. In this study, we perform a more general theoretical sensitivity evaluation considering the main ocean physical parameters such as SSS (Sea Surface Salinity), SST (Sea Surface Temperature), wind speed and direction, and measurement configuration such as radar operating frequency and incidence angles. We propose to evaluate the impact of salinity variations on the NRCS.

The first part of the manuscript recall the dielectric properties of seawater at different SAR frequencies (P, L and C-bands) and presents the models used for NRCS simulations. The second part highlights the main results of this theoretical study. The main challenge in this exercise is to disentangle in the SAR backscattered signal the sensitivity with the roughness and the sensitivity with the dielectric properties. Solutions to maximize the seawater dielectric properties impact and minimize the roughness impact based on physical consideration will be finally discussed at the end of the abstract.

II. Theoretical Background

A. Dielectric properties of seawater at SAR frequencies: Debye Model (Klein and Swift 1977 [5])

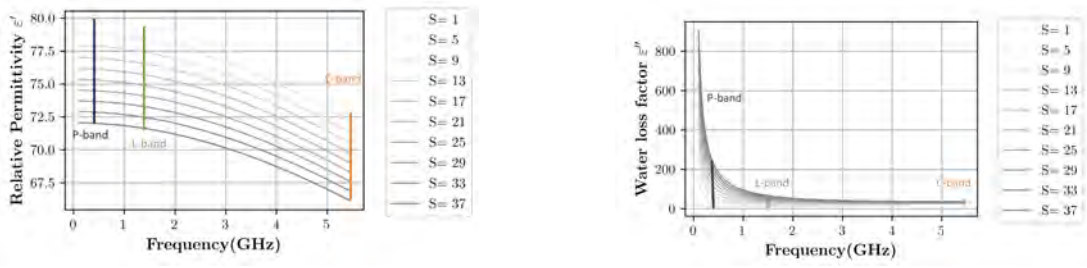

(a) Relative permittivity ε'

(b) Water loss factor ε''

Fig. 1: Dielectric constants of seawater at radar frequencies from VHF to C-band for different values of salinity from 0 to 38 psu (practical salinity unit, g/kg). The light shade indicate a low salinity as freshwater and the dark shade indicates high salinity close to seawater.

In this paper, we adopt the following convention: $\varepsilon = \varepsilon' - j\varepsilon''$. The real part ε' is denominated the relative permittivty and the imaginary part ε'' the loss factor. Figure 1 presents the real and imaginary part of the seawater dieletric permittivity for usual radar frequencies from VHF to C-band at T=25 °C. In Figure 1a is plotted the relative permittivity and in figure 1b the loss factor associated to the imaginary part of the dieletric permittivity.

We can observe in Figure 1a that ε' varies only a little with the salinity within the considered range of SAR frequencies (roughly from 70 to 80 at P and L-band and from 67 to 75 at C-band). On the contrary, ε'' associated to the imaginary part of

the dieletric permittivity is subject to strong variation at low frequencies depending on the salinity (at Biomass frequency from 0 to 300). The impact of the salinity can therefore be exploited at different frequencies of interest. We focus on the behaviours at the Biomass [6], [7] operating frequency (435MHz), ROSE-L [8] operating frequency (assumed 1.4 GHz) and Sentinel-1 [9] operating frequency (5.405 GHz).

B. NRCS (Normalized Radar Cross Section)

In the range 30 - 60 ° of incidence angle, the most significant contribution to the NRCS is the Bragg Scattering [10], therefore we allow ourselves for this preliminary study to use the tilted Bragg Model introduced in [11] to describe the NRCS σ_0. More accurate models taking into account the specular and breaking wave scattering contribution [12] have been developed, it can be interesting to implement them in the future to improve the NRCS modelisation. In short terms, the model that we considered for the study [11] takes into consideration Bragg waves (ripple process) and longer waves that modulates local processes. The outcome is a sum of pure Bragg contributions weighted by the probability density function of the local slopes considered as a random process. The standard deviation of the slopes are directly derived from the wave spectrum model. The pure Bragg σ_{0b} is expressed as follows:

$$\sigma_{0b}(\theta', \varphi) = 16\pi k_r^4 |G(\theta')|^2 \Psi(k_{bragg}, \varphi) \tag{1}$$

- k_r radar wave number
- $k_{bragg} = 2k_r \sin(\theta')$
- θ' Local incidence angle
- G Pure Bragg Coefficent =f(R_{pq})= $f(\theta', SSS, SST, k_r)$ with R_{pq} Fresnel Coefficient in polarization p, q
- Ψ 2D- Directional Elevation spectrum = f (Wind direction, wind speed)

Different development and strategies have been proposed for the 2D elevation spectrum Ψ, in the last 30 years (e.g. Elfouhaily [13], Kudryatsev [14] or Hwang (2015) [15]). We used the 2D spectrum developed by Elfouhaily et al. in this study because well established and recognized in oceanography literature [1].

III. Main Theoretical results

In this part we present an example of results obtained for the Bragg NRCS considering the salinity impact with different roughness (wind) assumptions, operating frequency and incidence angles. For this analysis, we consider salinity conditions from 1 to 40 psu (practical salinity unit, g/kg) with SAR configurations from 30 to 60 ° of incidence angle.

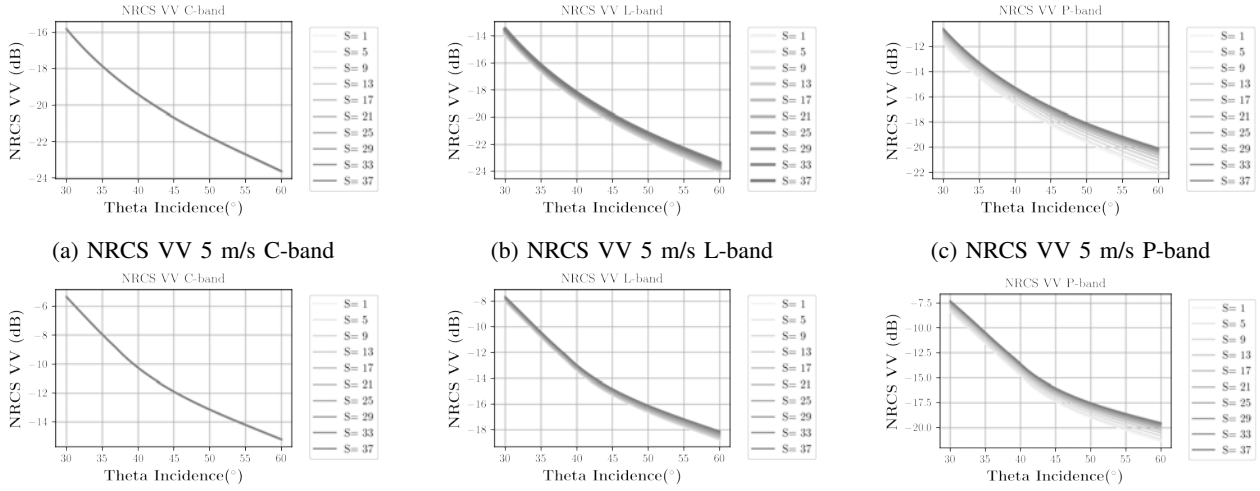

(a) NRCS VV 5 m/s C-band (b) NRCS VV 5 m/s L-band (c) NRCS VV 5 m/s P-band

(d) NRCS VV 15 m/s C-band (e) NRCS VV 15 m/s L-band (f) NRCS VV 15 m/s P-band

Fig. 2: NRCS VV modeled with Bragg scattering at 5 and 15 m/s of wind speed and wind direction toward the radar ($\varphi = 0$ degree) at C-, L- and P-bands. **a.** C-band wind=5m/s, **b.** l-band wind=5m/s, **c.** P-band wind=5m/s, **d.** C-band wind=15m/s, **e.** L-band wind=15m/s, and **f.** P-band wind=15m/s

Even though such model cannot describe with a high fidelity all configurations (strong wind, extreme incidence angles, surface current, breaking waves etc. [12]) it is a first approximation to evaluate the relative impact of wind and salinity in an operational retrieval strategy. As we can observe from the Figure 2, the salinity gains in impact on the NRCS from C-band (Figures 2a, 2d) to P-band (Figure 2c, 2f). However, the variation induced by the salinity remains quite low (few dBs on the

[1]useful tools and python librairies for SAR ocean scattering can be found in https://github.com/pakodekker/oceansar

range 0-40 psu at P-band).
Overall, L-band results represent a medium case both in term of sensitivity to salinity and roughness as we can see in Figures 2b and 2e. It can be however highlighted from the model results a crucial information, and it is intuitively consistent from the wavelength scale point of view, that the wind impact on the NRCS decreases from C-band to P-band. For instance between 5 m/s and 15 m/s a difference of around 10dB is observed for a given incidence angle at C-band in Figures 2a and 2d, whereas it is around 1 to 2dB at P-band in Figure 2c and 2f depending on incidence angles. Those results, even highlighting an higher sensitivity with salinity while decreasing the frequency, are encouraging but still challenging considering an operational retrieval framework.

IV. Discussion

From the previous section, the NRCS exhibits behaviors that may be interesting for SSS retrieval schemes, however, with variation close to the SAR sensors detection limits.
At C-band, the NRCS for VV polarization appears to be unaffected by salinity variation but is known to be sensitive to wind conditions: it is indeed an observable used to derive wind speed by inverting geophysical models such as CMOD5N [3].
P-band reveals as expected theoretically the most sensitive NRCS to salinity among the three frequency bands.
From a general point of view, it can be noticed that the consequence of decreasing the operating frequency seems to decrease the sensitivity of the NRCS to roughness and therefore decrease the possible errors associated to wind while injected into a SSS retrieval process. Even though the retrieval capabilities appears to be challenging from this theoretical sensitivity study, one advantage of SAR imaging is its intrinsic high resolution (meters to severals tens of meter). Therefore, a consequent averaging can be performed to improve the estimation (decreasing noise variance) of parameters and achieve an acceptable resolution for oceanographic applications (sub-kilometric).

V. Conclusion

The purpose of this work was to evaluate capabilities to retrieve SSS at high resolution from SAR images. This work focused firstly on the dielectric properties of sea water variations with salinity at different SAR frequency bands (P-, L- and C-bands) and then evaluated the consequences on the Normalized Radar Cross Section (NRCS). Retrieval schemes have been discussed and have to be further analyzed with in-situ data and SAR measurements to evaluate operational retrieval capabilities.

Acknowledgment

The authors would like to thank Philippe Paillou, Nicolas Reul, Klaus Scipal and Björn Rommen for interesting discussions on SAR and P-band scpecifities.

References

[1] Y. H. Kerr, P. Waldteufel, J.-P. Wigneron, S. Delwart, F. Cabot, J. Boutin, M.-J. Escorihuela, J. Font, N. Reul, C. Gruhier, S. E. Juglea, M. R. Drinkwater, A. Hahne, M. Martín-Neira, and S. Mecklenburg, "The smos mission: New tool for monitoring key elements ofthe global water cycle," *Proceedings of the IEEE*, vol. 98, no. 5, pp. 666–687, 2010.
[2] N. Reul, S. Grodsky, M. Arias, J. Boutin, R. Catany, B. Chapron, F. D'Amico, *et al.*, "Sea surface salinity estimates from spaceborne L-band radiometers: An overview of the first decade of observation (2010–2019)," *Remote Sensing of Environment*, vol. 242, p. 111769, 2020.
[3] H. Hersbach, "Comparison of C-Band Scatterometer CMOD5.N Equivalent Neutral Winds with ECMWF," *Journal of Atmospheric and Oceanic Technology*, vol. 27, no. 4, pp. 721 – 736, 2010.
[4] A. Dehouck, H. Dupuis, F. Gohin, B. Chapron, N. Reul, A. Jegou, and R. Garello, "Measuring sea surface salinity from an airborne sar in the gironde region, france," in *OCEANS '02 MTS/IEEE*, vol. 4, pp. 1962–1967 vol.4, 2002.
[5] L. Klein and C. T. Swift, "An improved model for the dielectric constant of sea water at microwave frequencies," *IEEE Transactions on Antennas and Propagation*, vol. 25, pp. 104–111, 1977.
[6] T. Le Toan, S. Quegan, M. Davidson, H. Balzter, P. Paillou, K. Papathanassiou, S. Plummer, F. Rocca, S. Saatchi, H. Shugart, and L. Ulander, "The BIOMASS mission: Mapping global forest biomass to better understand the terrestrial carbon cycle," *Remote Sensing of Environment*, vol. 115, no. 11, pp. 2850–2860, 2011. DESDynI VEG-3D Special Issue.
[7] "Biomass Mission." https://www.esa.int/Applications/Observing_the_Earth/FutureEO/Biomass, Accessed: 2022-09-14.
[8] M. Davidson, "Copernicus L-band SAR Mission Requirements Document," tech. rep., European Space Agency, 10 2018.
[9] "Sentinel-1 Mission." https://sentinel.esa.int/web/sentinel/missions/sentinel-1, Accessed: 2022-09-14.
[10] W. J. Plant, *Bragg Scattering of Electromagnetic Waves from the Air/Sea Interface*, pp. 41–108. Dordrecht: Springer Netherlands, 1990.
[11] V. Kudryavtsev, D. Hauser, G. Caudal, and B. Chapron, "A semiempirical model of the normalized radar cross-section of the sea surface 1. Background model," *Journal of Geophysical Research: Oceans*, vol. 108, no. C3, pp. FET 2–1–FET 2–24, 2003.
[12] V. Kudryavtsev, D. Akimov, J. Johannessen, and B. Chapron, "On radar imaging of current features: 1. Model and comparison with observations," *Journal of Geophysical Research: Oceans*, vol. 110, no. C7, 2005.
[13] T. Elfouhaily, B. Chapron, K. Katsaros, and D. Vandemark, "A unified directional spectrum for long and short wind-driven waves," *Journal of Geophysical Research: Oceans*, vol. 102, no. C7, pp. 15781–15796, 1997.
[14] V. N. Kudryavtsev, V. K. Makin, and B. Chapron, "Coupled sea surface-atmosphere model: 2. Spectrum of short wind waves," *Journal of Geophysical Research: Oceans*, vol. 104, no. C4, pp. 7625–7639, 1999.
[15] P. A. Hwang and F. Fois, "Inferring surface roughness and breaking wave properties from polarimetric radar backscattering," in *2015 IEEE International Geoscience and Remote Sensing Symposium (IGARSS)*, pp. 2529–2532, 2015.

Polar Low Recognition and Tracking from Multi-Temporal Synthetic Aperture Radar and Radiometer Observations

Biao Zhang[1, 2], William Perrie[2], Zhang Mingyu[1]

[1]Nanjing University of Information Science and Technology, Nanjing, China
[2]Fisheries and Oceans Canada, Bedford Institute of Oceanography, Dartmouth, Canada

Abstract: Polar lows are intense maritime mesoscale cyclones arising from cold air outbreaks and forming in poleward of the main baroclinic zone. Due to their short lifetime (<48 hours) and small horizontal scales (200~800 km), they remain difficult to monitor and forecast using sparse synoptic observing network and operational numerical weather prediction models. In this study, we use multi-temporal satellite data to recognize and track a strong and short-lived polar low occurring in Greenland Sea. This polar low was observed 8 times during its lifecycle (~12 hours) by spaceborne synthetic aperture radar (SAR) and passive radiometer on February 10, 2016. During its early development stage, the maximum wind speed from SAR-retrieved wind field is about 22 m/s. Based on an improved marker-controlled watershed transformation method, we identify polar low centers from three high-resolution SAR images acquired by RADARSAT-2 and Sentinel-1A. We use total atmospheric water vapor content data from radiometers (e.g., AMSR2, SSM/I, GMI) to recognize polar low, and apply a feature extraction algorithm to localize its center. The track of polar low is determined from the center locations derived from SAR and radiometer observations.

Index Terms– Polar low, synthetic aperture radar, radiometer

Satellite measurement of waves and currents: SAR vs Optical sensors

Nicolas Rascle[a,*], Antoine Grouazel[a], Alexis Mouche[a], Frederic Nouguier[a], Carlos Eduardo Villarreal Olavarrieta[b], Rodney Eduardo Mora Escalante[b], Guillermo Diaz Mendez[b], Bertrand Chapron[a], Francisco J. Ocampo-Torres[c]

[a] *Univ. Brest, CNRS, IRD, Ifremer, Laboratoire d'Océanographie Physique et Spatiale (LOPS), IUEM, Brest, France*
[b] *Departamento de Oceanografía Física, Centro de Investigación Científica y de Educación Superior de Ensenada, Baja California, México*
[c] *Centro Mexicano de Innovación en Energía Océano (CEMIE-Oceano), Inst. Ingeniería UNAM, México*

Keywords:
wave directional spectrum, surface current, near-surface current shear, multi-angle optical sunglint imagery, SAR Doppler imagery

1. SAR limitations

SAR measurements of waves and currents suffer limitations due to the complexity of the imaging mechanism and of the microwave backscatter mechanisms. More specifically, for wave retrieval, the non-linear SAR imaging process complicates the retrieval of the directional wave spectrum, as it can produce e.g. azimuth cut-off and different types of spectral distortions of wind sea components in the azimuth direction (Janssen and Alpers, 2006).

For current retrieval, mean Doppler velocities observed by radars and SARs include a component related to the wave orbital motion (Chapron et al., 2005). This wave orbital component is typically of similar magnitude as the ocean currents one aims to observe (e.g. Marié et al., 2020). To advance further, a precise separation between the respective contributions of waves, surface current and current at depth is needed.

2. Optical imagery

Optical measurements of waves and currents can help mitigate those limitations, as they provide direct imaging mechanism and direct measurement of the wave phase speed and its deviation due to current. As such they provide means of validation, calibration and synergy with SAR measurements.

2.1. Optical imagery to retrieve wave directional spectrum

We highlight here some on-going work on case studies where wave directional measurements are compared between SAR Sentinel-1, optical Sentinel-2 and in-situ sensors.

In-situ measurements are obtained from an ASIS buoy (Graber et al., 2000), where directional wave spectra are obtained from accelerometers and an array of capacitance wires (fig. 1). The spectra are processed over 10-minutes periods centered at the time of the satellite passes (fig. 2 center).

*Corresponding author: Nicolas Rascle, email: nrascle@ifremer.fr, tel: +33 2 98 22 45 33, postal address: IFREMER, 1625 route de Sainte Anne, 29280 Plouzane, France

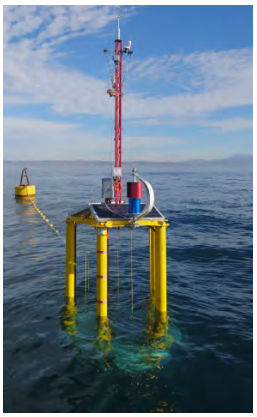

Figure 1: Instrumented buoy BOMM (Boya Oceanogrfica y de Meteorologa Marina) deployed in the coastal North-East Pacific.

SAR images are obtained from Sentinel-1 L1B data VV in mode IW. Spectra are computed using SLC intra burst real part cross spectrum (fig. 2 left). The expected azimuth cut-off of the SAR image is shown with the red lines (e.g. on the displayed day, the cut-off value was 244 m). Optical images are obtained from Sentinel-2 MSI band 2 and 4 within the sunglint. The brightness spectrum is computed first, and is complemented by the elevation spectrum computed under a tilt transfer function approximation (fig. 2 right). The singularity direction of the tilt transfer function is shown with the red line on the brightness spectrum (Kudryavtsev et al., 2017).

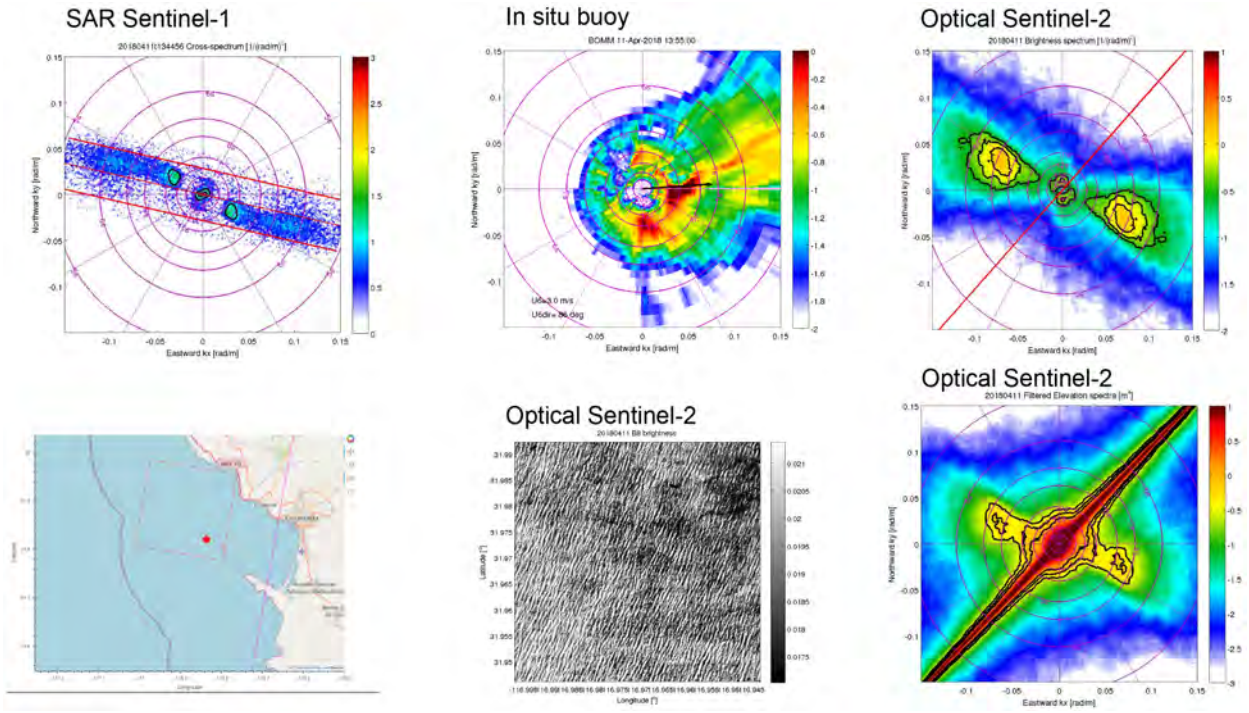

Figure 2: Successful case study of East Pacific swell. Day is 11 April 2018. (Left) SAR Sentinel-1 L1B IW3 SLC intra burst vv, real part cross spectrum, at 13:44 UTC. (Middle) In-situ buoy ASIS combining accelerometers and wired array. (Right) Optical Sentinel-2 brightness and elevation (under tilt hypothesis) spectra, at 18:19 UTC.

The fig. 2 shows measurements for 11 April 2018 over an East Pacific location (Todos Santos Island, Baja California, Mexico). We note that two wave systems are present, one swell and one wind-sea. The SAR-detected spectrum

has a swell peak period around 11 s and an wind-sea peak period around $6-7$ s. The optical spectrum has a wind-sea peak period about $7-8$ s and a swell peak period barely noticeable. The wave directions are also slightly shifted. Reproduction of those effects in numerical simulations (R3S, Nouguier, 2019) is under way within the SARWAVE ESA project (2022-2025).

2.2. Optical imagery to retrieve wave phase speed and current

Time series of optical images can help to retrieve wave phase speed and its deviation due to current. Several strategies are investigated, focusing either on sunglint or out of glint images. The wave decorrelation time is investigated using satellite videos of the sea surface. This will provide indications of the ideal viewing geometry of optical sensors dedicated to surface currents, depending on their available horizontal resolution. Confrontation with numerical simulations (R3S, Nouguier, 2019) will be reported within the ESA DopVisSat project (2023-2024).

3. Perspectives

This work is part of an effort towards a more systematic use of optical imagery to improve understanding of SAR imagery. Existing optical sensors like Sentinel-2 are considered, and future optical missions with different viewing geometry are also proposed to provide systematic means of calibration and validation of waves and current radar data (e.g the STREAM-O optical companion of STREAM-R mission EE11 proposal).

References

Chapron, B., Collard, F., Ardhuin, F., 2005. Direct measurements of ocean surface velocity from space: Interpretation and validation. J. Geophys. Res 110 (C07008).

Graber, H. C., Terray, E. A., Donelan, M. A., Drennan, W. M., Van Leer, J. C., Peters, D. B., 2000. Asisa new air–sea interaction spar buoy: Design and performance at sea. Journal of Atmospheric and Oceanic Technology 17 (5), 708–720.

Janssen, P., Alpers, W., 2006. Why sar wave mode data of ers and envisat are inadequate for giving the probability of occurrence of freak waves. In: Proceedings of SEASAR 2006, SP-613. ESA, ESA - ESRIN, Frascati, Italy.

Kudryavtsev, V., Yurovskaya, M., Chapron, B., Collard, F., Donlon, C., 2017. Sun glitter imagery of ocean surface waves. part 1: Directional spectrum retrieval and validation. Journal of Geophysical Research: Oceans 122 (2), 1369–1383.

Marié, L., Collard, F., Nouguier, F., Pineau-Guillou, L., Hauser, D., Boy, F., Méric, S., Sutherland, P., Peureux, C., Monnier, G., et al., 2020. Measuring ocean total surface current velocity with the kuros and karadoc airborne near-nadir doppler radars: a multi-scale analysis in preparation for the skim mission. Ocean Science 16 (6), 1399–1429.

Nouguier, F., 2019. Remote sensing spatial simulator (r3s). Tech. rep., Tech. Rep. SKIM-MPRC-TN6-V1. 0-LOPS-2019, European Space Agency, Noordwijk .

Abstract Submitted to ESA SeaSAR2023, Svalbard, May 2-6, 2023

Fronts, Eddies, and Other Features in the Western Pacific and Micronesia from SAR and Other Multi-Sensor Data

Benjamin Holt, Brittany Lockhart,
Jet Propulsion Laboratory, California Institute of Technology

Mitch Porter and Douglas Comer
CSRM Foundation

Abstract
Frontal features, indicating convergence along current shear boundaries and temperature boundaries, have often been observed by SAR imagery as enhanced lines of radar brightness. Conversely, the observation of marine slicks formed by convergence into narrow lines of reduced radar brightness indicates underlying surface flow of small eddies. Both types of convergence features have been observed in boundary currents such as the Gulf Stream, in coastal regions, and associated with islands. A highly cited study by Yoder et al. (1994) made use of astronaut sun glint imagery showing a linear feature in the equatorial Pacific and confirmed that the feature was located along a frontal boundary between warm waters and an upwelling zone. In this presentation, we will discuss frontal features and eddies seen with SAR imagery and multisensory data related to coral-reef islands and open-ocean features in the western Pacific.

This study is related to understanding migration patterns of native Pacific Islanders who populated the scattered island groups using traditional sailing techniques, primarily based on a detailed knowledge of navigating by stars and wave patterns. The primary area of interest is the Federated States of Micronesia, centered on the recently-designated World Heritage archaeological site of Nan Madol, located on the island of Pohnpei. To gain understanding of the fundamental ocean conditions and wave patterns as well as climatic forcing events in this region that may have impacted navigation routes and the development of this unique archaeological site, we examined SAR imagery in combination with ocean currents, sea surface temperature ocean color, and wind products derived from satellite data.

We identified a unique collection of SAR imagery from JAXA's ALOS-1 L-band SAR mission, collected in disparate locations in the western Pacific. Current convergence zones of enhanced, bright lines in the open ocean were observed, often away from nearby islands or strong boundary currents, which identify zones of enhanced surface roughness. We also identified dark, curvilinear marine slicks, composed of biogenic films, that are well-known to serve as tracers of the underlying current flow, particularly eddies of various scales. To determine if the frontal features are associated with strong temperature fronts, current gradients and shear, or a combination of both, we overly the SAR features onto coincident SST and current vector maps and then derive backscatter changes of the fronts in relation to surrounding ocean (Figure 1).

Returning to examining Micronesia's volcanic, coral reef island of Pohnpei, a substantial collection of Sentinel-1 imagery was analyzed. These data were obtained in standard beam mode

and provided detailed views of waves and refraction patterns, along with fine scale circulation features, including eddies associated with the island. Wind speed measurements were derived using the NOAA Coastwatch SAR winds algorithm (thanks to Chris Jackson). We will discuss steps taken to understand the seasonal patterns of winds, waves, and detailed island SAR features (Figure 2) associate with Pohnpei and an adjacent atoll.

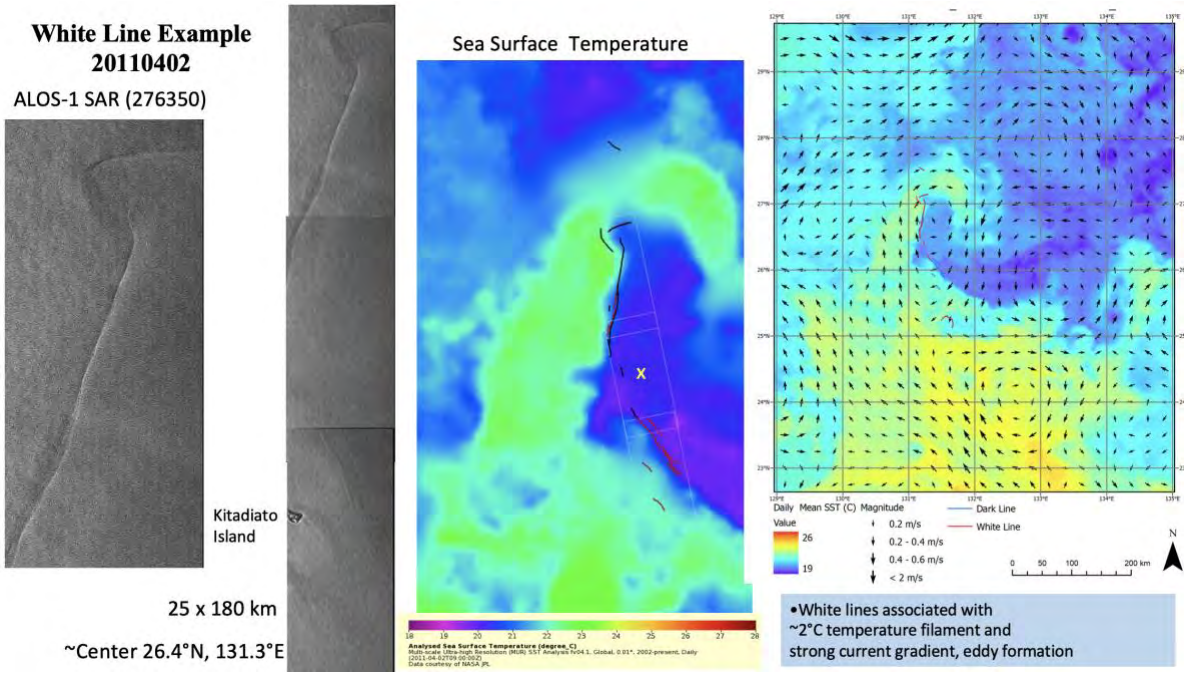

Figure 1. a) ALOS-1 SAR image showing enhanced convergence line. b) The linear features are traced and overlaid onto the sea surface temperature map of the same day, showing the alignment of the SAR feature along a filament; c) SAR features overlaid on the same SST map with ocean current vectors indicated.

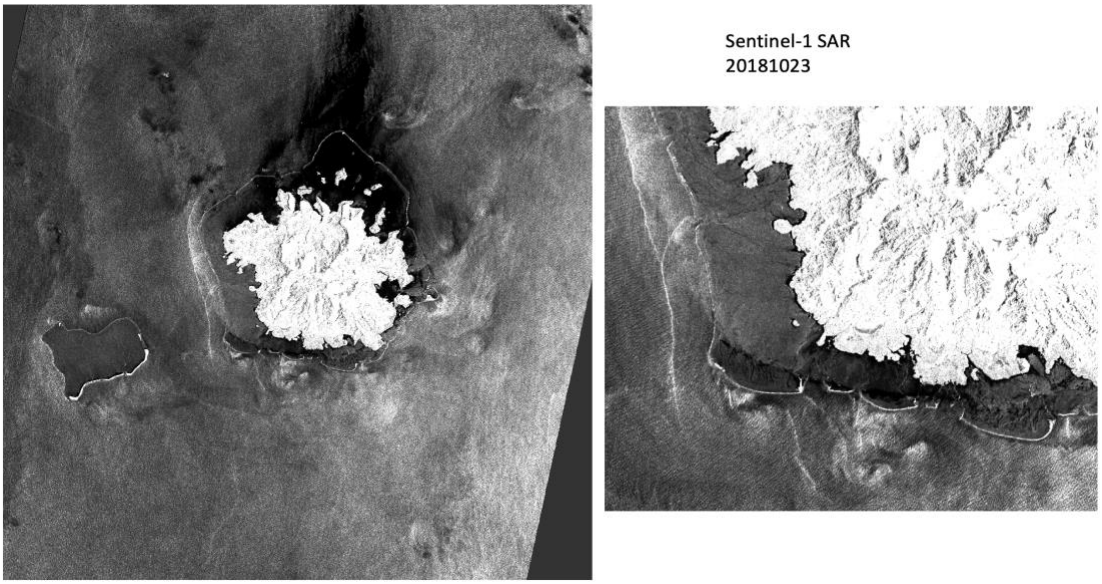

Figure 2. Sentinel-1 SAR image of Pohnpei, Micronesia. The enlargement on the right shows both a bright convergence line likely related to shallow bathymetry as well as small, anticyclonic, bright eddies related to flow through reef openings.

Comparing and combining S1 and SWIM spectral wave measurements

Husson Romain[1], Annabelle Ollivier[1], Bassam Chehade[1], Charles Peureux[1], Victor Quet[1], Gaël Goimard[1], François Soulat[1], Cedric Tourain[2], Jean-Michel Lachiver[2]

1-Collecte Localisation Satellites (CLS), Brest, France
2-CNES, Toulouse, France

Abstract

SWIM is a rotating Radar onboard the Chinese-French CFOSAT satellite providing directional wave spectra measurements. This sensor has been operating for 4 years and well complements Sentinel-1 wave measurements due to their different limitations. The loss of Sentinel-1B in December 2022 has reduced the global wave sampling capability with Sentinel-1 constellation and highlighted the relevance of combining these wave measurements. The present study uses the Sentinel-1 Level-2 OCN products from the Wave Mode acquisition mode and the SWIM Level-2P products distributed by ESA and CNES/CLS, respectively. The first part highlights the two sensors complementarities in terms of spatial coverage, sensitivity to varying wave regimes and directional limitations. The second part focuses on their commonly observed wave regimes, for waves with peak wavelength within ~200-500m. The swell measurement performances are assessed using model and in situ measurements and also co-locations between Sentinel-1 and SWIM measurements (also known as cross-overs in altimetry). This involves both static and dynamic co-locations where waves are propagated using a simple linear wave propagation model over a few hundred kilometers to maximize the number of co-locations. These comparisons show significant differences and suggest a need to propose an inter-calibration in order to propose a global and combined swell measurement product.

1. Introduction

Ocean surfaces are widely imaged by satellite altimeters providing a dense global coverage with more than 8 altimeters flying operationally today and whose wave products are distributed by the Copernicus Marine Service. These satellites only capture the significant wave height, the integrated energy of the co-existing wave systems. For long, the only sensors able to provide a more detailed sea state description have been Synthetic Aperture Radars (SAR) flying. The SWIM instrument, flying onboard the CFOSAT mission, carries a nadir pointing altimeter on top of its rotating radar and has provided a different point of view on the sea state description [1] with respect to Sentinel-1 with whom it has been operating since its 2018. They both observe the ocean surface and can image the wave spectra at global scale using a synthetic and rotating Radar. Yet, their sensing technology and their global coverage have huge impacts on their capability to observe waves in varying sea state conditions.

2. Data

The present study uses the Sentinel-1 Level-2 OCN products acquired in Wave Mode and the SWIM Level-2P products. They are distributed by ESA and CNES/CLS, respectively. They are also compared to directional wave spectra estimation provided by WAM numerical wave model outputs estimated at SWIM measurement's location. Finally, they are also compared to swell partitions extracted from directional wave spectral measurements from in buoys provided by the NDBC network (National Data Buoy Center).

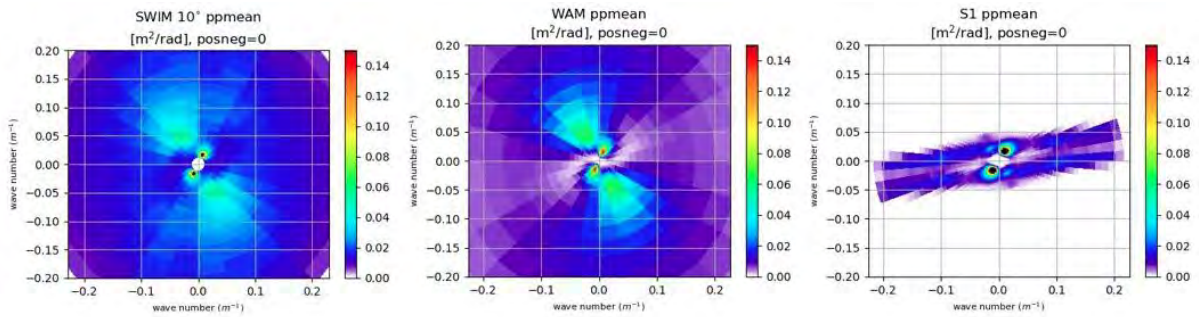

Figure 1: Co-located spectra observed with SWIM 10° beam (left), estimated with WAM and observed with Sentinel-1

3. SWIM and S1 specificities and complementarities for observing wave spectra

a. Wave classification

To simplify the analysis, the wave conditions are split in 3 different sets of waves according to their peak wavekength: [0-200m] corresponding to wind sea dominated sea states (Class 1), [200-500m] to a mix of long wind seas and swells (Class 2) and [500-800m], to very long swell (Class 3).

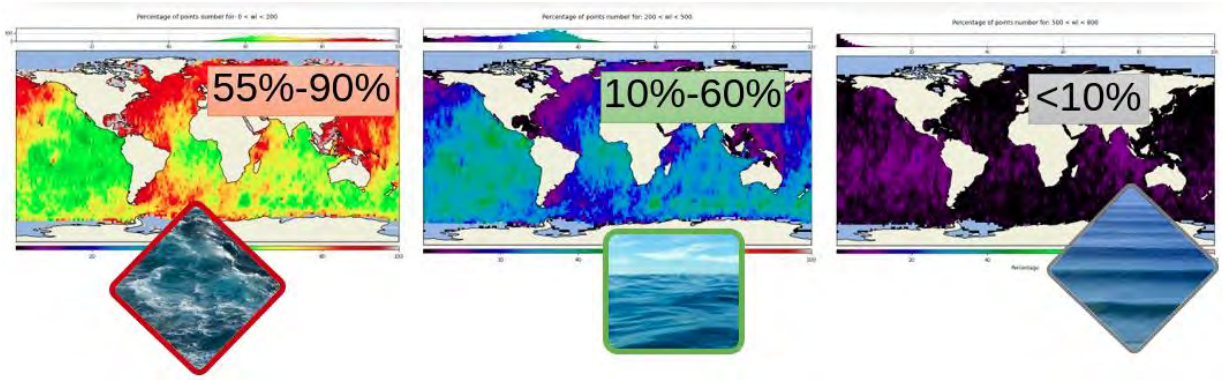

Figure 2: Percentage of occurrence and geographical distribution of the three wave classes according to WAM wave partitions: Class 1 on the left, Class 2 in the middle and Class 3 on the right for the time period April-May-Jun 2021.

b. SWIM and SWIM limitations

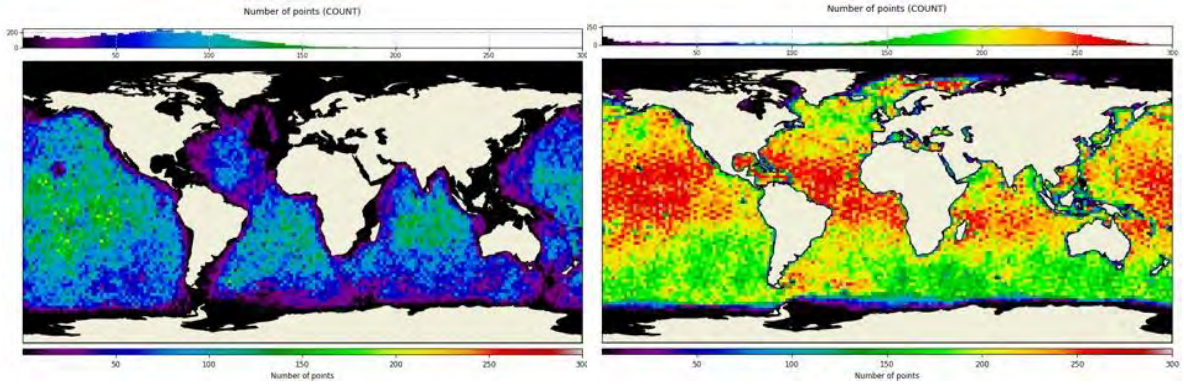

Figure 3: Geographical distribution of Sentinel-1 (left) and SWIM (right) depicted using a 2D histogram of the number of valid partitions acquired at global scale for April-May-Jun 2021.

Compared to SWIM, S1 misses some areas mainly near coasts and North Altlantic due to the change in acquisition mode (switching to Interferometric Wide Swath mode - IW).

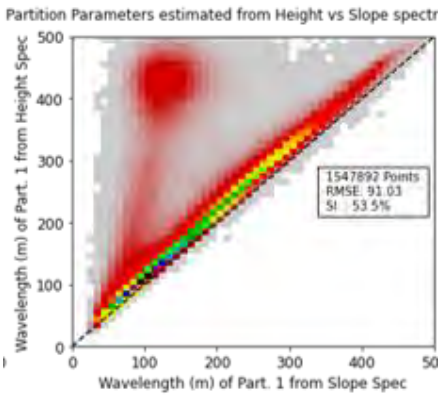

Figure 4: Scatterplots of peak wavelength estimated from wave height spectra wrt. estimation from slope spectra for a given wave partition domain (left) and histogram of the differences. Only the SWIM most energetic wave partition is considered here.

The analysis of the SWIM and S1 data over the various wave classes indicates that for SWIM:

- The wave sampling for the longest waves has been limited in the CNES L2 SWIM products to 500m. This threshold was chosen in order to avoid contributions from non-wave phenomena in the ocean waves spectra, possibly. The WAM analysis, indicates that this represents ~10% of the total number of wave partitions. Yet, the longest swell are also the ones associated with most intense storms. They can also greatly affect the sensing capabilities from Doppler altimeters or SWOT (Sea State Bias [3]).
- A higher speckly in the along-track direction, which required a very specific processing in order to compensate for the increased noise and energy in this wave spectra region.
- The presence of so-called “parasitic peaks”. They correspond to energy peaks becoming relevant whenever looking at wave height spectra while they are relatively weak in SWIM L2P products provided as slope spectra. They are associated with low Signal-to-Noise ratio. In Figure 4, they appear as outliers with a strong difference between the slope- and the height-estimated peak wavelength. For the other partitions, an average bias of 15 m exists.

For Sentinel-1, the main limitation lies in the azimuthal cut-off which prevents from imaging waves with azimuthal wavelength shorter than 200m on average. Overall, the SWIM and Sentinel-1 appear best suited for the Classes 1-2 and Classes 2-3, respectivly. The rest of the study focuses on the capability to accurately image wave for this common Class 2 wave category.

4. Merging SWIM and S1 swell measurements

a. Using S1 classification

S1 wave mode acquisition consists in high-resolution 20x20km imagettes that can be classified in metocean phenomena [4]. The estimation of SWIM performances wrt. WAM has demonstrated that co-localized and classified Sentinel-1 imagettes could be used to identify the metocean phenomena degrading SWIM measurements: rain cells, low winds and biological slicks (sea ice not considered).

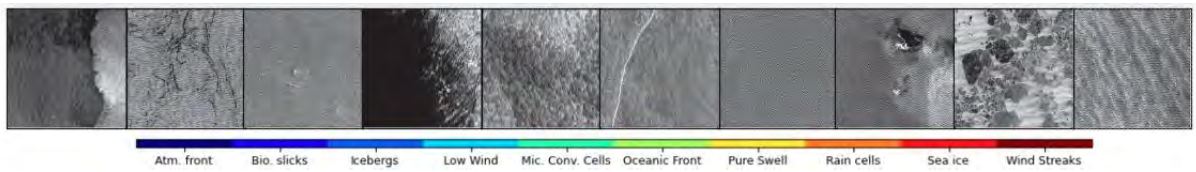

Figure 5: Illustration of the 10 metocean classes of TenGeo-P [4]

b. S1 vs. SWIM

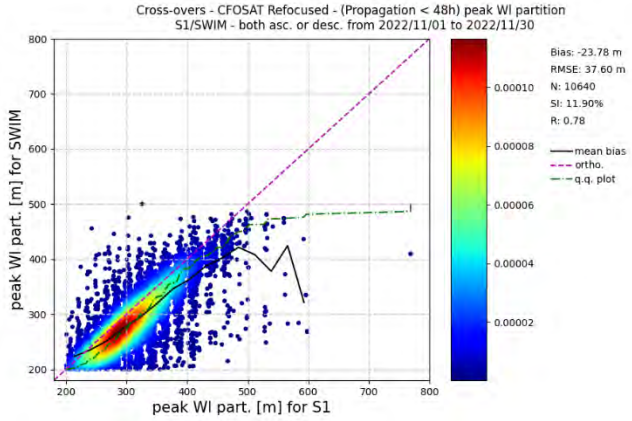

Figure 6: Scatterplot of peak partition wavelength between dynamically co-located SWIM wrt. S1 wave partitions

Using short propagation SWIM and S1 observations (<48h) from their observation location, wave partitions can be compared. This is shown her on Figure 6. A significant under-estimation of the SWIM partition peak wavelength is visible wrt. S1 (WV1 and WV2 measurements are mixed). This may be explained by the fact that the S1 azimuth cutoff limitation is not duplicated on SWIM spectra (-24m). This can also be partly explained that the SWIM partition peak wavelength is estimated from the slope spectra while S1 is estimated from the wave height spectra (cf. Figure 4).

a. S1 and SWIM vs. Buoy

Similarly, comparisons between S1, SWIM and buoys show a consistent difference for the peak wavelength, possibly due to the slope- versus wave height estimation.

5. Conclusions

Will be finished later

6. References

[1] Hauser, D., C. Tourain, L. Hermozo, D. Alraddawi, L. Aouf, B. Chapron, A. Dalphinet, et al. "New Observations From the SWIM Radar On-Board CFOSAT: Instrument Validation and Ocean Wave Measurement Assessment." *IEEE Transactions on Geoscience and Remote Sensing* 59, no. 1 (January 2021): 5–26. https://doi.org/10.1109/TGRS.2020.2994372.

[2] Wang, He, Alexis Mouche, Romain Husson, Bertrand Chapron, Jingsong Yang, Jianqiang Liu, and Lin Ren. "Quantifying Uncertainties in the Partitioned Swell Heights Observed From CFOSAT SWIM and Sentinel-1 SAR via Triple Collocation." *IEEE Transactions on Geoscience and Remote Sensing* 60 (2022): 1–16. https://doi.org/10.1109/TGRS.2022.3179511.

[3] Dubois, Pierre, and Bertr Chapron. "Characterization of the Ocean Waves Signature to Assess the Sea State Bias in Wide-Swath Interferometric Altimetry." *IGARSS 2018 - 2018 IEEE International Geoscience and Remote Sensing Symposium*, 2018, 3789–92. https://doi.org/10.1109/IGARSS.2018.8518813.

[4] Wang, Chen, Alexis Mouche, Pierre Tandeo, Justin Stopa, Nicolas Longépé, Guillaume Erhard, Ralph C. Foster, Douglas Vandemark, and Bertrand Chapron. "A Labelled Ocean SAR Imagery Dataset of Ten Geophysical Phenomena from Sentinel-1 Wave Mode." Geoscience Data Journal 6, no. 2 (November 1, 2019): 105–15. https://doi.org/10.1002/gdj3.73.

Methodology and Techniques

Methodology and Techniques

Tings, Björn; Pleskachevsky, Andrey; Wiehle, Stefan; Jacobsen, Sven
Ship Wake Detectability in TerraSAR X, CosmoSkymed, Sentinel 1 and RADARSAT 2 Imagery – Summary and Applications for Wake Detection

Arthurs, David
Open and Reproducible Science: The Role of Computing Platforms for Research and Applications that use SAR

Gade, Martin; Peters, Sebastian; Schäfers, Simon
On the Use of SAR Data to Monitor Coastal Erosion and Morphodynamics in Intertidal Areas

Hajduch, Guillaume; Pinheiro, Muriel; Valentino, Antonio; Vincent, Pauline; Recchia, Andrea; Cotrufo, Alessandro; Franceschi, Niccolo; Piantanida, Ricardo; Benchaabane, Amine; Peureux, Charles; Husson, Romain; Schmidt, Kersten; Mouche, Alexis; Grouazel, Antoine; Nouguier, Frédéric; Johnsen, Harald; Hindberg, Heidi; Guiton, Gilles; Collard, Fabrice
Sentinel-1 product performance

Shamshiri, Roghayeh; Eide, Egil; Rangriz Rostami, Fazel; Vilhelm Høyland, Knut
Sentinel-1 Extra Wide Thermal Noise Removal Using a Deep Learning Model

Yitayew, Temesgen Gebrie; Grydeland, Tom; Larsen, Yngvar; Engen, Geir
Processing of High Squint Bistatic SAR Data: The Case of Harmony

Hoffman, Lauren Alexandra; Mazloff, Matt R; Gille, Sarah T; Giglio, Donata; Bitz, Cecilia M; Heimbach, Patrick
Machine Learning for Evaluating the Drivers of Variability in Arctic Sea-ice Motion.

Grydeland, Tom; Yitayew, Temesgen Gabrie; Larsen, Yngvar;DuBois, Pierre; Armstrong, Thomas; Gombert, Baptiste; Soulat, Francois; Monnier, Goulven; Hellouvry, Yann-Herve; Camus, Benjamin; Lopez-Dekker, Paco; Lajas, Dulce; Rommen, Bjorn; deWitte, Erik
Signal Processing for Harmony: Illustrations with Simulated Data over Ocean

Colin, Aurélien; Tandeo, Pierre; Husson, Romain; Fablet, Ronan; Peureux, Charles
MediSAR: An Exhaustive Augmented Dataset Of Segmented Sentinel-1 SAR Ocean Observations Of The Mediterranean Sea and the Black Sea regions

Stopa, Justin E.; Foster, Ralph; Vandemark, Doug; Wang, Chen; Chapman, Jonathan; Glaser, Yannik; Sadowski, Peter; Mouche, Alexis; Chapron, Bertrand
Using Ocean Surface Imagery to Estimate Atmospheric Boundary Layer Stratification

Foster, Ralph; Mouche, Alexis; Chapron, Betrand
Using SAR Imagery to Diagnose Tropical Cyclone Boundary Layer Mean State

Larsen, Yngvar; Engen, Geir; Grydeland, Tom; Yitayew, Temesgen G.
An Alternative Approach for Estimation of Doppler Centroid Anomaly Based on Level-0 SAR Data

Alpers, Werner R.; Bignami, Franceco
Sar Observation Of Internal Waves Generated By Sub-mesoscale Features In The Strait of Sicily

Ship Wake Detectability in TerraSAR-X, CosmoSkymed, Sentinel-1 and RADARSAT-2 Imagery – Summary and Applications for Wake Detection

Björn Tings[a], Andrey Pleskachevsky[a], Stefan Wiehle[a], Sven Jacobsen[a]
[a] DLR, Maritime Safety and Security Lab Bremen, Am Fallturm 9, 28359 Bremen, Germany
Bjoern.Tings@dlr.de

1. Introduction

Ship wakes are produced by the interaction of the ship's hull with the ocean water and are result of multiple interacting wave systems closely beneath and on the ocean surface. The ship wake signatures in SAR imagery consists of various components. The most frequently encountered wake components are Kelvin wake arms, V-narrow wake arms and two parts of the turbulent wake: the near field and the far field [1]. The detectability of these four most important wake components in SAR imagery is influenced by several physical variables, which are in the following called influencing parameters. The influencing parameters can be categorized into ship properties, environmental conditions and SAR acquisition settings.

In a series of preceding studies of the authors [1, 2], the characteristics of the effects of influencing parameters on the detectability of individual wake components have been modelled using machine learning, categorized, and contrasted against the published state-of-the-art. For the latest study [3], the list of the satellites was extended and the detectability of wake components was investigated in terms of different radar frequency bands (C-Band and X-Band SAR) and different orbit altitudes (i.e. slant ranges).

This study summarizes the method and the results of the preceding studies [1,2,3] and the application of the results to the actual task of wake detection is demonstrated. The demonstration shows that the developed models can be applied to control the precision performance of wake detectors and to estimate vessel velocity with an accuracy coinciding with other published methods [4].

2. Materials and Method

The studies are based on four different SAR missions (Table 1). The ground truth wake samples listed for each sensor were created by a manual inspection procedure.

Table 1: Summary of wake component datasets

Sensor name	TerraSAR-X (TSX)	CosmoSkymed (CSK)	Sentinel-1 (S1)	RADARSAT-2 (RS2)
Frequency band /radar wavelength [cm]	X / 3.1	X / 3.1	C / 5.6	C / 5.6
Orbit-Altitude [km]	514	619	693	798
Approx. slant range [km] at 30°/50° incidence angle	593 / 800	715 / 963	800 / 1078	922 / 1242
Acquisition modes / product types	SL, SM / MGD	HIMAGE / DGM	IW / GRDH	MF, F, S / SGF
Number of total wake samples (HH / VV)	2881 (2429 / 452)	94 (94 / 0)	618 (0 / 618)	407 (407 / 0)

The detectability of each of the four wake components was modelled for each of the four sensors using the support vector regression (SVR) method. The length of each wake component is used as indicator for the wake component's detectability. The preceding studies have an intersecting set of five influencing parameters, which are listed in Table 2.

The SVR models predict which wake component lengths are expected depending to the conditions defined by the influencing parameters. The predicted wake component lengths are then linearly normalized between a minimum and maximum length boundary to obtain a measure of detectability with uniform scale. The so-called detectable length metric (DLM) for a sensor s and a wake component w is:

$$DLM_{w,s}(x_1, \dots, x_5) = \left(f_{w,s}(x_1, \dots, x_5) - l_w^{min}\right) / \left|l_w^{max} - l_w^{min}\right| \quad \text{(Eq. 1)}$$

where $x_1, \dots, x_5$ defines the five influencing parameters and $f_{w,s}$ the SVR model. l_w^{min} is the minimum length boundary and l_w^{max} maximum length boundary, both depending on the respective wake component.

The compositions of the created SVM models are analyzed and compared in order to derive statements on wake component detectability. A measure of the detectability models' uncertainty is provided to support the derived statements.

Table 2: List of the five influencing parameters with descriptions

Nr x_i	Parameter name	Description	Value range	
			x_i^{min}	x_i^{max}
x_1	AIS-Vessel-Velocity	Velocity of the vessel derived from AIS messages interpolated to the image acquisition time	1	10
x_2	AIS-Length	Length of the corresponding vessel based on AIS information	5	35
x_3	AIS-CoG	The Course over Ground (CoG) based on AIS information relative to the radar looking direction (0° means parallel to range, 90° mean parallel to Azimuth).	0	90
x_4	Incidence-Angle	Incidence angle of the radar cropped to TSX's full performance value range	20	45
x_5	SAR-Wind-Speed	Wind speed estimated from the SAR background around the vessel using the XMOD-2 (X-band) and CMOD-5 (C-band) geophysical model functions	2	9

The uncertainty measure quantifies, whether the models' compositions are learned systematically or randomly. The analysis is based on heatmaps as shown exemplarily in Figure 1. This example heatmap provides insight into the dependency of detectability of Kelvin wake arms on three influencing parameters describing ship properties [1, 2].

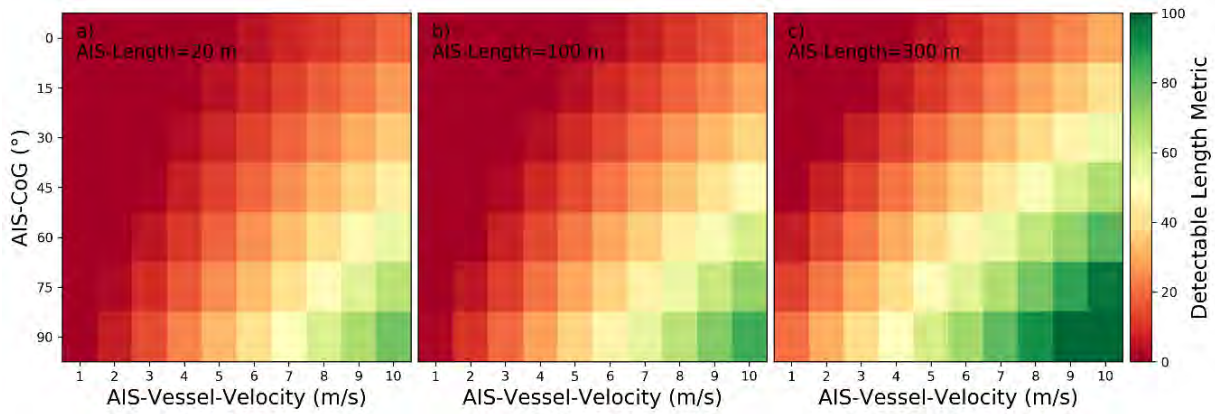

*Figure 1: Detectability heatmaps for accumulated port and starboard Kelvin wake arms based on AIS-Vessel-Velocity, AIS-CoG and from left to right AIS-Length with **a)** 20 m, **b)** 100 m, and **c)** 300 m.*

The comparison between models of two SAR sensors s_1 and s_2 is based on integrated differences in detectability [3]:

$$\overline{\Delta DLM_{w,s_1,s_2}} = \overline{DLM_{w,s_1}} - \overline{DLM_{w,s_2}} \quad \text{(Eq. 2)}$$

with

$$\overline{DLM_{w,s}} = \frac{1}{\Delta x_1 \dots \Delta x_5} \int \dots \int_V DLM_{w,s}(x_1, \dots, x_5)\ dx_1 \dots dx_5 \quad \text{(Eq. 3)}$$

where $\Delta x_i = x_i^{max} - x_i^{min}$ with $\left[x_i^{max}, x_i^{min}\right]$ is defined in Table 2. The multidimensional integration over the five-dimensional feature space is restricted by the volume $V = \left[x_1^{max}, x_1^{min}\right] \times \dots \times \left[x_5^{max}, x_5^{min}\right] \subseteq \mathbb{R}^5$.

3. Results

A summary of statements derived from studies [1, 2, 3] are summarized in The demonstration estimates that the total error of this method is RMSE=2.71 m/s
Table 3. It should be noted the statements from [1, 2] are revised in this study, as a measure for SVR models' uncertainties was developed in [3] and is additionally considered here.

4. Applications

The listed statements contribute primarily to the fundamental research of imaging and detection of ship wakes in SAR. The presented method for modelling of wake component detectability by SVR models,

consequently and systematically takes all selected influencing parameters into account. Due to this completeness, a new opportunity of applying the detectability models to the task of wake detection arises. For this purpose, a simple DeepLearning-based wake component detection system was developed. The applicability of the wake detectability models to wake detection is then demonstrated by two independent operations:

1. The sensitivity of wake detection systems can be controlled by the detectability models to increase precision while mainly maintaining the recall.
   The demonstration estimates that precision is increased by ~6% while recall only is decreased by ~3%
2. After detection of wake components by wake detection systems a reversion of the detectability models can be applied to estimate the ship velocity using the probability of detection PoD as substitute for $DLM_{w,s}\left|l_{w,s}^{max} - l_{w,s}^{min}\right| + l_{w,s}^{min}$ in reversed model:
   $$f_{w,s}^{x_1\,-1}\left(DLM_{w,s}\left|l_{w,s}^{max} - l_{w,s}^{min}\right| + l_{w,s}^{min}, x_2, x_3, x_4, x_5\right) = x_1 \qquad \text{(Eq. 4)}$$
   The demonstration estimates that the total error of this method is RMSE=2.71 m/s

Table 3: Summary on detectability of four wave components. Parameters with identical influence are marked by grey color

Influencing parameters	**Summary on detectability four wave components** **wake component detectability: "↑": better, "≈ ": hardly influenced**			
	near-hull turbulence	**turbulent wakes**	**Kelvin wake arms**	**V-narrow wake**
Vessel speed	↑ for faster moving vessels	↑ for faster moving vessels	↑ for faster moving vessels	↑ for faster moving vessels
Vessel length	↑ for larger vessels	↑ for larger vessels	↑ for larger vessels	↑ for larger vessels
Vessel moving direction	↑ for vessels moving parallel to range	≈ by vessels' moving direction	↑ for vessels moving parallel to azimuth	↑ for vessels moving parallel to azimuth
Incidence angle	↑ for larger incidence angles, when ship speeds are at least moderate	↑ for lower incidence angles	↑ for lower incidence angles	↑ for lower incidence angles
Local wind speed	↑ for lower wind speeds	↑ for lower wind speeds	↑ for lower wind speeds	↑ for lower wind speeds
Sea state wave height	≈ by wave heights	≈ by wave heights	≈ by wave heights	≈ by wave heights
Sea state wave length	↑ for longer wavelengths, when ship speeds are at least moderate	↑ for shorter wavelengths	↑ for longer wavelengths	↑ for longer wavelengths
Sea state Wave propagation direction	↑ for wave directions parallel to the vessel's movement	↑ for wave directions parallel to the vessel's movement	↑ wave directions parallel to the vessel's movement	≈ by wave propagation directions
Local Wind direction	≈ by wind direction	↑ for wave directions orthogonal to the vessel's movement	≈ by wind direction	↑ for wave directions orthogonal to the vessel's movement
SAR slant ranges	≈ by slant ranges	≈ by slant ranges	↑ for shorter slant ranges	≈ by slant ranges
SAR radar frequency	≈ by radar frequency	≈ by radar frequency	≈ by radar frequency	↑ for X-band

5. References

[1] B. Tings, "Non-Linear Modeling of Detectability of Ship Wake Components in Dependency to Influencing Parameters Using Spaceborne X-Band SAR," *Remote Sensing,* vol. 13, no. 2, p. 165, 2021.

[2] B. Tings, A. Pleskachevsky, D. Velotto and S. Jacobsen, "Extension of Ship Wake Detectability Model for Non-Linear Influences of Parameters Using Satellite Based X-Band Synthetic Aperture Radar," *Remote Sensing,* vol. 11, no. 5, p. 563, 2019.

[3] B. Tings, A. Pleskachevsky and S. Wiehle, "Comparison of detectability of ship wake components be-tween C-Band and X-Band synthetic aperture radar sensors operating under different slant ranges," *ISPRS Journal of Photogrammetry and Remote Sensing,* vol. 196, pp. 306-324, 2023.

SeaSAR2023 Workshop Abstract: "Open and Reproducible Science: The Role of Computing Platforms for Research and Applications that use SAR"

David Arthurs, Managing Director, Polar View

Open Science is a movement to make the entire research process more accessible and reproducible, including input data, analysis methods, results, and the dissemination and reception of those results. Its benefits include:

- Increased Transparency – all aspects of the research are explained and can be reproduced for better understanding by others (and even to help the original researcher remember in the future).
- Better Peer Review – others can replicate and test the research to ensure its accuracy and veracity.
- Amplified Impact and Efficiency – others can build on the research to augment its impact in subsequent work. The tendency to 'reinvent the wheel' is reduced.
- Improved Handling of Complexity – multiple researchers, working together or separately, can contribute to tackling difficult problems.

While science has always espoused the dissemination of methods and results so that they can be evaluated and tested by others, in many fields of science there has emerged a so-called "replication crises" in which it is asserted that the results of many scientific studies are difficult or impossible to reproduce. This situation is an impediment to the very underpinnings of the scientific method.

Technology and standards have an important and increasing role to play in supporting open and reproducible science at each stage of the research process:

- Collaboration – Forums, conferencing, chats, code sharing, and other tools allow researchers to work together, synchronously or asynchronously, regardless of their location or time-zone.
- Input Data – The FAIR data principles are that data is Findable, Accessible, Interoperable, and Reusable. FAIR data helps researchers obtain and use the inputs to their work and they pass those benefits along when they subsequently make their results FAIR.
- Analysis – While there has been significant progress in making research data FAIR, efforts to do the same for analysis methods and code are only just beginning. Interactive development environment tools such as Jupyter Notebooks enable researchers to combine code and results with explanations.
- Results – The importance of the management of research results is starting to be recognized. Too often, research results are kept in a box under the researcher's desk and are eventually lost to science or require expensive efforts to recover. Data needs to be properly archived for long-term preservation and assigned a Digital Object Identifier (DOI) so that it can be discovered, and the researcher given appropriate credit by others. All data and code should be made publicly available in a form that others can find, understand, and use them.
- Dissemination and Communication – Research will have an impact only if others are aware of it. Dissemination of research results can take many forms depending on the intended audience, which may include other researchers, decision makers, or the public.

Increasingly, computing platforms are emerging that incorporate tools to assist researchers in participating in all of the facets of open and reproducible science. The Polar Thematic Exploitation Platform (Polar TEP) is an example of such a platform.

ESA has developed a series of seven TEPs on different subjects to provide insight into how our oceans, atmosphere, land, and ice operate and interact as part of an interconnected earth system by exploiting the unprecedented flow of high-quality global data on the state of our planet, combined with long-term Earth Observation (EO) archives, in-situ networks, and models. Polar TEP was developed to address the particular needs of the polar community.

Polar TEP provides a complete working environment where users can access algorithms and data remotely to obtain computing resources and tools that they might not otherwise have and avoid the need to download and manage large volumes of data. This new approach removes the need to transfer large Earth Observation data sets around the world, while increasing the analytical power available to researchers and operational service providers. Polar TEP provides new ways to exploit EO and other large datasets for research scientists, industry, operational service providers, regional authorities, and policy analysts. Polar TEP provides:

- Collaboration

  Polar TEP provides capabilities for researchers to share algorithms and collaborate with others in a user forum.

- Data Discovery

  Polar TEP makes satellite and other polar data easily accessible for browsing or analysis within the cloud or within the user's own environment. The infrastructure takes care of the complexity of handling satellite imagery archives and makes the data available via web services. Users can instantly access petabytes of Sentinel, Landsat, and other Earth observation imagery, both historic and the latest acquisitions. Users can also bring their own data or connect to other data repositories to meet their data needs.

  SAR data is very important in the polar context. Polar TEP has the complete archive of Sentinel-1 data and is in the process of adding CEOS ARD compliant versions of Radarsat Constellation Mission (RCM) data.

- Interactive Development Environment

  Polar TEP offers a managed JupyterLab instance with curated base images. The platform provides different flavors of computational resources and a network file system for persistent data storage. Headless notebook execution is supported.

- Machine Learning

  Polar TEP has implemented the MLflow platform to support machine learning activities. MLflow manages all stages of the machine learning lifecycle, including experimentation, reproducibility, deployment, and a central model registry.

- Execution Environment

  Docker containers are used to provide processors with a separate custom environment having minimal execution overhead. The computing resources used by the execution environment are scaled to the current demand.

- Algorithm Hosting Environment

  Users can host their algorithms within the Polar TEP environment, making them available for others to invoke on-demand using the parameters and area of interest the end-user chooses. It

is possible to implement the algorithms under a pay-for-use model where the algorithm developer shares in the revenue from end-users.

- Results Dissemination and Story Telling

  Polar TEP provides tools to communicate analysis results to other researchers, decision makers, or the public.

Polar TEP is an integral part of the wider polar data ecosystem, contributing to data interoperability and fostering the use of information about the polar regions to support environmental protection, safety, and sustainable economic development.

Figure: Polar TEP Support for Open Science

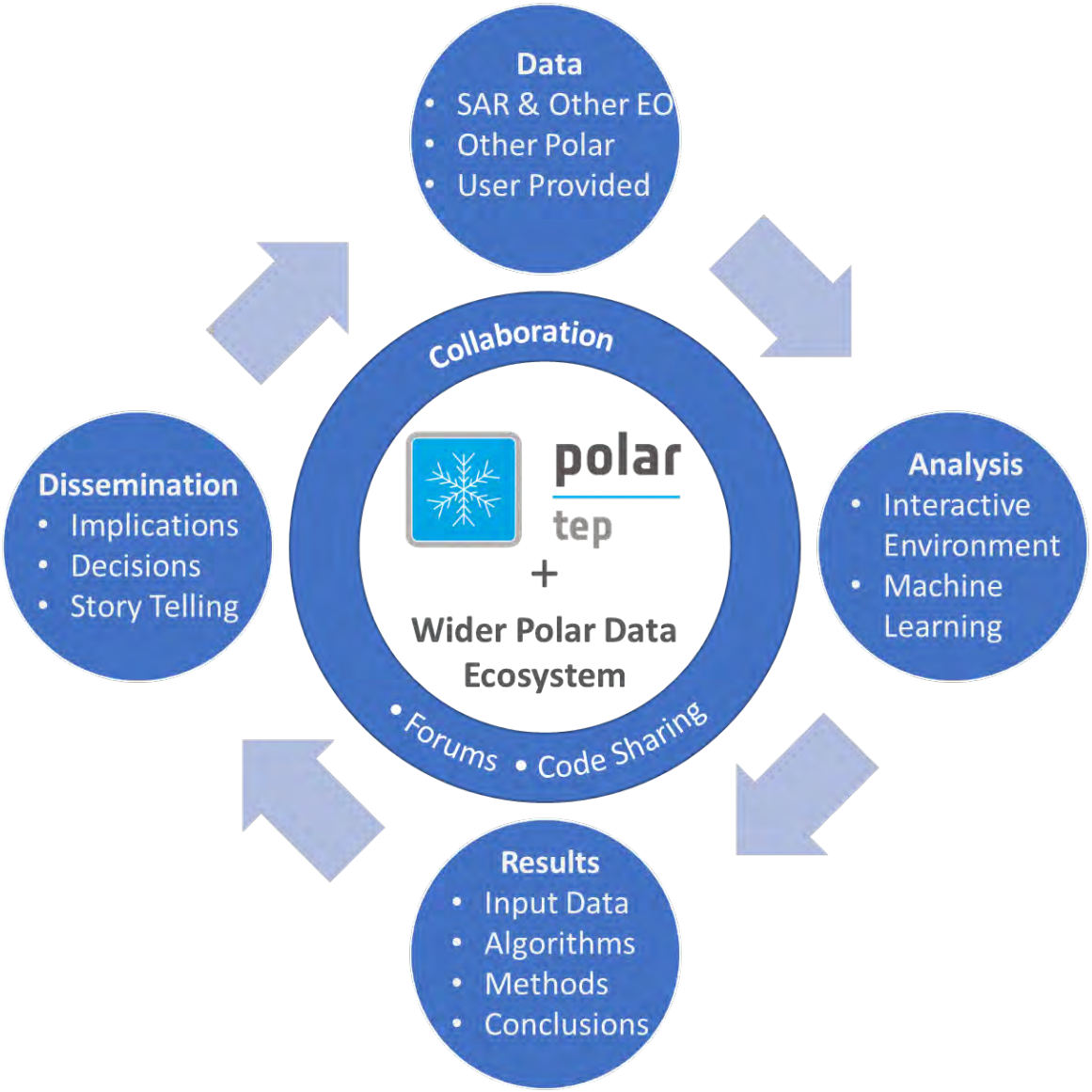

ON THE USE OF SAR DATA TO MONITOR COASTAL EROSION AND MORPHODYNAMICS IN INTERTIDAL AREAS

Martin Gade, Sebastian Peters and Simon Schäfers

Institut für Meereskunde, Universität Hamburg, Germany

The Wadden Sea on the continental North Sea coast is the World's largest coherent intertidal area and extends over an area of about 4700 km², reaching from the Dutch coast in the West to the Danish coast in the north. Most parts of the German part of the Wadden Sea are dominated by bare soils consisting of sandy and muddy sediments, whose actual distribution depends, among others, on dynamic forces induced by the tides and by wind and sea state. In contrast, vegetation such as sea grass stabilizes the upper sediment layer and reduces the hydrodynamic energy of tides and waves; therefore, sea grass meadows have great influence on the local sediment distribution. Being UNESCO World Heritage since 2011 the Wadden Sea forms a large natural ecosystem with a high biodiversity, and since it is increasingly exposed to anthropogenic threats such as (over-) fishing, high nutrient loads, oil and gas production, or tourism, according to national and international directives a continuous monitoring is mandatory. However, most areas are difficult to access by boat, foot or land vehicles, and in-situ observations are sparse, which makes remote sensing techniques an important and powerful tool for the mapping of key parameters.

Two areas of interest were identified on the German North Sea coast, within the National Park "North Frisian Wadden Sea", which represent areas of different sediment distribution and of high morphodynamics, i.e., strong erosion and accretion along the tidal creeks and channels. In addition, seagrass meadows and bivalve beds may be encountered, both being subject to frequent monitoring efforts by local (National Park) agencies. The two areas of interest are marked in the map shown in Figure 1. The aim of our studies was to demonstrate the way, in which monitoring programs may benefit from frequent synthetic aperture radar (SAR) observations of the marine coastal environment.

Figure 1. Map of the German North Sea coast, with the three National Parks ("Lower Saxon, Hamburg, and Schleswig-Holstein Wadden Sea") marked in light blue. The two areas of interest of this study are marked by the red rectangles.

We analyzed a great deal of SAR images acquired over the German part of the Wadden Sea by the L-, C-, and X-band SARs aboard ALOS-2, Radarsat-2 and Sentinel-1, and TerraSAR-X, respectively. Using this wide range of multi-frequency / multi-polarization SAR data we demonstrate which combinations of radar band and polarization are best suited for a classification of different Wadden Sea surface types, including sandy and muddy sediments, sea grass meadows, and bivalve beds. New

parameters, based on a decomposition of the complex SAR data, were used as input into a UNet-based semantic segmentation network with a texture-enhancement module to classify intertidal sediments and habitats. Here, a comparative study revealed that the combination of different radar bands yields best results [1].
Taking advantage of the high temporal coverage of the German North Sea coast by the SAR-C aboard the Sentinel-1 satellites, we generated digital elevation models (DEMs) of intertidal flats using the waterline method. The algorithm developed is based on a method for semi-automated waterline detection presented in [2], and it uses the so-called "Edge-Drawing" method [3]. For each image acquisition, absolute water levels derived from interpolated tide-gauge data were used to generate contour lines from the extracted waterlines. The resulting contour maps were then combined and interpolated into a DEM. Comparing DEMs for the spring of 2017 and the spring of 2020 (left and middle panels of Figure 2, respectively) allowed identifying areas of strong sediment loss (erosion) and gain (accretion), the former even resulting in a cut through an elongated sand flat. These results are shown in the right panel of Figure 2.

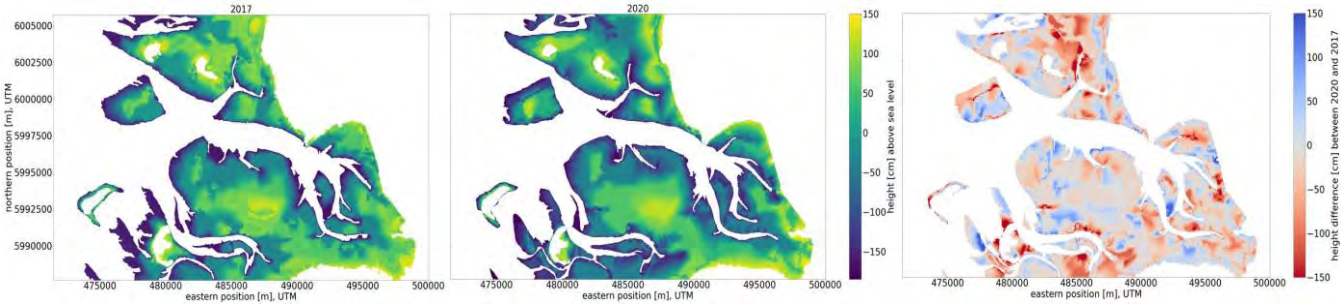

Figure 2. DEMs (28 km × 18 km) of a part of the Wadden Sea on the German North Sea coast, derived from Sentinel-1 SAR-C images of (left) spring 2017 and (middle) spring 2020. The right panel shows the difference of both, i.e., DEM2020 − DEM2017 .

The demonstrated method proved its usefulness for the identification of local hotspots of morphodynamic changes; however, it still requires manual fine-tuning of some parameters to generate optimal results. In another effort, therefore, we built a neural network for an automated detection of waterlines on Sentinel-1A/B SAR-C imagery. Our neural network is capable of segregating water from exposed intertidal flats at high spatial resolution (Figure 3).

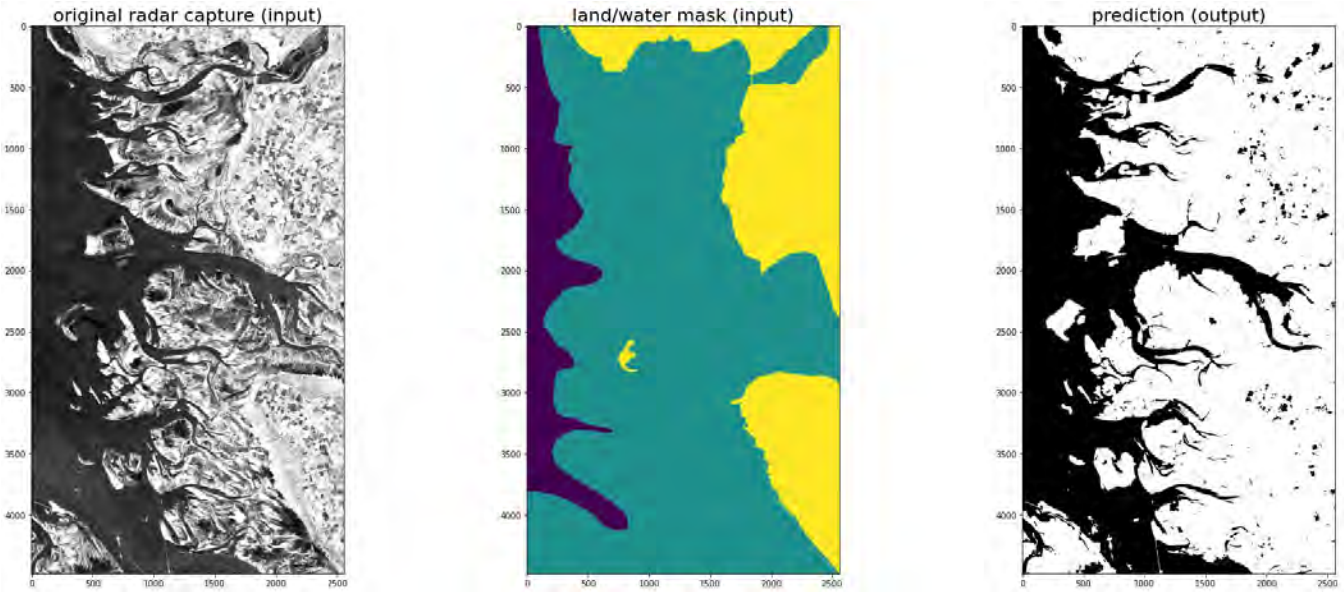

Figure 3. Automated classification of exposed intertidal flats by a neural network. Left: part of a Sentinel-1A SAR-C image of the German Wadden Sea acquired on 19 May 2020. Middle: manually generated land/water mask used as additional input; yellow: land; blue: open sea; green: potential intertidal flats. Right: resulting prediction of the neural network (classification).

The neural network is designed as an image-to-image network and uses SAR images and an ordinary land/water mask as input (left and middle panels of Figure 3, respectively). In order to detect large structures and at the same time, to preserve the high spatial resolution, it consists of two stages: the first stage generates a low-resolution (640 m × 640 m) allocation map, in which areas are classified that contain either mostly land, mostly water, or approximately equal parts of both. This allocation map is added as input to the second stage, in which islands and tidal channels are allocated. Within the second stage, only fractions of the original radar image are processed, thereby reducing the overall processing time, but also resulting in an accurate segregating of water and exposed intertidal flats at full SAR resolution (10 m × 10m, see the right panel of Figure 3).

Our network allows simplifying the SAR image analysis significantly, as only minor post-processing of the obtained results is required. However, further studies on its sensitivity to weather (wind) conditions are required. Moreover, an operational use of SAR data from wider coastal areas is not yet possible, because of a lack of labelled data.

REFERENCES

[1] Zhang, D., 2022: Synthetic Aperture Radar Image Interpretation Based on Deep Learning, PhD thesis, Univ. Hamburg, FB Informatik, 156 pp.

[2] Wiehle, S., and S. Lehner, 2015: Automated Waterline Detection in the Wadden Sea Using High-Resolution TerraSAR-X Images. *J. Sensors*. DOI: 10.1155/2015/450857

[3] Topal, C., and C. Akinlar, 2012: Edge Drawing: A combined real-time edge and segment detector. *J. Vis. Comm. Im. Repres. 23*, 862–872.

[4] Peters, S, 2022: Bestimmung morphodynamischer Veränderungen an der deutschen Nordseeküste mithilfe von Synthetik Apertur Radar Daten. BSc thesis (in German), Univ. Hamburg, FB Erdsystemwissenschaften, 26 pp.

Sentinel-1 product performance

Muriel Pinheiro[a], Guillaume Hajduch[b], Antonio Valentino[a], Pauline Vincent[b] , Andrea Recchia[c], Alessandro Cotrufo[c], Niccolò Franceschi[c], Riccardo Piantanida[c], Amine Benchaabane [b], Charles Peureux [b], Romain Husson [b], Kersten Schmidt[d] , Alexis Mouche[e], Antoine Grouazel[e], Frederic Nouguier[e], ,Harald Jonhsen [f], Heidi Hindberg [f], Gilles Guitton [g], Fabrice Collard [g]

[a] ESA/ESRIN, Frascati (Roma), Italy
[b] Collecte Localisation Satellites, CLS, Plouzané (Brest), France
[c] Aresys s.r.l., Milano, Italy
[d] German Aerospace Center (DLR), Oberpfaffenhofen, Germany
[e] IFREMER, Plouzané, (Brest), France
[f] NORCE, Tromsoe, Norway
[g] Ocean Data Lab, Loc Maria Plouzané (Brest) France

Abstract

The Copernicus program [1] and particularly Sentinel-1 [2] are among the largest Earth Observation SAR data providers, serving an ever-increasing number of services, users, and applications. A key aspect of the program is the constant provision of quality data, which requires long term engagement to carefully monitor, preserve, and even improve the system performances.
These tasks are mainly carried out within the SAR Mission Performance Cluster (SAR MPC), an international consortium of SAR experts in charge of the continuous monitoring of the SAR instruments status and of the L1 and L2 products quality. The SAR MPC is responsible of detecting any potential issues and implementing the necessary actions to ensure that no data quality degradation occurs for the users [3].
This paper provides an update on the monitoring and the actions implemented by the SAR MPC during the 2022 for what concerns the oceanographic applications. It is then a summary of the main elements of the Sentinel-1 Annual Performance Report for 2022 [5], with the objective to initiate a dialogue with the SAR Oceanographic community attending to the SeaSAR 2023 workshop.
As the end of mission for S-1B has officially been announced [4] after it suffered an anomaly resulting in its unavailability since the 23rd December 2021, this paper concerns only the performances of S-1A. The main results highlighted in this paper are the following:

Instrument status:
The gains and phases of the 280 individual Transmit Receive Modules (TRMs) composing the antenna are monitored via the RFC products to look for instrument aging or elements failures. Although this type of damage has occurred in the past, prompting for an electronic reconfiguration, the antenna status of S-1A has been stable throughout the 2022.
The instrument status is monitored via internal calibration products, describing the evolution of the product gain (PG) in time, and via noise products. The instrument pointing is also monitored by means of the Doppler Centroid estimates annotated in the L1 products.
The analysis of RFC and Internal Calibration products shows that S-1A instrument is stable. No major instrument events have been recorded during 2022. No quality degradation associated to issues happened in previous years is observed in S-1 products.
The analysis of Noise products shows that the instrument noise level is stable.
S-1 interferometric performances in terms of interferometric baseline, burst synchronization and instrument pointing are within the mission requirements. During the month of September 2022 collision avoidance manoeuvres caused an increase in the interferometric baseline and burst synchronization error.
S-1A DC is showing DC jumps up to 30 Hz when the STT configuration changes. The issue is continuously monitored and, in case the DC jumps get worse, could lead to the execution of a new STT alignment campaign during 2023.

Radiometric accuracy:
The instrument is radiometrically calibrated both in absolute and relative terms. Acquisitions over a calibration site comprising of both transponders and corner reflectors allow for the assessment of the absolute calibration constant.

The relative calibration is performed by considering acquisitions over a distributed target such as the rainforest, over which the gamma profile is assumed to be flat with respect to incidence angle.
The radiometric performance of S-1A has been monitored and the radiometric accuracy has been determined for IW mode DV polarization using point targets of the DLR calibration site. During 2022, the overall mean and standard deviation for the absolute calibration factor has been derived to be -0.08 dB ± 0.24 dB which includes the observation of both polarizations (VV and VH) and all three sub-swathes (IW1, IW2, and IW3). Including all error contributions, an absolute radiometric accuracy for the IW mode of 0.322 dB (1σ) could be verified. Furthermore, the radiometric performance for IW mode HH polarization has been monitored using CRs over Australia. With respect to the expected RCS, a small bias of –0.23 dB has been found with a standard deviation of 0.20 dB.
The channel imbalance in amplitude and phase has been derived from DLR transponder measurements. For both SAR instruments, the VV polarization channels show, in average, slightly higher values than VH polarization channels with remaining biases of 0.14 dB. The phases are also well balanced with remaining biases below 2 degrees. The co-registration of the IRF peaks for both polarizations show deviations below 0.1 m in average. The cross-talk of S-1A derived from DLR corner reflector measurements are in average -42.6 dB which confirms the very good quality concerning the separation of the co-and cross polarization channels of both SAR instruments.

Updates on the S-1 Instrument Processing Facility (IPF):
On 23rd March 2022, the IPF was updated for IPF v3.5.1, the most relevant changes are:

- Level 1 content:
  - Correction of the misalignment between the elevation antenna pattern and the annotated thermal noise vector
  - Reduction the number of false positives in RFI time-domain detection
  - Solving of inconsistency in the application of the results of the RFI pre-screening
- Level 2 content:
  - Implementation of a new algorithm for TotalHs computation
  - Review of the oswQualityFlag estimation (based on machine learning algorithm)
  - Rescalling of rvlNRCS
  - Wind inversion provided on the IceMask

For what concerns the RFI detection and mitigation: The number of Level 1 and Level 2 products impacted by RFI is reduced, however this process does not remove 100% of them. The number of products impacted by RFI before activation of the correction is not known with accuracy. However, since activation of the correction, the SAR processor flags around 20% of the products as being impacted by RFI signal on noise echo (even if not visible degradation on the product was observable). Furthermore, a systematic visual inspection of the products allows to assess that less than 1% of the products are impacted by residual RFI.

Level 2 Ocean Wind (OWI)
No major changes occurred in 2022 on OWI products for TOPS and SM modes acquisitions. Since the 18th May 2022, the products are generated using ECMWF wind forecast with a time step of 1hour instead of 3hours and a grid spacing of 0.1 degrees instead of 0.125 degrees. This increase of spatial and temporal resolution was not aimed to change the statistical performances of the Wind (OWI) measurement but may improve the performances on some specific products.

Level 2 Ocean Swell (OSW)
The OSW product is provided only for WV and SM modes (however the number of products acquired in SM mode is not sufficient to perform any geophysical validation). Since June 2021, an update of the instrument configuration for the wave mode beam 2 (WV2) allowed to introduce a significant improvement in significant wave height retrieval for this beam. Since March 2022, a new quality flag of the swell inversion is introduced allowed to classify the performances into five categories (“very good”, “good”, “medium”, “low”, “poor”). Since June 2022, additional

variables in OSW products provide the Total HS derived from machine learning method. Before this date, the variables were not populated.

Level 2 Radial Velocity (RVL)
The performances of the RVL products provided to end users did not evolve significantly in 2022. The Sentinel-1 Level 2 Doppler centroid anomaly (DCA) and radial velocity (RVL) measurements are currently coloured by the AOCS derived Doppler frequency. The predicted Doppler centroid (DC) frequency computed from the downlinked quaternions does not reflect the actual DC frequency as measured by the SAR. This prevents the current version of the Level 2 processor to provide calibrated DCA and RVL estimates. However, promising results are achieved off-line using restituted attitude (RESATT) estimated from calibrated Gyro data. A post-processing approach has been implemented as part of the "Copernicus Sentinel-1 RVL Assessment" project. The results are currently under validation.

References

[1] R. Torres and M. Davidson, "Overview of Copernicus SAR Space Component and its Evolution," IGARSS 2019 - 2019 IEEE International Geoscience and Remote Sensing Symposium, 2019

[2] M. Davidson et al.: *Sentinel-1 Mission Overview* 8th European Conference on Synthetic Aperture Radar (EUSAR), Aachen, 2010.

[3] Sentinel-1 Annual Performance Report 2021, on-line document, https://sentinels.copernicus.eu/web/sentinel/user-guides/sentinel-1-sar/document-library

[4] End of mission of the Copernicus Sentinel-1B satellite, https://sentinels.copernicus.eu/web/sentinel/-/end-of-mission-of-the-copernicus-sentinel-1b-satellite/1.5

[5] Sentinel-1 Annual Performance Report for 2022, under preparation at the date of submission of this abstract, and to be published as on-line document on the Sentinel-1 Online library https://sentinel.esa.int/nl/web/sentinel/user-guides/sentinel-1-sar/document-library

Acknowledgement

The SAR Mission Performance Cluster (MPC) Service is financed by the European Union, through the Copernicus Programme implemented by ESA.
Views and opinion expressed are however those of the author(s) only and the European Commission and/or ESA cannot be held responsible for any use which may be made of the information contained therein.

Sentinel-1 Extra Wide Thermal Noise Removal Using a Deep Learning Model

Roghayeh Shamshiri, Egil Eide, Fazel Rangriz Rostami, Knut Vilhelm Høyland

Department of Electronic Systems, Norwegian University of Science and Technology (NTNU), Norway

Abstract. The Sentinel-1 (S1) ground range detected (GRD) extra-wide (EW) swath data, particularly in the cross-polarization channel are strongly affected by thermal noise. This particular type of noise not only reduces the data interpretability and quality spatially but also troubles the creation of a clean and consistent time series of backscatter, which limits the full exploitation of the images in oceanographic applications. Especially, the time series applications on the GRD images in the Google Earth Engine (GEE) platform, which even though are denoised using the European Space Agency (ESA)-provided calibrated noise vectors, residual noises are still significant. Although the previously developed methods have shown an enhancement in the quality of the images, they are not yet feasible to be applied to the images in the GEE. The scope of this paper is therefore to present a novel method based on a deep-learning model with a U-Net Convolutional Neural Network (CNN) architecture for effectively reducing such noises from the S1 images in an automated way with competitive results with the conventional methods and with applicability in GEE.

Introduction. The Sentinel-1 (S1) mission with the open data policy, global coverage, improved revisit time, and rapid data dissemination offers a wide range of possibilities for monitoring the earth's surface and emergency management. The extra-wide (EW) ground range detected (GRD) products of the S1 images are also useful for generating high-resolution ice charts and understanding the long-term effects of climate change, and planning for a sustainable future. Despite the usability of the S1 EW swath images for oceanographic applications, they are affected by thermal noise, particularly in the cross-polarization channel, which restricts the application of these images. Therefore, precise thermal noise correction of the EW images in the cross-polarization is essential for acquiring useful information from S1 data. These noise effects can be reduced using the ESA-provided noise vectors. Although the denoising process improves the image quality, the residual noise is still significant in denoised images. Figure 1a and 1b show an intensity image of the S1 HV polarization in the EW swath mode and the corrected image using the ESA-provided noise vector, respectively.

Therefore to remove the noise from the EW data using the ESA-provided vectors, which is the preferable approach, a modification should be applied to the given noise information. A number of different approaches have addressed this problem for instance by proposing a quadratic objective function to model the mis-scale of the provided noise field using a least-squares solution [1], an effective denoising method, which finds the optimal scaling factors to modify the provided noise vectors to correct the additive [2] and remove the multiplicative noise [3]. Although these methods enhance the quality of the images, it is difficult or unfeasible to apply to the images ingested in the Google Earth Engine (GEE) [4, 5]. Since the noise vectors are lost in GEE and the thermal noise removal has been carried out using the ESA-provided vectors, the residual thermal noise causes difficulties in the time-series analysis in oceanographic applications [6]. To address this issue we propose a novel and efficient method, which provides the possibility of efficient thermal noise removal from the GRD images in GEE, without dealing with complex parameter optimization for each specific image. Utilizing a convolutional neural network (CNN) architecture called the "U-Net" [7], we

propose a method for thermal noise removal from the S1 GRD images, which has been recently used for image denoising and achieved good performance [8, 9, 10, 11].

Implementation Details. The most common CNN approaches to denoising require noise-free (clean) ground truth images for the training of the network. As such images from the S1 EW are not available, we employ the method presented in [3] with some modifications. We apply the method to more than 30 HV-polarized EW GRD images of S1 with the IPF after 2.9.0 over the Atlantic ocean, then choose 11 scenes with the best improvement and use eight of them as training and validation, and the rest as test datasets. We train our model using randomly selected image patches with the size of 256×512 pixels cropped with the overlap of 100 and 250 pixels in the azimuth and the range direction, respectively, and a batch size of 32. We use 75% of the patches (14421) as training data and the rest (4807) as a validation set for evaluating the performance of our model. The network is trained for 200 epochs, by randomly shuffling the training dataset before each training epoch. The output of the model in each epoch is compared to the corresponding clean ground truth patch using MSE loss. Fig. 1c shows the proposed U-net network to accomplish this denoising task. Our model is implemented in Python 3.8.10 using the Keras application programming interface (API) running on the Tensorflow 2.5.0 framework.

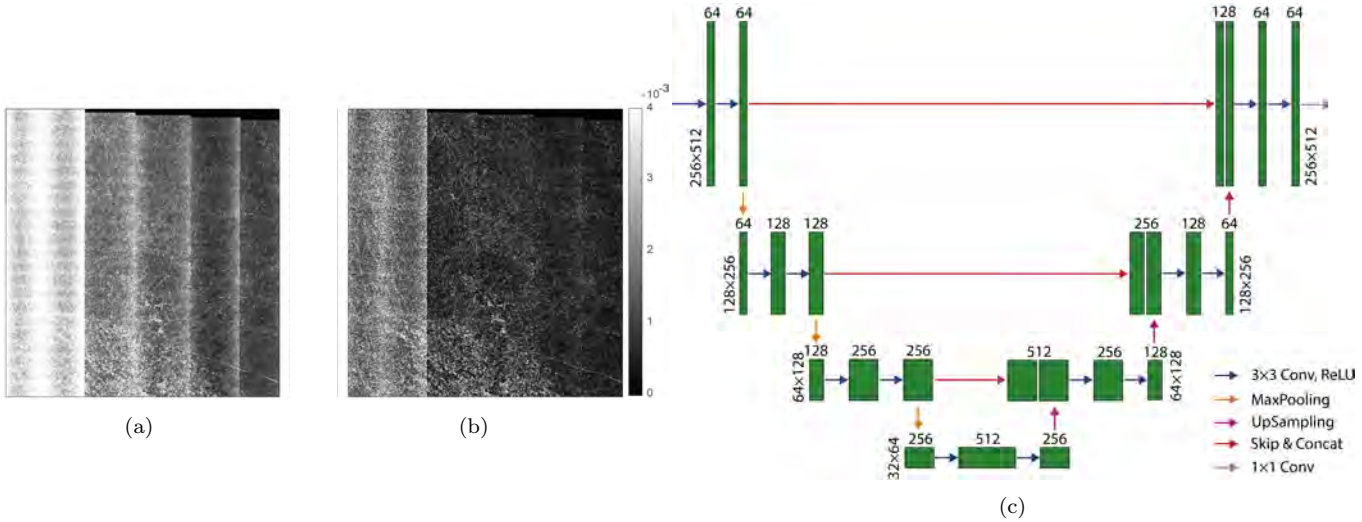

Figure 1: (a) S1 EW image in HV polarization (linear unit) without noise correction, (b) corrected using the ESA-provided noise vector.

Results. We evaluate the performance of the model on a hold-out test set, which includes three sets of noisy and clean images. Figure 2 shows the noisy, predicted, and clean for one of the images. Comparing the noisy image with the predicted (denoised using our method) one shows that the model has significantly removed the stripes and achieved a visually pleasing quality of the image. The peak signal-to-noise ratio (PSNR) value for this image is 36.67 dB, and the structural index similarity (SSIM) value is 0.93. The experimental results demonstrate the effectiveness of our proposed method in reducing the noises from the EW HV-polarized S1 images. In addition, unlike the conventional methods, our technique can be applied to the S1 GRD images ingested in the GEE platform, which leads to improving the quality of the time-series analysis on oceanographic applications.

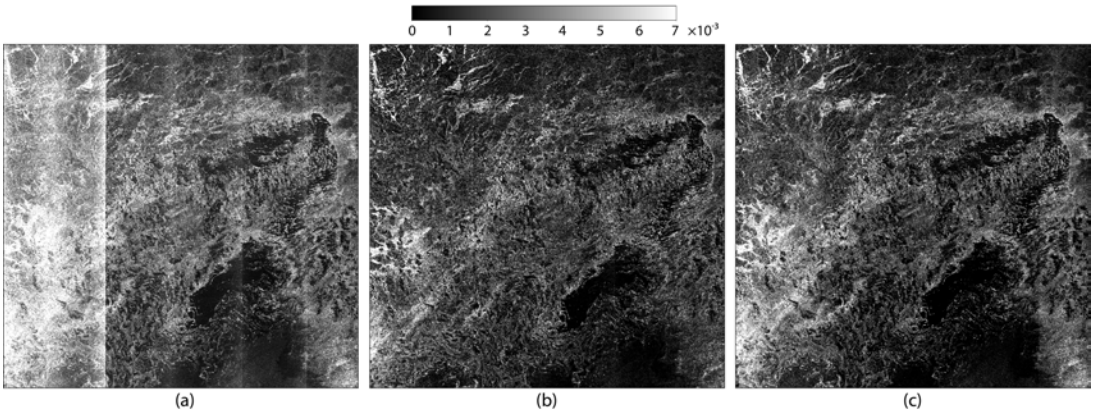

Figure 2: Model test result, (a) the noisy, (b) predicted using our model, and (c) clean image.

References

[1] P. Q. Lee, L. Xu, D. A. Clausi, Sentinel-1 additive noise removal from cross-polarization extra-wide TOPSAR with dynamic least-squares, Remote Sensing of Environment 248 (2020) 111982.

[2] J.-W. Park, A. A. Korosov, M. Babiker, S. Sandven, J.-S. Won, Efficient thermal noise removal for Sentinel-1 TOPSAR cross-polarization channel, IEEE Transactions on Geoscience and Remote Sensing 56 (2017) 1555–1565.

[3] Y. Sun, X.-M. Li, Denoising Sentinel-1 Extra-Wide Mode Cross-Polarization Images Over Sea Ice., IEEE Transactions on Geoscience and Remote Sensing 59 (2021) 2116–2131.

[4] N. Gorelick, M. Hancher, M. Dixon, S. Ilyushchenko, D. Thau, R. Moore, Google Earth Engine: Planetary-scale geospatial analysis for everyone, Remote Sensing of Environment 202 (2017) 18–27.

[5] O. Mutanga, L. Kumar, Google Earth Engine Applications, Remote Sensing 11 (2019). URL: `https://www.mdpi.com/2072-4292/11/5/591`. doi:10.3390/rs11050591.

[6] R. Shamshiri, E. Eide, K. V. Høyland, Spatio-temporal distribution of sea-ice thickness using a machine learning approach with Google Earth Engine and Sentinel-1 GRD data, Remote Sensing of Environment 270 (2022) 112851.

[7] O. Ronneberger, P. Fischer, T. Brox, U-net: Convolutional networks for biomedical image segmentation, in: International Conference on Medical Image Computing and Computer-assisted Intervention, Springer, 2015, pp. 234–241.

[8] B. Park, S. Yu, J. Jeong, Densely connected hierarchical network for image denoising, in: Proceedings of the IEEE/CVF Conference on Computer Vision and Pattern Recognition Workshops, 2019.

[9] S. Yu, B. Park, J. Jeong, Deep iterative down-up cnn for image denoising, in: Proceedings of the IEEE/CVF Conference on Computer Vision and Pattern Recognition Workshops, 2019.

[10] G. Zhang, Z. Li, X. Li, Y. Xu, Learning synthetic aperture radar image despeckling without clean data, Journal of Applied Remote Sensing 14 (2020) 026518.

[11] X. Cao, X. Fu, C. Xu, D. Meng, Deep Spatial-Spectral Global Reasoning Network for Hyperspectral Image Denoising, IEEE Transactions on Geoscience and Remote Sensing (2021).

Processing of high squint bistatic SAR data: The case of Harmony

Temesgen Gebrie Yitayew Tom Grydeland Yngvar Larsen Geir Engen

1 Introduction

The Harmony mission is a planned ESA mission which will feature two satellites flying in close formation with Sentinel-1 (S-1). Each of these companion satellites will carry a passive SAR instrument as a main payload which records echoes of pulses transmitted from S-1. One of the primary objectives of the mission is ocean parameter retrieval [ESA, 2022]. Due to many peculiar features of the acquisition geometry, processing of data needs a careful consideration. In this paper, we will discuss the main challenges that arise from the unique acquisition geometry and propose a solution for properly handling the data, with emphasis on focusing using full azimuth bandwidth, as is required for ocean parameter retrieval applications.

1.1 Observation geometry

Two different bistatic acquisition geometry configurations are envisioned in the Harmony mission. The first is the *Stereo configuration* where one of the companion satellites is leading and the other one trailing S-1. The spatial baseline between the companion satellites and S-1 is expected to be between 350 and 400 km. The envisioned applications with this configuration is mainly measurement of surface velocity vectors employing a variety of techniques. For example, along-track interferometry to measure instantaneous velocity vectors of ocean surfaces. For this application, the antenna in the companion satellites is expected to feature at least two phase centers displaced in azimuth (see Fig. 1(a)).

(a) (b)

Figure 1: Satellite configurations of the Harmony mission. (a) Stereo configuration, (b) Across-track interferometric configuration.

The second configuration is *Across-track interferometry configuration*, where the two companion satellites are expected to be separated by a baseline in the across-track direction to map topographic changes of the observed medium using single-pass across track InSAR technique. This is illustrated in Fig. 1(b). The baseline in the across-track direction is expected to vary between 400 and 800 m.

2 Considerations in processing high squint bistatic SAR data

Due to the large along-track separation between the transmitter and receiver satellites in the Harmony configuration, see Fig. 1, the system features a high squint bistatic geometry. Moreover, as the two companion satellites record the pulse transmitted by Sentinel-1, their antenna is expected to feature azimuth beam-steering when S-1 operates in TOPS mode (see section 2.3). These features need to be carefully considered in designing a frequency domain focusing kernel for Harmony. In the following section, we discuss the main signal properties arising from the unique high-squint bistatic acquisition geometry of Harmony.

2.1 Frequency domain SAR processing

Operational SAR processors are almost always based on frequency-domain focusing kernels due to their high computational efficiency. The SAR system is a linear system where the collected raw data is modelled by the convolution between the complex reflectivity of the imaged medium and the point target response also called the system Impulse Response Function (IRF). Therefore, given the raw data and the IRF of the SAR system, SAR focusing is the processes of retrieving the complex reflectivity by using the IRF as a matched filter. This can be efficiently done in the frequency domain by making use of the analytic Fourier transform of the IRF.

2.2 Range migration model

In frequency domain SAR processing, the range migration, i.e., the variation of the distance between the target and the platform(s) as a function of azimuth time is the single most important parameter. This model is employed to derive analytical expressions of frequency domain focusing kernels. Traditionally, a one-parameter hyperbolic Range Migration Model (RMM) has been used in combination with a zero-doppler coordinate system. This model is of adequate accuracy for monostatic acquisition with low to moderate squint. In addition, a semi-analytical solution to the inversion problem is available, resulting in the well-known ω-κ algorithm [Cumming and Wong, 2005]. However, for the high-squint bistatic acquisition geometry of Harmony, the hyperbolic RMM is not accurate enough, in particular when derived in a zero-doppler coordinate system. This is because, even though each of the transmitter- and receiver-range histories are hyperbolic, their sum is not hyperbolic. Therefore, an accurate range migration model coupled with a generalized SAR coordinate system is fundamental for deriving the ω-κ kernel for focusing data from the companion satellites. Our proposed approach is to expand the bistatic range history into a Nth-order polynomial model. This is used to derive the ω-κ kernel by making use of *series reversion* [Neo et al., 2007] and the principle of stationary phase approximation.

2.3 TOPS mode of operation

The Sentinel-1 SAR instrument makes extensive use of the azimuth scanning TOPS modes (IW and EW), which introduces a linear Doppler centroid variation within each burst of data. The PRF is high enough that the signal is properly sampled, but folded (aliased) within the azimuth frequency band [De Zan and Guarnieri, 2006]. The frequency dependence of the focusing kernel means that data must be unfolded in frequency before it can be applied. An efficient method to exchange frequency and time folding (and the inverse) without intermediate oversampling was introduced by [Engen and Larsen, 2011]. The combination of high squint and full bandwidth processing requires some modifications to the method, to be described below.

2.4 The squinted 2D spectrum

The Doppler centroid frequency is in general dependent on range frequency. In low-and moderate-squint SAR systems, which are characterized by small doppler centroid, this variation is very small relative to the Pulse Repetition Frequency (PRF), and can be ignored. However, for highly squinted acquisitions of Harmony, the Doppler centroid variation is large enough that the azimuth spectrum wraps in the 2D spectral domain. This is illustrated in figure 2.

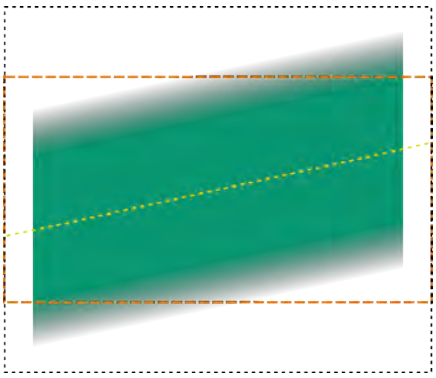

Figure 2: Azimuth bandwidth filtering and/or spectral extension for a squinted acquisition. The signal in the squinted SAR acquisition in the 2D frequency domain; range frequency on the horizontal axis, azimuth frequency on the vertical axis. Without spectral extension, pieces of the spectrum fall outside the band defined by the PRF (orange rectangle) and will be aliased (folded). Spectral extension creates more space in the azimuth frequency domain (black rectangle) so that the spectrum can be unfolded. If an azimuth bandwidth-limiting filter is required, it can be applied in this domain, such that it follows the shape of the spectrum (yellow dashed line) at each range frequency. If the resulting signal falls entirely within the orange box, spectral extension is not necessary.

When the processing azimuth bandwidth is to be limited, as is usual for non-ocean applications, care must be taken that the azimuth bandwidth filter is applied in the 2D frequency domain, and in such a way that it tracks the azimuth/range frequency dependence, shown with the dashed yellow line in the figure. Depending on the amount of squint and filtering, the total azimuth bandwidth may be within the limit given by the PRF and no further special precautions are necessary. Illustration with simulated data is presented in a companion paper in [Grydeland et al., 2023].

2.5 Full bandwidth processing for ocean applications

One parameter of interest that can be estimated from SAR data is the Doppler centroid anomaly (DCA) which in turn can be used to derive radial velocity of the observed ocean surface. Accurate retrieval of this parameter requires processing of the full azimuth bandwidth. In this case,[1] the 2D spectrum needs to be circularly extended after range compression, but before applying the focusing kernel [Davidson and Cumming, 1997]. This processing step is referred to as *azimuth spectral extension*. After the circular extension, the signal should be filtered down to the correct (unaliased) bandwidth using either a) for ocean applications: a boxcar filter corresponding to the full azimuth bandwidth, or b) the appropriate bandwidth-limiting filter. In either case, the filter should be applied as indicated in figure 2.

2.5.1 Stripmap-like modes

For modes without azimuth sweeping, *i.e.*, all modes except Spotlight and TOPS, data is brought to the 2D frequency domain by way of a 2D FFT. If necessary using short blocks in range. The expanded azimuth frequency domain implies a higher effective azimuth sampling rate for these cases.

2.5.2 High-squint TOPS modes

When a TOPS mode is used, the sweep of the antenna means that the azimuth frequency of the data varies over a band that is several times wider than the PRF, but the instantaneous bandwidth (determined by the azimuth antenna pattern) is adequately sampled. As hinted at above, the data are brought into the azimuth frequency domain by way of an efficient spectral mosaicing operation called the moving-band chirp-Z transform (MBCZT) [Engen and Larsen, 2011]. At the end of this operation, the data have been effectively resampled to a higher sampling rate that allows the full unwrapped spectral extent of the data to be represented without padding out to greater size. The MBCZT consists of three steps: the first and last steps are application of phase ramps (multiplication with chirps), while the middle step is a convolution with a chirp. The convolution is efficiently implemented as a multiplication in the frequency domain. Steps that require access to the azimuth frequency domain are then most conveniently applied in the middle of this convolution.

In the high-squint full-bandwidth case, the MBCZT as described previously must be modified by spectral extension. The spectral extension serves two purposes. The first is to unwrap the azimuth spectrum in a range-frequency dependent way. This is similar to what is described above, except for how the data was brought to the azimuth spectrum domain. Secondly, higher squint data will undergo significant dispersion during the focusing, meaning that it will spread out in azimuth time. The data must be prepared in such a way that there is enough space in the data array for the dispersion to occur without overlaying signal from different azimuth times. Such space can be secured by azimuth bandwidth filtering, by padding out the azimuth frequency domain, or by azimuth spectral extension.

It is perhaps surprising, and therefore worth emphasizing, that it is the azimuth frequency domain which must be bandwidth-limited, padded or extended inside the convolution in order to create space in the azimuth time domain. Spectral extension or padding at this step does not modify the effective azimuth sampling rate in the TOPS case.

2.5.3 The inverse moving-band chirp-Z transform for squinted modes

The IMBCZT is constructed from the same steps as the MBCZT, inversed and in the opposite order. The chirp rate is also a different one, arising from the combined effect of the antenna sweep and the doppler rate of the targets. For the transform to operate correctly, the signal must be centered in both azimuth frequency and azimuth time. There are multiple intricacies involved. These will be presented and discussed. An example using simulated data is shown in [Grydeland et al., 2023].

References

[Cumming and Wong, 2005] Cumming, I. G. and Wong, F. H. (2005). *Digital processing of synthetic aperture radar data.*

[Davidson and Cumming, 1997] Davidson, G. W. and Cumming, I. (1997). Signal properties of spaceborne squint-mode SAR. *IEEE Transactions on Geoscience and Remote Sensing*, 35(3):611–617.

[De Zan and Guarnieri, 2006] De Zan, F. and Guarnieri, A. M. (2006). TOPSAR: Terrain observation by progressive scans. *IEEE Transactions on Geoscience and Remote Sensing*, 44(9):2352–2360.

[Engen and Larsen, 2011] Engen, G. and Larsen, Y. (2011). Efficient full aperture processing of TOPS mode data using the moving band chirp Z-transform. *IEEE Transactions on Geoscience and Remote Sensing*, 49(10):3688–3693.

[ESA, 2022] ESA (2022). Report for Mission Selection: Earth Explorer 10 candidate mission Harmony. Technical Report ESA-EOPSM-HARM-RP-4129, European Space Agency, Noordwijk, The Netherlands.

[Grydeland et al., 2023] Grydeland, T., Yitayew, T. G., Larsen, Y., Dubois, P., Armstrong, T., Gombert, B., Soulat, F., Monnier, G., Hellouvry, Y.-H., Camus, B.and Lopez-Dekker, P., Lajas, D., Rommen, B., and deWitte, E. (2023). Signal processing for Harmony: Illustrations with simulated data over ocean. SeaSAR.

[Neo et al., 2007] Neo, Y. L., Wong, F., and Cumming, I. G. (2007). A two-dimensional spectrum for bistatic SAR processing using series reversion. *IEEE Geoscience and Remote Sensing Letters*, 4(1):93–96.

[1] or if the azimuth bandwidth exceeds the band given by the PRF even after filtering

Machine learning for evaluating the drivers of variability in Arctic sea-ice motion.

Physics-based simulations of Arctic sea ice are highly complex, involving transport between different phases, length scales, and time scales. Due to these complexities, numerical simulations of sea-ice dynamics have a high computational cost and a high model uncertainty. We employ **machine learning (ML)** to make predictions of sea-ice motion. The ML models are built to predict present-day sea-ice velocity given **present-day wind velocity** and previous-day sea-ice concentration and velocity. Models are trained using reanalysis winds and **satellite-derived sea-ice properties**. We compare the predictions of three different models: persistence (PS), linear regression (LR), and convolutional neural network (CNN). We quantify the spatio-temporal variability of the correlation between observations and model predictions. Additionally, we analyze model performance in comparison to variability in properties related to ice motion (wind velocity, ice velocity, ice concentration, distance from coast, bathymetric depth) to understand the processes related to decreases in model performance. Results indicate that a CNN can make skillful predictions of daily sea-ice velocity with a correlation as high as 0.80 between predicted and observed sea-ice velocity, while the LR and PS implementations exhibit correlations of 0.77 and 0.69, respectively. The correlation varies spatially and seasonally; lower values occur in shallow coastal regions and during times of minimum sea-ice extent (Figure 1). LR parameter analysis indicates that wind velocity plays the largest role in predicting sea-ice velocity on one-day timescales, particularly in the central Arctic (Figure 2). Regions where wind velocity dominates LR are regions where the CNN has higher predictive skill than the LR (Figures 1 and 2).

With a mind towards dynamical understanding and backwards propagation for assimilation we are using ‘explainable AI’ (XAI) techniques to understand how the CNN is making predictions. Similarly to LR, XAI analyses show that winds are the most important predictor overall, but that there are subtleties as to where the winds matter most for overall sea ice motion. Moreover, it shows the specific regions where knowledge beyond wind velocity is important. We compare the explainable AI outputs to LR parameters (Figure 2) and analyze both spatial and temporal patterns in efforts to understand how the relationship between wind and ice motion is changing as the ice melts.

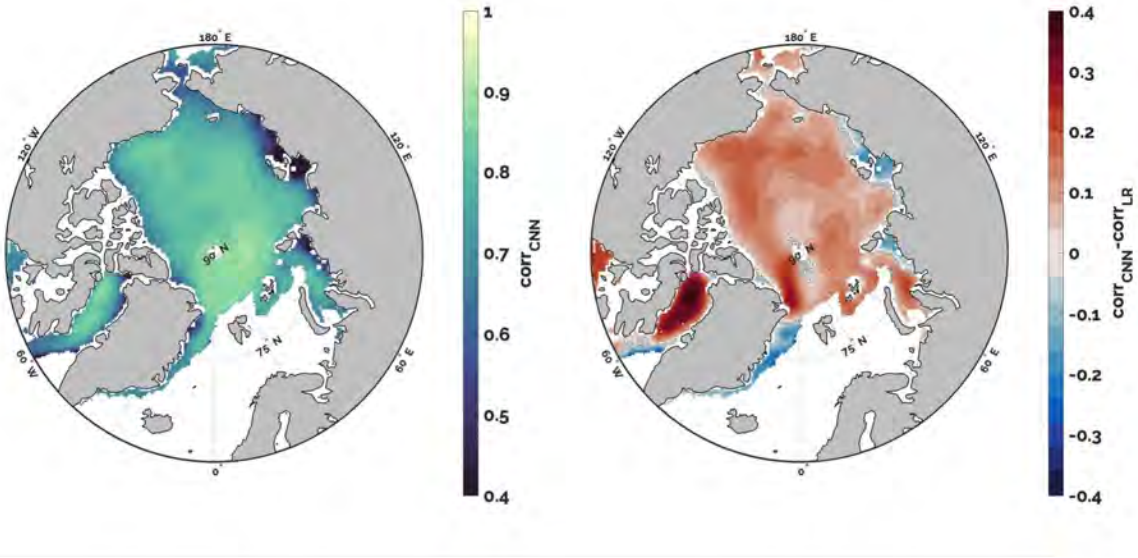

Figure 1: (a) Mapped correlation for predictions of sea-ice velocity made by the CNN. (b) The difference in correlation between the CNN and LR models. The gray regions in (b) represent locations where the difference in correlation between the two models is not statistically significant.

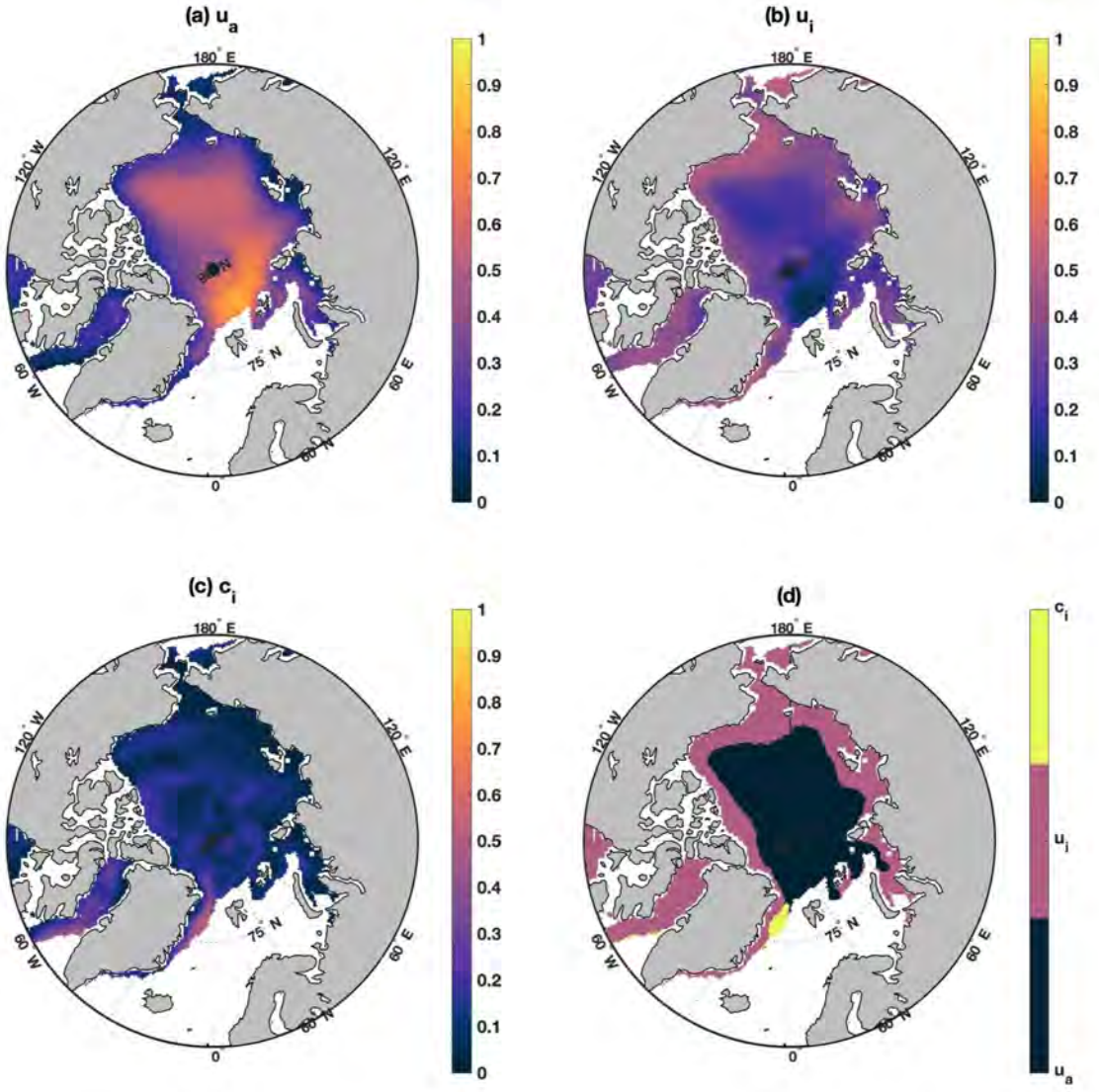

Figure 2: Magnitude of the normalized linear regression coefficient for the relationship between sea-ice velocity components and input parameters (a, wind speed, u_a; b, sea-ice speed, u_i; c, sea-ice concentration, c_i), normalized to the maximum of a-c. (d) Maximum linear regression parameter (a-c) for predicting sea-ice velocity at each location.

Signal processing for HARMONY: Illustrations with simulated data over ocean

T. Grydeland[1] T. G. Yitayew[1] Y. Larsen[1] P. Dubois[2]
T. Armstrong[2] B. Gombert[2] F. Soulat[2] G. Monnier[3]
Y-H Hellouvry[3] B. Camus[3] P. Lopez-Dekker[4] D. Lajas[5]
B. Rommen[5] E. deWitte[5]
([1]NORCE, [2]CLS, [3]Scalian Alyotech, [4]TU Delft, [5]ESA-ESTEC)

1 Introduction

The Harmony mission is a planned ESA mission which will feature two satellites flying in close formation with Sentinel-1. Each of these companion satellites will carry a passive Synthetic Aperture Radar instrument (SAR) as a main payload which records echoes of pulses transmitted from S-1. One of the primary objectives of the mission is ocean parameter retrieval [ESA, 2020]. Due to many peculiar features of the acquisition geometry, processing of data needs a careful consideration. In a companion paper [Yitayew et al., 2023], we discussed the main challenges that arise from the unique acquisition geometry and proposed solutions for properly handling the data, focusing in particular on ocean parameter retrieval applications. In this paper we apply the proposed solution to simulated bistatic SAR data which is simulated with an End-to-End Performance Simulator software that has been developed as part of the harmony mission validation study [Dubois et al., 2023]. Two different bistatic acquisition geometry configurations are envisioned in the Harmony mission. These are Stereo and Across-track interferometry configurations. In this paper, we will focus on the first of these, the *Stereo configuration*, where one of the companion satellites is leading and the other one trailing S-1. The spatial baseline between the companion satellites and S-1 is expected to be in the order of hundreds of kms (350 - 400 km). The envisioned applications with this configuration is mainly measurement of surface velocity vectors employing a variety of techniques. For example, along-track interferometry to measure instantaneous velocity vectors of ocean surfaces. For this application, the antenna in the companion satellites is expected to feature at least two phase centers displaced in azimuth. The second configuration, the *Across-track interferometry configuration*, is not discussed here.

1.1 Harmony End-to-End performance simulator

The end-to-end simulators are a classic tool for characterizing the performance of a mission, as defined by the science requirements. They integrate the definition of a set of geophysical scenarios (set as truths), the geometry and timing of the acquisition, the transfer function of the instrument, and the prototyping of all levels of processing (on-board L0, L1, L2). At the end of the L2 processing, the estimates of the geophysical parameters of interest can be compared to the geophysical truth used as an input into the simulation. Thus, the performance of the estimations can be quantified, mainly characterized by biases and errors. The main objective of the Harmony End-to-End Performance Simulator for ocean applications (HEEPS/Mare) is to validate the SAR derived products, as presented in [Dubois et al., 2023]. In this paper, simulated bistatic SAR data using one of the companion satellites will be used for illustration.

1.2 Simulation setup: Sea-state

The animated sea surface is modelled through a mesh with a resolution of 2.5 m. Topography and kinematics are simulated in the frame of the Choppy Wave Model [Nouguier et al., 2009]. Bistatic EM scattering is computed according to SSA-1, applied to intra-facet roughness. Fully polarized radar equation is applied at the facet level, accounting for realistic antenna patterns for each receiver/phase center/polarization channel. Complex contributions from illuminated facets are rasterized in range for all receiving channels. The resulting oversampled profiles are then convolved with the uncompressed waveform and under-sampled to produce raw IQ signals. In the simple simulation case used

hereafter, the sea state is homogeneous, comprising swell and wind-sea components, both oriented approximately across-track. The swell spectrum is gaussian, with a central wavelength of 200 m. It is intentionally made highly coherent, with correspondingly small spectral spread (FWHM is 0.003 rad.m-1 in wavenumber and 10° in azimuth). The wind-sea component resorts to the Elfouhaily spectrum [Elfouhaily et al., 1997], with U10=7 m/s and a fetch of 450 km.

2 Brief overview of TOPS SAR data processing

An efficient algorithm for processing TOPS SAR data has been presented in [Engen and Larsen, 2011] and revised in [Yitayew et al., 2023] for handling high-squint bistatic SAR data. In the low squint monostatic case, the focusing does not cause much dispersion. In the high-squint bistatic case however, the situation is very different. Figure 1 illustrates the problem. The left panel shows a spectrogram of time-wrapped raw data. There are clearly discernible bands of scattering, corresponding to the different spatial regions that contribute to this slice of range, but at different azimuth frequencies. After the focusing (right panel), the dispersion has caused signal to disperse in azimuth time (horizontally). While banding structure is still discernible, it is no longer possible to cleanly unfold the time folding. As presented in [Yitayew et al., 2023], the solution is to apply spectral extension.

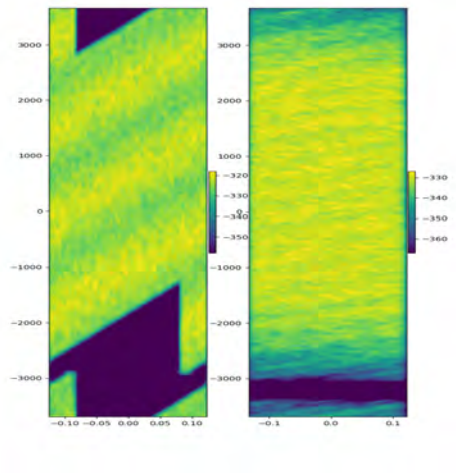

Figure 1: The problem with dispersion in the focusing. The time-wrapped raw data (left) have clearly identifiable bands of stronger scattering. After focusing (right) dispersion has caused the bands to bleed into each other such that scattering from distinct spatial regions can no longer be separated.

Spectral extension, figure 2, occurs in the middle of the convolution step of the (forward) MBCZT. For sea state characterization purposes, a boxcar filter corresponding to the full original bandwidth (i.e., the PRF) is used. After demodulation and deramping of the data (see [Yitayew et al., 2023]), there is a residual coupling between range frequency and azimuth frequency due to the high doppler centroid. Figure 2(a) shows the data in the 2D frequency domain for a small range block. The azimuth frequency dependence on range frequency is indicated by the red dashed line, while the yellow dashed lines indicate the limits of spectrum not afflicted by aliasing. The small triangles in top left and bottom right corners are pieces of spectrum that are wrapped (aliased) in azimuth frequency. Figure 2(b) shows the data after spectral extension. The data have been duplicated in the azimuth frequency direction and then filtered to the desired azimuth bandwidth with a filter that tracks the azimuth centre frequency for every range frequency. In this example, a boxcar filter with bandwidth corresponding to the original PRF was used. The feature at central range frequency is an artifact introduced in the data for illustration purposes. Observe that the scale on the vertical axis is different in the two panels.

Figure 3 shows that the space created through spectral extension allows the dispersion to occur in the focusing in a way which still allows the bands from distinct spatial regions to be cleanly separated.

2.1 The inverse moving-band chirp-Z transform for squinted data

After focusing, but before the final IFFT, the data are in the range-doppler domain, wrapped in azimuth time, albeit at a different rate than before focusing (*cf.* the difference between panels 1 and 2 of figure 4.

(a) (b)

Figure 2: Spectral extension of simulated bistatic TOPS data. (a): wrapped data in the 2D frequency domain, (b): extended 2D spectrum.

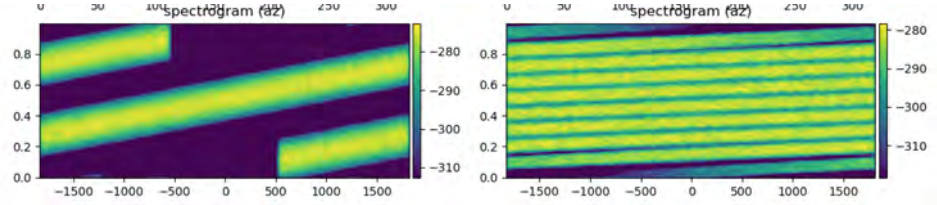

Figure 3: Allowing for dispersion in the focusing. The bands of signal in the time-wrapped raw data (left) are clearly separated thanks to the spectral extension procedure. After focusing (right) dispersion has caused the bands to come into close proximity, but without actual overlap. In this figure, unit sampling and normalized bandwidth is used on the axes.

Spectral mosaicing to bring these data to a frequency-wrapped time-domain representation is efficiently achieved using an inverse moving-band chirp-Z transform (IMBCZT) [Engen and Larsen, 2011], with some revisions outlined in [Yitayew et al., 2023] for the high-squint bistatic case.

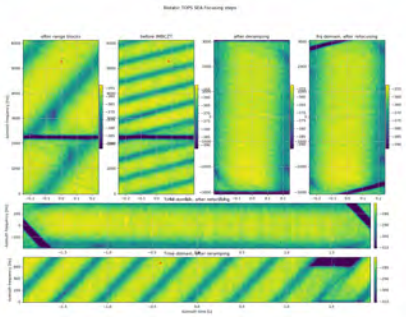

Figure 4: The steps of the inverse moving-band chirp-Z transform (IMBCZT) for high-squint data.

References

[Dubois et al., 2023] Dubois, P., Armstrong, T., Gombert, B., Soulat, F., Monnier, G., Hellouvry, Y.-H., Camus, B., Yitayew, T. G., Grydeland, T., Lopez-Dekker, P., Lajas, D., Rommen, B., and deWitte, E. (2023). Harmony end-to-end performance simulator: evaluating the performance of a bi-static ATI SAR mission for ocean observations. SeaSAR.

[Elfouhaily et al., 1997] Elfouhaily, T., Chapron, B.and Katsaros, K., and Vandemark, D. (1997). A unified directional spectrum for long and short wind-driven waves. *Journal of Geophysical Research: Oceans*, 502(7):15781–15796.

[Engen and Larsen, 2011] Engen, G. and Larsen, Y. (2011). Efficient full aperture processing of TOPS mode data using the moving band chirp z-transform. *IEEE Transactions on Geoscience and Remote Sensing*, 49(10):3688–3693.

[ESA, 2020] ESA (2020). ESA-EOPSM-HARM-RP-3784 - Earth Explorer 10 candidate mission Harmony report for assessment. Technical Report Issue 1, revision 0, Date of issue 13/11/2020, ESA.

[Nouguier et al., 2009] Nouguier, F., Guérin, C. A., and Chapron, B. (2009). "choppy wave" model for nonlinear gravity waves. *Journal of geophysical research: oceans*, 114.

[Yitayew et al., 2023] Yitayew, T. G., Grydeland, T., Larsen, Y., and Engen, G. (2023). Processing of high squint bistatic SAR data: The case of Harmony. SeaSAR.

MEDISAR: AN EXHAUSTIVE AUGMENTED DATASET OF SEGMENTED SENTINEL-1 SAR OCEAN OBSERVATIONS OF THE MEDITERRANEAN SEA AND THE BLACK SEA REGIONS

Aurélien COLIN[1,2], Pierre TANDEO[1], Romain HUSSON[2], Ronan FABLET[1], Charles PEUREUX[2]

1 - IMT Atlantique, Lab-STICC, UMR CNRS 6285, F-29238, France,
2 - Collecte Localisation Satellite (CLS), Brest, France

***Abstract*—With satellites observations being acquired routinely and producing large quantity of data, consideration is to be given to how to share these observations and the derived information computed from them. The observations are often time-consuming to obtain and need CPU and GPU capacity to be processed. We thereby introduce the MediSAR dataset. Dedicated to the Mediterranean and the Black Sea, it is designed to exhaustively encompass all Sentinel-1 mission observations. 102,504 observations acquired between 2014 and 2022 are combined with inferences from deep learning models. These models provide IA-derived geophysical information on biological slicks, wind speed, rainfall and convective processes using state-of-the-art methodologies. Collocation with non-SAR sensors (Sentinel-3/OLCI, MSG/Seviri) are planned. This dataset aims at sharing SAR observations and simplifies the study of metocean phenomena.**

I. INTRODUCTION

C-Band Synthetic Aperture Radar (C-SAR) is a valuable tool for studying ocean surfaces, particularly for wind speed [1] and direction [2], waves [3], and oil pollution [4]. It has the advantage of high resolution while not being affected by cloud cover. The Sentinel-1A and Sentinel-1B satellites have been using C-SAR since 2014, providing a large quantity of data that is difficult to manage. As meteorological and ocean (grouped under the name "metocean") processes rarely need the full resolution provided by SAR sensors, the estimation of metocean processes usually includes downloading the level-1 product at a resolution of 10 m/px, preprocessing, downscaling the SAR observation, and processing by a model. These considerations are even more relevant as deep learning models begin to appear with [5] categorizing thumbnails under ten metocean classes and [6] estimating the rainfall on coastal observations. Deep Learning (DL) models also require more computational capabilities and especially GPU acceleration. Altogether, the download and computational means can greatly hamper the uptake of SAR products for the study of metocean processes by a wide user community.

Recent SAR datasets have been published, such as the TenGeoP-SARwv dataset [7], which contains more than 37,000 observations of 20x20 kilometers at 50 m/px, or the OpenSARShip dataset [8], with 11,000 images centered on ships at 10 m/px. The present paper follows the same objectives and introduces the MediSAR dataset, which contains SAR observations as well as derived model estimates of rainfall, convective processes, and biological slicks. SAR-based wind speed, computed with a rain-invariant model, is also proposed. The also provides information from third party sensors or model. Wind speed for the reanalysis ERA5, chlorophyll contration from Sentinel-3 OLCI and brightness temperature from the Sentinel-3 mission.

The dataset is available at the following url: https://github.com/CIA-Oceanix/MediSAR

II. DATA

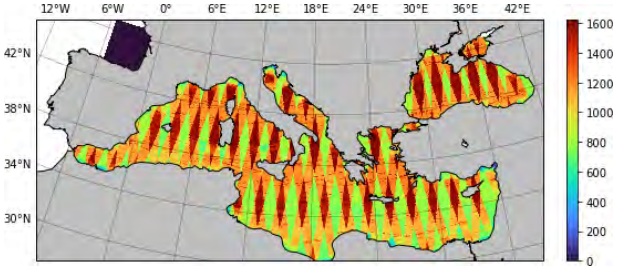

Fig. 1. Geographical distribution of Sentinel-1 IW observations from 2014/10/04 to 2022/12/31.

The dataset is composed of 102,000 IW observations from both Sentinel-1A and Sentinel-1B. As indicated by Fig. 1, they cover the Mediterranean Sea and the Black Sea. Each observation typically cover 160 x 200 km.

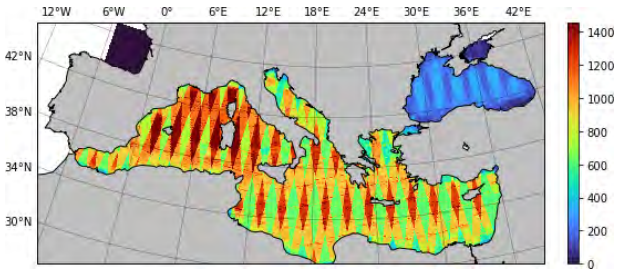

Fig. 2. Geographical distribution of Sentinel-1 IW observations with available level-2 products from 2014/10/04 to 2022/12/31.

The dataset contains both SAR channels and inferences from deep learning models. The co-polarized (vertical-vertical) and cross-polarized (vertical-horizontal) data are included, at a resolution of 200 m/px. These observations are computed from the GRDH product available from the ESA's Copernicus Service and NASA's Alaska Satellite Center at a native resolution of 10 m/px. Data from Sentinel-1A runs from October 17th, 2014 to December 31st, 2022, for a total of 61,232 observations. Sentinel-1B covers from September 26th, 2016 to December 23rd, 2021, for a total of 41,647 observations. However, Sentinel-1B satellite experienced issues with the power supply unit and is planned to be deorbited. Continuity of SAR observations will be ensured by the launch of Sentinel-1C in 2023. Each Sentinel-1 satellite is designed to have a revisit period of 12 days. However, as the tracks of the swaths overlap, the observation period ranges from 4 to 2 days, depending on the location.

To each SAR observation, there is an associated segmentation of meteorological and oceanographic processes. Biological slicks, oil-like surfactants produced by plankton, are visible on SAR observations because of the decreased sea surface roughness caused by the viscosity of the surfactant layer. They provide information on both the biological activity and surface meteorological and oceanographic situations as their dynamics depend on wind, waves, and currents. They are stored at 200 m/px and quantized to 8 values per pixel.

Convective processes indicate changes in wind characteristics (speed and direction). They help to understand moisture and heat transfer over the ocean. Similarly to biological slicks, they are quantized to 8 values per pixel but stored at 400 m/px as they are often large patterns that do not need higher resolution.

Rainfall segmentation maps obtained from [6] are stored at 400 m/px. They indicate qualitative information corresponding to thresholds at 1 mm/h, 3 mm/h, and 10 mm/h of estimated rainfall. Rainfall is a major source of discontinuities on SAR observations, otherwise mainly dominated by wind-related phenomena [9]. Usual SAR-based wind speed estimates rely on the Geophysical Model Function to retrieve the wind speed, but fail on rain-contaminated areas. Therefore, we add wind speed estimates obtained from a model specifically trained to reduce rain-related errors. The estimates are stored at 200 m/px, with a quantization step of 0.1 m/s, up to 51.2 m/s. However, wind speed estimates are computed only if OCN products are available. From August 2015 to March 2017, they cover only the Lion Gulf. Then, until April 2022 they are provided for the entire Mediterranean Sea. From then and continuing, they are available for each L1 product, including the Black Sea. The distribution of available OCN products is indicated in 2.

Segmentation examples are depicted in Table I.

III. Aggregated Maps

Due to multi-year measurements, the segmentation maps can be aggregated to observe the seasonal variability of the segmented phenomena. Fig. 3 contains the aggregation of the predicted biological slick segmentation during the summer and winter in the Alboran Sea, as well as the monthly evolution averaged between 2015 and 2022. The increased biological activity during the summer is clearly visible, rising interest in future collocation with other sensors such as Sentinel-3's radiometer. The distribution of the slicks also follows the Western Alboran Gyres, highlighting the capacity for biological slicks to provide information on currents.

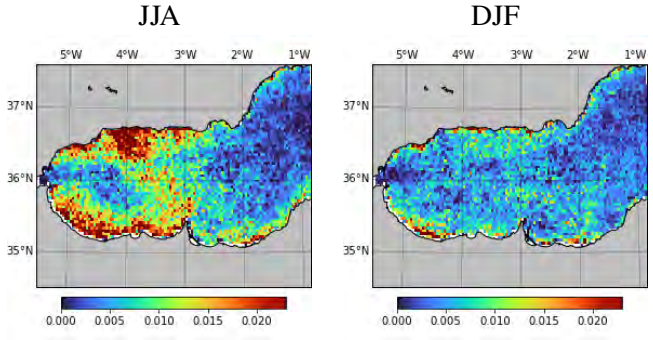

Fig. 3. Biological slick detection probability (restricted to points with wind speed between 6.5 and 12 m/s) during summer (left) and winter (right) in the Alboran Sea between 2015 and 2022.

Fig. 4 represents the probability of detecting convective processes in the Tyrrhenian Sea for wind speeds ranging from 6.5 to 15 m/s. Mean wind speed is also indicated. It highlights the impact of elevation on wind regimes over the sea surface. The correlation between convective processes and lower wind speeds is high, although some areas, such as the south and north of Sardinia, experience both high mean wind speeds and high probabilities of convection detection. We can also see a variation in mean wind speed in open waters with latitude that does not correspond to a variation in the probability of convection

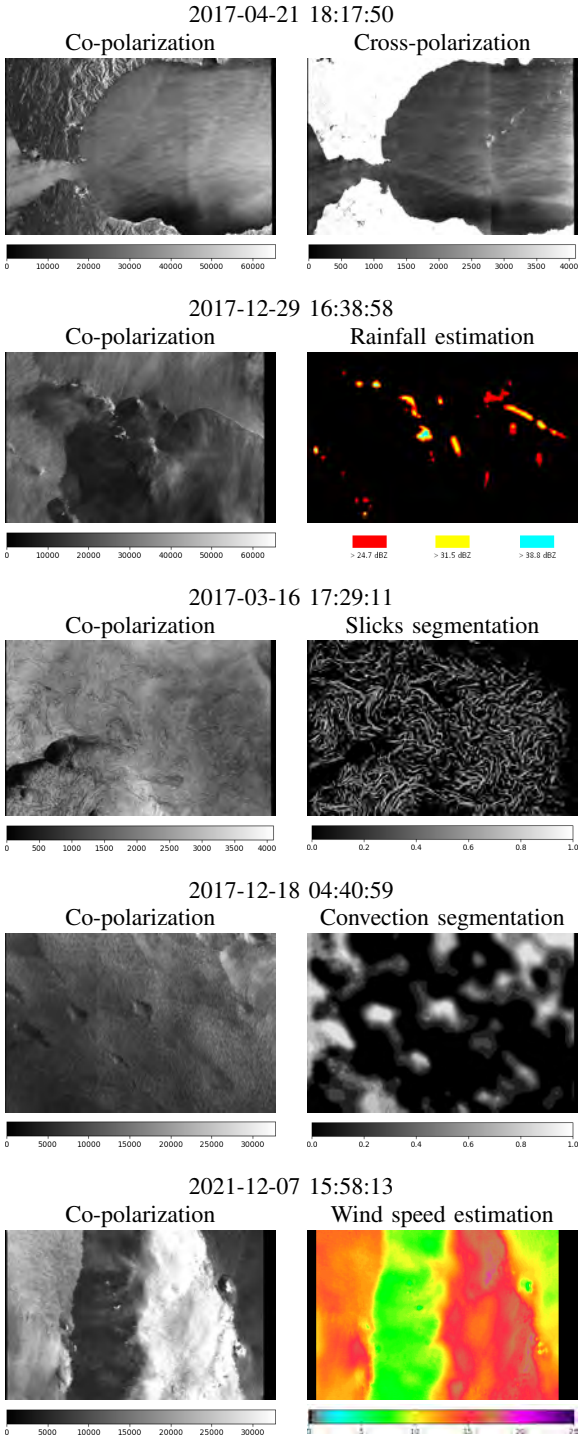

TABLE I
SAMPLES OF THE MEDISAR DATASET.

detection.

IV. CONCLUSION

To facilitate the diffusion of SAR-derived meteorological and oceanographic information, we present the MediSAR dataset. This dataset contains rainfall segmentation, biological slick delineation, convective process detection, and wind speed estimation. It includes the entirety of the Wide-Swath products over the Mediterranean Sea and the Black Sea from the Sentinel-1 mission as well as other satellite data from Sentinel-3 ans MSG. We hope this dataset will aid in the development of deep learning models, which heavily rely on large quantities of data, as well as simplify collocation with various sensors.

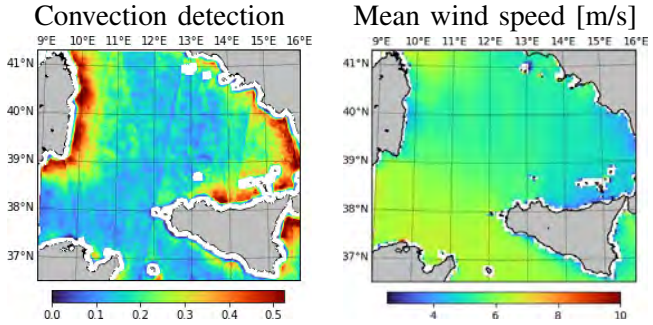

Fig. 4. Convection detection probability (left) and mean wind speed (right) in the Tyrrhenian Sea between 2017 and 2022.

REFERENCES

[1] Y. Lu, B. Zhang, W. Perrie, A. Mouche, X. Li, and H. Wang, "A c-band geophysical model function for determining coastal wind speed using synthetic aperture radar," in *2018 Progress in Electromagnetics Research Symposium (PIERS-Toyama)*, IEEE, Aug. 2018.

[2] A. Zanchetta and S. Zecchetto, "Wind direction retrieval from sentinel-1 SAR images using ResNet," *Remote Sensing of Environment*, vol. 253, p. 112178, Feb. 2021.

[3] J. Schulz-Stellenfleth, T. König, and S. Lehner, "An empirical approach for the retrieval of integral ocean wave parameters from synthetic aperture radar data," *Journal of Geophysical Research*, vol. 112, Mar. 2007.

[4] C. Alexandrov, N. Kolev, Y. Sivkov, A. Hristov, and M. Tsvetkov, "Oil spills detection on sea surface by using sentinel–1 SAR images," in *2020 21st International Symposium on Electrical Apparatus &amp Technologies (SIELA)*, IEEE, June 2020.

[5] C. Wang, P. Tandeo, A. Mouche, J. E. Stopa, V. Gressani, N. Longepe, D. Vandemark, R. C. Foster, and B. Chapron, "Classification of the global sentinel-1 SAR vignettes for ocean surface process studies," *Remote Sensing of Environment*, vol. 234, p. 111457, Dec. 2019.

[6] A. Colin, P. Tandeo, C. Peureux, R. Husson, N. Longepe, and R. Fablet, "Rain rate estimation with sar using nexrad measurements with convolutional neural networks," 2022.

[7] C. Wang, A. Mouche, P. Tandeo, J. E. Stopa, N. Longépé, G. Erhard, R. C. Foster, D. Vandemark, and B. Chapron, "A labelled ocean SAR imagery dataset of ten geophysical phenomena from sentinel-1 wave mode," *Geoscience Data Journal*, vol. 6, pp. 105–115, July 2019.

[8] L. Huang, B. Liu, B. Li, W. Guo, W. Yu, Z. Zhang, and W. Yu, "OpenSARShip: A dataset dedicated to sentinel-1 ship interpretation," *IEEE Journal of Selected Topics in Applied Earth Observations and Remote Sensing*, vol. 11, pp. 195–208, Jan. 2018.

[9] Y. Zhao, N. Longépé, A. Mouche, and R. Husson, "Automated rain detection by dual-polarization sentinel-1 data," *Remote Sensing*, vol. 13, p. 3155, Aug. 2021.

Using Ocean Surface Imagery to Estimate Atmospheric Boundary Layer Stratification

Justin E. Stopa - stopa@hawaii.edu
Ocean and Resources Engineering Department, University of Hawai`i at Manoa, USA

Ralph Foster - ralph@apl.washington.edu
Applied Physics Laboratory, University of Washington, USA

Doug Vandemark - doug.vandemark@unh.edu
Ocean Processes Analysis Laboratory, University of New Hampshire, Durham, USA

Chen Wang - cwang@nuist.edu.cn
School of Marine Sciences, Nanjing University of Information Science & Technology, Nanjing, China

Jonathan Chapman - jbchapma@hawaii.edu
Ocean and Resources Engineering Department, University of Hawai`i at Manoa, USA

Yannik Glaser and Peter Sadowski - yglaser@hawaii.edu, peter.sadowski@hawaii.edu
Information and Computer Sciences Department, University of Hawai`i Mānoa, USA

Alexis Mouche and Bertrand Chapron - Alexis.Mouche@ifremer.fr, Bertrand.Chapron@ifremer.fr
Univ. Brest, CNRS, IRD, Ifremer, Laboratoire d'Océanographie Physique et Spatiale (LOPS), IUEM, France

Statement of Problem

The air-sea fluxes of momentum, heat, and water vapor are crucial data records because they represent lower boundary conditions on the atmospheric circulation and upper boundary conditions of ocean waves and currents. They are of fundamental importance for improving our understanding of coupled atmosphere-ocean dynamics and efforts to model them. Global measurement of these fluxes using conventional fixed or moving systems is infeasible. Satellite-based measurements are the practical alternative source for estimating fluxes and this is one of the primary goals of satellite remote sensing. Sensible and latent heat fluxes are proportional to the imbalances between the near-surface temperature and humidity and their values at the sea surface multiplied by the difference between the near-surface wind speed and the surface currents. Standard remote sensing methods are capable of retrieving the surface values and the wind speed difference. However, retrieval of the near-surface temperature and humidity remains a major challenge. The proportionality factors are called bulk flux coefficients and they are functions of the air-sea stratification, which in turn describes the relative importance of shear and buoyancy in establishing the mean state of the turbulent near-surface atmospheric flow. While the coefficients vary continuously with stratification, one can think in terms of three basic states: buoyantly-driven, shear-driven, and stably-stratified as the stratification shifts from unstable to near-neutral to stable. Compared to unstable stratification, the sensitivity of the coefficients to stratification is higher in the near-neutral regime and the transition from near-neutral to stable is comparatively abrupt. Hence, the sensitivity of the fluxes to small errors

in temperature or humidity is high in the near-neutral regime. Since satellite retrieval of near-surface temperature and humidity at the precision and accuracy needed to estimate rather small imbalances is likely to remain quite difficult, novel remote sensing approaches providing independent information about air-sea stratification have a strong potential to improve ocean flux remote sensing.

Overview

Synthetic aperture radar (SAR) can implicitly measure the ocean surface roughness through the backscattered electromagnetic energy off the sea surface. Over the ocean, Sentinel-1 (S-1) defaults into wave mode (WV) and acquires very high resolution (5 m) small (20 km) images approximately every 100 km. It has been established that SAR captures information about ocean swells and the WV was originally designed to capture ocean gravity waves at the appropriate scales. However, WV has opened up new research opportunities to study the marine atmospheric boundary layer (MABL) because its high spatial resolution can resolve a wide range of MABL turbulent eddies and its 20 km field of view is large enough to capture many realizations of MABL-scale eddies. The two S-1 satellites, S-1A (2014-present) and S-1B (2016-2022), of the European Space Agency (ESA), each collect ~65,000 WV images covering approximately 3% of the globe every month. To date, more than 700TB of level-1 (L1) data has been accumulated. In order to take advantage of this vast resource, new methods are needed to extract useful information. Previous work from our team has established statistical image detection methods to automatically identify a wide range of geophysical phenomena including MABL organized eddy coherent structures (CS) that characterize unstable and near-neutral stratification. We further found that the lack of such characteristic MABL eddy structures (and frequently the ability to detect certain oceanic processes that can modulate the surface roughness) indicates stable stratification. The goal of this research is to further develop and expand this analysis and refine our predictions of air-sea stratification and consequently improve the retrieval of ocean surface fluxes. The following is an overview of the key outcomes of the work.

MABL State Detection:

We developed machine learning methods to sort millions of S-1 images into basic MABL state categories: wind streaks (WS), micro-scale convection (MC), and lack of any atmospheric signature with scales larger than 1000 m (negligible atmospheric variability ~NV). (Other interesting geophysical phenomena are also cataloged.) ERA5 atmospheric surface analyses have been time-space interpolated to each WV image providing consistent estimates of the air-sea stratification in terms of a bulk Richardson number (*Ri*). This systematic and global analysis of millions of SAR images shows that image textures are well correlated with *Ri* and define distinct unstable, near-neutral, and stable stratification regimes. That is, the different stratification regimes result in characteristic MABL mean states in which particular classes of coherent structures form and induce identifiable sea-surface roughness patterns. The bulk Richardson number is one of the key parameters controlling the bifurcation between the different turbulent states. The relationships between SAR-observed coherent structures and MABL state through *Ri* are robust and hold in overall averages, at seasonal/regional scales, and at MABL-process scales.

We expand the analysis to specific locations where we have detailed observations of the MABL turbulence and air-sea fluxes to check on the robustness of the results. We focus on two buoys: 1) the Coastal Pioneer Array buoy (CPA) off the US Northeast Coast and 2) the NTAS buoy in the

north Atlantic trade wind region near Barbados. The Pioneer buoy was selected because of the high interest in developing the area for offshore wind energy. The Barbados region and especially the MABL dynamics associated with its low-level clouds are of major climate research interest to understand how MABL processes affect Trade Wind Boundary Layer (TWBL) cloud formation and evolution. In both of these case studies, we rely on hand-labeled images to remove the potential uncertainties imposed by the machine learning detection model.

CPA is located in the mid-latitudes where stratification is generally closer to neutral. Of particular interest to the wind energy industry is the ability to characterize MABL stratification and the presence of MABL CS. This information is valuable because CS, especially MABL rolls can induce large wind stress divergence in the lower MABL and because the stratification plays an important role in characterizing energy production. We find that the NV, WS, mixed WS/MC, and MC cases are well mapped to *Ri* regimes. In particular, we find that the mixed WS/MC regime is intermediate to the WS and MC regimes, which indicates that the MABL bifurcation occurs through intermediate MABL states that combine the particular CS found in the extremes. This reinforces how closely tied the MABL state is to stratification. Consistent with the SAR/ERA5 results in the northern hemisphere mid-latitudes, we find that the more stable conditions are associated with predominantly southwesterly flow, the near-neutral flow with westerly flow, and unstable conditions with northwesterly flow.

At NTAS, one of our primary goals was to test Grossman's (1982) hypothesis that MABL underwent a major state bifurcation from roll to cells across a very narrow range of stratification. The hand-labeled images for this study refined the WS to MC transition regime across five categories and included surface features associated with boundary layer cloud processes. We confirm Grossman's hypothesis that the roll-to-cell transition occurs smoothly across a narrow range of *Ri* centered on the global WS/MC boundaries defined by the SAR/ERA5 comparison. We further found that the stratification/CS correlations hold even when significant sub-image variability is present.

Statistical Model Development:
One key aspect of this work is the continued development of statistical or machine learning models in order to analyze the continuing torrent of WV data. We place emphasis on improving the statistical models to detect phenomena in a more classic image detection problem. A novel approach through semi-supervised learning using uncategorized WV imagery has been implemented. Preliminary results suggest that this method is superior to more generalized models built on large and random sets of natural images. Besides the detection of the phenomena, we develop "regression" models to estimate air-sea stratification parameters like *Ri* and humidity-corrected air temperature directly from the SAR imagery. These regression models make no assumptions about what features are included in the SAR scenes. This leads us to the conclusion that atmospheric phenomena dominate the S-1 WV images. This new satellite-based approach that quantitatively estimates atmospheric stratification has implications for weather modeling and air-sea flux products.

Using SAR Imagery to Diagnose Tropical Cyclone Boundary Layer Mean State

Ralph Foster
Applied Physics Laboratory, University of Washington, Seattle, WA, USA

Alexis Mouche and Bertrand Chapron
Univ. Brest, CNRS, IRD, Ifremer, Laboratoire d'Océanographie Physique et Spatiale (LOPS), IUEM, 29280, Brest, France

The Canadian Space Agency (CSA) established the Hurricane Watch program in 1999 in collaboration with the Canada Centre for Remote Sensing (CCRS) and NOAA in order to capture wide-swath RadarSAT-1 C-band VV SAR images of the sea surface under Atlantic hurricanes. At the time this was a major challenge due to relatively long lead times for scheduling image acquisitions and comparatively less accurate tropical cyclone (TC) track forecasts. Over the years, lead times greatly shortened and track forecasts have become much more accurate. Presently we have nearly comprehensive global acquisitions of TCs through continuations of Hurricane Watch using RadarSAT-2 and RCM and through the Satellite Hurricane Observation Campaign (SHOC) at Ifremer in collaboration with the European Space Agency (ESA). SHOC was established in 2016 and its SAR component is mainly focused on Sentinel-1 C-band imagery, although RadarSAT images are frequently included. Importantly, these later SAR instruments provide both VV and VH images. This greatly expands the usefulness of the data since VV NRCS saturates in the range 35 to 40 m s^{-1} depending on the incidence angle. (Hurricane force wind is ~ 33 m s^{-1}.) VH NRCS, while being a much weaker signal, remains dependent on the surface wind speed to ~80 m s^{-1}, which puts major TCs in the range of quantitative analysis. Furthermore, VV NRCS has a strong dependency on the relative azimuth between the surface wind vector and the radar beam, while VH has only a weak azimuthal dependence. Hence, retrieving surface wind using VV alone requires relatively accurate surface wind directions while VV/VH TC imagery can be rapidly converted to wind speed with poor or no knowledge of the wind direction. Equally importantly, ESA has adapted a free-and-open data policy for Sentinel-1, which should soon lead to a major expansion of research and operational use of SAR TC data.

TCBLs are uniquely well-suited for quantitative study with SAR. TCs form and intensify over the ocean, which allows surface wind vector retrievals. They are quite compact storms so a single wide swath SAR image can capture most of “inner core”. Even though TCs are fueled by enormous air-sea enthalpy fluxes, the high winds force the TC boundary layer (TCBL) to a state of nearly-neutral stratification; the upper TCBL can even be weakly stably stratified. This simplifies the first-order analysis of the mean TCBL structure. A fluid dynamical consequence of the intense winds in near-neutral stratification is that the TCBL is essentially the paradigmatic boundary layer for the generation of turbulent coherent structures in the form of roll vortices. In fact, using data from both of the VV and VH images, the imprint of TCBL rolls, and a quantitative measurement of their orientation, is readily apparent in all regions of the TC. The routine combination of near-neutral stratification, reasonably accurate high-resolution surface wind vectors and TCBL roll orientation is unique in boundary layer studies. The value of this combination is due to the fact that TCBL roll orientation is highly sensitive to the vertical shear of the mean horizontal wind profiles.

This provides a possible pathway for diagnosing the mean state of the TCBL using SAR data in combination with a suite of analysis tools that were independently developed for TCBL studies.

The first tool is a nonlinear diagnostic similarity TCBL model framed as a boundary value problem. It includes the effects of curvature accelerations and both radial and vertical advection. Given reasonable estimates of the surface stress vector, the wind above the TCBL and an estimate of the eddy viscosity profile, it solves for the mean wind profiles. A first-order estimate of the surface stress can be made directly from the SAR surface wind vectors and suitable neutral drag coefficients (Cd). Recent field programs have provided much insight into Cd in the high wind regime, so the SAR images directly provide the lower boundary conditions (BCs). To first-order, TCs above the TCBL are in gradient and thermal wind balance. Hence, an estimate of the gradient wind can be used as upper BCs. It has been proven that for the same upper and lower BCs, quite different mean flow profiles result when a reasonable variety of assumed eddy viscosity models are used, including ones that are in general use in TC forecasting and research models. TCBL parameterization remains one of the major open questions in numerical modeling and comparatively little is known about the eddy viscosities in the TCBL. Most TCBL research flights were restricted to weaker regions of the storm and, for safety reasons, NOAA no longer flies in the TCBL. Since the TCBL model can accommodate essentially reasonable eddy viscosity profiles, the space of resulting mean flow profiles can be examined assuming there is a metric for evaluating the results.

The second tool provides the upper BCs for the similarity model. We employ a simplified version of the nonlinear similarity model to estimate the pressure gradient corresponding to each SAR surface wind vector. From this field of pressure gradients, we use ordinary least-squares to calculate the best fit pressure pattern, which can be converted to SLP given one or more pressure observations within the scene. Compared to drop sondes and depending on the metric used for evaluation, the SAR-derived TC SLP agree to ~4 mb. Gradient winds can be directly calculated from surface pressure gradients, which depend only on the shape of the sea-level pressure (SLP).

The third tool provides a means to evaluate the TCBL mean wind profiles that are inferred directly from the SAR images. TCBL roll orientation is highly sensitive to the mean shear profiles. This tool calculates the basic properties of the expected TCBL rolls given vertical profiles of the mean wind shear and eddy viscosity. The most fundamental property is the roll orientation. Hence, the evaluation steps after the generation of SAR surface wind vectors are: (1) Calculate the SLP pattern from the surface stress vector field; (2) Calculate the gradient vector for each SAR wind vector; (3) Map these results into a R-Z grid centered on the surface wind circulation center; (4) Calculate TCBL mean wind profiles for a range of eddy viscosity profiles designed to illuminate how details affect the resulting profiles; (5) Calculate expected roll orientations and compare against the SAR observations.

The results to date have been informative. The most commonly used TCBL parameterization is called YSU. Many recent investigations have challenged its validity, however, its simplicity and speed and robustness against model “blow-up” have kept it as the default in most applications. YSU enforces an eddy viscosity maximum at 1/3 the depth of the TCBL. Recent LES experiments indicate that the maximum should be closer to the surface. Our calculations support this contention, consistently better agreement in roll orientation occurs when the maximum value is closer to the surface, but the agreement reduces when it is too low. YSU also enforces a rapid

decrease in eddy viscosity with height above the maximum value, which has also been called into question. Again, we find improved roll orientation agreement when this assumption is relaxed. Preliminary comparisons of the SAR-derived mean TCBL wind profiles against aircraft tail Doppler radar along storm penetration radial flights are difficult. At present the SAR winds reproduce much of the variability, but seem to bias about 20% low. Example results for hurricane Fiona (2022) are below. Fiona is a very challenging case: very small Cat-2 storm close to land.

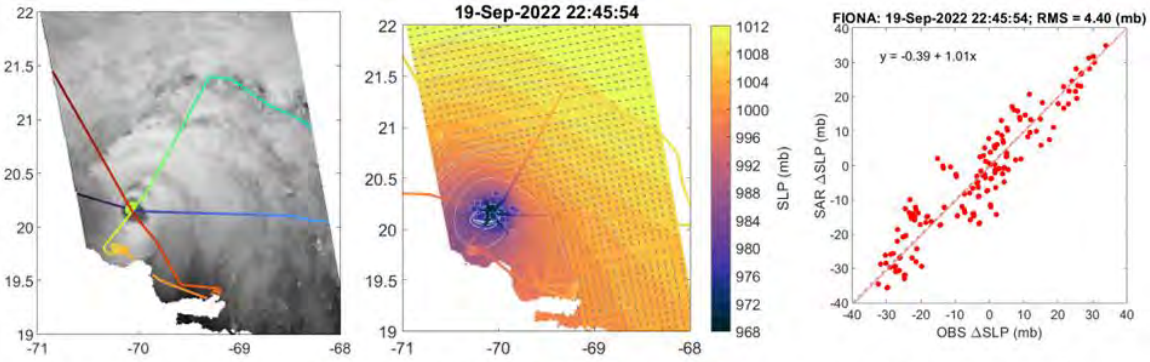

Figure 1: (a) Sentinel-1 image of hurricane Fiona (19 Sep, 2022) with P-3 flight tracks adjusted to overpass time. (b) SAR-derived SLP with TCBL roll orientations (gray). (C) N(N-1)/2 drop sonde pressure differences compared to SAR. Note that the Fiona was a very compact the RMW was heavily sampled, which leads to very high sensitivity to time-correction of observations to overpass time.

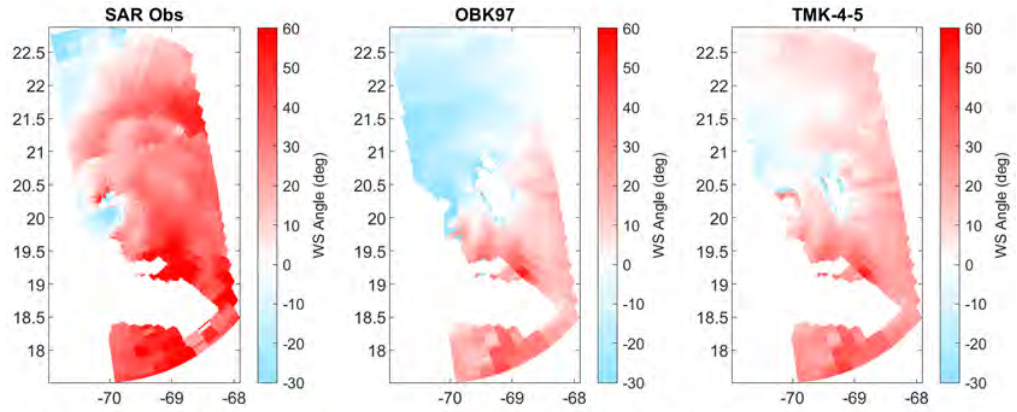

Figure 2: (a) SAR-observed roll orientation. (b) Calculated roll orientation using YSU-like eddy viscosity. (c) Calculated roll orientation with Zmax closer to the surface and reduced decrease of eddy viscosity above Zmax compared to YSU

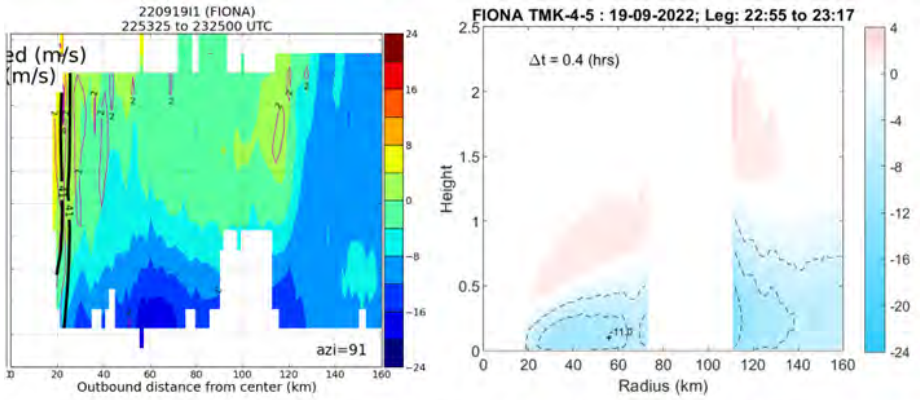

Figure 3: TCBL radial wind for hurricane Fiona (19 Sep 2022). (a) P-3 tail Doppler radar; (b) SAR-inferred.

An alternative approach for estimation of doppler centroid anomaly based on Level-0 SAR data

Yngvar Larsen, Geir Engen, Tom Grydeland, Temesgen Gebrie Yitayew

NORCE, Norway

Abstract

The radial velocity of the ocean surface is estimated from the doppler centroid anomaly (DCA), which is essentially the difference between the doppler centroid estimated from SAR data and the geometric doppler expected from a stationary target. DCA is usually estimated from azimuth correlation coeffients of an unfiltered Level-1 Single Look Complex (SLC) dataset in order to ensure spatial locality. Additionally, the use of focused data facilitate precise masking of land masses and strong targets, e.g. ships or icebergs.

However, algorithms for generation of SLC products have different performance criteria than DCA. In this work, we discuss an alternative approach for focusing of L0 SAR data, based on algorithmic variations that are more suited for the purpose of DCA estimation. The suggested approach is particularly relevant for data with range variable natural azimuth resolution, including Sentinel-1 TOPS and the Harmony mission.

1 Introduction

Estimation of the ocean radial velocity is an involved process [1]. In this work, we will limit the discussion to the precise estimation of the Doppler Centroid from SAR data. Other components of the DCA are system effects dependent on antenna patterns and satellite attitude. Analysis of these components are beyond the scope of this work.

2 Signal processing considerations

Estimation of the doppler centroid from SAR data with the precision required for the purpose of deriving the ocean radial velocity is challenging, and requires careful attention to azimuth temporal sampling. The basic estimator is based on the phase of the azimuth one-lag correlation coefficient [4]. However, in order to reach a precision of the order of 1 Hz, the basic estimator needs to be corrected by a sideband correction procedure due to the inherent azimuth aliasing of SAR data [1]. Successful sidelobe correction requires a critically sampled azimuth spectrum, and any azimuth resampling or bandwidth limitation in the azimuth direction will violate this.

2.1 The Sentinel-1 TOPS mode

The Sentinel-1 TOPS mode uses a linear electronic antenna sweep to enable scanning multiple subswaths, at the expense of azimuth resolution. The (range variable) azimuth time resolution

of TOPS SLC data is

$$\Delta t_{\mathrm{az}}(t_{\mathrm{rg}}) = \left(1 + \frac{\gamma}{|\beta(t_{\mathrm{rg}})|}\right) \mathrm{PRF}^{-1}, \tag{1}$$

where PRF is the pulse repetition frequency of the RAW SAR data, γ is the linear sweep rate of the antenna beam, and $\beta(t_{\mathrm{rg}})$ is the range variable doppler rate, see e.g. [2]. This range variable azimuth resolution is often referred to as *fan shape distortion*. In standard Sentinel-1 L1 products this spatial distortion is removed by resampling the data to a constant common azimuth pixel spacing. Furthermore, all bursts are additionally resampled to a common grid spacing. However, both these resampling operations are counterproductive and unnecessary for the purpose of DCA estimation.

We propose that for Sentinel-1 TOPS mode data, a better approach would be to simply avoid both these resampling operations. This leaves the azimuth spectrum sampled critically for all ranges, yielding essentially independent estimates of the azimuth correlation coefficients, and at the same time simplifying azimuth sideband correction.

2.2 The Harmony mission

The 10th Earth Explorer mission Harmony is a bistatic mission consisting of one of the Sentinel-1 satellites as the transmitter, and a pair of passive receiver satellites at a distance of 350 km in front of and behind Sentinel-1 in the orbit, respectively. Compared to the Sentinel-1 monostatic TOPS data, the high bistatic angle of this bistatic configuration poses some additional signal processing challenges that needs to be taken into account when designing a performant and accurate algorithm for DCA estimation. At high squint, the doppler centroid cannot be assumed to be wavelength independent. A procedure referred to as spectral extension is needed to ensure proper focusing of the azimuth spectrum [3]. However, spectral extension implies another resampling of the azimuth time axis that needs to be undone after focusing to facilitate azimuth sideband correction of the doppler centroid estimates.

3 Discussion

In this preliminary manuscript we have indicated an improved algorithm for precise doppler centroid estimation for the purpose of ocean radial velocity estimation, based on alternative processing of Level-0 SAR data. In the final version, we will elaborate on the details, and show the performance of the proposed approach using Sentinel-1 data. The implications for the Harmony mission will also be analyzed.

References

[1] Engen, G. ; H. Johnsen, "Sentinel-1 doppler and ocean radial velocity algorithm definition," ESA Doc. S1-TN-NRT-53-0658, ISBN 978-82-7492-311-9, ISSN 1890-5226, v1.6, 2022.

[2] Engen, G. ; Y. Larsen, "Efficient full aperture processing of TOPS mode data using the moving band Chirp Z-transform," IEEE Trans. Geosci. Remote Sens. 2011, 49, 3688–3693.

[3] Davidson, G.; I. Cumming, "Signal Properties of Spaceborne Squint-Mode SAR Gordon W. Davidson," IEEE Trans. Geosci. Remote Sens. 1997, 35, 611-617.

[4] Madsen, S. N. "Estimating the Doppler centroid of SAR data," IEEE Trans. Aerospace and Electronic Systems, 25, 134-140, 1989.

Applications: Maritime Security

Applications

Frost, Anja; Kortum, Karl; Wiehle, Stefan; Tings, Björn**.**
Ship Navigation Assistance For Polar Waters By Providing Information On Sea Ice Drift And Deformation Zones Using TerraSAR-X Data

Yang, Yi-Jie; Singha, Suman); Goldman, Ron
Integration of a Deep Learning Based Oil Spill Detection System into an Early Warning System for the Southeastern Mediterranean Sea

Blondeau-Patissier, David; Schroeder, Thomas; Suresh, Gopika; Li, Zhibin; Diakogiannis, Foivos; Steven, Andrew
Detection Of Marine Oil-like Features In Sentinel-1 SAR Images By Supplementary Use of Deep Learning and Empirical Methods

McGourty, Sara; Kaczor, Scott; Capsey, Austin
A Feasibility Study Into The Use of High-resolution Synthetic Aperture Radar (SAR) As A Novel Way Of Identifying Aids To Navigation

Gade, Martin; King, Dana
On the SAR Image Visibility of Heavy Fuel Leaking From the Wreck of a Sunken Vessel

Jones, Cathleen E, Johansson, Malin, Holt, Benjamin
Automation of Slick Detection and Classification for Improved Monitoring with SAR

Del Prete, Roberto; Graziano, Maria Daniela; Renga, Alfredo
AI-based Route Reconstruction on Multifrequency Multitemporal SAR Images

Ali, Muhammad; Schirinzi, Gilda; Afzal, Zeeshan; Hussain, Sajid
Impact of Sea Water Intrusion on Surface Deformation along the coastal areas of Pakistan using SAR Interferometry

Holt, Benjamin; Jones, Cathleen; Monaldo, Frank; Garcia, Oscar
Try, Try Again: Recent Steps Toward An Operational SAR-based Algorithm for Oil Spill Thickness Measurements

Bou-laouz, Moujahid; Vadaine, Rodolphe; Hajduch, Guillaume; Fablet, Ronan
Deep Learning For Ship Classification On Medium Resolution SAR Imagery

Zavagli, Massimo; Pastina, Debora; Santi, Fabrizio; Testa, Alejandro; Corvino, Michela; Morando, Elena; Pratola, Chiara; Costantini, Mario
Inverse SAR Processing for Maritime Situational Awareness

Lanz, Peter; Marino, Armando; Simpson, Morgan; Brinkhoff, Thomas; Köster, Frank; Möller, Matthias
Developing Refugee Vessel Detection Capabilities with Polarimetric SAR

Ship Navigation Assistance For Polar Waters By Providing Information On Sea Ice Drift And Deformation Zones Using TerraSAR-X Data

Anja Frost[1], Karl Kortum[1], Stefan Wiehle[1], Björn Tings[1]

[1]DLR (German Aerospace Center), Remote Sensing Technology Institute, Maritime Safety and Security Lab Bremen, Germany

Sea ice is subject to permanent changes. It arises as seawater freezes, and is drifted and deformed by winds and ocean currents, waves and temperature fluctuations. Within hours, leads of open water can be closed by drifting ice. If the drifting continues, pushing sections of sea ice together, floes are piled up forming an uneven surface, or pushed upright into pressure ridges. In other places, closed covers of sea ice can break, forming leads of open water. Hence, this can be either a severe hazard or a welcome opportunity for ships in polar waters.

Synthetic Aperture Radar (SAR) satellites make different structures within the sea ice visible. With their active radar antenna, they provide image data of the oceans and frozen waters through clouds and darkness. Since decades, national ice services utilize SAR images to create sea ice maps, which in turn are used for ship routing in polar waters. To further support the navigation in ice-infested waters, we established an operational data processing chain at the DLR ground segment. This allows to acquire and process SAR images of the German satellite mission TerraSAR-X along the planned ship course, as demonstrated in Figure 1, and provide them to navigators on board in near real time [1, 2]. The processing chain has been used in several research campaigns, amongst others the one-year-long MOSAiC expedition of *RV Polarstern*. It has been found that the support with these tailor-made, up-to-date TerraSAR-X data can help optimizing routes. To further support ship navigation, we aim to provide L2 products such as sea ice drift information automatically derived from subsequent SAR acquisitions.

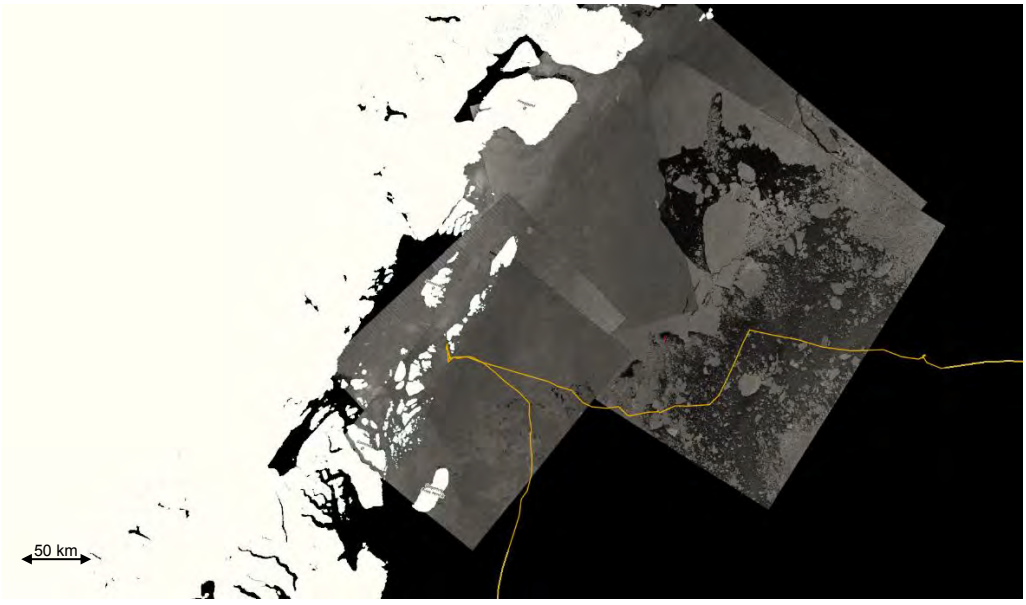

Figure 1: Ship navigation support during RV Polarstern expedition PS131 at east coast of Greenland through TerraSAR-X data supply along the planned ship route. Yellow: Ship track

In this contribution, we explore the capabilities of a new software processor that is intended to derive high resolution sea ice drift vector fields from subsequent SAR images, exemplarily shown in Figure 2. We quantize the accuracy of drift estimation using buoy data, and analyze the influence of different SAR parameters (i.e. incidence angle, heading, orbit direction), as well as different sea ice and metrological conditions. The drift vector estimation is based on the well-known phase correlation technique executed hierarchically in a multiscale Gaussian image pyramid. Phase correlation has first been applied in [3] for image pattern matching, and used for SAR based sea ice motion tracking in [4, 5]. We showed first experimental results of the general approach combining TerraSAR-X ScanSAR and RADARSAT-2 ScanSAR Wide acquisitions in [2] and [6] and first quantification of its accuracy using drift buoy data for validation in [7]. In the study presented here, we introduce a new iterative approach which fragments image patches in the last resolution level of the image pyramid in order to better represent sea ice drift at borders of different ice sheets. Inspired by the consistency check in [5], we re-estimate drift vectors iteratively in each resolution level until an update of zero indicates the best match is found, which results in increased accuracy.

Figure 2 exemplarily shows two drift vector fields derived from subsequent TerraSAR-X acquisitions taken on 25th, 26th, and 27th January 2020 during a storm event in Central Arctic. The drift vector fields show a quite homogeneous sea ice motion south- and eastwards, which supports the high reliability of the approach. Convergence and divergence zones become visible at the color jumps in the drift velocity map. Knowledge about the location and distribution of convergence and divergence zones as well as sheering zones helps for ship navigation in polar waters; in particular, convergence zones imply strong ice resistance difficult to pass even for icebreakers.

The sea ice drift retrieval presented here is part of the software suite SAINT developed at the DLR Maritime Safety and Security Lab Bremen. SAINT is integrated in the operational processing chain at the DLR ground segment in Neustrelitz and provides L2 products to maritime users, e.g. ship or iceberg detection. For reaching near real time requirements, we use parallel processing and hardware implementation on FPGAs.

References

[1] S. Lehner, T. Krumpen, A. Frost, R. Ressel, T. Busche, and E. Schwarz, “First Tests on Near Real Time Ice Type Classification in Antarctica,” *IEEE International Geoscience and Remote Sensing Symposium* (IGARSS), pp. 4876-4879, 2014.

[2] A. Frost, S. Wiehle, S. Singha, and D. Krause, „Sea Ice Motion Tracking from Near Real Time SAR Data Acquired During Antarctic Circumnavigation Expedition,” *IEEE International Geoscience and Remote Sensing Symposium* (IGARSS), pp. 2338-2341. 2018.

[3] E. De Castro, and C. Morandi. "Registration of translated and rotated images using finite Fourier transforms." *IEEE Transactions on Pattern Analysis & Machine Intelligence*, Vol. 5, pp. 700-703, 1987.

[4] J. Karvonen. Operational SAR-based sea ice drift monitoring over the Baltic Sea. In: *Ocean Science* 8.4: 473. 2012.

[5] T. Hollands. Motion tracking of sea ice with SAR satellite data. Diss. Universität Bremen, 2012.

[6] A. Frost, S. Jacobsen, and S. Singha, S., “High resolution sea ice drift estimation using combined TerraSAR-X and RADARSAT-2 data: First tests,” *IEEE International Geoscience and Remote Sensing Symposium (IGARSS)* (pp. 342-345). IEEE. 2017.

[7] A. Frost, S. Wiehle, and S. Jacobsen, “Accuracy of a Phase-Correlation Technique for Fully Automated Sea Ice Motion Retrieval based on Sequential SAR Images,” *SeaSAR* 2018.

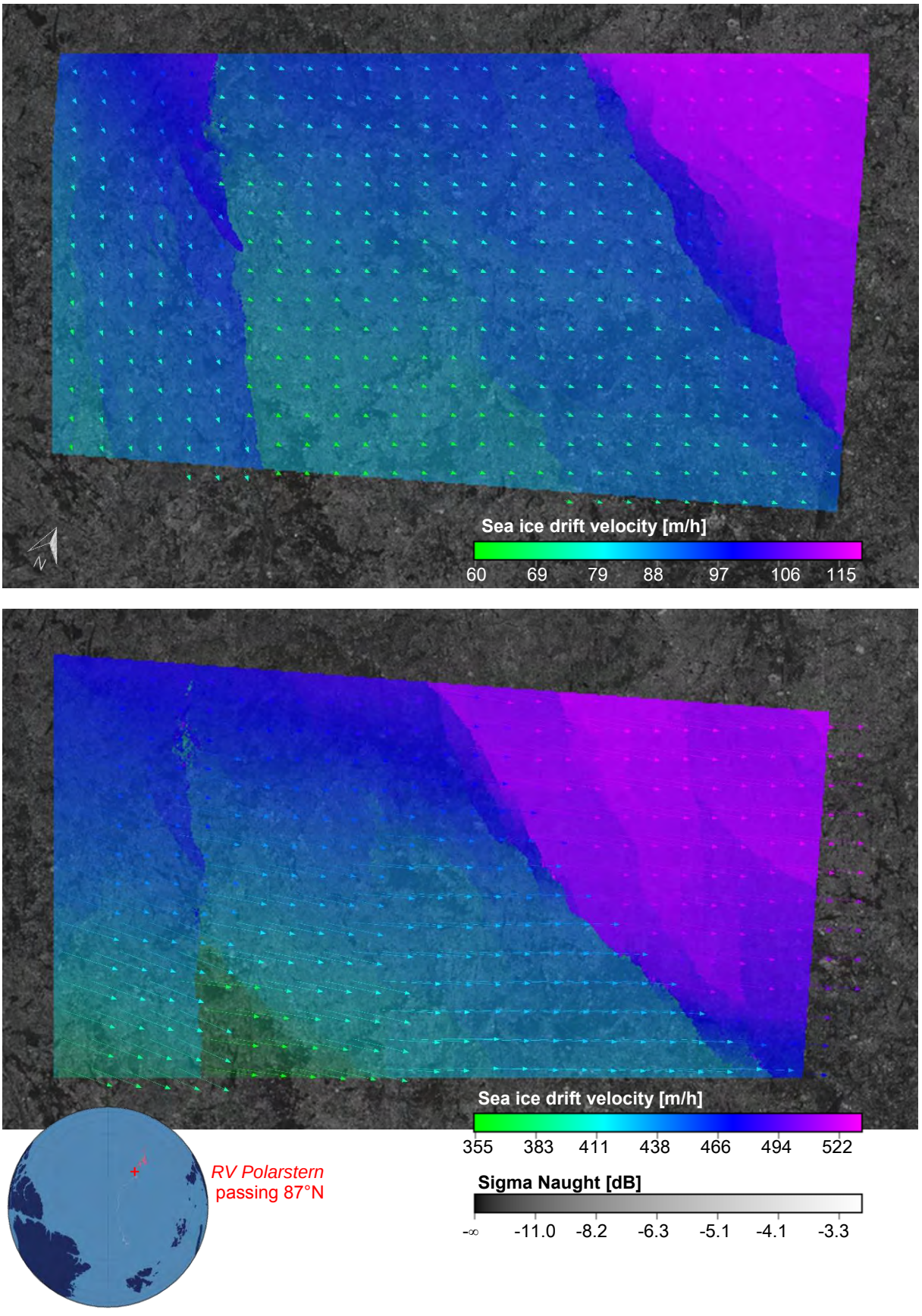

Figure 2: Examples for sea ice drift retrieval from TerraSAR-X data taken during MOSAiC expedition facing a storm event in late January 2020 in Arctic Ocean at 87°N. The background shows TerraSAR-X HH data from 2020/01/26 03:58 UTC (top) and 2020/01/27 03:41 UTC (bottom) in grey scale, calibrated to sigma naught. Overlaid colors represent retrieved sea ice drift velocity in 264 m resolution and arrows illustrate sea ice drift vectors (5 km spacing). The upper drift field is generated from TerraSAR-X acquisitions taken on 2020/01/25 and 2020/01/26, the lower from 2020/01/26 and 2020/01/27. Convergence and divergence zones become visible at the color jumps in the drift velocity map.

Integration of a Deep Learning Based Oil Spill Detection System into an Early Warning System for the Southeastern Mediterranean Sea

Yi-Jie Yang[1,2], Suman Singha[1†], Ron Goldman[3]
[1] Maritime Safety and Security Lab, Remote Sensing Technology Institute, German Aerospace Center (DLR), Bremen, Germany
[2] Research and Technology Centre Westcoast (FTZ), Kiel University, Büsum, Germany
[3] Israel Marine Data Center (ISRAMAR), Israel Oceanographic and Limnological Research (IOLR), Haifa, Israel
[†] Currently with National Centre for Climate Research (NCKF), Danish Meteorological Institute (DMI), Copenhagen, Denmark

Abstract

Deep learning based techniques have been applied in different environmental monitoring applications, including oil spill detection. This study aims to provide an oil spill detection and early warning system in order to take quick action for clean up operations for minimizing the environmental impact. Oil spills in the spaceborne Sentinel-1 Synthetic Aperture Radar (SAR) data are detected by a trained deep learning based object detector. The detections are then defined as binary masks by the segmentation method. Afterwards, the slick trajectory simulation is carried out. The system is running automatically on a regular basis when there are expected Sentinel-1 acquisitions. However, to avoid unnecessary clean up operations on false alarms, the system requires manual confirmation before sending a warning to the corresponding decision makers. The system performance should be evaluated with detailed analysis, but the feasibility of building such an automated oil spill detection and early warning system has been shown.

I. Introduction

Marine oil pollution from maritime accidents and illegal human-caused oil discharges can pose a great risk of environmental damage and have large-scale and long-term biological consequences. As an oil spill begins to weather and disintegrate into small fragments, it becomes difficult to recover the oil. Therefore, it is important to take action early to limit the spread of oil spills and predict their trajectory, which highlights the necessity of building an early surveillance system. With the advantages of wide coverage and frequent revisit, spaceborne SAR has been widely used in different environmental monitoring applications including oil spill detection. Oil spills appear as dark formations in SAR images as they dampen the gravity-capillary waves and thus reduce the backscatter. However, other phenomena also appear as dark formations (also known as look-alikes), which makes automated detection of oil spills challenging. Based on the large amount of accessible SAR data after the advent of Sentinel-1, a previous study highlights the possibility of detecting oil spills with a deep learning based object detection algorithm [1]. With this previous experience, this study aims to provide an automated oil spill detection system which targets oil spills in the Southeastern Mediterranean Sea on a regular basis. The detections are handed off to an existing oil spill trajectory simulator for predicting the influenced regions over time. The integration of the different parts into a complete early warning system can help with the oil combating response.

II. Methodology

This study focuses on oil spills in the Southeastern Mediterranean Sea within longitudes 31.5–36°E and latitudes 31–33.7°N. The overall structure of the proposed oil spill detection and early warning system is shown in Figure 1. The system includes four subsystems: satellite data processing, oil spill detection, forecast of synoptic condition and oil trajectory simulation. In the satellite data processing subsystem, Sentinel-1 SAR Level-1 Ground Range Detected (GRD) products are downloaded from Copernicus Open Access Hub on a regular basis and preprocessed with a series of corrections automatically with the use of Sentinel Application Platform (SNAP) Python API. Afterwards, a mosaic of latest preprocessed scenes covering the study area is formed and sent to the oil spill detection subsystem.

In the training stage of the oil spill detection subsystem, different scenarios were carried out to train the deep learning based You Only Look Once version 4 (YOLOv4) object detection algorithm [2] on detecting one-class (i.e. oil spill) objects. In the detection stage, the trained detector targets oil spills inside mosaics and defines their positions by bounding boxes. In order to obtain the exact areas covered by the respective oil spills, segmentation is applied. The output binary masks are handed off to the oil trajectory simulation subsystem. The simulation of oil spill trajectory and fate requires oil spill incident detail and forecasts of synoptic conditions, such as wind, sea current and sea water temperature. The MEDSLIK model [3] then simulates physical processes of oil spill incidents with respect to evaporation, diffusion, dispersion, emulsification, and beaching. The simulation results are available via an online interface enabling users to perform their own simulations and visualize the results.

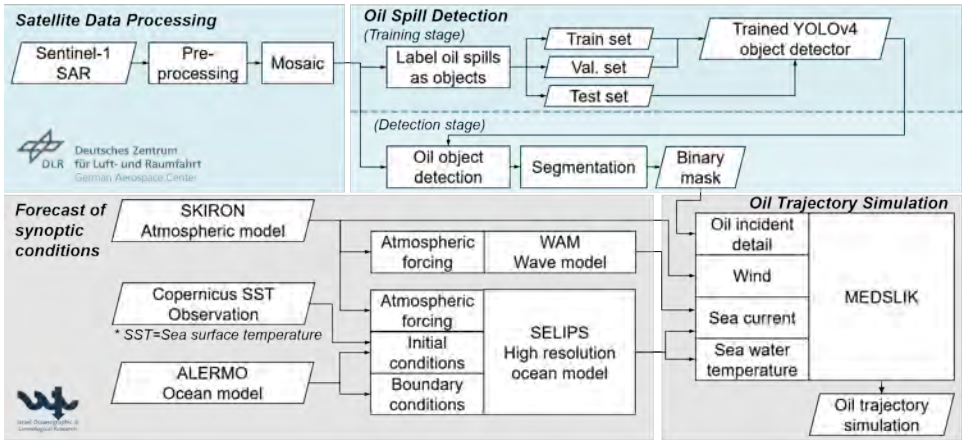

Fig. 1. An overview of the purposed oil spill detection and early warning system.

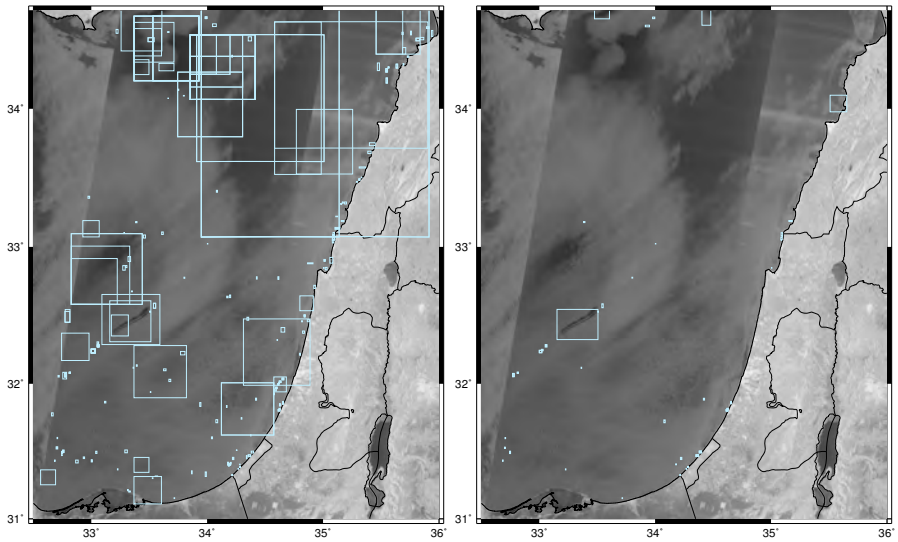

(a) (b)

Fig. 2. An example of detections from the oil spill detection subsystem using (a) the trained detector from the previous study [1] and (b) the implemented detector.

The satellite data processing and oil spill detection subsystems are developed and maintained by DLR. The forecast of synoptic winds is provided by the SKIRON system from the university of Athens, and the forecasts of sea currents and waves are performed by IOLR. The oil trajectory simulation subsystem and its connected user interface are maintained by IOLR.

III. Results

In the previous study, 9768 oil spills were used to train a YOLOv4 object detector. It reached an average precision (AP) of 69.10 % and 68.69 % on the validation and test sets, respectively [1]. This showed the ability of finding oil spills from the given image patches and highlighted the possibility of building an efficient oil spill detection system on regular SAR acquisitions based on the trained detector.

To illustrate how oil spills are detected in the oil spill detection subsystem, a selected case at 03:43 on 24 June 2019, with not only oil spills but also some other phenomena which appeared as dark formations, is used in the following. Figure 2(a) shows the detections from the trained detector. However, there are lots of false alarms. As all the image patches used for training the object detector include at least one oil spill, look-alikes were only learned as background information by the detector when they were near oil spills. Therefore, to further improve the detector, image patches without oil spills, but look-alikes or other remarkable features, were included in the training. Note that these image patches were not given any annotation and therefore considered as background. Figure 2(b) shows great improvement on avoiding the detection of look-alikes by the improved detector. Such an improved detector is applied in the oil spill detection subsystem running on a regular basis.

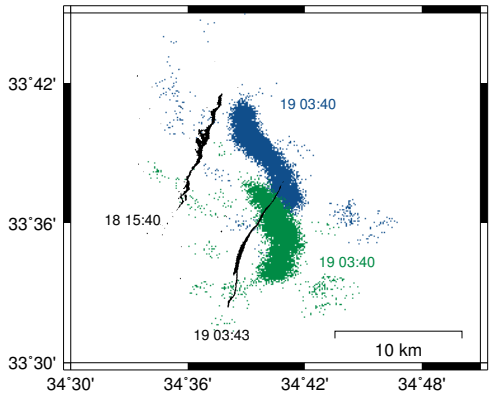

Fig. 3. An example of oil spill detections in consecutive Sentinel-1 SAR data at 15:40 on 18 August 2022 and at 03:43 on the next day (in black). With the second observation from Sentinel-1, additional information could be provided to validate and correct the trajectory forecast. The trajectory of the original simulation for 12 hours after the first observation is displayed in blue, and the corrected one is shown in green.

After the oil spills are detected, they are segmented into binary masks and delivered to the MEDSLIK model for trajectory simulation. It uses daily forecasts of synoptic conditions and generates hourly estimation of the slick trajectory. The trajectory simulation shows users the possible areas influenced by oil spills in the next few days. In some cases, the revisit time is short enough so that consecutive passes detect the same oil spill at different stages of its trajectory. In these cases, the new detection can be easily attributed by the users to the older detection and they may use the new information to validate the trajectory forecast. The system also provides an option to correct the simulation with the new location. This can be done internally in MEDSLIK, which adds a velocity modification computed from the displacement vector between the centroid of the new observation and the corresponding location in the original simulation. Alternatively, the system can search by external iteration for the optimal velocity modification. This is suitable when the spatial variation of the velocity (e.g. strong shear, circulation around bays or islands) makes the internal correction method inaccurate. As an example, Figure 4 illustrates a user-made simulation with internal MEDSLIK correction based on the new observation. The black oil spill binary masks shows the observations from Sentinel-1 at 15:40 on 18 August 2022 and the consecutive observation after 12 hours. The unmodified velocity in the original simulation (in blue) was westward with shear such that there is stronger velocity at the south of the slick. The corrected simulation (in green) pushed the slick southwest towards the observation. However, the resulting shear caused incorrect deformation of the slick.

IV. Conclusion

An automated and operational oil spill detection system was demonstrated and integrated into an early warning system in the Southeastern Mediterranean Sea for minimizing the environmental impact of oil spill events. The whole system is currently operating on a regular basis, which helps reduce the time spent on manual check and annotation. Based on the estimated slick trajectory, further information, which is often needed for large oil spills but not derivable from SAR, such as oil type and oil thickness, can be gathered with different sensors. Afterwards, strategies for combating the oil slicks can be developed according to oil type, sea state, the habitats of the influenced regions, available response resources, and so on. To avoid false alarms, the system requires manual confirmation before sending a warning to the corresponding decision makers. Further detailed analysis on performance regarding detectability, false alarm rate and accuracy of the numerical forecasting is required, but the feasibility of building an automated oil spill detection system is shown. Continuous tracking of small slicks can be used in future studies, to deduce velocities which will be assimilated back to correct the circulation model. Furthermore, with the experience of building such a system for the Southeastern Mediterranean Sea, extending the study area to global oil spill hotspots is foreseen.

Acknowledgements

This study is part of the DARTIS project, funded by the German Federal Ministry of Education and Research and the Israeli Ministry of Science and Technology under project ID 03F0823B and 03F0823A, respectively.

References

[1] Y.-J. Yang, S. Singha and R. Mayerle, “A Deep Learning Based Oil Spill Detector Using Sentinel-1 SAR imagery,” International Journal of Remote Sensing 43 (11), pp. 4287–4314, 2022.
[2] A. Bochkovskiy, C.-Y. Wang and H.-Y. M. Liao, “YOLOv4: Optimal Speed and Accuracy of Object Detection,” arXiv preprint arXiv:2004.10934, 2020.
[3] G. Zodiatis, R. Lardner, D. Solovyov, X. Panayidou and M. De Dominicis, “Predictions for Oil Slicks Detected from Satellite Images Using MyOcean Forecasting Data,” Ocean Science 8, pp. 1105–1115, 2012.

Detection of marine oil-like features in Sentinel-1 SAR images by supplementary use of deep learning and empirical methods: Performance assessment for the Great Barrier Reef marine park.

Abstract

Continuous monitoring of oil discharges in coastal and open ocean waters using Earth Observation (EO) has undeniably contributed to diminishing their occurrence wherever a detection system was in place, such as in Europe (EMSA's CleanSeaNet) or in the United States (NOAA's OR&R). This presentation will showcase the development and testing of a semi-automated oil slick detection system (**Figure 1**) tailored to the Great Barrier Reef marine park solely based on Sentinel-1 SAR data as no such service was routinely available in Australia until recently. We will also present portions of a large, curated, historical global dataset of SAR imagery (**Figure 2**) acquired by Sentinel-1 SAR that we have made publicly available specifically for the development and testing of deep learning models for marine oil-features detection. In this study, three different methods, namely a rule-based empirical approach, a deep learning model and a combination of the two in sequence, have been tested to discriminate between oil-like features and look-alikes (e.g **Figure 3**) in the scenes acquired over the marine park. We will show that the classifiers perform best when both the empirical and deep learning methods are combined, rather than when used separately. This study will demonstrate the benefit of sequentially combining classifiers to improve the detection and monitoring of unreported oil discharge events in SAR imagery. The workflow has also been tested outside the marine park, and examples applied to other regions such as Australia's Northwest Shelf and Southeast Asia will complement this presentation.

Key highlights

- Development of a semi-automated oil-like features detection system using C-band Sentinel-1 SAR.
- Classification of oil-like features based on a sequential approach combining machine learning and rule-based methods.
- The proposed approach achieves reliable oil-like features detection in the Great Barrier Reef marine park.
- An image dataset suitable for deep learning model development is made available publicly to the community.

Figures

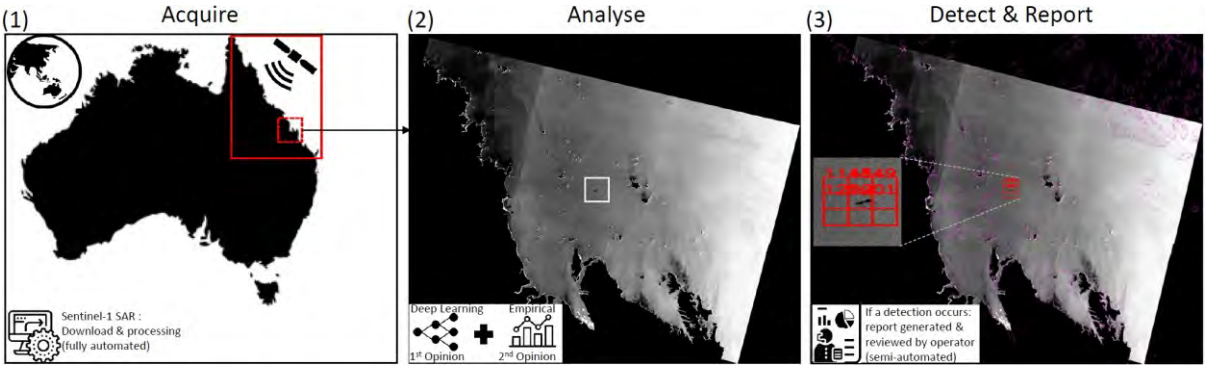

Figure 1 The study summarized in a 3-image sequence.

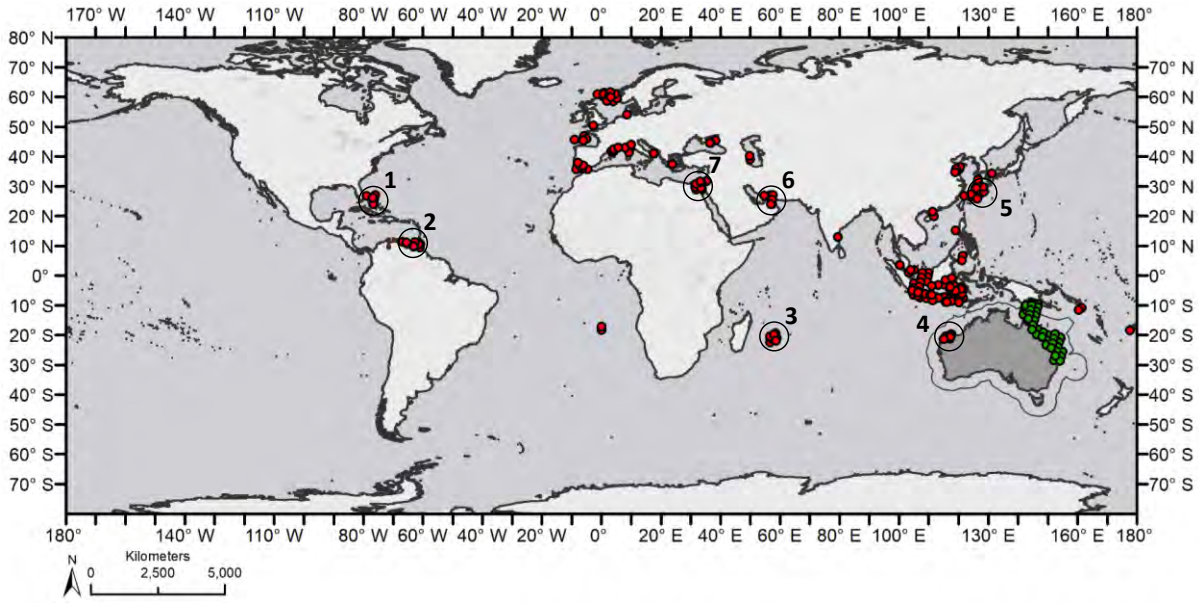

Figure 2 The CSIRO oil spills database: locations of oil spill events with matching SAR imagery from which the 400x400 pixel chips dataset has been derived and can be used for deep learning model development. (Publicly accessible at https://data.csiro.au/collection/csiro:57430)

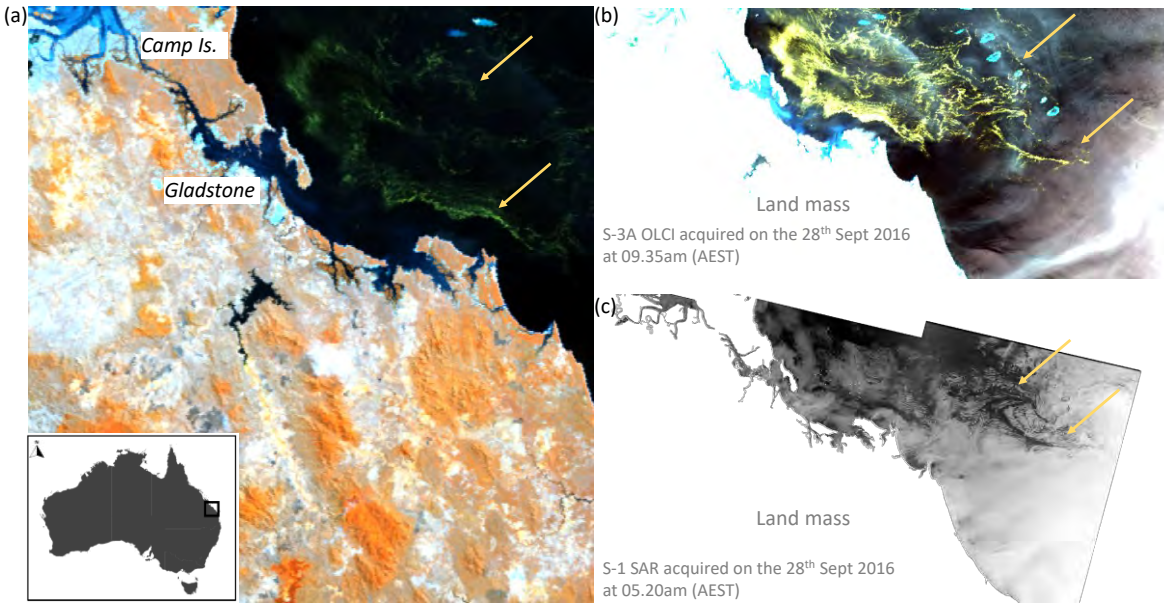

Figure 3 Trichodesmium spp. surface bloom event seen in coincident acquisitions by Sentinel-1A SAR and Sentinel-3A OLCI scenes on the 28 September 2016.

SEASAR2023 – Extended Abstract

A feasibility study into the use of high-resolution Synthetic Aperture Radar (SAR) as a novel way of identifying Aids to Navigation

Scott Kaczor & Sara McGourty - Remote Sensing Team, United Kingdom Hydrographic Office

There is an operational need to identify, position and monitor navigational buoys and beacons in distant or remote locations where persistent cloud cover precludes the use of optical imagery. Aids to Navigation (AtoN) vary in material composition and size therefore Sentinel-1 is of insufficient resolution to detect these smaller features (Figure 1). Launched in 2018, NovaSAR-1 was developed by SSTL (Surrey Satellite Technology Ltd) and AIRBUS and operates in S-Band frequency (Bird et al 2013, Whittaker et al 2021, Zhou et al 2020). In this investigation the higher resolution 6 m Stripmap product has been assessed for its performance in detection of AtoN. Backscattering from objects on a comparatively smooth horizontal sea surface will be expected to appear as bright targets in a SAR image. This has proven successful for the detection of larger objects such as ships where it has become a tried and tested approach (Crisp 2004, Iervolino et al 2013, Achiri et al 2018). Little research has been undertaken on applying the same methodologies to detecting smaller objects. This study utilises higher resolution SAR now that it has become more widely available.

This study posed the following questions:

1. Is high resolution S-band NovaSAR-1 suitable for detection of AtoN?
2. Does the physical size, shape, and construction material of the AtoN impact detectability?
3. Is there a limiting set of sea-surface conditions under which AtoN are no longer distinguishable from ambient sea surface roughness?
4. Is there a preferred combination of sensing parameters?
5. What is the horizontal positional accuracy of NovaSAR-1 without GCPs and to what degree would GCPs improve positional accuracy?
6. Is there correlation between presence of a radar reflector on the AtoNs and their visibility in NovaSAR-1?

Based on results from a selected range of AtoN present in Plymouth Sound and entrance to Tamar River, AtoN can be detected with NovaSAR-1 but not consistently or predictably. The size, shape, material, and angle at which the radar pulse reaches an AtoN are all influential in strength of the backscatter signal and therefore in its detection. Beacons such as Figure 1.A a steel pile with radar reflector resulted in a strong signature, the vertical nature of the construction produces a backscatter double bounce and possible volume scattering due to the complexity of its shape (Figure 2.A). The simpler form of the steel Admiralty Mooring Buoy with no radar reflector (Figure 1.H) elicits a much weaker backscatter signal (Figure 2.H) however this may also be due to orientation to radar pulses at time of image collect.

The evidence provided by assessment of weather conditions concurrent to the collection dates and times of the SAR images suggest weather conditions specifically windspeed have the most significant impact on detection. The increased surface roughness or 'sea clutter' due to wind reduces the contrast in backscatter between the surrounding water and AtoN decreasing the likelihood of positive identification (Figure 3). This may be exacerbated by relative directions of wind and tidal stream and can be localised across an image.

The images captured at night on a Descending orbit provided best results, this is assumed to be an artefact of the likelihood of lighter winds in coastal regions during the night resulting in smoother sea surfaces. HH polarity images provided most positive results, this is as expected from previous studies

but can also be linked to incidence angle (Crisp 2004: 21; Saini et al 2020: 117). With multiple combinations of environmental and geometric parameters affecting backscatter (Crisp 2004: 20-23), due to the small sample size of images in this study further investigation will need to be done to assess the impact of this with S-band NovaSAR-1.

The main issues have been quantifying the visibility of small structures and making this systematic when structures are variable in form, size, and material. A more significant number of images need to be assessed now it is clear objects such as AtoN are visible in high resolution S-band NovaSAR-1. A further study in a new geographic area is being undertaken to identify if these results can be replicated and improved on, identifying a method for quantifying visibility would reduce error in interpretation of results. Sea state was not measured directly at the time of capture due to a lack of appropriate instrumentation installed in the Plymouth locale. However, it has become possible to collect concurrent sea state data by GNSS Reflectometry (Yu et al 2022). This would allow sea surface roughness and its effects on image contrast to be assessed objectively in future studies.

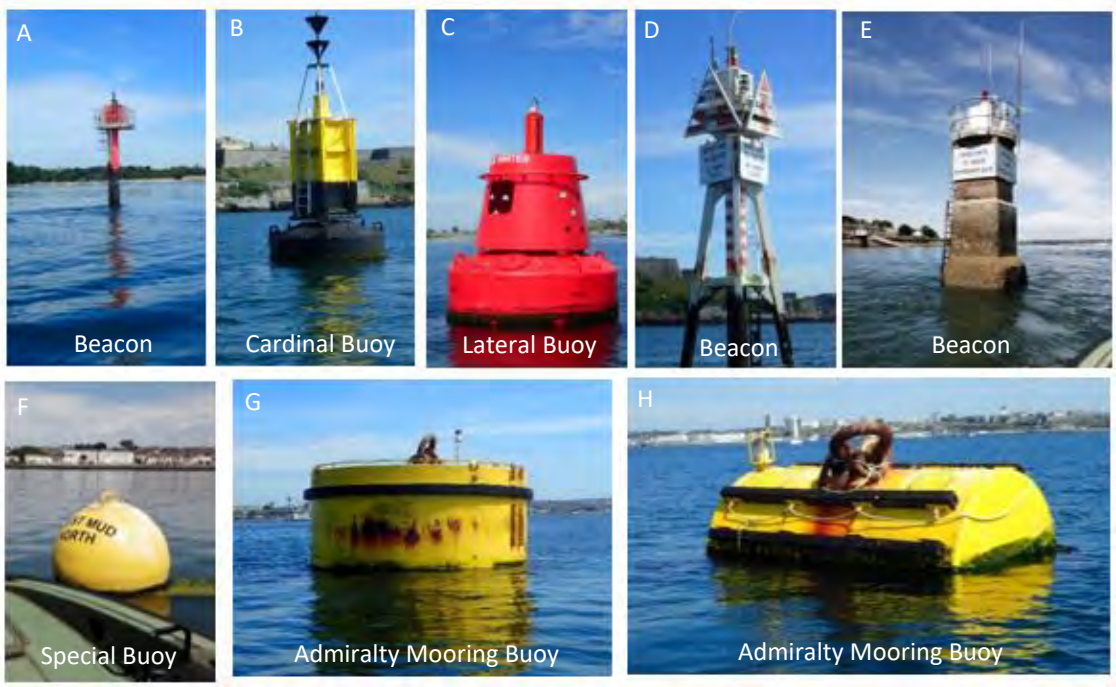

Figure 1. A – H show examples of the range of shapes, sizes and construction materials of AtoN in Plymouth Sound (Images©Sara McGourty).

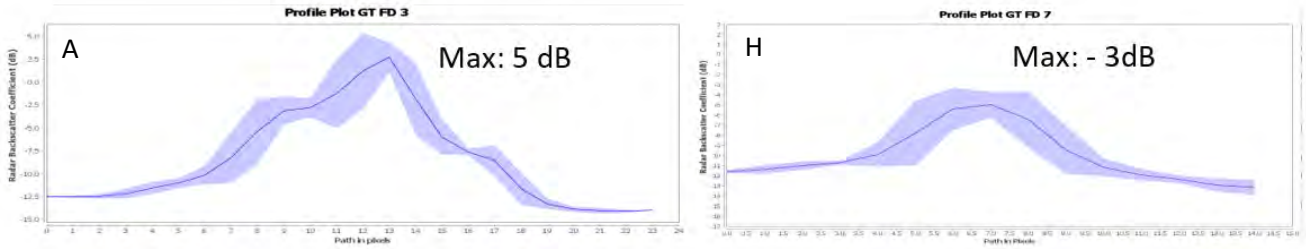

Figure 2. Example profile plots showing differences in strength and pattern of radar backscatter between forms of AtoN: Beacon A (Figure 1.A), Admiralty Mooring Buoy H (Figure 1.H)

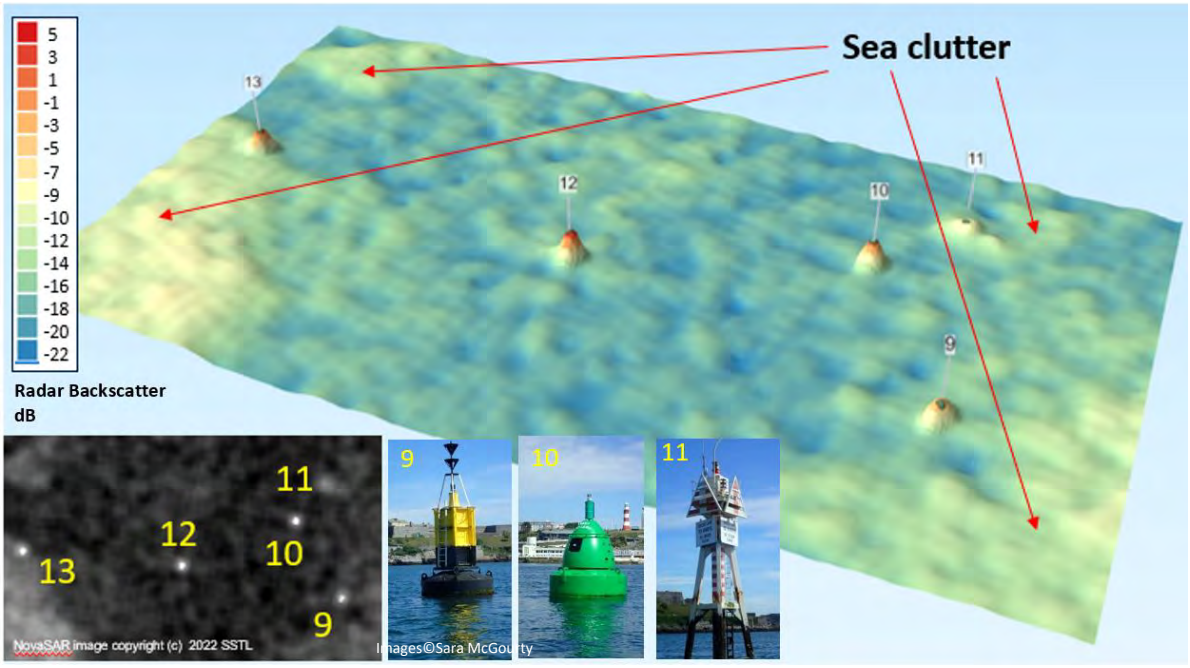

Figure 3. AtoN 9 to 13 visible in NovaSAR-1, the 'sea clutter' return from turbid water could mask backscatter signals from AtoN 11 without supporting ground truth data.

References

Achiri, L., Guida, R. and Iervolino, P., 2018, June. Collaborative use of SAR and AIS data from NovaSAR-S for Maritime Surveillance. In *EUSAR 2018; 12th European Conference on Synthetic Aperture Radar* (pp. 1-6). VDE.

Bird, R., Whittaker, P., Stern, B., Angli, N., Cohen, M., & Guida, R. "NovaSAR-S: A low-cost approach to SAR applications," Conf. Proc. 2013 Asia-Pacific Conf. Synth. Aperture Radar, APSAR 2013, pp. 84–87(2013).

Couchman-Crook, R., et al. "NovaSAR and SSTL S1-4: SAR and EO Data Fusion." Proceedings of SmallSat Conference, Logan, Utah, August 2020.

Crisp, D.J., 2004. *The state-of-the-art in ship detection in synthetic aperture radar imagery*. Defence Science and Technology Organisation Salisbury (Australia) Info Sciences Lab.

Iervolino, P., Guida, R. and Whittaker, P., 2013, July. NovaSAR-S and maritime surveillance. In *2013 IEEE International Geoscience and Remote Sensing Symposium-IGARSS* (pp. 1282-1285). IEEE.

Saini, O., Bhardwaj, A. and Chatterjee, R.S., (2020, March). Analysis of Back-Scattering Coefficient of NovaSAR-1 S-Band SAR. In *Proceedings of the National Seminar on Recent Advances in Geospatial Technology and Application, Dehradun, India* (pp. 117-122).

Whittaker, P., Doody, S., Cohen, M., Schwarz, B., Burbidge, G. and Bird, R., 2021, March. NovaSAR-1–Early mission achievements. In *EUSAR 2021; 13th European Conference on Synthetic Aperture Radar* (pp. 1-4). VDE.

Yu, K., Han, S., Bu, J., An, Y., Zhou, Z., Wang, C., Tabibi, S. and Cheong, J.W., 2022. Spaceborne GNSS Reflectometry. *Remote Sensing*, *14*(7), p.1605.

Zhou, Zheng-Shu & Parker, Amy & Brindle, Laura & Rosenqvist, Ake & Caccetta, Peter & Held, Alex. (2020). Initial NovaSAR-1 Data Processing and Imagery Evaluation. *IGARSS 2020 - 2020 IEEE International Geoscience and Remote Sensing Symposium*, Waikoloa, HI, USA, 2020, pp. 6154-6157.

SeaSAR 2023, Extended Abstract

SAR observation of internal waves generated by sub-mesoscale frontal features in the Strait of Sicily

Werner Alpers

University of Hamburg, Institute of Oceanography, Hamburg, Germany

Francesco Bignami

ISMAR-CNR Sede Secondaria di Roma, Rome, Italy

1. Introduction

SAR images acquired over the ocean from space have turned out to be game changers in internal wave research. It were Seasat SAR images that revealed for the first time that internal waves (IWs) are generated in the Strait of Messina (Italy) and that IWs are abundant off the coast of Portugal. Later satellites carrying SARs, among them ERS, Radarsat, ALOS, and Envisat detected IWs many areas in the World Ocean where the presence of IWs was not known before (Jackson, 2004). Based on these satellite observations, theoretical models have been developed to describe the generation and propagation of long-wavelength IWs generated by interaction of tidal flow with bottom topography. However, in the last years several authors suggested that short-wavelength (0.1 – 1 km) IWs may also be generated by sub-mesoscale features in the ocean without any external forcing, e.g., at sharp density fronts or by sub-mesoscale eddies (SMEs). In this regime, large strains and shears occur that should can give rise to emission of IWs. Several mechanisms have been proposed to model their generation, which include: 1) spontaneous generation in unbalanced, large Rossby number flows in the absence of direct forcing (Shakespeare and Hogg, 2017, 2018), 2) generation from a thermally stratified diurnal warm layer by Kelvin-Helmholtz instability (Wijesekera et al., 2020), and 3) generation from a turbulent mixed layer by the ‘‘mechanical oscillator effect’’ (Ansong and Sutherland, 2010) or the ‘‘obstacle mechanism’’ (Clark et al., 1986; Czechel and Eden, 2019). However, all these theories suffer from the fact that they are difficult to verify by means of observational data, since the phenomena have small scales and are very intermittent. Here we present Sentinel-1 SAR images, in conjunction with SST images, acquired over the Adventure Bank (AB) in the Strait of Sicily, showing sea surface signatures of short IWs generated by SMEs and filaments. Filaments are elongated structures of cold water (typically 100 km long and 10 km wide) that extend from the south coast of Sicily southwards into the Strait of Sicily, which are generated in the wake of upwelling events at the southern coast of Sicily. They become visible on infrared and optical images as bands of reduced SST and enhanced Chl-a values, respectively, and on SAR images as bands of reduced radar backscatter.

2. Oceanography of the study area.

The Adventure Bank is a shallow area in the western section of the Strait of Sicily, with an average depth of 80-100 m and a steep slope, in particular to the west and the south. Its topography is quite rough (due to its volcanic origin) with several small shallow (less than 50 m) bumps with width of order 1 km. In summer and early autumn, there is a strong warm

upper layer with an average depth of about 20 m present over the AB. The depth of this layer varies greatly with time and position and can attain values as thin as 5 m. The tidal flow in the AB region, which has a mix of diurnal and semi-diurnal periodicity, is generally quite weak (about 10 to 20 cm/s). Upwelling occurs between June and October typically 5 to 10 times each year, following strong northwesterly wind events, in particular Mistral outbreaks, issuing from the Gulf of Lions (NW Mediterranean Sea) and blowing along the south coast of southern Sicily.

3. Example of internal waves associated with a filament

Fig. 1a shows an SST image acquired over the AB on 13 July 2021 at 20:05 UTC. Visible is a filament as a band of reduced SST values (greenish color) emanating from the upwelling area at the southwest coast of Sicily and terminating in a mushroom-type feature. Fig. 1b shows a section of a Sentinel-1A image acquired over the area marked in Fig. 1a by a red rectangle on 13 July 2021 at 20:05 UTC. The darkish area is the area of cold surface water representing the filament. Internal waves are radiating from is sharp western boundary. The sharp front is a result of frontal sharpening.

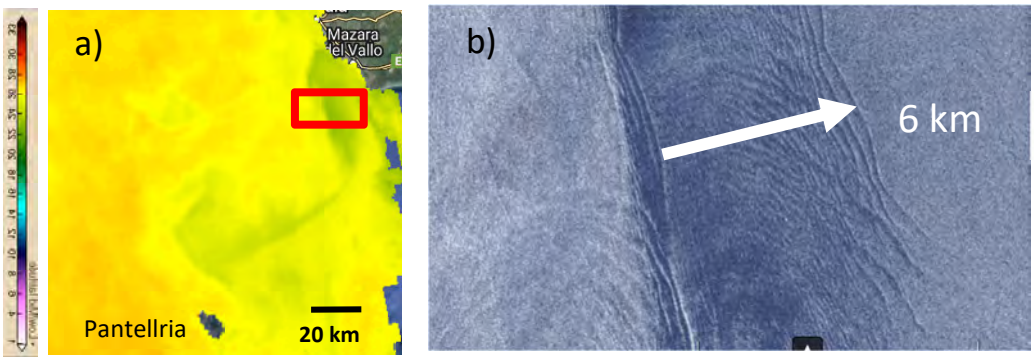

Fig. 1. a) Sentinel-3B SST image (SLSTR) acquired over the northwestern section of the Strait of Sicily on 13 July 2021 at 20:05 UTC; b) Sentinel-1A image acquired over the section marked by a red rectangle in Fig. 1a on 13 July 2021 at 17:13 UTC.

Fig. 2 shows two SST images acquired at a time separation of one day. Together with Fig. 1a, they demonstrate the strong dynamics of the filament. Its shape and position varies strongly from day to day causing a strong lateral displacement of cold water.

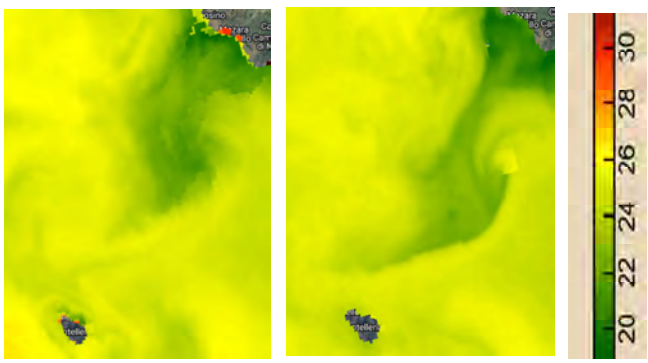

Fig. 2. a) Sentinel-3A SST image of 14 July 2021 at 21:13 UTC; b) Sentinel-3A SST mage of 15 July 2021 at 20:47 UTC. Color scale in ^{o}C

4. Example of internal waves associated with a sub-mesoscale eddy

Fig. 3a shows a GHRSST SST image acquired over the AB on 28 June 2017. Visible is a filament as a band of reduced SST values (yellow color), which terminates to the south in a broad patch (marked by a rectangle), which we interpret as the SST signature of a cyclonic SME. Cyclonic SMEs are a common phenomenon at the end of filaments, as often observed by their spiral arms on high-resolution Sentinel-3 SST images, which unfortunately are not available on this day. Fig. 3b shows a section of a Sentinel-1B SAR image acquired on the same day over the area marked by a black rectangle in Fig. 3a. At the time of the SAR data acquisition, a southeasterly wind of 2.5 m/s was blowing, which provided optimal conditions for SAR imaging of IWs. The position of the center of the area of reduced radar backscatter corresponds closely to the position of the center of the patch of slightly decreased SST values in the area marked by a rectangle in Fig. 3a. We interpret the dark patch as sea surface signature of an SME, where cold water rises to the sea surface and where the stability of the air-sea interface changes, which causes a reduction of the radar backscatter. Furthermore, we interpret the surrounding semi-circular wave pattern as the sea surface signature of IWs generated at the border of the rapidly moving SME.

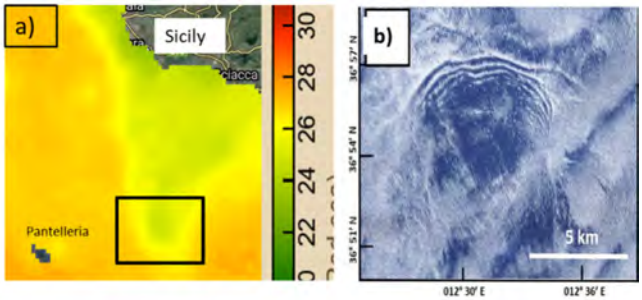

Fig. 3. a) GHRSST SST map (in °C) of 28 June 2017 showing a broad upwelling filament characterized by lower SST values than in the surrounding waters; b) Section of the Sentinel-1A SAR image acquired on 28 June 2017 at 17:12 UTC over the area marked by a dark rectangle in Fig. 3a.

5. Discussion

The analysis of Sentinel-1 SAR images acquired in the years between 2017 and 2022 over the Strait of Sicily has yielded the result that radar signatures of short-wavelength (0.3 - 1 km) IWs are present (1) only in the shallow AB region and its immediate surroundings, (2) only in the months between June and October, and (3) only near filaments and SMEs, which evolved over the AB after upwelling events along the south coast of Sicily. Their position does not show any periodicity or any relationship to prominent bathymetric features.

The observations suggest that the lateral motion of cold water within the filaments/SMEs is instrumental in their generation. When comparing position of the western boundary of the filament in the area marked by a red rectangle in Fig. 1a with the one in Fig. 2a, one obtains the result that it has shifted by 19 km in 24 hours. This implies a horizontal speed of the cold water of 0.22 m/s. This speed is much larger than the vertical speed of upwelling water, which is usually ≤ 5 m/day. Thus, we hypothesize that the rapid horizontal displacements and deformations of the upwelling front cause a perturbation of the pycnocline, which leads to generation of IWs. This generation mechanism has some similarity with generation of IWs by a river plume impinging into the ocean waters (Nash et al., 2005).

ON THE SAR IMAGE VISIBILITY OF HEAVY FUEL LEAKING FROM THE WRECK OF A SUNKEN VESSEL

Martin Gade, Dana M. King

Institut für Meereskunde, Universität Hamburg, Germany

Oil spills on the sea cause dark patches in C- and X-band Synthetic Aperture Radar (SAR) imagery, because they damping small-scale surface waves that are responsible for the radar backscattering. The wave damping, hence the radar contrast, is less pronounced at L-band, except for thick parts of the oil spills [1]. On global scales, the main source of marine oil pollution is operational ship traffic, though static sources such as oil seeps or oilrigs may also contribute. Routine oil-pollution monitoring of the western Black Sea using SAR imagery is being done through the CleanSeaNet System of the European Maritime Safety Agency (EMSA) [2]. There was, however, no static oil-pollution source reported for the Bulgarian Black Sea coast.

On 1 July 1921, the US cargo steamship *SS Mopang* sank off Sozopol on the Bulgarian Black Sea coast, close to the city of Burgas, after hitting a sea mine that was left from World War I. After the ship wreck had been lying at a depth of about 30 m for almost one century, in August 2018, local newspapers reported an oil leakage that was observed after a period of strong winds and currents in that area. Heavy fuel, of which the *SS Mopang* had originally loaded 650 tons, was leaking out of the wreck's tanks.

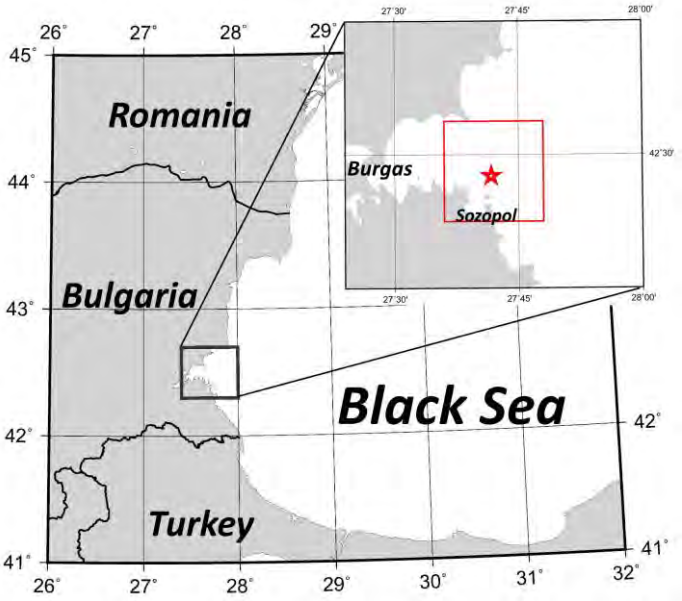

Figure 1. Map showing the location of the wreck of the *SS Mopang* on the Bulgarian Black Sea coast. The red square marks the position of the SAR image fragments shown herein.

We used 16 years of spaceborne SAR imagery, acquired between 2006 and 2021 by Sentinel-1A/B SAR-C, ALOS-1/2 PALSAR-1/2, and Envisat ASAR, to investigate for how long, and under which conditions, heavy fuel was leaking out of the wreck. The oil spill of the *SS Mopang* was visible on more than 100 SAR images; however, we could not find it on every SAR image acquired in the area, which implies that either the leakage of heavy fuel occurred only sporadically, or a continuous leakage of oil could not be seen on every SAR image. Figure 2 shows three examples of SAR images of the *Mopang* site, all showing manifestations of the heavy fuel leaking out of the ship wreck.

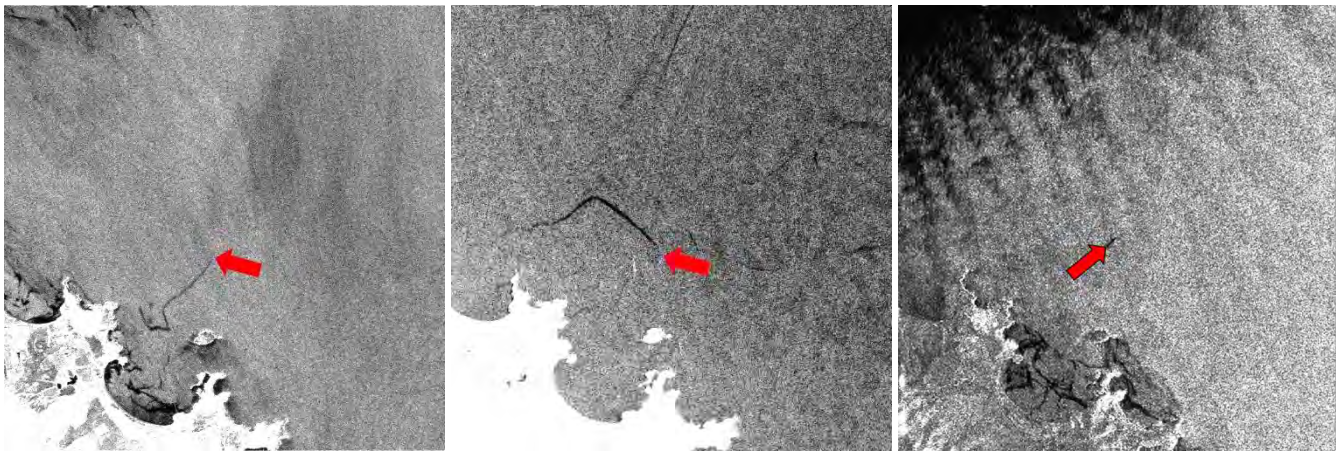

Figure 2. Three examples of SAR images of the *Mopang* site, acquired in 2018, 2016, and 2006 (left to right) and showing manifestations of the heavy fuel spill; image dimensions 16.6 km × 16.9 km. Left: ALOS-2 PALSAR-2 image acquired on 8 July 2018; middle: Sentinel-1A SAR-C image acquired on 9 September 2016; right: ENVISAT ASAR image acquired on 15 September 2006. Red arrows mark the position of the *SS Mopang*.

Further analyses revealed that oil spills, which could be attributed to the *Mopang* wreck, were detected only in the warmer season, from May to November, when the temperature of the bottom water layer exceeded 10 °C (Figure 3). Apparently, under these conditions the heavy fuel's viscosity was low enough to allow for its leakage and subsequent rise to the sea surface. In contrast, during colder months, when the bottom temperature was below 10 °C, the viscosity of the heavy fuel was too high and hence, we did not find any manifestation of the *Mopang* spill on SAR imagery acquired from December to April.

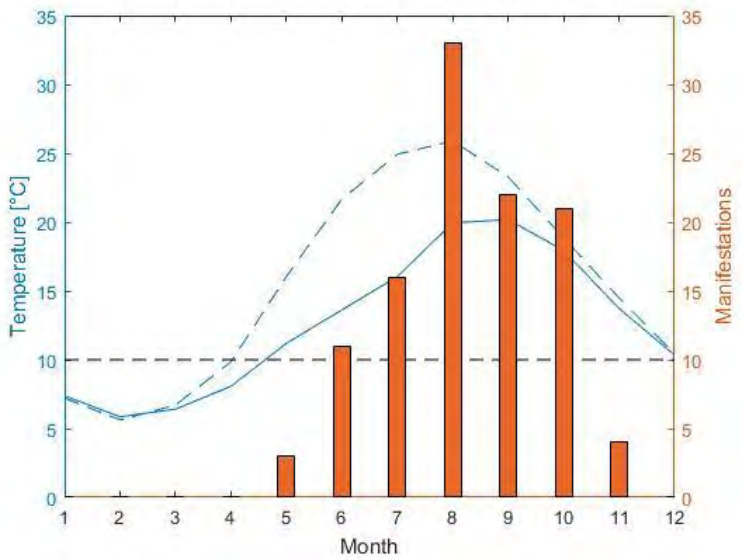

Figure 3. Seasonality of SAR image manifestations of the *Mopang* spill. The orange bars denote the number of manifestations in the respective months, the dashed and solid blue curves denote the mean water temperature and sea bottom temperature, respectively, in the area of the ship wreck.

We found similar patterns of the environmental conditions for all cases, in which we observed a *Mopang* spill on SAR imagery: periods of high winds, resulting in high sea state, were always preceding each oil spill detection, which implies that some mechanical action on the wreck's hull was needed to initiate further leakage. In addition, we always found a decrease in significant wave height, wind and current conditions shortly before the SAR image acquisition. We therefore hypothesize that

a period of increased mechanical stress on the wreck's hull was needed to force the leakage of heavy fuel, but that calmer conditions at the time of the SAR image acquisition were needed, likely to prevent the leaked heavy fuel from being mixed with sea water without forming a coherent spill at the sea surface, manifesting on the SAR imagery.

In cases when the *Mopang* spill also showed up on L-band SAR imagery, the leakage of heavy fuel must have been strong enough to form a thick oil spill that caused a detectable contrast on L-band SAR imagery. Estimates of the spill's thickness, however, were not possible.

REFERENCES

[1] Gade, M., W. Alpers, H. Hühnerfuss, H. Masuko, and T. Kobayashi, 1998: The imaging of biogenic and anthropogenic surface films by a multi-frequency multi-polarization synthetic aperture radar measured during the SIR-C/X-SAR missions, *J. Geophys. Res., 103*, 18851-18866.

[2] Berescu, S., 2013: Marine Environment Protection through CleanSeaNet with Black Sea, in *Marine Navigation and Safety of Sea Transportation – Maritime Transport & Shipping*, A Weintrit, Tomasz Neumann (Eds.), CRC Press Balkema, Leiden, 320 pp.

AUTOMATION OF SLICK DETECTION AND CLASSIFICATION FOR IMPROVED MONITORING WITH SAR

Cathleen E. Jones[1,2], Malin Johansson[2], Benjamin Holt[1]

[1]*Jet Propulsion Laboratory, California Institute of Technology*
[2]*UiT The Arctic University of Norway*

Synthetic aperture radar (SAR) is used to identify mineral oil spills at sea based on the contrast between the clean seawater and the surface slicks, which appear radar-dark [1]–[4]. The ocean contrast in SAR imagery is also used for other purposes [15] [30], e.g., to locate and characterize sea ice (see, e.g., [5]–[8], and in combination with optical data to monitor biogenic slicks, which are related to circulation, biological activity, and water quality [9] [10] [20] [31]. Furthermore, as the sea ice recedes and shipping potentially expands in the Arctic [11]–[12], there will be an increasing need to distinguish oil spills from young ice types that also appear radar dark [13]–[14], and to investigate oil transport in combination with sea ice [26].

Monitoring the ocean to identify and differentiate oil spills, marine slicks, and sea ice are all activities undertaken by operational agencies, and trained operators are frequently employed to distinguish the desired signal from a host of potential false positive signals[15]. Many SAR satellites are used by agencies to identify and monitor slicks, but are not sensitive to oil characteristics like thickness because the returns from the slicks are near-to-below the instrument noise floor [20] [21]. However, low noise SAR sensors have now demonstrated some sensitivity to the thickness and emulsification of mineral oil slicks on the ocean surface (e.g., [17]–[19]), so there is the chance to obtain additional information from SAR about the type and amount of material in the slicks. With ever-increasing SAR data volumes, the oil spill monitoring activities need to improve the automation of SAR processing.

Here we briefly describe a simple method for identifying radar-dark features in a SAR scene of the ocean and apply it on SAR imagery, demonstrating the ability to automatically delineate geometrically complex slicks from mineral oil and HABs. The method does not require a training data set or any other ancillary information, and is sufficiently general that it can be applied to any parameter used for distinguishing one feature from another on the open ocean, e.g., polarimetric decomposition products [16]. The contrast is then used to classify the radar-dark features based upon degree of contrast. For characterizing mineral oil slicks, the contrast in the VV-polarization normalized radar cross section (NRCS) is used because of that parameter's sensitivity to thickness or oil volumetric fraction [17] [25] [27].

The method starts by calculating the damping ratio (DR) [28] based upon the statistics of the ocean NRCS values in the scene. A mask is then needed to exclude any land areas in the scene. The DR is calculated as the ratio of the measured NRCS, σ, to that of unslicked (clean) water, $D = {}^{\sigma^{clean}}/_{\sigma}$. To calculate the DR, the clean water pixels must first be identified, ideally automatically and for any scene regardless of the complexity of the dark feature patterns. Here this is addressed using a statistical analysis, as described in [22], which can identify clean pixels even under challenging conditions. The clean water pixels show up as a peak in the probability distribution function, with the radar-dark pixels in the lower NRCS tail of the peak or in one or more peaks of lower NRCS, depending upon the extent of the scene covered by radar-dark features and the number of different types of phenomena that they represent. For slicks and PDFs with multiple peaks, the peak at the highest NRCS is identified as clean water. Generally, ships or structures and radar-bright fronts constitute relatively few pixels and show up in the high value tail of the clean water peak. High confidence clean water pixels are identified as those with values in a narrow band centered on the clean water peak value, and are used in calculating the DR for all pixels in the scene. Here we present three examples applying the method to airborne UAVSAR L-band images and a Radarsat-2 C-band image. Fig. 1(a)-(c) shows an example of the NRCS, the clean water mask, and the DR, generated automatically based on UAVSAR [29] data of oil slicks in the Gulf of Mexico. Note that the clean water mask at this point does not indicate where the slicks are, i.e., its complement is not the dark feature mask, but rather it identifies those pixels that represent the mean clean water NRCS. Fig. 2 shows the DR calculated for slicks from algal blooms in the Baltic Sea, derived from C-band Radarsat-2 images, and Fig. 3 compares the results from this algorithm applied to L-band UAVSAR data with PlanetScope imagery analyzed by the NOAA NESDIS personnel and reported in a Marine Pollution Surveillance Report.

At this stage the DR, calculated automatically, can be used by an analyst to manually identify features of interest, as in the example shown in Figure 3. However, the automated process can be taken a step further to make a dark feature mask and classify those pixels based upon intensity as an aid for analysis, a quick-look product for responders, or training data for machine learning algorithms. In Fig. 1(d), we show an example relative thickness classification of mineral oil slicks shown in Fig. 1(a). The DR is first classified using an unsupervised classifier (e.g., [23] [24]), and thereafter the slick/dark feature classes are selected based upon their mean and standard deviation relative to those of the clean water peak. These classes form the initial masks for clean water and slicks, which are then refined by removing pixels from the oil mask whose DR values fall within 2 SD of the clean water mean. Because the clean water mean is DR=1 in theory, this also provides a quality metric for the clean / oil separation. Finally, the oil pixels are classified based upon their DR values. The classification is adaptable in number of classes and thresholds, the latter of which are set based upon percentiles given the PDF of DR values for the oil pixels. Further analysis on validating the relationship between these classes and thickness, and on whether this classification can be used to differentiate mineral oil slicks from false positives is needed.

This kind of classification product could aid trained operators in identifying spills from SAR data of any frequency band, and, because the algorithm is fully automated, could be implemented to generate near-real-time (NRT) products to help direct responders as soon as remote sensing data is available, significantly reducing latency in providing preliminary assessments to field crews. Furthermore, because it works for all commonly available SAR frequency bands, the algorithm can be applied to any data, expanding the number of scenes that can readily be processed in NRT.

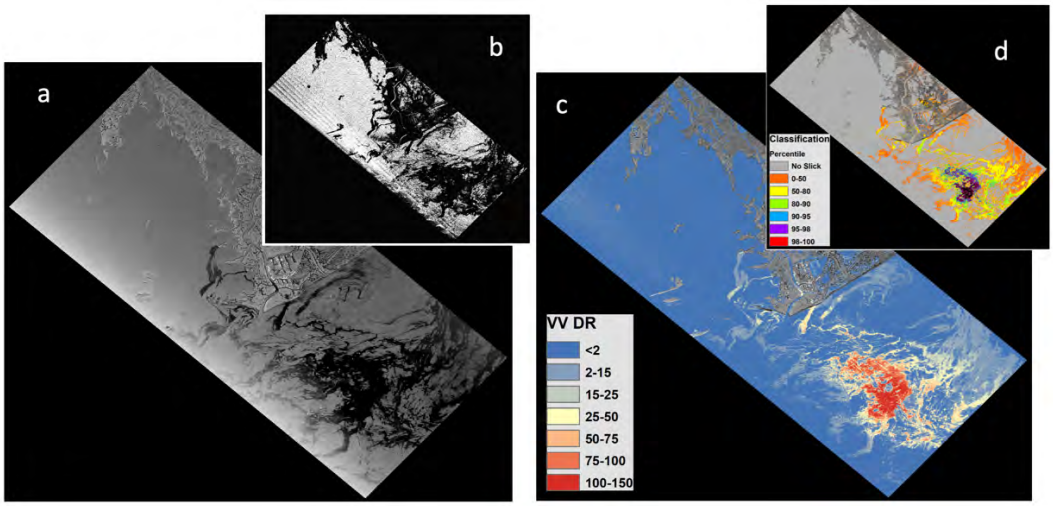

Fig. 1. (a) UAVSAR L-band VV-polarization image acquired on 6 Sept 2021 showing mineral oil slicks off the coast of Louisiana near Port Fourcon, the site of Hurricane Ida landfall on 29 Aug 2021. (b) The clean water mask identifying high confidence clean water pixels in white. (c) The calculated damping ratios. (d) Relative thickness classes for the oil slick derived from the damping ratio. Class thresholds were set based upon the distribution of the damping ratio values for pixels identified as oil, for the case shown having the lowest 50th percentile of the values in Class 1 and the highest 2% of values in Class 6.

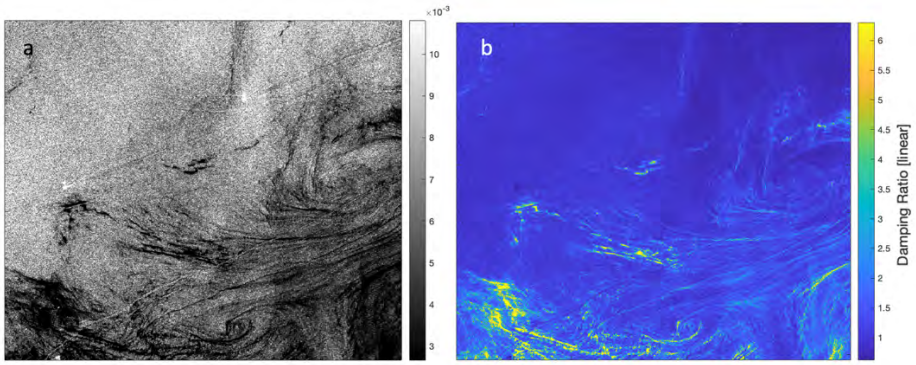

Fig. 2. (a) Radarsat-2 VV-polarization image acquired on 10 July 2017 showing slicks from algae in the Baltic Sea. (b) Damping ratio derived automatically.

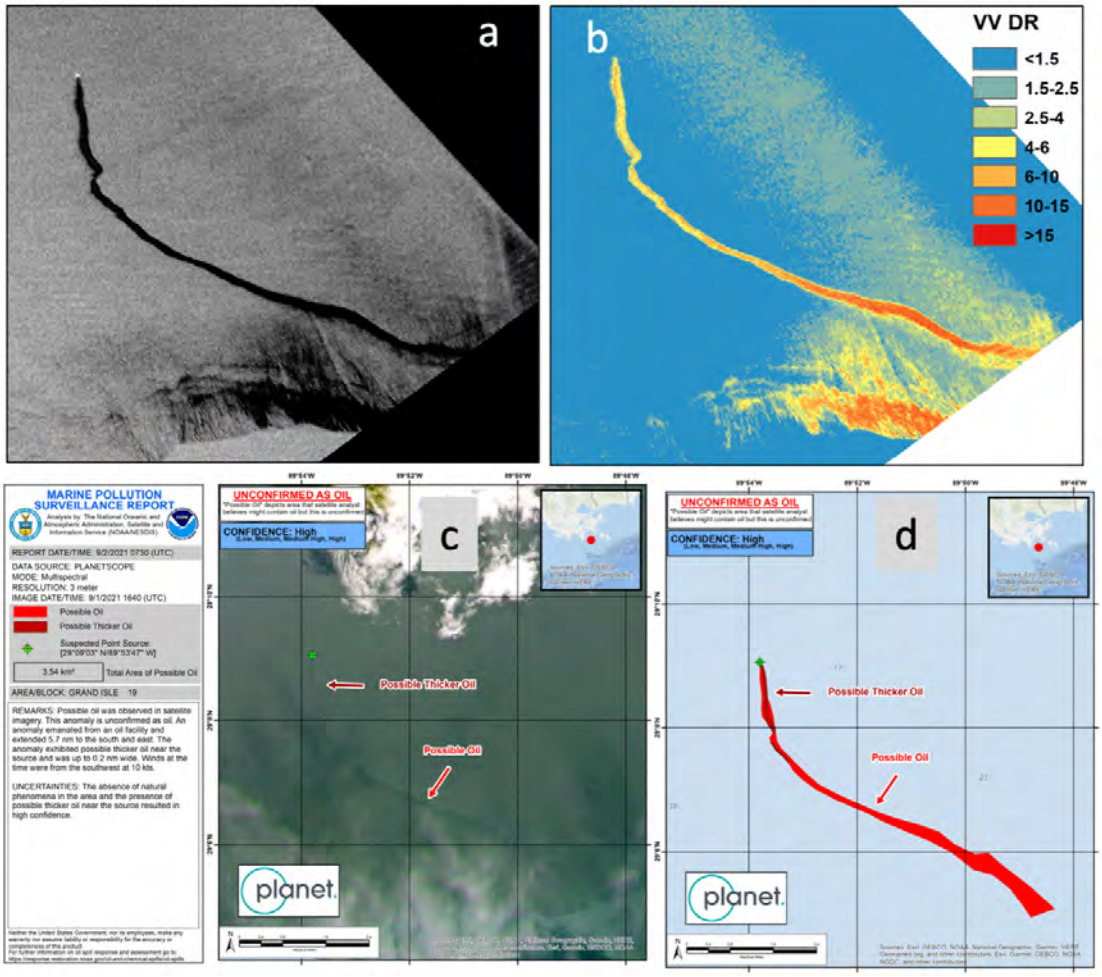

Fig. 3. (a) UAVSAR L-band VV image acquired on 1 Sept. 2021 1640 UTC near the location of the scene in Fig. 1 and (b) the calculated damping ratio, compared to (c) a NOAA Marine Pollution Surveillance Report derived from Planet optical imagery acquired 10 minutes earlier (shown) and (d) the analyst's delineated slick. The DR from the UAVSAR image shows the same delineated slick, but with more damping to the south than the north, and other slicks / radar-dark features to the south, which are also visible in unclouded areas in the PlanetScope image. Note that based on the DR alone, one would conclude that the thicker oil is to the south compared to the expert's identifying possible thicker oil at the north end of the slick. [MPSR image from NOAA]

ACKNOWLEDGEMENT

The research described in this paper was carried out in part at the Jet Propulsion Laboratory (JPL), California Institute of Technology, under a contract with the U.S. National Aeronautics and Space Administration (NASA). The UAVSAR data are courtesy NASA/JPL. M.J. was funded through the Research Council of Norway Grant no. 237906. RADARSAT-2 Data and Products © MDA Geospatial Services Inc. 2017, provided by NOSA/KSAT – All Rights Reserved.

REFERENCES

[1] Wahl, T., Skøelv, Å., Pedersen, J. P., Seljelv, L. G., Andersen, J. H., Follum, O. A., ... & Solberg, R. (1996). Radar satellites: A new tool for pollution monitoring in coastal waters. Coastal Management, 24(1), 61-71.

[2] Espedal, H. A., Johannessen, O. M., Johannessen, J. A., Dano, E., Lyzenga, D. R., & Knulst, J. C. (1998). COASTWATCH'95: ERS 1/2 SAR detection of natural film on the ocean surface. Journal of Geophysical Research: Oceans, 103(C11), 24969-24982.

[3] Wismann, V., Gade, M., Alpers, W., & Huhnerfuss, H. (1998). Radar signatures of marine mineral oil spills measured by an airborne multi-frequency radar. International Journal of Remote Sensing, 19(18), 3607-3623.

[4] Espedal, H. A. (1999). Satellite SAR oil spill detection using wind history information. International Journal of Remote Sensing, 20(1), 49-65.
[5] Kwok, R., Rignot, E., Holt, B., & Onstott, R. (1992). Identification of sea ice types in spaceborne synthetic aperture radar data. Journal of Geophysical Research: Oceans, 97(C2), 2391-2402.
[6] Dierking, W. (2009). Mapping of different sea ice regimes using images from Sentinel-1 and ALOS synthetic aperture radar. IEEE Transactions on Geoscience and Remote Sensing, 48(3), 1045-1058.
[7] Zakhvatkina, N. Y., Alexandrov, V. Y., Johannessen, O. M., Sandven, S., & Frolov, I. Y. (2012). Classification of sea ice types in ENVISAT synthetic aperture radar images. IEEE Transactions on Geoscience and Remote Sensing, 51(5), 2587-2600.
[8] Dierking, W. (2013). Sea ice monitoring by synthetic aperture radar. Oceanography, 26(2), 100-111.
[9] Bresciani, M., Adamo, M., De Carolis, G., Matta, E., Pasquariello, G., Vaičiūtė, D., & Giardino, C. (2014). Monitoring blooms and surface accumulation of cyanobacteria in the Curonian Lagoon by combining MERIS and ASAR data. Remote Sensing of Environment, 146, 124-135.
[10] Ma, Y., Wong, K., Tsou, J. Y., & Zhang, Y. (2022). Investigating spatial distribution of green-tide in the Yellow Sea in 2021 using combined optical and SAR images. Journal of Marine Science and Engineering, 10(2), 127.
[11] Melia, N., Haines, K., & Hawkins, E. (2016). Sea ice decline and 21st century trans-Arctic shipping routes. Geophysical Research Letters, 43(18), 9720-9728.
[12] Gascard, J. C., Riemann-Campe, K., Gerdes, R., Schyberg, H., Randriamampianina, R., Karcher, M., ... & Rafizadeh, M. (2017). Future sea ice conditions and weather forecasts in the Arctic: Implications for Arctic shipping. Ambio, 46(3), 355-367.
[13] Brekke, C., Holt, B., Jones, C., & Skrunes, S. (2014). Discrimination of oil spills from newly formed sea ice by synthetic aperture radar. Remote Sensing of Environment, 145, 1-14.
[14] Johansson, A. M., Espeseth, M. M., Brekke, C., & Holt, B. (2020). Can mineral oil slicks be distinguished from newly formed sea ice using synthetic aperture radar?. IEEE Journal of Selected Topics in Applied Earth Observations and Remote Sensing, 13, 4996-5010.
[15] Wang, C., Mouche, A., Tandeo, P., Stopa, J. E., Longépé, N., Erhard, G., ... & Chapron, B. (2019). A labelled ocean SAR imagery dataset of ten geophysical phenomena from Sentinel-1 wave mode. Geoscience Data Journal, 6(2), 105-115.
[16] Ressel, R., Singha, S., Lehner, S., Rösel, A., & Spreen, G. (2016). Investigation into different polarimetric features for sea ice classification using X-band synthetic aperture radar. IEEE Journal of Selected Topics in Applied Earth Observations and Remote Sensing, 9(7), 3131-3143.
[17] Minchew, B., Jones, C. E., & Holt, B. (2012). Polarimetric analysis of backscatter from the Deepwater Horizon oil spill using L-band synthetic aperture radar. IEEE Transactions on Geoscience and Remote Sensing, 50(10), 3812-3830.
[18] Boisot, O., Angelliaume, S., & Guérin, C. A. (2018). Marine oil slicks quantification from L-band dual-polarization SAR imagery. IEEE Transactions on Geoscience and Remote Sensing, 57(4), 2187-2197.
[19] Garcia-Pineda, O., Staples, G., Jones, C. E., Hu, C., Holt, B., Kourafalou, V., ... & Haces-Garcia, F. (2020). Classification of oil spill by thicknesses using multiple remote sensors. Remote Sensing of Environment, 236, 111421.
[20] Alpers, W., Holt, B., & Zeng, K. (2017). Oil spill detection by imaging radars: Challenges and pitfalls. Remote Sensing of Environment, 201, 133-147.
[21] Espeseth, M. M., Brekke, C., Jones, C. E., Holt, B., & Freeman, A. (2020). The impact of system noise in polarimetric SAR imagery on oil spill observations. IEEE Transactions on Geoscience and Remote Sensing, 58(6), 4194-4214.
[22] Jones, C. E. (2023). An automated algorithm for identifying marine oil slicks using synthetic aperture radar," Marine Pollution Bulletin, in review.
[23] Doulgeris, A. P., & Eltoft, T. (2009). Scale mixture of Gaussian modelling of polarimetric SAR data. EURASIP Journal on Advances in Signal Processing, 2010, 1-12.
[24] Doulgeris, A. P. (2013). A simple and extendable segmentation method for multi-polarization SAR images, https://munin.uit.no/handle/10037/6441, accessed 2023 Jan 19.
[25] Jones, C. E., & Holt, B. (2018). Experimental L-band airborne SAR for oil spill response at sea and in coastal waters. Sensors, 18(2), 641.
[26] Wilkinson, J., Beegle-Krause, C. J., Evers, K. U., Hughes, N., Lewis, A., Reed, M., & Wadhams, P. (2017). Oil spill response capabilities and technologies for ice-covered Arctic marine waters: A review of recent developments and established practices. Ambio, 46(3), 423-441.
[27] Angelliaume, S., Dubois-Fernandez, P. C., Jones, C. E., Holt, B., Minchew, B., Amri, E., & Miegebielle, V. (2018). SAR imagery for detecting sea surface slicks: Performance assessment of polarization-dependent parameters. IEEE Transactions on Geoscience and Remote Sensing, 56(8), 4237-4257
[28] Gade, M., Alpers, W., Hühnerfuss, H., Wismann, V. R., & Lange, P. A. (1998). On the reduction of the radar backscatter by oceanic surface films: Scatterometer measurements and their theoretical interpretation. Remote Sensing of Environment, 66(1), 52-70.
[29] Fore, A. G., Chapman, B. D., Hawkins, B. P., Hensley, S., Jones, C. E., Michel, T. R., & Muellerschoen, R. J. (2015). UAVSAR polarimetric calibration. IEEE Transactions on Geoscience and Remote Sensing, 53(6), 3481-3491.
[30] Cristea, A., Johansson, A. M., Doulgeris, A. P., & Brekke, C. (2022). Automatic Detection of Low-Backscatter Targets in the Arctic Using Wide Swath Sentinel-1 Imagery. IEEE Journal of Selected Topics in Applied Earth Observations and Remote Sensing, 15, 8870-8883.
[31] Qi, L., Wang, M., Hu, C., & Holt, B. (2022). On the capacity of Sentinel-1 synthetic aperture radar in detecting floating macroalgae and other floating matters. Remote Sensing of Environment, 280, 113188.

AI-BASED ROUTE RECONSTRUCTION ON MULTIFREQUENCY MULTITEMPORAL SAR IMAGES

Roberto Del Prete[1], Maria Daniela Graziano[1] and Alfredo Renga[1]

[1] Department of Industrial Engineering, University of Naples Federico II, Naples, Italy

E-mail: roberto.delprete@unina.it

1. Introduction

Ship wake retrieval using satellite imagery is one of the most useful applications for obtaining insights of moving vessels. Environmental monitoring, high-dimensional mapping, and ship tracking are just a few of the key applications that can benefit from the exploitation of such task. Regarding the ship tracking, this represents one of the primary reasons for the importance of ship wake detection as it allows for the monitoring of ship movements and activities. Indeed, ship wakes may reveal valuable information concerning vessel's speed, direction, and even its size and category [1]. This is especially valuable for marine applications such as port security and coastal surveillance, where it is critical to monitor ship movement to prevent smuggling, illicit fishing, and other types of maritime crime. Contrarily to optical sensors, the Synthetic Aperture Radar (SAR) imagers enable an all-weather and all-time detection capability [2]. Nonetheless, several problems arise when finding ship wakes in radar images mainly due to the presence of speckle noise. This one can interfere with the detection of ship wakes and make it difficult to extract useful information. To overcome this challenge, various methods have been proposed that exploit the linear characteristics of ship wakes and transform the lines in the spatial domain into bright or dark points in a transform domain, such as the Radon or Hough transforms [3]–[5]. However, such kind of approach assumes wakes as linear features which is not always true in practical in scenarios near coasts where ships typically change their route. It must be also considered that different wake appearances are produced by the coherent radar focusing mechanism, further complicating the detection problem. Currently, the insurgence of Artificial Intelligence (AI) has reached the remote sensing community, and Deep-Learning (DL) techniques for detecting wakes are present but still few in literature [6]–[8]. The topic is addressed in this paper by a different perspective, i.e, analysing the possibility of exploiting multifrequency multitemporal acquisitions to reconstruct ship route. To the knowledge of the authors, this research represents the first attempt of using AI for the sake of wake detection exploiting multi-temporal, multi-frequency, and multi-mission SAR data. The paper contributes in this under-studied topic illustrating a preliminary application of route reconstruction using mulitemporal multifrequency SAR data.

2. Method

In the field of computer vision, the identification of multiple instances within a single image goes under the task of Object Detection (OD). An OD architecture is built on top of a standard convolutional neural network (CNN) by adding a regression problem for bounding box detection around the objects. Region-based CNN (R-CNN) [9] was the first architectures developed for OD, which used region proposals or Regions of Interest (RoIs) to extract features from the image. R-CNN has mutated into countless architectures, but OD networks generally consist of three modules: a) the backbone, which collects image features; b) the neck, which links the backbone to the head; and c) the head, which classifies and detect image objects. The backbone can be a plain stack of convolutional and pooling layers, or a more engineered network such as EfficientNet [10] and ResNets [11]. As the number of output channels grows, the output size of feature maps decreases, generating a pyramidal structure. The neck module combines information at various scales, while the head module identifies and localizes picture objects. The proposals for the objects can be created using various processes, such as anchor boxes, keypoints, or transformers, and based on the proposal step, one-stage or two-stage detectors are often distinguished. The head module may include of basic convolutional layers or sophisticated DL ideas, such as transformer decoders. Typically, the loss function used for optimization is tailored to each model and is dependent on the proposal method and head layers. For the sake of route reconstruction, the architecture of Mask R-CNN was selected for the problem at hand. The backbone is ResNet-50 being a good trade-off between accuracy and efficiency.

3. Results

We train the model on the dataset of [6] with a hyper-parameter tuning strategy based on a grid-search algorithm. The learning rate varies in the range $2 \cdot 10^{-2}$ and $5 \cdot 10^{-4}$ with different scheduler, e.g., linear, stepwise, cosine-annealing. Regarding data augmentation, the same transforms techniques of [6] have been adopted. In the end, the model reached a mAP (mean Average Precision) of 83% for an Intersection over Union (IoU) of 0.5.

Presenting a practical application of route reconstruction, the Figure 1 shows the detection results of the same ship wake in two SAR images. Specifically, the first image is from COSMO-SkyMed (X-band, HH polarization) and the second one from Sentinel-1 (C-band, VH polarization) gathered at 17.04 and 17.13 CET, respectively. Products are paired from the dataset of [12] and have been gathered over the Egadi Islands on the 23 August 2020. The images have been complemented with ancillary AIS (Automatic Identification System) provided by [13]. Indeed, the Figure 1 reports a zoomed view referring to the same ship (MMSI: 247294400) which is a high-speed craft travelling at 10.28 knots with a course over ground of 166.5°. Essential to note is that these products come as SLC (Single Look Complex) differently from the GRD (Ground Range Detected) of the dataset of [6]. Nevertheless, still the model generazibility can recognize the visual pattern of a ship wake. As shown in Figure 1, multifrequency data reveals how the same wake appears differently under two frequencies (and polarizations). In addition, the route reconstruction is demonstrated thanks to the disposal of multifrequency multitemporal data allowing for discretizing the ship route in two non overlapped time frames.

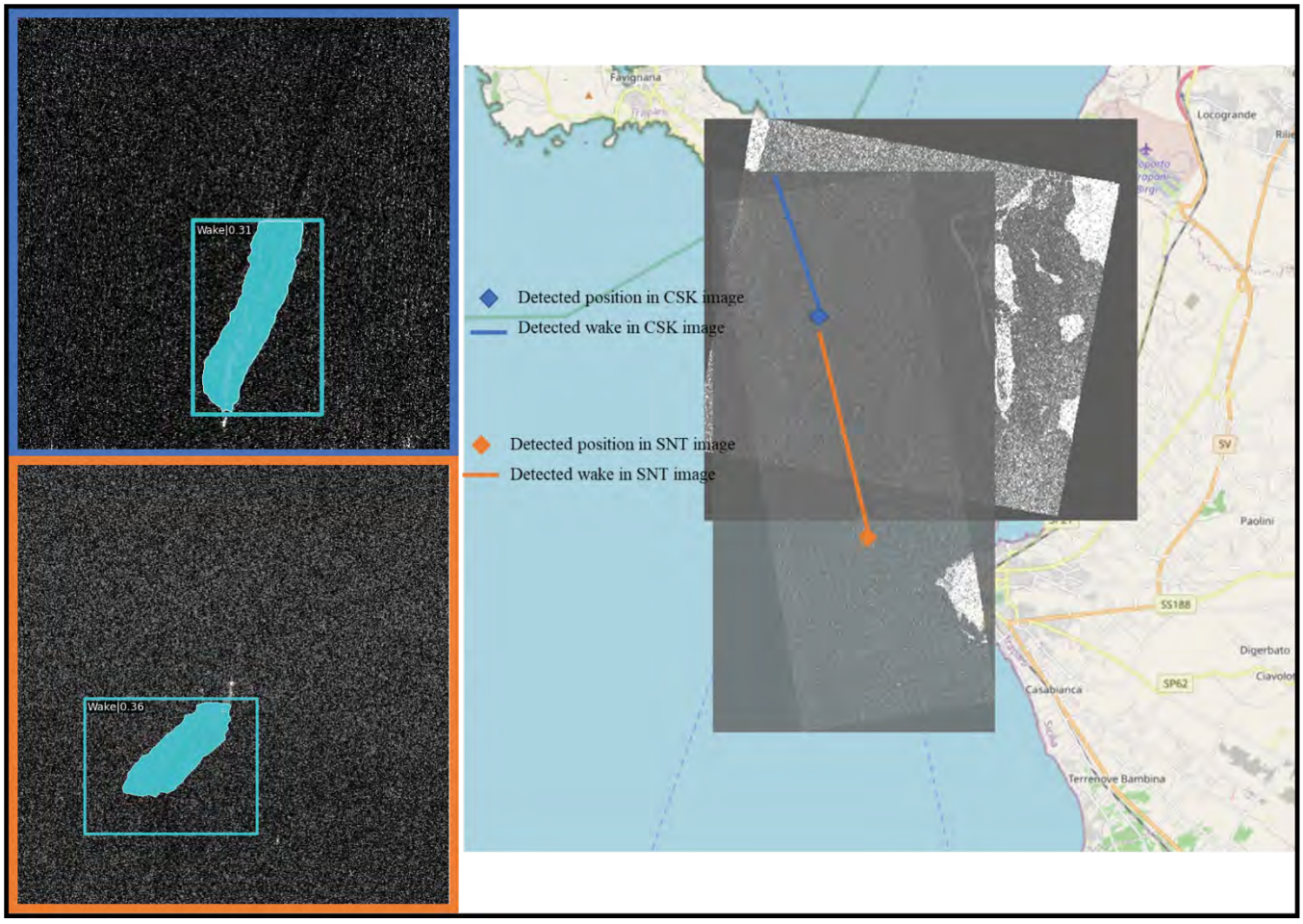

Figure 1 Route reconstruction by wake detection in multitemporal multifrequency SAR data. [a) COSMO-SkyMed (1418705), b) Sentinel-1 (S1A_IW_SLC__1SDV_20200823T171258_20200823T171325_034037_03F36B_5D18)]

The map in Figure 1 also reports a common route (dotted blue line) from the Favignana Island. This was reported purposely to show how the extracted wakes perfectly match it. This result hold significance demonstrating that ship wakes are not only a marker of the vessel presence but can be leveraged to gain knowledge of past movements of the vessel under analysis. In the

wake imaged by Sentinel-1, the distance between the wake vertex and the end of the visible wake is about 3 kilometres (i.e., wake vertex coordinates are *37°48'42"N, 12° 24'11"E*, end of wake coordinates are *37°50'22"N, 12°23'34"E*). Because the ship's velocity is 10.3 knots, the wake describes the ship locations starting around 9.45 minutes before the SAR acquisition. The upper tile is gathered by CSK, and the ship wake is 4.6 km long (i.e., 14.7 minutes). As a result of the synergic exploitation of consecutive photos (particularly of wakes captured in these photographs), the ship may be tracked from 16:50 (14 minutes before 17:04) to 17:13 as if the ship was continually providing AIS data.

4. Conclusions

The paper has addressed the ship wake detection problem from SAR images reporting a benchmark of several state-of-the art object detection network, both single- and multi-stage, anchor-free and anchor-based. Evidence on the different backbones analysed highlight how the problem is far away from the traditional OD for camera images. Finally, the first application of route reconstruction has been presented. The generalization capability of DL is exploited to detect the same wake gathered in two radar frequencies reporting how two acquisitions are much more than merely instantaneous marine images obtained at two epochs. Results show how the detected wakes can reconstruct ship route using multitemporal multifrequency images. In conclusion, this study demonstrates the potentialities of a synergic exploitation of SAR data for ship tracking.

Acknowledgements

This work has been developed in the framework of the Italian Space Agency's "Study of new methods and techniques based on the utilization of multimission/multifrequency SAR data", project "COastal Area monitoring with SAR data and multimission/multifrequency Techniques - COAST", ASI Contract N. 2021-11-U.0.

References

[1] I. G. Rizaev and A. Achim, "SynthWakeSAR: A Synthetic SAR Dataset for Deep Learning Classification of Ships at Sea," *Remote Sens (Basel)*, vol. 14, no. 16, p. 3999, 2022.

[2] I. G. Cumming and F. H. Wong, "Digital processing of synthetic aperture radar data: algorithms and implementation," pp. 225–248, 2005.

[3] M. D. Graziano, "Preliminary results of ship detection technique by wake pattern recognition in SAR images," *Remote Sens (Basel)*, vol. 12, no. 18, p. 2869, 2020.

[4] M. D. Graziano and A. Renga, "Towards automatic recognition of wakes generated by dark vessels in sentinel-1 images," *Remote Sens (Basel)*, vol. 13, no. 10, p. 1955, May 2021, doi: 10.3390/rs13101955.

[5] M. D. Graziano, M. D'Errico, and G. Rufino, "Wake component detection in X-band SAR images for ship heading and velocity estimation," *Remote Sens (Basel)*, vol. 8, no. 6, 2016, doi: 10.3390/rs8060498.

[6] R. del Prete, M. D. Graziano, and A. Renga, "First results on wake detection in SAR images by deep learning," *Remote Sens (Basel)*, vol. 13, no. 22, p. 4573, 2021.

[7] Y. Liu, J. Zhao, and Y. Qin, "A novel technique for ship wake detection from optical images," *Remote Sens Environ*, vol. 258, p. 112375, 2021, doi: https://doi.org/10.1016/j.rse.2021.112375.

[8] K. Ding *et al.*, "Towards real-time detection of ships and wakes with lightweight deep learning model in Gaofen-3 SAR images," *Remote Sens Environ*, vol. 284, p. 113345, 2023.

[9] P. Bharati and A. Pramanik, "Deep learning techniques—R-CNN to mask R-CNN: a survey," *Computational Intelligence in Pattern Recognition: Proceedings of CIPR 2019*, pp. 657–668, 2020.

[10] M. Tan and Q. Le, "Efficientnet: Rethinking model scaling for convolutional neural networks," in *International conference on machine learning*, 2019, pp. 6105–6114.

[11] K. He, X. Zhang, S. Ren, and J. Sun, "Deep residual learning," *Image Recognition*, vol. 7, 2015.

[12] M. D. Graziano, R. del Prete, and M. Grasso, "A NEW DATASET OF MULTI-MISSION/MULTI-FREQUENCY SAR DATA FOR MARITIME MONITORING: FIRST RESULTS AND CRITICAL ANALYSIS," in *IAC–73rd International Astronautical Congress 2022*, 2022.

[13] "exactEarth | AIS Vessel Tracking | Maritime Ship Monitoring | Home." https://www.exactearth.com/ (accessed Aug. 29, 2021).

Impact of Sea Water Intrusion on Surface Deformation along the coastal areas of Pakistan using SAR Interferometry

Muhammad Ali[1], Gilda Schirinzi[1], Zeeshan Afzal[2] and Sajid Hussain[3]

[1]Dipartimento di Ingegneria, Università degli Studi di Napoli "Parthenope", Napoli, Italy

[2]State Key Laboratory of Information Engineering in Surveying, Mapping and Remote Sensing, Wuhan University, Wuhan 430079, China

[3]School of Remote sensing and Information Engineering, Wuhan University, Wuhan 430079, China

Abstract-The growth of coastal megacities (those with populations of more than 8 million people) is concentrating populations in hazardous places, particularly in developing countries such as Pakistan. Similarly, more cities are expected to grow/develop along the coast of Pakistan such as the Baluchistan coast (Pasni, Omwara, Sumiani and Gwadar). These coastal areas are expected to be most vulnerable to seawater intrusion. The vulnerability of any coastal area increases with increasing land subsidence, deteriorating water drainage system, increase in sea level and local seismic activity (Elshinnawy & Almaliki, 2021).

Interferometric Synthetic Aperture Radar (InSAR) has become one of the most important and useful methods for the estimation of ground (Kumar et al., 2020; Ramzan et al., 2022). The enriched availability of new SAR tools and satellite collections has encouraged a solid development of processing procedures such as finding the small ground deformation signals linked to the different phases of the seismic cycle (Ali et al., 2021). Interferometric synthetic aperture radar (InSAR) is a radar technique that uses two or more synthetic aperture radar (SAR) images to produce images of surface deformation. This technique can measure sub-cm changes in deformation over spans of days to years (Ali et al., 2018; Lu et al., 2020). Interferometric Synthetic Aperture Radar (InSAR) is an effective way to measure changes in land surface altitude. InSAR makes high-density measurements over large areas by using radar signals from Earth-orbiting satellites to measure changes in the land-surface altitude at high degrees of measurement resolution and spatial detail (Khan et al., 2020).

The wide point in this study is the investigation of the potential significance of ground deformation for structural damage applications by measuring the magnitude and extent of surface deformation in the Makran subduction zone (Pasni, Omwara, Sumiani and

Gwadar) and the impact of Sea Water Intrusion to the land subsidence along the coastal areas. The coastal area of Pakistan lies in a high-risk zone. Disaster can strike anywhere related to drought, earthquake and tsunami. Indus Delta is facing many problems due to increasing seawater intrusion under prevailing climatic change where land deformation can augment its vulnerability. Therefore, this study will be helpful to assess the extreme changes in the coastal dynamics.

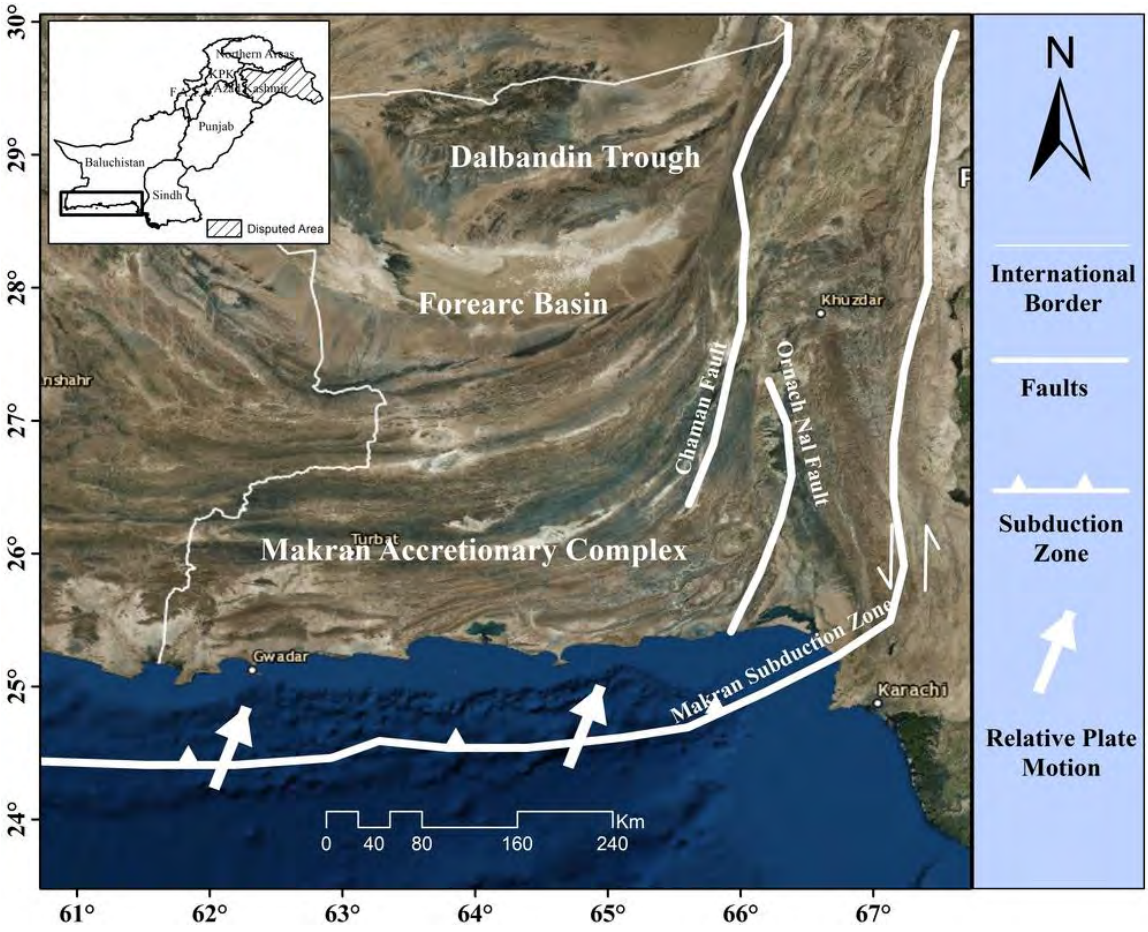

Figure 1: Map shows the study area (Coastal area of Pakistan) with regional tectonic margins of western Pakistan (Makran Subduction Zone).

References

Ali, M., Shahzad, M. I., Nazeer, M., & Kazmi, J. H. (2018). ESTIMATION OF SURFACE DEFORMATION DUE TO PASNI EARTHQUAKE USING SAR INTERFEROMETRY. *International Archives of the Photogrammetry, Remote Sensing & Spatial Information Sciences, 42*(3).

Ali, M., Shahzad, M. I., Nazeer, M., Mahmood, I., & Zia, I. (2021). Estimation of surface deformation due to Pasni earthquake using RADAR interferometry. *Geocarto International, 36*(14), 1630-1645.

Elshinnawy, I. A., & Almaliki, A. H. (2021). Vulnerability assessment for sea level rise impacts on coastal systems of Gamasa Ras El Bar Area, Nile Delta, Egypt. *Sustainability, 13*(7), 3624.

Khan, A., Gupta, S., & Gupta, S. K. (2020). Multi-hazard disaster studies: Monitoring, detection, recovery, and management, based on emerging technologies and optimal techniques. *International journal of disaster risk reduction, 47*, 101642.

Kumar, S., Kumar, D., Chaudhary, S. K., Singh, N., & Malik, K. K. (2020). Land subsidence mapping and monitoring using modified persistent scatterer interferometric synthetic aperture radar in Jharia Coalfield, India. *Journal of Earth System Science, 129*(1), 146.

Lu, C.-Y., Hu, J.-C., Chan, Y.-C., Su, Y.-F., & Chang, C.-H. (2020). The relationship between surface displacement and groundwater level change and its hydrogeological implications in an alluvial fan: case study of the Choshui River, Taiwan. *Remote Sensing, 12*(20), 3315.

Ramzan, U., Fan, H., Aeman, H., Ali, M., & A. A. Al-qaness, M. (2022). Combined analysis of PS-InSAR and hypsometry integral (HI) for comparing seismic vulnerability and assessment of various regions of Pakistan. *Scientific Reports, 12*(1), 22423. doi:10.1038/s41598-022-26159-1

SEASAR 2023, MAY 2-6, SVALBARD

Title: Try, Try Again: Recent Steps Toward An Operational SAR-based Algorithm for Oil Spill Thickness Measurements

Authors: Benjamin Holt[1], Cathleen E. Jones[1], Frank Monaldo[2], Oscar Garcia[3]

Affiliation:
[1]Jet Propulsion Laboratory, California Institute of Technology
[2]University of Maryland
[3]WaterMapping Inc.

Three field campaigns were conducted in the Santa Barbara oil seep region in 2021-2022 with the goal to develop a quantifiable approach for determining the thicker components of oil spills using microwave synthetic aperture radar (SAR) imagery to be utilized in an operational context to guide clean-up efforts. The challenging aspect of quantifying the thickness of oil on water is that oil is thin – order 10-100 μm, with the operational goal of identifying thickness >=50 μm, which is the threshold sought by responders as 'actionable' oil. This threshold is the part of a spill to be targeted for clean-up as thicknesses above this threshold are most harmful to the marine environment and ecosystem. In addition to this quantity, a lot more information is sought about an oil spill –extent, ocean conditions and transport, spill rates, composition, and so on - the list is long. As was observed particularly in the long-lasting and extensive Deepwater Horizon in 2010, there are many potential methods to derive key oil spill properties using remote sensing instrumentation as well as in-situ observations. Each type of remote sensing instrumentation has complications and challenges arising from the underlying physics of the sensing method as well as the environment and the oil itself. Flying the L-band NASA-UAVSAR during the Deepwater Horizon spill has led to a series of efforts to quantify oil thickness properties with field efforts, as well as separating oil from other marine slicks (Minchew et al., 2012; Skrunes et al., 2016; Jones and Holt, 2018; Espeseth et al. 2020A, 2020B).

This presentation will provide an overview of the Santa Barbara seep campaigns as well as the validation efforts to characterize oil thickness, with the ultimate goal of developing useful SAR-based quantitative algorithms that can be implemented by NOAA to derive operational products. The oil seep area off Santa Barbara has been utilized for decades for research and is one of the early sites for off-shore oil production. Two large oil spills have occurred there as well, in 1969 and 2015, with the earlier one causing considerable environmental damage and was the inspiration for Earth Day. The known seep areas are extensive and well mapped (Leifer, 2019) and happen to be readily accessible by boat. The campaigns focused on collecting SAR imagery using the airborne L-band NASA-UAVSAR SAR system during rapidly repeating acquisitions while ship-based observations were being obtained using ship-based drone multispectral imager collections, as well as direct oil thickness measurements and surface photography during the SAR overflights. Other aircraft and satellite observations were also obtained, as available, during each campaign. The UAVSAR provides fine resolution, low-noise radar imagery under all weather and solar conditions and is fully polarimetric, which enables evaluation of multiple methods to characterize the oil slick. The system noise floor of this instrument, considerably less than all satellite SAR instruments, enables a detailed examination of the zones of reduced backscatter caused by varying oil thickness levels. Previous campaigns have demonstrated the efficacy

and value of combining airborne and satellite SAR together with multispectral imagery from drones to determine oil thickness characterization (Garcia-Pineda et al, 2020).

The coastal region near Santa Barbara is subject to diurnal winds, characteristically low in the morning hours and increasing during the day into the afternoon, particularly in the summer months. During light winds, the oil spreads thinly over considerable extent, appearing as spreading slicks composed primarily of thinner sheens interspersed with thicker, narrow bands of brown-colored oil emanating from the source regions. As the winds increase, the slick area reduces as the thin sheen oil largely becomes mixed into the upper ocean, with the narrow bands remaining composed primarily of a range of thicker oil stages including emulsified oil. The narrow slicks are likely to be convergence zones indicative of underlying surface flow patterns, with the oil serving as tracers of the flow.

To identify the thicker narrow bands, the ship-based drone was deployed for local area reconnaissance, detectable in real-time on the drone operator display. The vessel was then directed to the more favorable areas for sampling, where multispectral drone imagery was obtained as well as surface photography and direct measurements of oil thickness and properties where desirable. The UAVSAR had an onboard processor which likewise could identity favorable slicks as well as see the vessel itself. There was regular communication between the UAVSAR crew and the vessel for guidance in order to optimize co-collections. The rapid change in appearance of the ocean surface and slicks with increasing wind, as well as the drift of the bands, made it challenging to conduct coincident observations needed for inter-sensor comparison and validation. Detailed comparisons of the drone-derived multispectral thickness classifications and those derived from the UAVSAR oil thickness classifications, based on using the L-band VV damping ratio (backscatter of oil over ocean), were derived. Both collections were able to identify the varying range of thicknesses within the slicks (Figure 1).

From these field campaigns and other coincident comparisons, an automated algorithm has been developed to estimate oil slick thickness, that is based on using the low-noise L-band imagery from UAVSAR (Jones, 2023). This algorithm can be readily applied to satellite L-band imagery as well, with a primary focus being on the planned launch of the NISAR mission in early 2024 and the potential for this algorithm to become operational. On the satellite side, both Sentinel-1 and Radarsat-2 imagery were also obtained during these Santa Barbara campaigns. While these were not coincident with the drone and UAVSAR collections, the results based on the contrast ratio (backscatter of water over oil), results can be compared with the field collections for consistency. An operational algorithm for oil thickness has also been developed using satellite C-band SAR data and is being staged in NOAA's SAR Ocean Product System (SAROPS) that currently produces SAR-derived wind speed and oil spill extent operationally, with the latter using the Texture-Classifying Neural Network (TCNNA) to automatically delineate oil versus non-oil covered areas (Garcia et al.. 2012).

References

Alpers, W., B. Holt, and K. Zeng (2017), Discriminating oil spills from biogenic slicks by imaging radars: challenges and pitfalls: Challenges and pitfalls, *Remote Sensing of the Environment*, 201, 133-147, http://dx.doi.org/10.1016/j.rse.2017.09.002.

Espeseth, M., C.E. Jones, B. Holt, C. Brekke, S. Skrunes (2020A), Quantitative measurements of oil slick evolution using a time series of SAR images, *J. Selected Topics in Applied Earth Obs. Remote Sens.,* 13, 10.1109/JSTARS.2020.3003686.

Espeseth, M., C. Brekke, C.E. Jones, B. Holt, A. Freeman (2020B), The impact of system noise in polarimetric SAR imagery on oil spill observations, *IEEE Trans. Geosci. Remote Sens.,* 2020, 10.1109/TGRS.2019.2961684.

Garcia-Pineda, MacDonald, I.R., Li, X., Jackson, C.R., Pichel, W.G., (2012), Oil spill mappingand measurement in the Gulf of Mexico with textural classifier neural network algorithm (TCNNA). *IEEE J. Sel. Top. Appl. Earth Observ. Remote Sens*. 6 (6), 2517–2525. https://doi.org/10.1109/JSTARS.2013.2244061.

Garcia-Pineda, O., G. Staples, C.E. Jones, C. Hu, B. Holt, V. Kourafalou, G. Graettinger, L. DiPinto, E. Ramirez, D. Street, J. Cho, G. Swayze, S. Sun (2020), Classification of oil spill thicknesses using satellite remote sensing for oil spill response, *Remote Sensing of the Environment*, 236, doi.org/10.1016/j.rse.2019.111421.

Jones, C. E. (2023), An automated algorithm for identifying oil slicks with synthetic aperture radar, *Marine Pollution Bulletin*, in review.

Jones, C. E., and B. Holt (2018), Experimental L-band airborne SAR for oil spill response at sea and in coastal waters. *Sensors*, 18 (641), doi:10.3390/s18020641.

Leifer, I., (2019), A Synthesis Review of Emissions and Fates for the Coal Oil Point Marine Hydrocarbon Seep Field and California Marine Seepage, *Geofluids*, doi.org/10.1155/2019/4724587.

Minchew, B., C. Jones, and B. Holt (2012), Polarimetric L-band SAR signatures of oil from the Deepwater Horizon spill, *IEEE Trans. Geoscience Remote Sensing*, doi:10.1109/TGRS.2012.2185804, 50(10), 3812-3820.

Skrunes, S., C. Brekke, C. Jones, and B. Holt (2016), A Multisensor Comparison of Experimental Oil Spills in Polarimetric SAR for High Wind Conditions, *J. Selected Topics in Applied Earth Obs. Remote Sens.*, doi: 10.1109/JSTARS.2016.2565063, 9 (11), 4948-4961.

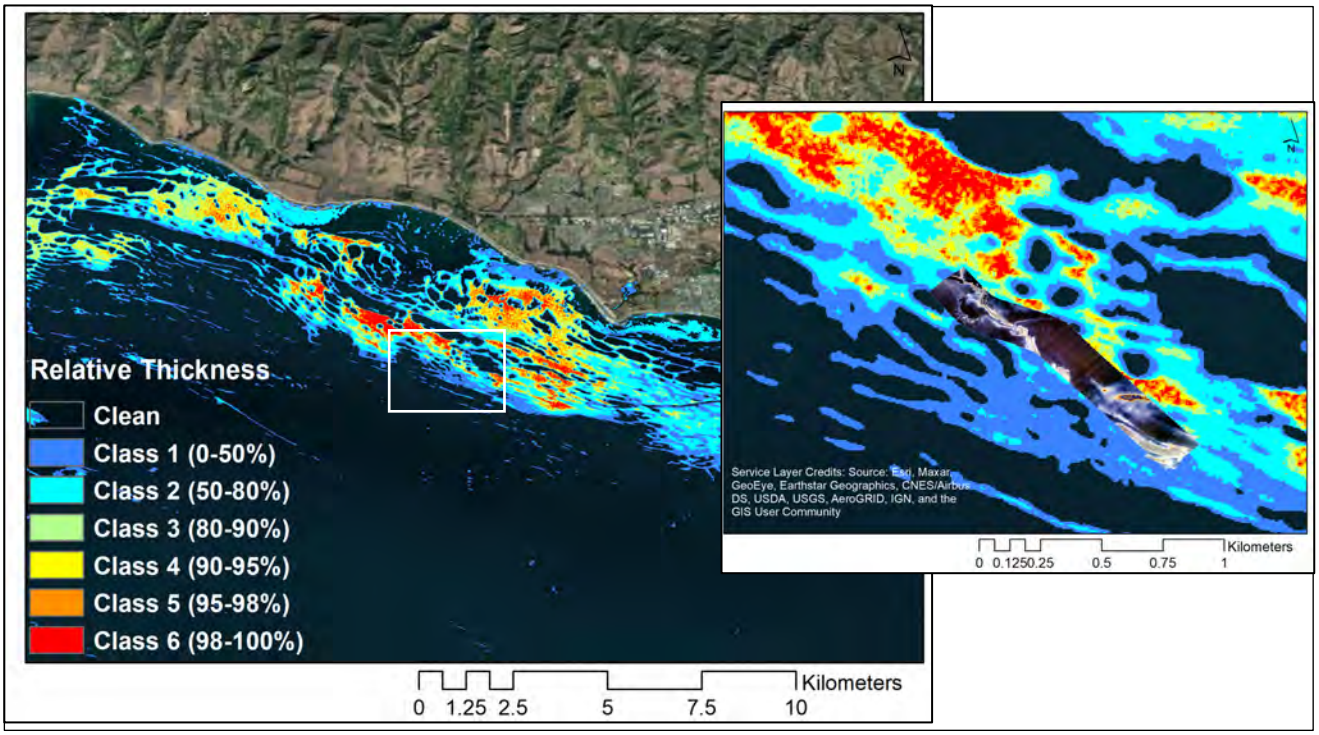

Figure 1. UAVSAR oil thickness classification with a comparison with drone multispectral imagery and classification. May 12, 2022

Deep Learning for ship classification on medium resolution SAR imagery

Bou Laouz Moujahid[1], Vadaine Rodolphe[2], Hajduch Guillaume[2], and Fablet Ronan[1]

[1]IMT Atlantique, Plouzané France
[2]CLS, Plouzané France

I. Introduction

The maritime traffic illustrates multiple types of activities ranging from economical to leasure activities. This traffic induces the need of surveillance by local authorities to address the challenges of maritime safety, maritime security, law enforcement and fisheries control [1]. Far off the coast, satellite observations allow collecting valuable information on the on-going activities using a wide range of sensors, including SAR sensors and AIS data collection. A large litterature is available on the use of a single source of data for the surveillance of maritime traffic for instance using SAR imagery [2][3] or AIS information [4] alone. The synergetic use of multiple source of data is however rapidely progressing [5]. Merging multiple type of data allows either to derive better processing for each data type separately [6] or a real merging of data information to improve the overal martime domain awareness [7].

Commercial SAR satellites deliver very high-resolution imagery [8][9] that can be aquired on specific regions of interest for instance for vessel detection. High-resolution observations make the classification of vessel types straightforward as illustrated by a large litterature on vessel classification for high-resolution satellite imagery [10]. However, few studies have addresse medium-resolution SAR imagery like the one of the Copernicus Sentinel-1 SAR constellation [11]. Sentinel-1 allows regular access to large dataset on European waters and large areas worldwide. Delivering automated vessel classification tools on such imagery would benefit to the analysis the maritime traffic and activities at sea.

This paper specifically adresses the vessel classification on medium resolution SAR images from the Sentinel-1 SAR mission and investigates the possibility to jointly exploit such satellite imagery datasets with AIS data streams to develop a learning-based classification framework.

In section II we present the data considered for the study. In section III we present the overall methodology of classification. In section IV we present the evaluation of performances. In section V we present the conclusion and proposition of applications of the results.

II. Presentation of data

The obsevation plan of the Sentinel-1 SAR constellation allows to collect over ocean mainly medium resolution imagery using the Interferometric Wide Swath (IW) acquisition mode. This data can be made available as detected images on two flavours being GRDM (medium) and GRDH (high) resolution. While the GRDH products are nominally processed by the ESA ground segment, the Collaborative ground stations can generate as well the GRDM flavour products [2].

In this study, we make use of the GRDH products, which has the following characteristics : a swath (rg x az [km]) of 250 x 170, a resolution (rg x az [m]) of 20 x 22 and a pixel spacing (rg x az [m]) of 10 x 10.

CLS made available series of AIS data collected from ground and space receivers. The AIS data collect the location of vessels reporting their positions and information on their speed, route, and type [12]. While the data broadcasted by AIS can be switched off or altered, it is broadly used by the Earth observation community as a proxy of vessel location and type [13].

With a view to implementing deep learning strategies, we created reference datasets using the synergy between AIS data and Sentinel-1 SAR data. Thanks to AIS data, we estimate the precise location of the ships in the SAR image and extract related information contained in AIS messages metadata (in our case, length and type). Based on this position and the positions of ships detected automatically on SAR satellite images (algorithm described in [14]), we extract the image of the ship by cropping the SAR image in the area where the ship is located.

III. Considered leraning-based methology

In this section, we detail our deep learning scheme for ship classification method and the associated rationale.

A. Vessel classification case-study

We focused on the categories "Tanker", "Cargo", and "Others". The "Others" category encompasses every other type of vessels. The motivations of this choice relate to the following facts:

- Neural networks are known to require large amounts of data in order to be effective. As a result, we selected the types of vessels that make up the majority of the data. Table I shows the most represented categories.
- The classification of vessels on medium-resolution radar images using deep learning techniques is a relatively new and under-explored field of research. For instance, the results presented in [6] are difficult to reproduce. In [15], the training was not done on a large dataset.

Therefore, the choice of a three-class problem offers a good starting testbed, as well as a perspective for more complex problems.

Vessel type	Tanker	Cargo	Fishing	Passenger	Others
# images	22569	36822	6981	3531	24678

TABLE I: Description of Data. The category "Others" includes every other type of vessel

B. Training and test datasets

The performance and accuracy of deep learning networks depend heavily on the quality of the data used for training and testing. The quality of the labeling issued from AIS data poses a significant challenge for our dataset. To reduce the impact of this quality shortage, we removed all the products that have the type of vessel "Unitised". These products contain a large amount of cargo, in addition to other types of vessels. Additionally, we removed the products that have a vessel size of zero or greater than 400 meters, as this data is likely to be falsified. The training is carried out on 80% of the data, while the test is done on 20% of the data. The data augmentation methods used includes oversampling and horizontal and vertical flips. Using other methods such as Gaussian noise or rotation proved to be disruptive for the models used. II represents the training and test sets.

Classes	Tanker	Cargo	Others
Number of images	22474	37173	20805
Training set	29739	29739	29739
Test set	4494	7435	4161

TABLE II: Description of training/Test data. The data augmentation is carried out on the categories "Tanker" and "Others"

C. Data preprocessing and choice of input

Due to nature of the SAR data, especially the range of observed pixel values and the occurence of outliers, we applied a logarithmic transformation to the data. This technique helps to minimize the effect of outliers and leads to faster convergence of the loss function.

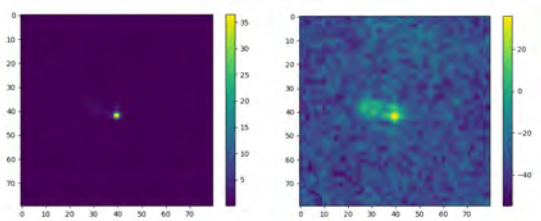

Fig. 1: A comparison of the effect of logarithmic transformation on a vessel image which has a very retro-diffusing point is shown. On the left is the original image, and on the right is the image with the logarithmic transformation applied

In terms of the input for our model, we chose to use a two-band image, which includes backscatter intensity and incidence angle. This selection was made because the incidence angle has a significant impact on the backscatter intensity and then on the contrast between vessel and sea surface. As a result, we did not use any pre-trained network, as we believed that they would not be able to handle these features relevantly.

D. Neural network architectures

To address the classification problem, we developed ensemble convolutional neural networks (CNNs). The overall architectures of the CNNs used in this work are illustrated in Table III. We used the most well-known concepts in the state-of-the-art in our models. In Model **A**, we used a Convolutional Block Attention Module [16], in Model **D**, we used residual layers [17], and in Model **E**, we used the inception module [18]. One can see that all models resemble more or less Model **A**. In fact, Model **A** is our main model. After many experiments, we believe that this is the best model compared to our data and problem.

We used the same parameters in all models. We exploited a categorical cross-entropy loss as a training loss function. We applied an end-to-end training using Adam Optimizer. We used batches of size 64 and a learning rate of 1e-4. This parametrization has shown good results for our classification task.

In our final model, we combined the output of the ensemble of CNN models using an "Averaging" merging. This configuration proved to be the best not only in terms of precision but also in terms of model calibration. It is worth mentioning that Model **A** is perfectly calibrated, while our final model is well calibrated, especially for large confidence values (> 0.8).

IV. Results

The experiments were conducted to evaluate the performance models **A**, **B**, **C**, **D**, and **E**, on the classification task. Table IV presents the total accuracy scores for each model, as well as our final model that was constructed by taking the average of the outputs from all five models. The results of the overall test dataset indicate that the total accuracy of our final model was 79%.

In this study, our objective is to attain an optimal balance between recall and precision for all classes, as there is no preference for classifying one class over another. However, some parts of our data pose a challenge in clearly distinguishing between cargo and tanker ships, causing a minor bias towards either the cargo or tanker class. To address this, we have chosen to lean slightly towards the cargo class as it is the most commonly encountered class in practical applications. The table V presents the confusion matrix and detailed metrics for each class.

V. Conclusion

This paper has studied the classification of vessels on medium resolution SAR images. To the best of our knowledge, this is the first time a Deep learning network has been trained to make this task on a relatively large dataset, and which provides a relatively good results.

A pratical use case for our network is the identification of discrepancies between a vessel's declared information and the network's predictions when those predictions are superior to

Block	Model A	Model B	Model C	Model D	Model E
1	128 - Conv	256 - Conv	128 - Conv	Concatenate(32 - Conv(k-s :1), 32 - Conv(k-s :2), 64 - Conv(k-s :3))	Concatenate(32 - Conv(k-s :1), 32 - Conv(k-s :2), 32 - Conv(k-s :3))
2	CBAM	CBAM	CBAM	256 - Conv	128 - Conv
3	256 - Conv	512 - Conv	256 - Conv	256 - Conv	128 - Conv
4	Average pooling	Average pooling	Average pooling	Dropout	128 - Conv
5	Dropout	Dropout	Dropout	.	Concatenate(Block 1 and 4)
6	.	.	256 - Conv	.	256 - Conv
7	.	.	512 - Conv	.	Average pooling
8	512 - Conv / Dropout / 128 - Conv / 256 - Conv / Average pooling / Dropout / 256 - Conv / 512 - Conv / 256 - FC / 3 - FC (Softmax)				

TABLE III: Structures of the models. In this table, "Conv" denotes a convolutional layer, "CBAM" denotes a convolutional block attention module using the same parameters cited in reference [16], "FC" denotes a fully-connected layer, "k-s" denotes kernel size, and "Concatenate" denotes a concatenation operation. Unless otherwise stated, we use in the convolution operations a kernel size of size 3, strides = 1, and padding = "same", we use in the pooling operations a pool size = 2, stride =1, and padding ="valid". We use a dropout rate of 0.3. All convolution and FC layers are followed by a RELU activation. Note that Block 8 is the same for all models

Models	A	B	C	D	E	Averaging
Total Accuracy	77.8%	77%	76%	77.4%	77.5%	**79%**

TABLE IV: Total Accuracy of Models **A**, **B**, **C**, **D**, **E**

Ground Truth \ Prediction	Tanker	Cargo	Others	Total
Tanker	3346	1026	123	4495
Cargo	844	6026	565	7435
Others	129	698	3334	4161
Total	4319	7750	4022	16091

Classes \ metrics	Precision (%)	Recall (%)	F1-Score (%)
Tanker	77.4	74.4	75.87
Cargo	77.7	81	79.33
Others	82.8	80.12	81.43
Overall	79.3%	78.5%	78.87%

TABLE V: Confusion matrix and evaluation metrics

0.9, which can trigger an alert for potentially-false AIS data. A large attention is placed in the field of maritime safety on *dark vessels* not reporting their location through AIS, while we believe that other alterations of AIS data are possible and under considered, including eroneous declaration of vessel's type (we could call them *bright vessels*).

This paper paves the way for future work to automatic vessel classification on medium-resolution SAR imagery without the need for AIS data. To our knowledge, the SAR imagery is more difficult to alter than the AIS information. This breakthrough could be achieved through the collection of more data and the development of deep learning methods.

AKNOWLEDGMENT

This work was performed under a research contract between CLS and IMT Atlantique. Part of the work was founded supported by "France Relance". We used Sentinel-1 data acquired between 2017 and 2022 as part of the Copernicus Sentinel programme.

REFERENCES

[1] EMSA, "Emsa outlook 2023," 2022.
[2] G. Hajduch, "Vigisat ground receiving station and emsa cleanseanet services," *Remote Detection and Maritime Pollution: Chemical Spill Studies*, pp. 77–86, 2021.
[3] D. J. Crisp, "The state-of-the-art in ship detection in synthetic aperture radar imagery," tech. rep., Defence Science and Technology Organisation Salisbury (Australia) Info ..., 2004.
[4] D. Nguyen, R. Vadaine, G. Hajduch, R. Garello, and R. Fablet, "A multi-task deep learning architecture for maritime surveillance using ais data streams," in *2018 IEEE 5th International Conference on Data Science and Advanced Analytics (DSAA)*, pp. 331–340, IEEE, 2018.
[5] R. Fablet, N. Bellec, L. Chapel, C. Friguet, R. Garello, P. Gloaguen, G. Hajduch, S. Lefèvre, F. Merciol, P. Morillon, *et al.*, "Next step for big data infrastructure and analytics for the surveillance of the maritime traffic from ais\& sentinel satellite data streams," in *BiDS 2017: Big Data from Space Conference*, 2017.
[6] C. Dechesne, S. Lefèvre, R. Vadaine, G. Hajduch, and R. Fablet, "Ship identification and characterization in sentinel-1 sar images with multi-task deep learning," *Remote Sensing*, vol. 11, no. 24, p. 2997, 2019.
[7] Z. Paladin, N. Kapidani, P. Scrima, G. Vosinakis, G. Hajduch, M. Moutzouris, C. Bolakis, and A. Astyakopoulos, "Maritime information sharing environment deployment using the advanced multilayered data lake capabilities: Effector project case study," *Pomorstvo*, vol. 36, no. 2, pp. 291–304, 2022.
[8] Airbus, "Terrasar-x image product guide: Basic and enhanced radar satellite imagery," *Airbus Defence Space*.
[9] D. MDA (MacDonald and A. Ltd.), "Radarsat-2 product description," 2016.
[10] C. Lu and W. Li, "Ship classification in high-resolution sar images via transfer learning with small training dataset," *Sensors*, vol. 19, no. 1, 2019.
[11] ESA, "Sentinel-1 what is it ?." https://sentinel.esa.int.
[12] "Automatic identification system," Jan 2023.
[13] P. W. Vachon, R. A. English, and J. Wolfe, "Validation of radarsat-1 vessel signatures with aislive data," *Canadian Journal of Remote Sensing*, vol. 33, no. 1, pp. 20–26, 2007.
[14] G. Hajduch, V. Kerbaol, and R. de Joux, "Ship detection: From processing to instrument characterization," in *Proceedings of SeaSAR 2008 workshop*, 2008.
[15] J. He, Y. Wang, and H. Liu, "Ship classification in medium-resolution sar images via densely connected triplet cnns integrating fisher discrimination regularized metric learning," *IEEE Transactions on Geoscience and Remote Sensing*, vol. 59, no. 4, pp. 3022–3039, 2021.
[16] S. Woo, J. Park, J.-Y. Lee, and I. S. Kweon, "Cbam: Convolutional block attention module," in *Computer Vision – ECCV 2018* (V. Ferrari, M. Hebert, C. Sminchisescu, and Y. Weiss, eds.), (Cham), pp. 3–19, Springer International Publishing, 2018.
[17] K. He, X. Zhang, S. Ren, and J. Sun, "Deep residual learning for image recognition," in *2016 IEEE Conference on Computer Vision and Pattern Recognition (CVPR)*, pp. 770–778, 2016.
[18] C. Szegedy, W. Liu, Y. Jia, P. Sermanet, S. Reed, D. Anguelov, D. Erhan, V. Vanhoucke, and A. Rabinovich, "Going deeper with convolutions," in *2015 IEEE Conference on Computer Vision and Pattern Recognition (CVPR)*, pp. 1–9, 2015.

INVERSE SAR PROCESSING FOR MARITIME SITUATIONAL AWARENESS

Massimo Zavagli+, Debora Pastina*, Fabrizio Santi*, Alejandro Testa*, Michela Corvino§, Elena Morando**, Chiara Pratola++, Mario Costantini+

*Department of Information Engineering, Electronics and Telecommunications
Sapienza University of Rome, ITALY
email: {alejandro.testa; debora.pastina; fabrizio.santi}@uniroma1.it
**Technische Universität Berlin
Berlin, GERMANY
email: elena.morando@campus.tu-berlin.de
+B-Open Solutions s.r.l.
Rome, ITALY
email: m.zavagli@bopen.eu
m.costantini@bopen.eu
++e-GEOS
Rome, ITALY
email: chiara.pratola@e-geos.it
§ESA ESRIN, Frascati, ITALY
email: michela.corvino@esa.int

1. Abstract

Remote sensing derived information is increasingly supporting the maritime situational awareness, addressing the effective understanding of global maritime domain, including environment, economy, safety and security. However, limitations to the current detection possibilities due to false alarms over the EO derived information, as well as to the extraction of target dynamics, still affect the operational suitability of EO based information services.
As part of the ESA funded project "Maritime Awareness Pre-Operational Demonstrations", the research activity described in this paper aimed at developing and testing ISAR techniques for SAR data processing, enabling refocusing of maritime targets to remove blurring effects caused by uncompensated target movements, and retrieval of the corresponding relevant motion parameters. Validation activities were performed, with specific focus on quantitative metrics assessing refocusing capabilities, by applying the developed processing chain on Stripmap and Spotlight COSMO SkyMed and Cosmo Second Generation images. The accuracy of the vessel speed estimation was also assessed by using AIS datasets as ground truth.

2. Introduction

By coherently processing echoes originating from the observed scene at varying aspect angles, synthetic aperture radar (SAR) and inverse SAR (ISAR) systems achieve the high cross-range resolution needed to get electromagnetic images. Standard SAR imaging relies on coherent echo processing assuming the observed scene stationary and the platform's motion in relation to the ground usually known. The use of standard focusing on moving targets results in defocusing effects that reduce range and azimuth resolutions and causes azimuthal displacements, [R1]. For a linear uniformly accelerated target motion, the range velocity component causes a shift in target imaging along the azimuth direction and smearing along the range, whereas the range acceleration and azimuth velocity component are responsible for the smearing effect along range, the defocusing along the azimuth direction, and for SNR losses. The refocusing process seeks to reduce blurring effects and estimate motion parameters. Conversely, the ISAR approach exploits the target own motion to achieve the synthetic aperture needed for radar imaging. It is based on the analysis of received echoes as a function of fast time and Doppler frequency, yielding a two-dimensional image. The time analysis offers the position of bright points along the range, whereas the Doppler analysis provides the position across the range. Since the relative motion between the target and the radar is typically unknown, it must be estimated directly from the radar signal by means of autofocusing technique. Previous work, [R2], has shown the effectiveness of the application of ISAR techniques at refocusing the images of such type of targets. Along this line, several

techniques for moving target motion compensation and motion parameter estimation have been tested in this research activity, demonstrating that SAR/ISAR configurations are effective for improving moving targets focusing in SAR imagery, as well as to derive vessels kinematic parameters, [R3]-[R5]. Noticeably, the effectiveness has be proved by analyzing an extended dataset nicely complemented by reference ground truth provided by recorded AIS data.

3. Architecture

The proposed service chain is developed to ingest Single Look Complex (SLC) SAR data product, taking advantage of the availability of the SLC layer for all satellite SAR missions. It is based on four main steps:

1) First, an inverse focusing, based on Chirp Scaling (CS) algorithm [R6], of the SLC SAR data is applied using metadata parameters, [R3]. This step aims at removing Range Migration Correction (RMC) and azimuth compression that were performed in the focusing process by incorrectly assuming scene stability. The result of this process is an instance of raw SAR data.

2) The raw SAR data is then processed through an autofocus algorithm that finds the optimal Doppler centroid and Doppler rate that maximize the quality of the SAR clip, [R2]. For this purpose, a global optimizer is used. The objective function of the optimization is the metric quantifying the quality of the focused SAR clip. Used metrics are: entropy, image contrast, spectral power density. Focusing is performed by using the efficient CS algorithm that can resolve migration correction without demanding interpolation computations. Finally, the velocity of the vessel, both the azimuth component for stripmap and spotlight 2 SAR data, and the range component for stripmap SAR data, are estimated from the optimal Doppler rate and centroid, respectively [R3].

3) The residual Doppler phase is then estimated through PGA, [R7], and removed. This step removes defocusing terms higher than second order (the parabolic component due to linear velocity has been removed from the autofocus) and stabilizes a point (fulcrum point), chosen as the one with the largest amplitude, which will be used in the next step.

4) The last step, the Cross-Range Scaling (CRS), aims to estimate the effective rotational velocity of the vessel, if any, for cross-range scaling and, if needed, to remove defocusing effects. As known, depending on SNR, target size and specific target motion, the performance achievable can be very poor, hence two different approaches have been tested and compared on specific representative case studies. The first approach exploits the quadratic component of the phase induced by the rotation motion, [R4], while the second exploits the slope of linear features in the target image to estimate the scale factor related to the rotation motion, [R5].

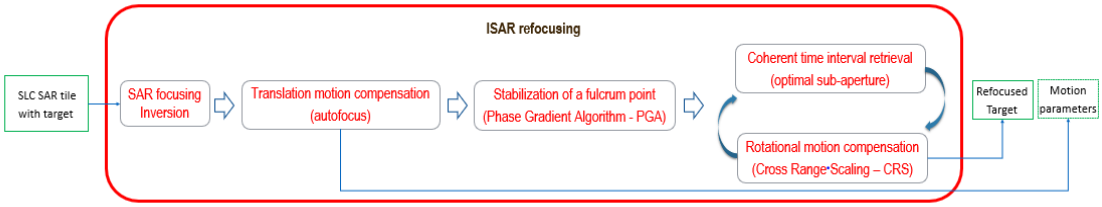

Figure 1 : ISAR Processing Chain

4. Validation and Results

The processing chain was tested over 3 areas of interest, exploiting a set of 24 SLC COSMO-SkyMed and COSMO-SkyMed Second Generation imagery, and AIS datasets provided by SPIRE. The performance assessment addressed two main aspects of the ISAR processing results:

1) The enhancement of the amplitude SAR image contrast.

The measurements of the contrasts have been calculated for all analyzed targets at different steps of the ISAR processing:

- Contrast of the original SAR image clip
- Contrast after the chirp-scaling refocusing
- Contrast after cross-range scaling

Based on these contrast estimations three key performance indicators have been retrieved:

- % mean contrast improvement due to refocusing step
- % mean contrast improvement due to cross-range scaling (CRS) step
- % mean contrast improvement due to the overall ISAR processing

The average improvement in image contrast, evaluated over 300 vessels, is about 18%. Most of the vessels showed defocusing effects due to linear motions and the refocusing is performed mainly by the autofocusing step. However, there are also different cases in which the rotation motion is relevant and produces strong defocusing effects that have been removed mostly by the last step based on CRS.

2) The estimation of the movement parameters.

The assessment of the retrieved movement parameters is based on a comparison with a reference set of motion parameters provided by the collected AIS data. In this analysis, only linear velocity parameters can be assessed, because the effective rotation velocities are not available in AIS data. Therefore, after a correlation process to link vessels in the SAR data to the corresponding AIS tracks, the AIS velocities of the vessels have been projected along the SAR azimuth and slant range direction. The quality of the correlation results, and therefore the effective reliability of the AIS velocities, depends on the linear distance (m) between the geographical position of the vessel in the SAR data and that reported in the correlated AIS tracks. The azimuth displacement in the SAR data of the vessel due to its range velocity has been calculated and compensated in the distance calculation. However, this distance is affected by different errors: inaccuracy of the SAR geometric information encoded in the state vectors, inaccuracy in the identification of the center of the vessel in the SAR data, unknown position of the AIS transmitter within the vessel and AIS positions inaccuracies. Higher is the distance between a vessel and its corresponding AIS track, less reliable is the AIS information content. For this reason, the assessment of the retrieved movement parameters has been performed considering only correlated target with distance smaller than 200 meters. Based on a comparison between velocity values (along azimuth and slant-range directions) of the vessels extracted by the AIS and those estimated by ISAR processing chain, two key performance indicators have been retrieved:

- Azimuth velocity root mean square (RMS)
- Range velocity root mean square (RMS)

The resulting velocity RMSEs are 1.90 [m/s] for the azimuth component, calculated on 220 vessels (in stripmap and spot-light-2 images), and 0.90 [m/s] for the range component, calculated on 24 vessels (in stripmap images). As an example figure 2 shows a comparison between the ship image as available in the CSK acquisition and the same image after refocusing: a clear improvement in the quality of the image is observed and, as a consequence, it is quite easy to identify in the radar image the main parts and the main characteristics of the considered target that are not recognizable in the original image.

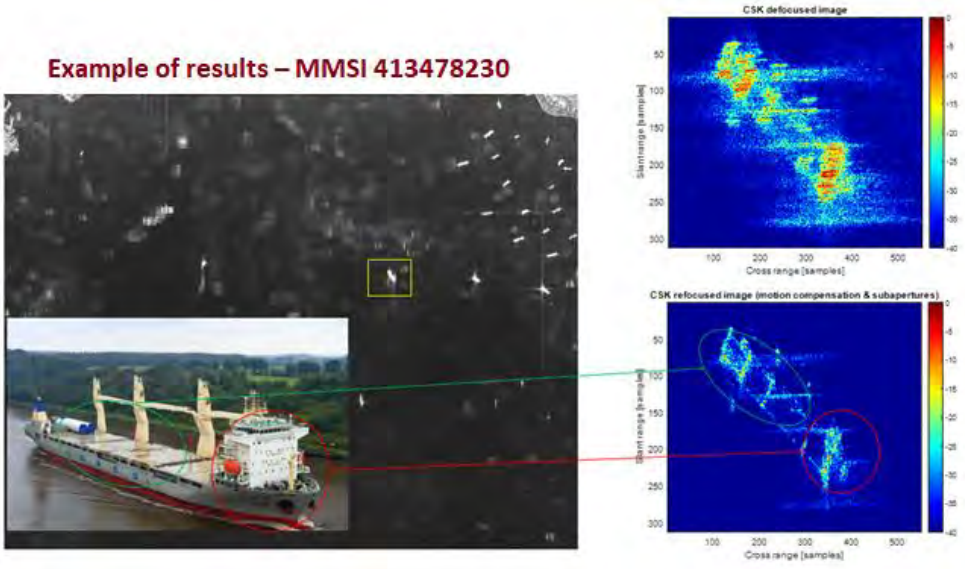

Figure 2: example of achievable results

5. Conclusions

The activity aimed at identifying shortcomings and advantages of inverse SAR algorithms in view of improving characterization of moving vessels by removing/mitigating defocusing effects due to linear and rotation motions of the target,

estimation of such motion parameters, and cross-range scaling of the target images. This activity demonstrated the impact of the ISAR processing in improving the characterization of moving targets in SAR imagery.

References

[R1]R. K. Raney, "Synthetic Aperture Imaging Radar and Moving Targets," in IEEE Transactions on Aerospace and Electronic Systems, vol. AES-7, no. 3, pp. 499-505, May 1971

[R2] M. Martorella, D. Pastina, F. Berizzi and P. Lombardo, "Spaceborne Radar Imaging of Maritime Moving Targets with the Cosmo-SkyMed SAR System," in IEEE Journal of Selected Topics in Applied Earth Observations and Remote Sensing, vol. 7, no. 7, pp. 2797-2810, July 2014, doi: 10.1109/JSTARS.2014.2321708.

[R3] Pastina, D., Turin, F., "Exploitation of the COSMO-SkyMed SAR System for GMTI Applications", (2015) IEEE Journal of Selected Topics in Applied Earth Observations and Remote Sensing, Volume 8, Issue 3, 1 March 2015, Article number 6919998, pp. 966-979.

[R4] D. Pastina, "Rotation motion estimation for high resolution ISAR and hybrid SAR/ISAR target imaging," 2008 IEEE Radar Conference, 2008, pp. 1-6, doi: 10.1109/RADAR.2008.4721055.

[R5] D. Pastina, C. Spina, "Slope-based frame selection and scaling technique for ship ISAR imaging", IET Proceedings on Signal Processing, Volume 3, Issue 3, September 2008, pp. 265-276.

[R6] Raney R. K., et al., "Precision SAR processing using chirp scaling", IEEE Trans. GRS, 1994, 32, (4), pp. 786-799.

[R7] D. E. Wahl, P. H. Eichel, D. C. Ghiglia, C. V. Jakowatz Jr, "Phase Gradient Autofocus – A Robust Tool for High Resolution SAR Phase Correction", IEEE Transactions on Aerospace and Electronic System, vol. 30, no. 3, July 1994.

Developing Refugee Vessel Detection Capabilities with Polarimetric SAR

Existing research in (semi-)automatic marine target detection using Synthetic Aperture Radar (SAR) data mainly concentrates on the detection and classification of large, metallic targets - mainly ships. This project focuses on the detection of small, non-metallic targets, i.e. inflatable rubber vessels. Such vessels are used by migrants attempting to cross from Africa to Europe. The physical attributes of such kind of targets, namely its small size and height and the absence of materials of high dielectric constant such as metals, decrease the detection capabilities of commonly known vessel detection systems. We tried to apply and test a range of detectors of different methodology to gain a better understanding of the target's backscattering properties and to identify the best approach to develop new, specially tailored detection algorithms. The science developed in this work builds on the shoulder of previous research (Lanz et al. 2020, Lanz et al. 2021) we have carried out on inflatable vessel detection.

We use multi-platform SAR data (mainly TerraSAR-X, accompanied by quad-pol Cosmo SkyMed (CSG) and ICEYE) holding "sea truth" to a 12m long rubber inflatable vessel identical in construction and material to those which are often used by human traffickers to send migrants to cross the central Mediterranean Sea. Data acquisition was done in a small lake near Berlin, Germany, which functioned as a test bed. The experiment setting is such to emulate the backscattering of 80 passengers on board and using two different orientations. We combined the two collections to create a testing environment as close as possible to the real situation. In experiments with a ground SAR system we identified wet clay pebbles, packed in 30x40cm air-tight plastic bags, as the best choice to simulate humans in SAR and filled the inflatable with them (Fig.1).

Figure 1: The data acquisition campaign setup.

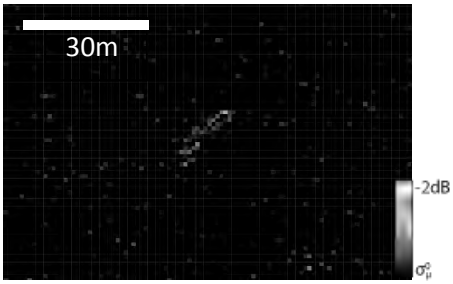

Figure 2: VV-pol ICEYE with the target in the center (©ESA 2022).

The collection comprises single, dual and quad-polarimetric data and covers a variety of different sensor and scene parameters. For detector testing we used different combinations of dual-pol TerraSAR-X data. With the high-resolution single-pol imagery from ICEYE we explored the location and the spatial distribution of the scattering intensity inside the vessel and in its close vicinity (Fig.2). The quad-pol CSG enabled us to apply a variety of coherent and incoherent polarimetric decompositions (Pauli, Cloude-Pottier, Yamaguchi and Cameron) to get insight about the different scattering mechanisms occurring on the inflatable. Fig.3 shows the entropy, which is high over the lake (red) and lower for the vessel (blue).

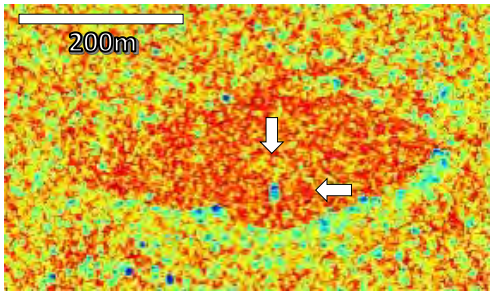

Figure 3: Entropy (©ASI 2022).

Different combinations of incidence angles (low, medium, high), polarimetric dual-pol channel-pairs (HH VV, HV HH, VH VV, vessel orientation relative to the LoS (45°, 90°) support the effort of identifying the main scattering mechanism and its detectability.

To facilitate the testing of vessel detector algorithms in a more realistic situation of different sea states, for the case of TSX, we put together a collection of dual-pol TSX data of wave heights between 0.5m and 6.5m, grouped by wind direction (up/down wind, cross wind), polarization (HH VV, HV HH, VH VV) and three categories of incidence angle (low, medium, high). We fused the inflatable backscattering with the datasets showing the open ocean. Respecting all important sensor parameters (resolution/acquisition mode, incidence angle and polarization), we placed pixels with the boat in a background made of pixels from the ocean.

We applied, apart from the intensity-based CA-CFAR detector, six Polarimetry-based and one sub-look-based detector following a qualitative evaluation of their detection capabilities regarding the special target. Amongst the polarimetry detectors are the Depolarization Ratio Anomaly Detector (iDPolRAD) (Marino et al. 2016), the Geometrical Perturbation-Polarimetric Notch Filter (GP-PNF) (Marino, 2013), the Polarimetric Match Filter (PMF) (Swartz et al. 1988, Novak et al. 1989), the polarimetric symmetry (PolSym), the polarimetric entropy (PolEntr) detector and the Polarimetric Whitening Filter (PWF) (Novak et al. 1989). The sublook-based detectors include the sublook correlation method (Marino et. al. 2015).

The novelty of this work lies in the innovative way we emulated the images of ocean with a fully boarded inflatable vessel. Second, the surface scattering detecting variant of the iDPolRAD, called 'SiDPolRAD'(Lanz et al. 2021), and the iDPolRAD were tested with co-pol (HH VV) data, adding dihedral scattering and Bragg scattering to the range of detectable scattering mechanisms of these detectors. Since the polarimetric decompositions resulted in a good contrast between the vessel and the lake surface when looking at volume scattering, we introduce a double bounce detection algorithm that uses the T22 element of the coherency matrix [T]. Further, we tested and benchmarked the combination of detectors to enhance the detection capabilities for the inflatable at higher sea states. We also worked on fusion of detectors, where we used both 'or' and 'and' operators for the combined detection masks.

The detector comparison showed very good results for the PWF, the PMF, the PolSym detector and the PNF. For dual cross-pol data, we tested different combinations of the polarimetric symmetry, the volume and surface detectors, CACFAR and the PWF. The best results could be obtained with the fusion of iDPolRAD with the SiDPolRAD, called 'PolRatioOR'. However, this fusion of detectors could not outperform the PolSym and the PWF (Fig.4).

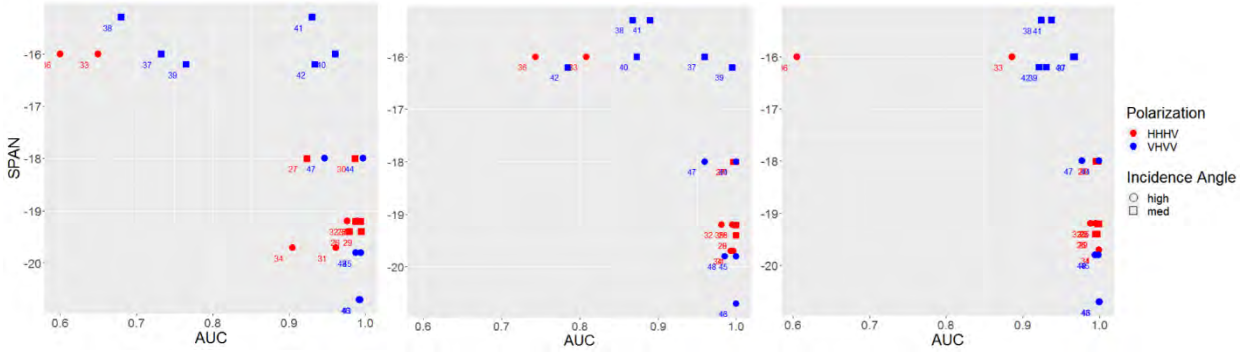

Figure 4: Detector comparison results for dual cross-pol data.
PolRatioOR (mean AUC: 0.91), PolSym (mean AUC: 0.951), PWF (mean AUC: 0.961).

For co-pol data, the combination of the PolEntr and the T22 detector delivers the best results, the PMF comes second (Fig.5). The testing showed, that the combination using the 'and' operator worked best and was therefore called 'HT22AND'. It is capable of generating very good

results even at high sea states, a quality which we attribute to the PolEntr.

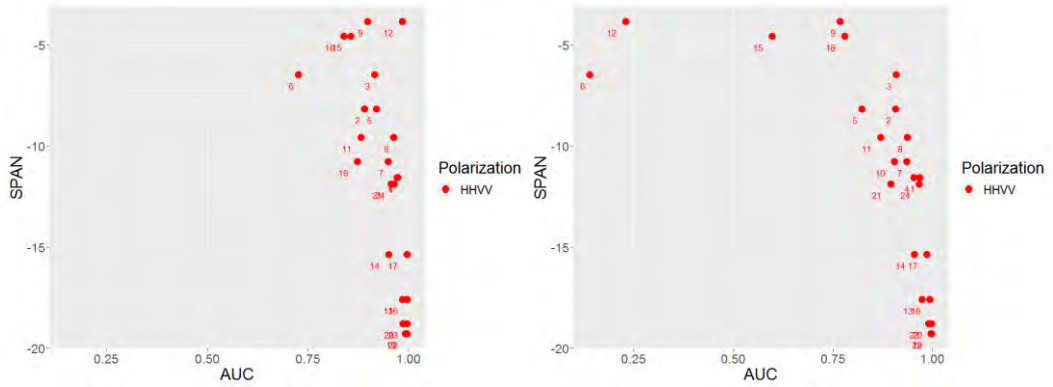

Figure 5: Detector comparison results for dual co-pol data. HT22AND (mean AUC: 0.936) and PMF (mean AUC: 0.884).

In case of low clutter, the main signal is produced by thermal noise. This state of high Entropy allows for target identification when there are clearly identifiable volume and/or surface scattering mechanisms and lower Entropy at the inflatable. In case of higher surface scattering, such as it is the case for higher sea states, the entropy of the water surface decreases and the vessel detector searches for higher entropy. The HT22AND reaches 95% positive true with a false alarm rate of less than 2% when only looking at medium and high incidence angles and wave heights of maximum 2 meters. In both scenarios, the detector searches for volume scattering as well and improves the detection result. The PMF and the PWF similarly show very good results, both in co-pol and cross-pol data.

The primary motivation of this research is to mitigate the ongoing humanitarian crisis at Europe's southern Sea border. The applicability of the project's results to the setting of the open sea, where stronger winds and seas could interfere with radar detection, will be discussed. This project builds a foundation to develop satellite based detection systems for inflatable rubber boats. Such systems could be integral to search and rescue infrastructure in reducing the number of lives lost at sea.

References:

Marino, A. (2013). A notch filter for ship detection with polarimetric SAR data. *Selected Topics in Applied Earth Observations and Remote Sensing, IEEE Journal Of*, *6*(3), 1219–1232.

Marino, A., Sanjuan-Ferrer, M. J., Hajnsek, I., & Ouchi, K. (2015). Ship Detection with Spectral Analysis of Synthetic Aperture Radar: A Comparison of New and Well-Known Algorithms. *Remote Sensing*, *7*(5), 5416–5439. https://doi.org/10.3390/rs70505416

Schneider, R. Z., Papathanassiou, K. P., Hajnsek, I., & Moreira, A. (2006). Polarimetric and interferometric characterization of coherent scatterers in urban areas. *IEEE Transactions on Geoscience and Remote Sensing*, *44*(4), 971–984. https://doi.org/10.1109/TGRS.2005.860950

Marino, A., Dierking, W., & Wesche, C. (2016). A Depolarization Ratio Anomaly Detector to Identify Icebergs in Sea Ice Using Dual-Polarization SAR Images. *IEEE Transactions on Geoscience and Remote Sensing*, *54*(9), 5602–5615. https://doi.org/10.1109/TGRS.2016.2569450

Swartz, A. A., Yueh, H. A., Kong, J. A., Novak, L. M., & Shin, R. T. (1988). Optimal polarizations for achieving maximum contrast in radar images. Journal of Geophysical Research: Solid Earth, 93(B12), 15252–15260.

Novak, L. M., Sechtin, M. B., & Burl, M. C. (1989). Algorithms for Optimal Processing of Polarimetric Radar Data. Massachusetts Inst. of Tech Lexington Lincoln Lab, 9

Future Missions

Future Missions

Garcia-Mondéjar, Albert; Freer, Bryony; López-Zaragoza, Juan Pedro; McKeown, Charlie; Gibert, Ferran; Mank, Enrico; Recchia, Lisa; Hendricks, Stefan; Scagliola, Michele; Fornari, Marco; Di Bella, Alessandro; Bouffard, Jerome; Cipollini, Paolo; Borde, Franck.
Enhanced Sea Ice Performances from CRISTAL Mission

Jawak, Shridhar; Lauknes, Tom Rune; Rouyet, Line; Sivertsen, Agnar
Airborne SAR Sensor in Svalbard; User Perspective on Mission Requirements and Observational Needs

Fu, Jiayu; Li, Yuanhao; Chen, Zhiyang; Hu, Cheng
A New Distributed ATI SAR System: GEO-LEO SAR ATI Concept

Suess, Martin; de Witte, Erik; Rommen, Björn
The Harmony SAR Instrument

Lauknes, Tom Rune; Sivertsen, Agnar; Gebrie Yitayew, Temesgen; Rouyet, Line; Werner, Charles; Jenning, Michael; Plettemeier, Dirk; D. Jawak, Shridhar
Development of a Dual-Frequency Airborne SAR Sensor in Svalbard

Donlon, Craig
Future Missions at the European Space Agency

Gommenginger, Christine; Martin, Adrien; Nagamine, Katia; Gracheva, Valeria; Egido, Alejandro; Hall, Kevin; Casal, Tania; Martin-Iglesias, Petronilo
SEASTAR - Earth Explorer 11 Mission Candidate: Imaging Small-Scale Ocean Dynamics

Lopez Dekker, Paco; Chapron, Bertrand; Pasquero, Claudia; Stoffelen, Ad; Buongiorno Nardelli, Bruno; Masina, Simona; Kleinherenbrink, Marcel; Theodosiou, Andreas; Rommen, Björn; Desbiolles, Fabien
Multistatic High-Resolution Observations of the Ocean with the Harmony Mission: Science, Products, and Expected Performances

Dubois, P.; Monnier, G.; Lopez-Dekker, P.; Yitayew, T. G.; Armstrong, T.; Gombert, B.; Soulat, F.; Hellouvry, Y.-H.; Camus, B.; Grydeland, T.; Lajas, D.; Rommen, B.; De Witte, E.
Harmony End-o-End Performance Simulator: Evaluating The Performance Of A Bi-static ATI SAR Mission For Ocean Observations

Lopez Dekker, Paco; Kleinherenbrink, Marcel; Theodosiou, Andreas; Eleveld, Marieke; Zijl, Firmijn; Macedo, Karlus; Luiz, Thiago; Kubanek, Julia
WaddenSAR campaign: first results

Enhanced Sea Ice Performances from CRISTAL Mission

Garcia-Mondéjar, Albert (1); Freer, Bryony (2,3), López-Zaragoza, Juan Pedro (1); McKeown, Charlie (1); Gibert, Ferran(1); Mank, Enrico (4); Recchia, Lisa (5); Hendricks, Stefan (6); Scagliola, Michele (7); Di Bella, Alessandro (7); Fornari, Marco (7); Bouffard, Jerome (8); Cipollini, Paolo (8); Borde, Franck (8)

Organisation(s): 1: isardSAT; 2: BAS, 3: University of Leeds, 4: Airbus; 5: Aresys; 6: AWI; 7: RHEA, ESA; 8: ESA
Email: Albert.Garcia@isardSAT.cat

The Copernicus polaR Ice and Snow Topography ALtimeter (CRISTAL) mission, planned to be launched in 2028, will incorporate a dual Ku/Ka band interferometric altimeter with specific transmission pulse sequences designed to enhance the sea ice performances. The open burst mode will enable the generation of Fully Focussed products with simultaneous estimations of snow depth and freeboard thanks to the dual-band range measurements. The target accuracy is 3 cm for sea ice freeboard, 5 cm for snow depth, and 0.15 m for the sea ice thickness at a scale of 25 km, which are not achievable with current radar altimeter missions.

Current sea ice freeboard measurements from satellite radar altimeters are obtained based on the procedure first introduced by RD. 1: waveforms along satellite tracks are classified as sea ice floes returns or leads by looking at their shape and maximum power, both determined mainly by surface roughness. The range from each of them is determined by tailored retrackers and later translated into elevation measurements. The lead heights are interpolated to estimate the SSH along the satellite track, which is then subtracted from the sea ice elevations to estimate freeboard heights.

Since the first altimeters launched in early 90s, the sea ice measurements have been improved from mission to mission by increasing the polar coverage, improving the along track resolution thanks to the SAR processing and providing interferometric capabilities to be able to properly geolocate off-track echoes. CRISTAL mission will keep improving the sea ice measurement being the first mission to incorporate Ku and Ka collocated measurements, open burst transmission mode to enable Fully Focussed processing and interferometric capabilities thanks to the two antennas. From the measurements point of view, it can be seen as having CryoSat-2, Sentinel-6 and SARAL/AltiKa on a single platform. Thanks to CryoSat-2 series of measurements over 13 years, recent publications (RD. 2, RD. 3, RD. 4) are stablishing the baseline methodologies and performances to be considered in the CRISTAL mission definition.

At this stage of the CRISTAL mission design, phase C, the expected performances are being evaluated against the requirements to verify the effectiveness of the mission configuration and assess its compliance. In this framework, an end-to-end validation environment has been designed.

Following the verification and validation plan defined during this first stage, the System and Instrument Simulator (SIS), the Ground Processor Prototype (GPP) and the Performance Assessment Tool (PAT) are in charge of providing the overall end-to-end performances of the mission over different scenarios (e.g. point targets, sea ice with different snow properties, sea ice with leads placed at different orientations, ocean tracks with different SWH, and wind conditions). In addition to the simulated data, real data from Sentinel-6, CryoSat-2 and SARAL/AltiKa can be also combined to assess the benefits from the interferometric, dual frequency and open burst Fully Focussed acquisitions.

On top of the requirements that should be met, CRISTAL mission can provide complementary types of measurements that have not been explored within the current altimetry missions. The work performed within the Sentinel-6 Validation Team [RD. 6] has demonstrated that it can be possible to make accurate distributed measurements (computation of areas) from the Fully Focussed radargrams when clear targets are located off-track.

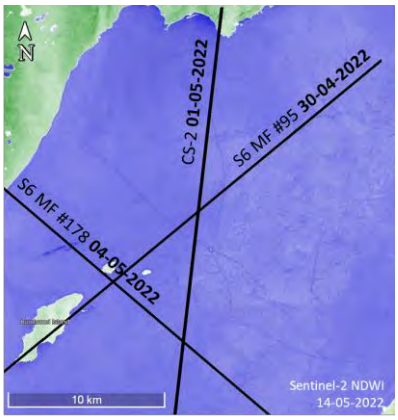

Figure 1. Sentinel-6 and CryoSat-2 ground tracks with the Sentinel-2 NDWI background image.

The improvement of this concept with CRISTAL mission is clear, we will not only be able to measure 2D features, but also to geolocate them properly thanks to the interferometric capabilities. We have provided an example of the potential capabilities of CRISTAL by looking at sea ice (frozen lake) area with time and space collocated Sentinel-6 (ascending pass #95 on the 30th of April and descending pass #178 on the 4th of May) and CryoSat-2 (1st of May pass) radargrams together with a Sentinel-2 (14th of May) NDWI image highlighting features that can be seen in the scene, Figure 1 .

In Figure 2 and Figure 3, we can see the radargrams from the different passes, comparing the features observed in the Unfocussed and Fully Focussed SAR.

As expected, the improved along track resolution from FFSAR (20 m vs 300 m in this example) allows us to better monitor smaller leads, being able to retrieve its dimensions (length and width) and location. Currently within the Sentinel-6 capabilities, we are not able to properly geolocate them but to derive the across track distance to the nadir without the possibility to determine towards which side. It can be appreciated from Figure 2 the "range folding" effect where signal from the Burntwood island is overlapped at the same range as the lead #2.

Comparing Figure 2 and Figure 3, we note how the lead #2 is observed from different points of view. Figure 2 presents a parallel observation, whereas Figure 3 shows the lead crossing the ground track. Extending this 2D feature extraction to the open sea ice environments, some other parameters such as the sea ice concentration or the sea ice roughness can be potentially derived based on the analysis of the backscattering of the echoes. Similar concepts are already being assess over open ocean by measuring the swell from the Fully Focussed waveforms tail, RD. 5.

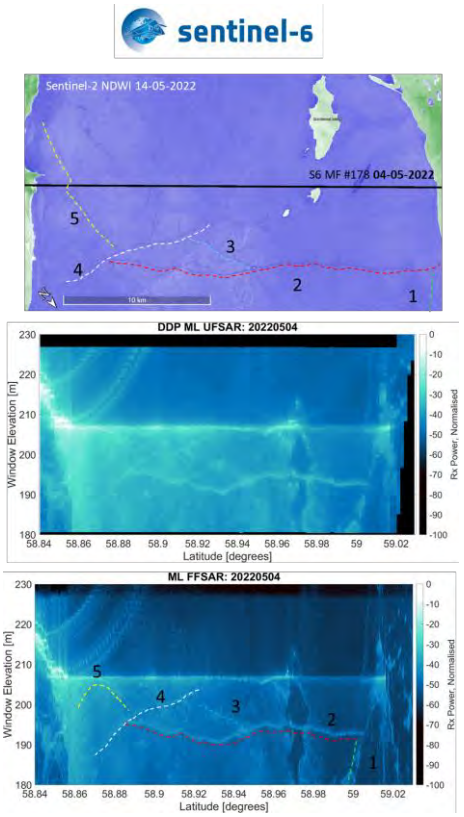

Figure 2. Sentinel 6-radargrams for pass #178 from Unfocussed and Fully focussed processing highlighting the leads that can be seen

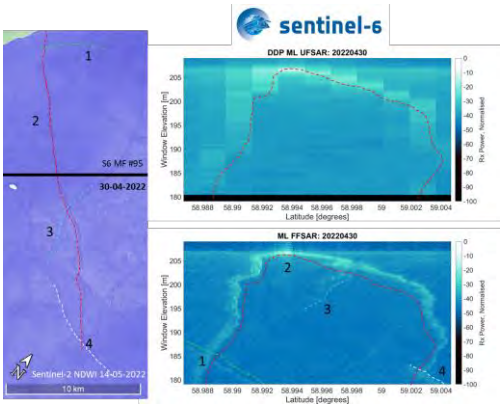

Figure 3. Sentinel-6 radargrams for pass #95 from Unfocussed and Fully focussed processing highlighting the features leads that can be seen.

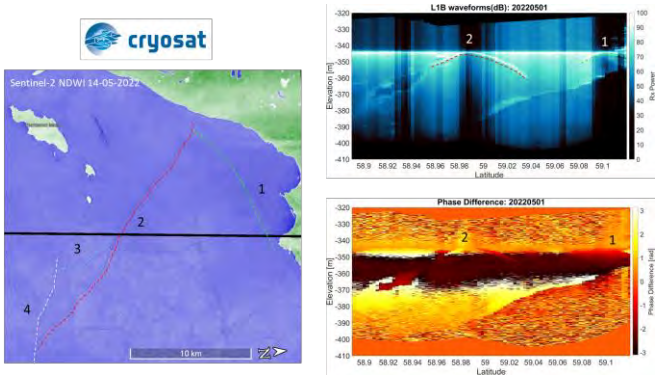

Figure 4. CryoSat-2 radargram and phase difference information highlighting the leads that can be seen.

In the CryoSat-2 pass from Figure 4, we can observe now how the phase difference measured by the interferometer is able to capture positives phase difference values in the lead#2 echoes that are on the east side of the trac and negative values on the west one. Not only the lead#2 but also Burntwood island present reliable phase difference values that will enable a proper geolocation of these range measurements and also enhanced 2D retrievals when using proper focused data.

A similar improvement is also expected with regards to the capabilities for measuring and detecting icebergs. The methods described in [RD. 7] will be used to generate iceberg retrievals, but the use of Fully Focussed waveforms instead of Unfocussed is opening the door to better retrieve distributed measurements such as shape of the icebergs. This improvement can be explored in Sentinel-6 data over icebergs, as shown in Figure 5 and Figure 6. Fully Focussed waveforms were generated every 25 metres, whereas the unfocussed SAR waveforms have the nominal 300 meters resolution.

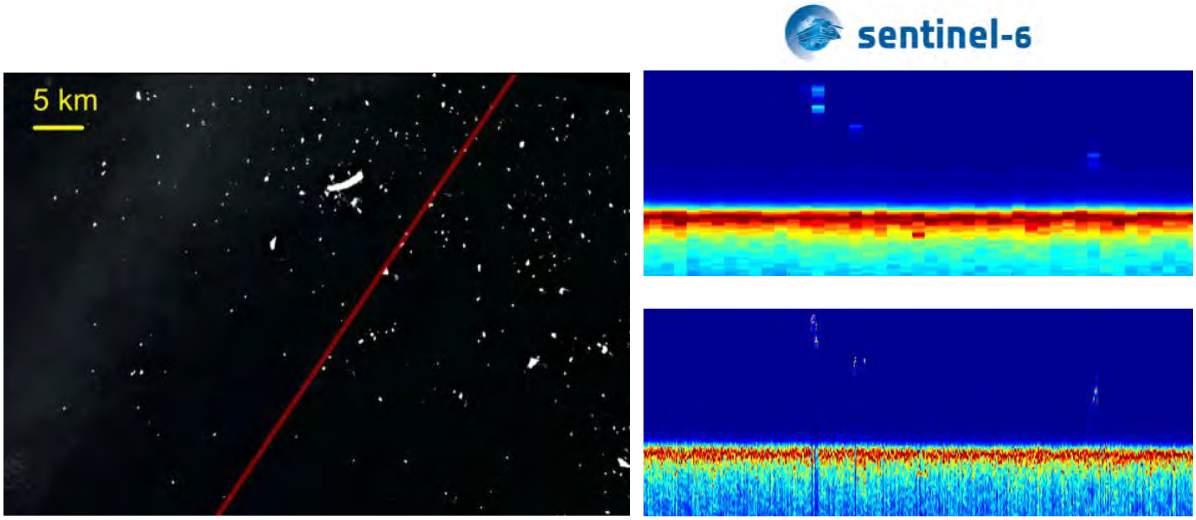

Figure 5. Sentinel-6 08/01/2021 12:26:34 ground track over Sentinel-2 07/01/2021 12:07:14 image (*left*), normalised waveforms, UF-SAR (*right top*), and FF-SAR (*right bottom*).

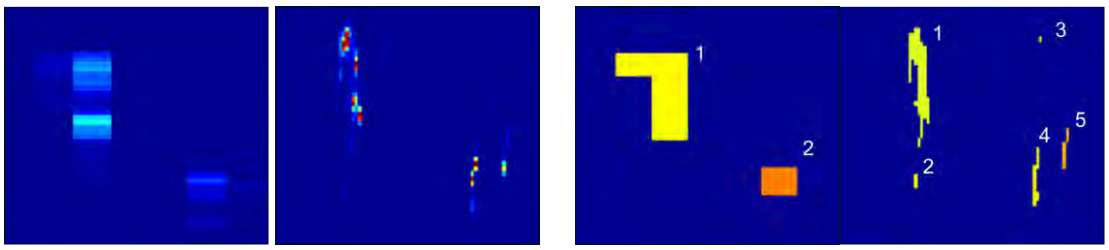

Figure 6. Iceberg echoes zoom (*left*), detection and labelling (*right*). Each colour represents a different iceberg detected for both UF-SAR (*third*) and FF (*fourth*).

References:

RD. 1 S. Laxon, N. Peacock, and D. Smith, "High interannual variability of sea ice thickness in the Arctic region," Nature, vol. 425, no. 6961, pp. 947–950, Oct. 2003.

RD. 2 Lawrence, Isobel R., et al. "Estimating snow depth over Arctic sea ice from calibrated dual-frequency radar freeboards." The Cryosphere 12.11 (2018): 3551-3564.

RD. 3 Di Bella, Alessandro, et al. "Multi-peak Retracking of CryoSat-2 SARIn Waveforms Over Arctic Sea Ice."IEEE Transactions on Geoscience and Remote Sensing 59.5 (2020): 3776-3792.

RD. 4 Landy, J.C., Dawson, G.J., Tsamados, M. et al. A year-round satellite sea-ice thickness record from CryoSat-2. Nature 609, 517–522 (2022). https://doi.org/10.1038/s41586-022-05058-5

RD. 5 Altiparmaki, O., Kleinherenbrink, M.,Naeije, M., Slobbe, C., & Visser, P.(2022). SAR altimetry data as a newsource for swell monitoring. GeophysicalResearch Letters, 49, e2021GL096224. https://doi.org/10.1029/2021GL096224

RD. 6 isardSAT, VALERIA - Water extent monitoring: preliminary results with FFSAR, Sentinel-6 Validation Team Meeting, 26-28 October 2021 (link).

RD. 7 Tournadre, J., K. Whitmer, and F. Girard-Ardhuin (2008), Iceberg detection in open water by altimeter waveform analysis, J. Geophys. Res., 113, C08040, doi:10.1029/2007JC004587.

Airborne SAR Sensor in Svalbard; User Perspective on Mission Requirements and Observational Needs

Shridhar D. Jawak[1], Tom Rune Lauknes[2], Line Rouyet[2], Agnar Sivertsen[2]

1 Svalbard Integrated Arctic Earth Observing System (SIOS), SIOS Knowledge Centre (SIOS-KC), Norway
2 NORCE Norwegian Research Centre, Tromsø, Norway

Svalbard Integrated Arctic Earth Observing System (SIOS) is an international collaboration of 28 scientific institutions from 10 countries to build a collaborative research infrastructure that will enable better estimates of future environmental and climate changes in the Arctic. SIOS's mission is to develop an efficient observing system in Svalbard, share technology and data using FAIR principles, fill knowledge gaps in Earth system science and reduce the environmental footprint of Arctic research. Since 2019, SIOS in collaboration with its member institution Norwegian Research Centre (NORCE) installed, tested, and operationalised optical imaging sensors in Lufttransport's Dornier (DO-228) (LN-LYR) passenger aircraft stationed in Longyearbyen under the SIOS-InfraNor project, making the acquired imagery compatible with research use in Svalbard. Two optical sensors are installed onboard the Dornier aircraft: (1) the PhaseOne IXU-150 RGB camera and (2) the HySpex VNIR-1800 hyperspectral sensor. The aircraft is configured to acquire aerial RGB imagery and hyperspectral remote sensing data during its regular logistics and transport operation in Svalbard. Since 2020, SIOS has supported around 50 flight hours to acquire Dornier aircraft and UAVs images used in about 20 scientific projects. However, the usage of airborne optical instrumentation is limited from March to October every year due to the polar night, and in addition limited by cloud cover which could be abundant in Svalbard, especially in summer.

NORCE has evaluated the potential of complementing the current optical instrumentation with a dual frequency Synthetic Aperture Radar (SAR), currently considering L- and X-band. A SAR is a microwave active sensor that has all-weather, all-day and all-season detection capability, beneficial for maritime surveillance, search & rescue, as well as for several maritime and terrestrial applications for polar research and environmental monitoring. Strong user involvement from the scientific community and relevant governmental organizations with activity in or around Svalbard is required to effectively define mission objectives and user requirements (UR). To get feedback on the interest and potential applications of an airborne SAR in Svalbard, NORCE and SIOS organised a user survey that was disseminated to the SIOS community and relevant stakeholders at the local, regional and national levels e.g. Norwegian coastal administration, Norwegian Coast Guard, Governor of Svalbard, governmental agencies, private companies and academic institutions with research or operational activities in and around Svalbard (e.g. Fram Center). We formulated fully anonymous survey questions into three categories: (1) general needs e.g. observational requirements, (2) L1/L2 product requirements (3) specific needs / high-level product requirements e.g. L4 products documenting geophysical variables. Between December 17th 2021 and February 7th 2022, 73 respondents partially and completely answered the survey. The present analysis is focused on the completely filled 54 responses.

The results show that survey respondents were mainly from academic institutions, private research institutes and governmental agencies (only a few from the industry). The majority of the respondents have a researcher position (26 out of 54) but the remaining respondents cover a wide range of positions (professors, engineers, advisers, students, managers, navigators, etc.). All the listed professional fields are represented in the survey. The main represented field was "radar remote sensing" (32), while "biology" was the least represented field (6). Among the other fields, "Optical remote sensing", "Glaciology", "Maritime surveillance", "Geology/Geomorphology", "Geophysics" had the highest scores (10–20 respondents). The survey participants use (or aim to use) remote sensing for a wide range of applications: snow mapping/characterization (25 people); sea ice mapping/characterization (22); sea ice drift (15); glacier motion (17); feature characterization (16). All listed applications are represented by at least 5 respondents. The respondents' work is mostly focusing on and around research bases (Ny-Ålesund/Hornsund), in Spitsbergen fjords and in maritime areas around Svalbard (Fram Strait, Arctic Ocean, Barents Sea, Greenland Sea, Norwegian Sea). Regarding the question on the appropriate revisit time, a high number of participants answered that weekly revisits or targeted missions (flexible revisits) are valuable to their applications. Sub-

daily, daily and monthly-annually are slightly less represented. However, the spread of answers both in terms of regional focus area and temporal resolution is significant, which is representative of the wide range of research fields covered by the survey participants. Most of the participants have experience with SAR data (76%) and a third (33%) has used (or is planning to use) optical data from the SIOS Dornier research aircraft (LN-LYR). Most users would use SAR data from Single-Look Complex format or a higher level. Only a few (6) are interested in level 0 (raw) data. There is a clear interest in a combination of radar frequencies. A total of 31 respondents believe that a combination of both X-/L-band is most appropriate, while 18 do not know. Only 5 people show a special interest towards one single frequency. The main value of the airborne SAR for the users is to complement field/in-situ measurements and calibrate/validate satellite remote sensing. Answers regarding technical specifications (real-time processing, polarization, across/along-track interferometry, left/right wide area mapping) are less clear, with a high percentage of participants answering that they don't know. It shows there is a need for further discussing the technical properties of the measurement methods with the stakeholders and organizing educational activities about SAR remote sensing.

The survey's results show that there is a strong interest in installing a SAR sensor onboard the Dornier aircraft. Based on the documented research needs, a SAR sensor would create many opportunities for data acquisition during the whole year in Svalbard. An airborne SAR will strengthen science, international collaboration, and capacity building in Svalbard through its airborne research infrastructure. Measurements are anticipated to complement in-situ and space-borne measurements and reduce the environmental footprint of research in Svalbard. An airborne SAR will enable a variety of applications within glaciology, hydrology, oceanography, and other fields of Earth system science to understand the state of the environment of Svalbard. Mapping glacier crevasses, generating DEMs for glaciological applications, snow and ice studies (e.g., sea ice, icebergs, glaciers and snow cover) and ocean surface features are examples of applications. The use of the Dornier passenger aircraft warrants the following benefits: (1) regular logistics and research activities can be coordinated to reduce flight hours in carrying scientific observations, (2) joint project proposals of using flight hours will facilitate international collaboration, (3) measurements conducted using both optical and SAR sensors will complement in variety of applications, (4) airborne data can be used to train the polar scientists as a part of the annual SIOS training course, and (5) data can also be useful for Arctic field safety as it can be used to make products such as high-resolution maps of crevassed areas on glaciers and sea-ice properties in Spitsbergen fjords.

A New Distributed ATI SAR System: GEO-LEO SAR ATI concept

The ocean (sea) surface velocity (SSV), which has always been an important parameter to understand the dynamic situation of the ocean. Spaceborne synthetic aperture Radar (SAR) has the capability of wide swath imaging in "area" measurement under various weather conditions at various times. The along-track interferometry (ATI) technique is implemented by using two receiving channels along the track direction, and the LOS velocity information between two short-time measurements can be obtained. It is a mainstream method for the estimation of SSV.

Traditional ATI measurements are mostly based on LEO monostatic systems, which have limited revisit and coverage capabilities, and can only obtain one-dimensional LOS velocity vector in a single measurement. Obtaining two-dimensional line-of-sight velocity vector has become a new development trend. To solve this problem, Steffen and Paco [1] proposed that the dual-beam interference mode could be used to obtain radial velocities in both sight directions. This idea was verified by the binary star system based on TDX and TSX [2], and the obtained Angle of forward and backward LOS velocities was about 4.4°. According to the above ideas, a new ATI measurement LOS angle can be provided through the distributed formation, which can provide the basis for 2D ocean current inversion. One of the distributed configurations is the GEO-LEO ATI SAR configuration, transmitted by GEO SAR and received by LEO SAR.

In GEO-LEO SAR system, the GEO SAR transmits signals to the target, at the same time, LEO SAR just act as passive satellites to receive high orbit satellite signals reflected from the ground and perform imaging processing. Zheng Lu and Yuekun Wang proposed a configuration optimization method based on Simulated Annealing (SA) algorithm to improve the GEO-LEO imaging performance, and studied the cross-orbit interference (XTI) ability of the system[3, 4]. In this paper, a configuration design method based on GEO-LEO distributed ATI SAR system is proposed, which not only meets the requirements of rough sea surface imaging performance, but also meets the requirements of ATI measurement. The results show that using GEO-LEO SAR system for ATI measurement can separate the LOS direction from the LEO platform and improve the sustainable measurement capability.

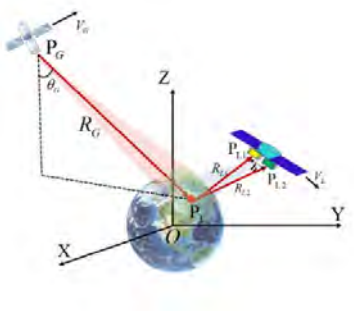

Figure 1. GEO-LEO ATI SAR system schematic diagram

The main work of this paper is as follows.

1. A theoretical phase model for GEO-LEO ATI SAR under large geometric difference is established

As shown in the figure below, we derived the ATI phase expression as (1.1), Δt is the time delay of the front and rear antennas, the superscript * represents the unit vector. It can be seen that the estimated radial velocity of the target is significantly offset due to the existence of the high-orbit emission source, and the new equivalent LOS direction is the sum of the LOS unit vectors of the

GEO and LEO.

$$\Delta\varphi_{ATI} = \frac{2\pi}{\lambda}\left[(\overrightarrow{S_0T_1^*} + \overrightarrow{S_1T_1^*})\cdot\overrightarrow{T_1T_2} - \overrightarrow{S_0T_0^*}\cdot\overrightarrow{v_0}\Delta t\right] \tag{1.1}$$

2. Performance analysis of ATI velocity measurement in GEO-LEO configuration

a) Baseline analysis

According to the above derivation, the two imaging delays can be expressed as (1.2):

$$\Delta t = \frac{\left\|\overrightarrow{S_1S_2}\right\|}{\left\|\overrightarrow{v_1}\right\|} \tag{1.2}$$

The length of the baseline mainly depends on LEO SAR, a longer baseline can obtain a higher phase resolution. However, the selection of ATI baselines should also be constrained by the sea surface decorrelation time.

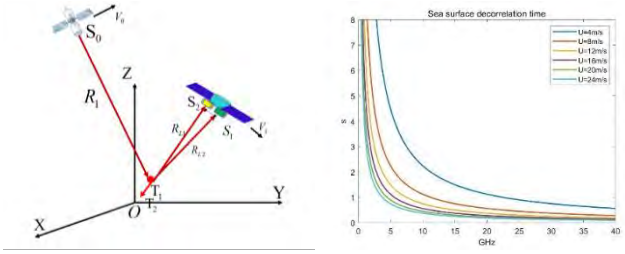

Figure 2. Illustration of the GEO-LEO SAR ATI interference model（left），Sea Surface decorrelation time under different sea conditions and radar frequencies（right）

b) Velocity resolution analysis

Fiedler and Krieger[5] gave the definition formula of the velocity resolution of ATI, which is defined as the ratio of the velocity resolution to the interferometric phase resolution. Combined with the ATI phase expression in our new regime, the velocity resolution can be expressed as (1.3)：

$$\frac{\Delta v_{ATI}}{\Delta\phi} = \frac{c}{720 f_0 \sin\theta_{inc}}\cdot\frac{1}{\tau}\left[\frac{m\cdot s^{-1}}{\deg}\right] \tag{1.3}$$

f_0 is the signal frequency，θ_{inc} is the incident angle of the equivalent LOS vector. Generally speaking, the maximum resolution of the interferometric phase of ATI system is 1°, and the velocity resolution of 0.05m/s can meet the requirements of actual ocean current velocity measurement.

3. Simulation is performed for a set of configuration parameters

Simulation results are as shown in figure 4. By optimization, we can achieve about 6*45 m^2 resolution performance, 89° resolution angle as well. At the same time, we can also get 0.04 ($m*s^{-1}$/deg) velocity resolution.

In the future, we will continue to explore more possibilities for 2-D ocean surface current filed inversion with GEO-LEO ATI SAR system, at the same time, focusing on accuracy compensation and signal-level & information-level data fusion. In order to improve GEO SAR utilization, we may also expand the number of satellites and system complexity at the LEO level.

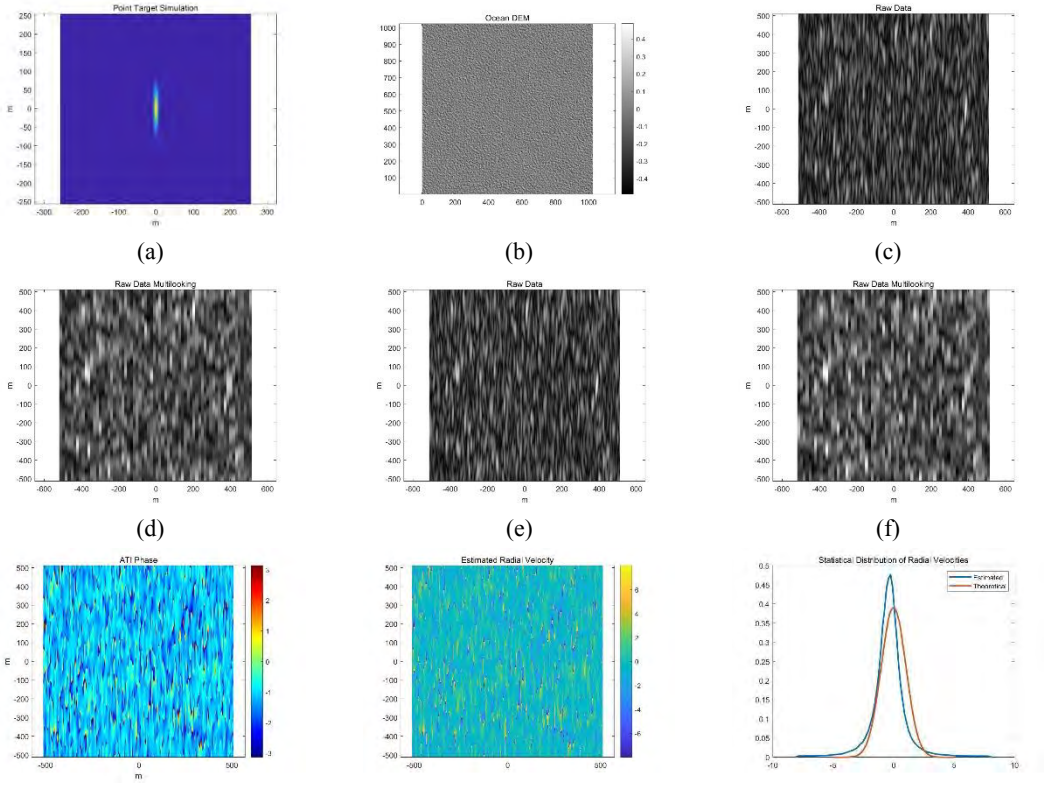

Figure 4. Our simulation is based on: about 36000km altitude GEO SAR with 580m/s velocity, 500km altitude LEO SAR with 7500m/s velocity. They all operate at 1.25GHz frequency, about 500MHz bandwidth, and synthetic aperture time about 400ms. A set of configuration parameters is obtained by using our optimization algorithm, which is based on NSGA-III[6]. GEO look angle is 5.67°, LEO look angle is 27.73°, LEO squint angle is 7.85°, the ground projection of the bistatic angle is 8.83°. Figure (a) is using point target to verify imaging performance. Figure (b) shows time-varying ocean DEM. Figure (c)~(f) are raw data from SAR imaging as well as multi-looking results. Figure (g)~(h) are our simulation ATI phase as well as estimated radial velocities. For the sake of evaluation of the estimation results, we analyzed the statistical distribution of radial velocities as shown in figure (i) in the end, the mean values of the true value and the estimated value are respectively, 0.00, -0.32 (m/s). The std values are about 1.01(True)&1.14(estimated), It's worth mentioning that we haven't done much precision compensation yet, the accuracy meets 10cm/s, which is expected to meet most requirements of ocean measurements.

References

[1] S. Wollstadt, P. López-Dekker, F. D. Zan, and M. Younis, "Design Principles and Considerations for Spaceborne ATI SAR-Based Observations of Ocean Surface Velocity Vectors," *IEEE Transactions on Geoscience and Remote Sensing,* vol. 55, no. 8, pp. 4500-4519, 2017.

[2] N. Caldarella *et al.*, "Retrieval of Wind- and Total Surface Current Vectors Using Experimental Bidirectional Along-Track Interferometric TanDEM-X Data," *IEEE Transactions on Geoscience and Remote Sensing,* pp. 1-1, 01/01 2022.

[3] Z. Lu, Y. Wang, H. Kuang, Y. Huang, Z. Wang, and Y. Zhu, "Formation Design and Accuracy Analysis of GEO-LEO Bistatic InSAR System," pp. 1-4, 2019.

[4] Y. Wang, Z. Lu, Z. Suo, Y. Zhu, Z. Li, and Q. Zhang, "Optimal configuration of spaceborne bistatic SAR with GEO transmitter and LEO receiver," *IET Radar, Sonar & Navigation,* https://doi.org/10.1049/iet-rsn.2018.5215 vol. 13, no. 2, pp. 229-235, 2019/02/01 2019.

[5] H. Fiedler, G. Krieger, F. Jochim, M. Kirschner, and A. Moreira, "Analysis Of Satellite Configurations For Spaceborne SAR Interferometry," 2002.

[6] K. Deb and H. Jain, "An Evolutionary Many-Objective Optimization Algorithm Using Reference-Point-Based Nondominated Sorting Approach, Part I: Solving Problems With Box Constraints," *IEEE Transactions on Evolutionary Computation,* vol. 18, no. 4, pp. 577-601, 2014.

The Harmony SAR Instrument

Abstract

The Harmony mission has been selected by ESA for implementation as Earth Explorer 10. The space segment consists of two receive only SAR satellites designed to use Sentinel-1 as illuminator. In this way, simultaneous acquisitions of the same scene from multiple viewing angles are obtained and can be combined to detect changes or velocities on the surface. The SAR instrument on each Harmony satellite receives all polarisations of the bi-static radar echo with an antenna divided in three sub-apertures and transfers the digitized signals to the mass memory for subsequent transmission to the ground.

This paper describes the SAR instruments and the expected instrument performance at the end of phase A as defined during the two parallel study contracts lead by Airbus Space and Defense (ADS) and Thales Alenia Space (TAS) which are referred to in the following as concept A and concept B respectively.

Observation Principles

The Harmony SAR instrument is receive only and designed to use S1 as illuminator. The pulses transmitted by Sentinel-1 are scattered by the target area and the echo signal is received by Sentinel-1 as well by the two Harmony satellites.

Due to the along track orbit distance between Sentinel-1 and the Harmony satellites a large bi-static angle is formed between transmitter and receiver. This results in an effective diversity in the line of sight or slant range direction and the scene is observed from three different directions in the Stereo configuration. This unique diversity in slant range direction is used to measure surface geo-physical parameters in all two dimensions instead of the single dimension than is accessible through a normal SAR observation.

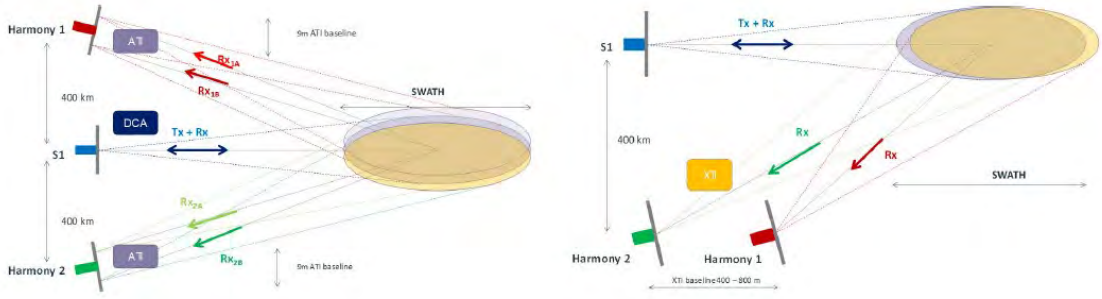

Figure 1: Observation geometry of Stereo (left) and XTI (right) configuration

The Harmony SAR instrument is compatible with, and optimised for, both the Stereo and Across-Track Interferometry (XTI) configurations of the Harmony formation, which are illustrated in Figure 1. It is planned to change several times between two configurations during the planned mission duration. With its forward, backward and side looking geometry, the Stereo configuration is optimized for detecting velocity vectors on the surface. This allows for the measurement of very slow velocities (mm/year) for solid Earth applications using repeat pass and permanent scatterers interferometry and the measurement of fast velocities (m/s) for ocean currents either with Along-Track Interferometry (ATI) or Doppler Centroid Anomaly (DCA) methods. The ATI is performed with short baselines formed between two wing antenna apertures on the same satellite. In addition, the viewing geometry allows the instrument to be used as a high-resolution scatterometer, for the

retrieval of surface wind from the radar backscatter images. The XTI configuration is optimised to detect vertical movements of the surface. The Single Pass Interferometry (SPI) observation technique requires a sufficiently large perpendicular baseline between the two Harmony satellites. In order to support these different modes of operation, the SAR antenna, shown in Figure 2 has three sub-apertures. A central part (which in the case of concept B is in itself broken up in two parts) and two wing antennas that are deployed on either side of the spacecraft. For the ATI mode, the ATI baseline is formed between the two wing antenna apertures while for the other measurement modes the signals from the full antenna are combined.

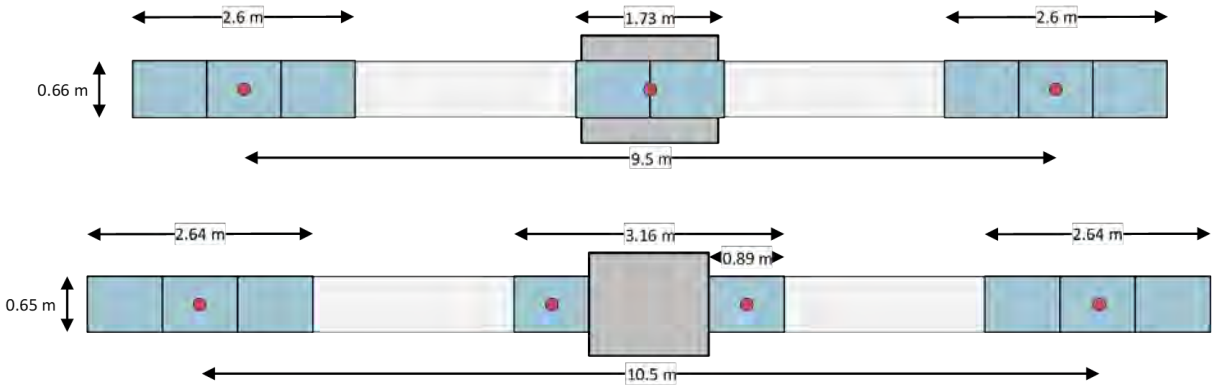

Figure 2: SAR antenna configuration of Concept A (top) and Concept B (bottom)

Instrument requirements

In order to receive the bi-static echo from S-1, the Harmony SAR instrument has to be capable of replicating all the S-1 SAR imaging modes including Stripmap, Interferometric Wide Swath, Extra Wide Swath and Wave Mode.

The Harmony SAR antenna needs to provide electronic beam steering in the cross-track direction over a wide angular range, in order to be fully compatible with the S-1 swath geometry. The TOPS steering within the bursts of the IW and EW modes requires steering in the along-track direction as well, however here the steering range is below +/- 1 degree. The Harmony antenna steering needs to take the squinted geometry of the bi-static observation into account as well.

For most areas, S-1 transmits in vertical polarisation with the exception of polar environment and sea-ice zones where horizontal polarization is preferred. Due to the bi-static geometry and the attitude of the Harmony satellite, the polarization vector with the strongest scattered signal is not aligned with the polarisation axis of the Harmony antenna. Therefore, Harmony always receives both polarisations, which allows to analyse the Harmony data in any desired polarisation reference frame. An overview on the required Harmony level-1 performance is provided in Table 1.

Requirement	Specification	Comment
Full antenna SLC Noise Equivalent Sigma Zero (NESZ)	< -20 dB	Over the full swath
Full antenna Distributed Total Ambiguity Ratio (DTAR)	< -17 dB	Over the full swath
Radiometric accuracy	< 0.6 dB	with a confidence level of 68%
Radiometric stability	< 0.3 dB	with a confidence level of 68%
Cross-polar isolation	< -30 dB	with a confidence level of 68%
Minimum NESZ dynamic range	-3 dB to +32 dB	

Table 1: Harmony Level-1 imaging performance requirements for the Single Look Complex image product

Instrument Architecture

The Harmony SAR instrument is composed of two major functional subsystems: the SAR Antenna Subsystem (SAS) which is split in three sub-apertures and the multi-receive-channel SAR Electronic Subsystem (SES).

The SAS is a deployable planar antenna of approximately 12-13 m length as shown in Figure 1. During launch, the antenna wings are folded and stowed on the side of the spacecraft body. Due to the instrument mass limitations the front surface of the antenna structure is not fully populated with antenna radiators but the SAS is split in three sub-apertures. The size and position of these three antenna sub-apertures has been carefully optimised to meet the required instrument performance with a minimum aperture. It is worth noting that concept B splits the central antenna in two parts places them on the antenna structure next to the satellite body, while concept A covers the top side of the satellite body with the central antenna. The along-track baseline for ATI measurements is governed by the distance between the two wing antenna phase centres.

The SAR antenna is built-up from eight antenna tiles, three for each wing aperture and two for the centre aperture. A tile comprises of a dual polarised radiating surface, a number of receive modules, and a beam forming and calibration network. The tiles of both consortia have very similar antenna surface and dimensions. Other important sub-systems of the SAS are the SAS level beamforming and calibration network, digital and power harness and the thermal subsystem. One key element for the instrument performance is the antenna radiator. Due to the mass constraints both consortia decided for the use of microstrip patch technology. The radiator for each panel is built-up out of 16 rows with 20 dual-polarised patch radiators. The signal from each sub-array is amplified and controlled in amplitude and phase in one of 64 dual channel receive modules (RMU).

The RF distribution network first combines the output signals from the RMUs per polarization on tile level. Then the signals from all tiles that are belonging to one sub-aperture are combined and transmitted through coaxial cables with high phase stability to the SES.

The SES provides all radar instrument control and antenna control, internal calibration signal generation, multi-channel radar echo signal reception, conditioning, digitisation, digital down conversion, data compression, formatting and transmission of the source packets to the platform mass memory. In concept A, the digitisation of all six receive signals, their digital processing as well as the generation of the internal calibration signal and the instrument and antenna control function is performed on a single electronic board called the Universal Processing Module (UPM). In concept B, these functions are distributed six electronic boards, which are specialised for the different functions.

Harmony SAR Image Performance

The SAR image performance SLC level is the basis for all the different higher-level products of the Harmony mission. For some of the products the signals of all three phase centres are combined.

Figure 3 shows the NESZ and the Total Ambiguity to Signal Ratio (TASR)) expected performances when operating in IW mode for consortium A. The TASR performance is driven almost entirely by the azimuth ambiguities. The different lines show the expected performance at the edges and the centre of the TOPS bursts. The analysis shows that the Level-1 imaging performance as given in Table 1 is meet.

Figure 4 shows the expected NESZ performance for a single wing antenna of both consortia and the Sentinel-1 SAR instrument. The analysed performance is compared with the results of the Harmony

End to End simulator (HEEPS), which includes dynamic scene generation, raw data generation and actual Level-1 processing.

Figure 5 shows the expected precision of the Geophysically equivalent surface velocities (USV) in along track direction when averaged over 2km for the reference mid wind condition.

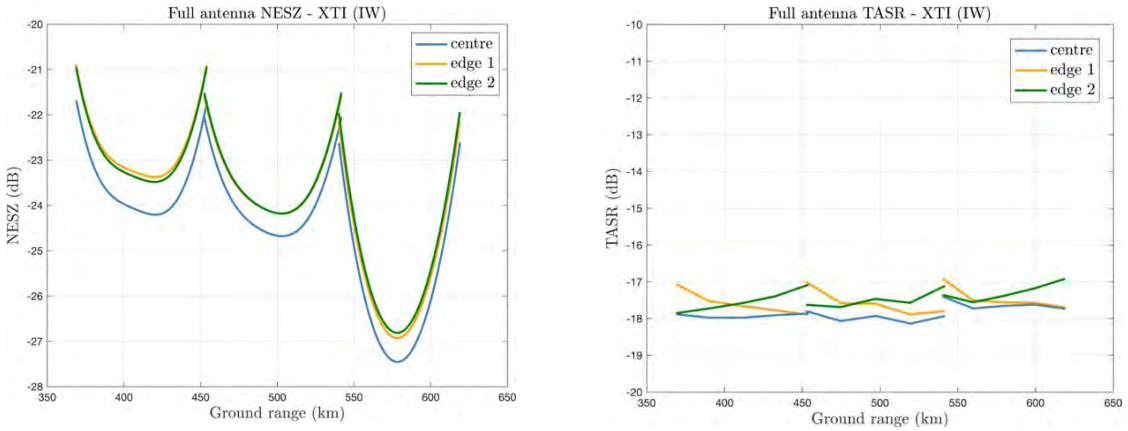

Figure 3: NESZ and the Total Ambiguity to Signal Ratio (TASR)) performances when operating in IW mode for consortium A

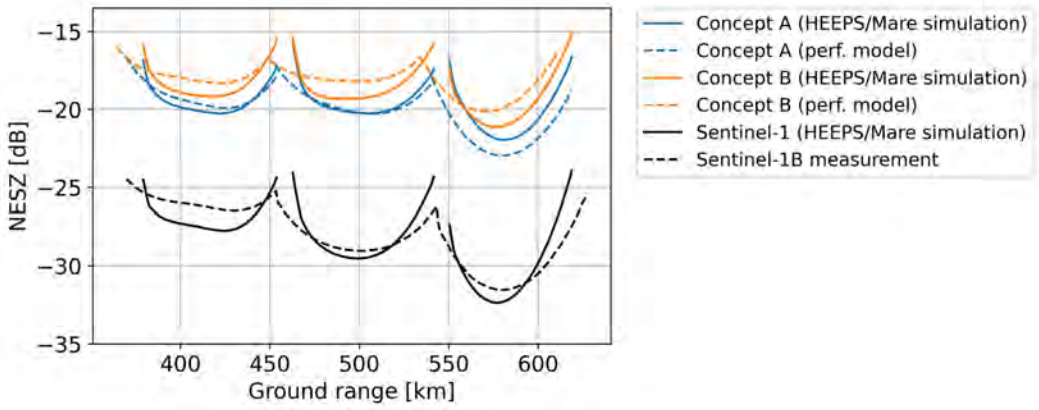

Figure 4: NESZ for a single wing antenna for both consortia and the S-1 performance in comparison with the results of the Harmony End to End simulator

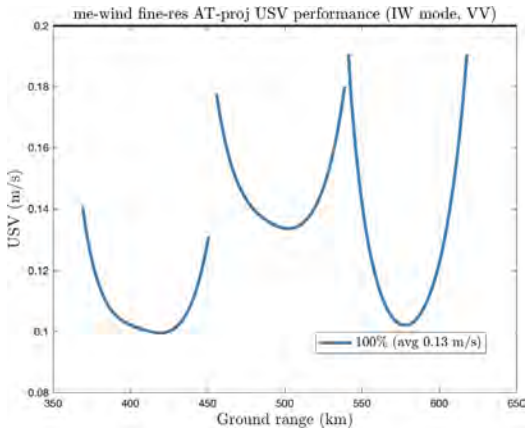

Figure 5: Along-track USV precision for fine resolution (2km) in IW mode (concept A)

Development of a Dual-Frequency Airborne SAR Sensor in Svalbard

Tom Rune Lauknes[1], Agnar Sivertsen[1], Temesgen Gebrie Yitayew[1], Line Rouyet[2], Charles Werner[2], Michael Jenning[3], Dirk Plettemeier[3], Shridhar D. Jawak[4]

1 NORCE Norwegian Research Centre, Tromsø, Norway
2 Gamma Remote Sensing, Gümlingen, Switzerland
4 Technische Universität Dresden, Dresden, Germany
4 Svalbard Integrated Arctic Earth Observing System (SIOS), SIOS Knowledge Centre (SIOS-KC), Longyearbyen, Svalbard, Norway

Increased activity in the Arctic imposes a growing need for improved maritime situational awareness. Safe and sustainable maritime operations in the Arctic require near-real-time information about sea ice, growlers, bergy bits, and icebergs, that pose a significant risk for maritime activities in this region. Year-round awareness can only be obtained by innovative combinations of remotely sensed synthetic aperture radar (SAR) imagery from air- and spaceborne platforms.

Figure 1. Search and Rescue responsibility area for Norway in the Arctic (Joint Rescue Coordination Centre - JRCC, 2019).

SAR systems provide all weather, all year, observational capacity. Spaceborne C-band SAR sensors have proven to be a key asset for maritime surveillance applications. However, the spatial and temporal coverage of current and planned spaceborne SAR observations is not sufficient for fully operational use in the Arctic, and the sensor capabilities and methodologies are not fully mature yet. Thus, there is a need to supplement spaceborne with airborne SAR observations that can fill in observational gaps, provide important Calibration and Validation (Cal/Val) data for satellite missions, and aid development of new products and methodologies.

Norway has an important responsibility regarding search and rescue in the Arctic (Figure 1). Airborne SAR provides all weather capability with unprecedented potential to improve observations of vessels, oil spills, icebergs, sea ice conditions, and floating debris, leading to improved safety and emergency response in the Arctic.

The Norwegian company Lufttransport AS currently operates two Dornier DO-228 aircraft, based in Longyearbyen, Svalbard. The aircraft operate mostly between Longyearbyen and Ny-Ålesund but have also frequent flights to North Greenland and mainland Norway. One of the aircraft (LN-LYR) has been equipped with a scientific pod containing a state-of-the-art hyperspectral imager (Figure 2).

In the fall of 2022, NORCE completed the first phase by defining mission requirements (MR) for a SAR system, to be installed on LN-LYR. The study was funded by Norwegian Space Agency and ESA.

The primary objectives of the airborne SAR mission are related to the major scientific observational gaps in the Arctic, to current and future needs for operational Cal/Val services specifically related to cryosphere applications, and to improve Norway's capabilities for increased situational awareness in the Arctic, as summarised below:

1. To provide high resolution imagery for the monitoring of sea ice, snow, glaciers, ice caps and permafrost in relation with the Global Climate Observing System (GCOS) **Essential Climate Variables**, and addressing the current knowledge gaps (e.g. Snow Water Equivalent (SWE) retrieval, ground ice content);
2. To improve safety by extending the **monitoring of geohazards** related to ground movement such as landslides and subsidence, and changes of snow properties related to e.g. snow avalanches, providing complimentary service to current Copernicus satellites;
3. To provide an all-weather sensor **for Search and Rescue and maritime surveillance** including localization of vessels and oil spills, categorization of sea ice types and detection of icebergs critical to safe navigation in Arctic areas, in compliance with the European Arctic policy;
4. To provide an airborne platform that can collect essential **Cal/Val data for satellite SAR missions**, such as ROSE-L and NISAR.

Based on a user survey, which was carried out in cooperation with SIOS, the following fundamental system and observational requirements have been defined:

- FMCW radar.
- L-band SAR.
- Higher-frequency SAR (e.g. X-band).
- Single-pass across– and along track capability (X-band).
- Repeat-pass capability (L-band).
- Polarimetric observations (one frequency).
- Simultaneous operation on both bands.
- Support SAR acquisitions during regular aircraft operations.
- SAR acquisitions simultaneous with hyperspectral.

First order antenna simulations have been completed and different antenna mounting positions on the aircraft are being considered. For X-band, there is a need to establish both an across-track and an along-track baseline, requiring careful antenna placement.

Based on the mission requirements, we are now preparing for the next phase which involves mission definition and system design. As part of this phase, we are planning an experiment SVALSAR2023, where we aim to collect multifrequency (Ku and L-band) SAR and hyperspectral data over different targets over both land, glacier, open water including vessels, icebergs, sea ice, and natural oil seepages. The experiment will be coordinated with simultaneous overflights by available satellite SAR sensors (e.g. ALOS-2 L-band, Sentinel-1 C-band).

Figure 2. Left: Ship detection in ice-infested waters based on Dual-Polarization SAR (Brekke & Anfinsen, 2011). Middle: Lufttransport's Dornier DO-228 aircraft (LN-LYR). Right: Sea ice identification and categorization based on SAR satellite images (Johansson et al., 2017).

In this work, we present the current system design of an airborne SAR to be installed on LN-LYR. The aircraft is available nearly 365 days per year, and a combination of a fully polarimetric, dual frequency, interferometrically capable SAR, plus a state-of-the art hyperspectral imager provides a unique asset for regular observations in the Arctic, and an available platform for validating geophysical parameters such as e.g. sea ice drift, estimated using other methods.

Future Missions at the European Space Agency

Craig Donlon
Organisation(s): European Space Agency, Netherlands, The

Submitted by: **Dr Craig Donlon**
(European Space Agency, NL)
, *ID: 1056*
Presenting Author: Donlon, Craig craig.donlon@esa.int
Topics: Future missions

The Arctic Ocean is changing dramatically responding to significant global atmospheric warming by pan-Arctic sea-ice retreat and thinning. Measurements of geophysical and societal change provide the evidence to underpin the establishment, implementation and monitoring of policy, policy decisions and their impact, not just in Europe, but across the world. Since changes in the Polar regions have profound impacts globally. Measurement evidence is required to support development implementation and monitoring the impact of the European Integrated Policy for the Arctic via the Copernicus Ocean, Land, Climate, and other Copernicus Service and down-stream application domains. The current fleet of Copernicus Sentinel satllites is being explanded by six Copernicus Expansion Missions that are being implemented by the European Space Agency and the European Commission. These missions include the Copernicus Imaging Microwave Radiometer (CIMR), the Radar Observation System for Europe in L-band (ROSE-L) and the Copernicus Polar Ice and Snow Topography Altimeter (CRISTAL). This presentation will review the current status of relevant future missions highlighting synergies and opportunities to develop a better insigt of ocean and ice processes.

SEASTAR - EARTH EXPLORER 11 MISSION CANDIDATE: IMAGING SMALL-SCALE OCEAN DYNAMICS

Christine Gommenginger[1], Adrien C. H. Martin[1], David L. McCann[1], Katia Nagamine Urata[2], Valeria Gracheva[2], Alejandro Egido[2], Kevin Hall[2], Tânia Casal[2], Petronilo Martin-Iglesias[2]

[1]National Oceanography Centre, Satellite Oceanography, Southampton, United Kingdom of Great Britain
[2]European Space Agency, ESTEC, Noordwijk, The Netherlands

SeaSTAR is a satellite mission candidate for ESA Earth Explorer 11 that proposes to measure small-scale ocean dynamics below 10 km at ocean/atmosphere/land/ice interfaces of the Earth System. SeaSTAR products consist of high-resolution images of total surface current vectors and wind vectors of unprecedented resolution (1 km) and accuracy over a wide swath.

A key objective of SeaSTAR is to characterize, for the first time, the magnitude, spatial structure, regional distribution and temporal variability of upper ocean dynamics on daily, seasonal and multi-annual time scales, with particular focus on coastal seas, shelf seas and Marginal Ice Zone boundaries. The mission addresses an urgent need for new measurements of small-scale ocean processes to help understand and model their impacts on air-sea interactions, horizontal water pathways, vertical mixing and marine productivity. High-resolution imaging of total currents with collocated wind and waves data would bring new means of validating and developing models to improve operational forecasts and climate projections.

The SEASTAR SAR instrument is an along-track interferometer (ATI) that can measure the phase difference between two SAR images of the same scene taken within a short time-lag. The system is currently assumed to function in Ku-band. SEASTAR has two pairs of antennas looking 45° forward and 45° backward to provide squinted ATI measurements, accompanied by a broadside beam, to provide measurements for a total of three different azimuth directions.

The Wavemill airborne demonstrator [2] validated the main principles of squinted ATI during an airborne campaign over the Irish Sea in 2011. The Wavemill system operated in X-band with two squinted antennas, but without a broadside beam. Comparisons against HF radar of the Wavemill retrieved TSCV were typically better than 0.1 m/s. Due to the absence of Normalised Radar Cross Section (NRCS) calibration, it was not possible to retrieved Ocean Surface Vector Wind (OSVW) from the airborne data, and wind information (needed to correct for the strong Wind-wave Artefact surface Velocity [3]) was taken from ground truth instrumentation (weather station). Despite the very successful campaign and promising results with the Wavemill airborne system, no further opportunities for airborne campaigns arose and the aircraft used to fly the Wavemill airborne demonstrator was decommissioned.

OSCAR is a Ku-band (13.5 GHz) SAR system with Doppler and scatterometry capabilities in three azimuth look directions as an evolution from the wavemill instrument. OSCAR was flown over the Iroise Sea (West of Brittany, France) in May 2022 during the SEASTARex campaign. The OSCAR operations and products are representative of the spaceborne concept, with geophysical parameters and accuracies that directly relate to those of the SeaSTAR satellite mission.

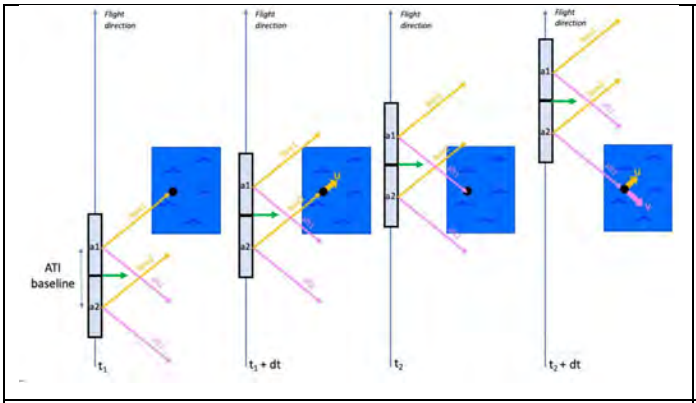

Figure 1 Observing principle: Squinted Along-track Interferometry.

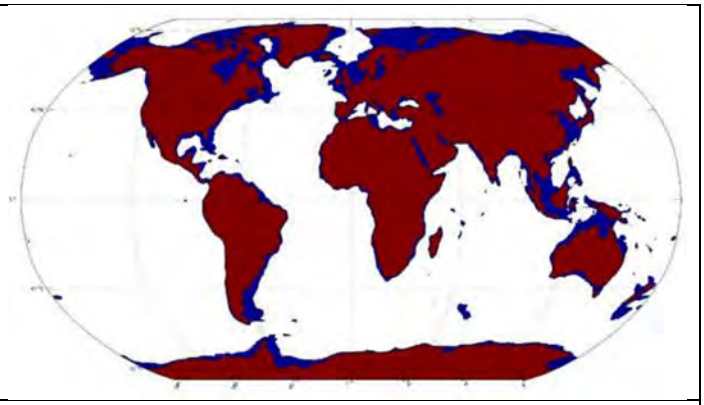

Figure 2 SEASTAR samples over all coastal/shelf seas and MIZs

The paper will outline the key elements of the mission and the latest status of the mission concept evolution, with the technical solutions and trade-offs that are being considered.

REFERENCES

[1] Gommenginger, Christine et al. , "SEASTAR: A Mission to Study Ocean Submesoscale Dynamics and Small-Scale Atmosphere-Ocean Processes in Coastal, Shelf and Polar Seas," *Frontiers in Marine Science*, Volume 6, p.457, 2019.

[2] Adrien C.H. Martin, Christine Gommenginger , "Towards wide-swath high-resolution mapping of total ocean surface current vectors from space: Airborne proof-of-concept and validation", *Remote Sensing of Environment*, Volume 197, 2017, Pages 58-71

[3] Adrien C.H. Martin, Christine Gommenginger, Jose Marquez, Sam Doody, Victor Navarro, Christopher Buck, "Wind-wave-induced velocity in ATI SAR ocean surface currents: First experimental evidence from an airborne campaign", *Journal of Geophysical Research: Oceans*, Volume121, Issue3, March 2016, Pages 1640-1653

Multistatic High-Resolution Observations of the Ocean with the Harmony Mission: Science, Products, and Expected Performances

Paco Lopez-Dekker[1], Bertrand Chapron[2], Claudia Pasquero[3], Ad Stoffelen[4], Bruno Buongiorno Nardelli[5], Simona Masina[6], Marcel Kleinherenbrink[1], Andreas Theodosiou[1], Fabien Desbiolles[3], and Björn Rommen[7]

[1]TU Delft, [3]University of Milan, [4]KNMI, [2]IFREMER, [5]CNR, [6]CMCC, [7]ESA

February 12, 2023

1 Introduction

After a successful User Consultation meeting in July 2022, the Harmony mission [1, 2] was confirmed as the European Space Agency's 10th Earth Explorer in September 2022. The Harmony mission will consists of two indentical spacecraft orbiting in formation with a Copernicus Sentinel-1 radar satellite. The Harmony satellites will carry two payloads: receive-only Synthetic Aperture Radar (SAR) and a multi-view Thermal Infrared (TIR) instrument. During at least 60% of it lifetime, Harmony will operate in a stereo formation [3] with one satellite flying 350 km ahead of Sentinel-1 and the other trailing it by the same distance. This formation is intended to maximize the geometric diversity needed to retrieve motion vectors. During the rest of the mission, in particular at the beginning and towards the end, one of the Harmony satellites will move to a close-formation with respect to its sibling to form a single-pass SAR interferometer. This configuration will provide dense and high resolution time-series of digital-elevation models of, for example, fast-evolving glaciers and volcanoes worldwide. Figure˜ 1 illustrates this two configurations as well as the associated obervation capabilities.

Being tightly linked to the Sentinel-1, Harmony is conceived as a multi-objective, multi-domain, mission. Over solid-earth, the main focus will be on the quantification of seismic-strain, in particular by providing precise estimates of North-South deformation components, which are largely missing in current observations. Over mountain and polar glaciers and other ice masses, the main objective of Harmony is to provide simultaneous observations of glacier motions and volume changes, which will be used to understand the underlying processes.

This paper discusses Harmony's science goals and observation capabilities over the oceans. Harmony will deliver data to improve our understanding of the upper ocean processes and of interactions between the lower atmosphere and the ocean surface. This will be achieved by providing, for the first time, large scale simultaneous measurements of wind, waves, surface currents, sea surface temperature differences and cloud motion vectors. The combination of these measurements will allow better understanding and interpretation of upper ocean small-scale processes and will yield an unprecedented view of the marine atmospheric boundary layer.

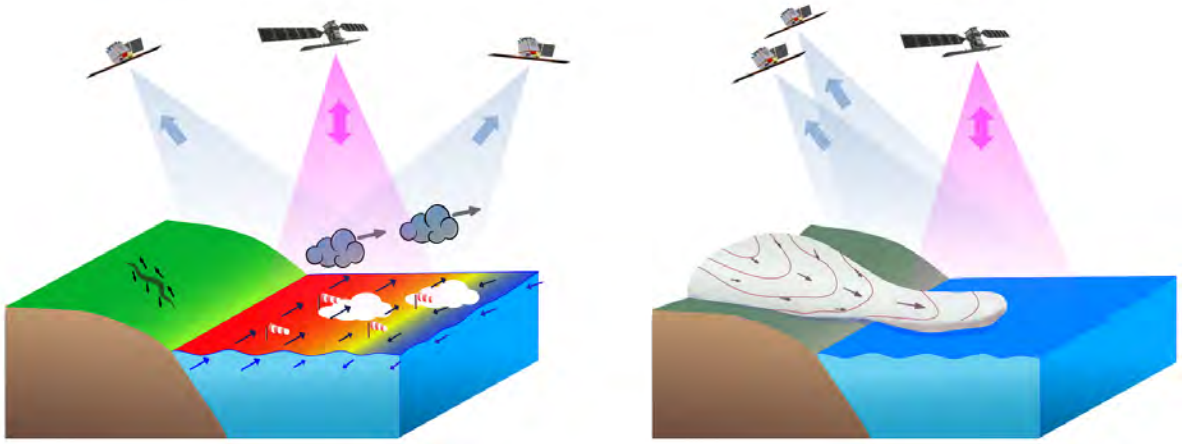

Figure 1: Cartoon illustrating Harmony's flight configuration and observation capabilities during the stereo (left) and XTI (right) phases.

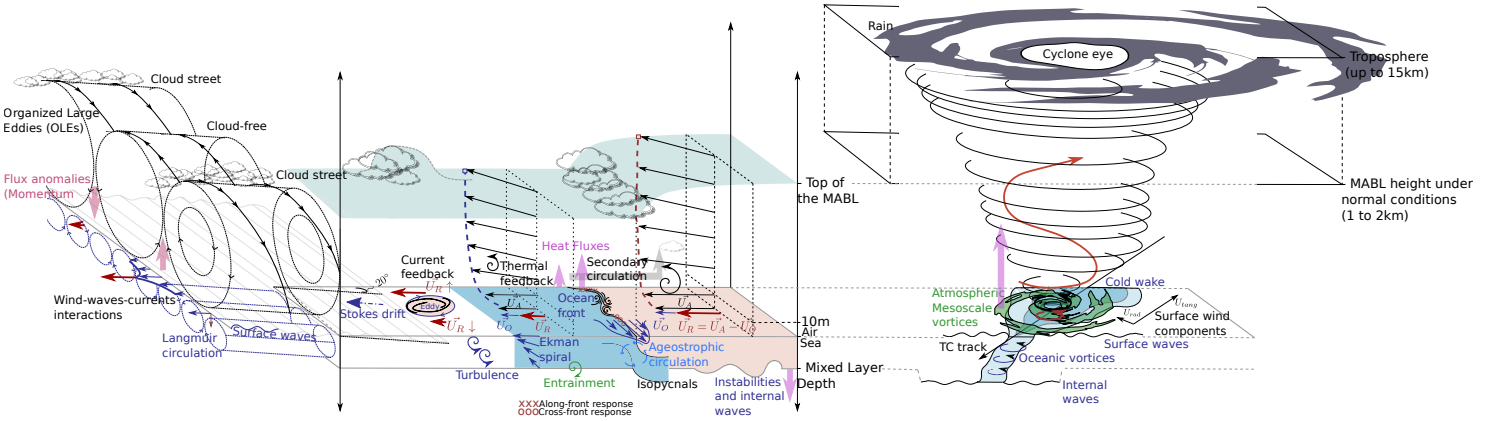

Figure 2: Left: illustration of many of the $\mathcal{O}$(km) scale processes in the Marine Atmospheric Boundary Layer and the oceanic Mixed Layer that contribute to vertical exchange of momentum, heat and gasses: Cartoon of a Tropical Cyclone, including its cold-wake.

2 Science goals

Numerical climate, Numerical Weather Prediction and Large Eddy Simulation models are all limited by the how well unresolved processes are represented and parameterized. A widely adopted strategy to address this source of uncertainty is to increase the resolution of the models, hereby creating a need for high resolution observations to validate and tune them. Another aspect that needs improvement is the representation of the coupling between different components, for example to correctly represent how the upper-ocean and the lower atmosphere interact. In that context, the overarching goal of Harmony is to provide the high-resolution observations urgently needed to drive the development of the next generation of high-resolution coupled models.

Specifically, Harmony aim at [4]:

- Quantifying and disentangling sub-mesoscale effects, i.e., the air-sea interactions and adjustment between ocean features (e.g., fronts and eddies) and the MABL and associated tropospheric clouds under different environmental conditions (Western boundary current systems, Eastern boundary upwelling systems, coastal and/or marginal ice zones), to consolidate empirical parameterisations, targeting momentum and heat exchanges, water cycle and CO_2 fluxes, leading to precise data-driven representations of these processes in new generation Earth System Models.

- Improving the prediction of the evolution of tropical and intense extratropical cyclones (notably, rapid intensification events), as well as evaluating the feedbacks between these extreme weather events and the upper ocean state.

- Resolving the high-latitude small mesoscale ocean surface dynamics and quantify the submesoscale surface current gradients over all latitudes and seasons, i.e., the upper ocean deformation, with the divergences and associated local vertical velocities in the upper ocean, strains and vorticities down to $\mathcal{O}$(1-5 km) horizontal resolution, to understand their contribution to ocean circulation, upper ocean ventilation, ocean heat uptake, CO_2 sequestration, water cycle, and related vertical ocean transport processes, and to develop data-driven downscaling parameterisations.

Figure 2 provides an illustration of many of the upper-ocean and MABL processes aimed to be studied, including phenomena associated to tropical cyclones and their cold-wake.

3 Measurements and Products

To achieve its science objectives, Harmony will generate a series of products combining a range of techniques. In this section we briefly discuss the different radar products.

Together with Sentinel-1, the Harmony satellites will provide measurements of the Normalized Radar Cross Section (NRCS) corresponding to three distinct azimuth directions, forming the analogous to a very high resolution wind scatterometer. The directional roughness of the ocean surface, and thus the NRCS, is controlled by the surface-stress vector, $\vec{\tau}$. Since it is difficult to directly retrieve surface stress vectors, the radar-scatterometry community usually uses stress-equivalent surface wind, $\mathbf{U}_{10s}$ [5], as a proxy variable that can be derived, for example, from buoy observations of the wind vector. Compared to a conventional three-beam wind-scatterometer, Harmony has roughly half so much azimuth diversity, but benefits from orders of magnitude higher resolution and from perfectly simultaneous observations (something only achievable with a multi-platform solution). The multistatic observation geometry makes the system behave similarly to a compact-pol system [6], which will provide additional information that can be exploited to identify areas where the backscatter is enhanced due to breaking waves.

Current performance analysis show that Harmony has the sensitivity to estimate variations of the $\mathbf{U}_{10s}$ vector at kilometer resolution (or better) with an error typically well below 5% of the actual value, which is enough to capture variations due to MABL phenomena such as convective rolls.

The second main observable is the Geophysical Doppler Centroid (GDC). To achieve high Doppler sensitivity, the Harmony radar antenna is designed to apply short-baseline Along-Track Interferometry (ATI), providing an ATI baseline in the order of 10 m. The combination of ATI capabilities with the very high nominal resolution of the measurements (20 m × 5 m or 5 m × 5 m, depending on the operating mode), results in a sensitivity typically in the range 0.05 m s^{-1} to 0.1 m s^{-1} at 2 km × 2 km resolution. However, it should be emphasized that for Harmony, like for any Doppler-oceanography mission, the retrieval of surface currents is limited by the capability to estimate and remove the so-called wave-Doppler, which, converted to velocity, amounts to 10 % to 20 % of the wind velocity [7]. Current simulations suggest that errors due to an incorrect estimation of the wave Doppler are likely to dominate the error budget.

Harmony will also provide an improved characterization of the directional wave-spectrum. For example, it will provide three estimates of the MeAn Cross Spectra (MACS) parameter [8] corresponding to the three effective observation geometries. This vectorized MACS can be used to further constrain the the wind-stress vector and to provide an improved estimate of the wave Doppler. For longer waves, Harmony will provide independent cross-spectra and extend the spectral region for which spectral components can be resolved.

During the XTI phases, the sensitivity to all the aforementioned products will be significantly reduced. In exchange, the particularities of the observation configuration allow for high geometric sensitivity to surface topography combined with effective inter-satellite along-track baselines that are small enough to ensure high coherence [9]. Preliminary analysis suggest a relative height uncertainty in the range 5 cm to 10 cm for a product resolution in the order of 3 km × 3 km for most of the IWS swath, although the final contribution of some systematic errors, in particular that of residual phase synchronization errors, remains to be investigated.

References

[1] P. López-Dekker, H. Rott, P. Prats-Iraola, B. Chapron, K. Scipal, and E. D. Witte, "Harmony: an Earth Explorer 10 Mission Candidate to Observe Land, Ice, and Ocean Surface Dynamics," in *IGARSS 2019 - 2019 IEEE International Geoscience and Remote Sensing Symposium*, pp. 8381–8384, July 2019. ISSN: 2153-6996.

[2] P. López-Dekker, J. Biggs, B. Chapron, A. Hooper, A. Kääb, S. Masina, J. Mouginot, B. B. Nardelli, C. Pasquero, P. Prats-Iraola, P. Rampal, J. Stroeve, and B. Rommen, "The Harmony Mission: End of Phase-0 Science Overview," in *2021 IEEE International Geoscience and Remote Sensing Symposium IGARSS*, pp. 7752–7755, July 2021. ISSN: 2153-7003.

[3] V. Boccia, E. D. Witte, J. Roselló, M. Tossaint, C. J. Donlon, K. Scipal, G. Burbidge, H. Johnsen, F. Fois, G. Engen, and D. Bibby, "StereoSAR: a multi-static SAR mission concept to enhance Sentinel-1 capabilities for measuring ocean dynamics," vol. 10423, p. 104230A, International Society for Optics and Photonics, Sept. 2017.

[4] ESA, "Report for Mission Selection: Earth Explorer 10 Candidate Mission Harmony," Tech. Rep. ESA-EOPSM-HARM-RP-4129, European Space Agency, Noordwijk, The Netherlands, 2022.

[5] J. de Kloe, A. Stoffelen, and A. Verhoef, "Improved Use of Scatterometer Measurements by Using Stress-Equivalent Reference Winds," *IEEE Journal of Selected Topics in Applied Earth Observations and Remote Sensing*, vol. 10, pp. 2340–2347, May 2017. Conference Name: IEEE Journal of Selected Topics in Applied Earth Observations and Remote Sensing.

[6] L. Iannini, D. Comite, N. Pierdicca, and P. Lopez-Dekker, "Rough-Surface Polarimetry in Companion SAR Missions," *IEEE Transactions on Geoscience and Remote Sensing*, vol. 60, pp. 1–15, 2022.

[7] B. Chapron, F. Collard, and F. Ardhuin, "Direct measurements of ocean surface velocity from space: Interpretation and validation," *Journal of Geophysical Research: Oceans*, vol. 110, no. C7, pp. n/a–n/a, 2005.

[8] H. Li, B. Chapron, A. Mouche, and J. E. Stopa, "A New Ocean SAR Cross-Spectral Parameter: Definition and Directional Property Using the Global Sentinel-1 Measurements," *Journal of Geophysical Research: Oceans*, vol. 124, no. 3, pp. 1566–1577, 2019.

[9] A. Theodosiou, M. Kleinherenbrink, and P. López-Dekker, "Wide-Swath Ocean Topography using Formation Flying Under Squinted Geometries: The Harmony Mission Case," in *2021 IEEE International Geoscience and Remote Sensing Symposium IGARSS*, pp. 2134–2137, July 2021. ISSN: 2153-7003.

Harmony end-to-end performance simulator: evaluating the performance of a bi-static ATI SAR mission for ocean observations.

P. Dubois[1], G. Monnier[2], P. Lopez-Dekker[3], T. G. Yitayew[4], T. Armstrong[1], B. Gombert[1], F. Soulat[1], Y-H Hellouvry[2], B. Camus[2], T. Grydeland[4], D. Lajas[5], B. Rommen[5], E. deWitte[5]
([1]CLS, [2]Scalian DS, [3]TU Delft, [4]NORUT, [5]ESA-ESTEC)

On September 22, 2022, the European Space Agency announced Harmony as the 10th Earth Explorer (EE10) mission. The Harmony concept comprises of two identical satellites that will fly in a constellation with a Copernicus Sentinel-1 satellite ([1]). Each satellite is being designed to carry a receive-only synthetic aperture radar as its main instrument. Working together with Sentinel-1's radar, Harmony will provide simultaneous measurements of wind, waves, and currents. These, along with measurements of sea surface thermal difference and cloud motion, will enable an unprecedented view of the marine atmospheric boundary layer.

The ocean products performance, derived in the early development phase with models and targeted simulations, was consolidated through the use of end-to-end (E2E) simulations, following ESA's proven process for EE selection ([2]). The E2E simulators are a classic tool for characterizing the performance of a mission, as defined by the science requirements. They integrate the definition of a set of geophysical truths, the geometry and timing of the acquisition, the transfer function of the instrument, and the prototyping of all levels of processing (On-board L0, L1, L2). At the end of the L2 processing, the estimates of the geophysical parameters of interest can be compared to the geophysical truth sets used as an input to the simulation.

The radar integration, modeled by the radar equation, is supported by a numerically processed spatial integral, whose complexity of computation is related to the spatial and temporal sampling of the surface, to the representativeness of radiometry and instrument model (antenna pattern, ...). In the context of a SAR system allowing, among other things, the estimation of surface currents vectors (with the ATI capability), the simulation of raw data requires a fine description of the ocean surface both spatially and temporally. Adding the number of phase centers, the variety of received polarization, and the extent of the scene (especially when Sentinel-1 emits in the IW mode), the resulting computational time is considerable and is the main challenge of the E2E design (called HEEPS/Mare for ocean application). The choice of models and implementation strategies made it possible to achieve a data production time compatible with performance studies.

1 Ocean scene modeling

The ocean scene is considered as a collection of layers, each consisting of a mesh that is defined at given spatial resolution and animated, if needed, at given temporal resolution. The layers are:

for the atmospheric conditions, the (spatially variant) (a) wind conditions, (b) clouds, wet troposphere.

for the time varying waves elevations, the (spatially variant) (a) aforementioned wind conditions layer, setting local wind sea elevation spectra by virtue of a modelled relationship between wind speed and friction velocity, (b) swell conditions, setting local swell elevation spectra, (c) surface currents, contributing to set the local waves dispersion relationship. The local waves spectra allow for the generation of local wave realizations thanks to the Fast-FT. Unfortunately, composing the entire surface using the tiles from the FFTs would result in strong discontinuities at the tile boundaries. An innovative approach is used to create smooth transitions between the local realizations.

for the surface radiometric model, a set-up that ensures a space-time cross-correlation of the back-scattered signal that coincides with a chosen Normalized Radar Cross Section (NRCS) model ([3]) at $t = 0$ and whose temporal spectrum coincides with a chosen Doppler spectra model ([4]). A mesh approach is applied, with the use of resolved waves elevation in the phase during the radar equation spatial integration, and the remaining contribution from the waves smaller than the mesh resolution (short waves) are accounted using time varying space random complex draws. For each of the mesh facets, the spectrum of the cross-correlation of the random variable is guaranteed to be the Doppler spectrum model computed for short waves only, and similarly for the NRCS. In doing so, it is ensured that the effect of short wave

motion on phase and amplitude (including its decorrelation) is taken into account. The setting of this statistical model is put in a table which is function of meshed slopes (that can be computed at the same time than meshed elevations, see previous item), facet size, wind speed and direction.

2 Geometry, Timing and Instrument transfer function

The spatially and temporally sampled data are acquired with respect to a specific line of sight pointing towards Earth. For Sentinel-1, the orbit and pointing information is determined using the Earth Observation CFI software and input state vectors. The Harmony satellites are propagated along the same orbit, taking into account a desired separation and the reception time given the bi-static observation geometry. The mechanical pointing is determined to be the same as that of the Sentinel-1 boresight, and the reception is configured based on a given Sentinel-1 acquisition mode. For the reception of the signal from the simulated ocean scene, the complex impulse response of the surface is computed utilizing input antenna models for both emission and reception, with narrow range gates to ensure precise estimate of the returned power. This result then undergoes a circular convolution with the chirp form to provide results expressed in sampling frequency domain, to which thermal noise is added.

3 Processing

The processing starts with the focusing of the raw data, as detailed in [5]. The following step is the retrieval of the main ocean products of interest in the relation to the ocean-atmosphere interactions [6].

The Doppler chain. The [L1b] Geophysical Doppler Centroid is estimated by removing the Along-Track Interferometry lag and the geometric phase contribution to the data. For Sentinel-1, this is the Doppler Centroid Anomaly (DCA) phase, as it delivers single phase-center data only, and the ATI phase for Harmony, exploiting the baseline between the wing antennas. The [L2] Relative Total Surface Current is the [L1b] geophysical Doppler where the so-called wave-Doppler contribution has been estimated by Geophysical Model Functions (GMFs) interpolation, and removed.

The amplitude chain. The Normalised Radar Cross-Section (NRCS) is, after appropriate calibration, a direct radar observable. The computation of the co- and cross-spectra includes the rotation of the polarisation basis, the tiling of the data, and processing steps similar to the S1-OSW processing. The surface stress and stress equivalent surface wind uses a GMFs that relates the stress equivalent surface wind and the NRCS.

There are at least three observations at different Lines of sight for the L2 estimates, which makes estimation of vectors possible (and over-determined). Parts of the Harmony L2 processing rely on the use of GMFs to correct/estimate geophysical contributions to the signals (amplitude and Doppler). These GMFs are one of the key elements of the mission performance study. Using GMFs based on real radar data in the E2E context can lead to uncertainties in the conclusions, since the ocean scene modelling is not the real ocean. A safe option has been to construct GMFs using the same models as those used in the E2E simulator.

4 Performance results

The main purpose of the simulator is to provide realistic estimates of expected Harmony performance. It can, for example, demonstrate the capacity of Harmony to retrieve a heterogeneous 2D wind velocity field (Figure 1) or a 2D wave spectra (Figure 2). In addition, the simulator allows to quantify performance metrics of L1 and L2 products such as the Noise Equivalent Sigma Zero and the standard deviation in retrieved wind and current homogeneous velocity fields. Initial results have been obtained during Phase A, and will be consolidated with updated processing algorithm definitions and more ocean scene variety.

References

[1] Harmony, eoportal. `https://www.eoportal.org/satellite-missions/harmony`. Accessed: 2023-01-23.

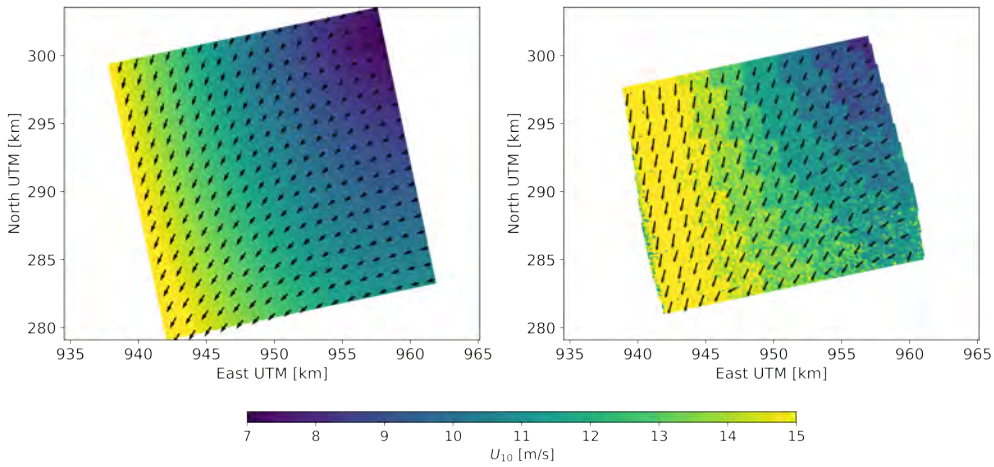

Figure 1: Capability of Harmony to retrieve a complex wind field in WV1 mode simulated using the HEEPS/Mare software. Left: input heterogenous wind field modelled as $\overline{U_{10}}(x, y) = (5 + 0.25x - 0.25y)\overline{x} + (5 + 0.5y)\overline{y}$. Right: retrieved wind field with a 125 m x 125 m sampling. Black arrows indicate wind direction

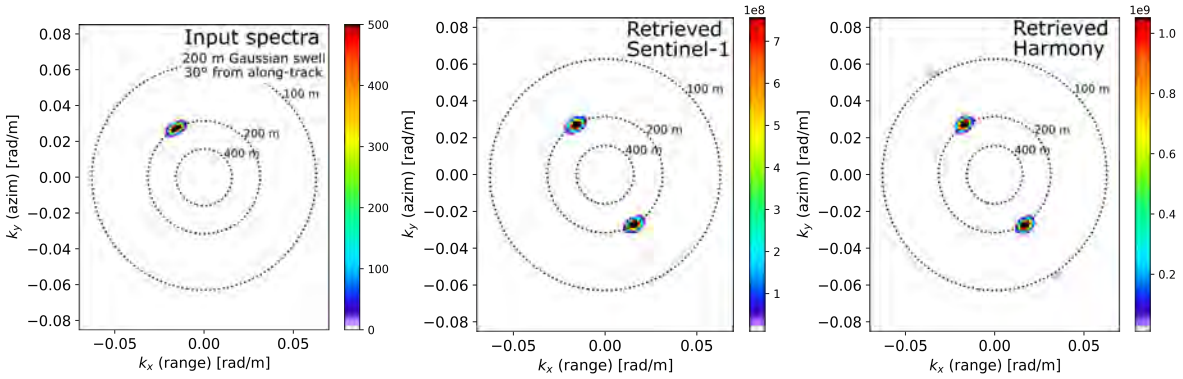

Figure 2: Capability of Harmony to retrieve an ocean swell spectrum in WV1 model using the HEEPS simulator. Left: input scene wave height spectrum. Middle and Right: retrieved modulation cross-spectrum for Sentinel-1 and Harmony-A, respectively. The difference in spectral power is explained by the Geophysical Model Function (GMF) that must be applied to the modulation spectra to obtain the wave height spectra.

[2] ESA. Report for Mission Selection: Earth Explorer 10 Candidate Mission Harmony. Technical Report ESA-EOPSM-HARM-RP-4129, European Space Agency, Noordwijk, The Netherlands, 2022.

[3] A Voronovich. Small-slope approximation for electromagnetic wave scattering at a rough interface of two dielectric half-spaces. *Waves in Random Media*, 4(3):337–367, 1994.

[4] F Nouguier, C-A Guerin, and G Soriano. Analytical Techniques for the Doppler Signature of Sea Surfaces in the Microwave Regime—I: Linear Surfaces. *IEEE Trans Geosci Remote Sens*, 49(12):4856–4864, 2011.

[5] Y. Larsen, Grydeland, T. G. T., Yitayew, and G. Engen. Processing of high squint bistatic sar data: The case of harmony. *SeaSAR*, 2023.

[6] P. Lopez Dekker, M. Kleinherenbrink, A. Payez, A. Stoffelen, and B. Chapron. Harmony Algorithm Theoretical Baseline Document: Oceans and Air-Sea Interactions. Technical report, TU Delft, 2022.

WaddenSAR campaign: first results

Paco Lopez-Dekker[1], Marcel Kleinherenbrink[1], Andreas Theodosiou[1], Marieke Eleveld[2], Firmijn Zijl[2], Karlus Macedo[3], Thiago Ruiz[3], and Julia Kubanek[4]

[1]TU Delft, [2]Deltares, [3]Metasensing, [7]ESA

February 13, 2023

1 Introduction

In September 2022, the Harmony mission [1, 2] was officially confirmed as the 10th ESA Earth Explorer. Harmony's space segment will consist of a pair of receive only-radar satellites that will fly in formation with Sentinel-1 which will act both as a common radar transmitter and, from a Harmony-mission perspective, as a third radar receiver. During most of the mission one of the Harmony satellites will fly 350 km ahead of Sentinel-1, with the other satellite trailing Sentinel-1 at the same distance. The resulting system will provide simultaneous measurements of the Normalized Radar Cross Section (NRCS) from three directions, implementing roughly the equivalent to a very high resolution scatterometer. In addition, Harmony will provide Doppler measurements using short-baseline Along-Track Interferometry (ATI) in the case of the companion satellites, and falling back to the much less sensitive Doppler Centroid Anomaly technique in the case of Sentinel-1.

The large inter-satellite separation, which is required to provide the directional diversity required to retrieve surface stress and surface current vectors, results in unprecedented large bistatic angles. While TanDEM-X [3] has been, from a system perspective, the first multistatic SAR mission, it is safe to say that Harmony will be the first multistatic mission from an electromagnetic scattering point of view. The characteristics of bistatic scattering at the ocean surface have been theoretically studied in depth [4, 5]. However, experimental data is required to fully validate and fine tune these scattering models. To serve that purpose, given the lack of available bistatic observations, ESA organized a multistatic airborne campaign in the Dutch Wadden Sea, with Metasensing as the prime contractor.

The main goals of the *WaddenSAR* campaign were:

1. To demonstrate the Harmony mission concept.
2. To test the proposed airborne implementation for use in future campaigns.
3. To confirm that the assumption that bistatic measurements behave largely like monostatic ones with a monostatic-equivalent geometry. Confirming this assumption allows using monostatic airborne data, which are much easier to collect, as a proxy for bistatic data in the development of, for example, retrieval algorithms.

The WaddenSAR flights took place on the 14th and 16th of March, 2022. This paper provides an overview of the campaign set-up and discusses some preliminary results.

2 Campaign description

During the campaign, Metasensing flew two Cessna C208 aircraft in a formation emulating Harmony's multistatic viewing geometry. As shown in Figure 1, the trailing aircraft carried a FMCW C-band radar, transmitting in V-polarization and receiving in two polarizations. The leading aircraft carried a receive-only radar payload with the dual-polarized antennas pitched 29.5° in order to align the receive-antenna footprint with that of the transmitter. Along-track interferometric observations where achieved by toggling in transmit between a pair of antennas separated about 0.8 meter. The raw data were focused on a regular ground-projected grid aligned with he flight direction using a back-projection algorithm. Table 1 provides a list of some relevant geometric and radar parameters.

On the first flight day, about 400 km of data was acquired flying a circuit in an open-sea region, North of the Wadden Islands. On the second day, after solving some technical issues, over 200 km were acquired mostly inside the Wadden Sea. Figure 2 shows the planned acquisition tracks overlayed on the total current predicted by the Dutch Continental Shelf Model in Flexible Mesh (DCSM-FM) model developed and implemented by Deltares.

Figure 1: Left: bistatic receive-only radar installed on the leading aircraft, with the dual-pol antenna tilted to provide overlapping antenna footprints. Right: transmit-receive system installed on trailing aircraft, with two transmit antennas toggled in order to implement ATI.

3 Results

Very preliminary results (not included in this abstract) show that both the monostatic and bistatic amplitudes are of good quality and generally similar to each other, as expected. The quality of the monostatic ATI phase should be enough to capture some of the strong tidal features shown in the model. At time of writing, the bistatic ATI phase shows large systematic range dependent phases, which the authors hope to have understood and mostly cleaned up during the workshop.

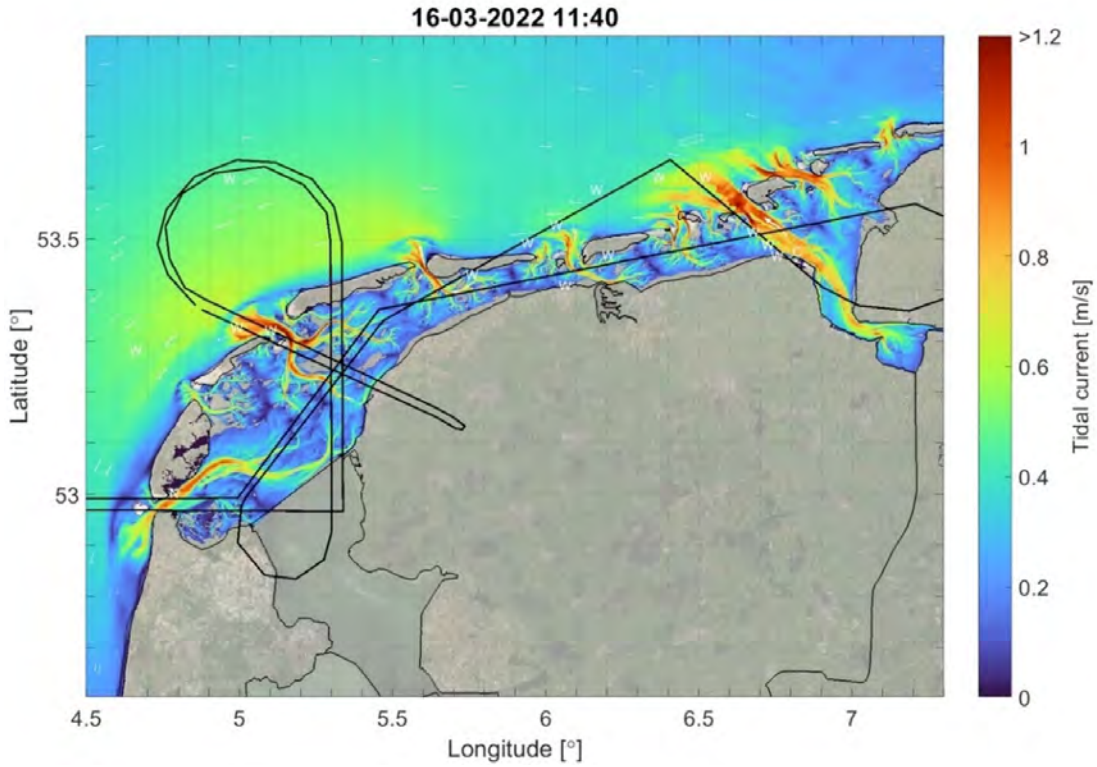

Figure 2: Planned flight tracks in the Wadden Sea overlayed on tidally dominated local currents predicted using the Dutch Continental Shelf Model in Flexible Mesh (DCSM-FM) model developed at Deltares.

References

[1] P. López-Dekker, H. Rott, P. Prats-Iraola, B. Chapron, K. Scipal, and E. D. Witte, "Harmony: an Earth Explorer 10 Mission Candidate to Observe Land, Ice, and Ocean Surface Dynamics," in *IGARSS 2019 - 2019 IEEE International Geoscience and Remote Sensing Symposium*, pp. 8381–8384, July 2019. ISSN: 2153-6996.

Flight & Observation geometry	
Flight altitude	$\sim$1550 m
Aircraft along-track distance	1100 m to 1400 m
Flight speed	$\sim$60 m s^{-1}
Angle of incidence (monostatic)	25° to 45°
Swath width	$\sim$1200 m
Radar parameters	
Center frequency	5.3 GHz
Azimuth single-look resolution	0.5 m
Slant-range single-look resolution	2.8 m
ATI baseline	0.8 m
Transmit polarization	V
Receive polarization	Dual (H and V)

Table 1: Radar and observation geometry characteristics

[2] P. López-Dekker, J. Biggs, B. Chapron, A. Hooper, A. Kääb, S. Masina, J. Mouginot, B. B. Nardelli, C. Pasquero, P. Prats-Iraola, P. Rampal, J. Stroeve, and B. Rommen, "The Harmony Mission: End of Phase-0 Science Overview," in *2021 IEEE International Geoscience and Remote Sensing Symposium IGARSS*, pp. 7752–7755, July 2021. ISSN: 2153-7003.

[3] G. Krieger, A. Moreira, H. Fiedler, I. Hajnsek, M. Werner, M. Younis, and M. Zink, "TanDEM-X: A Satellite Formation for High-Resolution SAR Interferometry," *IEEE Transactions on Geoscience and Remote Sensing*, vol. 45, pp. 3317–3341, Nov. 2007.

[4] T. Elfouhaily, D. R. Thompson, D. Vandemark, and B. Chapron, "A new bistatic model for electromagnetic scattering from perfectly conducting random surfaces," *Waves in Random Media*, vol. 9, pp. 281–294, July 1999.

[5] L. Iannini, D. Comite, N. Pierdicca, and P. Lopez-Dekker, "Rough-Surface Polarimetry in Companion SAR Missions," *IEEE Transactions on Geoscience and Remote Sensing*, vol. 60, pp. 1–15, 2022.

Proceedings Papers

List of Proceedings Papers

RECENT ADVANCES IN SAR REMOTE SENSING OF SEA ICE AND RECOMMENDATIONS FOR THE FUTURE: SUMMARY FROM SEASAR 2023

Anton Korosov[1], Malin Johansson[2], Anja Frost[3], Juha Karvonen[4], Ekaterina Kim[5], Ron Kwok[6], Nicolas Longépé[7], Johannes Lohse[2], Robert Shuchman[8], Catherine Taelman[2], Stefan Wiehle[3]

(1) Nansen Environmental and Remote Sensing Center, Bergen, Norway
(2) UiT The Arctic University of Norway, Tromsø, Norway
(3) DLR (German Aerospace Center), Germany
(4) Finnish Meteorological Institute, Helsinki, Finland
(5) Norwegian University of Science and Technology (NTNU), Trondheim, Norway
(6) University of Washington Applied Physics Laboratory, Seattle, WA, USA
(7) European Space Agency-ESRIN, Rome, Italy
(8) Michigan Technological University, USA

1. INTRODUCTION

Sea ice plays a crucial role in the Earth's climate system and global ecology. Its presence significantly influences the planet's energy balance by reflecting sunlight, helping regulate temperatures, and influencing ocean circulation patterns. Sea ice also serves as a habitat and a crucial feeding ground for various marine organisms, supporting complex ecosystems from microscopic algae to large mammals such as polar bears and seals. Additionally, the freezing and melting processes of sea ice impact ocean dynamics and, in turn, affect weather patterns and the livelihoods of coastal communities. Importantly, sea ice can be viewed also either as an obstacle for navigation or as an extension of land used by local communities for travel and hunting. Understanding the dynamics and importance of sea ice is essential for predicting climate changes and their potential impacts on both local and global scales.

Synthetic Aperture Radar (SAR) remote sensing is a key tool for monitoring and studying sea ice due to its unique capabilities in all-weather and day-and-night imaging. The importance of SAR remote sensing in the context of sea ice lies in its ability to provide high-resolution data, offering detailed information about sea ice distribution, type, and dynamics over vast and often remote regions. SAR sensors can penetrate through clouds and darkness, allowing continuous observation and monitoring of sea ice cover regardless of weather conditions. These observations are fundamental for understanding the changing patterns of sea ice extent, thickness, and movement, enabling the assessment of ice dynamics, identification of different ice types, such as ridged, deformed, or open water areas, and the tracking of ice movement and deformation. Such data is invaluable for climate studies, weather forecasting, fishing and hunting, safe navigation, ecosystem monitoring, and aiding in the understanding of the broader implications of climate change and human activities on polar regions. SAR remote sensing, therefore, plays a pivotal role in providing essential data for scientific research and policy-making concerning sea ice and its dynamic responses to changing environmental conditions. In this work we summarize recent advancements in SAR remote sensing of sea ice presented at the SeaSAR'23 conference and provide a synopsis of the main challenges and recommendations.

2. OVERVIEW OF RECENT ACHIEVEMENTS

2.1 Copernicus Marine Service SITAC SAR-Based Baltic Sea Ice Products

The Baltic Sea ice drift product in the Copernicus SITAC is provided by Finnish Meteorological Institute (FMI). The algorithm is a two resolution (referred as low and high resolution) level model. Co-registered dual-polarized (HH/HV) C-band SAR images from Sentinel-1, Radarsat-2 or

Radarsat Constellation Mission are first converted to single channel images by computing the SAR backscatter magnitude $M=(HH^2 + HV^2)^{1/2}$ from the two calibrated SAR channels. After this ORB (Oriented FAST and Rotated BRIEF, Rublee et al., 2011) is applied to detect ice drift in a reduced resolution of 500 m. This low-resolution result is then interpolated to cover the whole sea ice area. Optical flow (Horn and Schunck, 1981) is applied to high-resolution magnitude images using the low-resolution drift as an initial shift between the two images. The Lucas-Kanade Optical flow (Lucas and Kanade, 1981) is applied in the algorithm. Lucas-Kanade algorithm assumes that the optical flow equation holds for a block of pixels and the motion is solved by a least-squares fit. A simplified algorithm flow diagram is presented in Fig. 1.

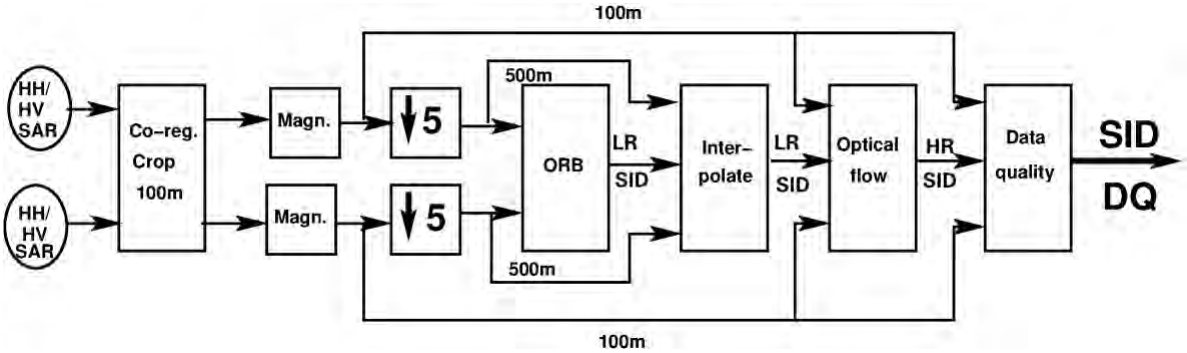

Figure 1. Structure of the operational FMI SITAC ice drift algorithm. A pair of overlapping images in input and first co-registered and resampled to 100 m resolution, then magnitude images of the two SAR channels are created, they are re-sampled to 500 m resolution and fed to the ORB feature detection and matching algorithm. The 500 m (low-resolution) drift detection is then interpolated to cover the image sea ice area. The low-resolution SID is then used as a starting point to the optical flow drift detection applied to the full-resolution magnitude images to refine the low-resolution ice drift estimation.

2.2 Tracking backscatter signatures of individual sea ice floes using in-situ drift observations

At present, most of the SAR data that is routinely available for sea ice monitoring is acquired in wide-swath mode at C-band, for example by Sentinel-1 (S1). For these sensors, the backscatter signal from a given sea ice type varies with incidence angle (IA) across the swath (Lohse et al., 2020), and it is strongly affected by changes in temperature and snow properties (Barber et al., 1992). Understanding these variations in backscatter is crucial for the interpretation and automated analysis of the imagery.

The seasonal evolution of C-band radar backscatter has been extensively studied for landfast ice (for example in (Yackel et al., 2000)), but seems rare for drifting ice. Tracking drifting ice floes in consecutive SAR images over long timespans has proven to work well in winter but remains challenging in melting conditions or in regions characterized by high drift speeds (Krumpen et al., 2019). In this study, we use a set of in-situ drift trajectories collected during the *CIRFA-22* campaign to track individual ice floes in the Fram Strait over several months, covering the transition from freezing conditions to warmer melting conditions.

We automatically identify the drifter locations in overlapping S1 imagery and manually identify and track distinct surface features (hereafter called 'ROIs') in the vicinity of the drifters that can be followed over time in the SAR images. On short timescales (days), this allows us to investigate the IA dependence of the backscatter signature for the exact same sea ice, while on longer timescales (weeks), we can study the temporal backscatter evolution of drifting ice as it undergoes physical changes at melt onset.

We investigate the IA dependence by estimating the slope relating IA to backscatter based on the backscatter values of a ROI imaged in two consecutive SAR scenes, once in near-range and

once in far-range. We only estimate slopes during freezing conditions, as we assume that no physical changes occur on the ice surface between two consecutive SAR acquisitions. The average slope estimate per ROI is then used to correct all backscatter values in the time series by projecting the values onto a common incidence angle. Next, we make a distinction between ROI's labeled on first-year ice (FYI) versus multiyear ice (MYI). We apply the incidence angle correction scheme individually for each ice type. An example based on one in-situ drift trajectory is shown in Fig. 2. As a general trend, we observe that backscatter values drop for MYI at melt onset, while backscatter values rise for FYI. The shift results in an inversion of the backscatter values per ice type shortly after melt onset. Note that at melt onset the backscatter values of both ice types overlap, which means that FYI and MYI are statistically inseparable in the SAR imagery at this moment. More case studies are needed to confirm that the backscatter intensity inversion consistently happens for FYI and MYI after melt onset.

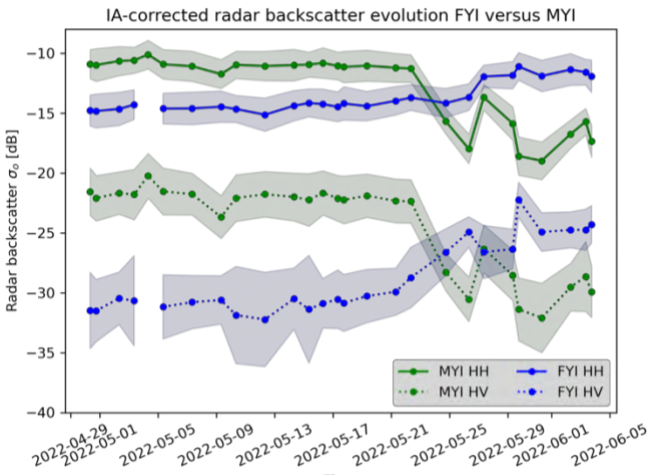

Figure 2. The seasonal evolution of incident angle-corrected radar backscatter values of first year ice (FYI) and multiyear ice (MYI), for HH and HV polarization channels.

2.3 Potential of the Earth Explorer 10 candidate "Harmony" for Studying Sea Ice Deformation

An alternative to sea ice drift observation on consecutive SAR images is estimation of instantaneous surface motion from Doppler shift anomaly fields (Kramer et al., 2018; Wang et al., 2023). However, data from only one SAR antenna can provide only one component of ice motion. Harmony, the candidate for the ESA Earth Explore 10 mission, promises to provide both components. Two Harmony satellites will fly in a reconfigurable formation with S1-D. Both will be equipped with a passive antenna, which receives the reflected S1-D signals. In the stereo formation, the Harmony satellites will fly approximately 300 km in front and behind S1, which allows for the estimation of instantaneous sea-ice drift vectors. As was shown by Kleinherenbrink et al. (2021) the sea ice drift and deformation can be derived from simulated Harmony data, but the signal-to-noise ratio is quite low.

Here we use the next generation sea ice model neXtSIM (Ólason et al., 2022) for simulating ice drift, and the end-to-end Harmony simulator (Kleinherenbrink, 2021a) to generate Doppler shift fields and derive ice motion from the synthetic Harmony data. We evaluate if we can use Harmony data for characterising sea ice deformation in the Arctic Ocean and validation of neXtSIM.

We compute 2D fields of Doppler shift from Concordia, Discordia, and Sentinel ($D_C(R,A)$, $D_D(R,A)$, $D_S(R,A)$) and the thermal noise equivalent sigma zero (NESZ) of the Doppler signal ($N_D(R,A)$) with the forward model (F_M) of (Kleinherenbrink et al., 2021b): D, $N_D = F_M(U)$, where U is the neXtSIM-simulated ice drift field. Thermal noise is added as a product of noise equivalent sigma zero (NESZ) profile and normally distributed noise (N): $D^N = N_D * N$.
Noise correction is performed for each field of D individually as follows. Given that the profile of NESZ is known *a priori* we can perform "texture noise" correction suggested by Park et al. (2019) for reducing amplitude of signal variations near inter-swath boundaries where NESZ is the highest: $D^1 = Gf(D^N)*N_N + D^N*(N_N - 1)$, where Gf is a 2D Gaussian filter with size of 10 pixels (20 km) and N_N is the N_D normalized into range $0 - N_{MAX}$, with $N_{MAX} = 0.7$ being found empirically. Next, we apply a low pass filter as suggested in (Kleinherenbrink et al. 2021b, Eqs. 19 – 22): D^2

= Kf(D^1, D). And finally, we apply the anisotropic diffusion filter (Perona and Malik, 1987) for smoothing homogeneous U/V fields and preserving high contrasts: D^3 = ADf(D^2, gamma=0.25, kappa=5).

Velocity fields (U^3) are reconstructed from the denoised Doppler shift fields D^3 using the retrieval model (R_M) of Kleinherenbrink et al. 2021b: $U^3 = R_M(D^3)$, and are denoised with clustering (grouping of pixels with similar velocities and coordinates). We apply clustering under the assumption that sea ice deforms as a solid body with low elasticity and ability for brittle break-up. Therefore, the neighbor elements can have either the same velocity (when they belong to an unbroken ice, i.e., an ice floe) or differ substantially (when they belong to different ice floes). After the clustering is performed, the small-scale variability on the edges of clustering is reduced by applying a median filter to the image with labels (Fig. 3).

For evaluating Harmony data and our inversion algorithms we simulate ice motion with neXtSIM on pan-Arctic scale and generate 15 swaths of Harmony observations for the 1 January 2019. We compute the divergence (Ñ) and shear (t) components of sea ice deformation from the velocity fields U^3 and U^4 using the method of Kleinherenbrink et al. 2021. A daily mean deformation map is created by averaging individual swaths.

Our results show (see Fig. 4) that realistic sea ice deformation fields can be derived from Harmony data: the major features north of Greenland, Canadian Archipelago and Laptev Sea are well visible. Method "4" seems to be better capturing also small deformation features and producing a less noisy map. Comparison of PDFs shows that deformations produced by both methods capture the strong, large-scale features with deformations rates of ~ 0.01 d-1. Nevertheless, only the method "4" reproduces the small magnitude deformation (< 0.001 d-1).

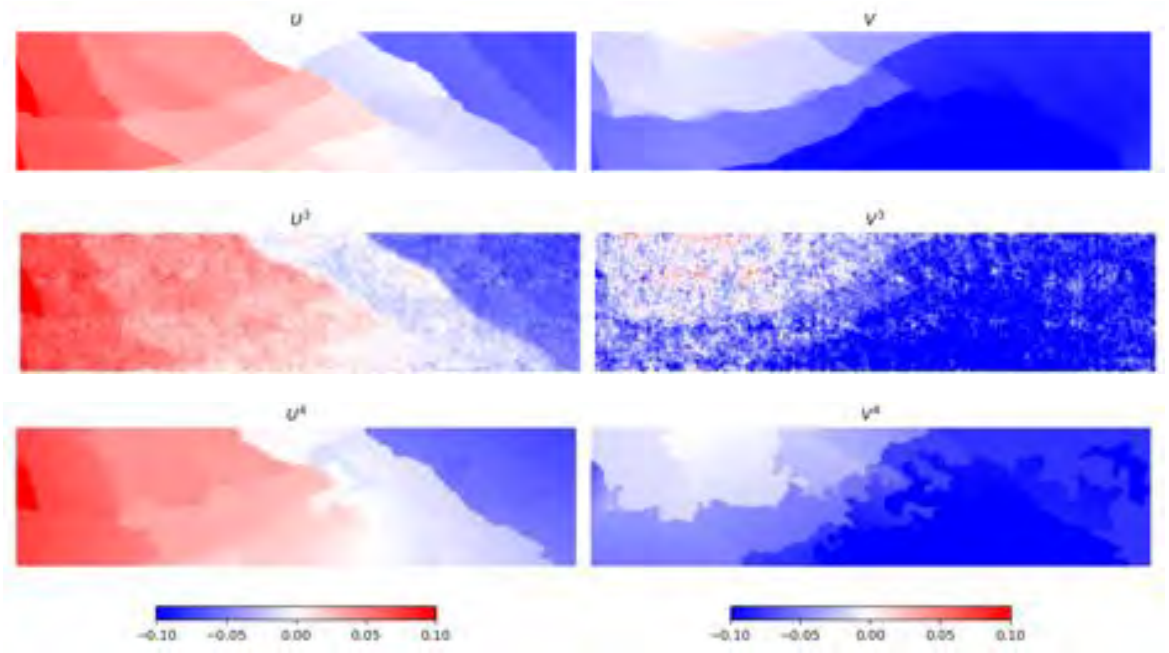

Figure 3. Velocity components after the steps of processing: U – initial range and azimuth components, U^3 – low-pass and anisotropic diffusion, U^4 – clustering.

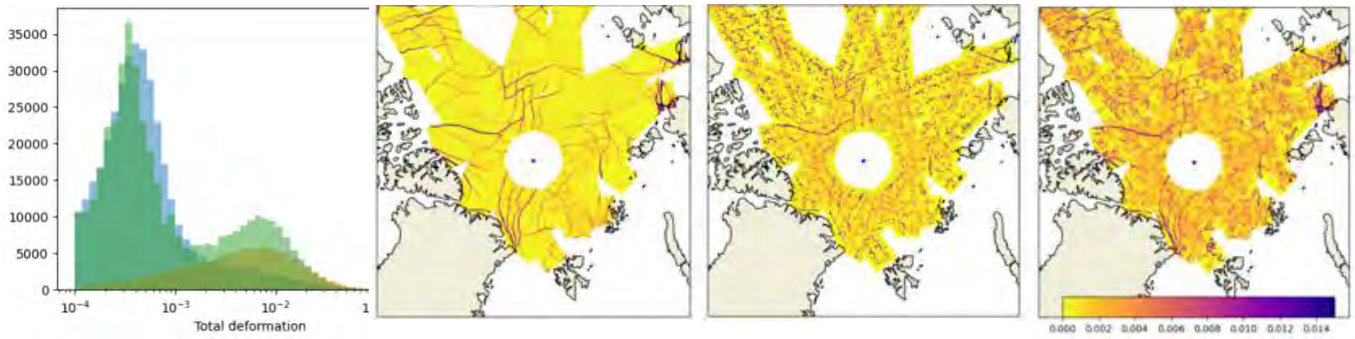

Figure 4. Maps of shear (t) computed from simulated velocities (1st column) and from Harmony denoised velocities using U^2 (2nd column) and U^3 (3rd column). PDFs of total deformation (blue – neXtSIM, orange – U^2, green – U^3).

2.4 Towards Multitemporal Sea Ice Classification by Means of Spaceborne SAR Image Time Series

Since the advent of satellite borne SAR, many approaches for SAR based sea ice type classification have been developed (Zakhvatkina et al., 2019). The most promising approaches have been transferred to operational services. Nevertheless, obtaining accurate classifications year-round is still a challenge. Different ice classes can show similar radar backscatter responses, which limits the performance of sea ice classification. Seasonally, the radar backscatter signal can be affected by precipitations, e.g., wet snow obscures information about underlying ice types (Kortum et al., 2022).

To stabilize automated classification, we describe here a new approach on multitemporal sea ice classification. The basic idea is to use collocated, sequential SAR acquisitions taken over a region of interest, and - in a first step - generate high resolution drift vector fields from these data, using, e.g., phase correlation as presented in (Frost et al., 2018). Using the retrieved drift vector information, we can track drifting pieces of ice (such as an ice floes) from one SAR acquisition to the next and collect more SAR measurements about the floe. The collected SAR measurements are then used jointly to classify the sea ice.

The core of our sea ice classification algorithm is an adjusted UNET++ convolutional neural network (CNN) architecture described by (Frost et al., 2018). In our specific implementation, the classification is done tile-wise, i.e. a SAR acquisition is divided into tiles, classified, and then the results are joined back to generate an ice map (Zhou et al., 2019). We differentiate MYI, FYI, young ice (YI), open leads (split in so-called dark leads (DL) and bright leads (BL)) and rough ice (RI). However, many classification methods allow to model a discrete probability distribution of sea ice types for each pixel. In general, the ice type with the highest probability is then selected as the final classification result. In contrast, in our multitemporal approach, several (sequential) discrete probability distributions of ice types are examined after drift compensation. For our first tests, we selected the most likely ice type from these subsequent probability distributions.

Our experimental results performed on a S1 image time series taken over the Arctic Ocean show that the multitemporal approach in parts improves the classification. It can correct obvious misclassifications that were generated from single SAR acquisitions. Overall, the multitemporal approach is a powerful tool to generate sea ice classifications with increased reliability and overcome short term surface changes that have no relevant influence on the sea ice in its core.

Note that for fusing probabilities, various approaches can be applied, namely Kalman filter, Bayesian networks, and Dempster-Shafer. In ongoing work, we consider Kalman filtering and incorporate a priori knowledge to forbid impossible class changes e.g. from YI to MYI and vice versa.

2.5 Preliminary results of Sea Ice Classification using combined Sentinel-1 and Sentinel-3 data

A sea ice classification was trained using a combination of SAR from S1 and an existing sea ice classification using optical-thermal data from the SLSTR sensor on board Sentinel-3 (König et al., 2021). In radar data, some ice classes exhibit a similar backscatter, limiting the applicability of radar-based classification. Sentinel-3 data contain optical/thermal information of water, ice, and snow, allowing a refined ice class separation after classification, but the observations are in lower resolution and clouds may obstruct the view.

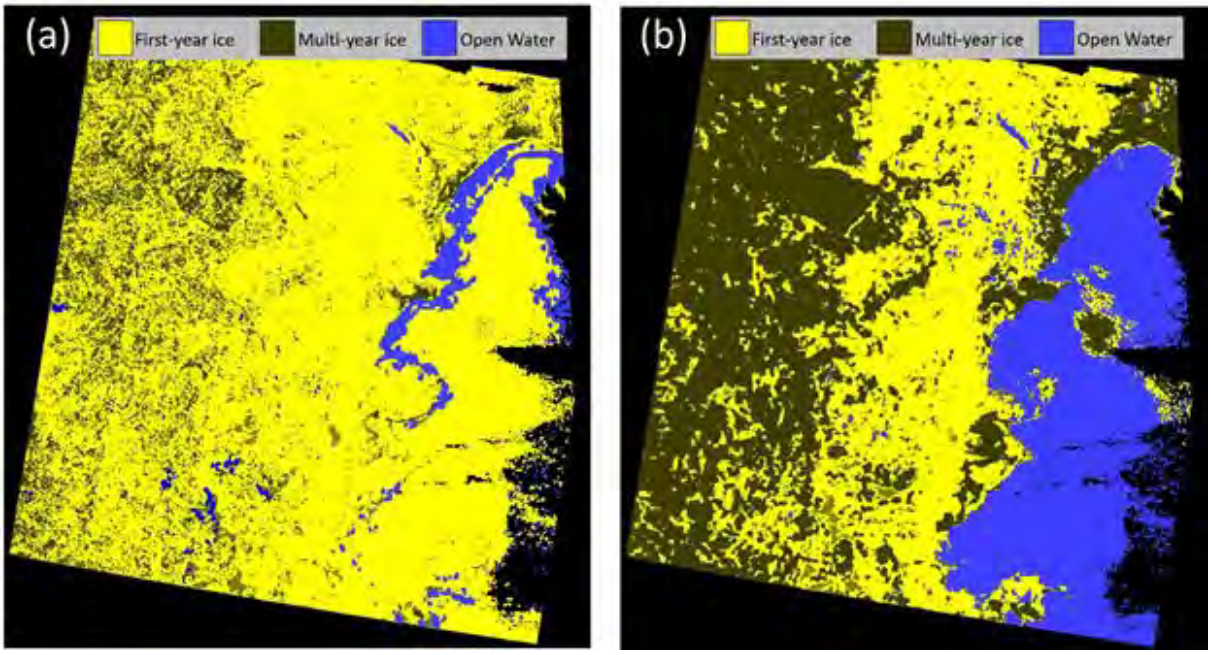

The fused classification is based on a Convolutional Neural Network (CNN) classifier and discriminates six sea ice types. A similar setup and method of classification was introduced before for SAR-only sea ice classification (Murashkin et al., 2021). The fusion input data are the HH and HV polarization channels of the S1 image plus classified Sentinel-3 SLSTR images with continuous RGB labels.

The results shown here are derived from an early, limited training data sample of 12 data stacks. Fig. 5 shows a comparison of the classification results between the SAR-only classification in panel (a), using only the SAR data for training and inference, and the fused classification in panel (b), which identifies the open water on the right correctly.

The presented preliminary results suggest that the fused sea ice classification from SAR and optical images can improve the results, especially in open water and lead detection. Further training and validation are currently ongoing. This fused classification is to become part of a near-real time sea ice information generation and delivery chain, where also the individual classifications from SAR and SLSTR are made available to the end users due to their much higher availability compared to fused results.

Figure 5. Example classification results. (a) SAR classification using only S1 data, (b) fused classification using SAR data and an SLSTR classification. Most open water areas are identified correctly by the fused classification. Note that the same cloud mask is applied to both scenes, causing the frayed black areas on the right.

2.6 Combining C- and L-band SAR imagery for automated sea ice classification and segmentation

In the light of ESA's upcoming L-band SAR mission ROSE-L, the benefits of combining C- and L-band SAR data for operational sea ice charting have been investigated in the project *Synergistic Use of L- and C-Band SAR Satellites for Sea Ice Monitoring (LC-ICE)*. Work package 3 of the project focused on the investigation of automated classification and segmentation.

In this study, we used a set of 161 aligned image pairs that were acquired over three different test sites in the Arctic (Belgica Bank, Fram Strait, and Lincoln Sea) and for which the sea ice drift during the time interval between the C- and L-band acquisition was compensated using an algorithm developed at Chalmers University of Technology (Demchev et al., 2023).

Figure 6. Example AOI with overlapping C- and L-band imagery (RGB: HV, HH, HH) and corresponding single- and multi-frequency classification results from the East Greenland test site. Training and validation ROIs are indicated on the SAR imagery. Ice type abbreviations are Open Water (OW), Young Ice (YI), Level Ice (LI), and Deformed Ice (DI).

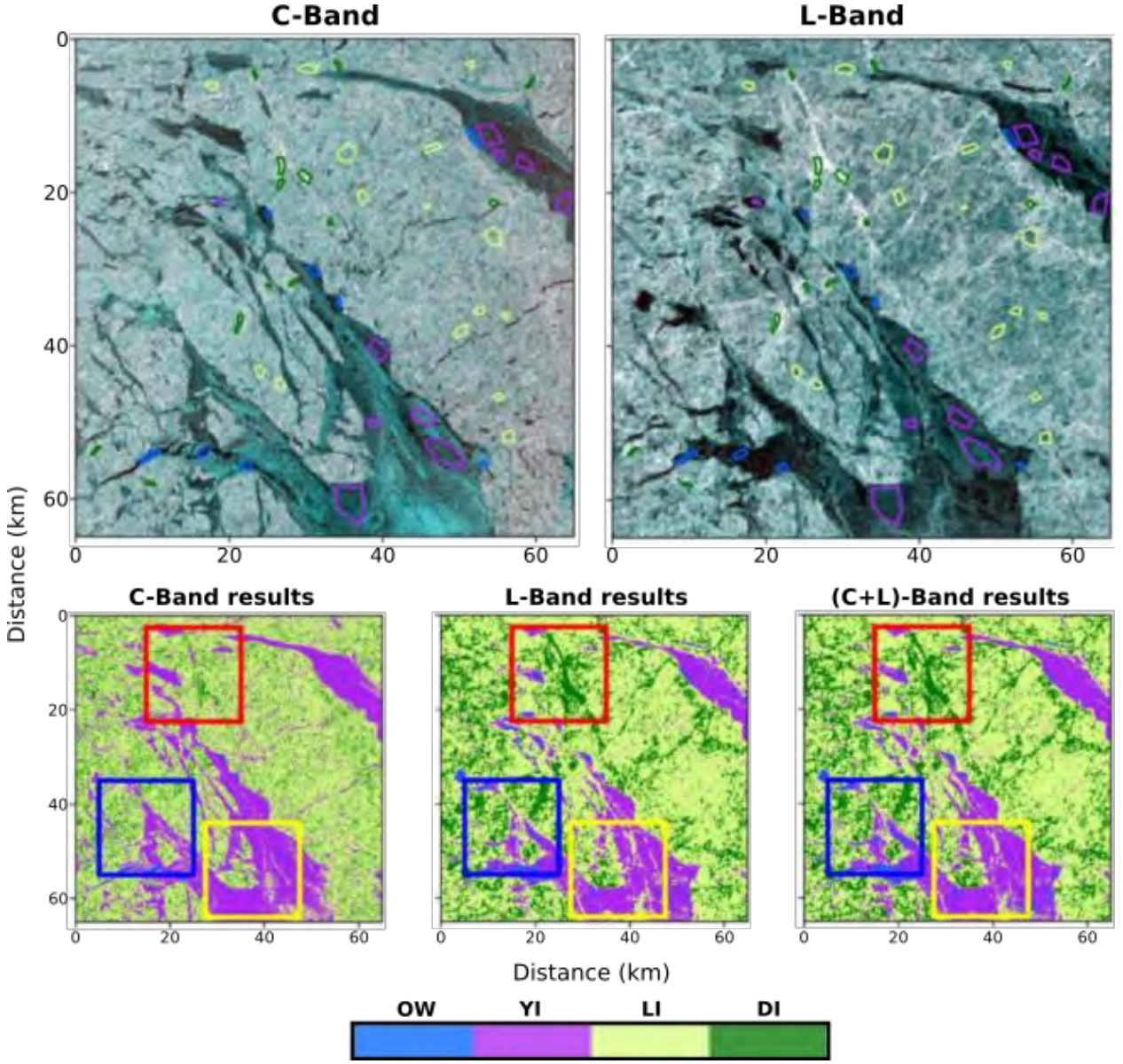

After visual inspection of the data, we selected an area of interest (AOI) within each pair that is suitable for the study of multi-frequency classification. The purpose of the AOI selection was to choose areas that are as large as possible, but small enough to avoid IA effects, visible swath boundaries, the influence of sensor noise, or artifacts from the image alignment process. We then applied both supervised classification and unsupervised segmentation algorithms on the selected AOIs using algorithms developed by Lohse et al. (2020) and Doulgeris (2015), respectively. Both methods were applied on each AOI for three separate test cases: (1) C-band stand-alone, (2) L-band stand-alone, (3) C+L-band. We evaluated the classification results in terms of per-class classification accuracy (CA) based on manually selected validation regions of interest (ROI)s.

Fig. 6 shows an example AOI and the corresponding classification results. Our unsupervised segmentation method automatically finds the number of clusters in data for a given sensitivity setting. As we increase the segmentation sensitivity and produce more clusters, we used the Jeffries-Matusita distance as a separability measure to find the maximum number of statistically separable classes for each case.

Our results show that the multi-frequency approach (C+L-band) generally outperforms the single-frequency approaches. For the supervised classification, we find that the dual-frequency approach achieves the highest CA in 98% of all test cases. In regions of deformed ice, the L-band stand-alone classification can sometimes perform almost equally as well as the dual-frequency classification. However, especially in lead areas with open water, newly formed ice, and young ice, the combination of C- and L-band is almost always superior to either of the single-frequency approaches. For the unsupervised segmentation, the combination of C- and L-band finds on average 2.4 more clusters than C-band alone, and 1.0 more clusters than L-band alone. This underlines the complementarity of the information content of both frequencies. Based on these findings, we conclude that a tandem flight pattern for the ROSE-L and the Sentinel-1 missions would be the most beneficial from a sea ice classification perspective.

2.7 High resolution L- and C-band polarimetric variability during MOSAiC

Separation between deformed sea ice and high-backscatter YI areas is one of the remaining challenges for automatic classification of sea ice types in synthetic aperture radar (SAR) images. Polarimetric features derived from fully-polarimetric or compact polarimetric imagery may aid this separation. Upcoming L-band missions such as NISAR, ALOS-4 and ROSE-L will offer the advantages of fully polarimetric acquisitions along with higher ground coverage to achieve an optimal scenario for L-band SAR based sea ice monitoring and will ensure a steady supply of L-band imagery in the years to come covering both the Artic and Antarctic sea ice.
Previous studies e.g., (Johansson et al., 2018; Mahmud et al., 2020; Toyota et al., 2020) have shown that L-band SAR can provide improved separability between different sea ice types. The different wavelengths mean e.g., different penetration depths and different sensitives to the onset of melting e.g. (Casey et al., 2016). In Mahmud et al., (2020) L-band data was shown to provide easier separation between FYI and MYI in the early and advanced melt season.

Here we investigate the usefulness of the polarization difference (PD: VV-HH) for the detection, separation, and characterization of YI areas in L- and C-band SAR images collected during the MOSAiC drift study. The drift lasted from the freeze-up to the early melt season, ensuring that the temperature dependency is also examined. We observed that PD has positive values for open water and new ice areas, i.e. HH > VV, whereas the values turn negative for the young ice stage and stabilize around 0 for the thicker sea ice types. The polarization difference was found to provide separability between younger ice types and thicker sea ice and provide good separability between high backscatter YI and MYI, in both C- and L-band SAR images, and hence provides a complement to the co-polarization ratio that can primarily separate the newer sea ice types. The variability in PD was in

L-band SAR was found to be a useful indicator of early melt stages, due to the shift from stronger VV to stronger HH data. The same trend could not be observed in the C-band images, and as such the two frequencies complemented one another. SAR images from the CIRFA cruise in 2022 at the Belgica Bank fast ice was found to confirm this analysis and the usefulness of PD will be further investigated using both the MOSAiC, N-ICE2015 and the CIRFA cruise data, utilizing overlapping L- and C-band images that co-inside with in-situ measurements.

2.8 Quadruple Helix Framework for Sea Ice Monitoring: Next Steps

Ice covered Arctic areas remain severely under-monitored and not well known to the broad public. Current ecosystem mapping proposals via the EU's Biodiversity Strategy for 2030 do not explicitly include in-situ measurements as a part of the mapping. Without in-situ monitoring, rapid localized changes in ecosystem's conditions cannot be detected. As a result, our ability to predict rapid changes of the environment and manage the effects of environmental change will remain severely limited. Furthermore, as waves of urbanization and immigration as well as the widespread of digitalization continue, there is limited human engagement, and participation in monitoring of nature and a further disassociation with it. We illustrate the above challenges using a quadruplex helix framework for monitoring of sea ice as an example. The framework (shown in Fig. 7) relates sea ice knowledge at different spatial and temporal resolutions to each other (i.e., remote sensing, in-situ scientific measurements, citizen science, and indigenous knowledge)

Users from the maritime sector are not always able to validate and trust satellite products when looking at rapid and localized events or changes in sea ice conditions. This shortcoming can be addressed using technology for automated collection, processing, and quality control of the ground-truth sea ice data. A three-stage approach for the automated analysis of close-range optical images containing floating ice is described in Panchi et al. (2021). The proposed system is based on an ensemble of deep learning models and conditional random field postprocessing.

Figure 7. Quadruplex helix framework for sea ice monitoring and its challenges.

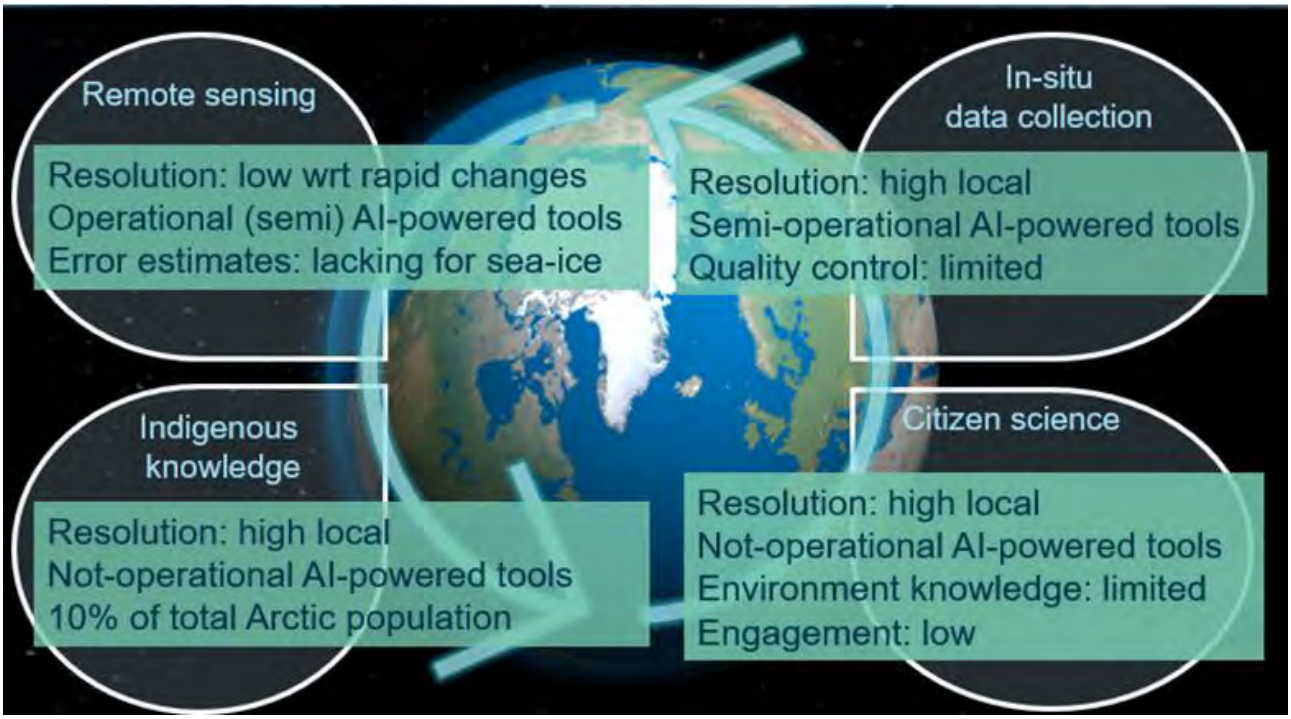

The following surface ice formations are considered: icebergs, deformed ice, level ice, broken ice, ice floes, floe bergs, floe bits, pancake ice, and brash ice as well as additional five non-surface ice categories: sky, open water, shore, underwater ice, and melt ponds. The best performance is achieved using an ensemble of models having pyramid pooling layers (PSPNet, PSPDenseNet, DeepLabV3+, and UPerNet) and convolutional random field postprocessing, and this outperformed the best single-model approach. The results show that when per-class performance was considered, the sky is the easiest class to predict, followed by deformed ice and open water. Melt pond is the most challenging class to predict. More efforts will be needed to make this automated image segmentation and analysis fully operational for remote sensing applications—especially the collection and labelling of more images containing floeberg, floebit, and melt ponds and introducing new labels. In situ verification, validation, and possible corrections to ice segmentation would go a long way in providing more training data and improving the proposed approach. When coupled with optical sensors and GNSS, such an approach can serve as a supplementary source of large-scale 'ground truth' data for validation of satellite-based sea-ice products.

In addition, sea ice data users (e.g., maritime sector) increasingly require spatially explicit information on the uncertainty of sea ice parameters for evaluating the risk that a specific outcome of further analysis of the information will be incorrect. It is, therefore, a priority to develop and standardize methods to compute consistent and comparable error estimates for sea ice datasets. This is particularly important for in-situ observations since realistic uncertainty estimates are essential for meaningful integration of these data in remote sensing and other higher-level products and studies (automated sea ice charting, climate modelling, etc.).

3. REMAINING KNOWLEDGE GAPS AND CHALLENGES

In the field of SAR remote sensing of sea ice, several knowledge gaps persist, necessitating further investigation and development. One critical issue is the presence of high thermal or speckle noise. Effective noise suppression techniques that maintain image resolution are essential. The implications of noise on the accuracy of ice drift and deformation measurements need thorough examination. The loss of the Sentinel-1B satellite has reduced data coverage, emphasizing the need for access to RCM data and algorithm adaptation. Thermal noise reduction is particularly needed for the RCM cross-polarization channel due to the strong scalloping effect and significant noise patterns, which affect automated SAR interpretation algorithms.

Another challenge is the low contrast in SAR images, particularly in wet snow conditions during summer and broken ice within the MIZ. Enhancing the informativeness of SAR image patches is crucial for robust sea ice drift retrieval based on Maximum Cross-Correlation (MCC) methods. Utilizing HH and HV polarization channels simultaneously may offer a solution, but efficient methodologies need to be developed.

Rapidly changing surface conditions, such as melting in summer and heterogeneous drift in the MIZ, complicate image analysis. Adapting the time delta between images is necessary, and identifying the optimal time interval is critical. The inherently different patterns observed in C-band and L-band SAR imagery further complicate MCC and alignment evaluation, necessitating methods to compare and align these datasets effectively. At the same time image alignment algorithms face significant challenges due to floe rotation and other fast surface changes, which complicate image morphing. More efficient image generation and morphing techniques are needed, as well as new metrics for evaluating aligned multi-frequency imagery.

Sea ice numerical models need a proper Lagrangian Sea Ice Drift product for thorough

calibration and validation. However, despite current SAR missions, such as S1, Radarsat-2 (RS2), and the RCM provide vast amounts of SAR imagery, there is currently no replacement for the ice drift product produced by the Radarsat Ground Processing System (RGPS) (Kwok et al., 1998). Obviously, the handling of large SAR datasets (Big Data) demands optimized algorithms and adequate hardware resources.
Sea ice is highly diverse, and some categories, such as new ice, are underrepresented. Improving the representation of all ice types in SAR data and addressing low prediction accuracy in under-represented categories is critical. Strong winds and the presence of new or young ice further complicate classification, necessitating improved quality of label data and mitigation of systematic biases in ice charts.

The role of snow in influencing radar signatures, including snow metamorphism and the effects under dry freezing conditions, must be better understood. Investigating the impact of wind-compacted layers, rain-on-snow events, ice lenses within the snowpack, and the brine layer at the snow-ice interface, particularly in relation to C- and X-band SAR, will improve the interpretation of radar data. The L-band's relative insensitivity to these factors should also be considered.

Inconsistent classification results across multi-temporal images presents another challenge. Developing methods to improve consistency and address these inconsistencies is necessary. Furthermore, machine learning (ML) and deep learning (DL) models, often considered black boxes, require efforts to elucidate the physical relationships between input features and the theoretical informativeness of SAR images to infer multiple ice types.

Multi-sensor synergy offers enhanced temporal and spatial coverage when combining data from multiple sensors. However, the time delays between acquisitions, particularly in regions with high sea ice drift speeds like Fram Strait, pose significant challenges. Data alignment is crucial, but temporal gaps in multi-sensor data can be problematic. Combining SAR with optical satellite data may offer advantages for various sea ice tasks, for instance, infrared sensors can differentiate between thin and thick ice by heat fluxes, optical sensors can identify open water, snow-covered sea ice, and ridges under favorable illumination, and SAR can penetrate snow and reveal ice structures, although separating ice from water remains challenging. However, overcoming the time separation between image acquisitions remains a key issue.

Upscaling and downscaling between different observational modes, from in-situ to drones, airborne, and satellite data, to models, requires careful consideration of ice motion. Large spatial coverage over study sites can help mitigate issues with overlapping drifting in-situ campaigns, enhancing the overall understanding and monitoring of sea ice dynamics.

4. OUTLOOK AND RECOMMENDATIONS

4.1 Algorithm Improvement

To enhance the retrieval of sea ice drift from SAR imagery, the implementation of deep learning techniques is recommended. Post-processing methods such as discarding, optimization, and interpolation of drift vectors should be developed to refine the data quality. Furthermore, the optimization of time intervals between SAR image acquisitions is crucial for improving the accuracy of ice drift measurements. Algorithms must be optimized for parallel processing, and more resources should be allocated for processing.

4.2 More Input Data

An operational L-band SAR constellation should be launched to improve data coverage and quality. Collocating datasets from various missions, including passive microwave, altimetry, scatterometry, and SAR, will enable synergetic use and enhance the robustness of sea ice monitoring. Incorporating additional variables into automatic algorithms will improve their accuracy. These variables include wind speed, solar radiation, optical data VIIRS, PMW data from AMSR2, RS2, RCM, high-resolution Sea Surface Temperature (SST), radar and laser

altimetry, multi-frequency and multi-polarization data, and sea ice deformation data.

Improving time separation between different SAR sensors and leveraging tandem missions like S1 and ROSE-L for automated ice type classification are recommended. A fleet of mixed micro-satellites, such as those from Capella Space, could be an option when time delays of less than one hour are acceptable. The use of RCM mode HH+VV over polar regions in summer, and combining sea ice deformation with thermodynamics for classification, should be explored. Identifying the contributions of L-band SAR for improved sea ice products and enhancing collaboration between different sensor acquisitions will maximize the potential of multi-sensor synergy.

4.3 Better Training and Validation Data

High-resolution verification data from other satellites or in-situ measurements coinciding with SAR data are crucial for accurate training and validation. Ridges, leads, and roughness data from altimetry, which are free from inherent biases in manual ice charts, should be utilized. Building a solid training dataset, including challenging conditions such as wet ice in summer and windy water, with many scenes similar to AI4Arctic, will improve model robustness. Cross-calibration of ice experts through evaluation of ice charts is also necessary.

4.4 Better output Products

Increasing the temporal resolution of ice drift products is essential. Developing a high-resolution, long-term Lagrangian sea ice drift dataset will provide valuable insights into sea ice dynamics. Additionally, combining sea ice drift data with thermodynamic models can facilitate the retrieval of sea ice thickness, thereby improving the overall understanding of sea ice properties. Satellite data should also be used to derive new variables, such as the probability of belonging to an ice category, deformation, ridges, leads, and aerodynamic roughness. Developing fit-for-purpose ice products tailored for ice charts or for models is essential for providing relevant and actionable information.

4.5 Improved Applications

A move towards integrated systems combining satellite observations, data assimilation, and modeling is recommended. The use of Structural Similarity (SSIM) as a metric for evaluating the alignment of multiple SAR images should be explored. Sea ice drift and alignment algorithms must be tested under various weather and drift conditions to ensure robustness. Reducing noise in Harmony data and using it to detect the MIZ, where mobile ice with high concentrations is present, will enhance detection capabilities. Practical predictability of linear kinematic features in sea ice should be estimated and improved. Developing new metrics for model calibration and validation using ice drift and deformation data is necessary.

Integrating ML-based ice type products into ice service routines will aid ice analysts. Combining ice type observations with ice drift forecasts to predict ice types and ship routes will enhance navigation safety. Forecasting SAR images by integrating them with ice drift forecasts will improve operational planning.

Different products should be assimilated in various regions for both operational and reanalysis purposes. The impact of assimilating different products, such as Sea Ice Concentration (SIC) and Sea Ice Drift (SoD), must be evaluated, and uncertainties characterized better.
Interpreting the results of 'black box' Convolutional Neural Networks (CNNs) will transform machine learning insights into human learning. Developing a forward model for sea ice backscatter, where SAR image texture reflects the history of ice deformation, is essential for advancing sea ice physics understanding.

4.6 Targeted In-Situ Data Collection and Sharing

Targeting in-situ data campaigns for satellite product validation and overlapping permanent stations with repeated satellite passes will

improve data quality. In-situ data collection should be tailored to address specific scientific questions, and connections between ground radar observations, drones, and SAR for upscaling should be established. Openly available multi-sensor API for routine overlapping in-situ + satellite sensor planning. Coordinating observations from space, drones, above sea ice, and below sea ice will enhance data integration. Improving procedures for quality control of in-situ data and deploying more drifters on underrepresented sea ice types, such as FYI and fast-drifting sea ice, are critical.

Increased use of georeferenced drone images for training and validation of satellite data products is recommended. Drone flights should be planned to address scientific and operational questions, and used for instantaneous sea ice drift retrieval connected with SAR observations. Drones' long-distance capabilities allow for detailed optical and infrared mapping below cloud cover and simultaneous with SAR acquisitions.

By addressing these recommendations, significant advancements can be made in the field of SAR remote sensing of sea ice, enhancing the accuracy and reliability of sea ice monitoring and forecasting.

REFERENCES

Barber D., E. LeDrew, D. Flett, M. Shokr, and J. Falkingham, “Seasonal and diurnal variations in SAR signatures of landfast sea ice,” IEEE transactions on geoscience and remote sensing, vol. 30, no. 3, pp. 638–642, 1992.

Casey J. A., S. E. Howell, A. Tivy, and C. Haas, “Separability of sea ice types from wide swath C- and L-band synthetic aperture radar imagery acquired during the melt season,” Remote Sensing of Environment, vol. 174, pp. 314 – 328, 2016.

Demchev, D., L. E. B. Eriksson, A. Hildeman and W. Dierking: "Alignment of Multifrequency SAR Images Acquired Over Sea Ice Using Drift Compensation,", *IEEE Journal of Selected Topics in Applied Earth Observations and Remote Sensing*, vol. 16, pp. 7393-7402, 2023, doi: 10.1109/JSTARS.2023.3302576.

Doulgeris, A.P.: An Automatic U-Distribution and Markov Random Field Segmentation Algorithm for PolSAR Images, IEEE Transactions on Geoscience and Remote Sensing, vol. 53, no. 4, pp. 1819–1827, 2015.

Frost, A., Wiehle, S., Singha, S., & Krause, D. (2018, July). Sea Ice Motion Tracking from Near Real Time Sar Data Acquired During Antarctic Circumnavigation Expedition. In IGARSS 2018-2018 IEEE International Geoscience and Remote Sensing Symposium (pp. 2338-2341). IEEE.

Horn, B. K. P. and Schunck, B. G., Determining optical flow, Artif. Intell., 17, 185–203, 1981.

Johansson A. M., C. Brekke, G. Spreen, and J. A. King, “X-, C-, and L-band SAR signatures of newly formed sea ice in Arctic leads during winter and spring,” Remote Sensing of Environment, vol. 204, pp. 162 – 180, 2018.

Karvonen, J., Baltic Sea Ice Concentration Estimation Using SENTINEL-1 SAR and AMSR2 Microwave Radiometer Data, in IEEE Transactions on Geoscience and Remote Sensing, vol. 55, no. 5, pp. 2871-2883, May 2017, doi: 10.1109/TGRS.2017.2655567.

Karvonen, J., Baltic Sea Ice Concentration Estimation From C-Band Dual-Polarized SAR Imagery by Image Segmentation and Convolutional Neural Networks, in IEEE Transactions on Geoscience and Remote Sensing, vol. 60, pp. 1-11, 2022, Art no. 4301411, doi: 10.1109/TGRS.2021.3097885.

Kleinherenbrink, M.: Harmony sea-ice dynamics code and Notebooks, Zenodo, https://doi.org/10.5281/zenodo.5055737, 2021a.

Kleinherenbrink, M., Korosov, A., Newman, T., Theodosiou, A., Komarov, A. S., Li, Y., Mulder, G., Rampal, P., Stroeve, J., and Lopez-Dekker, P.: Estimating instantaneous sea-ice dynamics from space using the bi-static radar measurements of Earth Explorer 10 candidate Harmony, The Cryosphere, 15, 3101–3118, https://doi.org/10.5194/tc-15-3101-2021, 2021b.

Kleinherenbrink, M., Korosov, A., Newman, T., Theodosiou, A., Komarov, A. S., Li, Y., Mulder, G., Rampal, P., Stroeve, J., and Lopez-Dekker, P.: Estimating instantaneous sea-ice dynamics from space using the bi-

static radar measurements of Earth Explorer 10 candidate Harmony, The Cryosphere, 15, 3101–3118, https://doi.org/10.5194/tc-15-3101-2021, 2021b.
König C., T. König, S. Singha, A. Frost, and S. Jacobsen, “Combined ¨ Use of Space Borne Optical and SAR Data to Improve Knowledge about Sea Ice for Shipping,” Remote Sensing, vol. 13, no. 23, 2021.
Kortum, K., Singha, S., & Spreen, G. (2022). Robust Multiseasonal Ice Classification From High-Resolution X-Band SAR. IEEE Transactions on Geoscience and Remote Sensing, 60, 1-12.
Kræmer T., H. Johnsen, C. Brekke and G. Engen, "Comparing SAR-Based Short Time-Lag Cross Correlation and Doppler-Derived Sea Ice Drift Velocities," in IEEE Transactions on Geoscience and Remote Sensing, vol. 56, no. 4, pp. 1898-1908, April 2018, doi: 10.1109/TGRS.2017.2769222. keywords: {Doppler effect;Satellites;Sea ice;Synthetic aperture radar;Antennas;Global Positioning System;Doppler measurement;motion estimation;sea ice;synthetic aperture radar}.
Krumpen, Thomas, et al. "Arctic warming interrupts the Transpolar Drift and affects long-range transport of sea ice and ice-rafted matter." Scientific Reports 9.1 (2019): 5459.
Kwok, R.: The RADARSAT Geophysical Processor System, in: Analysis of SAR Data of the Polar Oceans, Springer Berlin Heidelberg, 235–257, https://doi.org/10.1007/978-3-642-60282-5_11, 1998. a, b
Lohse, J and Doulgeris, A.P. and Dierking, W.: Mapping sea-ice types from Sentinel-1 considering the surface-type dependent effect of incidence angle, Annals of Glaciology, vol. 61, no. 83, pp. 260–270, https://doi.org/10.1017/aog.2020.45, 2020.
Lucas, B. and Kanade, T., An iterative image registration technique with an application to stereo vision, in: Proceedings of the 7th International Joint Conference on Artificial Intelligence (IJCAI), 24–28 August 1981, Vancouver, Canada, vol. 2, 674–679, 1981.
Mahmud M., V. Nandan, S. Howell, T. Geldsetzer, and J. Yackel, “Seasonal evolution of l-band SARbackscatter over landfast arctic sea ice,” Remote Sensing of Environment, vol. 251, p. 112049, 2020.
Murashkin D., and A. Frost, “Arctic Sea Ice Mapping Using Sentinel-1 SAR Scenes with a Convolutional Neural Network,” IEEE International Geoscience and Remote Sensing Symposium, pp. 5660-5663. 2021.
Olason, E., Boutin, G., Korosov, A., Rampal, P., Williams, T., Kimmritz, M., et al. (2022). A new brittle rheology and numerical framework for large-scale sea-ice models. Journal of Advances in Modeling Earth Systems, 14, e2021MS002685. https://doi.org/10.1029/2021MS002685.
Panchi N., E. Kim and A. Bhattacharyya, "Supplementing Remote Sensing of Ice: Deep Learning-Based Image Segmentation System for Automatic Detection and Localization of Sea-ice Formations From Close-Range Optical Images," IEEE Sensors Journal, vol. 21, no. 16, pp. 18004-18019, 2021.
Perona P., J. Malik, Scale space and edge detection using anisotropic diffusion, Proc. IEEE Comp. Soc. Workshop on Computer Vision (Miami Beach, Nov. 30 – Dec. 2, 1987), IEEE Computer Society Press, Washington, 16–22, 1987.
Rublee, E., V. Rabaud, K. Konolige and G. Bradski, ORB: An efficient alternative to SIFT or SURF, 2011 International Conference on Computer Vision, Barcelona, Spain, 2011, pp. 2564-2571, doi: 10.1109/ICCV.2011.6126544.
Toyota T., J. Ishiyama, and N. Kimura, “Measuring deformed sea ice in seasonal ice zones using l-band SAR images,” IEEE Trans. Geosci. Remote Sens., vol. 59, no. 11, pp. 9361–9381, 2020.
Wang R., W. Zhu, X. Zhang, Y. Zhang and J. Zhu, "Comparison of Doppler-Derived Sea Ice Radial Surface Velocity Measurement Methods From Sentinel-1A IW Data," in IEEE Journal of Selected Topics in Applied Earth Observations and Remote Sensing, vol. 16, pp. 2178-2191, 2023.
Yackel J., and D. Barber, “Melt ponds on sea ice in the Canadian Archipelago: 2. On the use of RADARSAT-1 synthetic aperture radar for geophysical inversion,” Journal of

Geophysical Research: Oceans, vol. 105, no. C9, pp. 22 061–22 070, 2000.
Zakhvatkina, N., Smirnov, V., & Bychkova, I. (2019). Satellite SAR data-based sea ice classification: An overview. Geosciences, 9(4), 152.
Zhou Z., M. M. R. Siddiquee, N. Tajbakhsh, and J. Liang, "Unet++: Redesigning skip connections to exploit multiscale features in image segmentation," IEEE transactions on medical imaging, 39(6), 1856-1867. 2019.

Satellite Sensor Synergy to strengthen spatial and temporal coverage and shortcut interpretation challenges

Johnny A. Johannessen[1], Bertrand Chapron[2], Fabrice Collard[3], Ben Holt[4], Jose da Silva[5], Artem Moiseev[1], Werner Alpers[6], Thibault Taillade[7], Lucile Gaultier[3], Biao Zhang[8], William Perrie[8], Antonio Bonaduce[1], Nicolas Rascle[2], Romain Husson[9], Lasse H. Pettersson[1] and Craig Donlon[7]
[1]NERSC, [2]Ifremer, [3]ODL, [4]JPL,[5]Univ. of Porto, [6]Univ. of Hamburg, [7]ESA, [8]Bedford Inst. of Oceanography, [9]CLS.

1. Background

Numerous new satellites and sensors have emerged together with continuity missions during the past two decades (https://database.eohandbook.com). Altogether they provide a wide range of imaging capabilities for studies of the marine atmospheric boundary layer (MABL) and physical and biological structures and processes at the ocean surface, at various spatial and temporal scales. Consistent and regular visualization, co-location and overlay of these heterogeneous datasets in a simple, fast and convenient way is now also possible thanks to the free and open online visualization portals such as (https://ovl.oceandatalab.com; https://seascope.oceandatalab.com). The ability to take optimum advantage of satellite sensor synergy combining active and passive microwaves, optical and infrared sensing jointly with in-situ observations for investigation of mesoscale to sub-mesoscale upper ocean currents is therefore highly feasible as indicated in Figure 1.

A common challenge in using satellite sensors for retrievals of upper ocean currents is lack of quantitative understanding of near-surface ocean processes and their interactions with the atmospheric boundary layer. Direct in-situ observations of the exchanges between the ocean and atmosphere are rarely made as they are difficult and costly. Yet, air-sea interaction is strongly connected to weather development, storm intensity and storm track pathways as well as the exchanges of carbon, water and energy that are of key importance for the climate of the Earth system (see Figure 2). Evaporation, for instance, is a major driver of changes in regional rainfall patterns and affect both storm tracks and hurricane development. Variability in the heating through the ocean surface combined with changes in wind-driven ocean circulations moreover drives annual climate variations, such as El Niño/Southern Oscillation and affect regional sea level variability and long-term sea level rise.

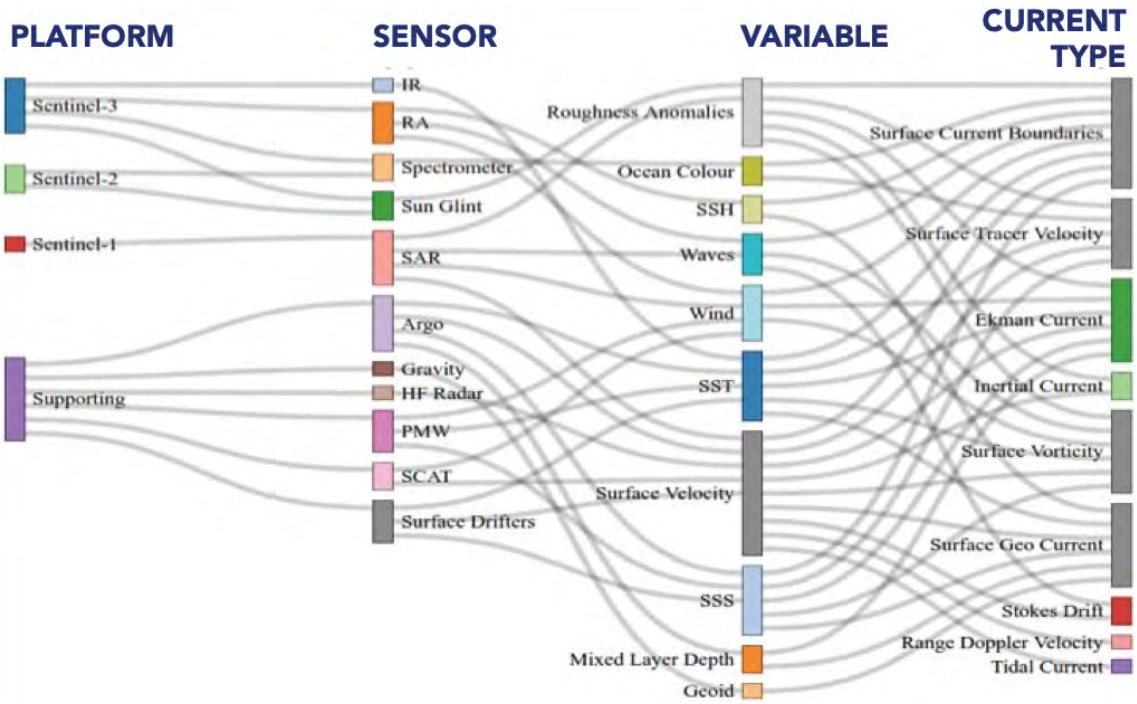

Figure 1. *Example of satellite sensor synergy for upper ocean current monitoring based on the Sentinel-1,-2,-3 combinations of infrared (IR) and microwave radiometer (PMW); imaging spectrometer; radar altimeter (RA); SAR-based surface roughness and range Doppler velocity; scatterometer based surface roughness and wind field; and Visible-derived sun-glint.*

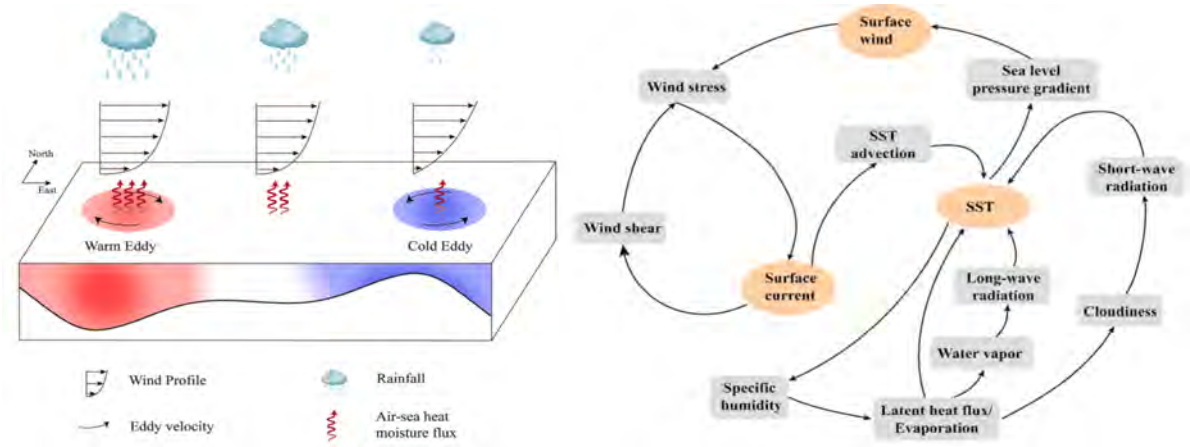

Figure 2. *Schematic illustration of ocean-atmosphere exchanges in the presence of warm and cold eddies versus reference background (left) and local and non-local multi-scale interactions (right). (Courtesy Paco Lopez-Dekker).*

As suggested in Figure 2 (right) the motion of the ocean surface is intrinsically entwined with the atmosphere through air-sea interactions across a large domain of spatial and temporal scales. However, as we lack proper knowledge of the satellite-based retrieval accuracy, we are limited in quantifying how the uncertainty in the estimation of one quantity may propagate to other quantities and processes.

In this proceeding paper the importance of synergetic combination of multi-modal atmosphere-ocean EO sensor observations, theoretical dynamical frameworks, machine-learning techniques and numerical simulations will be highlighted. The strength in sensor synergy is presented and evidenced in Section 2 followed by presentation of distinct gaps and limitations in Section 3. Section 4 then closes the paper with an outlook including account of future approved satellite missions. Note that more details on sensor synergy for sea ice research and application development are addressed in Korosov et al., (this issue).

2. Strength of Sensor Synergy

During the last decades the advances in free and open access to near real time satellite data have greatly improved our ability to apply sensor synergy for studies of the MABL, air sea interaction, upper ocean dynamics and lower-level marine biogeochemical conditions (see for instance Johannessen et al., (2005), Kudryavtsev et al., (2012). In addition, we have seen significant development in visualization and multi-sensor co-location capabilities (https://ovl.oceandatalab.com; https://narval.nersc.no). In particular, this have been evidenced for upper ocean mesoscale dynamics in intense current regimes such as the Agulhas Current, the Gulf Stream and other regions including the western Mediterranean Sea, the Lofoten Basin within the Norwegian Sea, and the coastal area of the California Current.

However, the expressions of these dynamic features are often challenging to fully interpret and quantify in the satellite data. As such, the systematic use of satellite sensor synergy often strengthens the temporal coverage and shortcuts detection limitations by individual sensors to advance the interpretation. Moreover, although in-situ data are sparse at mesoscale coverage they offer high temporal sampling within the water column that importantly complement satellite-based remote sensing observations. Jointly with numerical model fields a multi-modal approach has demonstrated advances in discovery, understanding and monitoring of mesoscale to sub-mesoscale surface signatures and their connection to upper ocean processes (e.g. Klein et al., 2009). Other evidence, for instance, are tailored to:

- Wind-current and wave-current interactions retrieved from Sentinel-1 combined with Sentinel-2 and Sentinel-3. The wind stress drives the upper ocean circulation by means of an interplay with the vertical turbulent friction and the Coriolis force, generating horizontal wind drift currents which spiral and decay with depth (e.g. Bressan and Constantin (2019); Chapron et al (2018); Bourassa, M. A. (2018)). In addition, detailed wave propagation analysis helps reveal spatial variations of the directional wave spectra, directly linked to the ocean surface current variations as demonstrated by jointly combining Sentinel-3, Sentinel-1 and Sentinel-2 with the CFOSAT mission and the new SWOT mission (https://en.wikipedia.org/wiki/Surface_Water_and_Ocean_Topography).
- Novel colocation of SWOT sea surface height and Sentinel-1 range Doppler velocity (see Figure 3) revealing the ability to examine the spatial co-variability of the mesoscale sea surface height structures and the range directed surface velocities as indicated by the presence of the cyclonic and anticyclonic eddies.
- Linking 2D surface velocity structures to 3D upper ocean dynamics (Beron-Vera et al., 2019) using collocated satellite and in-situ data, jointly with model simulations (Le Guillou et al., 2024) with whereby for instance surface drifter data and Argo profiling floats ensure quantitative estimates of the

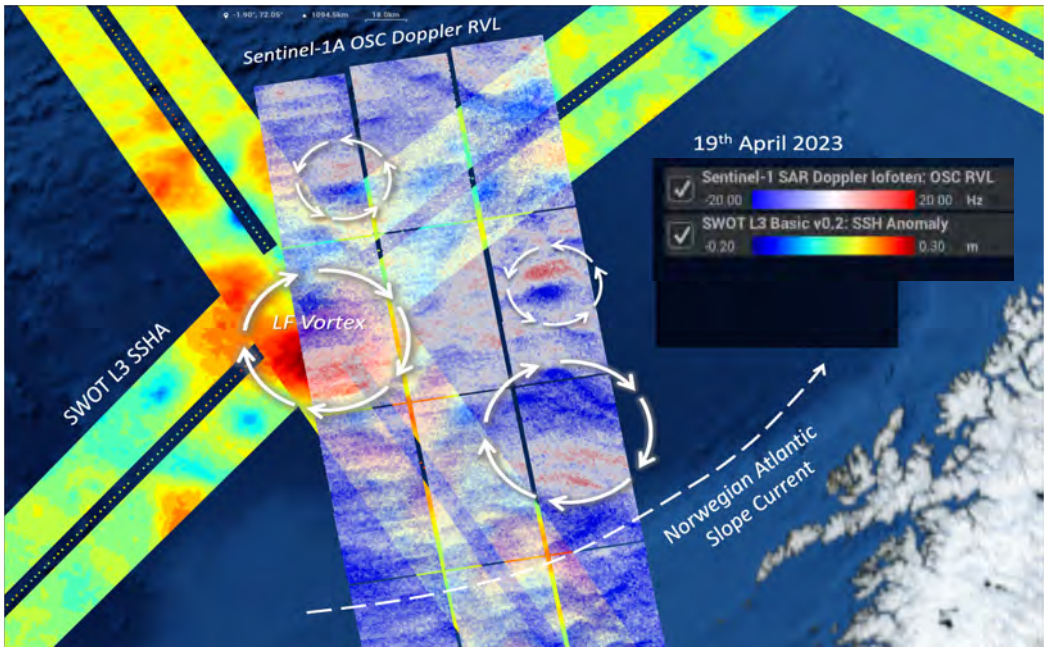

Figure 3. *Collocated SWOT sea surface height and Sentinel-1 range Doppler velocity in the Lofoten Basin acquired on 19 April 2023. White circles mark presence of cyclonic and anticyclonic eddies. Colour scale marks Sentinel-1Doppler shift (Hz) and SWOT SSH (m)*

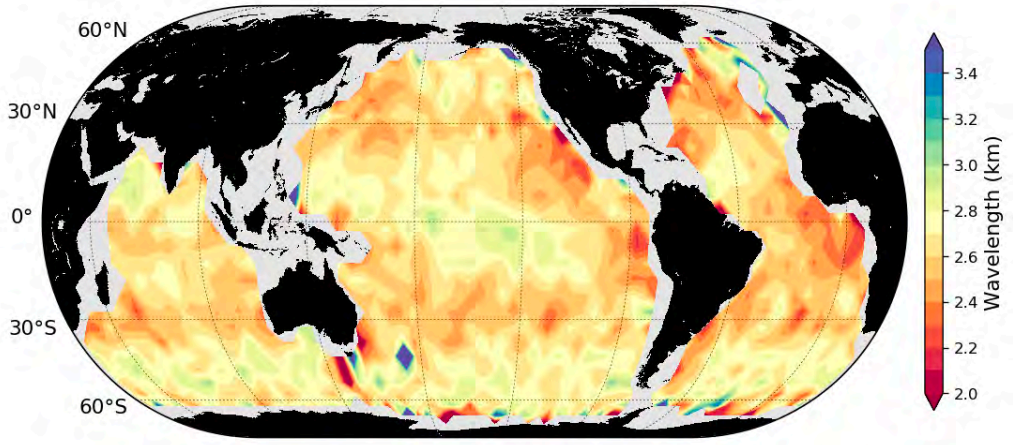

Figure 4. *Global distribution of extracted roll wavelengths from the most energetic peak of the identified WV SAR images. Colour donates the average in 5 by 5 grid boxes. (Courtesy of C. Wang.)*

total surface current, upper layer water mass properties and mixed layer depth.

- Thanks to the massive number of Sentinel-1 SAR wave mode (~20 * 20 km) acquisitions Wang et. al (2019a) developed a machine learning (convolutional neural network) approach to produce a novel dataset in support to MABL studies over the world's ocean as demonstrated in Figure 4 (Wang et. al (2019b)). These coherent boundary layer wind driven roll structures evidence air-sea interactions that is also of relevance in the context of both local weather development, exchanges of momentum, heat and carbon and thus global climate change.

Gaps and Limitations

Instantaneous ocean surface observation from satellite sensor synergy, at synoptic scale O (100 km) and resolution of 100 m to 10 km, reveal a mixture of oceanic and atmospheric features and processes, e.g. ocean surface waves, internal waves, vector wind, wind streaks, hurricanes, polar lows, filaments, upwelling, meanders, fronts, spiral eddies, convergence/divergence, and biogenic, surfactants. These features and underlying processes are expressed due to a broad range of imaging mechanisms, that unfortunately are rarely collocated and retrieved from in situ ocean observations. It is therefore challenging to derive quantitative insight and specify uncertainty levels on how these processes and features influence the interactive pathways between the MABL and the upper ocean. This is illustrated in Figure 5, including how they impact the carbon, heat and momentum exchanges, the

3D motions in the upper ocean and in the MABL, the physical-biological interactions in the upper ocean, and the structures and concentrations of floating material.

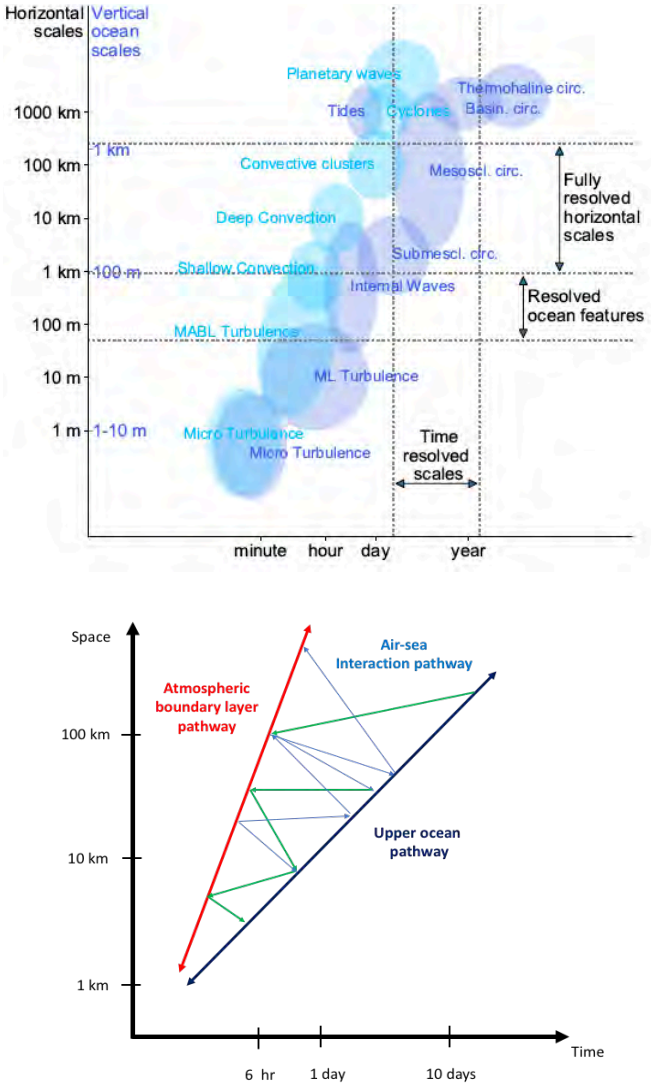

Figure 5. *(upper) Schematic illustration of the time-space scales of dominant ocean-atmosphere phenomena and interactive processes, including a range of vertical scales where these processes occur. (lower) Indications of the multiple pathways of atmosphere-ocean interactions.*

Regular and systematic comparison of model fields and satellite-based surface 2D expressions of mesoscale to sub-mesoscale features are also yet to become routine. The ocean surface layer is usually well mixed and mediates the transfers between the atmosphere and the deeper ocean. This can be exemplified with the expression shown in Figure 6 connected with model-based mixed layer depth estimations for a region in the Northeast Atlantic. The snapshot image depicts how the depth of this mixed layer varies from very shallow (~10 m) mixed layers (light yellow) to several hundred (purple) metres at horizontal scales from a few km to 100 km. Such fields yield promising capabilities to compare to multi-sensor satellite-based mesoscale 2D surface feature expressions.

The state-of-the-art of atmospheric Large Eddy Simulation (LES) models that resolve the most energetic 3D boundary layer turbulence cannot yet explicitly simulate capillary waves and their excitation by the atmospheric turbulent eddies near the surface. But LES models are presently undergoing rapid development and expansion of meteorological and physical capabilities (Maronga et al., 2020; Kim et al., 2023). In particular, their ability to explicitly resolve small-scale turbulent dynamics has improved with implementation of internal multi-level nesting capabilities (Hellsten et al., 2021; Lin et al., 2021).

Marine surfactants, an indicator of upper ocean biological activity, are observed by multiple radar sensors and in sun glint at low winds and they also form within spiral eddies and internal waves. The sea surface microlayer has been shown to have importance for CO2 and air-sea gas exchange (Mustaffa et al., 2020). Recent studies have shown the value of SAR for the detection of floating algae including Sargassum (Qi et al., 2022) and kelp (Jones et al., 2024) through changes in surface roughness, indicating that the synergetic observations of SAR can extend the observational time series of the marine ecosystem established by optical sensors (Qi et al., 2020). Moreover, surfactants that have been considered to be primarily observed in coastal regions by SAR are now also detected in the SAR-based wave mode products throughout the world ocean's (Wang et al., 2019b). This suggests that the radar detection of surfactants may have an unexpected role to play in observing marine ecosystems on a global scale. So is their potential influence on air-sea interaction and uptake of CO2.

Outlook

As demonstrated above systematic satellite sensor synergy in combination with high-resolution numerical models including dynamical joint-reconstructions of sea surface height and temperature fields from multi-sensor satellite observations clearly strengthen multi-variable Earth system process studies, use of ML methods and design of digital twin components as indicated in Table 1.

High-resolution, collocated and simultaneous estimates of the SSH and the SST are highly important, but yields no direct ability to retrieve accurate estimates of the mixed layer depth. On the other hand, improved quantitative interpretation and classification of the abundant and rich manifestations of the mesoscale and sub-mesoscale upper ocean dynamic features (e.g. converging/diverging frontal boundaries, eddies, IWs, upwelling, etc.) is now becoming feasible following a dynamical framework, such as VarDyn (Le Guillou et al., 2024), which combines minimal physically-based constraints with a variational scheme to enhance the mapping capabilities of upper ocean dynamics. By synthesizing multi-modal satellite observations, VarDyn aims at improving the accuracy of SSH and SST maps in comparison to operational products, both in terms of RMSE and effective spatial resolution. It is

Figure 6. *Snapshot of the Mixed Layer Depth in the Northeast Atlantic for one day in March derived from the ocean model eNATL60 OGCM. Iceland is seen at the top, the Fareo Island to the right and Scotland at the lower right. (Courtesy of L. Brodeau and J. Le Sommer IGE, Grenoble.)*

Sensors & spatial resolution	**Key derived variables**	**Connection to surface current**	**Dynamic Interpretation**
Gravity & altimetry 10-100 km	SSH, MDT, ADT= MDT+SLA	Mean and varying Surface geostrophic current	SQG and Streamfunction estimation, eddies, VarDyn*
Radiometer and spectrometer 0.5 - 1 km (4 km, 25 km)	SST, ΔSST, OC, ΔOC, Chlorophyll	SST fronts, OC fronts, Sun glint obey geostrophic balance, express impact of convergence/divergence	SQG and Streamfunction estimation, MCC, Omega equation for ageostrophic motion, VarDyn
SAR Spectrometer 0.1-1 km	σ and Δσ MSS and ΔMSS	Surface roughness and gradients related to mean square slope and gradient	Near surface wind speed, TC, PL, Constrain Ds to DMSS using RIM, VarDyn
SAR Doppler shift 1 – 5 km	Range surface velocity	Total surface current in range direction	Use of DOPRIM and CDOP, VarDyn
Scatterometer 10-25 km	Vector wind and wind stress	Surface stress, drag coefficient	CMOD4 and CMOD5 Wind stress curl express large scale ocean current fronts, VarDyn
Passive microwave 10 - 25 km	Wind speed, SST, SSS	Near surface vector wind, SST, SSS	Hurricanes, fronts, eddies, Wake of hurricanes

Table 1. *Characterization of a dynamical frameworks that account for synergies between different sensors to establish more consistent and better estimates of surface current dynamics and corresponding relation to for instance the stream function, vorticity and convergence/divergence in the upper ocean. Details of VarDyn is found here https://sciencehub.esa.int/projects/vardyn-dynamical-joint-reconstructions-of-sea-surface-height-and-temperature-from-multi-sensor-satellite-observations/*

also anticipated that by using a surface quasi-geostrophic/quasi-geostrophic (SQG/QG) framework the 3D dynamics within the first 500 m below the ocean upper mixed layer could be very efficiently diagnosed using high resolution satellite-based sea surface height (SSH) and SST observations, jointly with in-situ data (Buongiorno Nardelli, 2020; Asdar et al., 2024).

Guided by simulated model fields from fine-resolution numerical ocean models, the routine production of high-resolution 2-dimensional multi-sensor satellite data can then help to uncover the 3-dimensional dynamics in the upper 200-500 m of the ocean in combination with use of ML methods (e.g. Martin et al., 2023; Manucharyan et al., 2020). In collaborations with the numerical community this would, in turn, yield regular and novel abilities to validate the 3D structures in ocean models. Such a multi-modal approach would also optimize the opportunities to fill spatial and temporal observation gaps and provide a new analyses and interpretation framework for studies and monitoring of mesoscale to sub-mesoscale upper ocean variability and dynamics. However, it would significantly rely on implementation of comprehensive field campaigns ensuring sustainable access to high quality in-situ data over extended observation periods to advance process understanding, model validation and development of ML/digital twins.

In turn, more reliable estimates of the uncertainties in the model fields may be achieved.

Moreover, by regular exploration of linkages between SAR observed MABL imprints jointly with sea surface temperature and near-surface air temperature measurements, it may be possible to identify the relationship between SAR observed MABL imprints and the atmospheric stratification. In combination with LES this might, in turn, advance the understanding of wave-affects in the atmospheric surface layer and help constrain satellite-based surface flux estimates directly.

Recent improved processing and corrections of Sentinel-1 SAR image data are highly promising to secure reliable Satellite-based Doppler retrievals and Doppler simulations following the DOPRIM approach (Li et al., (2019; Moiseev et al., (2022); Kudryavtsev et al., (2023)). In addition, systematic benefit of the time-lagged inter-channel Sentinel-2 acquisitions under cloud free conditions (e.g. Kudryavtsev et al., (2017a, b); Villas Boas et al., (2019; Yurovskaya et al., (2018), jointly with the new high resolution 2D SSH observations across the 100 km will further strengthen satellite sensor synergy. The SWOT mission, together with Sentinel-3, Sentinel-1 SAR and HARMONY, will therefore herald a new era in Doppler retrieval-based oceanography. Moreover, combining these missions with the expansion missions including CIMR (Kilic et al, (2018), CRISTAL, ROSE-L together with NISAR, S3NGT and EPS next generation high-resolution scatterometer (see Donlon et al., this issue) a new realm of satellite sensor synergy analysis and interpretation will emerge. This is also expected to further advances the near real time use of visualization tools (e.g. https://ovl.oceandatalab.com; https://narval.nersc.no) and also strengthen ability to collocate, overlay and examine the spatial and temporal evolution of larger scale to mesoscale surface expressions associated with the MABL and upper ocean dynamics and their interactive processes.

In summary the outlook for advances in multi-modal synergy is clearly in line with the objectives of the United Nations SDGs (#13 and #14) and the Decade of Ocean Science for Sustainable Development (2021-2030). It is also linking scientific analyses to applications within fields such as tailored to Safe Ocean Navigation, Renewable Marine Energy, Pollution Monitoring and Sustainable Fisheries. Finally, it might become a valuable tool for Observing System Simulation Experiment (OSSE) and could become an integral part of the design and implementation of the new missions as well as for planning of optimum orbit phasing.

References

Ardhuin, F. (2019). SKIM, an ESA satellite mission for exploring global ocean currents and waves. *Frontiers in Marine Science, 09 April 2019, doi: 10.3389/fmars.2019.00124.*

Asdar, Sarah, Daniele Ciani, and Bruno Buongiorno Nardelli (2024), 3D reconstruction of horizontal and vertical quasi-geostrophic currents in the North Atlantic Ocean, *Earth System Science Data,* Volume 16, issue 2, 1029–1046, 2024.

Beron-Vera, F. J., A. Hadjighasem, Q. Xia, M. J. Olascoaga and G. Haller (2019), Coherent Lagrangian swirls among submesoscale motions, *PNAS,* September 10, 2019, vol. 116, no. 37, 18251–18256, www.pnas.org/cgi/doi/10.1073/pnas.1701392115.

Bourassa, M. A. (2018). Strong coupled air-sea interaction through winds, currents and waves. *Frontiers in Marine Science, 23 August 2019, doi: 10.3389/fmars.2019.00443. something is wrong with this reference- doi points to a different paper and paper title does not appear*

Bressan, A. and A. Constantin (2019), The Deflection Angle of Surface Ocean Currents From the Wind Direction, *JGR-Oceans,* 10.1029/2019JC015454, Oct. 2019.

Buongiorno Nardelli, Bruno (2020) A multi-year time series of observation-based 3D horizontal and vertical quasi-geostrophic global ocean currents, *Earth System Science Data, Volume 12, issue 3, 1711–1723, 2020, https://doi.org/10.5194/essd-12-1711-2020*

Chapron, B., and the GlobCurrent Team, January 2018, GlobCurrent Analyses and Interpretation Framework, Technical Report available at http://www.globcurrent.org

Hellsten, A., Ketelsen, K., Sühring, M., Auvinen, M., Maronga, B., Knigge, C., Barmpas, F., Tsegas, G., Moussiopoulos, N., & Raasch, S. (2021). A nested multi-scale system implemented in the large-eddy simulation model PALM model system 6.0. *Geoscientific Model Development*, *14*(6), 3185–3214. https://doi.org/10.5194/gmd-14-3185-2021

Johannessen, J.A., V.Kudryavtsev, D.Akimov, T. Eldevik, N. Winther, and B. Chapron, On Radar Imaging of Current Features; Part 2: Mesoscale Eddy and Current Front detection. *Journal of Geophysical Research*, Vol. 110, C07017, 2005.

Jones, C. E., K. An, and B. Holt (2024), The Capability of Multi-frequency SAR for Monitoring Giant Kelp (*Macrocystis pyrifera*), *Remote Sensing of the Environment*, under revision.

Kilic, L., C. Prigent, F. Aires, J. Boutin, G. heygster, R.T. Tonboe, H. Roquet, C. Jimenez and C. Donlon (2018) , Expected Performances of the Copernicus Imaging Microwave Radiometer (CIMR) for an All-Weather and High Spatial Resolution Estimation of Ocean and Sea Ice Parameters, JGR-Oceans https://doi.org/10.1029/2018JC014408

Kim, E., Choi, K., Park, S., Kim, M.-H., Kim, S.-W., Park, M.-S., Ahn, M.-H., Park, Y.-S., & Song, C.-K. (2023). Turbulent characteristics in complex coastal areas assessed using BSWO observations and WRF-LES simulation results. *Atmospheric Research*, *289*(March), 106756. https://doi.org/10.1016/j.atmosres.2023.106756

Klein, P., G Lapeyre (2009), The oceanic vertical pump induced by mesoscale and submesoscale turbulence, *Annual Review of Marine Science 1 (1), 351-375, 2009.*

Korosov, Anton, Malin Johansson, Anja Frost, Johnny A. Johannessen, Juha Karvonen, Ekaterina Kim, Ron Kwok, Nicolas Longépé, Johannes Lohse, Robert Shuchman, Catherine Taelman, Stefan Wiehle (2024), Recent advancements in SAR remote sensing of sea ice

and recommendations for future: summary from SeaSAR'23, *In Seasar2023 Workshop Proceedings, Spitsbergen, Svalbard*.

Kudryavtsev, V., M. Yurovskaya, B. Chapron, F. Collard, and C. Donlon (2017a), Sun glitter imagery of ocean surface waves. Part 1: Directional spectrum retrieval and validation, *Journal of Geophys. Res. Oceans*, doi:10.1002/2016JC012426

Kudryavtsev, Vladimir, Maria Yurovskaya, Bertrand Chapron, Fabrice Collard, and Craig Donlon (2017b), Sun glitter imagery of surface waves. Part 2: waves transformation on ocean currents, *Journal of Geophys. Res. Oceans*, doi:10.1002/2016JC012426.

Kudryavtsev, Vladimir, Alexander Myasoedov, Bertrand Chapron, **Johnny A. Johannessen,** Fabrice Collard, (2012), Imaging mesoscale upper ocean dynamics using SAR and optical data, *Journal of Geophysical Research,* Vol. 117, C04029, 2012.

Kudryavtsev, Vladimir, Shengren Fan, Biao Zhang, Bertrand Chapron, Johnny A. Johannessen and Artem Moiseev (2023), Sea Surface Doppler Velocity Model Based on Dual Co-Polarized Radar Data - Part 1: Approach, *Transactions on Geoscience and Remote Sensing, Vol. 61, 2023.*

Le Guillou, Florian, Bertrand Chapron, Marie-Hélène Rio (2024). VarDyn: Dynamical joint-reconstructions of Sea Surface Height and Temperature from multi-sensor satellite observations. *ESS Open Archive* . September 12, 2024., **DOI:** 10.22541/essoar.172616118.81277809/v1

Li, H., Chapron, B., Mouche, A. A., & Stopa, J. E. (2019). A new ocean SAR cross-spectral parameter: Definition and directional property using the global Sentinel-1 measurements. *Journal of Geophysical Research: Oceans*, 124, 1566– 1577. https://doi.org/10.1029/2018JC014638

Lin, D., Khan, B., Katurji, M., Bird, L., Faria, R., & Revell, L. E. (2021). WRF4PALM v1.0: a mesoscale dynamical driver for the microscale PALM model system 6.0. *Geoscientific Model Development*, *14*(5), 2503–2524. https://doi.org/10.5194/gmd-14-2503-2021

Maronga, B., Banzhaf, S., Burmeister, C., Esch, T., Forkel, R., Fröhlich, D., Fuka, V., Gehrke, K. F., Geletič, J., Giersch, S., Gronemeier, T., Groß, G., Heldens, W., Hellsten, A., Hoffmann, F., Inagaki, A., Kadasch, E., Kanani-Sühring, F., Ketelsen, K., … Raasch, S. (2020). Overview of the PALM model system 6.0.

Martin, Scott A., Georgy E. Manucharyan, Patrice Klein (2023), Synthesizing Sea Surface Temperature and Satellite Altimetry Observations Using Deep Learning Improves the Accuracy and Resolution of Gridded Sea Surface Height Anomalies, *Journal of Advances in Modelling Earth Systems, Vol 15, Issue 5, May 2023, https://doi.org/10.1029/2022MS003589*

Manucharyan, Georgy E., Lia Siegelman, Patrice Klein (2020), A Deep Learning Approach to Spatiotemporal Sea Surface Height Interpolation and Estimation of Deep Currents in Geostrophic Ocean Turbulence, *Journal of Advances in Modelling Earth Systems, Vol 13, Issue 1, Jan. 2020,* https://doi.org/10.1029/2019MS001965

Moiseev, A., J.A. Johannessen, H. Johnsen (2022). Towards retrieving reliable ocean surface currents in the coastal zone from the Sentinel-1 Doppler shift observations. *Journal of Geophysical Research: Oceans, 127, e2021JC018201. https://doi.org/10.1029/2021JC018201*

Mustaffa, NIH, Ribas-Ribas M, Banko-Kubis HM,Wurl O. (2020) Global reduction of in situ CO2 transfer velocity by natural surfactants in the sea-surface microlayer. *Proc. R. Soc. A* 476: 20190763, doi.org/10.1098/rspa.2019.0763

Qi, Lin,Menghua Wang, Chuanmin Hu, Benjamin Holt (2022), On the capacity of Sentinel-1 synthetic aperture radar in detecting floating macroalgae and other floating matters, *Remote Sensing of Environment,* Vol. 280, October 2022, https://doi.org/10.1016/j.rse.2022.113188.

Qi, L., C. Hu, K. Mikelsons, M. Wang, V. Lance, S. Sun, B. B. Barnes, J. Zhao, and D. Van der Zande (2020), In search of floating algae and other organisms in global oceans and lakes, *Remote Sensing of Environment, 239,* doi.org/10.1016/j.rse.2020.111659.

Yurovskaya, Maria, Nicolas Rascle, Vladimir Kudryavtsev, Bertrand Chapron, Louis Marie, Jeroen Molemaker (2018), Wave spectrum retrieval from airborne sunglitter images, *Remote Sensing of Environment*, 2018,https://doi.org/10.1016/j.rse.2018.07.026

Villas Bôas A. B., F. Ardhuin, A. Ayet, M. A. Bourassa, P. Brandt, B. Chapron, B. D. Cornuelle, J. T. Farrar, M. R. Fewings, B. Fox-Kemper, S. T. Gille, C. Gommenginger, P. Heimbach, C. Hell Momme, Q. Li, M. R. Mazloff, S. T. Merrifield, A. Mouche, M.-H. Rio, E. Rodriguez, J. D. Shutler, A. C. Subramanian, E. J. Terrill, M. Tsamados, C. Ubelman, E. van Sebille (2019): Integrated Observations of Global Surface Winds, Currents, and Waves: Requirements and Challenges for the Next Decade. *Frontiers in Marine Science, Vol. 6*, doi=10.3389/fmars.2019.00425.

Wang, Chen, Alexis Mouche, Pierre Tandeo, Justin E. Stopa, Nicolas Long, Guillaume Erhard, Ralph C. Foster, Douglas Vandemark, Bertrand Chapron (2019a), A labelled ocean SAR imagery dataset of ten geophysical phenomena from Sentinel-1 wave mode, *Geoscience Data Journal*, https ://doi.org/10.17882/ 56796.

Wang, Chen, Douglas Vandemark, Alexis Mouche, Bertrand Chapron, Huimin Lid, Ralph C. Foster (2019b), Global assessment of marine atmospheric boundary layer roll detection using Sentinel-1 SAR data. *In revision Remote Sensing of Environment*

ADVANCEMENTS IN METHODOLOGIES USING MACHINE LEARNING - SEASAR 2023

Justin Stopa[1], Ralph Foster[2], Aurélien Colin[3,4], Martin Gade[5], Lauren Alexandra Hoffman[6], Roghayeh Shamshir[7], Björn Tings[8]

[1] Resources Engineering Department, University of Hawai`i at Manoa, USA
[2]Applied Physics Laboratory, University of Washington, USA
[3]IMT Atlantique, Lab-STICC, UMR CNRS, France
[4]Collecte Localisation Satellite (CLS), Brest, France
[5]Universität Hamburg, Germany
[6]Scripps Institution of Oceanography, USA
[7] Norwegian University of Science and Technology (NTNU),Trondheim, Norway
[8]DLR, Maritime Safety and Security Lab, Bremen, Germany

1. INTRODUCTION

SEASAT equipped with L-band synthetic aperture radar (SAR), launched in 1978 by NOAA, started the modern satellite-based ocean observation era. During the following decade, a significant research effort was dedicated to interpreting the 80-day record of SEASAT SAR imagery of the ocean surface. A multitude of atmospheric and oceanic phenomena were observable in SEASAR's imagery because the phenomena frequently leave their imprint on the ocean surface. These included structures embedded in atmospheric turbulence such as rolls and cells, rain, biological slicks, and oceanic fronts. Many of these phenomena observed in SAR imagery are summarized in NOAA's SAR Manual (Jackson and Apel, 2004). The European Space Agency (ESA) has been persistent in the collection of SAR data starting with the European Remote Sensing satellite, ERS-1, launched in 1991. This marked a significant milestone in understanding Earth's integrated system. Motivated by environmental concerns, it aimed to provide continuous global datasets, particularly for monitoring the oceans and the ocean-atmosphere interface. Equipped with a multi-component Active Microwave Instrument (AMI), including a scatterometer, radar altimeter, and SAR, ERS-1 was designed for 24-hour, all-weather global capability. Building on the legacy of NASA-NOAA's SEASAT, ERS-1 capitalized on microwave technology's ability to penetrate clouds and operate independently of sunlight, offering valuable insights into sea surface heights, winds, wave heights, and structural ocean phenomena. The success of ERS-1 and its successors, ERS-2, ENVISAT, and the Sentinel-1 missions greatly contributed to ocean research, providing crucial wind and wave data for numerical wave models and propelling advancements in our understanding of atmosphere/ocean dynamics.

There are many different satellites equipped with SARs currently in operation such as Advanced Land Observing Satellite 2 (ALOS2), RADARSAT2, RADARSAT Constellation Mission (RCM), Sentinel-1, CosmoSkyMed second generation, TerraSAR-X/Tandem-X, Gaofen-3, Capella, and ICEYE. Out of all of these active SAR satellites, only Sentinel-1 (S-1) data is openly available. ESA has adopted a free-and-open

data policy for S-1, which is leading to a major expansion of research and operational use of SAR data.

There are four mutually exclusive imaging modes of S-1 and they include the Interferometric Wide swath (IW), Extra Wide swath (EW), Strip Map (SM), and Wave Mode (WV). Each acquisition mode has its different configurations of field of view and pixel resolution where the WV has the smallest footprint and highest spatial resolution. ESA has made strides to make the data as accessible as possible by making the data accessible through Copernicus data servers and the Alaska Satellite Facility and has developed openly available analysis tools like Sentinel Application Platform (SNAP). The large datasets of Sentinel-1, exceeding petabytes of raw data, demand that new methodologies and tools be developed to best exploit its rich details of the ocean and atmosphere. This paper summarizes new methodologies developed to handle such large datasets. All these examples of new methodologies were part of the May 2023 SEASAR workshop that took place in Longyearbyen, Svalbard, Norway. This summary is not meant to be a robust literature review of all available new methods to process SAR datasets but rather a snapshot in time of experts from the SAR research community.

A commonality of many of the methodologies presented was machine learning (ML) which is a broad range of statistical techniques used to efficiently extract information from multi-dimensional, high-resolution, and large SAR datasets. These studies are all based on SAR data over the oceans and they have applications for atmospheric or oceanic research. Likely because of its free and open data policy, data from the S-1 mission was commonly used in the studies, and we briefly describe the mission. S-1 is a constellation of identical polar-orbiting, sun-synchronous satellites with a local time of ascending node 18:00 (Torres et al., 2012). S-1A was launched in April 2014 and is still operating. S-1B was launched in April 2016 and stopped collecting data in December 2021 due to a power issue. S-1C is expected to be launched in 2024. S-1 operates in the C-band SAR with a center frequency of 5.405 GHz or wavelength of 5.5 cm. S-1 has a 12-day repeat cycle, flies with an altitude of 690 km, has an inclination of 98.2°, and a repeat period of 98.7 minutes. When both S-1A and S-1B were in operation they were 180° out of phase equating to a 6-day repeat cycle. The following seven studies utilize the S-1 mission by developing new methods to extract new information, remove noise, or automate workflows. The paper is organized as follows. The SEASAR 2023 methodology contributions are summarized in section 2 by describing their unique challenges, methods, and representative results. A summary and outlook are provided in section 3.

2. RESULTS

The following describes the various contributions to the methodology theme at the 2023 SEASAR workshop. There are two commonalities of all works. The first is the use of the S-1 acquisitions. The second is the use of statistical techniques often including machine learning (ML). The use of ML is often motivated by the reduction of computational resources, image recognition capabilities, or automated workflows that can readily be implemented to process large datasets. Since S-1 is used in all methodologies presented here, we summarize the update from Hajduch et al., (2023) regarding the operational S-1A satellite in terms of the instrument performance, radiometric accuracy, and level 1 and level 2 products. A key aspect of the S-1 program is the constant provision of quality data, which

requires long-term engagement to carefully monitor, preserve, and improve the system.

S-1A Instrument update

- The S-1A antenna has been stable throughout 2022 without product quality degradation.
- The instrument noise level is stable.
- The September 2022 collision avoidance maneuver caused an increase in the interferometric baseline and burst synchronization error.
- Changes in DC of 30 Hz are being continuously monitored but it does not appear to impacting the products.

S-1A Radiometric accuracy update

- IW calibration at the calibration site in Germany shows the overall mean and standard deviation for the absolute calibration factor is -0.08 dB ± 0.24 dB for both VV and HH polarizations.
- An absolute radiometric accuracy for the IW mode is 0.322 dB.
- An absolute calibration accuracy of –0.23 dB with a standard deviation of 0.20 dB was determined using corner reflectors over Australia.

S-1A Level-1 algorithm update

- Correction of the misalignment between the elevation antenna pattern and the annotated thermal noise vector.
- Reduction in the number of false positives in radio frequency interference time-domain detection.
- Reduction in the inconsistencies of the radio frequency interference pre-screening

S-1A Level-2 algorithm update

- Implementation of a new algorithm for TotalHs computation of Quach et al., (2022).
- Review of the oswQualityFlag estimation is based on a machine learning algorithm.
- Recalling the radial velocity from the normalized radar cross-section is updated.
- Wind inversion provided is now provided on the IceMask.

2.1 Using Ocean Surface Imagery to Estimate Atmospheric Boundary Layer Stratification

Justin E. Stopa, Ralph Foster, Doug Vandemark, Chen Wang, Yannik Glaser, Peter Sadowski, Alexis Mouche, Bertrand Chapron

Over the ocean, S-1 acquisitions are wave mode (WV) and S-1 acquires very high resolution (5 m) small (20 km) images approximately every 100 km. It has been established that SAR captures information about ocean swell and the WV was originally designed to capture ocean gravity waves at the appropriate scales. However, WV has opened up new research opportunities to study the marine atmospheric boundary layer (MABL) because its high spatial resolution can resolve a wide range of MABL turbulent eddies and its 20 km field of view is large enough to capture many realizations of MABL-scale eddies. The two S-1 satellites, A and B collect ~65,000 WV images every month resulting in more than 700TB of level-1 imagery. ML models were developed using convolutional neural networks (CNN) to detect oceanic or atmospheric phenomena that leave their imprint on the ocean surface (Wang et al., 2019). The method is used to sort millions of S-1 images into basic MABL state categories: wind streaks (WS), micro-scale convection (MC), and lack of any atmospheric signature with scales larger than 1000 m (negligible atmospheric variability ~NV). ERA5 atmospheric surface analyses have been time-space interpolated to each WV image providing consistent estimates of

the air-sea stratification through a bulk Richardson number (*Ri*). This systematic and global analysis of millions of SAR images shows that image textures are well correlated with the Richardson number and define distinct unstable, near-neutral, and stable stratification regimes as shown in Figure 1. That is, the different stratification regimes result in characteristic MABL mean states in which particular classes of coherent structures form and induce identifiable sea-surface roughness patterns. The Richardson number is one of the key parameters controlling the bifurcation between the different turbulent states. The relationships between SAR-observed coherent structures and MABL state through *Ri* are robust and hold in overall averages, at seasonal/regional scales, and MABL-process scales.

Figure 1: (a) PDFs of MABL Ri estimated from ERA5 for cells (unstable), streaks (near stable), and negligible atmospheric variability (stable) detection from SAR. The shaded gray PDF denotes the entire WV2 population. Representative SAR images for (b) unstable Ri = −0.032, U10N = 5.3 ms^{-1}, ΔTv = −2.81°, (c) near-neutral Ri = −0.006, U10N=9.8 ms^{-1}, ΔTv = −1.74°, and (d) stable Ri =AA 0.005, U10N=7.6 ms^{-1}, ΔTv = 0.84° MABL states. The white dashed arrow points north and the red solid arrow is the ERA5 wind direction.

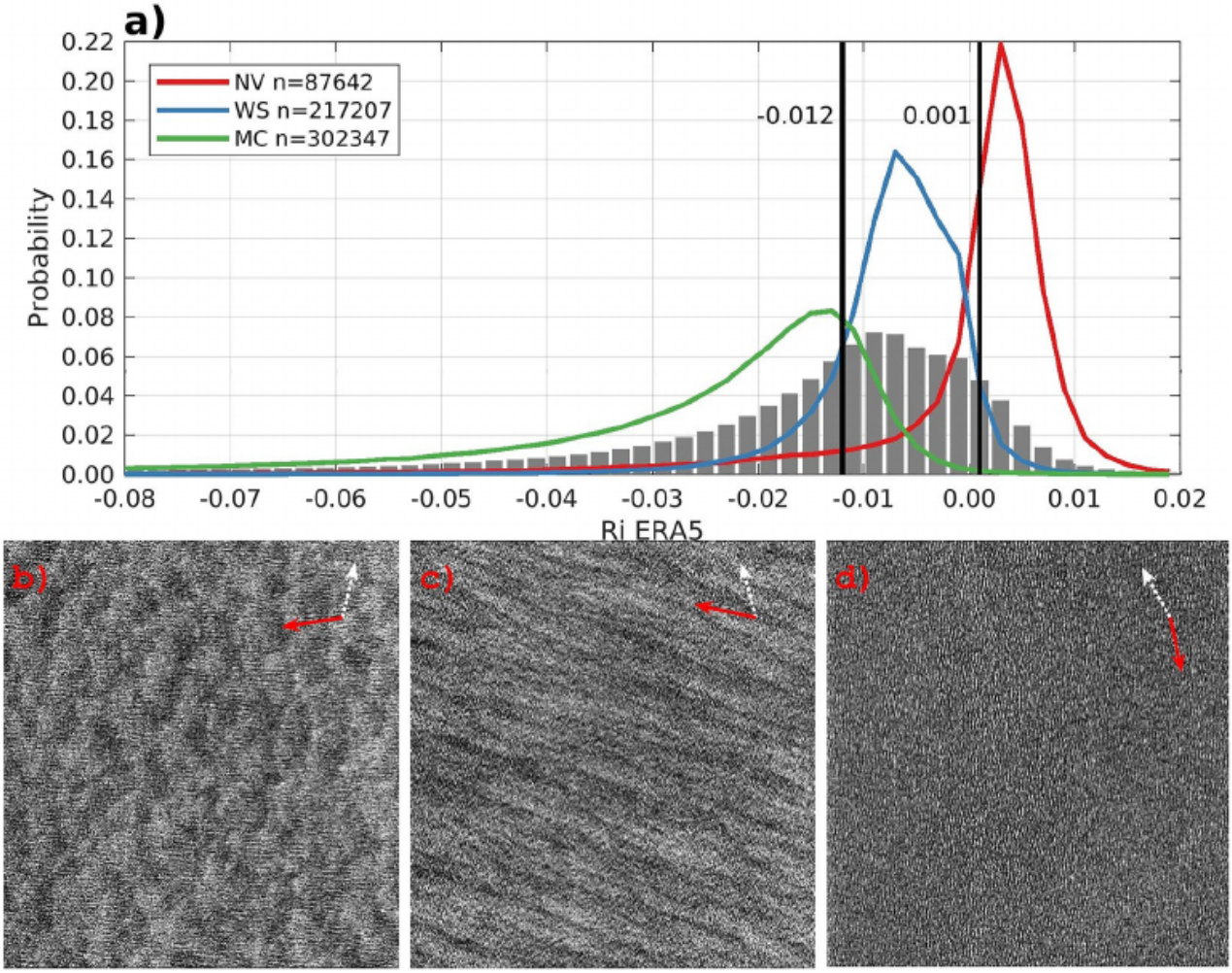

2.2 Using SAR Imagery to Diagnose Tropical Cyclone Boundary Layer Mean State

Ralph Foster, Alexis Mouch, Bertrand Chapron

Tropical cyclones (TC) form and intensify over the ocean and are quite compact storms, so high-resolution observations in remote locations are a necessity. A single wide swath SAR image can capture most of a TC's "inner core". The Satellite Hurricane Observation Campaign (SHOC) was established in 2016 and its goal is focused on collecting high-resolution SAR imagery in tropical cyclones with the S-1, RadarSAT2 (RSAT2) and RadarSAT Constellation (RCM) missions. S-1, RADARSAT2, and RCM can acquire simultaneous imagery in both co-pol (VV or HH) and cross-pol (VH). The cross-polarization acquisitions (VH) do not saturate at high wind speeds like VV normalized radar cross-sections. This offers the opportunity to estimate accurate wind speeds in tropical cyclones (33 to 80 m s^{-1}). The high winds force the tropical cyclone boundary layer (TCBL) to a state of near-neutral stratification even though the surface enthalpy fluxes can be enormous; the upper TCBL can even be weakly stably stratified. The consequence of the near-neutral stratification is that the TCBL is essentially the paradigmatic boundary layer for the generation of turbulent coherent structures in the form of roll vortices. TCBL roll orientation is highly sensitive to the vertical shear of the mean horizontal wind profiles. The rich dataset collected by SAR through SHOC and the routine observations of roll orientation in the imagery offer an opportunity to explore the atmospheric dynamics within tropical cyclones. Three different tools were used to exploit the SHOC archive. The first tool is a similarity boundary value model for the mean wind profiles in the TCBL. The lower boundary conditions are provided by the SAR surface wind vector field. The second tool provides the upper boundary conditions. It uses a simplified version of the nonlinear similarity model to estimate the pressure gradient field at the top of the boundary layer, from which we can directly calculate the sea-level pressure (SLP) pattern and consequently the gradient wind vectors representative of the forcing wind at the top of the TCBL. Ordinary least squares is used to calculate the pressure surface from the pressure gradient vectors. If one or more pressure observations are available, the SLP pattern can be converted to SLP.

The missing information for the similarity model is the turbulent eddy viscosity profile in the TCBL, which we infer indirectly from the orientation of the TCBL rolls extracted from the SAR image. TCBL roll orientation is mainly determined by the mean shear profiles, which in turn is sensitive to the eddy viscosity profile. The third tool calculates the roll orientation for trial eddy viscosity profiles that are variations of standard numerical model parameterizations. A consistent solution has a minimum RMS between measured and calculated roll orientations. Example results for Hurricane Fiona (2022) are shown in Figure 2. Fiona is a very challenging case because it is a very small Cat-2 storm close to land.

Figure 2 (below): (a) Sentinel-1 backscatter image of Hurricane Fiona (19 September 2022) with the P-3 flight tracks adjusted to the overpass time. (b) SAR-derived SLP with TCBl roll orientations (gray). (c) N/(N-1)/2 dropsonde pressure differences compared to SAR. Note that Fiona was a very compact storm and the storm was heavily sampled which leads to very high sensitivity to time-correction of observations to the overpass time.

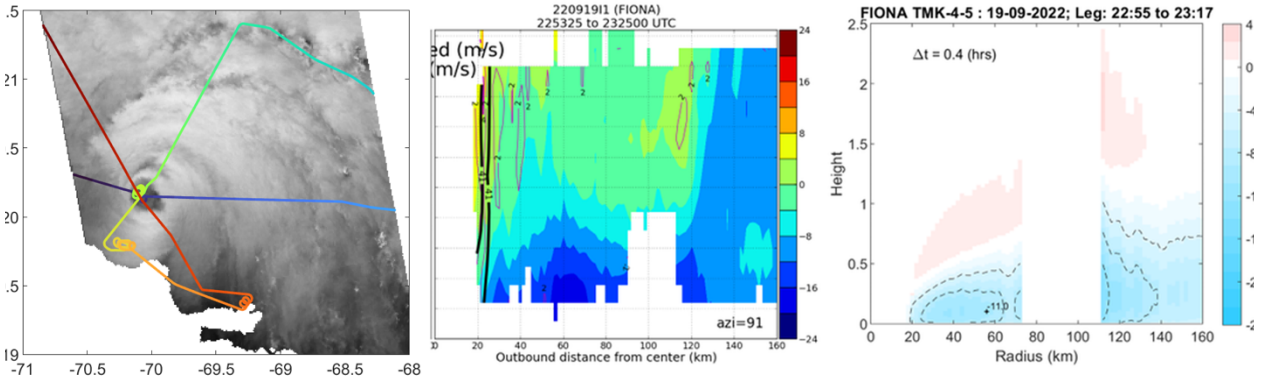

2.3 MediSAR: An Exhaustive Augmented Dataset of Segmented Sentinel-1 SAR Ocean Observations of the Mediterranean Sea and the Black Sea Regions

Aurélien Colin, Pierre Tandeo, Romain Husson, Ronan Fablet, Charles Peureux

Wide swath S-1 images are routinely collected over Europe. This dataset is high resolution and rich with information about ocean and atmospheric phenomena which leave their imprint within the SRA backscatter. Due to the high resolution and large footprint of the wide swath SAR imagery, a considerable amount of computational effort from both CPUs and GPUs is needed to process the S-1 IW archive composed of 102,504 images which typically cover 160x200 km. The work uses the hand-tagged dataset of Wang et al., (2019) to train deep-learning models to detect various ocean and atmospheric phenomena in the S-1 IW database. The effort exhaustively includes all SAR images between 2014-2022 and covers the Mediterranean and Black Seas. The methodology effectively utilizes high-resolution SAR textures to provide geophysical information about biological slicks, wind speed, rainfall, and atmospheric convective processes. As an example, Figure 3 shows the biological slick detection probability during the summer (June-July-August~JJA) and winter (December-January-February~DJF) in the Alboran Sea. The increased biological activity during the summer is visible. The distribution of the slicks also follows the Western Alboran Gyres, highlighting the capacity for biological slicks to provide information on currents. Future work will evaluate the ML models relative to other satellite technologies such as the Sentinel-3/OLCI and MSB/Seviri. The dataset is called MediSAR and its goal is to share SAR observations for the study of metocean phenomena more readily.

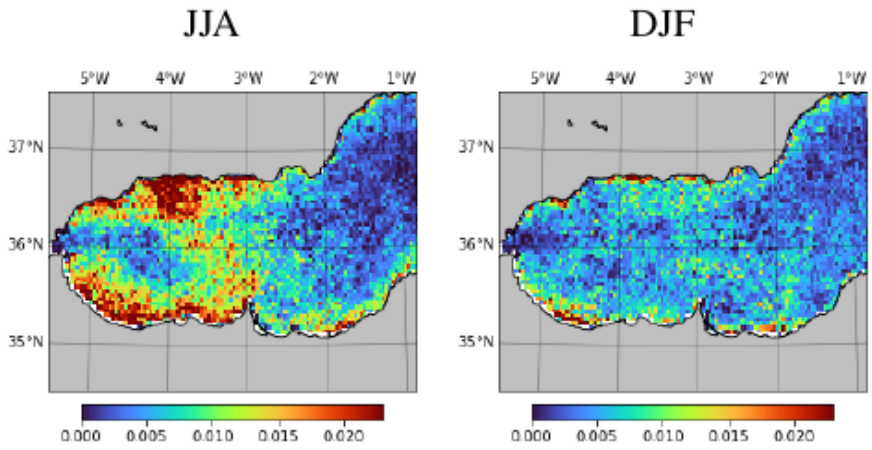

Figure 3: Biological slick detection probability (restricted to points with wind speed between 6.5 and 12 m/s) during summer (left) and winter (right) in the Alboran Sea between 2015 and 2022.

2.4 Machine learning for evaluating trends in the drivers of variability in Arctic sea-ice dynamics

Lauren Alexandra Hoffman, Matt R Mazloff, Sarah T Gille, Donata Giglio, Cecilia M Bitz, Patrick Heimbach

Arctic sea ice simulations are complex due to various factors, leading to high computational costs and model uncertainties. Classical numerical models need help to accurately represent sea-ice motion due to the complexity of simulating multi-phase, multi-physics problems. Machine learning (ML) offers a promising approach by serving as a surrogate for the dynamical component of sea ice, potentially enhancing computational efficiency and revealing emergent behaviors. ML models are developed using sea-ice velocity, ice concentration, and wind velocity from satellite and reanalysis data sources. Hoffman et al., (2023) developed these ML models and show the viability in predicting sea-ice motion, achieving a correlation of up to 0.8 with observed data. Efforts were extended to use explainable ML (XML) techniques and find that wind velocity is a key predictor of ice motion in the central Arctic, aligning with established statistical relationships. Example heat maps show the relevance of each of the inputs to an ML model to predict sea ice motion in Figure 4. Results from the XML method known as layerwise relevance propagation (LRP) applied to a CNN show that wind velocity is the most important predictor of ice motion for regions in the central Arctic (red in Figure 4d). It found that the physics-based and ML models have the largest uncertainties in the coastal regions where ice stress is significant. Ongoing work is utilizing SAR and XML methods to understand the role of linear kinematic features in ice dynamics and to improve the predictability of sea ice motions in coastal regions.

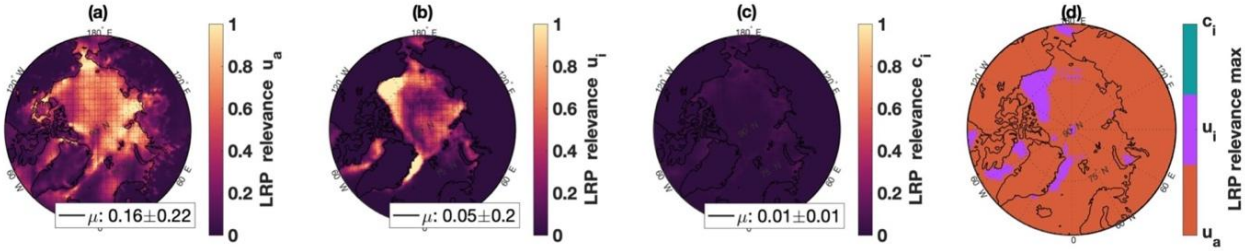

Figure 4: (a–c) Heat maps show the relevance of each of the inputs to an ML model for making predictions of sea-ice motion. These relevance heat maps are from an explainable machine learning (XML) method known as layerwise relevance propagation (LRP) applied to a CNN trained to make one-day predictions of sea-ice motion from inputs of wind velocity (ua) in panel (a), ice velocity (ui) in panel (b), and ice concentration (ci) in panel (c). (d) Map showing which input is the most important predictor of sea-ice motion for the ML model at each location in the Arctic.

2.5 Sentinel-1 Extra Wide Thermal Noise Removal Using a Deep Learning Model

Roghayeh Shamshiri, Egil Eide, Fazel Rangriz Rostami, Knut Vilhelm Høyland

The Sentinel-1 (S1) ground range detected (GRD) extra-wide (EW) swath data, particularly in the cross-polarization channel is strongly affected by thermal noise. This particular type of noise not only reduces the data interpretability and spatial quality but also creates challenges of a consistent backscatter time series. Even though GRD images undergo denoising using calibrated

noise vectors provided by the ESA, residual noises persist in time series applications on the Google Earth Engine platform. Previously developed methods enhance the image quality; but, these methods are not feasible in cloud computing using the Google Earth Engine. Therefore, a novel method using deep learning through a U-Net Convolutional Neural Network (CNN) architecture was developed to reduce noise in S-1 wide swath imagery automatically. There are two further constraints: the results should be competitive with those produced by existing conventional methods and the method can be implemented on the Google Earth Engine. Figure 5 shows the noisy, predicted, and clean images for example GRD S-1 acquisition. The CNN has significantly removed the stripes and the backscatter is continuous across the swath. The results demonstrate the effectiveness of the CNN in reducing the noises from the EW HV-polarized S1 images and the method can effectively be implemented on Google Earth Engine.

Figure 5: Model test result, (a) the noisy, (b) predicted using our model, and (c) clean image.

2.6 Monitoring coastal erosion and morphodynamics in intertidal areas

Martin Gade, Sebastian Peters, and Simon Schäfers

The Wadden Sea on the continental North Sea coast is the World's largest coherent intertidal area and extends over an area of about 4700 km^2, extending from the Dutch coast in the West to the Danish coast in the north. Intertidal areas are crucial for ecosystems and protect infrastructure from damaging storms. Due to the large area, remote sensing methods are best suited to monitor coastal changes related to land type (sediment, sea grass, etc.) or morphological changes (coastline change). Small-scale changes (<1 km) need to be resolved and SAR is the ideal sensor with its high resolution. A large number of SAR images were acquired over the German part of the Wadden Sea by the L-, C-, and X-band SARs aboard ALOS-2, Radarsat-2 and Sentinel-1, and TerraSAR-X, respectively. Using this wide range of multi-frequency / multipolarization SAR data it is determined which combinations of radar band and polarization are best suited for the classification of different Wadden Sea surface types, including sandy and muddy sediments, seagrass meadows, and bivalve beds. A neural network was built for the automated detection of waterlines on

Sentinel-1A/B SAR-C imagery. The neural network is capable of segregating water from exposed intertidal flats at high spatial resolution (Figure 6). The neural network is designed as an image-to-image network and uses SAR images and an ordinary land/water mask as input (left and middle panels of Figure 6, respectively). The neural network simplified the SAR image analysis significantly, as only minor post-processing of the obtained results is required.

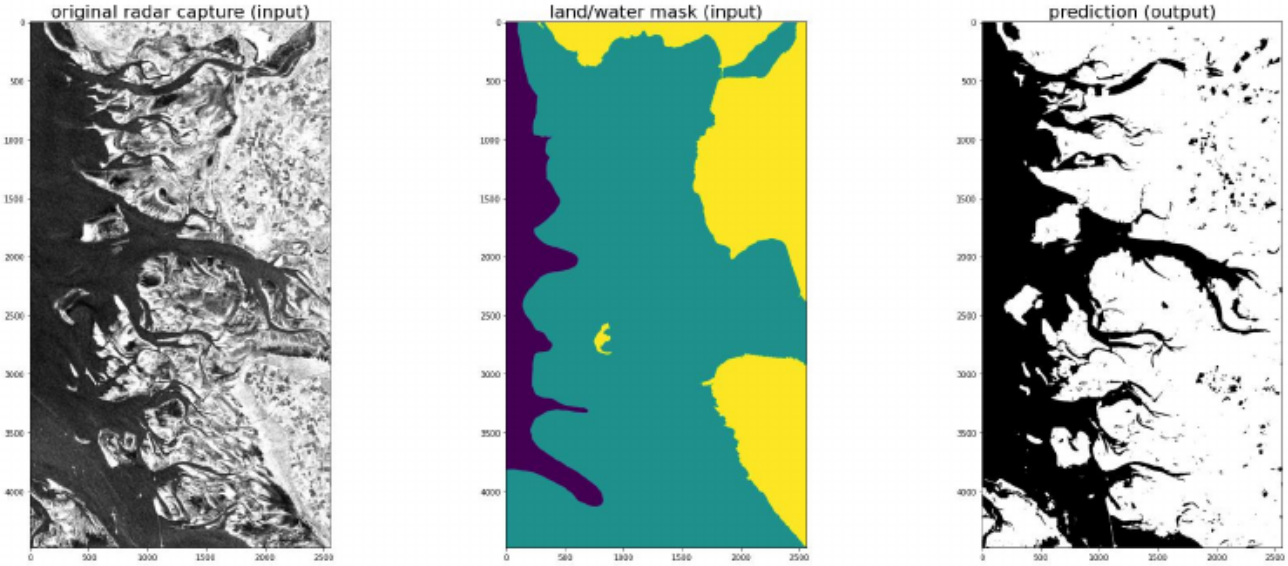

Figure 6. Automated classification of exposed intertidal flats by a neural network. Left: part of a Sentinel-1A SAR-C image of the German Wadden Sea acquired on 19 May 2020. Middle: manually generated land/water mask used as additional input; yellow: land; blue: open sea; green: potential intertidal flats. Right: resulting prediction of the neural network (classification).

2.7 Ship Wake Detectability

Björn Tings, Andrey Pleskachevsky, Stefan Wiehle, Sven Jacobsen

Ship wakes are produced by the interaction of the ship's hull with the ocean water and result from multiple interacting wave systems closely beneath and on the ocean surface. The ship wake signatures in SAR imagery consist of four components including Kelvin wake arms, V-narrow wake arms, and near-field and far-field turbulent components of the wake. The detectability of wakes in SAR imagery is influenced by ship properties, environmental conditions, and SAR acquisition properties (frequency and incidence angle). Machine learning through support vector machines was used to understand the detectability of individual wake components. This approach allows various influencing parameters to be isolated for the four different wake attributes. TerraSAR-X (2881), CosmoSkyMed (94), Sentinel-1 (618), and RADARSAT-2 (407) in C-band and X-band were used in this study. Ship information from the Automatic Identification System (AIS) was used as a reference. The results are provided in Table 1.

Table 1: Summary of detectability for the four wake components. Parameters with identical influence are marked by grey color.

Influencing Parameter	**Summary of detectability of the four wake components wake component detectability: "↑": better, "≈ ": hardly influenced**			
	Near-hull turbulence	**Turbulent wakes**	**Kelvin wake arms**	**V-narrow wakes**
Vessel speed	↑ for faster moving vessels	↑ for faster moving vessels	↑ for faster moving vessels	↑ for faster moving vessels
Vessel length	↑ for larger vessels	↑ for larger vessels	↑ for larger vessels	↑ for larger vessels
Vessel moving direction	↑ for vessels moving parallel to range	≈ by vessels' moving direction	↑ for vessels moving parallel to azimuth	↑ for vessels moving parallel to azimuth
Incidence angle	↑ for larger incidence angles, when ship speeds are at least moderate	↑ for lower incidence angles	↑ for lower incidence angles	↑ for lower incidence angles
Local wind speed	↑ for lower wind speeds	↑ for lower wind speeds	↑ for lower wind speeds	↑ for lower wind speeds
Sea state - wave height	≈ by wave heights	≈ by wave heights	≈ by wave heights	≈ by wave heights
Sea state - wavelength	↑ for longer wavelengths, when ship speeds are at least moderate	↑ for shorter wavelengths	↑ for shorter wavelengths	↑ for longer wavelengths
Sea state - wave propagation direction	↑ for wave directions parallel to the vessel's movement	↑ for wave directions parallel to the vessel's movement	↑ for wave directions parallel to the vessel's movement	≈ by wave propagation directions
Local wind direction	≈ by wind direction	↑ for wave directions orthogonal to the vessel's movement	≈ by wind direction	↑ for wave directions orthogonal to the vessel's movement
SAR slant ranges	≈ by slant ranges	≈ by slant ranges	↑ for shorter slant ranges	≈ by slant ranges
SAR radar frequency	≈ by radar frequency	≈ by radar frequency	≈ by radar frequency	↑ for X-band

3. SUMMARY AND OUTLOOK

3.1 Summary

The open-data policy of ESA has allowed SAR data to be more easily used in a broad range of applications. While the examples here are not exhaustive, the seven works show how surface textures from SAR can be exploited for study of atmospheric phenomena (Stopa et al., 2023; Foster et al., 2023; Colin et al., 2023), ocean phenomena (Colin et al., 2023), refinement of sea ice motion in coastal regions (Hoffman et al., 2023), monitoring and the detection of the coastline variability in intertidal regions (Gade et al., 2023), and the detection of ship waves in SAR imagery (Tings et al., 2023).

For wide swath imagery, the correction of overlapping SAR swaths often creates erroneous data issues and ML can be used to effectively correct the swaths and is comparable to existing methods (Shamshiri et al., 2023). This broad range of applications requires different ML approaches to be developed and implemented. A commonality of using ML is that the methods are often easily automated and require fewer computational resources than other methods. For example, Colin et al., (2023) and Stopa et al., (2023) use ML for image detection from convolutional neural networks through deep learning which effectively extracts information about the ocean surface textures. Image detection through ML allows the large S-1 archive that contains sub-mesoscale features across basin scales through the WV mode (now exceeding 1 Pb) and the >100,000 IW (400 Tb ~4 Gb per single polarization images) in the Mediterranean and Black Seas to be utilized. ML models are also being used to determine important input parameters as in the case of Hoffman et al., (2023) for predicting sea ice motion or Tings et al., (2023) for determining the radar settings in influencing the detectability of ship wakes.

3.2 Outlook

Machine learning is a rapidly changing field and we expect that these new advancements in the methods will be further refined to meet the needs of remote sensing specialists using high-resolution imagery. ESA is dedicated to providing SAR data until at least 2030 with Sentinel-1 with satellites C and D yet to be launched. NASA's NiSAR mission will be launched in 2024 and like ESA they will have an open data policy. We strongly attribute the wider use of SAR data for research and applications to the open data policy and ease of data access.

4. REFERENCES

SEASAR Contributions

Colin, A., Tandeo, P., Husson, R., Fablet, R., Peureux, C., 2023. MediSAR: An Exhaustive Augmented Dataset Of Segmented Sentinel-1 SAR Ocean Observations Of The Mediterranean Sea and the Black Sea regions, SEASAR, May 2-6, 2023, Longyearbyen, Svalbard.

Foster, R., Mouche, A., Chapron, B., 2023. Using SAR Imagery to Diagnose Tropical Cyclone Boundary Layer Mean State, SEASAR, May 2-6, 2023, Longyearbyen, Svalbard.

Gade, M., Peters, S., Schäfers, S., 2023. On the Use of SAR Data to Monitor Coastal Erosion and Morphodynamics in Intertidal Areas, SEASAR, May 2-6, 2023, Longyearbyen, Svalbard.

Hajduch, G., Pinheiro, M., Valentino, A., Vincent, P., Recchia, A., Cotrufo, A., Franceschi, N., Piantanida, R., Benchaabane, A., Peureux, C., Husson, R., Schmidt, K., Mouche, A., Grouazel, A., Nouguier, F., Johnsen, H., Hindberg, H., Guiton, G., Collard, F., 2023. Sentinel-1 product performance, SEASAR, May 2-6, 2023, Longyearbyen, Svalbard.

Hoffman, L., Mazloff, M. R., Gille, S. T., Giglio, D., Bitz, C. M., Heimbach, P.,

data policy for S-1, which is leading to a major expansion of research and operational use of SAR data.

There are four mutually exclusive imaging modes of S-1 and they include the Interferometric Wide swath (IW), Extra Wide swath (EW), Strip Map (SM), and Wave Mode (WV). Each acquisition mode has its different configurations of field of view and pixel resolution where the WV has the smallest footprint and highest spatial resolution. ESA has made strides to make the data as accessible as possible by making the data accessible through Copernicus data servers and the Alaska Satellite Facility and has developed openly available analysis tools like Sentinel Application Platform (SNAP). The large datasets of Sentinel-1, exceeding petabytes of raw data, demand that new methodologies and tools be developed to best exploit its rich details of the ocean and atmosphere. This paper summarizes new methodologies developed to handle such large datasets. All these examples of new methodologies were part of the May 2023 SEASAR workshop that took place in Longyearbyen, Svalbard, Norway. This summary is not meant to be a robust literature review of all available new methods to process SAR datasets but rather a snapshot in time of experts from the SAR research community.

A commonality of many of the methodologies presented was machine learning (ML) which is a broad range of statistical techniques used to efficiently extract information from multi-dimensional, high-resolution, and large SAR datasets. These studies are all based on SAR data over the oceans and they have applications for atmospheric or oceanic research. Likely because of its free and open data policy, data from the S-1 mission was commonly used in the studies, and we briefly describe the mission. S-1 is a constellation of identical polar-orbiting, sun-synchronous satellites with a local time of ascending node 18:00 (Torres et al., 2012). S-1A was launched in April 2014 and is still operating. S-1B was launched in April 2016 and stopped collecting data in December 2021 due to a power issue. S-1C is expected to be launched in 2024. S-1 operates in the C-band SAR with a center frequency of 5.405 GHz or wavelength of 5.5 cm. S-1 has a 12-day repeat cycle, flies with an altitude of 690 km, has an inclination of 98.2°, and a repeat period of 98.7 minutes. When both S-1A and S-1B were in operation they were 180° out of phase equating to a 6-day repeat cycle. The following seven studies utilize the S-1 mission by developing new methods to extract new information, remove noise, or automate workflows. The paper is organized as follows. The SEASAR 2023 methodology contributions are summarized in section 2 by describing their unique challenges, methods, and representative results. A summary and outlook are provided in section 3.

2. RESULTS

The following describes the various contributions to the methodology theme at the 2023 SEASAR workshop. There are two commonalities of all works. The first is the use of the S-1 acquisitions. The second is the use of statistical techniques often including machine learning (ML). The use of ML is often motivated by the reduction of computational resources, image recognition capabilities, or automated workflows that can readily be implemented to process large datasets. Since S-1 is used in all methodologies presented here, we summarize the update from Hajduch et al., (2023) regarding the operational S-1A satellite in terms of the instrument performance, radiometric accuracy, and level 1 and level 2 products. A key aspect of the S-1 program is the constant provision of quality data, which

requires long-term engagement to carefully monitor, preserve, and improve the system.

S-1A Instrument update

- The S-1A antenna has been stable throughout 2022 without product quality degradation.
- The instrument noise level is stable.
- The September 2022 collision avoidance maneuver caused an increase in the interferometric baseline and burst synchronization error.
- Changes in DC of 30 Hz are being continuously monitored but it does not appear to impacting the products.

S-1A Radiometric accuracy update

- IW calibration at the calibration site in Germany shows the overall mean and standard deviation for the absolute calibration factor is -0.08 dB ± 0.24 dB for both VV and HH polarizations.
- An absolute radiometric accuracy for the IW mode is 0.322 dB.
- An absolute calibration accuracy of –0.23 dB with a standard deviation of 0.20 dB was determined using corner reflectors over Australia.

S-1A Level-1 algorithm update

- Correction of the misalignment between the elevation antenna pattern and the annotated thermal noise vector.
- Reduction in the number of false positives in radio frequency interference time-domain detection.
- Reduction in the inconsistencies of the radio frequency interference pre-screening

S-1A Level-2 algorithm update

- Implementation of a new algorithm for TotalHs computation of Quach et al., (2022).
- Review of the oswQualityFlag estimation is based on a machine learning algorithm.
- Recalling the radial velocity from the normalized radar cross-section is updated.
- Wind inversion provided is now provided on the IceMask.

2.1 Using Ocean Surface Imagery to Estimate Atmospheric Boundary Layer Stratification

Justin E. Stopa, Ralph Foster, Doug Vandemark, Chen Wang, Yannik Glaser, Peter Sadowski, Alexis Mouche, Bertrand Chapron

Over the ocean, S-1 acquisitions are wave mode (WV) and S-1 acquires very high resolution (5 m) small (20 km) images approximately every 100 km. It has been established that SAR captures information about ocean swell and the WV was originally designed to capture ocean gravity waves at the appropriate scales. However, WV has opened up new research opportunities to study the marine atmospheric boundary layer (MABL) because its high spatial resolution can resolve a wide range of MABL turbulent eddies and its 20 km field of view is large enough to capture many realizations of MABL-scale eddies. The two S-1 satellites, A and B collect ~65,000 WV images every month resulting in more than 700TB of level-1 imagery. ML models were developed using convolutional neural networks (CNN) to detect oceanic or atmospheric phenomena that leave their imprint on the ocean surface (Wang et al., 2019). The method is used to sort millions of S-1 images into basic MABL state categories: wind streaks (WS), micro-scale convection (MC), and lack of any atmospheric signature with scales larger than 1000 m (negligible atmospheric variability ~NV). ERA5 atmospheric surface analyses have been time-space interpolated to each WV image providing consistent estimates of

the air-sea stratification through a bulk Richardson number (*Ri*). This systematic and global analysis of millions of SAR images shows that image textures are well correlated with the Richardson number and define distinct unstable, near-neutral, and stable stratification regimes as shown in Figure 1. That is, the different stratification regimes result in characteristic MABL mean states in which particular classes of coherent structures form and induce identifiable sea-surface roughness patterns. The Richardson number is one of the key parameters controlling the bifurcation between the different turbulent states. The relationships between SAR-observed coherent structures and MABL state through *Ri* are robust and hold in overall averages, at seasonal/regional scales, and MABL-process scales.

Figure 1: (a) PDFs of MABL Ri estimated from ERA5 for cells (unstable), streaks (near stable), and negligible atmospheric variability (stable) detection from SAR. The shaded gray PDF denotes the entire WV2 population. Representative SAR images for (b) unstable Ri = −0.032, U10N = 5.3 ms^{-1}, ΔTv = −2.81°, (c) near-neutral Ri = −0.006, U10N=9.8 ms^{-1}, ΔTv = −1.74°, and (d) stable Ri =AA 0.005, U10N=7.6 ms^{-1}, ΔTv = 0.84° MABL states. The white dashed arrow points north and the red solid arrow is the ERA5 wind direction.

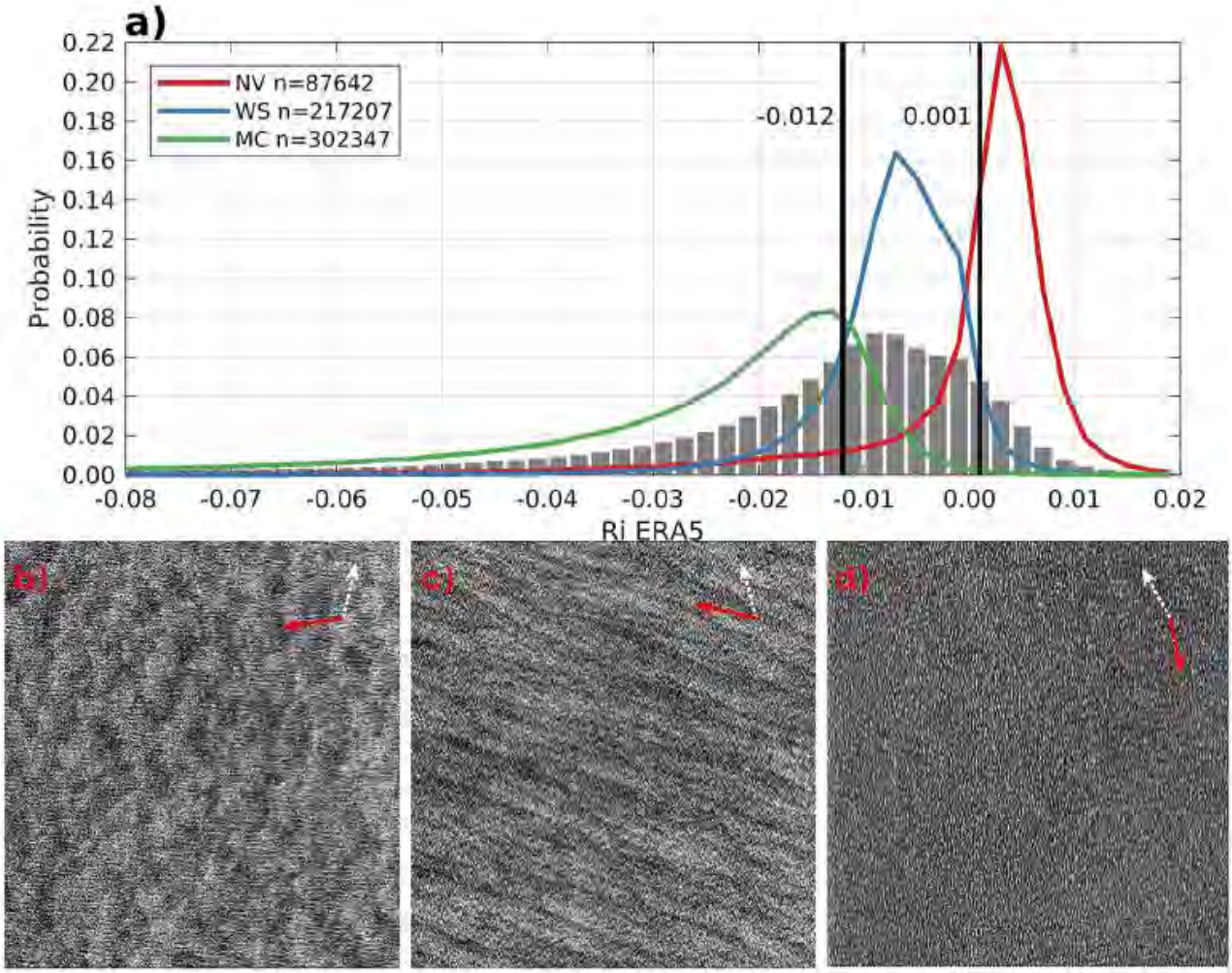

2.2 Using SAR Imagery to Diagnose Tropical Cyclone Boundary Layer Mean State

Ralph Foster, Alexis Mouch, Bertrand Chapron

Tropical cyclones (TC) form and intensify over the ocean and are quite compact storms, so high-resolution observations in remote locations are a necessity. A single wide swath SAR image can capture most of a TC's "inner core". The Satellite Hurricane Observation Campaign (SHOC) was established in 2016 and its goal is focused on collecting high-resolution SAR imagery in tropical cyclones with the S-1, RadarSAT2 (RSAT2) and RadarSAT Constellation (RCM) missions. S-1, RADARSAT2, and RCM can acquire simultaneous imagery in both co-pol (VV or HH) and cross-pol (VH). The cross-polarization acquisitions (VH) do not saturate at high wind speeds like VV normalized radar cross-sections. This offers the opportunity to estimate accurate wind speeds in tropical cyclones (33 to 80 m s^{-1}). The high winds force the tropical cyclone boundary layer (TCBL) to a state of near-neutral stratification even though the surface enthalpy fluxes can be enormous; the upper TCBL can even be weakly stably stratified. The consequence of the near-neutral stratification is that the TCBL is essentially the paradigmatic boundary layer for the generation of turbulent coherent structures in the form of roll vortices. TCBL roll orientation is highly sensitive to the vertical shear of the mean horizontal wind profiles. The rich dataset collected by SAR through SHOC and the routine observations of roll orientation in the imagery offer an opportunity to explore the atmospheric dynamics within tropical cyclones. Three different tools were used to exploit the SHOC archive. The first tool is a similarity boundary value model for the mean wind profiles in the TCBL. The lower boundary conditions are provided by the SAR surface wind vector field. The second tool provides the upper boundary conditions. It uses a simplified version of the nonlinear similarity model to estimate the pressure gradient field at the top of the boundary layer, from which we can directly calculate the sea-level pressure (SLP) pattern and consequently the gradient wind vectors representative of the forcing wind at the top of the TCBL. Ordinary least squares is used to calculate the pressure surface from the pressure gradient vectors. If one or more pressure observations are available, the SLP pattern can be converted to SLP.

The missing information for the similarity model is the turbulent eddy viscosity profile in the TCBL, which we infer indirectly from the orientation of the TCBL rolls extracted from the SAR image. TCBL roll orientation is mainly determined by the mean shear profiles, which in turn is sensitive to the eddy viscosity profile. The third tool calculates the roll orientation for trial eddy viscosity profiles that are variations of standard numerical model parameterizations. A consistent solution has a minimum RMS between measured and calculated roll orientations. Example results for Hurricane Fiona (2022) are shown in Figure 2. Fiona is a very challenging case because it is a very small Cat-2 storm close to land.

Figure 2 (below): (a) Sentinel-1 backscatter image of Hurricane Fiona (19 September 2022) with the P-3 flight tracks adjusted to the overpass time. (b) SAR-derived SLP with TCBl roll orientations (gray). (c) N/(N-1)/2 dropsonde pressure differences compared to SAR. Note that Fiona was a very compact storm and the storm was heavily sampled which leads to very high sensitivity to time-correction of observations to the overpass time.

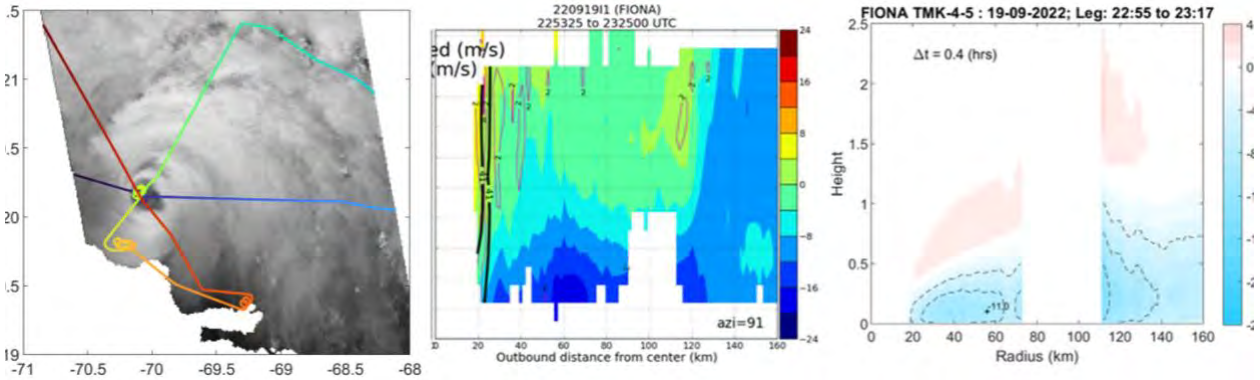

2.3 MediSAR: An Exhaustive Augmented Dataset of Segmented Sentinel-1 SAR Ocean Observations of the Mediterranean Sea and the Black Sea Regions

Aurélien Colin, Pierre Tandeo, Romain Husson, Ronan Fablet, Charles Peureux

Wide swath S-1 images are routinely collected over Europe. This dataset is high resolution and rich with information about ocean and atmospheric phenomena which leave their imprint within the SRA backscatter. Due to the high resolution and large footprint of the wide swath SAR imagery, a considerable amount of computational effort from both CPUs and GPUs is needed to process the S-1 IW archive composed of 102,504 images which typically cover 160x200 km. The work uses the hand-tagged dataset of Wang et al., (2019) to train deep-learning models to detect various ocean and atmospheric phenomena in the S-1 IW database. The effort exhaustively includes all SAR images between 2014-2022 and covers the Mediterranean and Black Seas. The methodology effectively utilizes high-resolution SAR textures to provide geophysical information about biological slicks, wind speed, rainfall, and atmospheric convective processes. As an example, Figure 3 shows the biological slick detection probability during the summer (June-July-August~JJA) and winter (December-January-February~DJF) in the Alboran Sea. The increased biological activity during the summer is visible. The distribution of the slicks also follows the Western Alboran Gyres, highlighting the capacity for biological slicks to provide information on currents. Future work will evaluate the ML models relative to other satellite technologies such as the Sentinel-3/OLCI and MSB/Seviri. The dataset is called MediSAR and its goal is to share SAR observations for the study of metocean phenomena more readily.

Figure 3: Biological slick detection probability (restricted to points with wind speed between 6.5 and 12 m/s) during summer (left) and winter (right) in the Alboran Sea between 2015 and 2022.

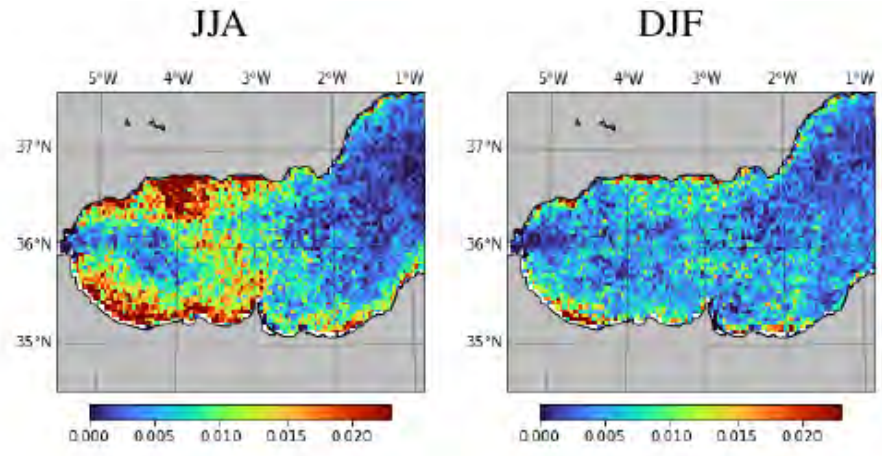

2.4 Machine learning for evaluating trends in the drivers of variability in Arctic sea-ice dynamics

Lauren Alexandra Hoffman, Matt R Mazloff, Sarah T Gille, Donata Giglio, Cecilia M Bitz, Patrick Heimbach

Arctic sea ice simulations are complex due to various factors, leading to high computational costs and model uncertainties. Classical numerical models need help to accurately represent sea-ice motion due to the complexity of simulating multi-phase, multi-physics problems. Machine learning (ML) offers a promising approach by serving as a surrogate for the dynamical component of sea ice, potentially enhancing computational efficiency and revealing emergent behaviors. ML models are developed using sea-ice velocity, ice concentration, and wind velocity from satellite and reanalysis data sources. Hoffman et al., (2023) developed these ML models and show the viability in predicting sea-ice motion, achieving a correlation of up to 0.8 with observed data. Efforts were extended to use explainable ML (XML) techniques and find that wind velocity is a key predictor of ice motion in the central Arctic, aligning with established statistical relationships. Example heat maps show the relevance of each of the inputs to an ML model to predict sea ice motion in Figure 4. Results from the XML method known as layerwise relevance propagation (LRP) applied to a CNN show that wind velocity is the most important predictor of ice motion for regions in the central Arctic (red in Figure 4d). It found that the physics-based and ML models have the largest uncertainties in the coastal regions where ice stress is significant. Ongoing work is utilizing SAR and XML methods to understand the role of linear kinematic features in ice dynamics and to improve the predictability of sea ice motions in coastal regions.

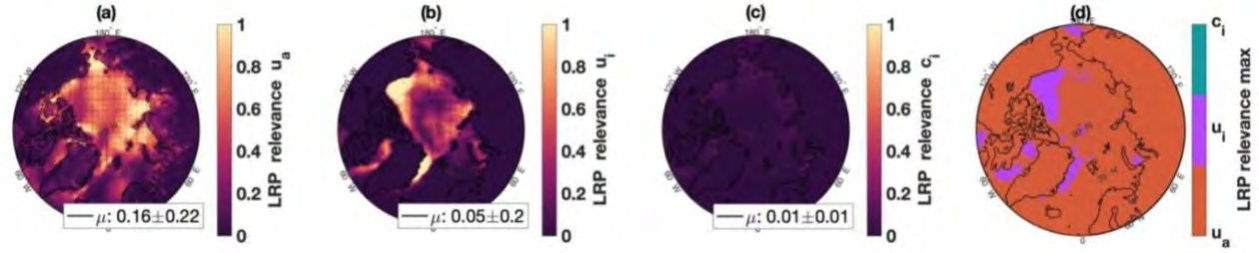

Figure 4: (a–c) Heat maps show the relevance of each of the inputs to an ML model for making predictions of sea-ice motion. These relevance heat maps are from an explainable machine learning (XML) method known as layerwise relevance propagation (LRP) applied to a CNN trained to make one-day predictions of sea-ice motion from inputs of wind velocity (ua) in panel (a), ice velocity (ui) in panel (b), and ice concentration (ci) in panel (c). (d) Map showing which input is the most important predictor of sea-ice motion for the ML model at each location in the Arctic.

2.5 Sentinel-1 Extra Wide Thermal Noise Removal Using a Deep Learning Model

Roghayeh Shamshiri, Egil Eide, Fazel Rangriz Rostami, Knut Vilhelm Høyland

The Sentinel-1 (S1) ground range detected (GRD) extra-wide (EW) swath data, particularly in the cross-polarization channel is strongly affected by thermal noise. This particular type of noise not only reduces the data interpretability and spatial quality but also creates challenges of a consistent backscatter time series. Even though GRD images undergo denoising using calibrated

noise vectors provided by the ESA, residual noises persist in time series applications on the Google Earth Engine platform. Previously developed methods enhance the image quality; but, these methods are not feasible in cloud computing using the Google Earth Engine. Therefore, a novel method using deep learning through a U-Net Convolutional Neural Network (CNN) architecture was developed to reduce noise in S-1 wide swath imagery automatically. There are two further constraints: the results should be competitive with those produced by existing conventional methods and the method can be implemented on the Google Earth Engine. Figure 5 shows the noisy, predicted, and clean images for example GRD S-1 acquisition. The CNN has significantly removed the stripes and the backscatter is continuous across the swath. The results demonstrate the effectiveness of the CNN in reducing the noises from the EW HV-polarized S1 images and the method can effectively be implemented on Google Earth Engine.

Figure 5: Model test result, (a) the noisy, (b) predicted using our model, and (c) clean image.

2.6 Monitoring coastal erosion and morphodynamics in intertidal areas

Martin Gade, Sebastian Peters, and Simon Schäfers

The Wadden Sea on the continental North Sea coast is the World's largest coherent intertidal area and extends over an area of about 4700 km^2, extending from the Dutch coast in the West to the Danish coast in the north. Intertidal areas are crucial for ecosystems and protect infrastructure from damaging storms. Due to the large area, remote sensing methods are best suited to monitor coastal changes related to land type (sediment, sea grass, etc.) or morphological changes (coastline change). Small-scale changes (<1 km) need to be resolved and SAR is the ideal sensor with its high resolution. A large number of SAR images were acquired over the German part of the Wadden Sea by the L-, C-, and X-band SARs aboard ALOS-2, Radarsat-2 and Sentinel-1, and TerraSAR-X, respectively. Using this wide range of multi-frequency / multipolarization SAR data it is determined which combinations of radar band and polarization are best suited for the classification of different Wadden Sea surface types, including sandy and muddy sediments, seagrass meadows, and bivalve beds. A neural network was built for the automated detection of waterlines on

Sentinel-1A/B SAR-C imagery. The neural network is capable of segregating water from exposed intertidal flats at high spatial resolution (Figure 6). The neural network is designed as an image-to-image network and uses SAR images and an ordinary land/water mask as input (left and middle panels of Figure 6, respectively). The neural network simplified the SAR image analysis significantly, as only minor post-processing of the obtained results is required.

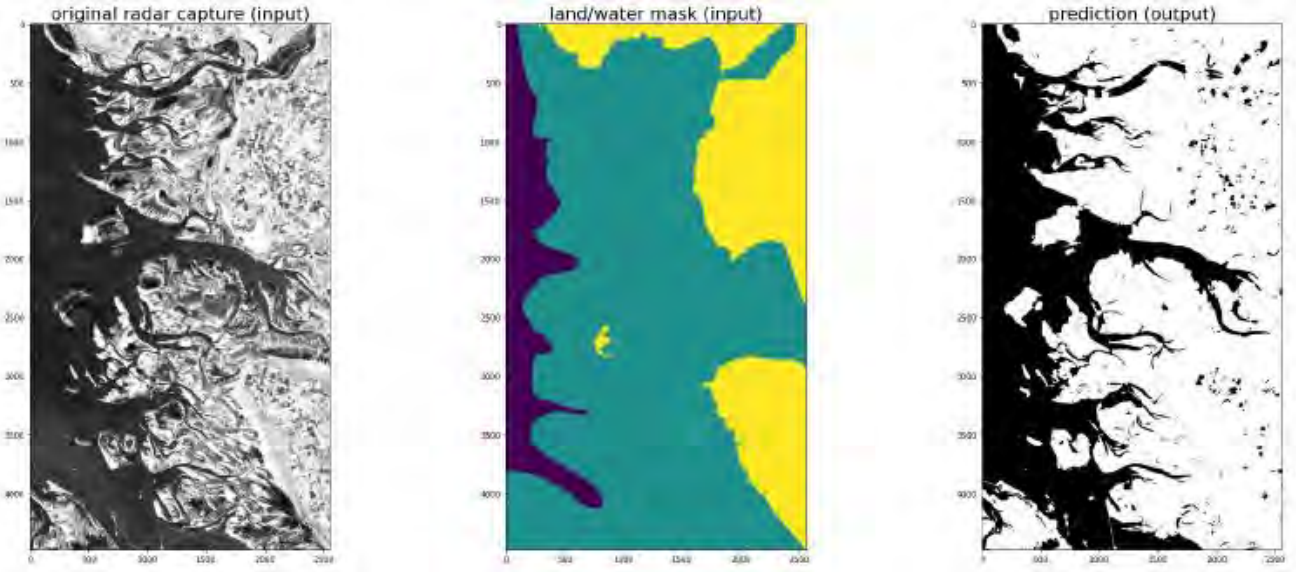

Figure 6. Automated classification of exposed intertidal flats by a neural network. Left: part of a Sentinel-1A SAR-C image of the German Wadden Sea acquired on 19 May 2020. Middle: manually generated land/water mask used as additional input; yellow: land; blue: open sea; green: potential intertidal flats. Right: resulting prediction of the neural network (classification).

2.7 Ship Wake Detectability

Björn Tings, Andrey Pleskachevsky, Stefan Wiehle, Sven Jacobsen

Ship wakes are produced by the interaction of the ship's hull with the ocean water and result from multiple interacting wave systems closely beneath and on the ocean surface. The ship wake signatures in SAR imagery consist of four components including Kelvin wake arms, V-narrow wake arms, and near-field and far-field turbulent components of the wake. The detectability of wakes in SAR imagery is influenced by ship properties, environmental conditions, and SAR acquisition properties (frequency and incidence angle). Machine learning through support vector machines was used to understand the detectability of individual wake components. This approach allows various influencing parameters to be isolated for the four different wake attributes. TerraSAR-X (2881), CosmoSkyMed (94), Sentinel-1 (618), and RADARSAT-2 (407) in C-band and X-band were used in this study. Ship information from the Automatic Identification System (AIS) was used as a reference. The results are provided in Table 1.

Table 1: Summary of detectability for the four wake components. Parameters with identical influence are marked by grey color.

Influencing Parameter	**Summary of detectability of the four wake components wake component detectability: "↑": better, "≈ ": hardly influenced**			
	Near-hull turbulence	**Turbulent wakes**	**Kelvin wake arms**	**V-narrow wakes**
Vessel speed	↑ for faster moving vessels	↑ for faster moving vessels	↑ for faster moving vessels	↑ for faster moving vessels
Vessel length	↑ for larger vessels	↑ for larger vessels	↑ for larger vessels	↑ for larger vessels
Vessel moving direction	↑ for vessels moving parallel to range	≈ by vessels' moving direction	↑ for vessels moving parallel to azimuth	↑ for vessels moving parallel to azimuth
Incidence angle	↑ for larger incidence angles, when ship speeds are at least moderate	↑ for lower incidence angles	↑ for lower incidence angles	↑ for lower incidence angles
Local wind speed	↑ for lower wind speeds	↑ for lower wind speeds	↑ for lower wind speeds	↑ for lower wind speeds
Sea state - wave height	≈ by wave heights	≈ by wave heights	≈ by wave heights	≈ by wave heights
Sea state - wavelength	↑ for longer wavelengths, when ship speeds are at least moderate	↑ for shorter wavelengths	↑ for shorter wavelengths	↑ for longer wavelengths
Sea state - wave propagation direction	↑ for wave directions parallel to the vessel's movement	↑ for wave directions parallel to the vessel's movement	↑ for wave directions parallel to the vessel's movement	≈ by wave propagation directions
Local wind direction	≈ by wind direction	↑ for wave directions orthogonal to the vessel's movement	≈ by wind direction	↑ for wave directions orthogonal to the vessel's movement
SAR slant ranges	≈ by slant ranges	≈ by slant ranges	↑ for shorter slant ranges	≈ by slant ranges
SAR radar frequency	≈ by radar frequency	≈ by radar frequency	≈ by radar frequency	↑ for X-band

3. SUMMARY AND OUTLOOK

3.1 Summary

The open-data policy of ESA has allowed SAR data to be more easily used in a broad range of applications. While the examples here are not exhaustive, the seven works show how surface textures from SAR can be exploited for study of atmospheric phenomena (Stopa et al., 2023; Foster et al., 2023; Colin et al., 2023), ocean phenomena (Colin et al., 2023), refinement of sea ice motion in coastal regions (Hoffman et al., 2023), monitoring and the detection of the coastline variability in intertidal regions (Gade et al., 2023), and the detection of ship waves in SAR imagery (Tings et al., 2023).

For wide swath imagery, the correction of overlapping SAR swaths often creates erroneous data issues and ML can be used to effectively correct the swaths and is comparable to existing methods (Shamshiri et al., 2023). This broad range of applications requires different ML approaches to be developed and implemented. A commonality of using ML is that the methods are often easily automated and require fewer computational resources than other methods. For example, Colin et al., (2023) and Stopa et al., (2023) use ML for image detection from convolutional neural networks through deep learning which effectively extracts information about the ocean surface textures. Image detection through ML allows the large S-1 archive that contains sub-mesoscale features across basin scales through the WV mode (now exceeding 1 Pb) and the >100,000 IW (400 Tb ~4 Gb per single polarization images) in the Mediterranean and Black Seas to be utilized. ML models are also being used to determine important input parameters as in the case of Hoffman et al., (2023) for predicting sea ice motion or Tings et al., (2023) for determining the radar settings in influencing the detectability of ship wakes.

3.2 Outlook

Machine learning is a rapidly changing field and we expect that these new advancements in the methods will be further refined to meet the needs of remote sensing specialists using high-resolution imagery. ESA is dedicated to providing SAR data until at least 2030 with Sentinel-1 with satellites C and D yet to be launched. NASA's NiSAR mission will be launched in 2024 and like ESA they will have an open data policy. We strongly attribute the wider use of SAR data for research and applications to the open data policy and ease of data access.

4. REFERENCES

SEASAR Contributions

Colin, A., Tandeo, P., Husson, R., Fablet, R., Peureux, C., 2023. MediSAR: An Exhaustive Augmented Dataset Of Segmented Sentinel-1 SAR Ocean Observations Of The Mediterranean Sea and the Black Sea regions, SEASAR, May 2-6, 2023, Longyearbyen, Svalbard.

Foster, R., Mouche, A., Chapron, B., 2023. Using SAR Imagery to Diagnose Tropical Cyclone Boundary Layer Mean State, SEASAR, May 2-6, 2023, Longyearbyen, Svalbard.

Gade, M., Peters, S., Schäfers, S., 2023. On the Use of SAR Data to Monitor Coastal Erosion and Morphodynamics in Intertidal Areas, SEASAR, May 2-6, 2023, Longyearbyen, Svalbard.

Hajduch, G., Pinheiro, M., Valentino, A., Vincent, P., Recchia, A., Cotrufo, A., Franceschi, N., Piantanida, R., Benchaabane, A., Peureux, C., Husson, R., Schmidt, K., Mouche, A., Grouazel, A., Nouguier, F., Johnsen, H., Hindberg, H., Guiton, G., Collard, F., 2023. Sentinel-1 product performance, SEASAR, May 2-6, 2023, Longyearbyen, Svalbard.

Hoffman, L., Mazloff, M. R., Gille, S. T., Giglio, D., Bitz, C. M., Heimbach, P.,

2023. Machine Learning for Evaluating the Drivers of Variability in Arctic Sea-ice Motion, SEASAR, May 2-6, 2023, Longyearbyen, Svalbard.

Shamshiri, R., Eide, E., Rangriz, Rostami, F. R., Høyland, K. V., 2023. Sentinel-1 Extra Wide Thermal Noise Removal Using a Deep Learning Model, SEASAR, May 2-6, 2023, Longyearbyen, Svalbard.

Stopa, J. E., Foster, R., Vandemark, D., Wang, C., Glaser, Y., Sadowski, P., Mouche, A., Chapron, B., 2023. Using Ocean Surface Imagery to Estimate Atmospheric Boundary Layer Stratification, SEASAR, May 2-6, 2023, Longyearbyen, Svalbard.

Tings, B., Pleskachevsky, A., Wiehle, S., Jacobsen, S., 2023. Ship Wake Detectability in TerraSAR X, CosmoSkymed, Sentinel 1 and RADARSAT 2 Imagery – Summary and Applications for Wake Detection, SEASAR, May 2-6, 2023, Longyearbyen, Svalbard.

SEASAR APPLICATIONS: STATUS AND OUTLOOK

Cathleen E. Jones[1,2], Maria Michela Corvino[3], Benjamin Holt[1], Elena Morando[3], Roberto Del Prete[4], Martin Gade[5], Scott Kaczor[6], Peter Lanz[7], Bou-Laouz Moujahid[8], Yi-Jie Yang[9,10]

[(1)] Jet Propulsion Laboratory, California Institute of Technology, Pasadena, California, USA
[(2)] UiT The Arctic University of Norway, Tromsø, Norway
[(3)] European Space Agency-ESRIN, Rome, Italy
[(4)] University of Naples Federico II, Napoli, Italy
[(5)] Institute of Oceanography, University of Hamburg, Hamburg, Germany
[(6)] United Kingdom Hydrographic Office, Taunton, UK
[(7)] Carl von Ossietzky University of Oldenburg, Oldenburg, Germany
[(8)] IMT Atlantique, Plouzane, France
[(9)] German Aerospace Center (DLR), Bremen, Germany
[(10)] Research and Technology Centre West Coast, Büsum, Germany

ABSTRACT

SAR is a vital source of information for monitoring the coastal oceans, particularly for oil spill detection and identifying and tracking vessels. Major advances in understanding how SAR can be used to detect, track, and characterize slicks has resulted from observations with low noise instruments, but determining thickness and discriminating mineral oil from other radar-dark phenomena remain challenges. Remote sensing information is playing a crucial role in enhancing maritime situational awareness, addressing detection of illegal trafficking at sea and illegal fishing, and monitoring integrity and operations of surface/sub-surface critical infrastructures. The availability of free and low-cost SAR data, development of new processing techniques, and deep learning methods applied to object identification in SAR imagery supports continued advancement. This paper summarizes advancements in the ~20 years since SeaSAR was last held on Svalbard, remaining major gaps in knowledge and capability, and activities to continue advancement in the coming decades.

1. INTRODUCTION

The progress made since the last SeaSAR meeting on Svalbard, ESA's 2003 Workshop on Coastal and Marine Applications of SAR, was discussed at the May 2023 SeaSAR meeting with the goal of identifying knowledge gaps and actions that can be taken in the next 10 years to advance studies of the ocean based on Synthetic Aperture Radar (SAR), considering both fundamental and applied science. The sessions on applications were separated into three topics, two of which covered generally related applications and a third that covered other notable marine and coastal ocean applications:

1. Maritime Security / Navigation / Ship Identification
2. Marine Mineral Oil Slicks / Spills
3. Others (Macroalgae/algal blooms, oil in arctic ice, iceberg detection, biogenic surfactants)

There are numerous other topics that could have been included as SeaSAR applications and some of those were relegated to other sessions: an abstract on coastal erosion in the Methodology and Techniques session; wave-driven flooding, submergence, and erosion necessarily related to wave retrieval; iceberg detection and impact to shipping closely related to sea ice detection. In some cases, the topics were not discussed at the meeting, e.g. the impact of man-made pollution on marine water quality and SAR-based measurements of coastal bathymetry. A variety of ocean applications were covered by submitted abstracts (included in this volume), all addressing the first two topics.

The sections in this paper are separated by the three topics listed above, each covering the state-of-the-art in each field, knowledge gaps and critical processes that are still not well understood, and studies and measurements through airborne and space missions or field campaigns that can lead to the next level of advancements. The references cited cannot cover the vast amount of research done in the last 15–20 years, so those given here are selected as exemplars; the references therein and their citing articles serve to document the volume of research in these study areas.

The topic-specific sections are followed by a summary identifying the theme-specific recommendations and commonalities in gap-filling activities among the different marine and coastal applications for which SAR observations provide key information. These include what we identified to be the highest priorities given the upcoming ESA, NASA, and JAXA missions. The abstracts and short papers submitted to the SeaSAR Applications session and provided by the coauthors are included in the volume and cited herein.

2. MARITIME SECURITY AND NAVIGATION

2.1 Overview

Maritime situational awareness is related to the effective understanding of targets at sea that could impact

environment, economy, safety, and security. The use of satellite data in maritime applications allows sea waters to be monitored worldwide, in a cost-effective and reliable manner, and, thanks to the use of SAR satellites, independently of the time of the day and weather conditions. The current baseline of higher revisit times of Earth Observation (EO) missions and constellations than previously possible provides a strong foundation for the development of routine applications and services integrating new processing techniques.

Several techniques ranging from classical statistical ship detection methods to more modern Artificial Intelligence (AI)-based techniques are being used to perform ship detection from satellite imagery [Morando et al., 2023]. Furthermore, the correlation between positioning data transmitted by vessels, using AIS, LRIT, and VMS reporting systems, and satellite ship detections allows to track and retrieve information about the behaviour of ships.
The main areas of development related to the operational exploitation of EO for maritime situational awareness can be identified as follows:

- new techniques considering a more persistent temporal coverage thanks to the increased availability of data;
- new processing techniques to improve accuracy for target detection, identification, characterization and tracking;
- faster access to satellite acquisitions and reduction of latency time, focusing on tipping and cueing capabilities and cloud processing techniques.

2.2 Advancements in methods - maritime security

The 'New Space' sector's rise, alongside advancements in processing and computer vision, is transforming the space industry. This evolution opens new research avenues, especially in using EO data for maritime surveillance. Recent satellite constellations, primarily made of small- and nano-satellites, have enhanced global monitoring capabilities. These satellites are outfitted with standard sensors like Optical and SAR, as well as cutting-edge ones such as AIS and Radio Frequency (RF) detectors. This payload diversity yields a rich mix of varied and complex datasets. While these diverse datasets present challenges in terms of data processing and fusion due to varying resolutions in time and space, they also offer actionable information more efficiently and cost-effectively.

Furthermore, advancements in data processing techniques together with increased data availability, offer improved object detection and tracking capabilities compared to traditional image processing methods. An example are pattern-of-life-based alerting functions which direct attention to specific target behaviors.

Traditional ship detection methods typically rely on segmentation-based algorithms that analyze SAR image characteristics statistically to distinguish targets from the background, such as the classical Constant False Alarm Rate (CFAR) method. In this context, innovative techniques like advanced data augmentation, few-shot learning, transfer learning, and automated Deep Learning (DL) operations are being explored to provide new solutions for automatic vessel detection or port activity recognition. One of the widely adopted DL methods, including for ship detection is Convolutional Neural Networks (CNNs). DL-based ship detection often involves extracting patches from SAR images and using CNNs to determine if these patches belong to the target ship. The advantages of DL methods include their processing speed and accuracy.

Furthermore, leveraging innovative DL-based restoration techniques can potentially improve the spatial resolution of imagery and video data, enabling new applications in maritime surveillance. The industrialization of these academic studies has the potential to enhance the value of low-resolution and openly available EO data for addressing novel applications. To fully leverage the increased data availability, dedicated research is focused on designing innovative signal processing techniques. These techniques aim to enhance the focus on moving targets in SAR imagery and derive kinematic parameters for vessels. The combined use of traditional satellite SAR and Inverse SAR (ISAR) techniques applied to SAR data are currently being examined to assess their impact on feature extraction processes and, consequently, on improvements in data fusion results. Differently from SAR, ISAR uses the motion of the target rather than the radar platform to generate the synthetic aperture antenna for radar imaging. The two-dimensional image is then produced by analysing received echoes based on fast time and Doppler frequency. The analysis in time provides the position of bright points along-range, while the Doppler analysis provides the cross-range position. The outcome of an ISAR system can be a one-, two-, or three-dimensional (and possibly temporal) description of the target's spatial electromagnetic reflectivity distribution, depending on the sensor characteristics and the relative target-sensor motion. It is important to note that ISAR images of moving targets, which are processed assuming the radar platform is stationary and the target moving, are well-focused. This contrasts with standard SAR images of moving targets, where the moving target appears blurred because the data are processed as if the scene is stationary and only the radar platform is moving, causing target motion to remain uncompensated. Furthermore, ISAR enables to retrieve target motion parameters (such as speed and direction), providing invaluable information for characterizing the target and its activities.

Another processing technique under evaluation involves the modelling and exploitation of radar micro-Doppler effects to determine the dynamic properties of targets, with further developments anticipated in this area [Chen, 2023]. An interesting definition of the micro-Doppler

effect is given by Victor Chen [2023]: "The micro-Doppler signature is the intricate frequency modulation that is imparted on the backscatter signal by the moving components of a radar target." Mechanical vibrations or rotations of a target can induce frequency modulation of radar returns, generating sidebands about the Doppler frequency, known as micro-Doppler effects. Modulations produced by rotational, vibrational, or non-uniform movements can be considered features of interest in the target signature. Therefore, the analysis of micro-Doppler effects and the real time extraction of micro-Doppler information is considered of relevance, in combination with other techniques, to improve target detection and classification.

An additional research line is based on traditional subaperture techniques applied to SAR datasets acquired with new modes. New microsatellites feature an active phased array antenna with beam steering capabilities in the along and cross-track directions, that allow ScanSAR and TOPSAR modes to be operated. Lightweight platforms are more agile and exhibit more flexible mechanical pointing capabilities that enable very long dwell and staring Spotlight modes, creating new data products from which to derive information on moving targets (e.g. VideoSAR).

SAR video is generated by focusing adjacent portions of the synthetic aperture, with each focused sub-aperture corresponding to one video frame. During the extended acquisition time, a continuous sequence of images is generated and mapped onto a consistent Cartesian grid while the radar platform moves towards, by, or around the target area. The resulting imagery exhibits a video-like nature due to the overlapping synthetic apertures used for its production, allowing for output frame rates comparable to those of traditional video systems, hence VideoSAR [Palm et al., 2014; Gu & Chang, 2016; Liu et al., 2016; Yamaoka et al., 2016]. The key characteristic of VideoSAR imaging is the ability to maintain consistent antenna illumination on the target, regardless of changes in the squint angle. However certain theoretical and practical limitations to this capability exist. To fully exploit the potential of VideoSAR, it is crucial to maintain the phase coherence in the imagery and to control the acquisition geometries. These measures allow the generation of secondary products such as coherence images or maps, which are valuable for change detection and other advanced analysis techniques.

Another interesting capability is distributed sensing, provided by bistatic and multistatic spaceborne satellite systems. These have proven effective for interferometric and imaging applications. Examples come from companies such as Iceye and Capella whose new SAR constellations are enhancing the ability to explore scene characteristics by leveraging multiple observation angles. These constellations are also contributing to global and continuous monitoring of the planet, offering actionable information in a better, faster, and more cost-effective manner. Moreover, distributed missions such as Chinese LuTan-1 Mission, European Space Agency Harmony Mission, German Aerospace Center (DLR) TanDEM-L Mission, Italian Space Agency RODiO Mission, Netherlands Institute for Space Research (SRON) SwarmSAR Mission, and the distributed geosynchronous SAR (GEO SAR) are in the preparation or planning stage. Distributed spaceborne SAR systems offer significant advantages when compared to monostatic SAR platforms. They provide a shorter revisit time, broader imaging coverage, and a wider range of remote sensing applications, thanks to their system flexibility and inter-satellite collaboration. Furthermore, the combination of sensors, such as spaceborne-airborne bistatic SAR configurations, enhances SAR capabilities, providing more comprehensive information about scattering properties and enabling forward-looking SAR imaging. As a result, these distributed systems can effectively overcome challenges like temporal decorrelation and atmospheric interference, leading to improved performance in topography and deformation retrieval, moving target detection, and three-dimensional (3D) imaging.

In terms of data fusion, the integration of SAR and RF signals for active targets offers substantial improvements in recognition and status characterization, even in complex environments with multiple targets. SAR sensors can also incorporate ground-based transmissions within their field of view into the focused image, supporting the mapping and location of ground-based transmitters operating within the SAR's frequency spectrum. New satellite technologies capable of detecting and geolocating electromagnetic signals emitted by vessels, such as those from L-band satellites, GSM, VHF maritime emitters, and X-band maritime radars, are already operational and in further development by commercial and public/private partnerships. These technologies are not affected by weather conditions and can complement traditional satellite remote sensing products. Commercially available RF datasets provide information on maritime radar pulses, aiding in the detection of changes in navigation equipment and profiling maritime radars operating in X and S bands. ESA-funded activities include analyzing and implementing data fusion algorithms to enhance the detection and tracking of non-cooperative targets and analyzing anomalous behaviors. Additionally, algorithms for route prediction and forecasting based on AI methodologies are being developed to reduce the uncertainty in the fusion process.

2.3 Gaps - maritime security and navigation

In terms of detection of targets, DL techniques applied to EO datasets have demonstrated unprecedented performance compared to conventional algorithms.

However, current DL-based SAR ship detection still faces challenges, such as complex scenes and different-sized targets, particularly in port scenarios. The algorithms utilizing medium resolution, but free, SAR, e.g. from Sentinel-1 and soon from NISAR, have not been as well studied because of the focus on high resolution SAR.

A remaining issue is the availability of very large training datasets for the DL models both for ship identification [Moujahid et al., 2024] and ship wake retrieval [Del Prete et al., 2024]. Currently, AIS positioning data is not transmitted by all vessels, does not adequately label the vessel type, is not publicly available for many areas, much of it being proprietary, and is not attached as ancillary data to SAR datasets. There is also a notable deficiency in obtaining multi-temporal images with minimal time delays.

Challenges remain in the quantification of the visibility of small structures on the ocean surface and making this systematic when structures that need to be identified vary in form, size, and material. A detector fusion approach was used to improve the ability to detect small, non-magnetic vessels, such as inflatable rubber boats used by refugees to cross the Mediterranean Sea. The developed detection capabilities for those boats are good up to a wave height of 2.5 meters [Lanz et al., 2024]. This problem extends to detecting floating debris from wreckage of vessels and structures in cases where slicks do not indicate their location. There is also an operational need to identify, position, and monitor navigational buoys and beacons in distant or remote locations where persistent cloud cover precludes the use of optical imagery. Because of their small size, high resolution SARs have been investigated for this purpose [e.g. Kaczor et al., 2024], but more work including other frequency SAR is needed. Finally, the methods must be reliable, repeatable, and cost-effective for wide-spread adoption. This requires testing in a variety of locations, integration with ancillary information or other remote sensing data, quantification of accuracy and limitations, lower temporal resolution, and easy and low latency data access. Ideally, the SAR data are free or inexpensive, which is currently not the case with constellations such as COSMO-SkyMed and TerraSAR/Tandem-X.

3. MARINE OIL SLICKS AND SPILLS

3.1 Overview

SAR has long been used for identifying and tracking mineral oil slicks on the ocean surface based upon contrast with the clean ocean surface, often called the 'damping ratio' in this context [Gade et al., 1998a]. This works for winds speeds in the range 2–12 m/s depending on the instrument operating frequency and transmit power. In general, the contrast decreases as the wind speed increases [Gade et al., 1998a,b]. Slick detection with SAR is challenged at low wind speeds by the lack of contrast because the calm surface of clean sea water generally has very low SAR returns also, and it is challenged at high wind speeds by slicks not persisting on the surface, but rapidly mixing into the water column driven predominantly by wave breaking. Examples of look-alikes for mineral oil slicks are low wind areas, natural biogenic films, algal blooms and macroalgae (in some radar bands), rain cells, and grease ice.

Some key information available through SAR remote sensing is needed for oil spill response and remediation, namely the location and extent of the slick, and characterization of the oil by thickness and degree of emulsification. Models initiated or updated with the information can be used to forecast the likely transport path of the slick, and for hindcasting to identify the source location of the oil for accidental or intentional releases. Given information about the extent and thickness of the surface slick and time since release, a 3-dimensional transport and evolution model can be used to estimate the volume of released material, information required to assess environmental and economic damages.

3.2 Advancements in methods - oil slicks and spills

Significant progress has been made in oil spill detection, tracking, and characterization based on SAR data in the last 15 years, in no small part because of the plethora of SAR data that was collected with spaceborne and airborne sensors during the 2010 Deepwater Horizon spill in the Gulf of Mexico [Latini et al., 2016]. Prior to this, it was widely thought that SAR was not useful for doing more than detecting slicks [Fingas & Brown, 2014], but since 2010 that has been shown to be incorrect in studies using the low noise floor airborne SARs like UAVSAR (L-band) [e.g. Minchew et al., 2012], FSAR (X-, S-, and L-band) [e.g. Quigley et al., 2023], and SETHI (X- and L-band) [e.g. Angelliaume et al., 2017; Angelliaume et al., 2018], and the low noise floor quad-pol mode of the C-band Radarsat-2 satellite-borne SAR [Garcia-Pineda et al., 2020].

During the late 2000s and early 2010s, many studies were undertaken to evaluate the capabilities of polarimetric SAR for characterizing oil slicks, i.e., determining oil thickness or differentiating mineral oil from various false positives, primarily biogenic slicks. Many different polarimetric parameters were suggested (see lists in Skrunes et al., 2014; Espeseth et al., 2017), including but not limited to entropy calculated via the H/A/α polarimetric decomposition. Studies with low noise instruments have shown that many of those studies were impacted by instrument noise and that polarimetric parameters are not necessarily the best option, for L-band at least [Minchew et al., 2012; Espeseth et al., 2020a]. In fact, studies have shown that the VV and HV damping ratios and the HH/VV copolarization ratio [Espeseth et al., 2017; Angelliaume et al., 2018] are the most sensitive to oil slick characteristics, including thickness. Given sufficient margin above the instrument noise floor (~6 dB

based on Minchew et al., 2012; Espeseth et al., 2020), the damping ratios can identify zones of thicker oil within a slick [Wismann et al., 1998; Gade et al., 1998b; Jones & Holt, 2018]. This identifies areas of relatively thicker oil, as opposed to measuring the thickness of the oil (Figure 1).

Theoretical modeling has shown that obtaining the absolute thickness by this method is not feasible given the range of values that bulk and interfacial properties can have, some of which change by orders of magnitude as the oil weathers [Jaruwatanadilok et al., 2023]. Based on data collected during the Deepwater Horizon spill, the damping ratios have also been used to relate the backscatter to the dielectric constant of a thick oil layer, hence obtaining information about emulsification by estimating the oil:water ratio based on the dielectric constant derived from a backscattering model [Minchew, 2012; Minchew et al., 2012]. Automated ML methods for identifying slicks based on contrast using data from the operational satellite-borne imaging SARs and suitable for use by oil slick detection services have been developed [e.g. Garcia-Pineda et al., 2013; Bianchi et al., 2020; Yang et al., 2024]. A computationally inexpensive algorithm applicable to SAR of any frequency and polarization, which is based on statistical analysis, is under development and test by NOAA and NASA/Jet Propulsion Laboratory [Jones, 2023; Holt et al., 2024; Jones et al., 2024]. This is also suitable for implementation on-board aircraft for real-time acquisition and processing during response.

Another advancement has been in the use of rapid repeat SAR imaging to measure slick transport, including identifying probable locations of thicker oil [Espeseth et al., 2020b] and identifying oil slicks in low wind situations where single images cannot resolve the similar low backscatter features [Quigley et al., 2024]. Modeling of oil slick evolution and transport has advanced significantly [Lehr, 2021; Keramea et al., 2021], and the model parameters can be refined when constrained by SAR data from rapid repeat imaging [Jones et al., 2016; Röhrs et al., 2018].

A particular challenge under study is differentiating slicks in the presence of false positives. Early work used spatial, contextual, and statistical features to label and discriminate the slicks [Brekke and Solberg, 2005], but machine learning / deep learning (ML/DL) methods have been applied for automated detection of oil spills based on satellite SAR imagery. Many studies have been published in the last 10 years, and examples of the methods applied can be found in Cao et al. [2017], Bianchi et al. [2020], Shaban et al. [2021], Amri et al. [2022] and references therein. Few of these studies are multi-class - most classify the scene as oil vs. not oil, although [De Laurentiis et al., 2020] differentiates mineral oil from clean ocean and biogenic slicks based on airborne SAR data acquired near the Louisiana coast in the Gulf of Mexico. Many include look-alikes in the 'not oil' training dataset, e.g. Yang et al. [2024].

Starting in the early 2000s, the increasing amount of available single- and multi-mission SAR data has been used for statistical analyses of spatio-temporal pollution densities in European marginal seas [Ferraro et al., 2006, 2008] and, more recently, in Indonesian waters [Mohr and Gade, 2022]. Despite being based on relatively small numbers of SAR images, such studies have already demonstrated the necessity of routine oil pollution monitoring of ecologically sensitive marine environments using multi-mission spaceborne SAR.

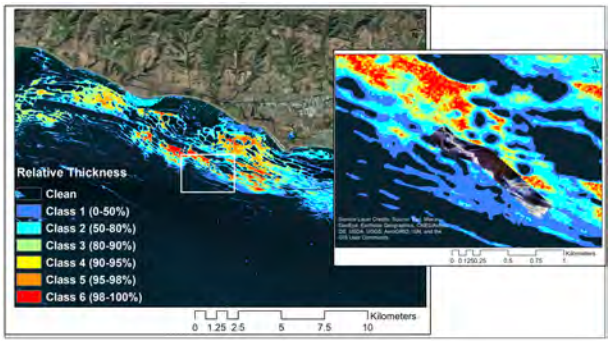

Figure 1. Relative thickness classification of mineral oil slicks in the Coal Oil Point seep field derived from L-band VV-polarization data acquired by UAVSAR. The inset shows the area in the white box, overlain with multispectral imagery collected simultaneously by drone from a boat. [From Holt et al., 2024]

3.3 Gaps - marine oil slicks and spills

There are several gaps in knowledge that remain, the most significant being the ability to differentiate mineral oil slicks from radar-dark look-alikes, e.g. low wind, biogenic oil, rain cells. In the context of disaster response, this includes differentiating spills from natural seeps, a potential problem in some areas. ML methods offer promise but are hampered by the lack of open-source training datasets that include false positives, including those classified by type. An issue is finding verified spills/slicks for those datasets. Another understudied topic is the value of multifrequency SAR for differentiating mineral oil from false positives.

There is a need to better identify the thicker oil within a slick, particularly those areas with oil thickness > 50 µm, the 'actionable' oil that is more easily removed from the surface [Holt et al., 2024]. Oil transport and weathering models should continue to be improved to forecast and hindcast evolution and to better estimate the release volume and the ecological impact from a spill.

With ever-increasing SAR data volumes, the operational spill monitoring agencies and services need to improve automation of SAR processing to identify slicks, specifically algorithms to identify potential slicks quickly

and with higher true positive and lower false positive rates. Computationally inexpensive methods of oil slick identification and classification that work for all the typically used SAR bands (X, C, S, L) are needed for this purpose and to support on-board and near-real-time monitoring from aircraft. As identified for maritime security, the methods must be reliable, repeatable, and cost-effective, and developed and tested in a variety of locations.

Studies with UAVSAR have shown the capability of rapid repeat imaging to support response in new ways, and the value of the data for improved oil transport forecasting, but the studies have been very limited in the types of slicks studies and the environmental conditions under which the data has been collected. The capabilities of the new SmallSat SARs for supporting oil spill response has been largely unstudied, although they potentially offer the most frequent image repeats of all the satellite SARs.

4. **OTHER APPLICATIONS**

4.1 Overview

The extended and routine observations from Sentinel-1 have benefitted areas of investigations focused on marine application topics, including topics that have relied more heavily on multispectral observations such as marine algae. A recent overview study provided an extensive listing of studies that have detected macroalgae, algae blooms, and other water organisms using optical imagery (Qi et al., 2020), as optical imagery has more well-known detection capabilities. In this section, we briefly look at marine algae and some of its many forms being observed by SAR, studies of which have shown a recent proliferation in publications, including macroalgae and other forms of algae that generate marine slicks. SAR has been used to detect algal blooms, notably in regional seas, which appear on SAR as dark surface slicks. One notable form of algae not included in the Qi et al. (2022) overview paper is coastal kelp (*Macrocystis*), which is attached to the bottom but is floating and spreads across the ocean surface. In this section, we will briefly review SAR studies of macroalgae, algal blooms and slicks, and kelp. Continuity in both SAR and fine resolution multispectral missions including Sentinel-2 are particularly beneficial for comparison and potentially for cross-validation of features of interest.

4.2 Marine Algae

4.2.1 Macroaglae

In recent years, there have been extensive blooms of floating macroalgae including species of *Ulva* and *Sargassum* in global seas, often related to warming and an increase in nutrients, leading to hazards in coastal conditions by massive incursions of biomass. A study by Qi et al. (2022) made use of extensive collections of Sentinel-2 data, with previously identified mapping capabilities for many forms of macroalgae, to examine the likewise extensive and coincident collections of Sentinel-1 imagery to determine the detection capabilities of SAR imagery, particularly as a means to increase the number of observations. Based on coincident observations and machine learning techniques, the study found that two species of macroalgae were detected clearly on SAR imagery, *Ulva prolifera* in the Yellow Sea and *Sargassum fuitans/natans* in the Caribbean Sea. The detected macroalgae was found to have enhanced radar backscatter compared to the surrounding seas under moderate wind speeds, with the enhanced returns attributed to various components of the dense macroalgae biomass appearing above the ocean surface, increasing sea surface roughness and reflecting radar returns. The macroalgae species that were not detected showed little difference in backscatter compared to the surrounding ocean rather than reduced backscatter as might be expected, due most likely to either reduced density and/or most of the algae remaining below the surface, although the SAR brightness relative to the surrounding water may depend upon the radar frequency and the instrument noise floor.

4.2.2 Algal blooms and slicks

Algal blooms have often been observed with SAR imagery in regional seas (Gade et al., 1998c; Lin et al., 2002: Shen et al., 2014), primarily being identified as marine slicks, where wind-driven short gravity waves are smoothed by the presence of a surface film composed of biogenic material released by the growth and decay of marine life (e.g. Alpers et al., 2017). Some exceptions have been identified where the blooms have also been detected by increased contrast compared to the surround ocean (Shen et al., 2014; Gade et al., 1998c). Biogenic films or slicks are ubiquitous in the global seas especially in the coastal regions (Wurl et al., 2011) and may impact air-sea CO2 exchange (Wurl et al., 2016). Marine slicks are associated with areas of productivity, likely increasing after bloom events but appearing to maintain a presence for longer periods of time well after bloom events. The slicks frequently also serve as surface tracers of underlying surface currents including submesoscale cyclonic slicks (e.g. Stuhlmacher and Gade, 2020).

4.2.3 Kelp

Kelp (*Macrocystis sp*) is present in the global temporal coastal zone and is a foundational species for rocky coastal ecosystems. Kelp has also been found to be subject to warming and pollution. Kelp has been observed extensively with optical sensors but only in a cursory way with SAR imagery. Recently Landsat and other optical imagery have been used to generate kelp products of extent and biomass (e.g. Bell et al., 2020) along the California coast. SAR studies of kelp are extremely limited, however. Jensen et al. (1980) compared both X-band and L-band images of kelp beds

off Santa Barbara CA, which appeared as bright targets in X-band but could not be distinguished from open water in L-band. A preliminary study is underway utilizing a unique collection of L- and S-band airborne SAR imagery along with near-coincident Sentinel-1 imagery (Jones et al., 2024). Initial results over the same kelp beds with a more sensitive SAR indicate that kelp has a bright signature at C-band, a signature at S-band that shows little-to-no difference compared to the surrounding sea, and a reduced, radar-dark signature at L-band. While not definitive, early results suggest that SAR may be useful in extending the observations of kelp in conjunction with cloud-free optical imagery.

4.3 Oil in Sea Ice

The need to identify oil spills in the Arctic, particularly in ice infested waters, has become a topic of some urgency in the past 20 years as sea ice has declined and shipping begins to expand in the Arctic [Vergeynst et al., 2018]. Both the overall extent of sea ice coverage has declined [Parkinson& DiGirolamo, 2021) and the amount of multi-year ice in the Arctic has declined [Howell et al., 2023]. Furthermore, the evolution of oil in sea ice and very cold water is more complicated than for oil in the typical ocean environments usually encountered in spills [see, e.g. Fingas & Hollebone, 2003; Afenyo et al., 2016]. It is doubtful that oil will remain on the surface of the ice in thicker ice and closed packs [Oggier et al., 2020], so it is likely to be more observable with SAR when mixing at the ice margin and in new ice, which is also radar-dark, or in open pack conditions [Dickens, 2011]. Also, few studies have modeled the transport of oil in the Arctic, although this is a topic of increasing interest [Nordam et al., 2019].

Whether and how best to use SAR to support spill in the Arctic has been the topic of study since 2014 [e.g., Brekke et al., 2014; Johansson et al., 2020], and in the last few years there have been several studies using C-band SAR in laboratory settings [e.g., Asihene et al., 2021; Zabihi Mayvan et al., 2024]. However, the full capabilities of SAR, particularly multi-frequency observations, remains unknown. Fortunately, there has not been a major spill in the Arctic to test SAR in the actual environment.

4.4 Gaps – Other applications

As discussed in Section 3.3, a remaining challenge is distinguishing low backscatter signatures, i.e. isolating low winds from marine oil spills from biogenic slicks and new/young ice using SAR imagery. In addition, there are improvements to be made in modeling of oil slick transport, and the study of oil transport in combination with sea ice is in its infancy.

Both satellite and airborne platforms carrying SARs have different instrument configurations and observational capabilities. Coupled with the vagaries of the ocean surface and conditions that may be present, it has been difficult to quantitatively and definitely determine the optimum methodology. Perhaps machine learning will enable these steps to be determined, but these new developments require sufficient validated training data to determine clear differentiation.

5. RECOMMENDATIONS

5.1 Recommendations - maritime security and navigation

The increasing number of constellations and the developments in sensor technology have led to greater availability of higher resolution SAR data, attracting an audience new to radar imagery applications. Stakeholders unfamiliar with radar remote sensing have been expressing their interest in remote sensing surveillance products to ESA. Although the basic use of fast revisit intensity images and InSAR data is becoming more standard, there are a variety of processing approaches that provide layers of information with significant added value over traditional SAR data.

Advanced signal processing techniques for imaging, motion estimation, and feature extraction from moving targets exploiting spatial, temporal, and polarimetric diversity for radar imaging systems shall be further developed and tested for surveillance and security applications, including for surveillance of slow-moving targets in portal areas. The industrialization of these academic studies has the potential to enhance the value of low-resolution and openly available EO data for addressing novel applications.

ML is proving useful for maritime security applications. To provide the large datasets required for training DL algorithms, AIS and similar vessel positioning data needs to become routinely available, at low or no cost, and offer world-wide coverage. More accurate and fine details regarding vessel classes need to accompany positioning data. Integrating AIS vessel class and positioning data with SAR products will facilitate the development of training datasets for DL algorithms. Sentinel-1C/D satellites will be outfitted with AIS receivers, but there is a need to also populate the Sentinel-1A/B archive with correlated AIS datasets, at least for locations with high maritime traffic.

The current reliable and extensive baseline of high revisit times offered by ESA, third-party, and other commercial SAR missions provides a credible foundation for the development of routine applications and services that integrate these techniques. Scalable cloud-based processing and platform-based environments ensure that the required complex processing and data integration can be performed within reasonable timeframes and with the required level of reliability. Therefore, ESA should continue to engage with industry partners, the research community, and maritime surveillance stakeholders to evaluate emerging methods of utilizing EO data in terms of attainable performance for wider use and adoption.

ESA-funded activities should continue to include the analysis and implementation of data fusion algorithms to better detect and track non-cooperative targets and identify anomalous actions.

Further work is needed on the detection of small targets of different composition and shape to support the detection of small vessels, Aids to Navigation, and debris detection. We recommend research and mission design and observation coordination between missions and space agencies for multifrequency studies and more frequent imaging. Given their high resolution, adaptive pointing, and rapid revisit potential, the capabilities of SmallSat SARs for contributing to this should be explored with a short-term goal of determining their value for these applications.

5.2 Recommendations - mineral oil slicks and spills

More accurate classification of SAR images for automated detection of mineral oil slicks is needed. There are three recommended avenue for advancement. The first is to explore the use of multi-frequency data for this purpose; the second to explore the use of short timescale repeat imaging with or without multi-frequency and/or multi-polarization data; and the third is development of more sophisticated ML algorithms, including those that incorporate relevant physical information about the wind and sea states and the instrument characteristics (noise floor, incidence angle).

Multi-frequency studies can be done with dual-frequency satellite SARs (of which NISAR is the only one in operation or soon to launch), joint observations from SARs of different frequency including commercial providers to increase frequency diversity, field campaigns with a multi-frequency airborne SAR or a combination of airborne and spaceborne SARs operating at different frequencies. Fusion of SAR and multispectral data should be considered.

Rapid repeat imaging with SAR deserves more study with SAR constellations that can provide repeat imaging on the time scale of hours. More frequent imaging could use any of the SAR constellations or a combination of instruments, possibly including the commercial SmallSat constellations if they are suitable. We recommend systematically evaluating the SmallSat constellations (e.g. Iceye, Cappela, Umbra Space) for this application in the near future. These small instruments generally have a higher noise floor than the SARs from the major space agencies, hence are less likely to be useful for applications involving radar-dark features.

A major limitation in the development of ML algorithms for spill detection is the scarcity of training data. A concerted effort needs to be made to develop a large and diverse training dataset including images containing the full range of false positive phenomena, classified, and providing this to the community through open-access. There also needs to be new DL models developed for sensors like NISAR and the SmallSat SAR constellations, e.g. X-band from Iceye, Cappela, and Umbra Space if their sensors have sufficiently high NESZ to be useful.

The necessary next step beyond detecting and tracking oil slicks to make SAR significantly more useful for emergency response is to identify the 'actionable' oil, slicks of thickness > 50 μm, to target collection and dispersion more accurately. SAR has shown promise for this, but more research is needed specifically with low noise SARs. Field campaigns are needed under different environmental conditions and with different amounts and types of oil. Higher power spaceborne SARs could supply the data, but this is not necessarily feasible. Data from instruments like UAVSAR have been useful, but those instruments were designed for a wide range of science, not specifically for oil spill response, and generally have InSAR capability, which is not needed for the ocean applications. Less expensive, single or dual polarization instruments could do the job, flying at lower altitude to improve SNR [Jones & Holt, 2018]. We recommend that ESA support development and test of these instruments, and campaigns using them. Ideally, this would lead to commercialization of the capabilities or operation by response agencies if research shows the value of the technology.

5.3 Recommendations - other applications

Recommendations for algae monitoring and detecting oil in sea ice are the same as those for mineral oil spills (Section 5.2). In addition, continued and frequent observations of the Arctic in all bands is needed, particularly with ALOS-2/4 because NISAR, the other L-band SAR that is near launch, will not image above 77.5°N.

5.4 Commonalities in Recommendations

Further study of SmallSat constellations is recommended for all applications, along with additional multi-frequency, multi-polarization, multi-viewing-angle observations. Coordination of observation plans, and in the future even coordination of missions, is recommended to decrease the time between imaging considering all assets.

Development of larger and more diverse datasets (in sites covered, environmental conditions, and instruments) for ML algorithm development is needed. Continued support for research is always needed. Support for field campaigns is requested, including to support oil slick characterization, particularly thickness, and validation of new algorithms.

Establishment of 'supersites' with in situ instruments or additional remote sensing observations and freely available products from ESA, NASA, JAXA, DLR, and, if possible ASI, ISRO, and other agencies operating SARs are needed to support algorithm development and

validation. Possible supersites should include areas with significant amounts of marine debris and severe and sustained oil pollution (i.e., the Niger Delta).

The attendees at SeaSAR 2023 identified a need for a curated public repository for resources, similar to the Ocean Virtual Portal, that archives the datasets necessary for the ocean applications identified here, and is funded and staffed at a level where it becomes a reliable resource for the community. This would allow searching, viewing, and downloading collocated SAR and optical data, along with ancillary datasets (wind, waves, currents), and any in-situ data made publicly available. Science traceability is required for the archive datasets. The archived datasets should have standardized metadata and associated documentation on their sources, processing, and how the information was derived. DOIs must be assigned so that they can be cited in literature. An open-access site is also needed for sharing open-source code, maintaining released, vetted versions, documenting the full providence of the code, and including example output. There is also a need for assets facilitating cloud processing, preferably at low or no cost to those with a true need for the information, but without resources to cover the costs otherwise.

6. SUMMARY

As SAR data has become more accessible to researchers and operational users in the last decade, its value for ocean applications has become clear. SAR is now a vital source of information for monitoring the coastal oceans, particularly for oil spill detection and identifying and tracking vessels. Major advances in understanding how SAR can be used to detect, track, and characterize slicks have come about because of observations with low noise SAR instruments operating at frequencies from X-band to L-band. Remote sensing information is playing a crucial role in enhancing maritime situational awareness, addressing detection of illegal trafficking at sea and illegal fishing, but also hybrid threats - including monitoring integrity and operations of surface/sub-surface critical infrastructures and assessing the depletion of natural resources. Including vessel class and position data with SAR products will enable development of training data sets for DL algorithms.

Decreasing the temporal baseline between imaging, considering the full constellation of SARs, is very important for ocean observations. Besides providing support for research, the space agencies can support advancement by coordination of their observation plans, and even in the future of their missions to the extent possible given individual objectives. This will enable the community to obtain multi-frequency and multi-look-direction observations with shorter imaging interval.

The availability of free and low-cost SAR data, development of new processing techniques, and deep learning methods applied to object identification in SAR imagery supports continued advancement for both maritime navigation and oil spill surveillance. Other identified high priority actions are supporting the development of training datasets for ML and establishing and maintaining an archive for ocean application datasets.

ACKNOWLEDGEMENT

This research was carried out in part at the Jet Propulsion Laboratory, California Institute of Technology, under contract with the U.S. National Aeronautics and Space Administration.

REFERENCES

Afenyo, M., Veitch, B., & Khan, F. (2016). A state-of-the-art review of fate and transport of oil spills in open and ice-covered water. Ocean Engineering, 119, 233-248.

Alpers, W., Holt, B., & Zeng, K. (2017). Oil spill detection by imaging radars: Challenges and pitfalls, Remote Sensing of Environment, 201, 133-147.

Amri, E., Dardouillet, P., Benoit, A., Courteille, H., Bolon, P., Dubucq, D., & Credoz, A. (2022). Offshore oil slick detection: From photo-interpreter to explainable multi-modal deep learning models using SAR images and contextual data. Remote Sensing, 14(15), 3565.

Angelliaume, S., Ceamanos, X., Viallefont-Robinet, F., Baqué, R., Déliot, P., & Miegebielle, V. (2017, October). Radar and optical remote sensing in offshore domain to detect, characterize, and quantify ocean surface oil slicks. In Remote Sensing of the Ocean, Sea Ice, Coastal Waters, and Large Water Regions 2017 (Vol. 10422, pp. 17-23). SPIE.

Angelliaume, S., Dubois-Fernandez, P. C., Jones, C. E., Holt, B., Minchew, B., Amri, E., & Miegebielle, V. (2018). SAR imagery for detecting sea surface slicks: Performance assessment of polarization-dependent parameters. IEEE Transactions on Geoscience and Remote Sensing, 56(8), 4237-4257.

Asihene, E., Desmond, D. S., Harasyn, M. L., Landry, D., Veenaas, C., Mansoori, A., ... & Isleifson, D. (2021). Toward the detection of oil spills in newly formed sea ice using c-band multipolarization radar. IEEE Transactions on Geoscience and Remote Sensing, 60, 1-15.

Bell, T. W., Allen, J. G., Cavanaugh, K. C., & Siegel, D. A. (2020). Three decades of variability in California's giant kelp forests from the Landsat satellites. Remote Sensing of Environment, 238, 110811.

Bianchi, F. M., Espeseth, M. M., & Borch, N. (2020). Large-scale detection and categorization of oil spills from SAR images with deep learning. Remote Sensing, 12(14), 2260.

Brekke, C., & Solberg, A. H. (2005). Oil spill detection

by satellite remote sensing. Remote Sensing of Environment, 95(1), 1-13.

Brekke, C., Holt, B., Jones, C., & Skrunes, S. (2014). Discrimination of oil spills from newly formed sea ice by synthetic aperture radar. Remote Sensing of Environment, 145, 1-14.

Cao, Y., Xu, L., & Clausi, D. (2017). Exploring the potential of active learning for automatic identification of marine oil spills using 10-year (2004–2013) RADARSAT data. Remote Sensing, 9(10), 1041.

Chen, V. (2019). The Micro-Doppler Effect in Radar, 2nd ed.; Artech House Radar Library; Artech House: Norwood, MA, USA.

De Laurentiis, L., Jones, C. E., Holt, B., Schiavon, G., & Del Frate, F. (2020). Deep learning for mineral and biogenic oil slick classification with airborne synthetic aperture radar data. IEEE Transactions on Geoscience and Remote Sensing, 59(10), 8455-8469.

Del Prete, R., Graziano, M. D., & Renga, A. (2024). AI-based route reconstruction on multifrequency multitemporal SAR images. Abstracts, this volume.

Dickins, D. (2011, February). Behavior of oil spills in ice and implications for Arctic spill response. In OTC Arctic Technology Conference (pp. OTC-22126). OTC.

Espeseth, M. M., Skrunes, S., Jones, C. E., Brekke, C., Holt, B., & Doulgeris, A. P. (2017). Analysis of evolving oil spills in full-polarimetric and hybrid-polarity SAR. IEEE Transactions on Geoscience and Remote Sensing, 55(7), 4190-4210.

Espeseth, M. M., Brekke, C., Jones, C. E., Holt, B., & Freeman, A. (2020a). The impact of system noise in polarimetric SAR imagery on oil spill observations. IEEE Transactions on Geoscience and Remote Sensing, 58(6), 4194-4214.

Espeseth, M. M., Jones, C. E., Holt, B., Brekke, C., & Skrunes, S. (2020b). Oil-spill-response-oriented information products derived from a rapid-repeat time series of SAR images. IEEE Journal of Selected Topics in Applied Earth Observations and Remote Sensing, 13, 3448-3461.

Ferraro, G., Tarchi, D., Fortuny, J., & Sieber, A. (2006). Satellite monitoring of accidental and deliberate marine pollution. In: Gade, M., Hühnerfuss, H., Korenowski, G.M. (eds), Marine Surface Films: Chemical Characteristics, Influence on Air-Sea Interactions and Remote Sensing. Springer, Heidelberg, 273-288.

Ferraro, G., Bulgarelli, B., Meyer-Roux, S., Muellenhoff, O., Tarchi, D. & Topouzelis, K. (2008). The use of satellite imagery from archives to monitor oil spills in the Mediterranean Sea. In: Barale, V., & Gade, M. (eds), Remote Sensing of the European Seas. Springer, Dordrecht, 371-382.

Fingas, M., & Brown, C. (2014). Review of oil spill remote sensing. Marine Pollution Bulletin, 83(1), 9-23.

Fingas, M. F., & Hollebone, B. P. (2003). Review of behaviour of oil in freezing environments. Marine pollution bulletin, 47(9-12), 333-340.

Gade, M., Alpers, W., Hühnerfuss, H., Wismann, V. R., & Lange, P. A. (1998a). On the reduction of the radar backscatter by oceanic surface films: Scatterometer measurements and their theoretical interpretation. Remote Sensing of Environment, 66(1), 52-70.

Gade, M., Alpers, W., Hühnerfuss, H., Masuko, H., & Kobayashi, T. (1998b). The imaging of biogenic and anthropogenic surface films by a multi-frequency multi-polarization synthetic aperture radar measured during the SIR-C/X-SAR missions, Journal of Geophysical Research: Oceans, 103, 18851-18866.

Gade, M., Rud, O., Ishii, M. (1998c). Monitoring algae blooms in the Baltic Sea by using spaceborne optical and microwave sensors. In: IGARSS '98. Sensing and Managing the Environment. 1998 IEEE International Geoscience and Remote Sensing. Symposium Proceedings. (Cat. No.98CH36174), 6–10. https://doi.org/10.1109/ IGARSS.1998.699573.

Garcia-Pineda, O., MacDonald, I. R., Li, X., Jackson, C. R., & Pichel, W. G. (2013). Oil spill mapping and measurement in the Gulf of Mexico with textural classifier neural network algorithm (TCNNA). IEEE Journal of Selected Topics in Applied Earth Observations and Remote Sensing, 6(6), 2517-2525.

Garcia-Pineda, O., Staples, G., Jones, C. E., Hu, C., Holt, B., Kourafalou, V., ... & Haces-Garcia, F. (2020). Classification of oil spill by thicknesses using multiple remote sensors. Remote Sensing of Environment, 236, 111421.

Gu, C., & Chang, W. (2016, May). An efficient geometric distortion correction method for SAR video formation. In 2016 5th International Conference on Modern Circuits and Systems Technologies (MOCAST) (pp. 1-4). IEEE.

Holt, B. Jones, C. E., Monaldo, F., Garcia, O. (2024). Try, try again: recent steps towards an operational SAR-based algorithm for oil spill thickness measurements. Abstracts, this volume.

Howell, S. E., Babb, D. G., Landy, J. C., & Brady, M. (2023). Multi-year sea ice conditions in the Northwest Passage: 1968–2020. Atmosphere-Ocean, 61(4), 202-216.

Huang, X., Zhang, B., Perrie, W., Lu, Y., & Wang, C. (2022). A novel deep learning method for marine oil spill detection from satellite synthetic aperture radar imagery. Marine Pollution Bulletin, 179, 113666.

Jaruwatanadilok, S., Duan, X., Holt, B., & Jones, C. E. (2023). A study of the sensitivity of SAR ocean backscatter to oil slick properties using an electromagnetic scattering model. IEEE Transactions on Geoscience and Remote Sensing, 61, 2004516.

Jensen, J. R., Estes, J. E., & Tinney, L. (1980). Remote sensing techniques for kelp surveys. Photogrammetric Engineering and Remote Sensing, 46(6), 743-755.

Johansson, A. M., Espeseth, M. M., Brekke, C., & Holt, B. (2020). Can mineral oil slicks be distinguished from

newly formed sea ice using synthetic aperture radar?. IEEE Journal of Selected Topics in Applied Earth Observations and Remote Sensing, 13, 4996-5010.

Jones, C. E., Dagestad, K. F., Breivik, Ø., Holt, B., Röhrs, J., Christensen, K. H., ... & Skrunes, S. (2016). Measurement and modeling of oil slick transport. Journal of Geophysical Research: Oceans, 121(10), 7759-7775.

Jones, C. E., & Holt, B. (2018). Experimental L-band airborne SAR for oil spill response at sea and in coastal waters. Sensors, 18(2), 641.

Jones, C. E. (2023). An automated algorithm for calculating the ocean contrast in support of oil spill response. Marine Pollution Bulletin, 191, 114952.

Jones, C. E., Johansson, M., Holt, B. (2024). Automation of slick detection and classification for improved monitoring with SAR. Abstracts, this volume.

Jones, C. E., An, K., & Holt, B. (2024). The value of multi-frequency SAR for monitoring giant kelp, manuscript in preparation.

Kaczor, S., McGourty, S., Capsey, A. (2024). A feasibility study into the use of high-resolution synthetic aperture radar as a novel way of identifying aids to navigation. Abstracts, this volume.

Keramea, P., Spanoudaki, K., Zodiatis, G., Gikas, G., & Sylaios, G. (2021). Oil spill modeling: A critical review on current trends, perspectives, and challenges. Journal of Marine Science and Engineering, 9(2), 181.

Lanz, P., Marino, A., Simpson, M. Brinkhoff, T., Köster, F., & Möller, M. (2024). Developing refugee vessel detection capabilities with polarimetric SAR, Abstracts, this volume.

Latini, D., Del Frate, F., Jones, C. E. (2016). Multi-frequency and polarimetric quantitative analysis of the Gulf of Mexico oil spill event comparing different SAR systems. Remote Sensing of Environment, 183, 26-42.

Lehr, W. J. (2021). A brief survey of oil spill weathering models. In eds. Oleg Makarynskyy, Marine Hydrocarbon Spill Assessments, 27-57, Elsevier.

Lin, I.I., Wen, L.S., Liu, K.K., Tsai, W.T., & Liu, A.K., (2002). Evidence and quantification of the correlation between radar backscatter and ocean colour supported by simultaneously acquired in situ sea truth. *Geophys. Res. Lett*. 29 (10), 102-1-102-4.

Liu, B., Zhang, X., Tang, K., Liu, M., & Liu, L. (2016, July). Spaceborne Video-SAR moving target surveillance system. In 2016 IEEE International Geoscience and Remote Sensing Symposium (IGARSS) (pp. 2348-2351). IEEE.

Minchew, B. (2012). Determining the mixing of oil and sea water using polarimetric synthetic aperture radar. Geophysical Research Letters, 39(16).

Minchew, B., Jones, C. E., & Holt, B. (2012). Polarimetric analysis of backscatter from the Deepwater Horizon oil spill using L-band synthetic aperture radar. IEEE Transactions on Geoscience and Remote Sensing, 50(10), 3812-3830.

Mohr, V., & Gade, M. (2022). Marine oil pollution in an area of high economic use: Statistical analyses of SAR data from the Western Java Sea. Remote Sensing, 14(4), 880.

Morando, E., Corvino, M., Campbell, G. (2023). New Earth Observation and AI based capabilities for maritime situational awareness. Euro-Atlantic Resilience Journal*,* 1/2023, 93-102.

Nordam, T., Beegle-Krause, C. J., Skancke, J., Nepstad, R., & Reed, M. (2019). Improving oil spill trajectory modelling in the Arctic. Marine pollution bulletin, 140, 65-74.

Oggier, M., Eicken, H., Wilkinson, J., Petrich, C., & O'Sadnick, M. (2020). Crude oil migration in sea-ice: laboratory studies of constraints on oil mobilization and seasonal evolution. Cold Regions Science and Technology, 174, 102924.

Palm, S., Wahlen, A., Stanko, S., Pohl, N., Wellig, P., & Stilla, U. (2014, June). Real-time onboard processing and ground-based monitoring of FMCW-SAR videos. In EUSAR 2014; 10th European Conference on Synthetic Aperture Radar (pp. 1-4). VDE.

Parkinson, C. L., & DiGirolamo, N. E. (2021). Sea ice extents continue to set new records: Arctic, Antarctic, and global results. Remote Sensing of Environment, 267, 112753.

Qi., L., Hu, C., Mikelsons, K., ... & Van der Zande, D. (2020). In search of floating algae and other organisms in global oceans and lakes, Remote Sensing of the Environment. 239, 111659.

Qi, L., Wang, M., Hu, C., and Holt, B. (2022). On the capacity of Sentinel-1 synthetic aperture radar in detecting floating macroalgae and other floating matters. Remote Sensing of Environment, 280, 113188.

Quigley, C., Johansson, A. M., Jones, C. E., Holt, B. (2024). Distinguishing mineral oil slicks from low wind areas using rapid repeat synthetic aperture radar imagery, IEEE Journal of Selected Topics in Applied Earth Observations and Remote Sensing, 17, 7323-7342.

Röhrs, J., Dagestad, K. F., Asbjørnsen, H., Nordam, T., Skancke, J., Jones, C. E., & Brekke, C. (2018). The effect of vertical mixing on the horizontal drift of oil spills. Ocean Science, 14(6), 1581-1601.

Shaban, M., Salim, R., Abu Khalifeh, H., Khelifi, A., Shalaby, A., El-Mashad, S., ... & El-Baz, A. (2021). A deep-learning framework for the detection of oil spills from SAR data. Sensors, 21(7), 2351.

Shen, H., Perrie, W., Liu, Q., and He, Y. (2014). Detection of macroalgae blooms by complex SAR imagery. Marine Pollution Bulletin. 78, 190-195.

Skrunes, S., Brekke, C., & Eltoft, T. (2013). Characterization of marine surface slicks by Radarsat-2 multipolarization features. IEEE Transactions on Geoscience and Remote Sensing, 52(9), 5302-5319.

Stuhlmacher, A., & Gade, M. (2020). Statistical analyses of eddies in the western Mediterranean Sea based on

synthetic aperture radar imagery, Remote Sensing of Environment. 250, 112023.

Vergeynst, L., Wegeberg, S., Aamand, J., Lassen, P., Gosewinkel, U., Fritt-Rasmussen, J., ... & Mosbech, A. (2018). Biodegradation of marine oil spills in the Arctic with a Greenland perspective. Science of the Total Environment, 626, 1243-1258.

Wismann, V., Gade, M. Alpers, W. & Hühnerfuss, H. (1998). Radar signatures of marine mineral oil spills measured by an airborne multi-frequency multi-polarization microwave scatterometer, International Journal of Remote Sensing, 19, 3607-3623.

Wurl, O., Wurl, E., Miller, L., Johnson, K., Vagle, & S. (2011). Formation and global distribution of sea-surface microlayers. Biogeosciences, 8, 121–135.

Wurl, O., Stolle, Ch., Thuoc, Ch.V., Thu, Ph., & Mari, X. (2016). Biofilm-like properties of the sea surface and predicted effects on air–sea CO2 exchange. Progress in Oceanography. 144, 15–24.

Yamaoka, T., Suwa, K., Hara, T., & Nakano, Y. (2016, July). Radar video generated from synthetic aperture radar image. In 2016 IEEE International Geoscience and Remote Sensing Symposium (IGARSS) (pp. 6509-6512). IEEE.

Yang, Y.-J., Suman, S., Goldman, R. (2024). Integration of a deep learning-based oil spill detection system into an early warning system for the southeastern Mediterranean Sea. Abstracts, this volume.

Zabihi Mayvan, M., Asihene, E., Desmond, D., Hicks, L., Polcwiartek, K., Stern, G. A., & Isleifson, D. (2024). Monitoring diesel spills in freezing seawater under windy conditions using C-band polarimetric radar. Remote Sensing, 16(2), 379.

List of Participants

Name			Organization	Country
Mr	Ali	Muhammad	Università degli Studi di Napoli "Parthenope", Napoli, Italy	Italy
Prof	Alpers	Werner R.	University of Hamburg	Germany
Mr	Amir	Haris	Sant'Anna Institute of Advanced Studies	Italy
Dr	Aouf	Lotfi	Meteo France	France
Dr	Arthurs	David	Polar View	Canada
Mr	Bou-laouz	Moujahid	IMT Atlantique	France
Dr	Chapron	Bertrand	ifremer	France
Dr	Collard	Fabrice	Oceandatalab	France
Ms	Corvino	Michela	ESA	Italy
Dr.	da Silva	Jose	University of Porto	Portugal
Mr	Del Prete	Roberto	University Of Naples Federico II	Italy
Dr	Demchev	Denis	Chalmers University of Technology	Sweden
Dr	Dimitriadou	Krystallia	Technical University of Denmark	Denmark
Dr	Domps	Baptiste	Degreane Horizon	France
Dr	Donlon	Craig	European Space Agency	Netherlands
Ms	Downy	Catherine	NERSC	Norway
Dr	Dubois	Pierre	CLS	France
Dr	Egido	Alejandro	European Space Agency	Netherlands
Mr	Eltoft	Torbjørn	UiT the Arctic University of Norway	Norway
Mr	Elyouncha	Anis	Chalmers University of Technology	Sweden
Dr	Foster	Ralph	APL/University of Washington	USA
Dr	Frost	Anja	DLR (German Aerospace Center)	Germany
Dr	Gade	Martin	Universität Hamburg	Germany
Mr	Garcia-Mondéjar	Albert	isardSAT	Spain
Prof	Gommenginger	Christine	National Oceanography Centre	UK
Dr	Graber	Hans Christian	CSTARS - University of Miami	USA
Mr	Guitton	Gilles	OceanDataLab	France
Dr	Hajduch	Guillaume S.A.	CLS	France
Dr	Hindberg	Heidi	NORCE	Norway
Ms	Hoffman	Lauren Alexandra	Scripps Institution of Oceanography	USA
Mr	Holt	Benjamin	Jet Propulsion Laboratory	USA
Dr	Husson	Romain	CLS	France
Mr	Ideström	Petter Fritiof	UNIS	Norway
Dr	Jawak	Shridhar	Svalbard Integrated Arctic Earth Observing System (SIOS)	Norway
Mr	Jiayu	Fu	Beijing institute of technology	China
Prof	Johannessen	Johnny A.	NERSC	Norway

Dr	Johansson	Malin	UiT The Arctic University of Norway	Norway
Prof	Johnsen	Harald	NORCE - Norwegian Research Center	Norway
Dr	Jones	Cathleen E	Jet Propulsion Laboratory	USA
Mr	Kaczor	Scott	UK Hydrographic Office	UK
Dr	Karvonen	Juha	Finnish Meteorological Institute	Finland
Dr	Kim	Ekaterina	Norwegian University of Science and Technology	Norway
Dr	Kleinherenbrink	Marcel	TU Delft	Netherlands
Dr	Korosov	Anton	Nansen Environmental and Remote Sensing Center	Norway
Ms	Kreiner	Matilde Brandt	Danish Meteorological Institute	Denmark
Mr	Lanz	Peter	Carl von Ossietzky Univ. of Oldenburg | Jade Univ. of Applied Sciences Oldenburg	Germany
Dr	Larsen	Yngvar	NORCE	Norway
Dr	Lauknes	Tom Rune	NORCE Norwegian Research Centre	Norway
Prof	Li	Xiao-Ming	Aerospace Information Research Institute, Chinese Academy of Sciences	China
Ms	Lodadio	Sabrina	Serco Spa c/o ESA	Italy
Dr	Lohse	Johannes	UiT The Arctic University of Norway	Norway
Dr	Longepe	Nicolas	ESA	Italy
Dr	Lopez Dekker	Paco	TU Delft	Netherlands
Dr	Martin	Adrien	National Oceanography Centre	UK
Ms	McGourty	Sara	United Kingdom Hydrographic Office	UK
Prof	Moen	Jøran	UNIS	Norway
Dr	Moiseev	Artem	The Nansen center	Norway
Ms	Morando	Elena	Technische Universiät Berlin	Germany
Dr	Nouguier	Frederic	Ifremer	France
Dr	Ocampo-Torres	Francisco J	CEMIE-Océano	Mexico
Mr	Pera	Fabrizio	Serco Spa c/o ESA	Italy
Dr	Perrie	Will	DFO, Bedford Institute of Oceanography	Canada
Mr	Pettersson	Lasse H.	Nansen Environmental and Remote Sesning Center (NERSC)	Norway
Dr	Pinheiro	Muriel Aline	ESA	Italy
Dr	Portabella	Marcos	Institute of Marine Sciences (ICM-CSIC)	Spain
Mr	Pouplin	Clément	Ifremer	France
Ms	Richter	Dominik	DLR	Germany
Dr	Rikka	Sander	Tallinn University of Technology	Estonia
Dr	Rinne	Eero	UNIS	Svalbard and Jan Mayen
Dr	Romeiser	Roland	University of Miami	USA
Dr	Shamshiri	Roghayeh	NTNU	Norway

Dr	Shuchman	Robert Allan	Michigan Technological University, USA	USA
Ms	Staffansdotter	Anna Gölin	UNIS	Svalbard and Jan Mayen
Dr	Stoffelen	Ad	Royal Netherlands Meteorological Institute (KNMI)	Netherlands
Dr	Stopa	Justin	University of Hawai`i at Manoa	United States
Mr	Suess	Martin	ESA/ESTEC	Netherlands
Ms	Taelman	Catherine	UiT The Arctic University of Norway	Norway
Dr	Taillade	Thibault	ESA	Italy
Mr	Tings	Björn	DLR	Germany
Prof	Vandemark	Douglas	UNH	USA
Ms	von Goedeke	Lena	Satellite Institute Svalbard	Norway
Mr	Wang	Qiang	The Arctic University of Norway	Norway
Mr	Watkins	Ray Howard	Michigan Tech University	United States
Dr	Wiehle	Stefan	German Aerospace Center (DLR)	Germany
Mr	Wulf	Tore	Danish Meteorological Institute (DMI)	Denmark
Ms	Yang	Yi-Jie	Deutsches Zentrum für Luft- und Raumfahrt e.V.	Germany
Ms	Yang	Yanli	Nanjing University of Information Science and & Technology	China
Dr	Yitayew	Temesgen Gebrie	Norce	Norway
Dr	Zecchetto	Stefano	National research council of Italy	Italy

= online participant only